1.0

1.1

1.25

4.5
50

2.8

3.2

3.6

4.0

2.5

2.2

2.0

1.8

1.4

1.6

MICROCOPY RESOLUTION TEST CHART

NATIONAL BUREAU OF STANDARDS 1963 A

NR80H-76

⑫

ADA111527

PROGRESS TOWARDS A THEORY

OF JET FLAP THRUST RECOVERY

P.M. Bevilaqua, P.E. Cole, E.F. Schum

Rockwell International
North American Aircraft Operations
Columbus, Ohio 43216

DTIC
ELECTE
MAR 0 2 1982

E

Contract F49620-78-C-0069
30 September, 1980

FINAL REPORT FOR PERIOD MAY 1978 – SEPTEMBER 1980

DTIC FILE COPY

82

REPORT DOCUMENTATION PAGE		READ INSTRUCTIONS BEFORE COMPLETING FORM
1. REPORT NUMBER A	2. GOVT ACCESSION NO.	3. RECIPIENT'S CATALOG NUMBER
4. TITLE (and Subtitle) Progress Towards a Theory of Jet Flap Thrust Recovery		5. TYPE OF REPORT & PERIOD COVERED Final Report May 1978 - September 1980
		6. PERFORMING ORG. REPORT NUMBER NR80H-76
7. AUTHOR(s) P. M. Bevilaqua, P. E. Cole & E. F. Schum		8. CONTRACT OR GRANT NUMBER(s) F49620-78-C-0069
9. PERFORMING ORGANIZATION NAME AND ADDRESS Rockwell International Corporation North American Aircraft Operations Columbus, Ohio 43216		10. PROGRAM ELEMENT, PROJECT, TASK AREA & WORK UNIT NUMBERS 61102F
11. CONTROLLING OFFICE NAME AND ADDRESS Air Force Office of Scientific Research Bolling Air Force Base		12. REPORT DATE 30 September 1980
		13. NUMBER OF PAGES
14. MONITORING AGENCY NAME & ADDRESS(if different from Controlling Office)		15. SECURITY CLASS. (of this report) Unclassified
		15a. DECLASSIFICATION/DOWNGRADING SCHEDULE

16. DISTRIBUTION STATEMENT (of this Report)

17. DISTRIBUTION STATEMENT (of the abstract entered in Block 20, if different from Report)

18. SUPPLEMENTARY NOTES

19. KEY WORDS (Continue on reverse side if necessary and identify by block number)

Jet Flap   V/STOL Aerodynamics
Thrust Recovery   Powered Lift

20. ABSTRACT (Continue on reverse side if necessary and identify by block number)

A combination of analysis and testing has been utilized to develop a theory of jet flap thrust recovery at the low speeds and large deflection angles characteristic of V/STOL lift systems. The contribution of jet drag to the reduction in recovery has been computed with a viscid/inviscid interaction analysis. The results of this computation are compared to wake survey and airfoil surface pressure measurements made with a two-dimensional jet flapped airfoil model. The thrust recovery is nearly complete for small values of the jet deflection angle, but for larger angles, the recovery decreases as

the thrust coefficient increases. It is concluded that the loss of recovery is due to the jet drag for values of the thrust coefficient less than unity; for larger values, the loss is increased by flow separation from the airfoil.

ACKNOWLEDGEMENTS

Accession For

A

iii

TABLE OF CONTENTS

LIST OF FIGURES

LIST OF FIGURES

LIST OF TABLES

I. INTRODUCTION

A jet sheet directed downwards from the trailing edge of a wing, as
shown in Figure 1, significantly increases the wing lift, especially at
low speeds. Lift is generated both as a direct reaction to the jet
impulse and as a result of changes in the wing surface pressure distribu-
tion induced by deflection of the main stream. This phenomenon is called
the jet flap effect by analogy to the action of a mechanical flap. It
makes some contribution to the forces induced by all powered lift systems.

In addition to generating a total lift on the wing greater than the
vertical component of the jet impulse, the jet flap also induces a
thrust greater than the horizontal component of the jet impulse. This
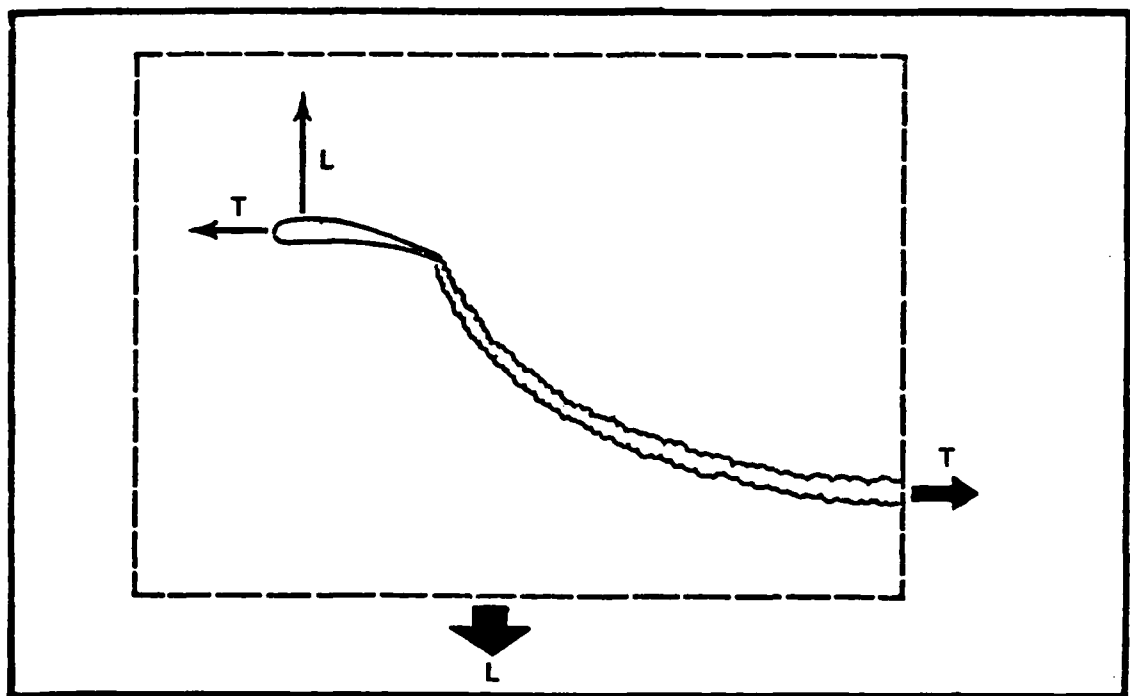was discovered during testing of jet flapped airfoils at the British

Figure 1. Jet Flap Thrust Recovery Hypothesis

1

National Gas Turbine Establishment. As a result of this discovery, Stratford (ref 1) suggested the hypothesis that, in ideal flow, the total jet thrust is always recovered as a horizontal force, regardless of the initial deflection angle, because the jet is ultimately turned in the direction of the free stream. He did not attempt a formal proof of this hypothesis, but reasoned from first principles that the force on the airfoil must be equal but opposite to the momentum of the deflected jet.

This thrust recovery hypothesis was received with considerable skepticism, but the existence of the phenomenon was established by tests performed at Stanford University, when Foley (ref 2) measured almost complete thrust recovery for jet deflection angles, θ, up to 60°. However, Stratford (ref 3) and Williams, et al (ref 4) measured only partial recovery at all deflection angles, with large decreases in recovery as the jet deflection angle increased to 90°. In subsequent tests with Foley's model, Tsongas (ref 5) also found a decrease in recovery when the deflection angle was increased beyond 60°, although Hynes (ref 6) found that the flow separated from the tunnel wall in this case.

The loss in thrust recovery has been attributed to various three-dimensional and real fluid effects: Maskell and Spence (ref 7) pointed out that deflection of the jet wake by the downwash behind a finite wing would reduce the recovery, even in ideal flow. Stratford (ref 3) and Wygnanski (ref 8) reasoned that the thrust recovery is decreased in real fluids by the jet entrainment, which induces a form drag on the airfoil; they suggested that the entrainment and, therefore, the jet drag increases with the jet deflection angle. More recently, Wilson (ref 9) used an empirical entrainment function to compute the jet drag and show that it is on the order of the observed loss in recovery. On the other hand, Williams, et al (ref 4) argued that flow separation on the airfoil would also cause a loss of thrust, while Tsongas (ref 5) suggested that separation of the main stream from the jet flap was the loss mechanism. Thus, while there is clear evidence of a thrust recovery phenomenon, the real fluid effects which reduce the recovery are incompletely understood.

Various analytic methods have been developed to predict the increments of aerodynamic lift and pitching moment induced by the jet flap. These methods are based on Spence's (ref 10) now classical jet flap theory, in which the inertia of the jet sheet is related to the strength of an equivalent vortex sheet. The original theory has been extended to include, for example, three dimensional effects (Maskell and Spence, ref 7), ground effects, (Lissaman, ref 11), and jet oscillations (Simmons and Platzer, ref 12). In addition, the theory has been applied to over-wing-blowing (Lan, ref 13) and ejector wing (Wilson, ref 9) configurations.

Although good predictions of the lift and moment have been obtained, none of these methods predict the loss of thrust recovery. In current practice, complete recovery is assumed for calculating lift, while an empirical function derived from the Stanford data is used to specify a reduction in the thrust recovery. Entrainment functions have been useful for estimating the magnitude of the thrust loss, but such functions treat just half of the jet/airfoil interaction, the jet drag induced on the airfoil; the other half of the interaction, the equal but opposite reduction of the jet thrust, is neglected. Since the reduction in thrust affects the computed position of the jet, which in turn affects the computed force on the airfoil, a method for predicting the effect of the jet flap should include this interaction.

The jet flap methods are further limited by linearizing assumptions to low values of the jet thrust coefficient and small airfoil and jet deflection angles. Thus, they cannot be used to predict the takeoff or landing performance of V/STOL aircraft for which current interest in the jet flap effect is greatest. Addessio and Skiftad (ref 14) recently addressed some of these low speed effects, but made the usual assumption of complete thrust recovery.

Such semi-empirical methods are only useful for small variations from the original data base. An essentially complete range of jet deflection

3

angles has been tested, but all of the data are for jet thrust co-
effocients less than unity. Since the thrust coefficient is much
greater than unity for most of the V/STOL flight regime, there are no
data for either the force on the airfoil or the trajectory of the jet
sheet in this case.

The purpose of this report is to describe progress in developing a
theory of jet flap thrust recovery at the low speeds and large deflec-
tion angles characteristic of V/STOL lift systems. A combination of
analysis and testing has been utilized to develop this theory. A viscid/
inviscid interaction analysis of the jet flap has been devised to
compute the contribution of the jet drag to the reduction in thrust
recovery. In addition, wake survey and airfoil surface pressure measure-
ments have been made for a two-dimensional, jet flapped airfoil over a
range of jet thrust coefficients. In the next section of this report,
the mechanism of thrust recovery and the way in which entrainment and
separation reduce the recovery are discussed. The jet drag analysis is
then presented in the following section. The experimental apparatus and
test procedure are described in the section after that. In the last
section, the analytical results are compared to the measured thrust
recovery. It is concluded that the thrust recovery is nearly complete
for small values of the jet deflection angle; but for larger angles,
the recovery decreases as the thrust coefficient increases. For values
of the thrust coefficient on the order of unity, the thrust loss is due
to jet drag; for larger values, the loss is increased by flow separation
from the airfoil.

II. JET FLAP THEORY

MECHANISM OF THRUST RECOVERY

The thrust recovery is generated by equal but opposite pressure
forces induced on the airfoil and jet sheet. According to Spence's
(ref 10) theory, the inertial forces which resist deflection of the jet
sheet are balanced by a pressure difference in the external flow along
the upper and lower boundaries of the jet. This pressure difference
can be related to the strength of an equivalent vortex sheet located
along the jet axis. Then, in mathematical terms, the vorticity in a
section of the jet sheet induces an upwash velocity of magnitude,
$\Gamma_j/2\pi r$, on a vortex segment bound in the wing, as shown in Figure 2.
An upstream force, $\rho\Gamma_w(\Gamma_j/2\pi r)$, is therefore induced on the wing.
Similarly, the wing vortex induces a downwash, $\Gamma_w/2\pi r$ on the jet vortex
which then experiences an equal force $\rho\Gamma_j(\Gamma_w/2\pi r)$ directed downstream.
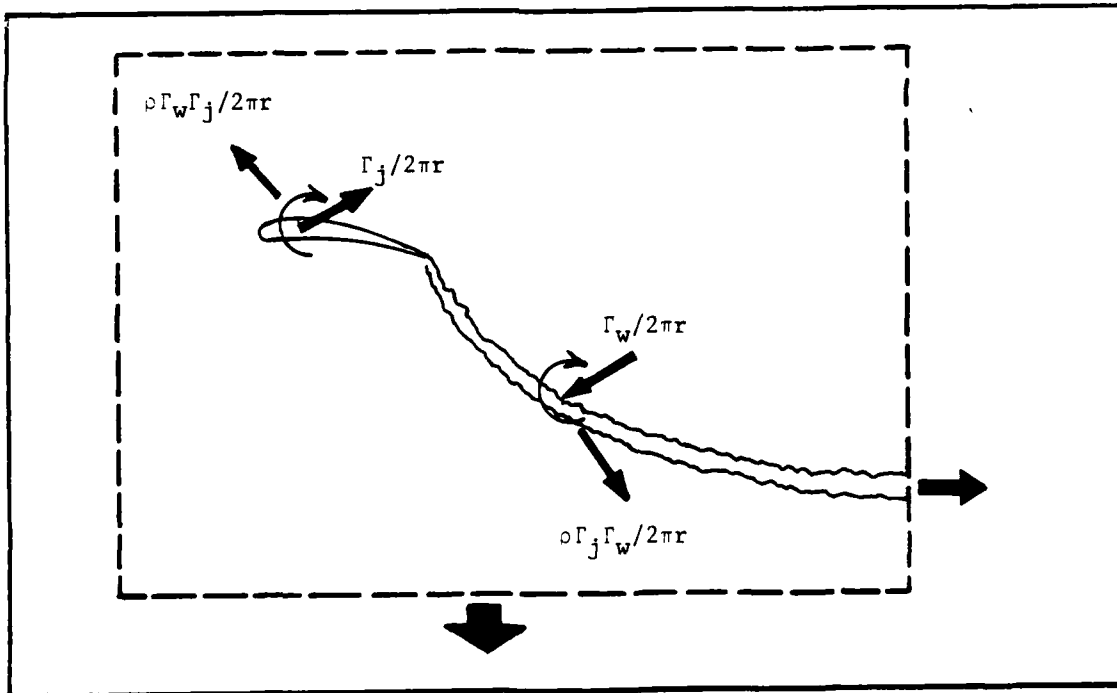
Figure 2. Mutually Induced Forces on a Vortex Pair

It is the integrated effect of all such vortex pairs which results in the apparent "thrust recovery." Figure 3 is a sketch of the forces on the airfoil, jet, and a surrounding control volume. As seen in the figure, the jet is not actually deflected, as by a vane. Rather, the interaction between the airfoil and jet induces a horizontal force, $\rho w \gamma$ on the jet and a corresponding reaction force on the airfoil. Simultaneously, the interaction of the main stream with the jet cancels the vertical component of the jet thrust and produces an equal reaction on the main stream. Thus, the horizontal thrust of the jet is increased, without any reduction in the vertical reaction force on the airfoil.

If the entrainment of the jet is neglected, Spence's theory predicts recovery of the total jet thrust as a horizontal force. This can be shown from the equilibrium of the forces which then act on the jet. Consider the segment of the jet shown in Figure 4. The forces due to the main stream and the wing vortex system deflect the jet through an angle, θ,
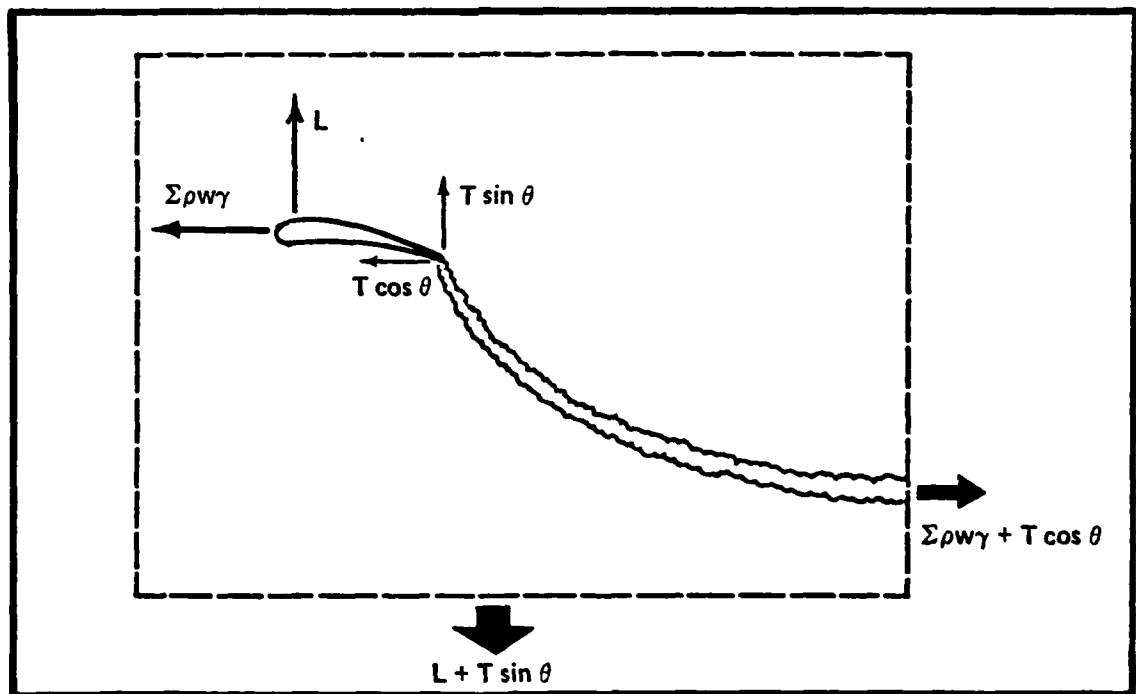
Figure 3. Forces Induced on an Airfoil and Jet Flap

6
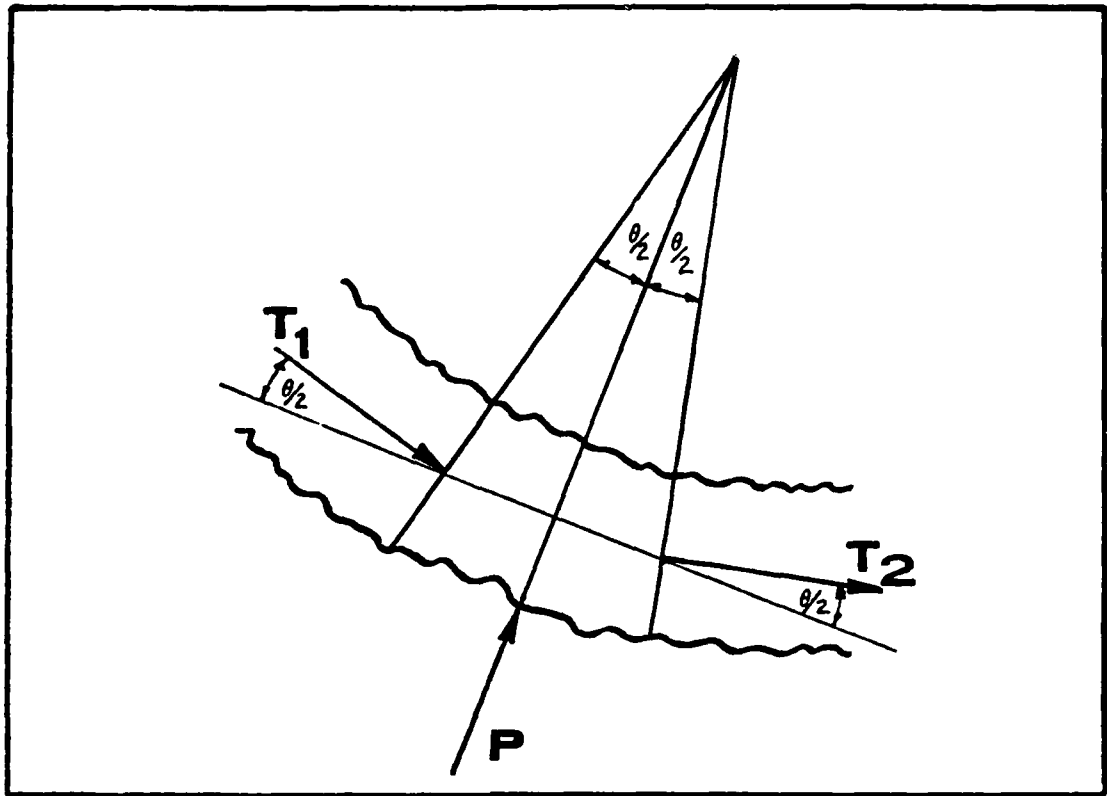
Figure 4. Forces on a Section of the Jet Sheet

as shown. The initial thrust of the jet is T_1 and the final thrust is T_2. Since entrainment has been neglected, the jet will be a streamline of the flow and the pressure force, P, must therefore act normal to the segment.

The summation of forces in the direction of T_2 yields

$$T_2 = T_1 \cos \theta + P \sin \frac{\theta}{2} \qquad\qquad 2\text{-}1$$

The summation of forces normal to the direction of T_2 gives

$$P \cos \frac{\theta}{2} = T_1 \sin \theta \qquad\qquad 2\text{-}2$$

7

Solving this equation for P and substituting in Equation 2-1 gives $T_2 = T_1$. Therefore, the thrust of the jet is conserved. Because the jet consists of a series of these segments, its total thrust is ultimately recovered in the far wake as a horizontal force.

The horizontal force induced on the jet is the integral of the corresponding pressure difference across the jet; that is,

$$\Sigma\rho w\gamma = \int_0^\infty dP \sin \theta \, d\theta \qquad\qquad 2\text{-}3$$

According to Spence (ref 10), $dP = T/R$. Since T is constant and $ds = Rd\theta$, integration yields

$$\Sigma\rho w\gamma = T(1 - \cos \theta) \qquad\qquad 2\text{-}4$$

The sum of this force and the horizontal component of the initial jet momentum gives the total jet thrust. The vertical force on the jet is similarly found to be $T \sin \theta$.

This thrust recovery mechanism was not verified by the Stanford experiments: Quambeck (ref 15) integrated the surface pressure distributions as the jet deflection angle was varied and, finding that the horizontal force did not change, he concluded that the entire jet thrust was felt as an internal pressure on the nozzle. However, in these tests, the jet was deflected by utilizing the Coanda effect (Metral and Zerner, ref 16) to turn it over a short flap. The reaction to the force which deflects the jet over the flap appears as a reduction in the static pressures on the Coanda surface. The resulting pressure drag is equal

8

but opposite to the thrust induced by the jet flap because the force initially required to deflect the jet over the flap must be the same as the force necessary to bend it back in the direction of the free stream. As a result, the net horizontal force is independent of the jet deflection angle. Today, it is no longer doubted that the thrust recovery is induced on the airfoil surface, primarily as a leading edge suction.

THRUST LOSS HYPOTHESES

Real fluid effects reduce the thrust recovery through two separate mechanisms. The very large suction peak generated near the leading edge of the airfoil increases the possibility of flow separation in this region. If the flow does separate, the resulting loss of suction reduces the thrust on the airfoil, while entrainment of the low momentum wake fluid by the jet causes a corresponding loss of thrust. Separation becomes more likely as the jet thrust coefficient and deflection angle are increased.

However, even if the flow does not separate from the airfoil, entrainment reduces the thrust recovery. A jet drag is induced by the mutually induced forces on the vortex sheet bound in the wing and a sink distribution which represents the entrainment of the jet. The origin of the force on the wing is relatively easy to understand; the jet sinks change the surface pressure distribution so as to increase the wing drag. There are two contributions to this force, as shown in Figure 5. The jet drag due to thickness originates in the interaction between the jet sinks and the source distribution which defines the airfoil thickness. The jet drag due to lift originates in the interaction between the jet sinks and vortex distribution which determines the wing lift.

The origin of the reaction force on the jet may not be as apparent. This force is conceptually similar to the drag experienced by a sink

9
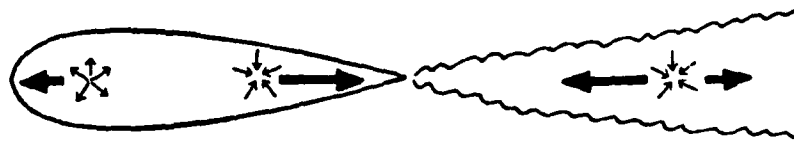
SINK-SINK DRAG DUE TO MIXING
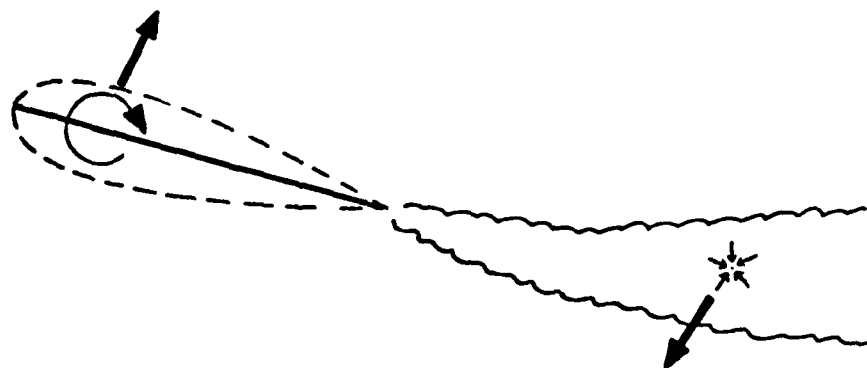
VORTEX-SINK DRAG DUE TO MIXING

Figure 5. Origin of the Mixing Loss

in an external stream. However, the sink/vortex interaction is only
an irrotational simulation of the jet mechan sm. The fluid entrained
into the jet becomes rotational, so that an understanding of how the
reaction force actually develops requires consideration of the jet
mixing process.

This process is basically an inelastic collision between the jet and
surrounding fluid. As such, jet mixing is governed by the same laws of
momentum and energy conservation as simple collisions between discrete
particles. If the mixing occurs in a region of constant static pres-
sure, the thrust of the jet is conserved. But if the jet passes through

10

a region where the static pressure, P^*, is different from the undis-
tributed pressure at infinity, P_∞, the mixing changes the momentum flux.
The following simple analysis illustrates this phenomenon.

Inside the region where the pressure is P^*, the velocities in the
jet and coflowing stream, before mixing, are assumed to be

$$U_j^* = \left[\frac{2(P_0 - P_*)}{\rho} \right]^{1/2} \qquad \qquad 2\text{-}5$$

and

$$U_s^* = \left[U_\infty^2 + \frac{2(P_\infty - P_*)}{\rho} \right]^{1/2} \qquad \qquad 2\text{-}6$$

in which P_0 is the stagnation pressure of the jet and U_∞ is the velocity
of the coflowing stream at infinity. Momentum is conserved during the
mixing process itself, so that

$$\dot{m}_j U_j^* + \dot{m}_s U_s^* = (\dot{m}_j + \dot{m}_s) \, U_m^* \qquad \qquad 2\text{-}7$$

in which $\dot{m}_j$ is the initial mass flux of the jet, $\dot{m}_s$ is the quantity of
mass entrained by the jet, and U_m^* is the average velocity of the mixed
flow.

The velocity of the mixed stream changes as it passes into the region
of undisturbed pressure; the velocity becomes

$$U_m = \left[U_m^{*2} - \frac{2(P_\infty - P_*)}{\rho} \right]^{1/2} \qquad \qquad 2\text{-}8$$

The ratio of the final thrust of the mixed stream, $(\dot{m}_p + \dot{m}_s) \, U_m$, to the
thrust, $\dot{m}_p U_j$, obtained by an isentropic expansion of the jet, without

11

mixing, to the final pressure may be evaluated by substituting in turn for U_m, then U_m^*, and finally for U_j^* and U_s^*. Performing these substitutions yields for this ratio

$$\phi = \left[1 + 2M \left\langle (1+H)^{1/2} (U^2+H)^{1/2} - H \right\rangle + M^2 U^2 \right]^{1/2} - MU \qquad 2\text{-}9$$

in which $M = \dot{m}_s/\dot{m}_p$, is the entrainment ratio, $U = U_\infty/U_j$ is the velocity ratio, and $H = 2(P_\infty - P*)/ U_j^2$ is the normalized pressure change.

If there is no mixing between the jet and the coflowing stream, then $M = 0$ and the thrust of the jet is conserved; that is, $\phi = 1$. Similarly, if there is no pressure change, then $H = 0$ and the solution reduces to that for free jet mixing; the thrust is conserved in this case, also. However, if the pressure in the mixing region is less than the pressure at infinity, then $H < 0$ and the thrust of the jet increases. For the case in which $U_\infty = 0$, the thrust ratio has the simple form,

$$\phi = (1 + M)^{1/2} \qquad 2\text{-}10$$

and the jet thrust increases with increasing entrainment. This is the basic mechanism of ejector thrust augmentation, which has been discussed in greater detail by Bevilaqua (ref 17).

If the pressure in the mixing region is above ambient, the thrust of the jet is reduced. For the case in which $U_s^* = 0$, the thrust ratio also has a simple form

$$\phi = 1 - MU \qquad 2\text{-}11$$

and in this case the jet thrust decreases with increasing entrainment. Because there is a region of increased static pressure behind the trailing edge of the wing, the mixing loss mechanism will reduce the

12

jet thrust. According to Newton's law of action and reaction, the net
loss of thrust must be equal to the jet drag on the wing.

The thrust loss is specified by a thrust recovery coefficient, r,
which is defined to be a fraction of the total thrust; that is,

$$rT \equiv S + T \cos \theta_o \qquad \text{2-12}$$

in which $T \cos \theta_o$ is the horizontal component of the jet thrust within
the nozzle, and S is the horizontal component of the airfoil surface
pressure distribution. In ideal, two-dimensional flow $S = T(1 - \cos \theta_o)$
and so $r = 1$. If a Coanda flap is used to deflect the jet, the pressure
drag due to the Coanda effect, $T(1 - \cos \theta_o)$, is included in S.
Therefore, the recovery is defined as

$$rT \equiv S + T \qquad \text{2-13}$$

In this case, $S = 0$ for ideal, two-dimensional flow so that $r = 1$,
again. The evaluation of the recovery coefficient will be discussed in
greater detail in Section 4.1, on data reduction.

In order to determine the relative importance of separation and jet
drag in reducing the thrust recovery, the jet drag will be computed for
unseparated flow and compared to the drag actually obtained on a wind
tunnel model under the same conditions. Differences between these cases
will be studied to quantify the loss mechanisms. In the next section,
the method of calculating the jet drag will be developed from the
principles outlined in this section.

13

III.   COMPUTATIONAL METHODS

The Navier-Stokes equations for steady fluid motion are elliptic,
which means that the domain of influence of a point disturbance is the
entire flow volume. That is, pressure and stress gradients transmit
the effect of local disturbances to every other point in the flow.
Thus, the forces induced on the airfoil depend on the jet position,
while the jet position, in turn, depends upon the forces on the airfoil.
The basis of our analysis is the division of the flow field into two
regions: the region of turbulent mixing within the jet, and the inviscid
region surrounding it. The equal but opposite forces on the airfoil
and jet will be computed by matching a viscous solution for the jet to
a potential flow solution for the airfoil and jet flap. The significant
elliptic effects are then transmitted through the pressure field of the
external flow.

For the viscous jet solution, a finite difference analysis utilizing
a two-equation turbulence model was developed. The basic scheme
was that devised by Patankar and Spalding (ref 18) for thin shear
layers: the full Navier-Stokes equations are reduced to a simpler set
by the assumption that there is a primary direction of flow (along the
jet), and that the diffusion of fluid properties is negligible in that
direction. The effects of curvature on the development of the jet will
be treated as a perturbation of this basic scheme. A jet flap panel
method, in which the thrust of the jet is not assumed to be constant,
was used for the inviscid solution.

INVISCID JET ANALYSIS

In the inviscid program, the potential flow continuity equation takes
the form of the Laplace equation in terms of the velocity potential,
$\nabla^2 \phi = 0$. The mathematical problem to be solved requires finding a
velocity potential which is harmonic, and satisfies the boundary condi-
tion of uniform flow at infinity and flow tangent to the surface of the

14

airfoil and the centerline of the jet. Since the shape of the jet is
initially unknown, Spence (ref 10) made the important contribution to
solving this problem by relating the inertia force in the jet to the
strength of an equivalent vortex sheet,

$$T/R = \rho U \gamma \qquad\qquad 3-1$$

In this equation T is the jet thrust (which Spence assumed constant),
R is the local radius of jet curvature, and γ is the vortex strength
per unit length along the jet.

This force balance becomes an additional, dynamic boundary condition
at each point on the jet sheet. In the inviscid analysis, the jet thrust is
considered to vary in a known way. This variation is determined from the
viscous solution for the turbulent jet computed in the previous itera-
tion. The inviscid solution is obtained by iterating between the jet
shape and the jet vorticity. For each iteration, the problem reduces
to solving a set of linear influence equations with unknown vortex
strengths. The boundary condition on both the airfoil and jet is that
of no net normal velocity at each panel control point. A Gaussian
elimination solution of the simultaneous equation is used.

The airfoil is described by an input set of X and Y coordinate points.
These points may be used as the vortex panel endpoints, or an increased
number of panels may be calculated using cosine spacing on the upper
and lower surfaces and nonlinear interpolation of the input points.
An airfoil geometry subroutine performs the interpolations if required
and computes the individual panel angles and control point (panel
centroid) coordinates. If an angle of attack case is run, all geometry
is rotated, and all displacements are included.

In the solution, the airfoil is represented by distributions of
linearly varying vorticity. The paneling scheme begins at the airfoil

trailing edge and proceeds forward over the lower surface and back over the upper surface to the trailing edge. Each vortex distribution, with the exception of the first consists of a ramp-up (increasing from zero) vorticity over one airfoil panel and a ramp-down (decreasing to zero) vorticity over the next airfoil panel. The first vortex distribution uses a constant vorticity over the first airfoil panel and a ramp down over the second airfoil panel. (This distribution was used to better represent the near constant pressure in this region under conditions of large jet deflection and high jet momentum.) This paneling scheme gives a number of unknown vortex strengths which is one less than the number of airfoil panel control points, at which the boundary conditions were defined. This over-specified problem is solved by the method of uniform error, (Bristow, ref 19). Figure 6 illustrates the airfoil vorticity paneling scheme. The jet was modeled as a thin sheet of vorticity using the assumptions of Spence (ref 10). Within each iteration, the jet shape was assumed to be known. For the first iteration, the

Linear Vorticity Distribution

N Unknown Vortex Strengths,

N + 1 Control Points
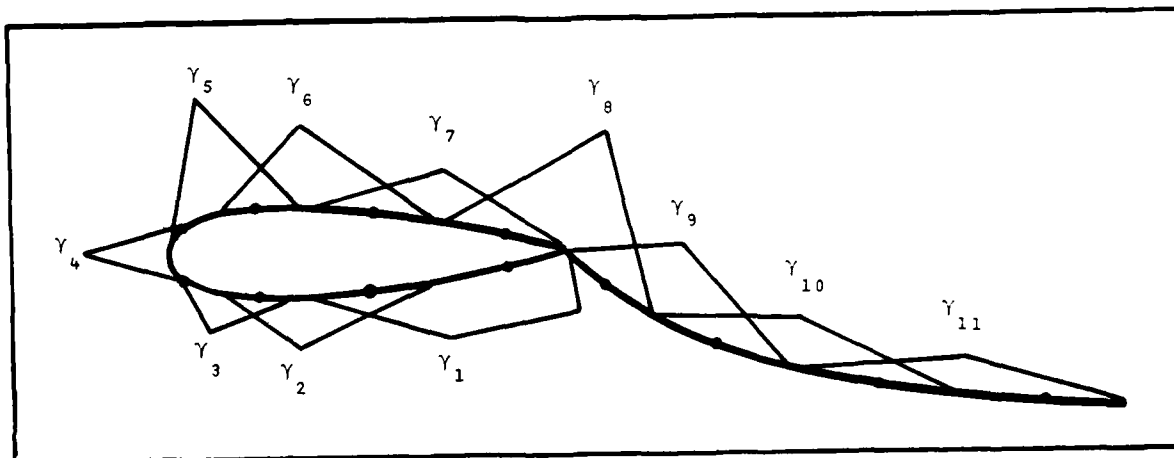
Figure 6. Vorticity Distributions on the Airfoil and Jet

16

empirical jet shape equation from Chandra (ref 20) was used. For sub-
sequent iterations, the jet panel angles were computed using an itera-
tion scheme described in a later section. Briefly, this scheme used
the previous jet shape (panel angles) modified as guided by a new shape,
computed from satisfying the dynamic jet boundary condition, Equation 3-1.

Jet panel lengths were set by a simple geometric progression factor,
usually between 1.05 and 1.15. Thus, each panel length was larger than
the one just upstream by the factor chosen. The first jet panel length
was similarly related to the last airfoil upper surface panel length.
This scheme had the distinct advantage of minimizing numerical problems
associated with rapidly changing panel sizes. The jet panel lengths
and angles were used to calculate the panel endpoint and control point
(centroid) coordinates using a summation beginning at the airfoil
trailing edge.

The jet was represented by distributions of linearly varying vorticity.
The first jet vortex was a single ramp down function over the first panel.
Subsequent vortex distributions were a ramp up over one panel and a ramp
down over the next downstream panel. The second jet vortex distribution
begins on the first jet panel. The last jet vortex distribution ramps
down to zero strength at the trailing edge of the last jet panel.

When required, the jet entrainment effects are represented by a
number of sink panels, coinciding with the jet panels, and a numerically
integrated sink strength which decays as $X^{-1/2}$ from the jet trailing edge
to a point far downstream (typically 1000 chord lengths). The sink
strengths are computed from entrainment output from the viscous program
and are modeled as constant over each jet panel. The initial value of
the decaying sink function is set equal to the last panel's constant
strength. The effect of these jet sinks is to modify the boundary con-
ditions imposed at each control point. The jet sink panels are
illustrated in Figure 7.

17
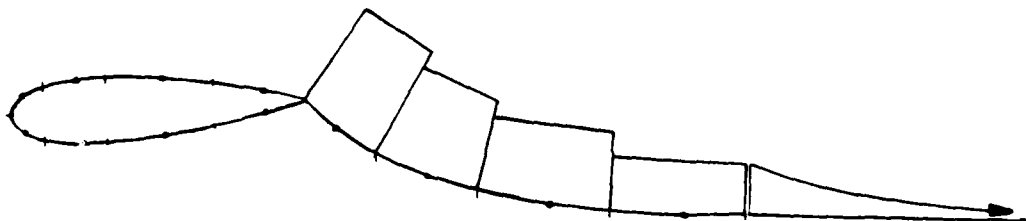
Figure 7. Sink Distributions on the Jet Panels

Vortex and Sink Influence Equations

The equations used to compute the velocities induced by each of the
linearly varying singularities (vortices or sinks) used in the inviscid
flow analysis are given below. These equations were developed by
Dvorak and Woodward (ref 21). Note that each equation is written in a
coordinate system with its origin at the left hand edge of the singu-
larity panel and with its ordinate axis lying along the singularity.
Routines within the inviscid program handle rotation and translation of
an influenced point into the panel coordinate system, and resolve the
induced velocities into velocities normal and tangential to the
influenced panel control point. The terms in the equations are defined
in the sketch of the singularity coordinate system sketched in Figure 8.

The velocities induced by a ramp up vortex or sink distribution are:

$$U_v = W_s = \frac{S}{2\pi} \left\{ \frac{z}{c} \log \frac{\sqrt{(x-c)^2 + z^2}}{\sqrt{x^2 + z^2}} - \frac{x}{c} \left[\tan^{-1} \frac{z}{x} - \tan^{-1} \frac{z}{x-c} \right] \right\} \qquad 3-2$$

18
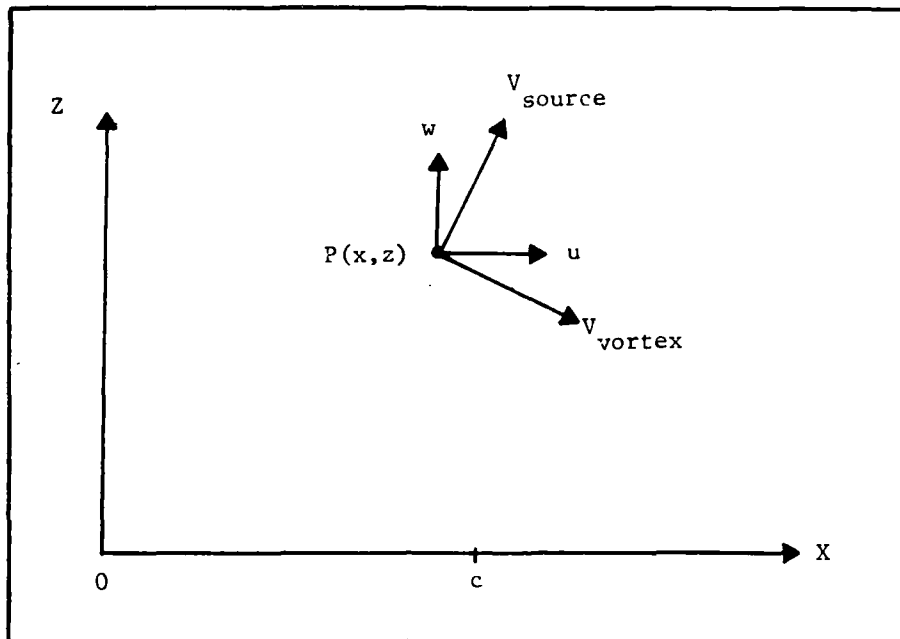
Figure 8. Singularity Coordinate System

$$-W_v = U_s = \frac{-S}{2\pi} \left\{ 1 + \frac{z}{c} \left[\tan^{-1} \frac{z}{x} - \tan^{-1} \frac{z}{x-c} \right] + \frac{x}{c} \log \frac{\sqrt{(x-c)^2 + z^2}}{\sqrt{x^2 + z^2}} \right\} \quad \text{3-3}$$

The velocities induced by a constant vortex or sink distribution are:

$$U_v = W_s = \frac{S}{2\pi} \left[\tan^{-1} \frac{z}{x-c} - \tan^{-1} \frac{z}{x} \right] \quad \text{3-4}$$

$$-W_v = U_s = \frac{-S}{2\pi} \log \sqrt{\frac{(x-c)^2 + z^2}{x^2 + z^2}} \quad \text{3-5}$$

where s is the singularity strength, which is known for the sink distributions and set equal to V_∞ for the calculation of the vortex influence coefficients.

19

The velocities induced by a ramp down singularity distribution are calculated by subtracting the ramp up velocities from the constant singularity velocities. Velocities induced by the composite singularities (ramp up on one panel and ramp down on the next panel) are simply the sum of the two contributions computed separately.

Initial Jet Shape

While the initial jet shape is not critical with the iteration scheme used, a good first guess minimized computer run time. For the present inviscid flow program, the initial jet shape (in terms of panel angles) was obtained from the empirical jet angle function derived by Chandra (ref 20).

$$\frac{\theta}{\theta_0} = 0.64 \exp (-.82 \ s/C_\mu) + 0.36 \exp (-11.7 \ s/C_\mu) \qquad 3\text{-}6$$

For any initial jet deflection, θ_0, and jet momentum coefficient, C_μ, the jet angle at a given distance, s, along the jet arc could be computed. Jet panel lengths were computed as described above, and the initial panel angles were then the average of the angles at the panel endpoints. Initial jet position was computed from the individual panel angles and lengths.

Solution for Singularity Strengths

The airfoil and jet panel geometries and the influence equations, 3-2 to 3-5 are used to compute the influence coefficient matrix and the boundary condition vector. Terms in the influence coefficient matrix, A_{ij}, are the normal velocity induced by unit strength vortex distribution, i, at the control point, j. The terms in the boundary condition vector, B_j, are equal but opposite to the normal velocities which exist

20

at each control point due to the freestream velocity, V_∞, and the jet
sinks, if present. The following matrix equation results:

$$A_{ij} \, \gamma_i = B_j \qquad\qquad 3\text{-}7$$

This system of equations is solved for γ_i by a Gaussian elimination
procedure.

Pressure and Force Coefficients

The resulting pressure coefficients, C_{p_i}, are computed from the
singularity strengths as follows:

On the airfoil:

$$C_p = \frac{P_{local} - P}{q} = 1 - V_T^2 \qquad\qquad 3\text{-}8$$

where V_T is the total tangential velocity at the control point due to
V_∞ and all singularities.

On the jet:

$$C_p = \frac{P_u - P_L}{q} = -2 V_T \, \gamma_{avg} \qquad\qquad 3\text{-}9$$

where γ_{avg} is the average of the vortex strengths at the panel endpoints.

Airfoil and jet normal force and axial force coefficients are computed
by summing the product of the panel pressure coefficient and its
respective projected area.

Calculation of "New" Panel Angles

"New" jet panel angle refers to the panel angles computed from the
jet vorticity distribution and the dynamic boundary condition,
Equation 3-1. They are different from the next iteration jet panel
angles, which are computed from the last iteration angles by the
iteration scheme described below. In terms of the local jet radius, R,
and panel length, ΔS, the change in jet flow angle from one end of a
panel to the other is

$$\Delta\theta = \Delta S/R \qquad\qquad 3-10$$

but, from Equation 3-1, $R = T/\rho V\gamma$. Thus,

$$\Delta\theta = \Delta S\, \rho V\gamma/T \qquad\qquad 3-11$$

In terms of the local pressure coefficient, $C_p = \rho V\gamma/q$ and jet thrust
coefficient $C_\mu = T/qc$, the change in angle is

$$\Delta\theta = -C_p\, \Delta S/C_\mu C \qquad\qquad 3-12$$

Each "new" jet panel angle is then the average of the panel endpoint
angles found from the panel pressure coefficients, local momentum co-
efficient (input from the viscous program) and panel length.

Iteration Scheme

An iteration scheme was written which eliminates some of the problems
associated with ordinary relaxation techniques. This scheme provides
rapid convergence initially, is not as sensitive to oscillations near
the jet trailing edge, and does not require the user to chose a weight-
ing factor.

22

This iteration scheme does not use the "new" jet panel angles directly. Instead, they are used only as an indication of the direction of change. The magnitude of the change in panel angle is determined by the factor $1 - \frac{1}{2^n}$, where n is a positive integer which may be different for each panel. Initially, n = 1 and n is incremented by 1 each time the required direction of change is reversed. If the "new" panel angle is less than the angle used in the previous iteration, the previous angle is multiplied by the factor $1 - \frac{1}{2^n}$ using the current value of n. If the "new" panel angle is larger than the angle used in the previous iteration, the previous angle is divided by the factor $1 - \frac{1}{2^n}$. In either case, the next iteration jet panel angle is never allowed to change by an amount greater than "new" angle - "old" angle.

The iteration continues until a convergence criterion is met. The criterion used is that the average change in panel angle must be less than 0.01 times the initial jet deflection.

TURBULENT JET ANALYSIS

The sink strengths which represent the effect of the jet mixing are calculated from a viscous solution for the turbulent jet. It is possible to compute the mixing without including the elliptic effects by taking advantage of the flow geometry. Since there is a primary direction of flow (along the jet), the thin shear layer approximation can be applied. This reduces the governing elliptic equations to a parabolic set which can be solved by marching along the jet in the streamwise direction. By treating the radial pressure gradient as a perturbation of the axial pressure gradient, additional simplifications are achieved. These assumptions result in considerable savings in computer storage and running time compared to a solution of the complete elliptic problem.

23

The governing equations are derived from Reynolds equations for turbulent flow by neglecting streamwise diffusion and upstream convection. Thus, the effect of a local disturbance is transmitted downstream by pressure and convection and across the flow by pressure, convection and diffusion. In cylindrical coordinates, (r, θ), the equations take the general form:

Conservation of Mass

$$\frac{\partial U}{r \partial \theta} + \frac{\partial V}{\partial r} + \frac{V}{r} = 0 \qquad \text{3-13}$$

Streamwise Momentum

$$U \frac{\partial U}{r \partial \theta} + V \frac{\partial U}{\partial r} + \frac{UV}{r} \approx - \frac{1}{\rho} \frac{\partial P}{r d\theta} - \frac{\partial \overline{u'v'}}{\partial r} - \frac{2\overline{u'v'}}{r} \qquad \text{3-14}$$

Radial Momentum

$$U \frac{\partial V}{r d\theta} + V \frac{\partial V}{\partial r} - \frac{U^2}{r} = - \frac{1}{\rho} \frac{\partial}{\partial r} (P + p') \qquad \text{3-15}$$

in which U and V are the streamwise and radial velocity components. The radial perturbation pressure $p'(r, \theta)$ is decoupled from the mean streamwise pressure, $P(\theta)$.

These equations do not describe the effect of curvature on the flow. The "extra" terms originate in the choice of coordinate system and do not imply any additional physical processes. The Coriolis acceleration, $UV/r = \omega V$ and the centrifugal acceleration $U^2/r = \omega U$, arise from rotation of the velocity vector with respect to the coordinate system. Similarly, the extra stress term is a consequence of having chosen a cylindrical volume element; that is, since the sides of the element are not parallel,

the shear stress has a component, $\overline{u'v'}/r$, in the streamwise direction. Thus, the use of cylindrical coordinates is a convenience in this case, and the additional terms merely account for the difference between the actual accelerations of the fluid and those which appear to take place in the curvilinear coordinate system.

To facilitate solution, the governing equations are transformed into an ω-x coordinate system as shown in Figure 9. This provides the advantage of expanding the grid point spacing as the jet spreads. Thus, the maximum number of grid points are always contained within the jet, and there is no need to include additional, unnecessary grid points for the external stream. The stream function, ψ is defined as

$$\frac{\partial \psi}{\partial y} = \rho U \qquad\qquad 3\text{-}16$$
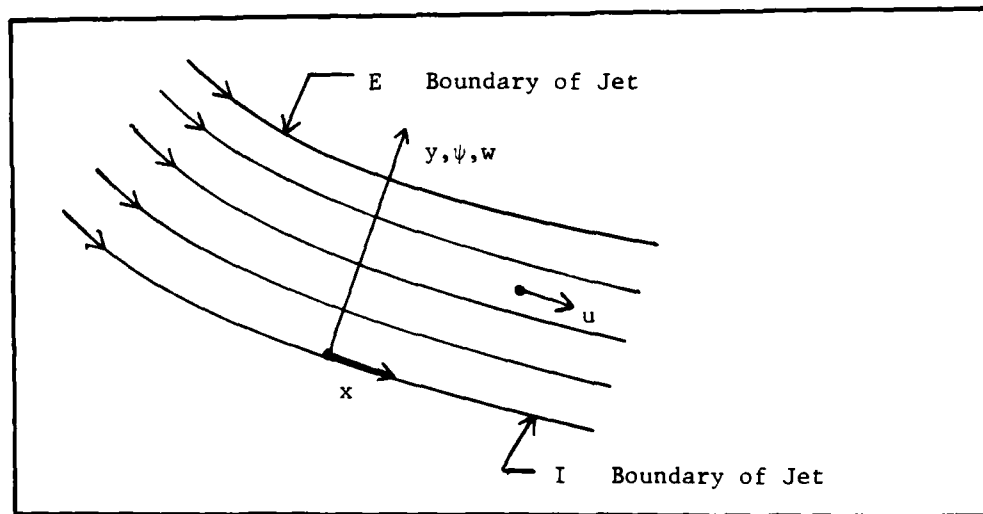
Figure 9. Transformed Coordinate System for Turbulent Jet

The variable, ω, is a dimensionless stream function defined by:

$$\omega = \frac{\psi - \psi_I}{\psi_E - \psi_I} \qquad \text{3-17}$$

The ψ coordinate lines are not true stream lines. They are used as a convenient method to handle flow in the cross stream direction.

Turbulence Equations

The effect of curvature is to increase the turbulent mixing rate. Recent proposals to model this effect have been based on the turbulence kinetic energy equation. According to the usual eddy viscosity assumption, the turbulent stress is first expressed in terms of a turbulent viscosity, μ_t, and the mean strain rates

$$\overline{u'v'} = \mu_t \left(\frac{\partial U}{\partial r} - \frac{U}{r}\right) \qquad \text{3-18}$$

Again, no new physical process is implied by the extra strain rate, U/r. Following Launder and Spalding (ref 22), the turbulent viscosity is assumed to depend on two parameters: the turbulence kinetic energy, k, and its rate of dissipation, ϵ. From dimensional arguments, the expression for the turbulent viscosity is

$$\mu_t = \frac{c_\mu \rho k^2}{\epsilon} \qquad \text{3-19}$$

in which c_μ is an empirical constant. A procedure for modifying the turbulence kinetic energy equations to account for the effect of curvature has been developed by Schum, et al. (ref 23). This method has been used here. Briefly, the effect of curvature is to transfer energy from the streamwise component of the turbulence to the transverse component.

Since it is the transverse component which produces most of the mixing in thin shear layers (Bradshaw, ref 24), this transfer of energy increases the mixing.

However, curvature has no effect on the total turbulence energy, because energy is simply transferred from one component to another. Thus, the turbulence kinetic energy equation cannot be used to calculate the effects of curvature. An additional production term was therefore added to the total turbulence energy equation to represent the increase of the transverse energy component by the curvature. In cylindrical coordinates, the equation for the turbulence energy becomes

$$\rho \, \frac{dk}{dt} = \overline{u'v'} \left(\frac{\partial U}{\partial r} - \frac{U}{r} \right) - \rho \epsilon + \frac{\partial}{\partial r} \left(\frac{\mu_t}{\sigma_k} \frac{\partial k}{\partial r} \right) + \overline{u'v'} \, \frac{2U}{r} \qquad 3\text{-}20$$

in which the first term on the right hand side represents the usual production mechanism, the second term represents dissipation, the third term represents diffusion, and the last term represents the effect of curvature.

An equation derived by Chambers and Wilcox (ref 25) was used to compute ϵ, the dissipation of the turbulence energy. It contains the same curvature correction as the turbulence energy equation:

$$\rho \, \frac{d\epsilon}{dt} = (c_1 G - c_2 \rho \epsilon) \, \frac{\epsilon}{k} + \frac{\partial}{\partial r} \left(\frac{\mu_t}{\sigma_\epsilon} \frac{\partial \epsilon}{\partial r} \right) + \overline{u'v'} \, \frac{2U}{r} \qquad 3\text{-}21$$

This turbulence model has five empirical constants: c_μ, c_1, c_2, σ_k, and σ_ϵ. The values of these constants recommended by Launder and Spalding (ref 22) were used for this analysis.

27

Finite Difference Equations

The governing mean flow and turbulence equations are solved simul-
taneously by iteration. In order to simplify the program logic, the
momentum and turbulence equations are expressed in the general form:

$$\frac{\partial \phi}{\partial x} + (a + b\omega) \frac{\partial \phi}{\partial \omega} = \frac{\partial}{\partial \omega} (\Gamma \frac{\partial \phi}{\partial \omega}) + \frac{s}{\rho u} \qquad 3\text{-}22$$

in which

$$a = \frac{\dot{m}_I}{\psi_E - \psi_I} \quad \text{and} \quad b = \frac{\dot{m}_E - \dot{m}_I}{\psi_E - \psi_I} \qquad 3\text{-}23$$

The general dependent variable ϕ represents either U, V, k, or ϵ,
while Γ and S represent the corresponding diffusion and source terms.
Also, $\dot{m}$ represents the mass flux across the jet boundaries shown in
Figure 9. With all the equations expressed in this same form, the
same solution procedure can be used.

A marching solution is performed in which the task is to obtain
values of the flow variables at a downstream station when the values
at the upstream station are known. With a given set of initial con-
ditions, one can then make a series of forward steps in the streamwise
direction to obtain the solution for the entire flow field. The flow
field is modeled by specifying a number of control volumes across the
flow in a direction normal to the mainstream direction, x, with grid
points centered at the control volume faces upstream and downstream
(Figure 10).

The method of specifying control volumes in the program is one where
the control volume boundaries are input in the ω coordinate system (at
x = 0) and the respective grid points are then located in the center of
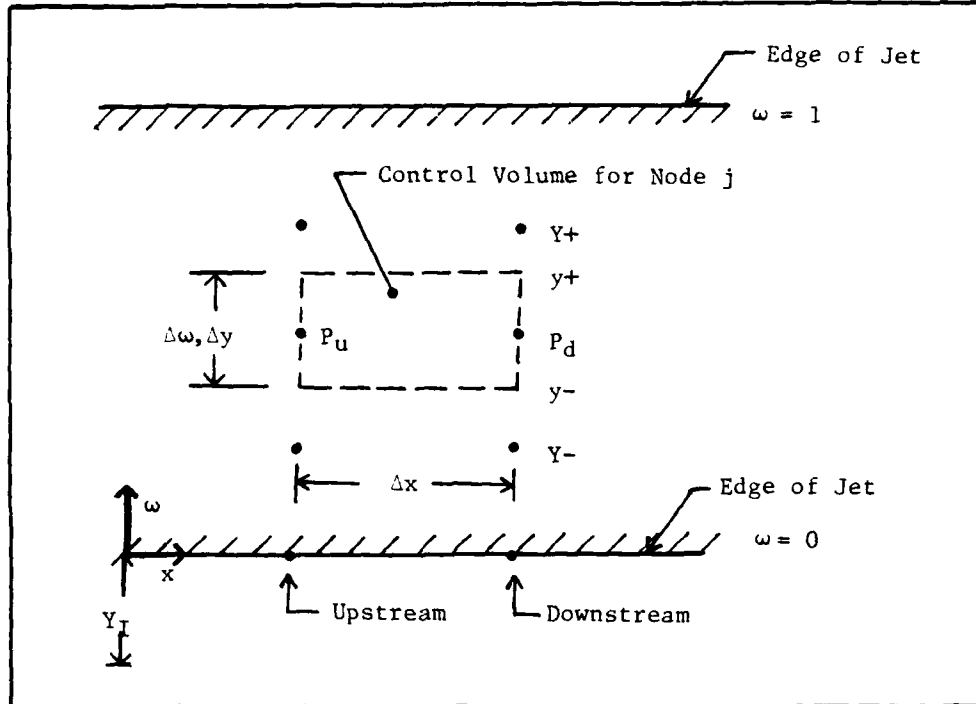
Figure 10. Control Volume and Coordinate System

each control volume (midway between y^+ and y^-). The points Y^+ and Y^- represent adjacent grid points, above and below grid point P_d. The values of Δy can change in the x direction, depending on the values of the U velocities in the control volume. The finite-difference equations are then formed by integrating the governing partial differential equations over the control volumes. In order to express the various terms in the equations in algebraic form, the following practices are used:

1) The value of the variable at the central grid point is assumed to prevail over the entire face of the control volume.

2) The downstream values are considered to prevail over the entire forward step.

3) The dependent variables are assumed to vary linearly between the grid points (this is modified when convection is large).

29

4) Strict compatibility is maintained between the neighboring control volumes, ie., the flux leaving a control volume through a face is made exactly equal to the flux entering the adjacent control volume through the same face.

The resulting algebraic equations (finite-difference equations) for each grid point have the following general form:

$$A_P \ \phi_{Pd} = A_{Y+} \ \phi_{Y+} + A_{Y-} \ \phi_{Y-} + A_{Pu} \ \phi_{Pu} + B \qquad \text{3-24}$$

where A_{Y+} and A_{Y-} represent the effect of cross stream convection and diffusion; A_{Pu} represents the upstream convection; B is the constant part of the source term

$$S = B + S_P \ \phi \qquad \text{3-25}$$

and A_P is defined by

$$A_P = A_{Y+} + A_{Y-} + A_{Pu} - S_P \qquad \text{3-26}$$

The symbolic term, ϕ, is used to represent the U, k, or ϵ parameters at grid locations, Y^+, Y^-, u or d. Table I presents the corresponding source terms. The value of the A coefficients depend on which parameter is being considered. The coefficients A_{Y+} and A_{Y-} in Equation 3-24 are defined as:

$$A_{Y+} = D^*_{y+} - \frac{1}{2} \ C_{y+} \qquad \text{3-27}$$

$$A_{Y-} = D^*_{y-} + \frac{1}{2} \ C_{y-} \qquad \text{3-28}$$

D represents diffusion and C represents convection through the y^+ or y^- boundary. The subscripts for D and C indicate that these quanti are

30

Table I. Source Terms

ϕ	S_P	B
U	-	$-\dfrac{dP}{dx} - \dfrac{\partial}{\partial y}\left(\mu_t\,\dfrac{U}{r}\right) - \dfrac{dP'}{dx}$
k	$-\dfrac{\rho\epsilon}{k}$	$\mu_t\left(\dfrac{\partial U}{\partial y} - \dfrac{U}{r}\right)^2 - 2\,\dfrac{U\mu_t}{r}\,\dfrac{\partial U}{\partial r}$
ϵ	$-\dfrac{c_2\rho\epsilon}{k}$	$\rho c_1 c_\mu k\left(\dfrac{\partial U}{\partial y} - \dfrac{U}{r}\right)^2 - 2\,\dfrac{U\mu_r}{r}\,\dfrac{\partial U}{\partial r}\,\dfrac{\epsilon}{k}$

There are two special things to note in the representations of the source terms

(1) In the k equation, the $\rho\epsilon$ term has been reformed to $\left(\dfrac{\rho\epsilon}{k}\right)k^*$. This procedure improves the mathematical convergence accuracy.

(2) In the ϵ equation, the $c_1 G$ term has been reformed by expressing the μ_t in G as $\dfrac{\rho C_D k^2}{\epsilon}$.

to be evaluated at the control volume boundary indicated by the subscript. D^* is the modified form of D depending on the size of C compared to D. This is called the "hybrid scheme" and represents a central difference scheme when C is less than twice D and an upwind difference scheme when C is twice D:

$$C = \left\{ m_I + \omega(m_E - m_I) \right\} \Delta X \qquad 3\text{-}29$$

$$D = \frac{\Gamma\,\Delta X}{\Delta y'} \qquad 3\text{-}30$$

and $D^* = D$ if $|C| < 2D$

      $= 1/2C$ $|C| \ge 2D$ and C positive

      $= -1/2C$ $|C| \ge 2D$ and C negative

31

where Γ , ω, and Δx are the values of the exchange coefficient, dimensionless stream function, and x stepsize, respectively, of the control volume boundary being considered. $\Delta y'$ is the distance between the two grid points on either side of the control volume boundary.

The coefficient Ap_u represents the convection from upstream and is calculated by

$$Ap_u = (\psi_E - \psi_I)_u \, \Delta\omega \qquad\qquad 3\text{-}31$$

where $(\psi_E - \psi_I)_u$ is the total upstream flow rate and $\Delta\omega$ is the change in ω across the control volume being considered.
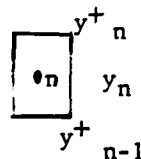
Once the solution of the differential equations is complete and values of the U velocities and ΔP have been calculated, the locations of the grid points and control volume boundaries in terms of y must be found. This is done by using the definitions of ψ and ω to obtain

$$dy = \frac{(\psi_E - \psi_I)}{\rho U} \, d\omega \qquad\qquad 3\text{-}32$$

Now by using this expression and the known ω values that are input for the control volume boundaries the corresponding Δy can be found from

$$(\Delta y)_n = \frac{(\psi_E - \psi_I)}{(\rho U)_n} (\Delta\omega)_n \qquad n = 2,3,\ldots,N \qquad 3\text{-}33$$

for each nth control volume. The y values of the control volume boundaries, y^+, are then easily found by knowing the boundary value, y_I, (which can be set to 0) and the $(\Delta y)_n$ values:

$$y^+_{\,n} = \frac{(\psi_E - \psi_I)}{(\rho U)_n} + y^+_{\,n-1} \qquad n = 2,3,\ldots,N+1 \qquad 3\text{-}34$$

where $y^+_1 = y_I$ and y^+_{N+1} will equal y_E.

The y location of the grid point n is calculated by using the centered grid point approach so

$$y_n = \frac{1}{2}(y^+_n + y^+_{n-1}) \qquad n = 2,3,\ldots, N=1 \qquad\qquad 3\text{-}35$$

Pressure Equations for Curved Flow

In the viscous program, two pressure gradients are considered--one in the streamwise direction and the other in the cross stream direction, a result of jet curvature. With the addition of curvature effects, the change in the local pressure due to the centrifugal forces must be included in the mainstream momentum equation. However, in parabolic flow, these pressure changes must not change the total integrated mean pressure difference times area term for a cross section. In other words, only one value of mean pressure exists at a particular x station. The local pressure variation due to curvature is calculated by creating an additional pressure value, P', from

$$\frac{\partial P'}{\partial y} = \frac{\rho U^2}{r} \qquad\qquad 3\text{-}36$$

where r is the local curvature. Upstream values of the velocity, U_u, are used for downstream values since the latter have yet to be determined. With small Δx steps, as used here, this is a good approximation.

For the mean or global pressure to have only one value at a particular x station, it is necessary that:

$$\Sigma P'_j \, dA_j = 0 \qquad j = 1, 2,\ldots N \qquad\qquad 3\text{-}37$$

where N is the number of control volumes. The values of P_j' are used to determine a gradient dP'/dx for use in the source term in the U momentum equation (Table I).

Boundary Conditions

The viscous program requires boundary conditions to be specified at the inlet plane and along the jet surfaces. At the inlet plane (nozzle exit) a top hat velocity profile is used. The radial perturbation pressures are determined from Equation 3-36 in which the radius of curvature is specified by the inviscid program. The U velocity at the inlet is derived from a stream tube analysis, Figure 11. By combining the Bernoulli and continuity equations with the definition of C_μ, the initial jet velocity, $U_{J,i}$ can be obtained.
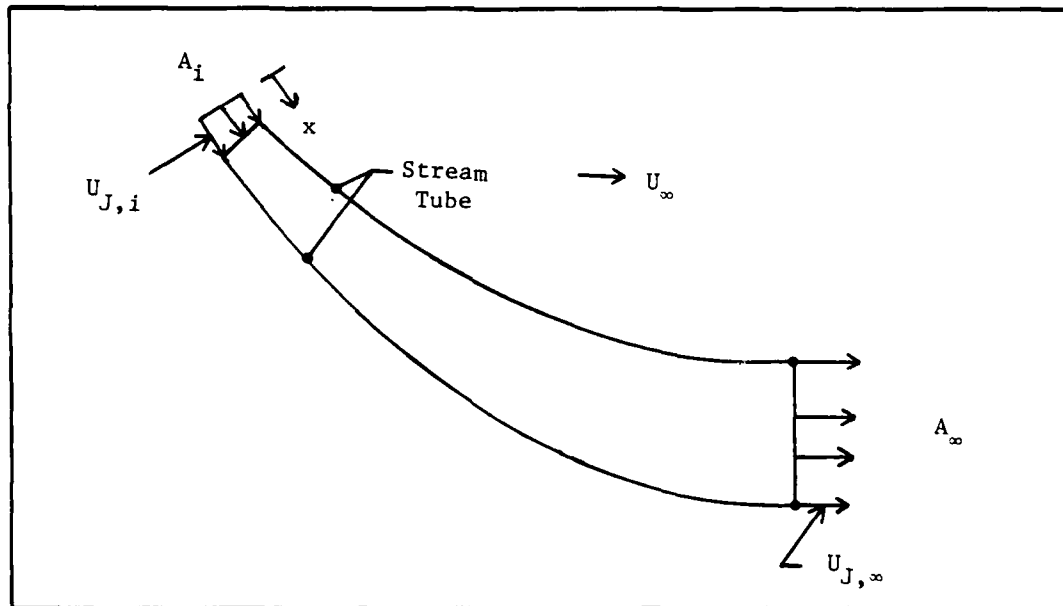
Figure 11. Stream Tube for the Deflected Jet

34

From Bernoulli

$$P_i + \frac{1}{2}\rho U_{J,i}^2 = P_\infty + \frac{1}{2}\rho U_{J,\infty}^2 \qquad\qquad 3\text{-}38$$

and continuity

$$\rho U_{J,i} A_i = \rho U_{J,\infty} A_\infty \qquad\qquad 3\text{-}39$$

It can be shown that $U_{J,i}$ can be obtained from the quadratic

$$(U_{J,i}^2)^2 + \frac{2(P_i - P_\infty)U_{J,i}^2}{\rho} - \left(\frac{U_\infty^2 C_\mu C}{2 A_i}\right)^2 = 0 \qquad\qquad 3\text{-}40$$

At any downstream distance, x, the velocity profile is dependent on
the solution of the momentum equations with prescribed velocities as
boundary conditions at the inner and outer surface of the jet. There
are two ways to obtain the edge velocities, one is to use the velocities
from the inviscid program and the other is to use the upstream radial pressures
from the viscous program. The latter approach was used in the iteration
procedure involving the inviscid and viscous programs. This serves as
a check on the degree of convergence between the two programs since the
velocities at corresponding locations should be the same when convergence
is achieved. The inner and outer jet surface velocities are determined
from:

$$(U_I)_{Viscous} = \sqrt{\frac{2}{\rho}(\overline{P} + P_I')} \qquad\qquad 3\text{-}41$$

$$(U_E)_{Viscous} = \sqrt{\frac{2}{\rho}(\overline{P} + P_E')} \qquad\qquad 3\text{-}42$$

in which P_I' and P_E' are determined from the previous upstream radial pres-
sure distribution (Eq. 3-36), calculated in the viscous program. The mean

pressure, $\overline{P}$, is obtained from the inviscid velocities.

$$\overline{P} = \frac{1}{2}\rho\left(\frac{U_I + U_E}{2}\right)^2_{\text{Inviscid}} \qquad\qquad 3\text{-}43$$

The velocity profiles in the jet are also dependent upon the entrainment at the inner and outer jet surface, $\dot{m}_E$ and $\dot{m}_I$. The values are obtained from the relation given by Patankar and Spalding (ref 18)

$$\dot{m} = \left(\frac{\partial\mu_t}{\partial y}\right)_{\text{jet edge}} \qquad\qquad 3\text{-}44$$

in which the viscosity is calculated in the solution of the momentum and turbulence equations. In some cases, step-to-step oscillations in the width of the jet can occur. One of the many approaches to minimize these oscillations (Patankar and Spalding, ref 18) is to utilize a multiplication factor, F, in the entrainment calculations, such that

$$\dot{m} = F\left(\frac{\partial\mu_t}{\partial y}\right)_{\text{jet edge}} \qquad\qquad 3\text{-}45$$

where F is altered from one Δx step to the next by

$$F_{\text{new}} = F_{\text{old}}\left[\frac{|U_{N+1} - U_N|}{\Delta U^*}\right]^n \qquad\qquad 3\text{-}46$$

where $|U_{N+1} - U_N|$ is the absolute value of the difference in velocity between the boundary and adjacent grid point, and ΔU^* is the velocity difference specified by the user as the minimum to which he wants the difference between U_{N+1} and U_N to fall. The exponent controls the rate of change of thickness if oscillations are a problem. Setting it equal to 0.05 has generally worked well. ΔU^* is generally specified as a

36

percentage of the maximum change in velocity in the velocity profile, say one or two percent of $U_{max} - U_{min}$. Even though the value of F may vary from step to step, on the average, the correct entrainment is calculated.

Solution of Finite Difference Equations

For each grid node (excluding boundary nodes) there is a corresponding finite difference equation (Equation 3-24) representing the momentum and turbulence equations. If there are M nodes used, there are (M - 2) equations to be solved. These finite-difference equations are solved by using the tri-diagonal matrix algorithm having the generalized format:

$$A_j \ \phi_j = B_j \ \phi_{j+1} + C\phi_{j-1} + D_j^* \qquad\qquad 3\text{-}47$$

for $j = 2,3,\ldots,M\text{-}1$. ϕ_1 and ϕ_M are prescribed boundary conditions, such as the jet edge velocities. Equation 3-47 represents Equation 3-24 in which the last two terms have been combined into the single value, D_j^*.

When calculating the coefficients for the equations, several values of flow variables and distances are needed. Upstream values are used when downstream values are not available. No iterations per forward step are performed. These iterations could improve the solution; however, the improvement is insufficient to warrant the increased work for two-dimensional parabolic problems. This lack of iteration is only a problem if the forward steps become too large and one is covering an area where the flow variables change a lot over one step. For the cases studied here, the forward Δx step was only 0.0005 ft over a total jet length of about 10 ft. Changes in the flow variables over such a small distance as 0.0005 ft are relatively small.

37

The only readily available data for a turbulent jet in a coflowing stream with a streamwise pressure gradient is that of Fekete (ref 26). Tests were conducted so as to provide self preservation. According to Newman (ref 27), self preservation is possible only if:

$$\frac{U_o}{U_\infty} = \text{constant} \qquad\qquad 3\text{-}48$$

and
$$U_\infty \propto X^{\,m} \qquad\qquad 3\text{-}49$$

where

$$m = -\frac{\sqrt{2} + U_o/U_\infty}{3\sqrt{2} + 2\,U_o/U_\infty} \qquad\qquad 3\text{-}50$$

Measured velocity profiles of Fekete showed that self preservation was achieved. Velocity profiles were also calculated with the viscous program for a set of conditions identical to Fekete, namely for $U_o/U_\infty = 0.95$. Analytically predicted velocity profiles also had similarity and are shown in Figure 12 to be in good agreement with measured values.

Experimental values of the excess momentum were obtained by integrating Fekete's similarity solution for the jet velocity profiles. Computed values of the excess momentum were within six percent of the measured values. The computed jet spreading rate of 0.037 agreed favorably with the measured value of 0.036, and the computed gradient of the excess momentum was within 2% of the measured values. Since the turbulence constants were not adjusted, this is very good agreement.
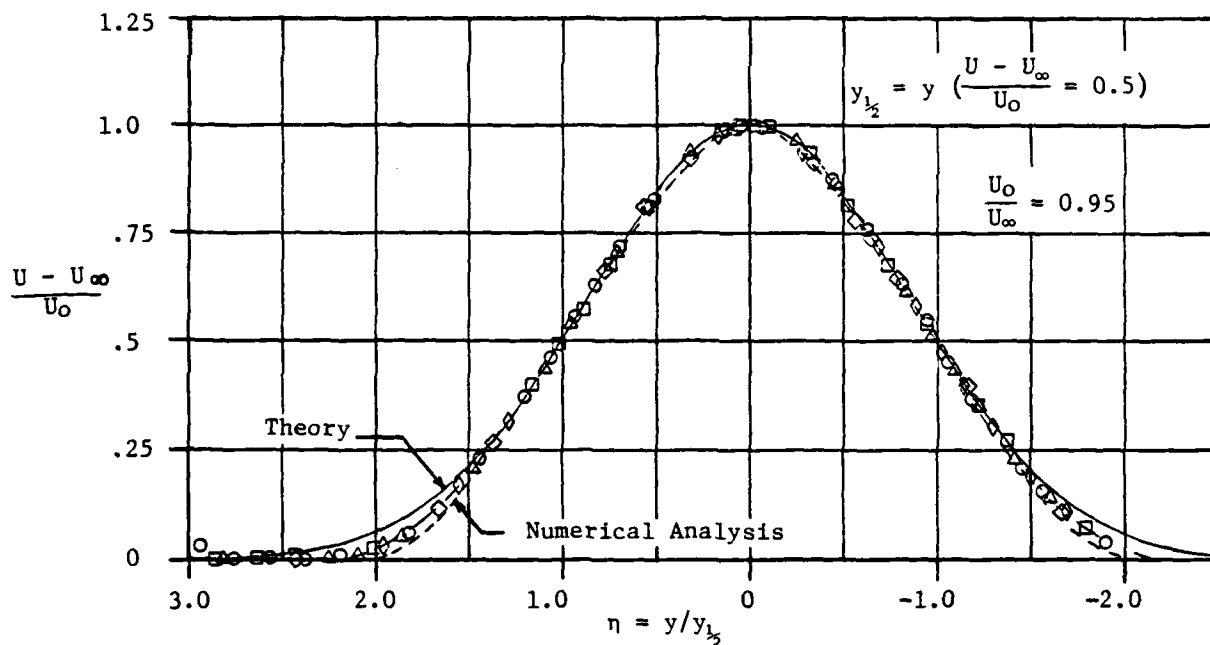
Figure 12. Comparison of Calculated and Measured Jet
Velocities

MATCHING PROCEDURE

The analysis of the jet flap is matched to the analysis of the
turbulent jet by iterating between solutions for the shape of the jet
flap and the variation of the jet thrust, as follows: for given dis-
tributions of jet thrust and sink strength, the inviscid jet flap
program yields an estimate of the jet shape. The curvature and pres-
sure distribution along the jet sheet then provides a set of boundary
conditions for calculating the jet thrust and sink strengths with the
turbulent mixing program. These solutions are iterated until the
computed reduction of jet thrust and the jet drag induced on the
airfoil converge to within acceptable limits.   The iterations are
started with a classical jet flap solution in which the thrust

39

of the jet is assumed to be constant, and the sink strengths are all
zero. Generally, three to four iterations are required to obtain con-
vergence.

The thrust and momentum of the jet are evaluated in the following
way: The net thrust on the airfoil can be calculated by integrating
the computed velocity profile at any point in the wake. For simplicity,
consider the case in which the jet is undeflected, as shown in Figure
13. If the upstream control surface is far enough away for the flow
across it to be undisturbed, the momentum equation yields:

$$T = \int_S (P + \rho U^2)dy - \int_1 (P_\infty + \rho U_\infty^2)dy \qquad 3\text{-}51$$

By factoring and recombining the terms, we get

$$T = \rho \int_{-\infty}^{+\infty} U(U - U_\infty)dy + \rho U_\infty \int_{-\infty}^{+\infty} (U - U_\infty)dy + \int_{-\infty}^{+\infty} (P - P_\infty)dy \qquad 3\text{-}52$$

The continuity equation expresses the fact that the difference in mass
flow between the upstream and downstream stations is equal to the mass
added by the jet; that is,

$$\rho \int_{-\infty}^{+\infty} (U - U_\infty)dy = \dot{m}_j \qquad 3\text{-}53$$

Substituting this relation into the momentum equation then yields the
following expression for the net thrust on the airfoil:

$$T = \dot{m}_j U_\infty + \rho \int_{-\infty}^{+\infty} U(U - U_\infty)dy + \int_{-\infty}^{+\infty} (P - P_\infty)dy \qquad 3\text{-}54$$
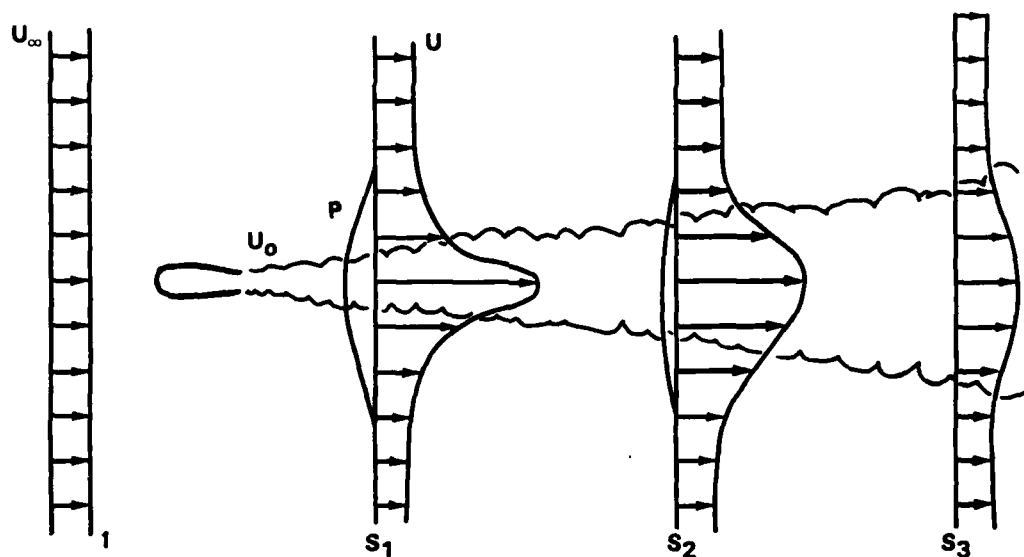
Figure 13.   Control Surfaces for Evaluating Jet Thrust

The first term is the source thrust generated by the added mass of the jet. For turbojet engines, which draw the initial mass of the jet from the atmosphere (except for a very small fuel fraction) the source thrust is negligably small. This term is also zero in a pure wake. On the other hand, for rocket engines, which generate the initial jet mass from internal fuel, this term is significant. It must also be included in evaluating the thrust of the jet flap model since the jet mass is added to the tunnel mass flow from inside the model. The second term is the integral of the excess momentum; it represents the part of the initial jet momentum which is greater than the displaced free stream momentum. In a pure wake, it would represent the drag of the body. The last term represents the pressure force due to the perturbations of the velocity field. Close to the model, this pressure term is siʒnificant. However, it vanishes at points far downstream. As it does, the excess momentum increases, because the net thrust is the same at every station behind *the model.*

The deflection of the jet flap is determined by the momentum flux of the jet, not the net thrust. Thus, the variation of the jet momentum flux,

$$T_M \equiv \dot{m}_j \, U_S + \rho \int_{-\infty}^{+\infty} U(U - U_S) dy \qquad \text{3-55}$$

is used in the inviscid program for calculating the jet shape. U_S is the velocity in the main stream on either side of the jet. An average of the values at the jet boundaries is used for the value of U_S within the jet. Outside the jet, where $U = U_S$, the integral vanishes. At downstram infinity, where $U_S = U_\infty$, the jet momentum flux does equal the net thrust of the jet.

The sink distribution represents the drag induced on the airfoil by the jet. In principle, the sinks can be determined from the streamwise variation of the excess mass within the jet (The variation of the excess mass must be used, rather than the total entrainment, because only the change in excess mass affects the flow outside the jet.) However, due to the arbitrary way in which the jet boundary is defined, it is more accurate to evaluate the sink strengths directly from the change in jet thrust.

The force on a section of the jet and the equal but opposite reaction on the airfoil are shown in Figure 14. The reaction force on the airfoil has two components: $\rho U_Q \Gamma$, a component due to the interaction between the sink and airfoil singularities, and $\rho U_\infty d\Gamma$, a component due to the change which the sink produces in the strength of the airfoil singularities. These are also shown in the figure. Since the horizontal force induced by the sink must equal the horizontal component of the thrust loss, an estimate of the sink strength at each point on the jet is obtained from the relation

42
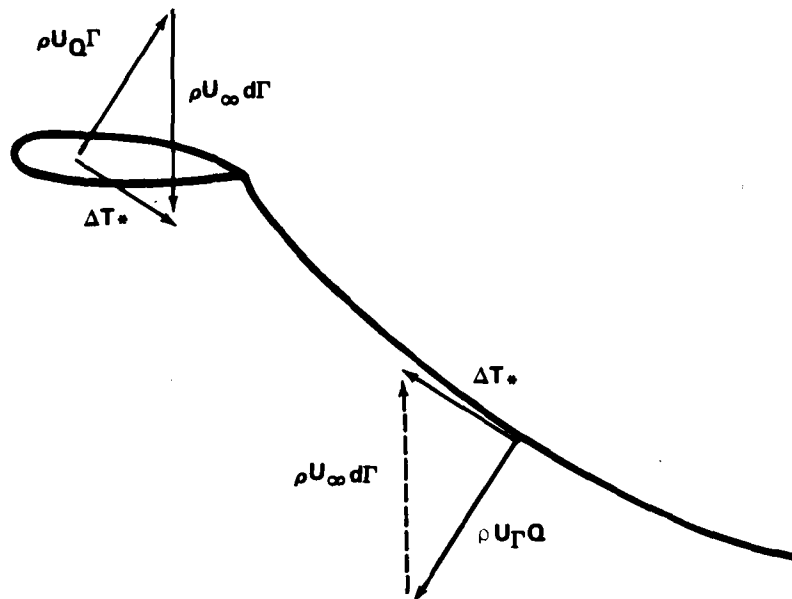
Figure 14. The Equal but Opposite Drag Forces on the Airfoil and Jet

$$\Delta T_* \cos \theta = \rho U_Q \Gamma \cos \lambda \qquad\qquad 3\text{-}56$$

in which ΔT_* is the local change in the actual thrust of the jet, and $\rho U_Q \Gamma \cos \lambda$ is the net horizontal force induced on all the other singularities by the sink. Alternately, the equal but opposite force induced on the sink by all the other singularities may be used on the right hand side. In the next inviscid calculation, the strength of the airfoil singularities are corrected to include the influence of the sink distribution. Therefore, when the iterations have converged, both components of the force on the airfoil are determined.

The local thrust of the jet, T_*, is defined to be the thrust obtained by an isentropic expansion (without additional mixing) of the local mass

43

of the jet to the pressure at infinity. It is necessary to use the local thrust for defining the sink strengths, rather than the local excess momentum because the excess momentum does not include the contribution of the pressure term to the jet thrust.

The local thrust of the jet is evaluated from the local jet velocities in the following way. The local thrust is defined as

$$T_* = \dot{m}_j U_\infty + \rho \int_{-\infty}^{+\infty} U_*(U_* - U_\infty) dy \qquad \text{3-57}$$

in which U_* prescribes the velocity distribution of the expanded jet. Since the expansion is assumed to occur without mixing, the continuity equation for each stream tube yields

$$\rho U_* dy_* = \rho U dy \qquad \text{3-58}$$

Thus, the local thrust can be written

$$T_{*\cdot} = \dot{m}_j U_\infty + \rho \int_{-\infty}^{+\infty} U(U_* - U_\infty) dy \qquad \text{3-59}$$

Then, since U_* is defined by Bernoulli's equation,

$$\frac{1}{2} \rho U_*^2 + P_\infty \equiv \frac{1}{2} \rho U^2 + P \qquad \text{3-60}$$

the local thrust can be expressed in terms of the local jet velocity distribution:

$$T_* = \dot{m}_j U_\infty + \rho \int_{-\infty}^{+\infty} U([U^2 + 2(P - P_\infty)/\rho]^{\frac{1}{2}} - U_\infty) dy \qquad \text{3-61}$$

In the irrotational flow on each side of the jet, $U = U_S$ and

$$2(P - P_\infty)/\rho = U_\infty^2 - U_S^2 \qquad \text{3-62}$$

44

(U_S has a different value on each side of the jet.) As a result, this
integral differs from zero only within the jet so that the local thrust
can be evaluated from the computed velocity profiles within the jet.

As a footnote to this discussion, Jones (Schlichting, ref 28) derived
Equation 3-61 for use in determining airfoil drag from a wake survey.
However, by expanding the radical in powers of $2\Delta P/\rho U^2$, it can be seen
that this equation does not give the drag (or thrust) on the airfoil:

$$T_* = \dot{m}_j U_\infty + \rho \int_{-\infty}^{+\infty} U(U - U_\infty)dy + \int_{-\infty}^{+\infty} (\Delta P - \frac{1}{2} \Delta P^2 + \ldots)dy \qquad 3\text{-}63$$

This series converges for $\Delta P < \rho U^2$, but is equal to the actual drag only
when $\Delta P << \rho U^2$. Thus, Jones' method does not yield the actual drag when
$\Delta P \sim \rho U^2$. His error was the assumption that evaluating U_* with Bernoulli's
equation gives the actual drag. To obtain the drag, U_* must be defined
from the drag equation

$$\rho \int_{-\infty}^{+\infty} U_*(U_* - U_\infty)dy_* \equiv \rho \int_{-\infty}^{+\infty} U(U - U_\infty)dy + \int_{-\infty}^{+\infty} \Delta Pdy \qquad 3\text{-}64$$

which yields

$$U_* \equiv U(1 + \Delta P/\rho U^2) \qquad 3\text{-}65$$

On the other hand, the integrand does not go to zero outside the jet with
this definition of U_*, so that there is no advantage over using Equation
3-54. We have therefore used the method of Betz (Schlichting, ref 28) to
measure the jet thrust in the experimental phase of this study.

Jet Drag of a Cylinder

In order to illustrate the results of this matching technique, the
jet drag induced on a cylinder has been calculated. A total of 36
vortex panels were used to represent the cylinder, and 100 sink panels
were used for the jet. The jet was considered to originate at the rear

stagnation point and trail straight back along the stagnation streamline.
A Reynolds number of Re = 500,000 and jet thrust coefficient of $C_\mu = 1$
were used. However, it was assumed that the viscous drag of the
cylinder was zero and that there was no separated wake.

A total of three iterations were required for convergence. In
Figure 15 the computed surface pressure distribution for this case is
compared to the computed distribution for the classical case without a
jet. It can be seen that the effect of the jet is to accelerate the
flow around the cylinder and reduce the base pressure. This produces
a net pressure drag of magnitude $D/T_j = .207$ on the cylinder.

The streamwise variation of the excess momentum in the jet is shown
in Figure 16. At downstream infinity, the excess momentum plus the
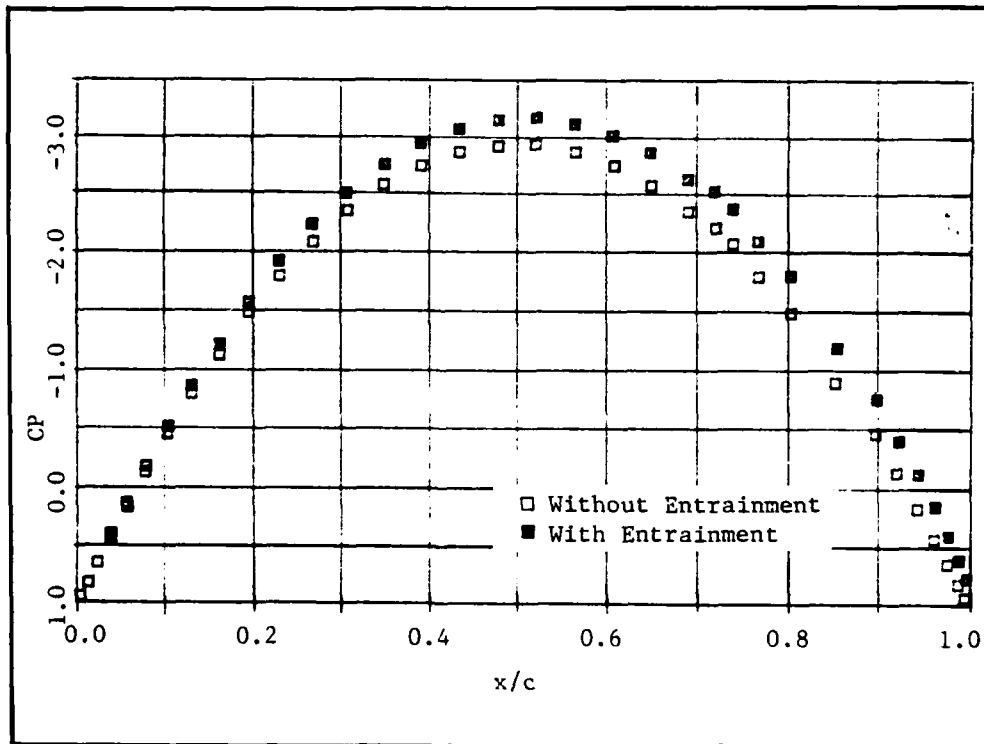
Figure 15.   Comparison of Cylinder Surface Pressure Distributions

46
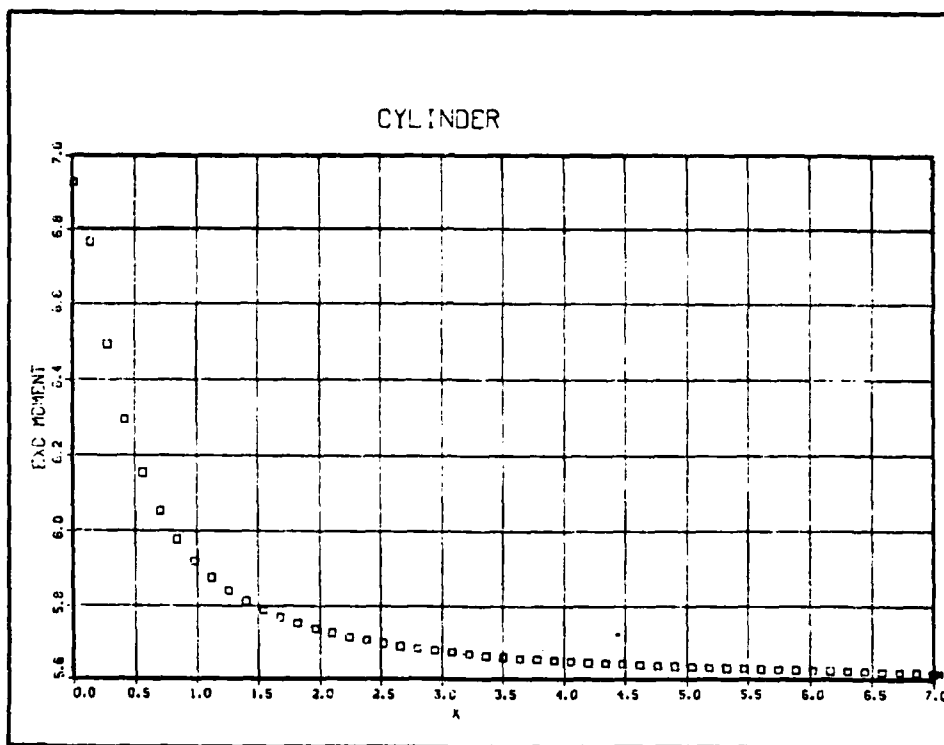
Figure 16.   Variation of Excess Momentum in the Jet

source thrust give the net force on the cylinder. By X/D = 7, the reduction in jet thrust is $\Delta T/T_j$ = .189. Considering the difficulty in accurately determining the drag from surface pressure integrations, this was felt to be good agreement, and additional iterations were not performed. A solution was also attempted using the sink strengths given by the total jet entrainment, but the jet drag on the cylinder approached a value near D/T_j = 0.5, which was roughly twice the change in jet thrust.

47

IV. EXPERIMENTAL METHODS

WIND TUNNEL FACILITY

Tunnel Description

The wind tunnel in which the jet flap model was tested is a two-dimensional tunnel designed especially for powered lift testing. A photograph of this tunnel is shown in Figure 17. The tunnel is an open circuit return type driven by a downstream multi-tube ejector.

The test section is 51 cm wide and 366 cm high. With the 20 cm chord model of this test, the height-to-chord ratio for this tunnel is 18.0. This ratio minimizes wall effects and allows sufficient space for the jet to develop downstream for the large jet deflections and momentum coefficients tested. For example, with $C_\mu \sim 50°$, the velocity overspeed is estimated to be $1.001\ U_\infty$. The test section extends approximately 8 chord lengths (158 cm) upstream and 12 chord lengths (23 cm) downstream of the model quarter chord. A smooth entrance to the test section is provided by a 61 cm long elliptical bellmouth. The vertical walls of the tunnel diverge from 51 cm apart at the downstream end of the bellmouth to 55 cm apart at the tunnel exit to allow for wall boundary layer growth. The model was mounted in the test section 213 cm above the tunnel floor. The tunnel was constructed of plywood and lumber.

A multi-tube ejector was located at the downstream end of the test section to power the tunnel. The ejector primary nozzle arrangement consisted of 304 separate .457 cm I.D. nozzles uniformly spaced in the ejector plane. These nozzles were fed by two 10 cm diameter steel plenums, located outside the tunnel, one on either side. The ejector gives an entrained to primary mass flow ratio of 20. With the air

48

Figure 17.   Two-Dimensional Wind Tunnel

49

supply available for this test, the maximum tunnel speed was approximately 24 meters per second.

The model was mounted in aluminum plates set flush in the tunnel's wooden walls. These plates contained circular insets which allow the model to be rotated to angles of attack between -10 and +20 degrees. Windows were provided in the inserts to review the model during testing. A photograph of the aluminum plates is shown in Figure 18.
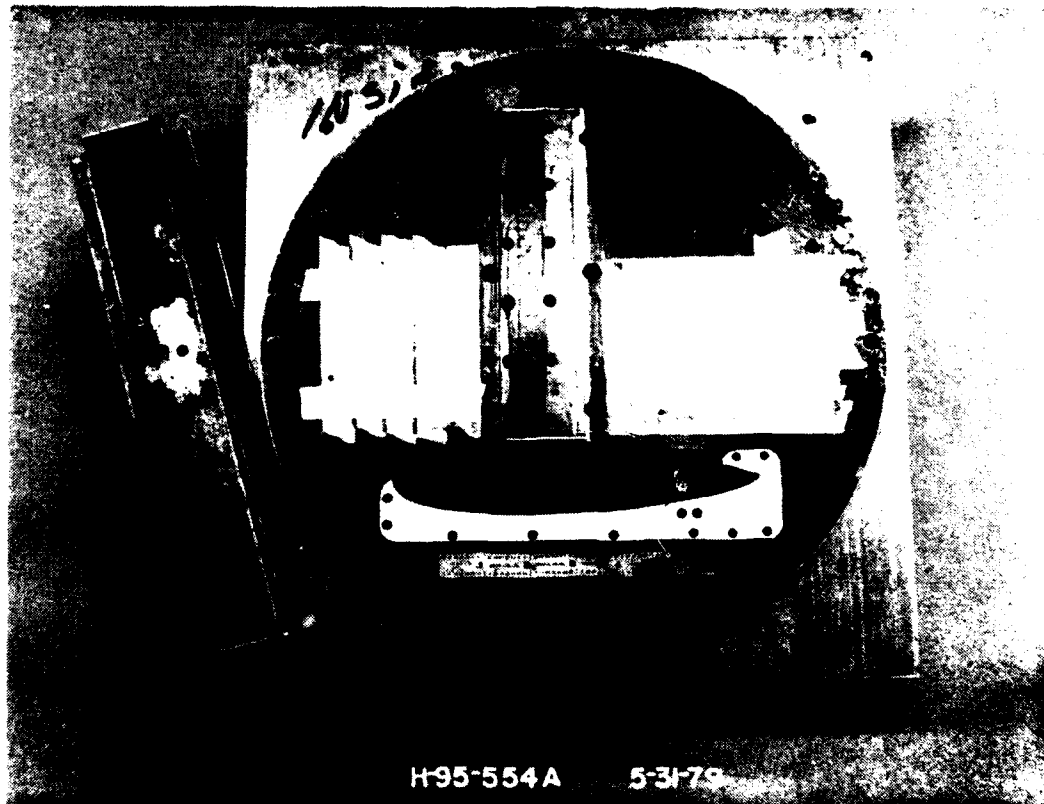
Figure 18. Airfoil Model Endplates

50

Two boundary layer blowers were mounted on each test section side-wall. A 30 cm long BLC blower was located 7.6 cm upstream of the model leading edge and was set at an angle of 15 degrees from the vertical. A 15 cm long blower was attached to the model mount inserts, with the nozzle located at the midchord blowing parallel to the chordline. All four blowers were fed from a common supply line and operated at the same supply pressure. The blower nozzle gaps were set to .100 cm.

Tunnel Calibration

Calibration of the wind tunnel test section was performed in two steps. The first stage was to adjust the vertical wall divergence to obtain a constant static pressure distribution along the entire length of the test section. Then the total and static pressure distributions in the area where the model would be located were surveyed. This survey data was used to generate a calibration curve of test section conditions versus a measured sidewall surface static pressure. The results of the calibration procedures are discussed below.

A 5 cm diameter pipe containing static pressure taps every 15.25 cm was mounted equidistant between the tunnel walls and 213 cm above the tunnel floor (at the future model chord line). The first static tap was at the downstream end of the bellmouth at the inlet. The tunnel walls were set with a total of 3.8 cm divergence in width (51 cm at the entrance, 55 cm at the exit). Longitudinal static pressure distributions were measured for a range of tunnel speeds. These showed no systematic variations.

The total and static pressure distributions in the region of the model locations were measured in the second phase of the tunnel calibration. A rake consisting of 10 total pressure tubes mounted 5 cm apart and 6 static pressure tubes mounted 5 cm above the total pressure tubes was used. The rake data were taken from 30 cm above the model location to 40 cm below the model location at 5 cm intervals. The resulting pressure data are shown in Figure 19.

The tunnel sidewall static pressure was measured at taps on each sidewall approximately 10 cm downstream of the bellmouth and 2.3 cm above the tunnel floor (on the model chord line). This sidewall static pressure was measured at each tunnel set condition at which the test section pressure distributions were taken. These data were used to generate the tunnel speed calibration factor which relates the tunnel dynamic pressure to the sidewall static pressure drop below atmospheric pressure. This calibration gave

$$q = 1.03 \ (P_q - P_s) \qquad\qquad 4\text{-}1$$
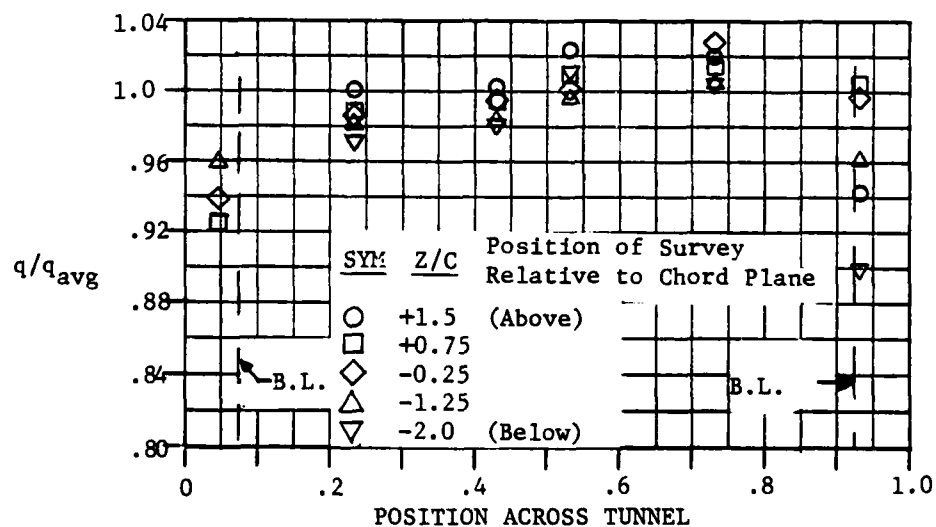
Figure 19. Dynamic Pressure Distribution At Model Location

52

AIRFOIL MODEL

Model Description

The airfoil model had a thickness to chord ratio of 0.20 and was symmetrical except in the area of the blowing slot and upper flap contour. The model chord was 20 cm and the installed model span was 51 cm. A sketch of the model cross section is shown in Figure 20 and a photograph is shown in Figure 21.
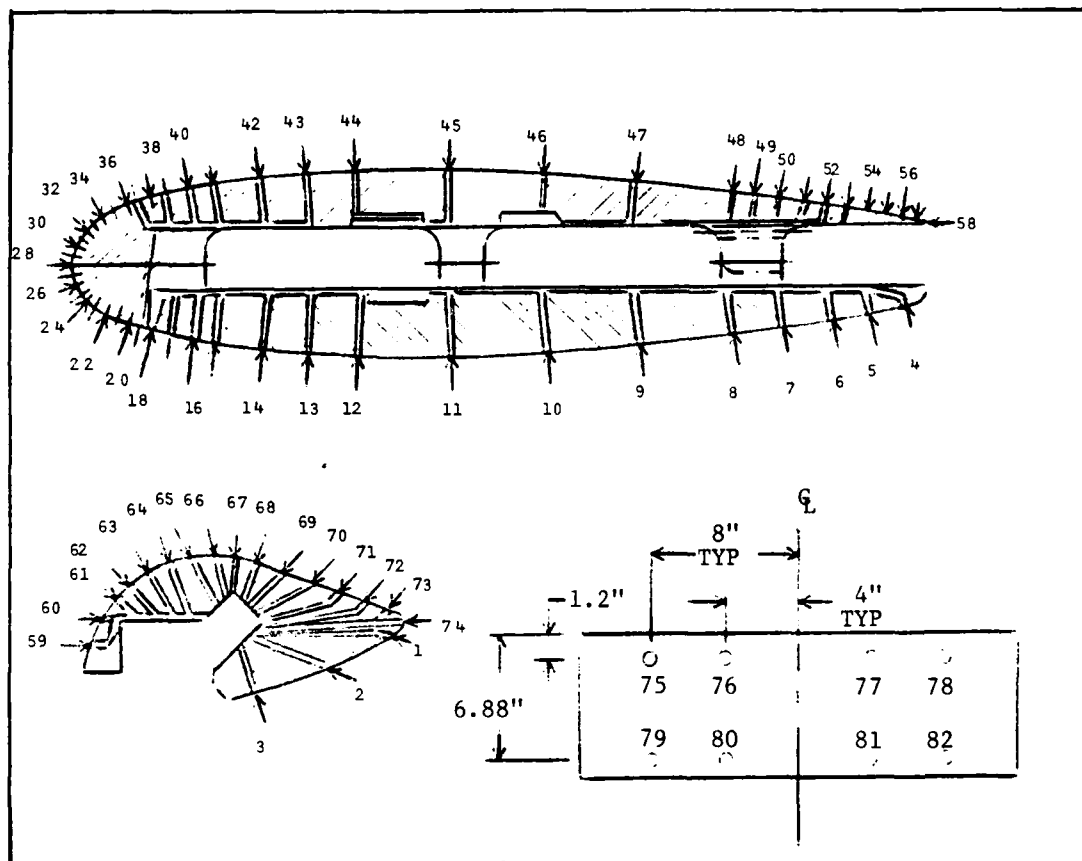
Figure 20. Location of Pressure Taps on Airfoil Model

53

Figure 21. Airfoil Model Mounted on Wind Tunnel Balance

Forward of the maximum thickness ordinate (X/C = 0.4), the model
contour is described by an ellipse which gave an effective leading edge
radius of approximately 5.5% of the chord. Aft of the maximum thickness,
a different ellipse was used to describe the contour. The jet blowing
slot was located on the upper surface at X/C = 0.9. The upper nozzle lip
had a thickness equal 0.005% of the model chord. The 10% chord flap had
a circular Coanda turning surface with a radius equal to 1.4 cm which was
tangent to the flat upper surface trailing edge at X/C = 0.93. The airfoil
trailing edge was slightly blunt, with a thickness equal 0.01% of the air-
foil chord. The lower surface trailing edge was modified slightly from the
ellipse to give a sharp edge at the trailing edge. The model was con-
structed of aluminum. Model contours in the center 5 cm of span were held
to ±.005 cm.

The model flap was attached to the forward portion of the model with
one of five separate flap brackets. These brackets were attached inter-
nally, and did not break the airfoil mold line. The flap could be
mounted at angles of 0°, 10°, 30°, 50°, and 70° relative to the airfoil chord
plane. The flap upper surface made an angle of 20° relative to the chord.
Thus, the flap surface and hence the nominal jet deflection angle could
be set to 20°, 30°, 50°, 70°, and 90° relative to the airfoil chord. The
effective flap pivot point is at X/C = .9 Y/C = 0.05.

The total span of the constant model cross section was 61 cm. The
model therefore pierced the tunnel walls and the nozzle gap was plugged
to the correct tunnel span of 51 cm. The nozzle plugs installed at each
end were given a bellmouth shape in the planform to maintain a constant
nozzle total pressure distribution up to the wind tunnel walls.

A large portion of the model interior was open and acted as the
nozzle feed plenum. The flow passage from the plenum to the nozzle
convergence was designed with two 90° turns with flow areas approximately
twice the nozzle area. This was done to improve the spanwise jet total

pressure distribution. The convergence to the nozzle exit was formed by a flat upper surface and the circular extension of the Coanda surface. The flap brackets were designed such that the nozzle convergence was the same for all flap settings. The nozzle exit was located at 90% chord and designed to have the jet exit parallel to the airfoil chord. Ambient temperature compressed air was supplied to the model through steel endplates to which were welded 10 cm pipe fittings. A portion of the right steel endplate could be removed to ease flap changes. Sealing of all mating surfaces was provided by O-rings.

The model was instrumented with a total of 82 pressure taps. Seventy-four taps were arranged in a streamwise row on the airfoil and flap at mid-span. Of these, two taps were located on the blunt, aft facing surfaces, the nozzle lip, and the flap trailing edge. An additional eight pressure taps were arranged in two spanwise rows to monitor test two-dimensionality. Figure 20 shows the location of all of the pressure taps.

Model Calibration

The model's jet nozzle pressure distribution and actual jet reaction force and angle were calibrated prior to installation in the two-dimensional tunnel.

The nozzle was plugged to the correct span as discussed in the model description section. The model was then mounted on the six component pyramidal balance located in the low speed wind tunnel at Rockwell International's Columbus Plant. The air supply plumbing to the model closely matched that to be used in the 2-D tunnel installation. A venturi and associated instrumentation were installed in the air supply line. A pressure tap in one of the steel model end fittings was used as the calibration reference pressure. One objective of the calibration was to generate a curve relating this reference pressure to the nozzle exit total pressure.

56

Nozzle exit total pressure distributions were measured at each flap
angle for a range of pressure ratios from 1.1 to 2.2. These distributions
were quite uniform. At each test condition, the model plenum reference
pressure was recorded. These data were then used throughout the test to
compute exit total pressure.

For each flap angle, a set of force data were taken over a pressure
ratio range of 1.1 to 2.1. The resultant thrust angle was computed from
the model lift and drag forces and this is shown in Figure 22. Model
isentropic thrust was calculated from the venturi measured mass flow and
the nozzle isentropic velocity. The isentropic velocity was computed
assuming an expansion from the nozzle total pressure (obtained from the
calibration curve) to the ambient pressure. Jet temperature was measured
at the venturi as experience has shown this to be within a few degrees
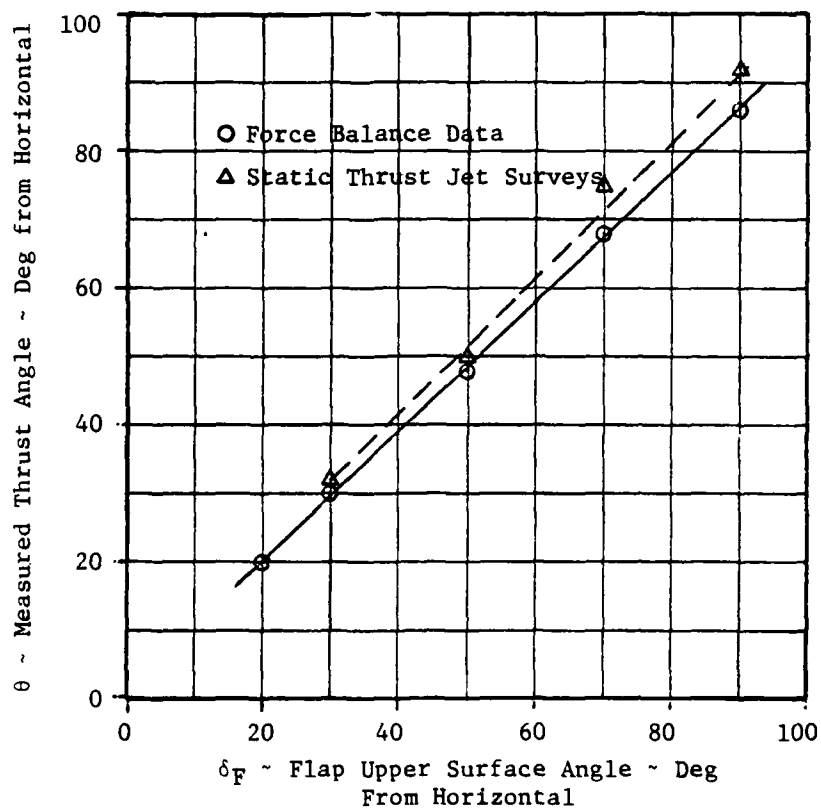
Figure 22. Comparison of Balance and Survey Measured Thrust Angles

Rankine of the temperature at the nozzle exit. Figure 23 shows the variation of the ratio of the actual thrust to the isentropic thrust as a function of the model flap angle.
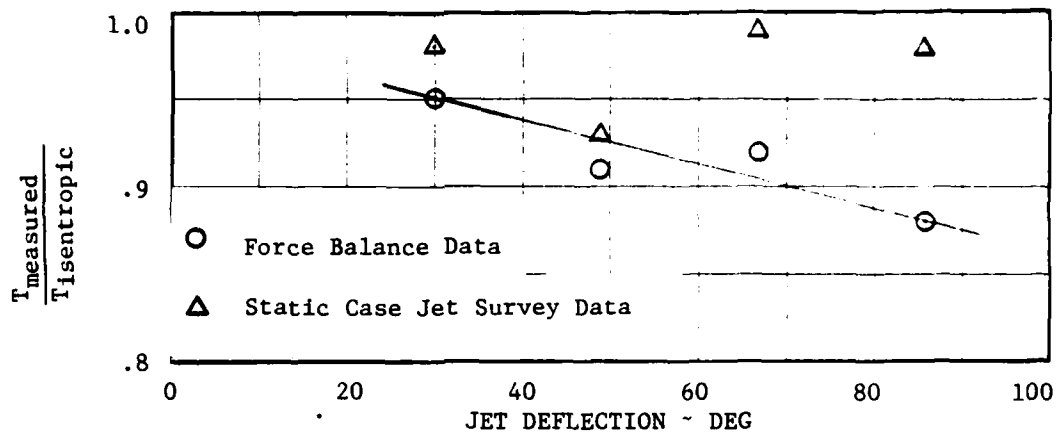
Figure 23. Jet Flap Nozzle Thrust Calibration

INSTRUMENTATION AND EQUIPMENT

Survey Probe

Downstream jet/wake surveys were made using a United Sensor
three-dimensional directional flow probe, type DC-125. This probe has
a stepped conical sensing head with one pressure tap at its center and
four taps located on the conical surface. This probe was calibrated as
described below to accurately measure total and static pressure and
flow angle over a flow angle range of ±50 degrees in pitch and ±20 degrees
in yaw. A photograph of this probe is shown in Figure 24.

Figure 24. Five Port Directional Flow Probe

The probe was calibrated by testing it in a jet of air of known
total and static pressure and flow direction. Data were taken at a
matrix of probe angles of ± 50 degrees in pitch and ± 20 degrees in yaw,
in 5° increments. At each position, the five separate probe pressures
were recorded. These data were repeated in calibration jets of 2.6,
5.2, and 7.75 cm Hg gage total pressure. At each point, the following
calibration constants were calculated:

$$KP = \frac{P5-P1}{P5-P3} - 1 \quad (+ \text{ Pitch, i.e., } P1 < P3)$$

$$= \frac{P3-P5}{P5-P1} + 1 \quad (- \text{ Pitch, i.e., } P1 > P3)$$

$$KY = \frac{P5-P4}{P5-P2} - 1 \quad (+ \text{ Yaw, i.e., } P4 > P2)$$

$$= \frac{P2-P5}{P5-P4} + 1 \quad (- \text{ Yaw, i.e., } P4 < P2)$$

$$KPT = \frac{P5-PT}{PT-PS} \quad \begin{array}{l} (PT = \text{jet total pressure} \\ PS = \text{jet static pressure}) \end{array}$$

$$KPS = \frac{P5 \dfrac{-P1+P2+P3+P4}{4}}{PT-PS}$$

These data are then used to generate calibration matrices for pitch
angle (function of KP and KY), yaw angle (function of KP and KY), total
pressure factor (KPT as function of pitch and yaw angle), and static
pressure factor (KPS as function of pitch and yaw angle).

In an unknown flow field, the five probe pressures are measured, and
used to compute KP and KY. These values are used as the independent
variables in two dimensional interpolations in the calibration matrices
to give the pitch and yaw angles of the flow. These two angles are then
used as the independent variables in two dimensional interpolations to
give the flow's total and static pressure factors, KPT and KPS. These
factors and the five probe pressures are used to compute the unknown
flow's total and static pressure.

60

The four required calibration matrices were generated using the data taken in the 7.75 cm Hg total pressure jet. The calibration was then checked by using the calibration to reduce the data taken at the other two jet pressures. Flow angles were generally good to ±2 degrees. Total static pressures were within ±.05 cm Hg.

During the test, the 3-D probe was mounted on a traversing rig attached to the tunnel sidewall. This rig consisted of two support rails and a motorized screw jack which could position the probe support arm anywhere along 76 cm travel. The motor was under either manual or computer control as discussed in the test procedure section. The traversing rig could be bolted to the tunnel wall at any location. The probe could be positioned at any spanwise location and at eight discrete downstream locations for any rig position.

Instrumentation

The following data channels were used during the 2-D wind tunnel test:

- Wind tunnel sidewall static pressure
- Model plenum calibration pressure
- Model air supply venturi upstream pressure
- Model air supply venturi differential pressure
- Model air supply venturi temperature
- Model surface pressures - 5 module scanivalve
- Jet/wake 3-D survey probe - 5 low range and 5 high range transducers
- Jet/wake 3-D survey probe traversing rig position
- Two-dimensional wind tunnel ejector supply pressure
- Test section sidewall boundary layer control blower plenum pressure

All transducers were calibrated prior to the first test series and were recalibrated prior to the second test series.

All instrumentation output signals w re amplified and filtered before
going to the multiplexed analog to digital converter in the IBM 1800 data
acquisition computer. Readings were then converted to engineering units
and preliminary integrations of lift (from surface pressures) and drag
(from both wake data and surface pressures) were performed.

The model surface pressures were assigned to the various Scanivalve
modules on the basis of expected maximum pressures. Each Scanivalve module
had the transducer reference pressure (the tunnel sidewall pressure) con-
nected to the first and last ports. Each model pressure connected to the
two low range (± 1 cm Hg max. input) modules was connected to two consecu-
tive scanivalve ports. This was done to give an effective settling time
of twice the normal settling time which was two seconds.

The data acquisition program was written to read every other port on
these two modules. The maximum number of ports read was set by the
higher range modules which then allowed this technique to be used.

The 3-D wake probe was required to measure the flow properties in both
the low total pressure tunnel airflow and the higher total pressure jet
sheet. To improve the accuracy of the readings in the low pressure flow,
the following scheme was used. Each of the five probe pressures were
routed to two transducers, one set for approximately .775 cm Hg maximum
input (data system saturation limit) and the other set for approximately
26 cm Hg max input. A pressure relief valve was installed in the tube
leading to the low pressure transducer. This valve was set to shut off
this pressure line at about 1.5 cm Hg, well below the 2.5 cm Hg trans-
ducer physical limit. With this setup, in the low pressure tunnel flow,
each pressure was read on two transducers, and the data reduction program
used the output from the lower range transducer. As a probe entered the
jet, the low range transducer data channel reached saturation, but the
relief valve protected the transducer from over pressure damage. The
data reduction program recognized this saturation value and instead used

62

the high range transducer output for calculations. As the probe emerged from the jet, the relief valve reopened, the low range transducer fell below saturation, and its more accurate output was again used for that pressure. The over-lapping ranges of transducer electrical saturation, relief valve operation, and transducer physical pressure limits allowed the scheme to work well in the region of large pressure fluctuations at the edge of the jet.

TEST PROCEDURES

Data Acquisition

The major problem with two-dimensional testing is the effect of the
sidewall boundary layer. The sectional wing lift is reduced in the wall
boundary layer which gives rise to three-dimensionality and the associated
induced drag. A more serious effect may occur when the wall boundary layer
is forced to separate by the adverse pressure gradients on the model. The
strength of these adverse gradients is significantly increased by the
large lifts generated by a jet flap device.

There are several ways to mount a two-dimensional model on a balance,
but each has significant problems for this particular test. If the entire
model is metric (on the balance), with or without a portion of the sidewalls,
the measured loads will include the non-uniform load near the walls due to
the boundary layer. In this case, a decision must also be made whether or
not to attach a portion of the walls to the model. In the first case, the
tip sealing problem is alleviated, but the forces on the endplates must be
accounted for. In the second case, a force free seal must be made at the
model tip/wall juncture.

A second approach is to mount only a center span portion of the model
on the balance. This eliminates the direct force effects of the tip
loading, but again introduces joints and seals, near the region of
interest. This approach is substantially complicated on a jet flap
model by the need to segment the nozzle.

Any balance installation on a jet powered model faces the problem
of bridging the balance with the air supply pipes. This problem has
been successfully solved many times in the past. But each installation
is generally unique and there is usually a development phase before a

64

useable set-up is obtained. In any case, the balance must be calibrated
with the air supply system installed and pressure effects must be con-
sidered. All these effects reduce the two-dimensionality of the pressure
distributions and measured forces.

In view of the above complications, the decision was made to obtain
lift from airfoil surface pressures and drag from wake surveys.
Integration of the drag component of the surface pressures was also per-
formed as a secondary drag calculation. Use of this technique also
provides information on the qualitative nature of the flow.

Each run during these tests acquired data for one test condition
(angle of attack, jet deflection, and momentum coefficient). Model angle
of attack was set by rotating the circular wall inserts. The wake probe
traversing rig was positioned such that the probe would pass the desired
distance downstream of the model (approximately 15 cm). The rig tilt
angle was set such that the expected flow angles would be within the
probe's acceptance limits (±50 degrees from the probe axis). The desired
tunnel speed was set by adjusting a pressure regulating valve while moni-
toring the sidewall static pressure displayed on a digital voltmeter (DVM).
Model thrust was set by operating a pressure control valve to achieve the
precomputed model plenum reference pressure also displayed on a DVM.
Sidewall BLC operating pressure was set in the same way as the model
pressure. Proper set pressures were determined by observing tufts
attached on the sidewall and model upper surface and by monitoring the
model spanwise row of pressure taps.

With the desired test conditions set, data acquisition was under
computer control. Model and tunnel operating conditions were read
followed by the scanivalve data. The computer then commanded the tra-
versing rig travel based on a predetermined number of datapoints and
desired distance between points. Different numbers of points and point
spacing could be requested in each of three survey regions (nominally
above the jet, in the jet, and below the jet). After each step of probe
travel, a pressure setting time of two seconds was allowed before data
were acquired.

For each channel of data acquired, the computer took ten readings over a 1/2 second period. These readings were averaged and this average was stored for later conversion to engineering units.

Each run required approximately 15 minutes and required about 190 wake probe positions. Test conditions were held constant during this time by two technicians. The test engineer was able to monitor these conditions and progress of the test from the data acquisition system.

Two test series were run several months apart. The objective of the first series was to obtain lift and drag data for jet deflection angles of 30°, 50°, 70°, 90°, and momentum coefficients between 0.5 and 24.0. The objective of the second test was to survey the jet at five downstream locations for a range of test conditions to quantify the jet thrust and mass flow changes as the jet develops downstream.

Data Reduction Procedures

The following section discusses the data reduction procedures for the wind tunnel and model operating conditions, airfoil surface pressure lift and drag integrations, wake drag integration, and jet profile thrust and mass flow integrations.

The wind tunnel operating conditions are computed from the measured sidewall static pressure and ambient pressure and temperature. Because of the suck down type tunnel design, the test section total pressure is equal to the ambient pressure; this was confirmed by the test section calibration.

$$P_{T_{Test Section}} = P_{ambient}$$

This calibration provided the following relationship between the sidewall static pressure and the calibrated test section uncorrected dynamic pressure.

$$q_{test section uncorrected} = 1.03 \times (P_{sidewall} - P_{ambient})$$

66

A solid blockage correction was included to give the corrected test section dynamic pressure.

$$q_{test\ section} = q_{uncorrected}\ (1.0 + .0006)^2$$

Test section static pressure is then:

$$P_{test\ section} - P_{T_{TS}} - q_{TS}$$

Test section Mach number

$$M_{TS} = \sqrt{\left[\left(\frac{P_T}{P}\right)^{.28571} - 1\right] \times 5} \qquad 4-2$$

Model Reynold's number (based on model chord):

$$R_n = 10^6\ (1.798)\ q_{TS}\ \left[\frac{1+.2M^2}{M}\right]\left[\frac{T_{TS} + 1.986\ (1+.2M^2)}{T_{TS}^2}\right] \qquad 4-3$$

Where T_{TS} is ambient temperature.

The model jet isentropic thrust was computed from venturi measured mass flow and jet isentropic velocity. The venturi data ($P_{upstream}$, $P_{differential}$, and Temperature) were reduced to a mass flow using standard computations. Isentropic velocity was computed as follows:

The nozzle exit total pressure was obtained from the model plenum calibration pressure and the calibration. The jet temperature was assumed to be equal to the measured venturi temperature as discussed earlier. The isentropic velocity is then calculated assuming isentropic expansion from the nozzle total pressure to the test section static pressure.

$$V_{isen} = \sqrt{\gamma \cdot R \cdot T_v}\ \sqrt{5.\left[1 - \frac{P_{Test\ Section}}{P_{T_{nozzle}}}\right]^{.28571}} \qquad 4-4$$

Where γ is the ratio of specific heats and R is the universal gas constant.

67

The model jet Mach number was computed:

$$M_j = \sqrt{5 \times \left[\left(\frac{P_{T_{nozzle}}}{P_{Test\ Section}}\right)^{.28571} - 1\right]} \qquad 4\text{-}5$$

$(M_J \leq 1.0)$

and used in the calculation of a theoretical mass flow:

$$\dot{m} = \sqrt{\frac{\gamma}{RT_v}} \left[\frac{A_{nozzle} \cdot {}^{P_{T_{nozzle}}} \cdot M_j}{(1.0 + .2M_j^2)3}\right] \qquad 4\text{-}6$$

Comparing the theoretical and venturi measured mass flows gave a further check on instrumentation and test setup.

The model momentum coefficient is then defined:

$$C_\mu = \frac{M_{venturi} \cdot V_{isen}}{q_{TS} \cdot S_{ref}} \qquad 4\text{-}7$$

The pressure coefficients were then integrated as functions of their X/C and Y/C locations to give lift and drag force coefficients, respectively.

Each integration was performed piecewise over surface of the airfoil.

A complete set of plotted airfoil pressure coefficient data from the first test series (Test 272) is included in Appendix I.

Each of the wake/jet sheet surveys from both test series has been integrated to give an airfoil drag coefficient. This integration was performed using the method of Betz, (Schlichting, ref 28), modified to include the effect of the large flow deflection angle. Direct application of the Betz method of wake survey integration does not give the correct value of drag, if the survey is made before the jet has completely turned

to the free stream direction. In that case, there is a static pressure
difference which makes a contribution to the horizontal force. This con-
tribution must be equal to the difference between the horizontal component
of the local jet thrust and the thrust of the completely deflected jet.
Since the jet approaches the free stream direction asymptotically, the
actual thrust can, in principle, only be determined from a jet survey at
downstream infinity, or from a survey which extends to infinity above and
below the jet. However, if the jet is nearly parallel to the free stream,
the tangential component of the jet thrust is equal to the value recovered
at infinity, within experimental error. This will be seen in the analytic
results. Thus, the measured tangential thrust was used to determine the
thrust recovery.

V. RESULTS AND DISCUSSION

SURFACE PRESSURE DISTRIBUTIONS

   The character of the measured surface pressure distributions changes
as the jet thrust coefficient and deflection angle are increased. For
low thrust coefficients (C_μ < 1) and small deflection angles (θ = 30°),
the pressure distributions have a saddle shape, typical of that predicted
by classical, inviscid jet flap theory. A representative case is shown in
Figure 25. The saddle shape is due to the suctions peaks at the leading
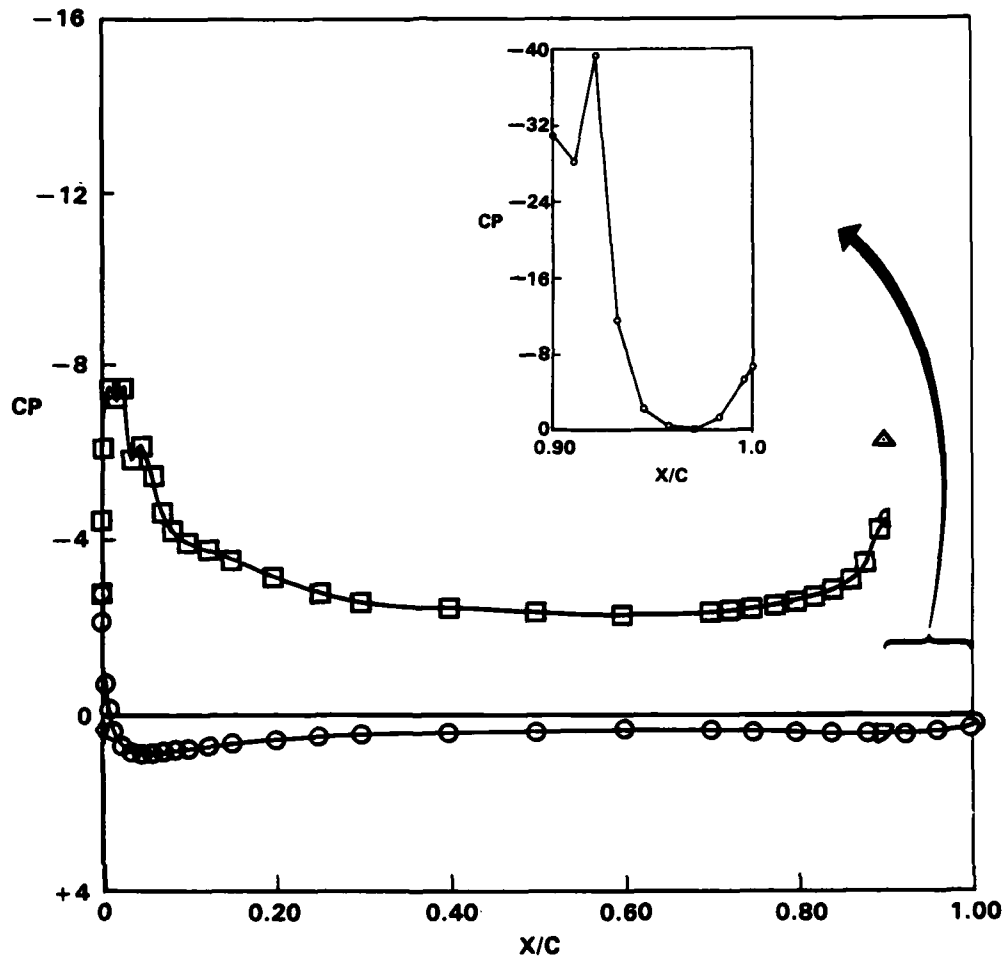
Figure 25.   Surface Pressure Distribution for Attached Flow, C_μ = 2, θ_0 = 30°

edge of the airfoil and the knee of the flap. The pressure is further
reduced on the upper surface of the flap by the suction which deflects
the jet over the Coanda surface. Since the radial pressure gradient
balances the inertia of the jet, the reduction in flap surface pressure
is given by

$$\Delta C_p = C_\mu c/R \qquad\qquad 5\text{-}1$$

The sudden pressure rise at the point where the surface of the flap changes
from a circular arc to a straight section causes a separation bubble to
develop; the suction peak near the nozzle exit is due to this bubble. The
smaller rise at the trailing edge of the flap is due to the jet flap effect:
The jet leaves the airfoil along a tangent to the upper surface of the flap,
and therefore deflects the trailing edge streamline relative to the mean
line of the airfoil. This produces a suction peak similar to the one which
occurs at the knee of a flap.

For moderate values of the thrust coefficient ($2 < C_\mu < 8$) and deflection
angles ($\theta = 30°$, $50°$), a separation bubble appears on the upper surface of
the airfoil. The flow separates from the leading edge of the airfoil and
reattaches at some point on the upper surface. In this case, the pressure
is nearly constant over the front of the airfoil, but returns to the ideal
saddle shape over the rear section. A typical example is shown in Figure
26.

For large values of the thrust coefficient ($C_\mu > 8$) and large deflection
angles ($\theta > 50°$) the separation bubble does not reattach to the surface of
the airfoil. In this case, the pressure distribution is flat or even
slightly arched, as seen in Figure 27. Since the combined effect of the
jet and flap accelerates the flow over the unblown section at the rear of
the airfoil, trailing edge separation did not occur for any case tested.
The complete set of surface pressure distributions may be found in
Appendix I.

71
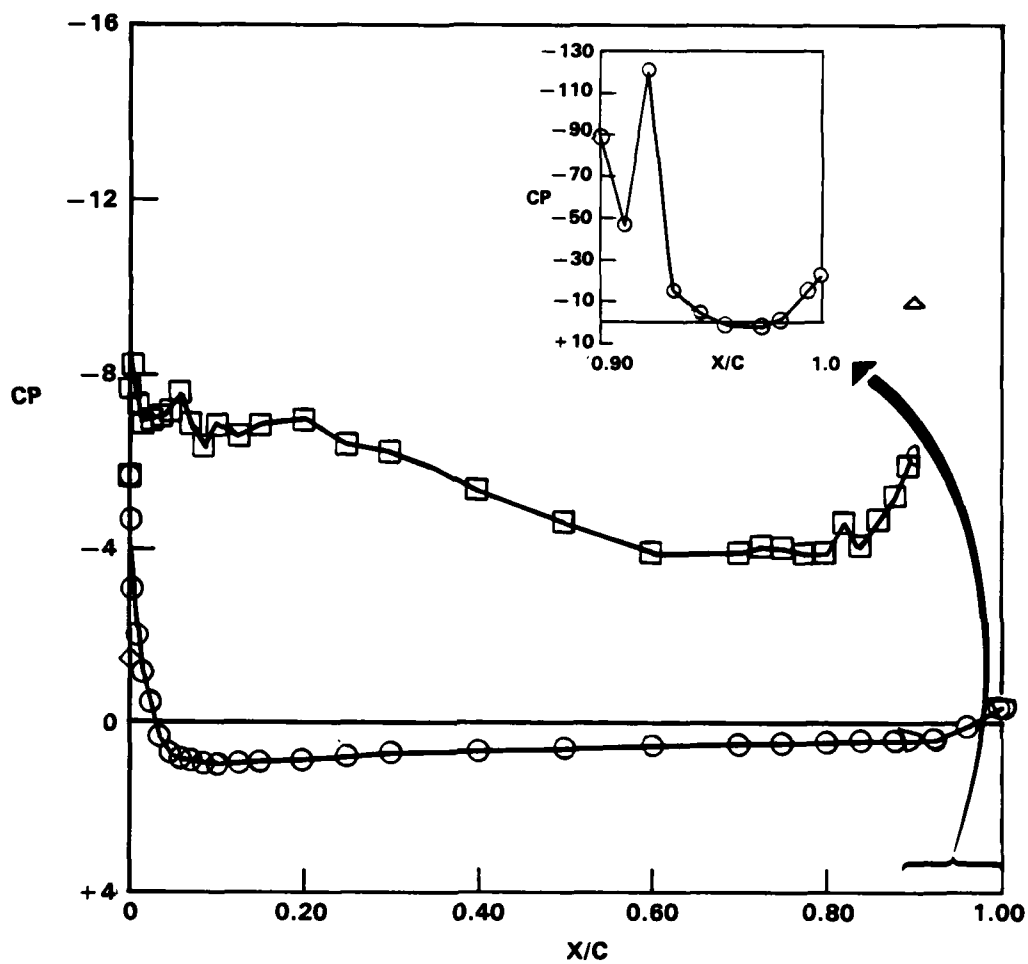
Figure 26.   Surface Pressure Distribution for Leading Edge
Separation, $C_\mu = 6$, $\theta_o = 30°$

72
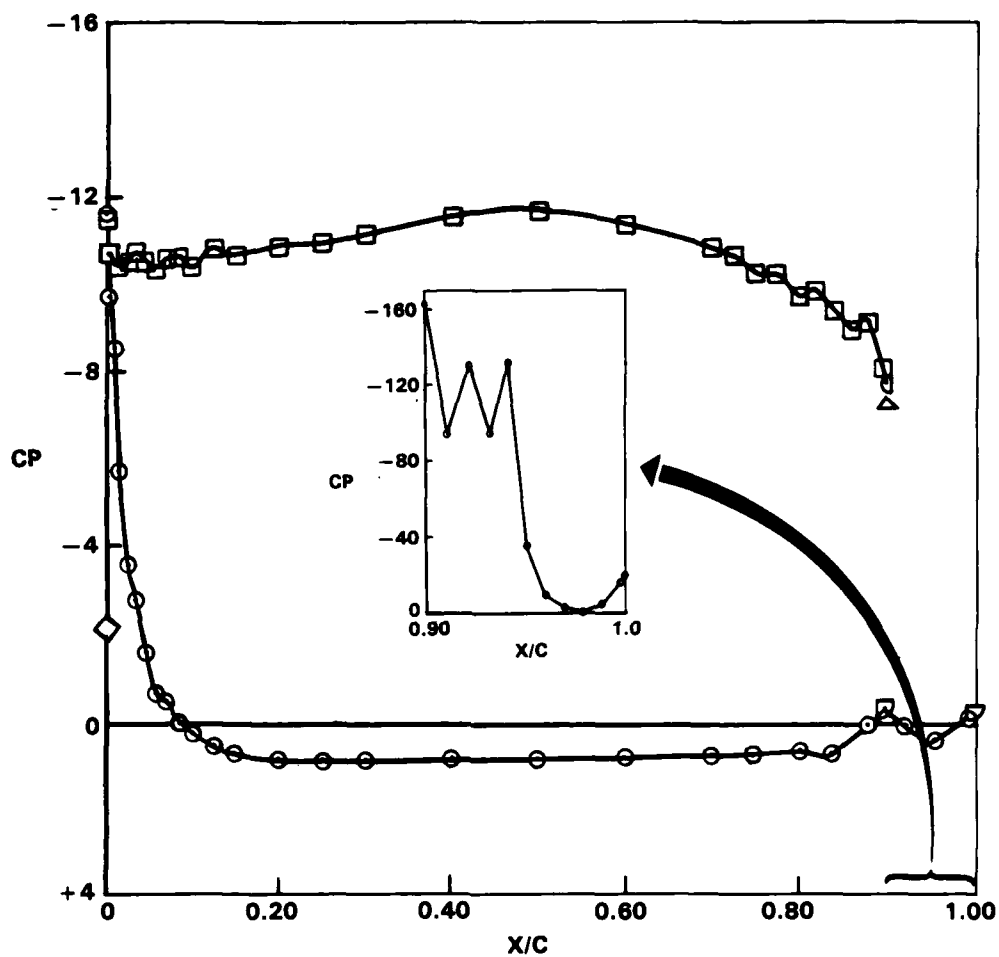
Figure 27. Surface Pressure Distribution for Upper Surface Separation, $C_\mu = 8$, $\theta_o = 50°$

WAKE PRESSURE DISTRIBUTIONS

Distributions of the total and static pressure, as well as the flow
angularity, were obtained in the near wake. The trend of the wake data
was consistent with the surface pressure distributions. A representative
set of pressure profiles for the case in which the flow did not separate
from the airfoil is shown in Figure 28. The total pressure profile has
the classical bell shape, and the static pressure is less above the jet
than below it. In Spence's (ref 10) theory, this pressure jump is
represented by the vortex sheet. The reduction in static pressure within
the jet is due to the jet turbulence, which causes an actual reduction
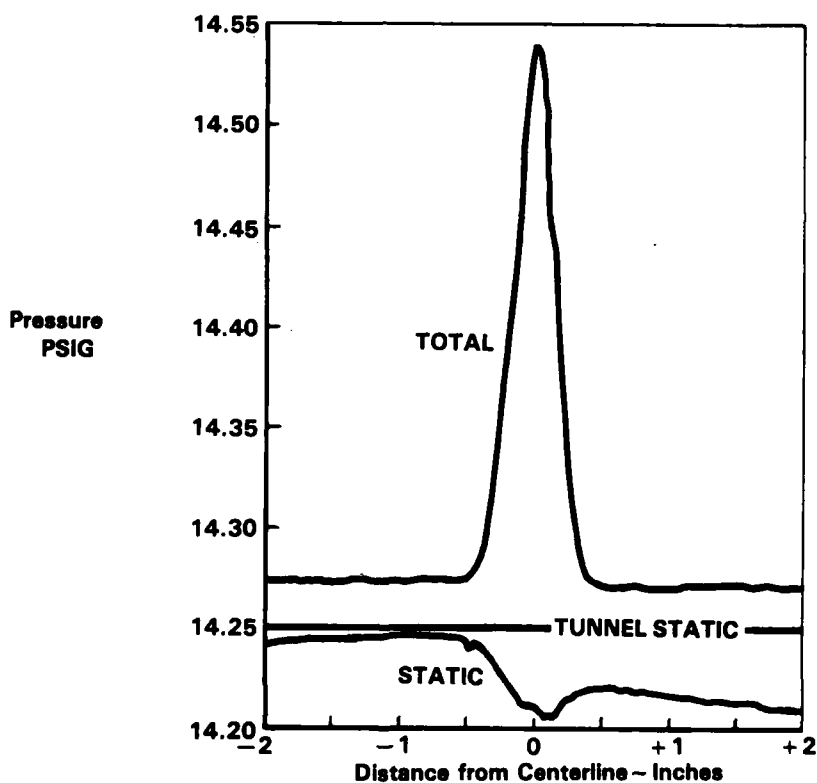
Figure 28. Total and Static Pressure Surveys in the Jet Wake for C_μ = 1
and θ = 50°

74

in the pressure and introduces an error in the probe reading. Since the error is small, no correction was used. When the flow did separate from the airfoil, a region of low total pressure was seen above the jet. The wake survey data are contained in Appendix II.

The wake of every configuration was surveyed at the same station. But in addition, some configurations were surveyed at several stations, in order to determine the jet development. In Figure 29, the variation of the jet trajectory with the initial jet deflection angle is shown for the
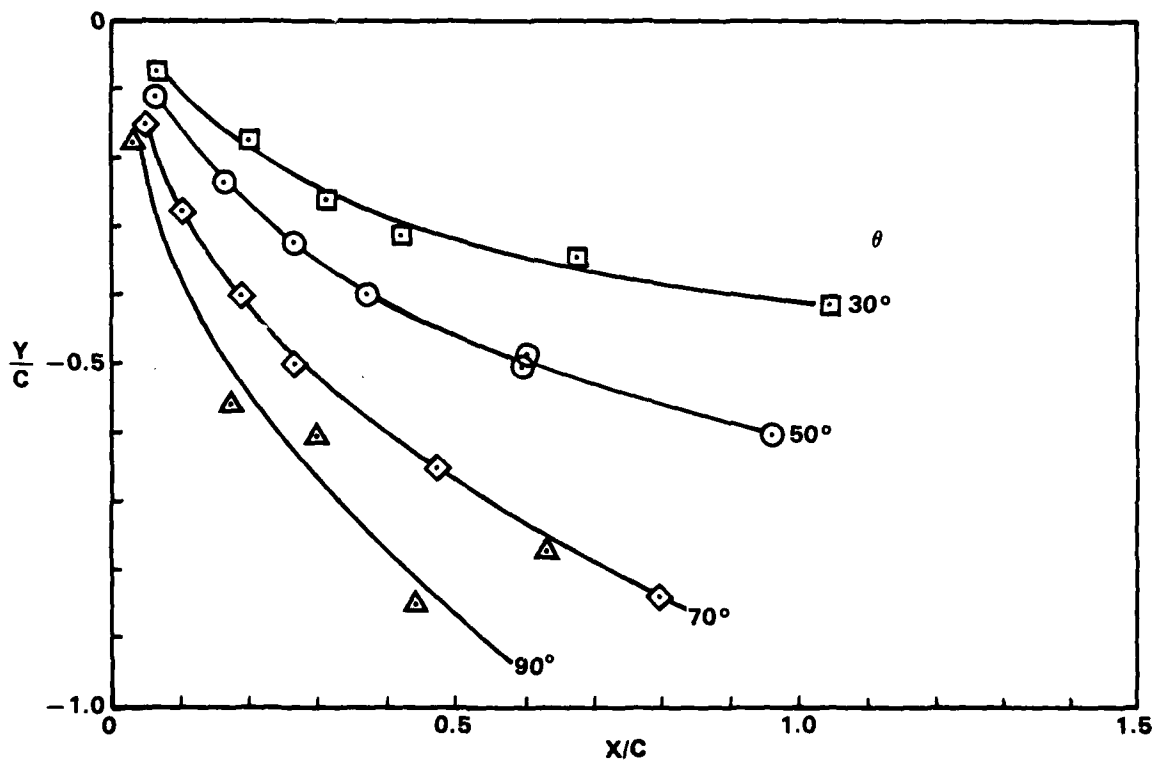
Figure 29. Variation of Jet Shape with Initial Jet Deflection Angle, θ

case with $C_\mu = 1$. As might be expected, the penetration of the jet increases with the initial deflection angle. The effect of the jet momentum coefficient on the trajectory is shown in Figure 30 for two values of the initial deflection angle. As the blowing coefficient is increased, the jet tends to straighten out. In the limit as $C_\mu \to \infty$, the jet continues along the initial trajectory and the horizontal force on the airfoil becomes $T\cos\theta$. These wake survey data are contained in Appendix III.
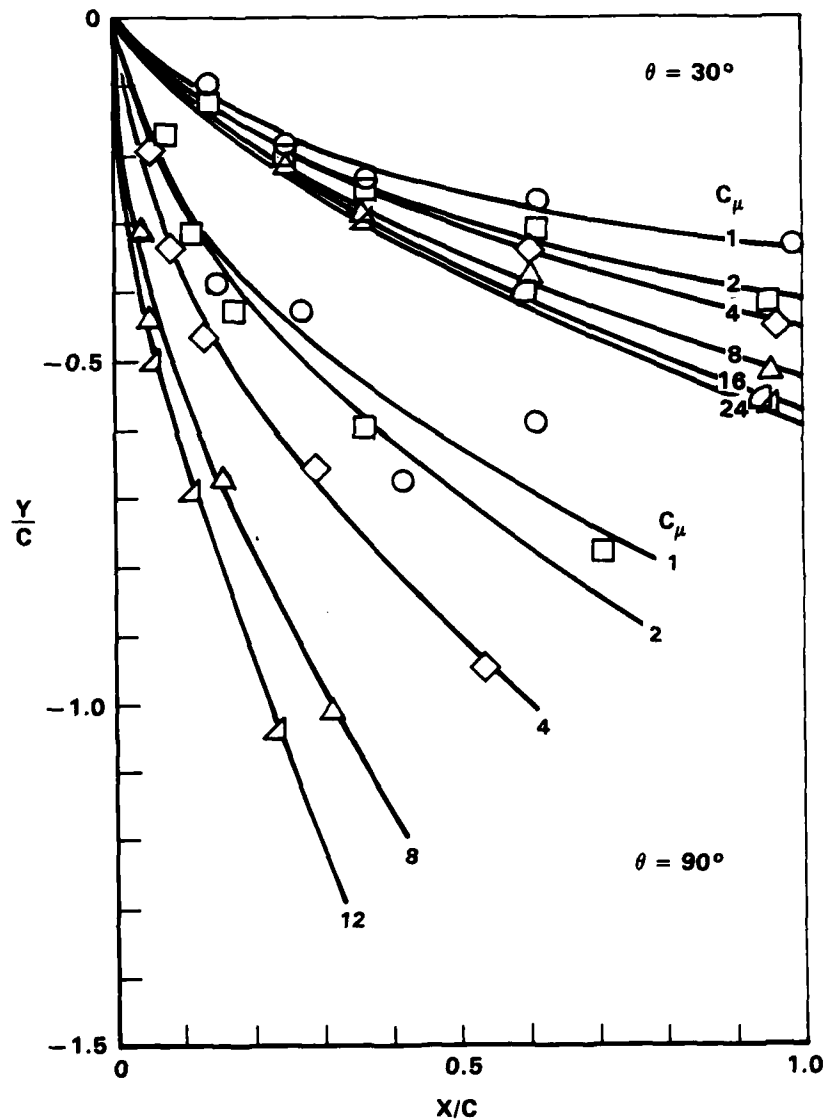
Figure 30. Variation of Jet Shape with Jet Momentum, C_μ

76

LIFT AND THRUST INTEGRALS

The measured surface pressure distributions were integrated to obtain
the lift on the airfoil. In Figure 31 the total lift coefficient is shown
as a function of the jet thrust coefficient. The total lift on the airfoil
is equal to the sum of the circulation lift and the vertical reaction to
the jet thrust, which appears as a suction on the flap surface. For the
smaller jet deflection angles (30°, 50°) the data are well represented by
the theoretical results obtained by Spence (ref 10). However, for the
larger deflection angles, there is a loss of circulation lift due to
separation from the airfoil. Impingement of the jet on the tunnel floor
causes the lift to increase again at large values of C_μ and θ, but this is
a blockage effect and not representative of the force that would be induced
by an unconfined jet.
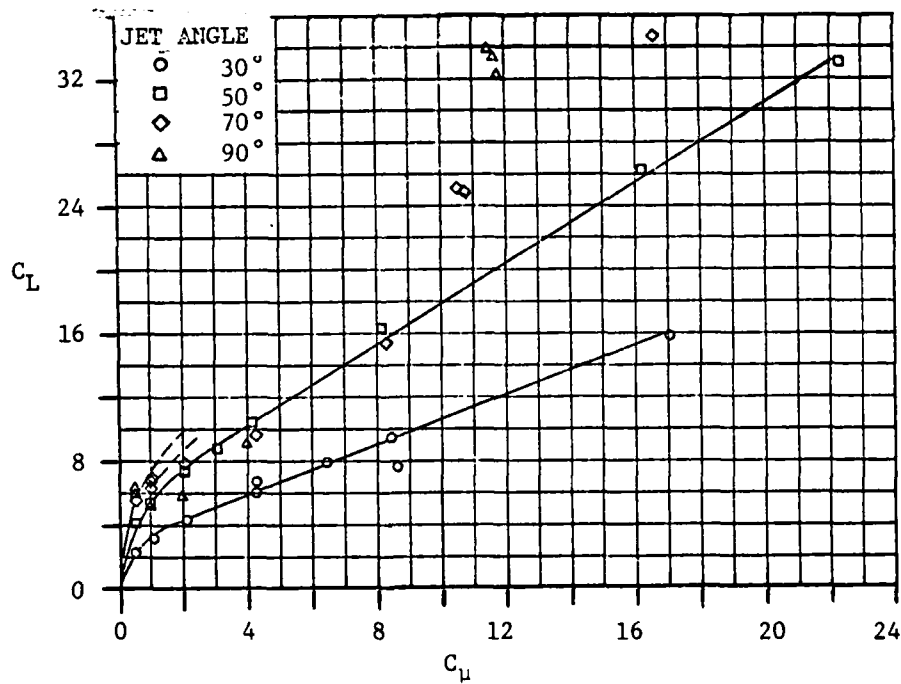
Figure 31.   Lift Coefficient as a Function of Momentum Coefficient

77

In order to provide a check on the experimental methods, the thrust
recovery was calculated from both the wake survey data and the airfoil
surface pressures. As previously explained, the method of Betz (Schlichting,
ref 28) was used to evaluate the excess momentum integral from the wake
pressure distributions. The net thrust on the airfoil is then obtained
by adding the source thrust of the initial jet mass to the momentum
integral. Since the thrust recovery is defined relative to the viscous
drag of the unblown airfoil, this baseline drag is added to the net thrust
of the jet flap. Thus, the loss of recovery is taken to be the increase
in the profile drag of the unblown airfoil due to jet entrainment and
flow separation induced by the jet. The wake recovery factor is there-
fore given by

$$r_w = \frac{T_x + T_q + |D_v|}{T}$$
<div style="text-align:right">5-2</div>

in which T_x is the excess momentum integral, T_q is the source thrust, and
D_v is the viscous drag.

The viscous drag of the airfoil was estimated by computing the pressure
and velocity distributions on the unblown airfoil. The actual airfoil
coordinates and test Reynolds number were used. Variations in lift were
obtained by changing the angle of attack. In Figure 32 the predictions
of this program are compared to measurements for 10° angle of attack. The
excellent agreement of the measured and predicted surface pressure distribu-
tions is an indication that good two dimensionality was achieved in the
wi: ! tunnel test. The agreement between the lift coefficients is also
good. The measured axial force coefficient is within 10% of the computed
value; since integration of the surface pressure data to obtain the axial
force is difficult, this is considered good agreement. The computed
viscous drag coefficient of the airfoil is described by the function

$$C_v = .007C_L{}^2 + .022$$
<div style="text-align:right">5-3</div>

78
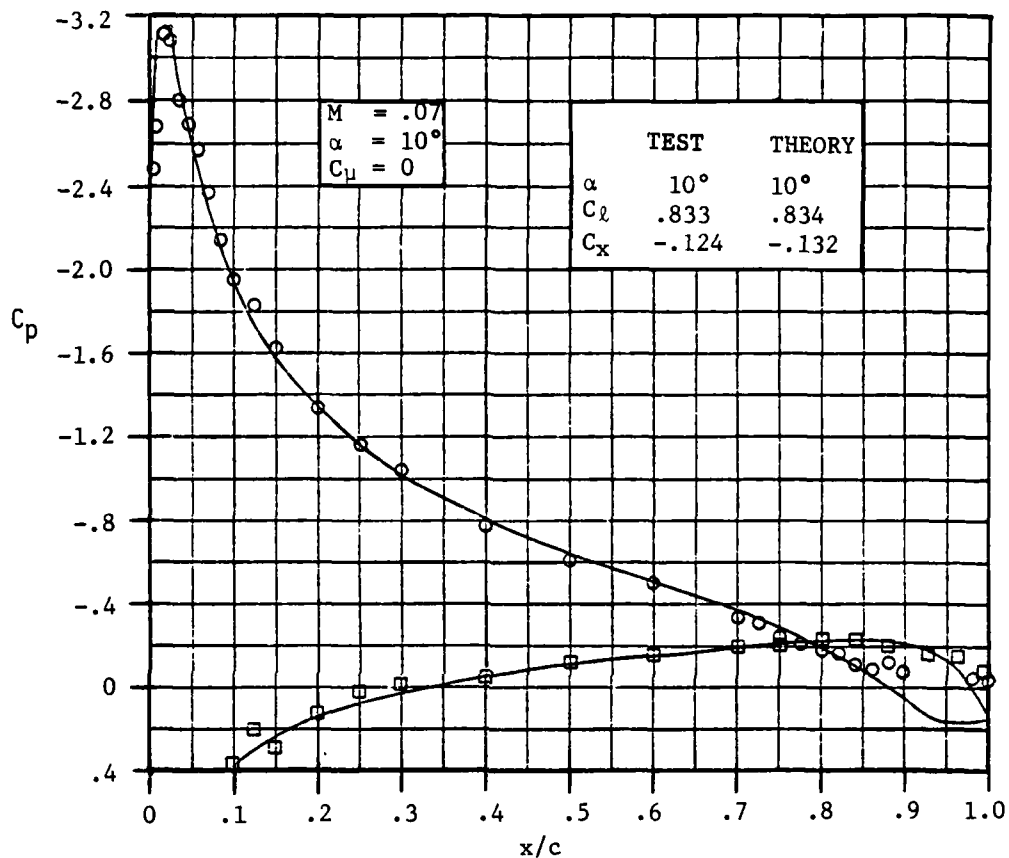
Figure 32. Comparison of Measured and Predicted Surface Pressure
Distributions

in which C_L is the circulation lift coefficient. The viscous drag
includes both the skin friction drag and the pressure dra$_0$ due to the
displacement effect of the boundary layer.

The drag obtained by integrating the airfoil surface pressures also
includes the pressure drag due to viscosity, but not the skin friction

drag. Thus, the pressure drag of the unblown airfoil is added to the measured surface pressure drag. In addition, however, an induced drag correction must be made because end effects introduce some three dimensionality in the surface pressure distributions. The airfoil recovery factor is therefore given by

$$r_a = 1 - \left| \frac{D_s + D_p + D_i}{T} \right| \qquad 5\text{-}4$$

in which D_s is the integral of the surface pressures, D_p is the computed viscous pressure drag of the unblown airfoil, and D_i is the induced drag correction.

Foley (ref 2) estimated the induced drag by extrapolating the linear section of the drag polar of the unblown airfoil to the large lift coefficients of the jet flapped airfoil. This is equivalent to assuming that the lift and jet thrust are elliptically distributed along the span. A similar approach was taken in this study, but the large values of the thrust coefficient considered here required using the expression for the induced drag of a jet flapped wing devised by Maskel and Spence (ref 7),

$$C_{D_i} = \frac{C_L^2}{\pi ARe + 2C_\mu} \qquad 5\text{-}5$$

In effect, Foley (ref 2) neglected the thrust coefficient term, but over the range of values he examined ($C_\mu < 1$), the error is small. In this study, the effective aspect ratio of the airfoil was determined by subtracting the computed viscous drag from the measured total drag of the unblown airfoil. The measured drag polar is shown in Figure 33. The total drag is described by the function

$$C_D = .011 C_L^2 + .022 \qquad 5\text{-}6$$

The effective aspect ratio of the airfoil is then obtained from the relation

80

$$C_D = .022 + .011 \, C_L^2$$
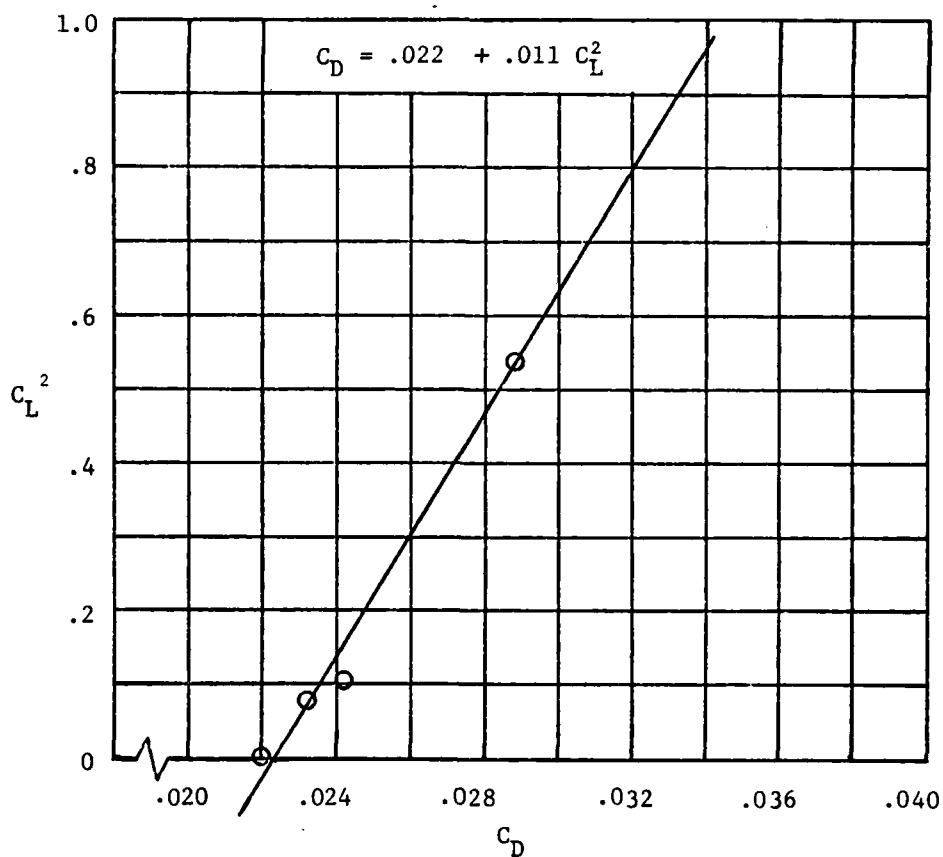
Figure 33. Drag Polar of the Unblown Airfoil

$$ARe = \frac{C_L^2}{\pi(C_D - C_v)} \qquad \qquad 5\text{-}7$$

This gives ARe = 77, which was then assumed to be independent of variations in C_μ and θ_o.

The values of the thrust recovery factor obtained by both methods are compared in Figure 34. There is surprisingly good agreement between the methods, although the surface pressure data gives consistently higher
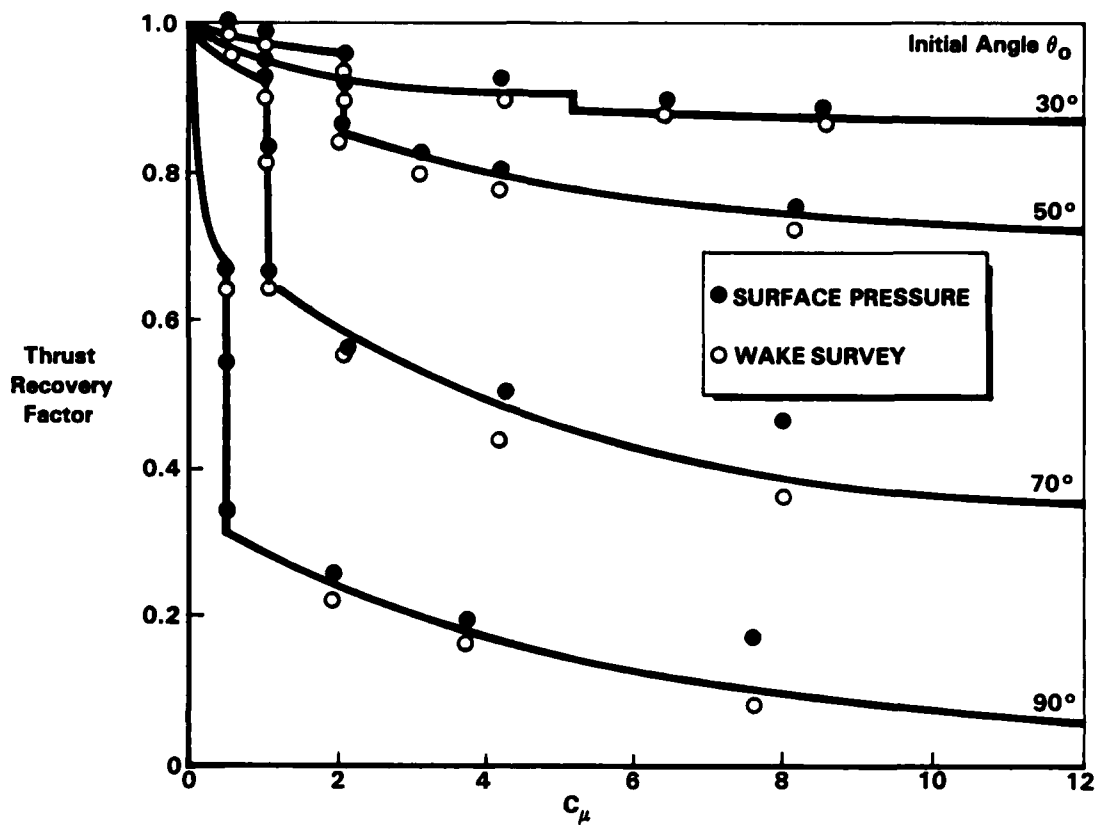
Figure 34. Variation of the Thrust Recovery Factor

recovery. Based on our prior experience with wake and surface pressure integrations, it is our feeling that the wake survey data is more reliable. However, the differences observed are within the 16% range of experimental error associated with previous measurements of thrust recovery (Leaman and Plotkin, ref 29). The increase in the recovery factor observed for large values of C_μ and θ_0 is due to jet impingement on the tunnel floor, and is not representative of the thrust recovery of an unconfined jet.

ANALYSIS OF RESULTS

In general, the thrust recovery decreases as the jet thrust coefficient and initial deflection angle are increased. However, the variation is not

continuous. For every value of the deflection angle there is a discon-
tinuous change in the recovery for a value of the thrust coefficient of
approximately $C_\mu = 2$. During the test, a distinct increase in noise
level could be heard when the discontinuity occurred. Comparison of the
measured airfoil surface pressure distributions just before and after the
discontinuity reveals that it is due to the bursting of the leading edge
separation bubble. This is shown in Figure 35 for the $\theta_0 = 50°$ case.
There is a change between a short separation bubble, which gives larger
recovery and a long bubble which gives less recovery. Although the
thrust recovery continues to decrease as the long bubble grows, there is
no change when the bubble ultimately fails to reattach to the surface of
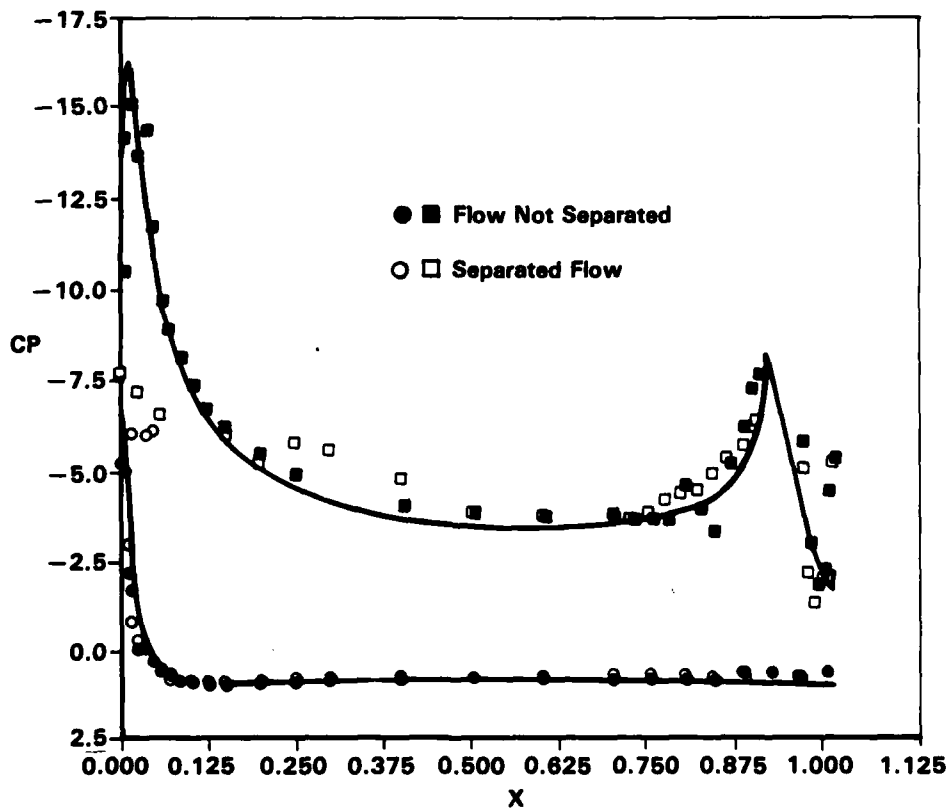
Figure 35. Comparison of Measured and Ideal Airfoil Pressure Distributions,
$C_\mu = 2$, $\theta = 50°$

the airfoil at all. Because earlier studies were conducted at small values of C_μ, this discontinuity has not been previously known.

The bursting of the bubble depends on the Reynolds number and Mach number of the flow, and the leading edge radius of the airfoil, so that these trends cannot be generally applied. However, the value of the thrust recovery factor is well predicted by the jet flap analysis up to the point of bursting. Thus, it can be concluded that the loss of recovery up to the burst point is due to jet entrainment drag, and that the short bubble does not significantly affect either the lift or thrust integrals.

In Figure 36 the computed surface pressure distribution on the unblown airfoil is compared to the computed distribution on an airfoil with an
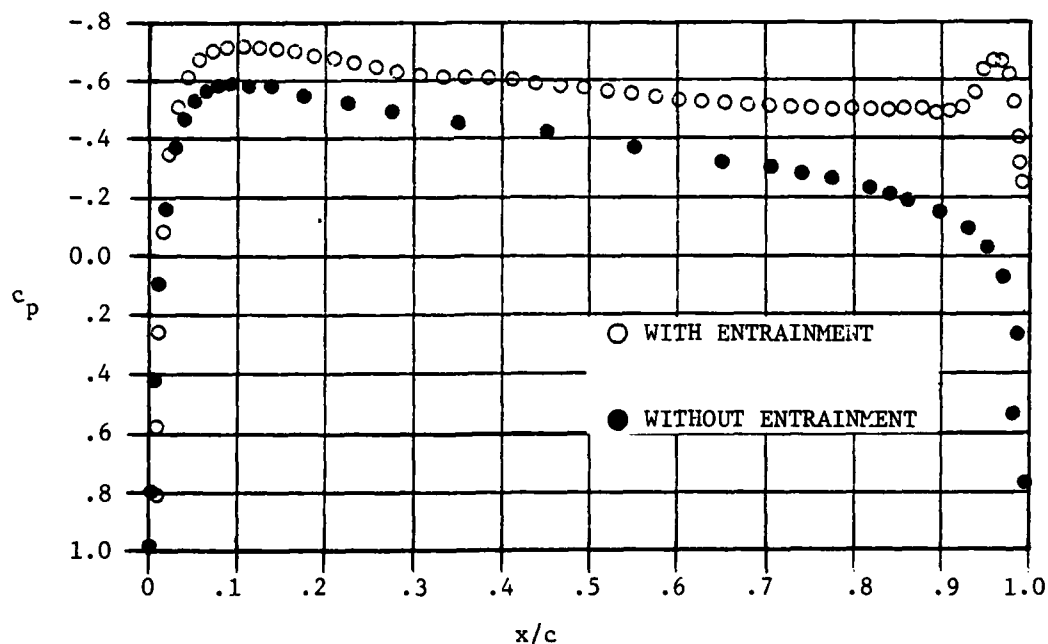
Figure 36. Comparison of Airfoil Surface Pressure Distributions

84

undeflected jet, for $C_\mu = 1$. The effect of the jet is to increase the base drag on the airfoil. Integration of the surface pressures gives $r = 0.050$ for the thrust recovery. The corresponding variation in the excess momentum of the jet is shown in Figure 37. By the last station shown, the jet thrust has decreased to give $r = 0.051$.

For small values of the jet thrust coefficient, the thrust recovery actually increases slightly as the jet deflection angle is increased from 30° to 50°. Similar behavior was seen in Foley's (ref 2) data, and predicted by the jet flap analysis. Because the static pressure on the upper surface of the jet becomes more negative as the jet is deflected, there may actually be some thrust augmentation in this case. However, the effect is small and not sufficient to overcome the entrainment drag which occurs farther downstream.
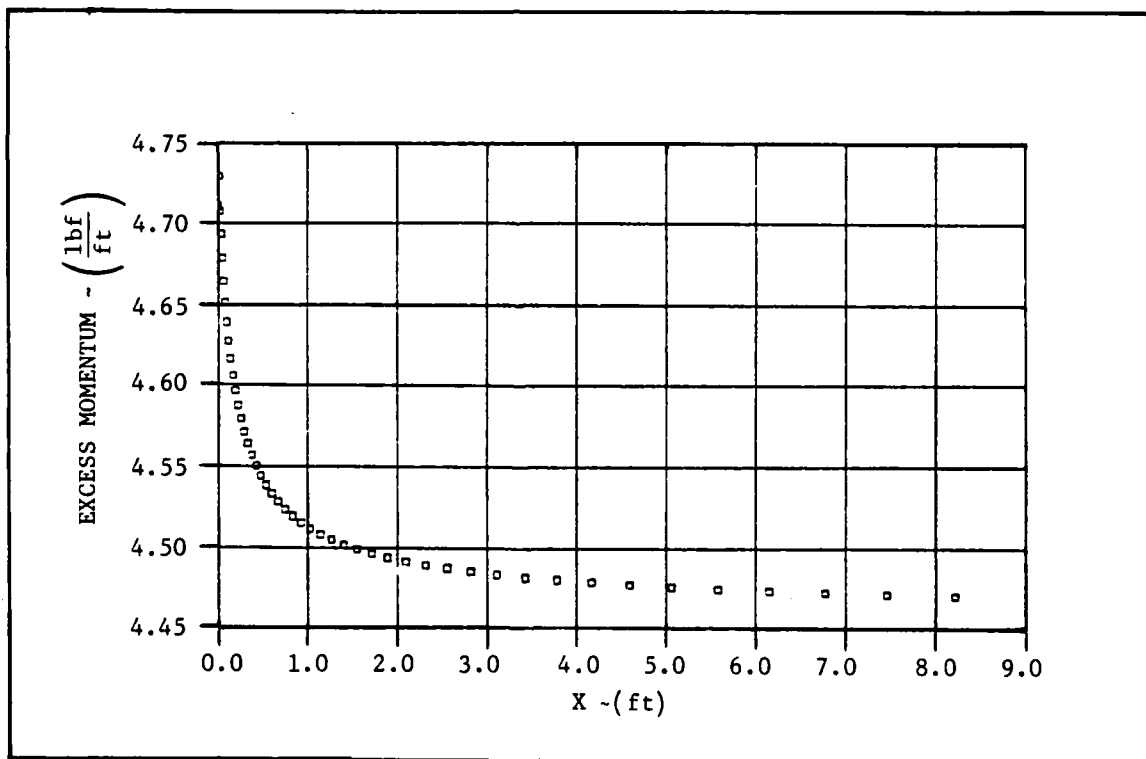
Figure 37. Streamwise Variation of Excess Momentum in Jet

VI. CONCLUSIONS AND RECOMMENDATIONS

The thrust recovery is generated by equal but opposite pressure forces induced on the airfoil and the jet flap. If the mixing of the jet is neglected, the jet is a streamline of the flow, and the net pressure force is everywhere normal to the jet. In this case, the thrust of the jet is conserved and ultimately recovered as a horizontal force in the far wake. This gives complete thrust recovery. Real fluid effects reduce the actual recovery both by inducing a jet drag on the airfoil and by causing separation of flow from the airfoil.

The thrust recovery is a function of both the thrust coefficient and jet deflection angle. In general, the recovery is nearly complete for small values of the thrust coefficient ($C_\mu < 1$), but decreases to the horizontal component of the jet reaction force at large values of thrust ($C_\mu > 15$). The effect of jet mixing is to reduce the thrust recovery about 10% at small values of the thrust coefficient and deflect... angle. As these parameters are increased, flow separation causes a further loss in recovery. For a fixed deflection angle, there is a discontinuous change in the recovery factor at $C_\mu \sim 2$, as the character of the separation changes from a "short" bubble which reattaches to the airfoil near the leading edge, to a "long" bubble which reattaches near the trailing edge. The flow is bistable in the transition region. At higher values of C_μ, the bubble does not reattach to the airfoil at all, but is entrained into the wake.

A viscid/inviscid interaction analysis has been developed to compute the contribution of the jet drag to the reduction in thrust recovery. It was found that the entrainment drag accounts for all the variation in recovery before bursting occurs. Thus, such an analysis can be used to predict the thrust recovery of various jet flap concepts if the flow is prevented from separating by the use of slats, etc.

Because flow separation plays such an important part in determining the thrust recovery at large values of the thrust coefficient, further development of jet flap theory should focus on predicting the effects of separation.

86

VII. REFERENCES

1. Stratford, B. S., "Mixing and the Jet Flap," Aeronautical Quarterly, May 1956.

2. Foley, W. M., "An Experimental Study of Jet Flap Thrust Recovery," Stanford University, SUDAER No. 136, Sept. 1962.

3. Stratford, B. S., "A Further Discussion on Mixing and the Jet Flap," The Aeronautical Quarterly, Vol. VII, August 1956.

4. Williams, J., Butler, S. F., and Wood, M. N., "The Aerodynamics of Jet Flaps," ARC R&M 3304, January 1961.

5. Tsongas, G. A., "Verification and Explanation of the Controllability of Jet Flap Thrust," SUDAER No. 138, October 1962.

6. Hynes, C. S., "The Lift, Stalling, and Wake Characteristics of a Jet-Flapped Airfoil in a Two-Dimensional Channel," Thesis, Stanford University (SUDAAR No. 363) 1968.

7. Maskell, E. C. and Spence, D. A., "Theory of the Jet Flap in Three-Dimensions," Proceedings of the Royal Society of London, Vol. A251, 1959, pp. 407-425.

8. Wygnanski, I., "The Effect of Jet Entrainment on Loss of Thrust for a Two-Dimensional Symmetrical Jet-Flap Aerofoil," The Aeronautical Quarterly, Vol XVII, February 1966.

9. Wilson, J., "Thrust Augmented Wing Sections in Potential Flow," PhD Thesis, West Virginia University, 1973.

10. Spence, D. A., "Lift Coefficient of a Thin, Jet-Flapped Wing," Proceedings of the Royal Society of London, Vol. A238, 1956, pp. 46-68.

11. Lissaman, P. B. S., "Linear Theory of the Jet Flap in Ground Effect," AIAA Journal, Vol. 6, July 1968, pp. 1356-1362.

12. Simmons, J. M., Platzer, M. F. and Smith, T. C., "Velocity Measurements in an Oscillating Plane Jet Issuing into a Moving Airstream," J. Fluid Mech., Vol. 84, pp. 33-53, 1978.

13. Lan, C. E., "Theoretical Aerodynamics of Over-Wing-Blowing Configurations," Journal of Aircraft, Vol. 14, June 1977, pp. 517-518.

14. Addessio, F. L. and Skifstad, J. G., "Aerodynamics of a Finite Aspect Ratio Jet Flap at Low Flight Speeds," Journal of Aircraft, Vol. 14, Oct. 1977, pp. 936-943.

15. Quanbeck, A. H., "Further Verification of Jet Flap Thrust Recovery and Identification of its Mechanism," PhD Thesis, Stanford University, 1963.

16. Metral, A. and Zerner, F., "The Coanda Effect," Publication Scientifiques et Techniques du Ministere dé Í Air, No. 218 (1948), M.O.S., TIB/T4027, 1953.

17. Bevilaqua, P. M., "Lifting Surface Theory for Thrust Augmenting Ejectors," AIAA Journal, May 1978, pp. 475-481.

18. Patankar, S. V. and Spalding, D. B., "Heat and Mass Transfer in Boundary Layers," International Textbook Co., Ltd., London, 1970.

19. Bristow, D. R., "Recent Improvements in Surface Singularity Methods for the Flow Field Analysis about Two-Dimensional Airfoils," AIAA Paper 77-641, 1977.

20. Chandra, S., "Asymmetric Entrainment of Two-Dimensional Curved Jets," PhD Thesis, West Virginia University, 1975.

21. Dvorak, F. A. and Woodward, F. A., "A Viscous/Potential Flow Inter- action Analysis Method for Multi-element Infinite Swept Wings," NASA CR-2476, Vol. I, November 1974.

22. Launder, B. E. and Spalding, D. B., "Mathematical Models of Turbulence," Academic Press, 1972.

23. Schum, E. F., Bevilaqua, P. M., and Patankar, S. V., "Computation of the Turbulent Mixing in Curved Ejectors," ONR CR212-249-2F, April 1980.

24. Bradshaw, P., "Review-Complex Turbulent Flows," ASME Trans., June 1975.

25. Chambers, T. and Wilcox, D., "Critical Examination of Two-Equation Turbulence Closure Models," AIAA Paper 76-352, July 1976.

26. Fekete, G. I., "Two-Dimensional, Self Preserving Turbulent Jets in Streamline Flow," Report No. 70-11, McGill University, December 1970.

27. Newman, B. G., "Turbulent Jets and Wakes in a Pressure Gradient," Proc. G. M. Conference on Fluid Mechanics of Internal Flow, Elsevier Publishing Co., Amsterdam, 1967.

28. Schlichting, H., "Boundary Layer Theory," McGraw-Hill Book Co., New York, 1979.

29. Leamon, R. G. and Plotkin, A., "An Improved Solution of the Two-Dimensional Jet Flapped Airfoil Problem," Journal of Aircraft, Vol. 9, No. 9, September 1972, pp. 631-635.

MICROCOPY RESOLUTION TEST CHART
NATIONAL BUREAU OF STANDARDS 1963 A
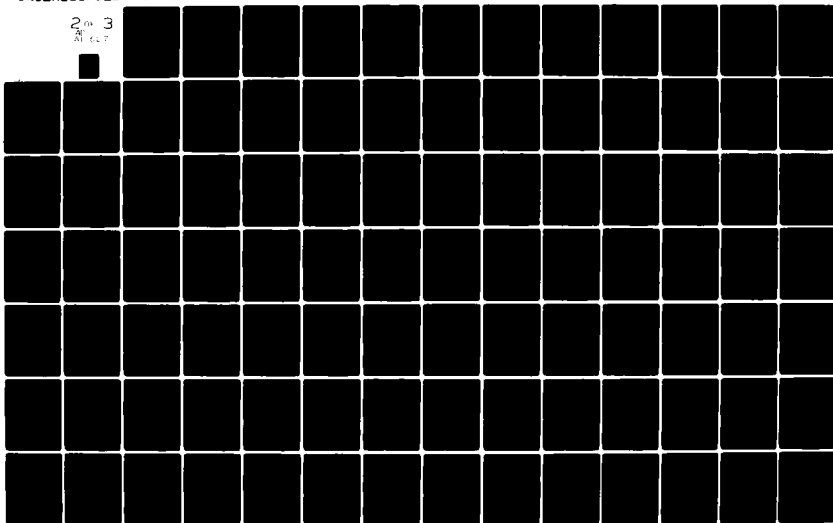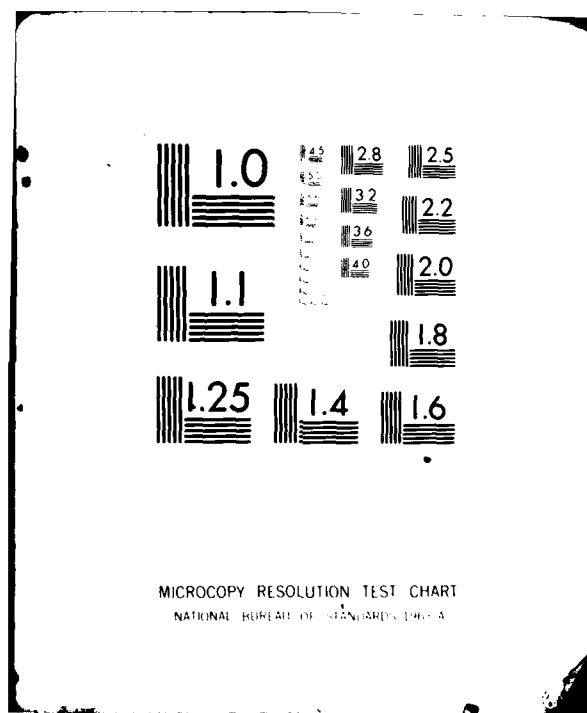
APPENDIX I

AIRFOIL SURFACE PRESSURE DISTRIBUTION
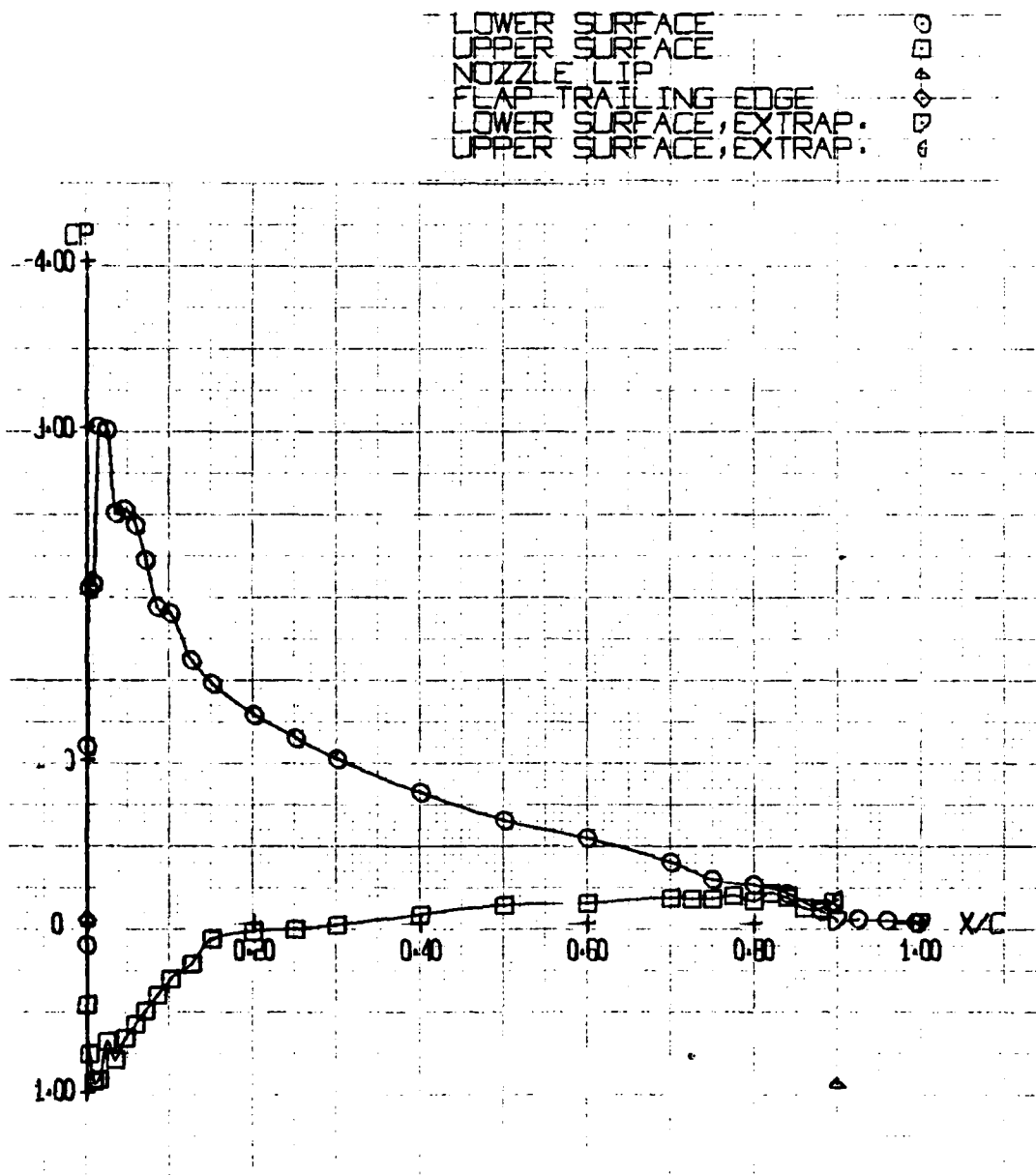
Figure I-1. $C_\mu = 0$, Theta $= 0°$, Alpha $= -10°$ (Test 272, Run 2)
Q = 7.18 psf

90
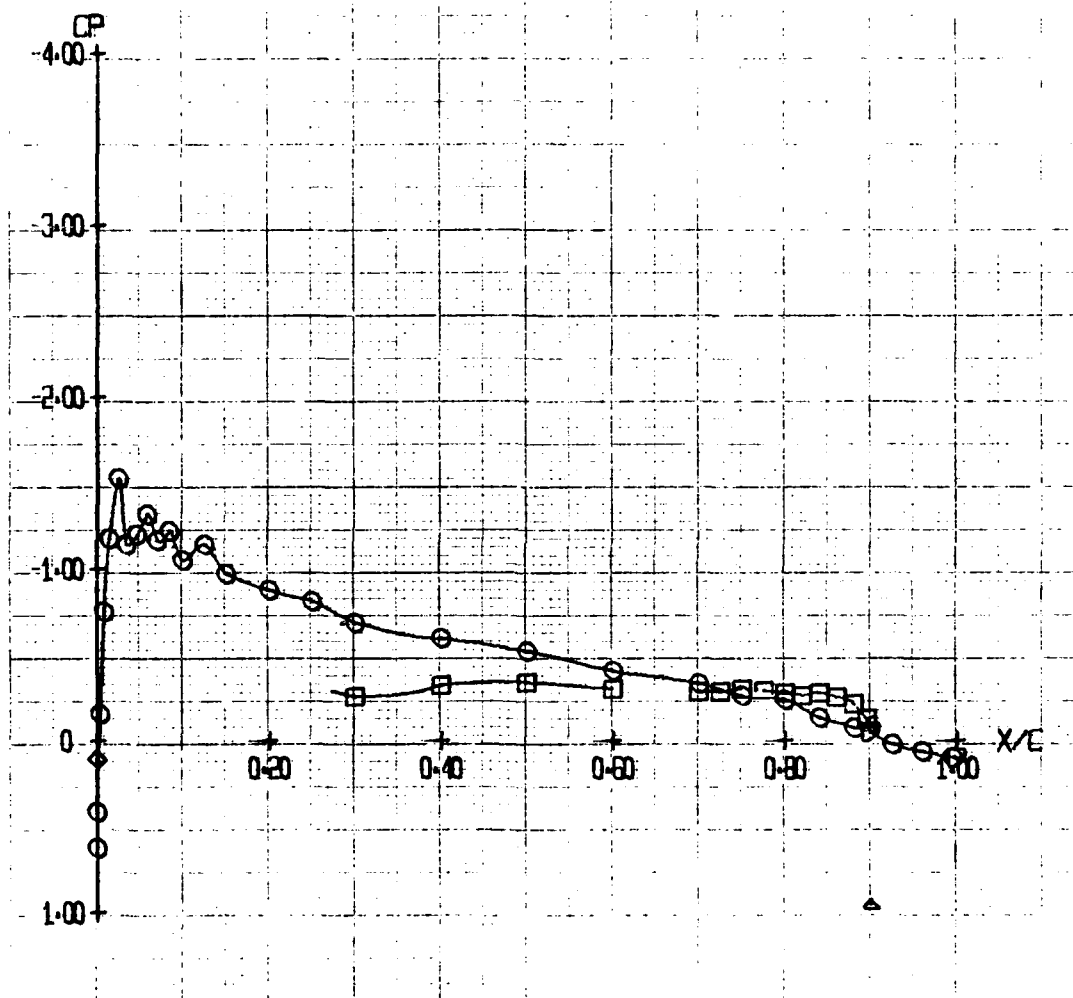
Figure I-2. $C_\mu = 0$, Theta = 0°, Alpha = -5° (Test 272, Run 3)
$Q = 7.28$ psf
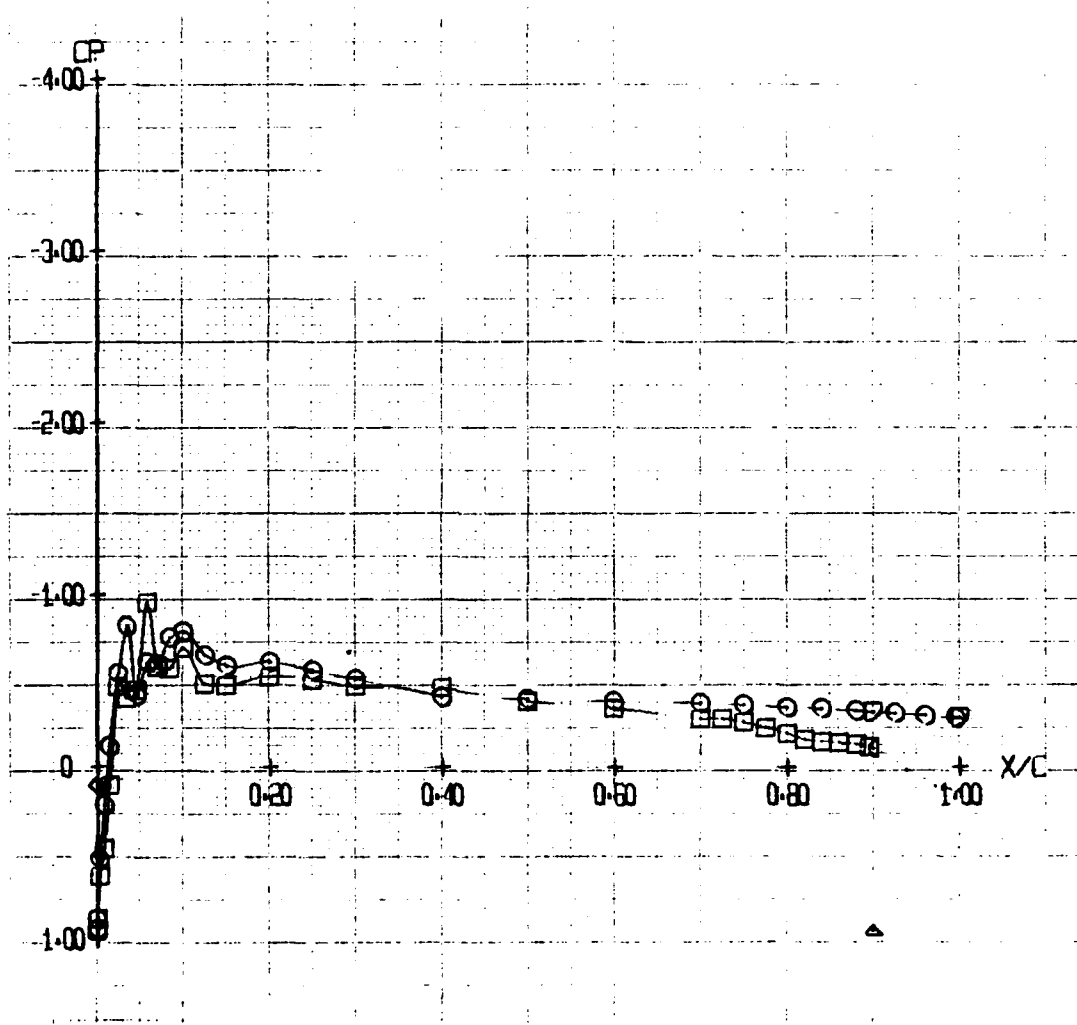
Figure I-3. $C_\mu = 0°$, Theta = 0°, Alpha = 0° (Test 272, Run 1)
$Q = 7.27$ psf

92
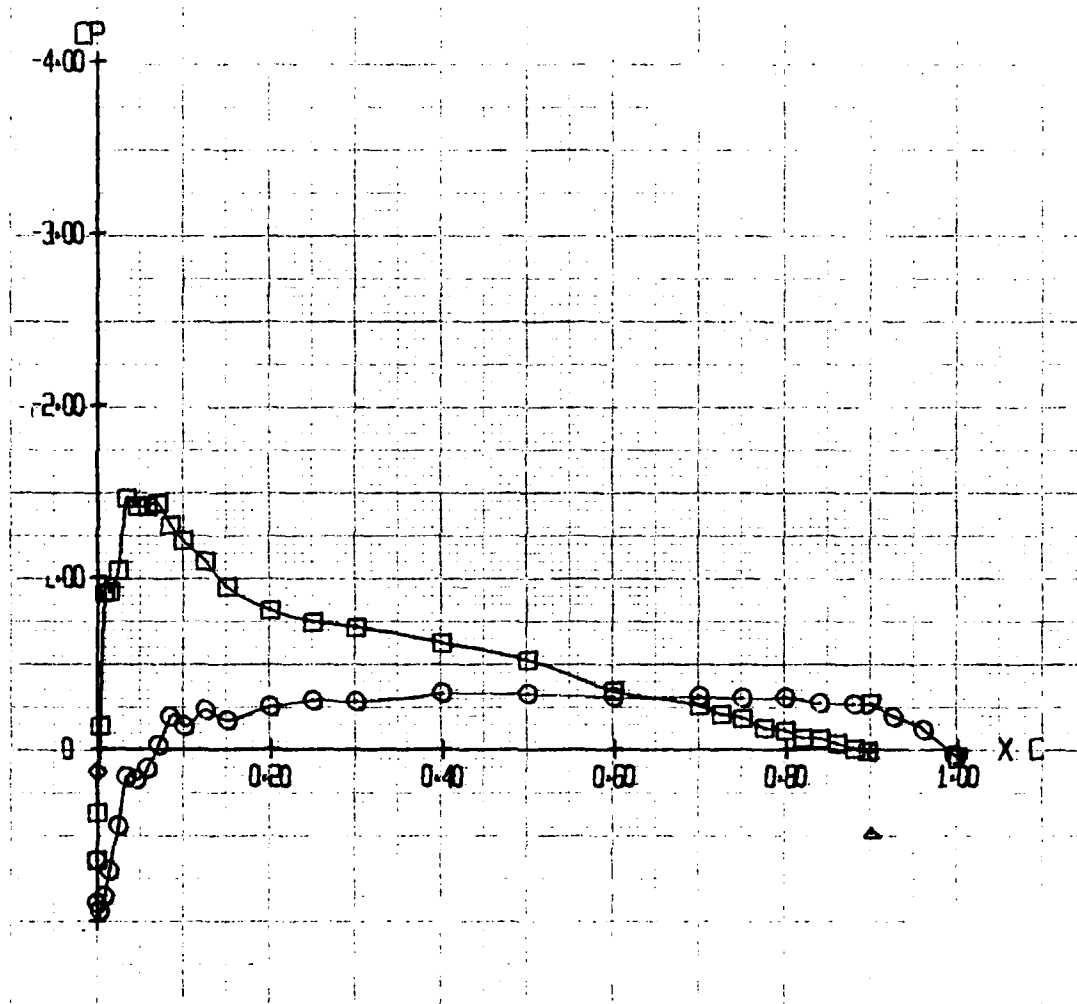
Figure I-4. $C_\mu = 0$, Theta $= 0°$, Alpha $= 0°$ (Test 272, Run 4)
            $Q = 7.25$ psf

93
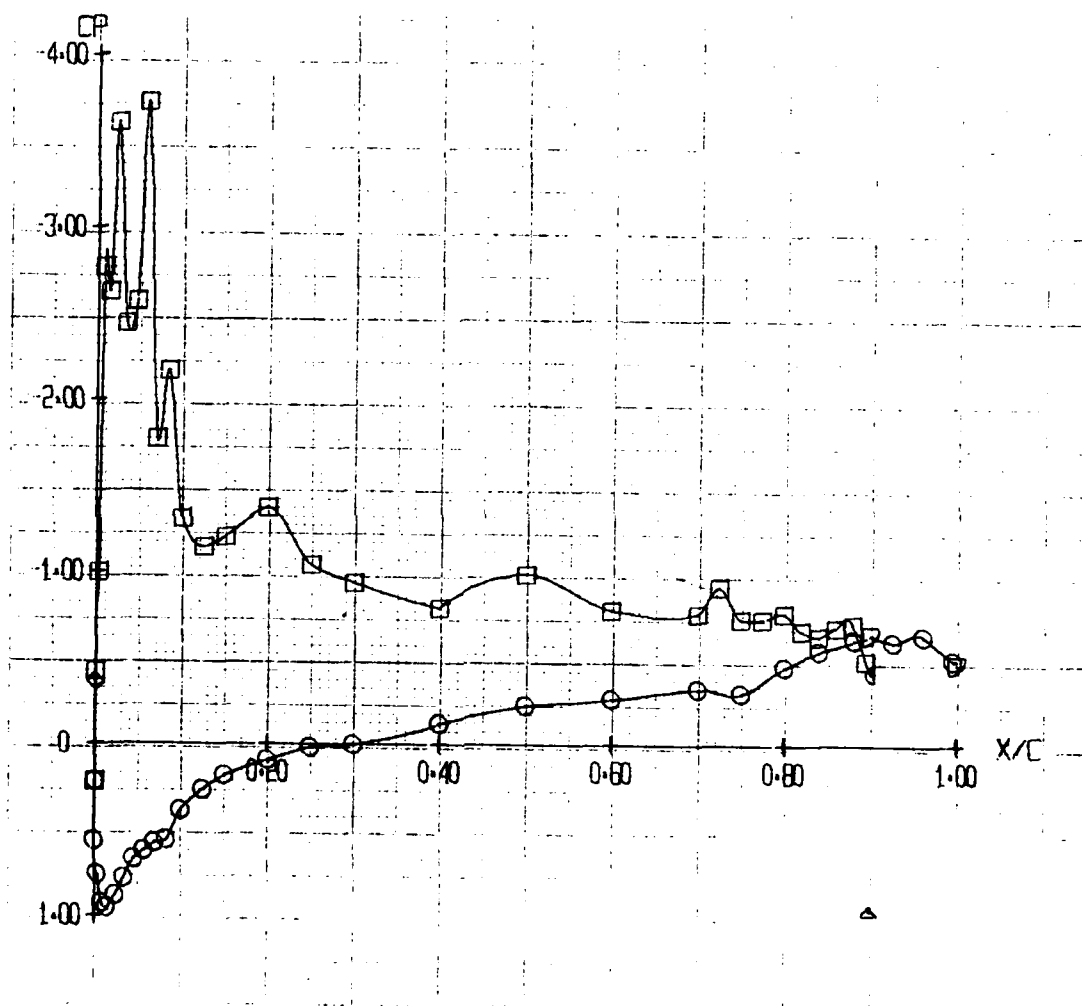
Figure I-5. $C_\mu = 0$, Theta = 0°, Alpha = 15° (Test 272, Run 8)
$Q = 7.22$ psf

94
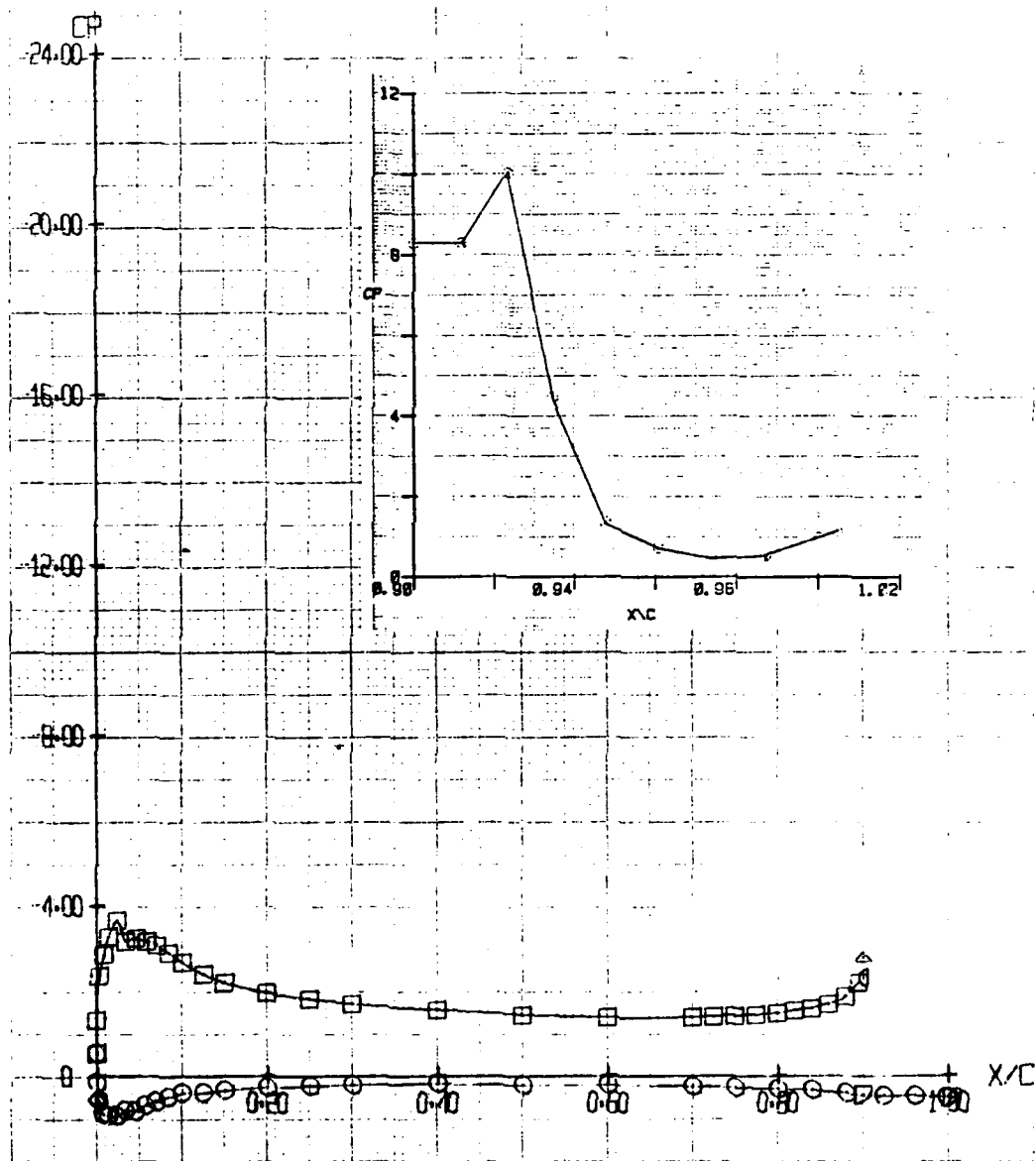
Figure I-6. C_μ = 0.53, Theta = 30°, Alpha = 0° (Test 272, Run 9)
Q = 6.91 psf

95
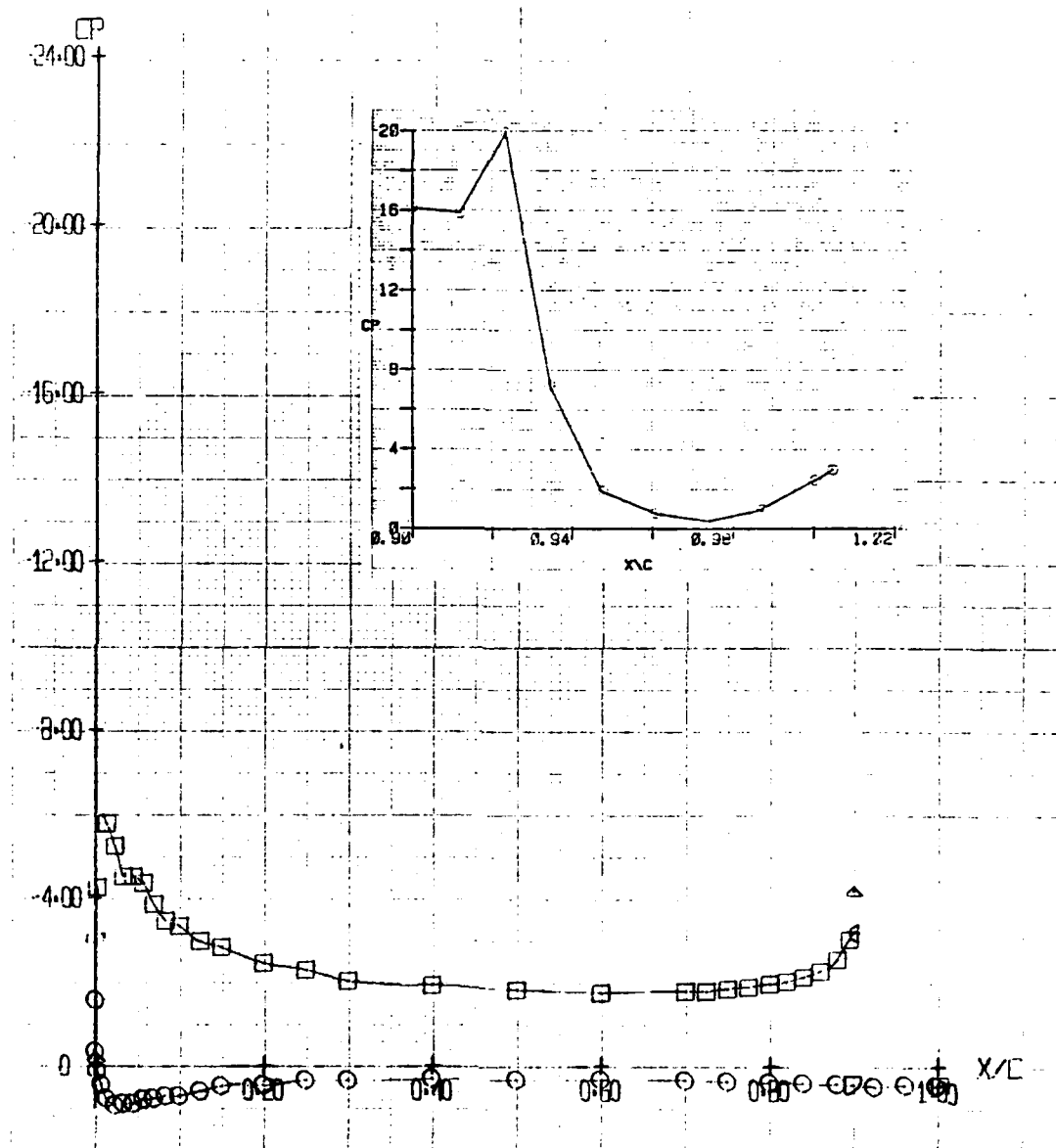
Figure I-7. C_μ = 1.07, Theta = 30°, Alpha = 0° (Test 272, Run 10)
Q = 7.07 psf

96
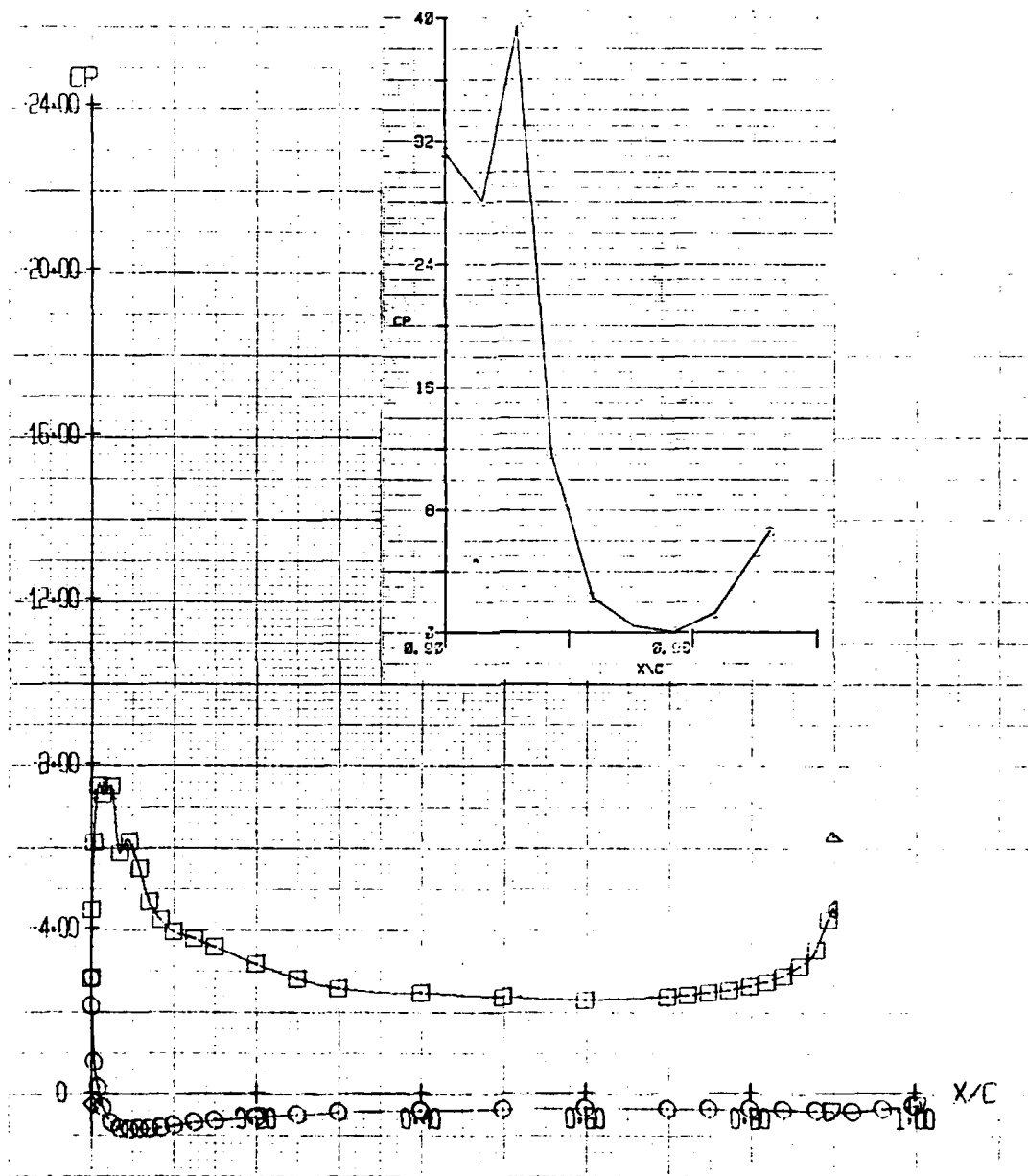
Figure I-8. C_μ = 2.11, Theta = 30°, Alpha = 0° (Test 272, Run 11)
Q = 7.16 psf
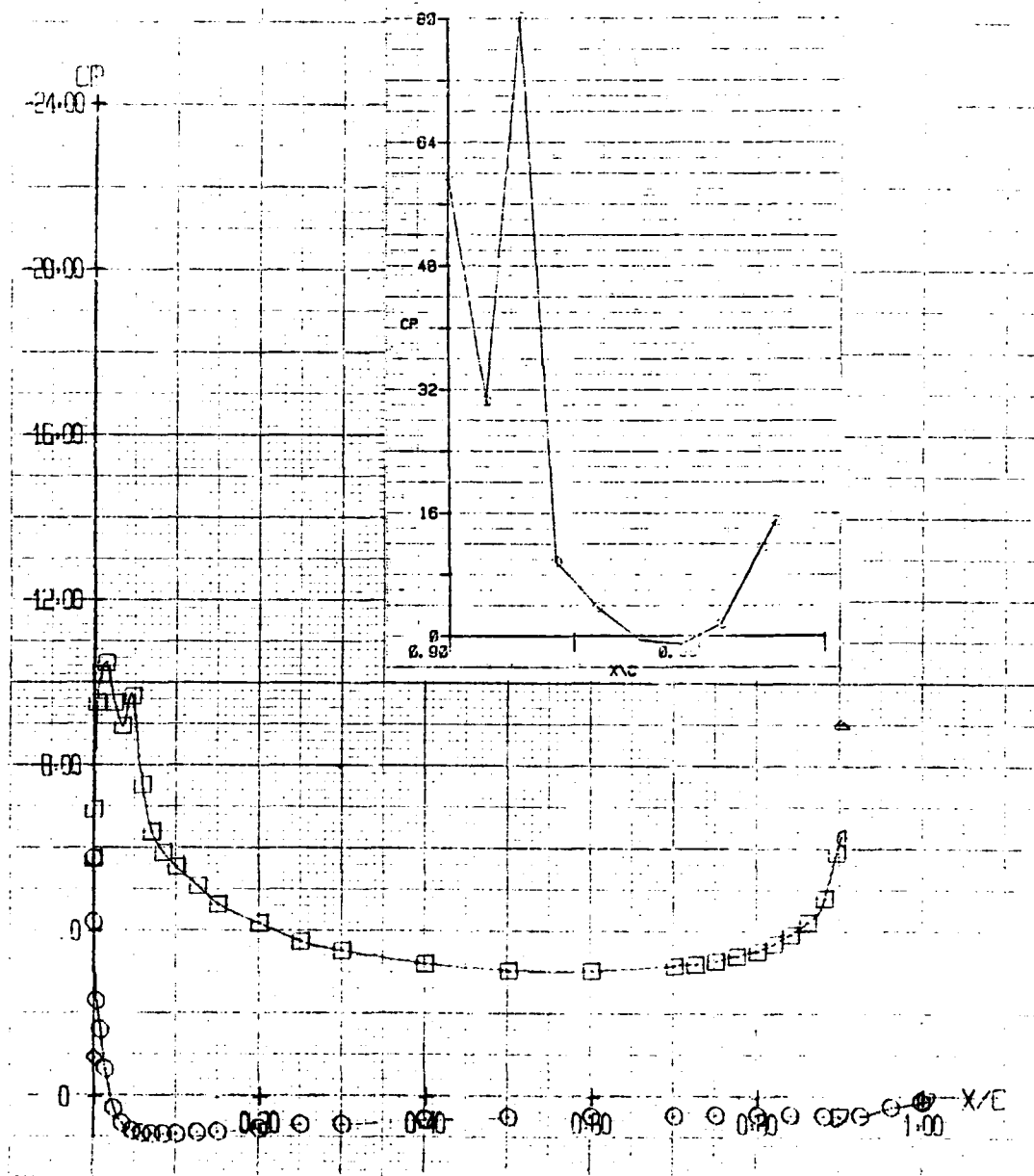
Figure I-9. C_μ = 4.26, Theta = 30°, Alpha = 0° (Test 272, Run 13)
            Q = 6.13 psf

98
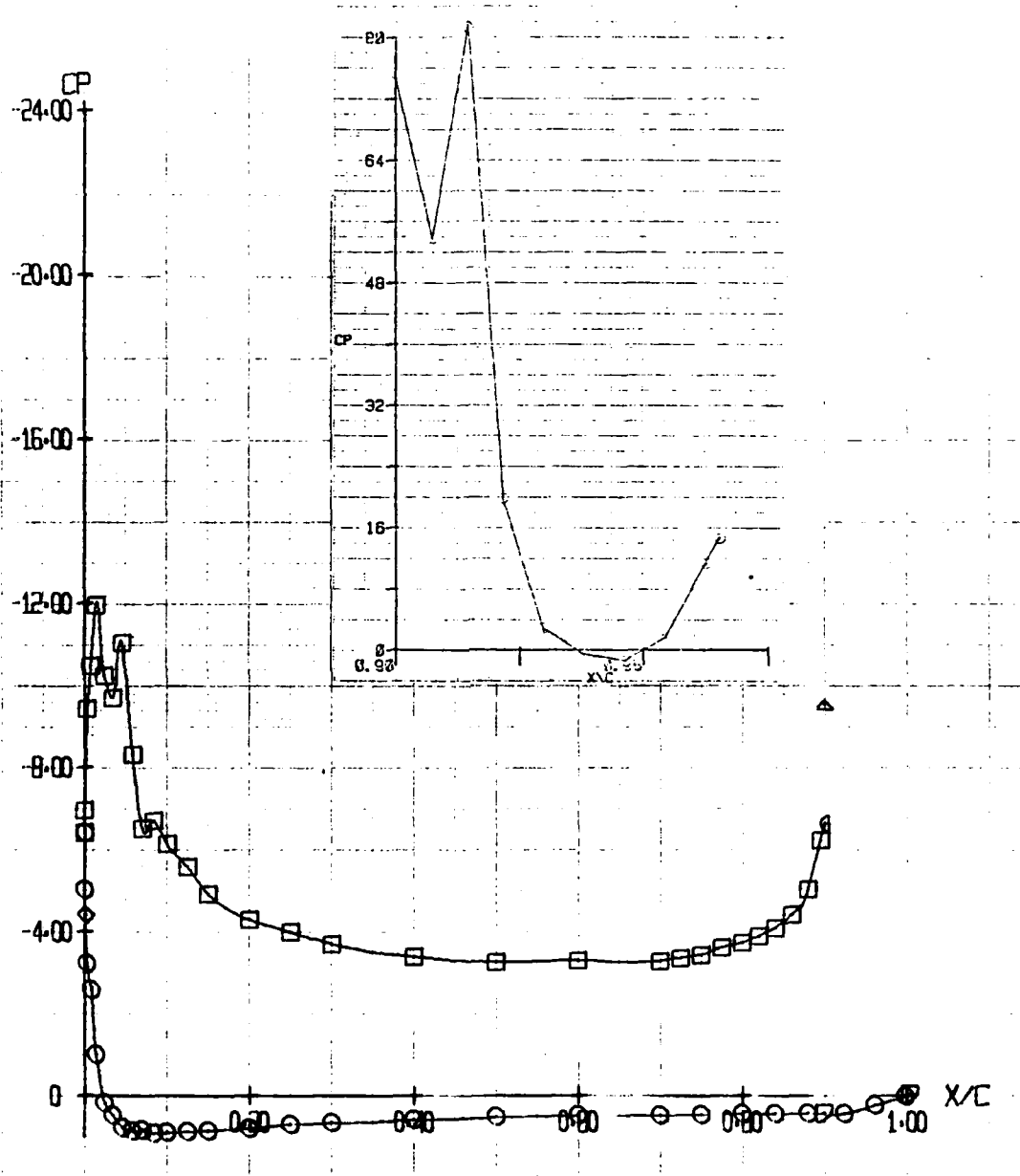
Figure I-10. $C_\mu = 4.26$, Theta = 30°, Alpha = 0° (Test 272, Run 14)
$Q = 4.52$ psf

99
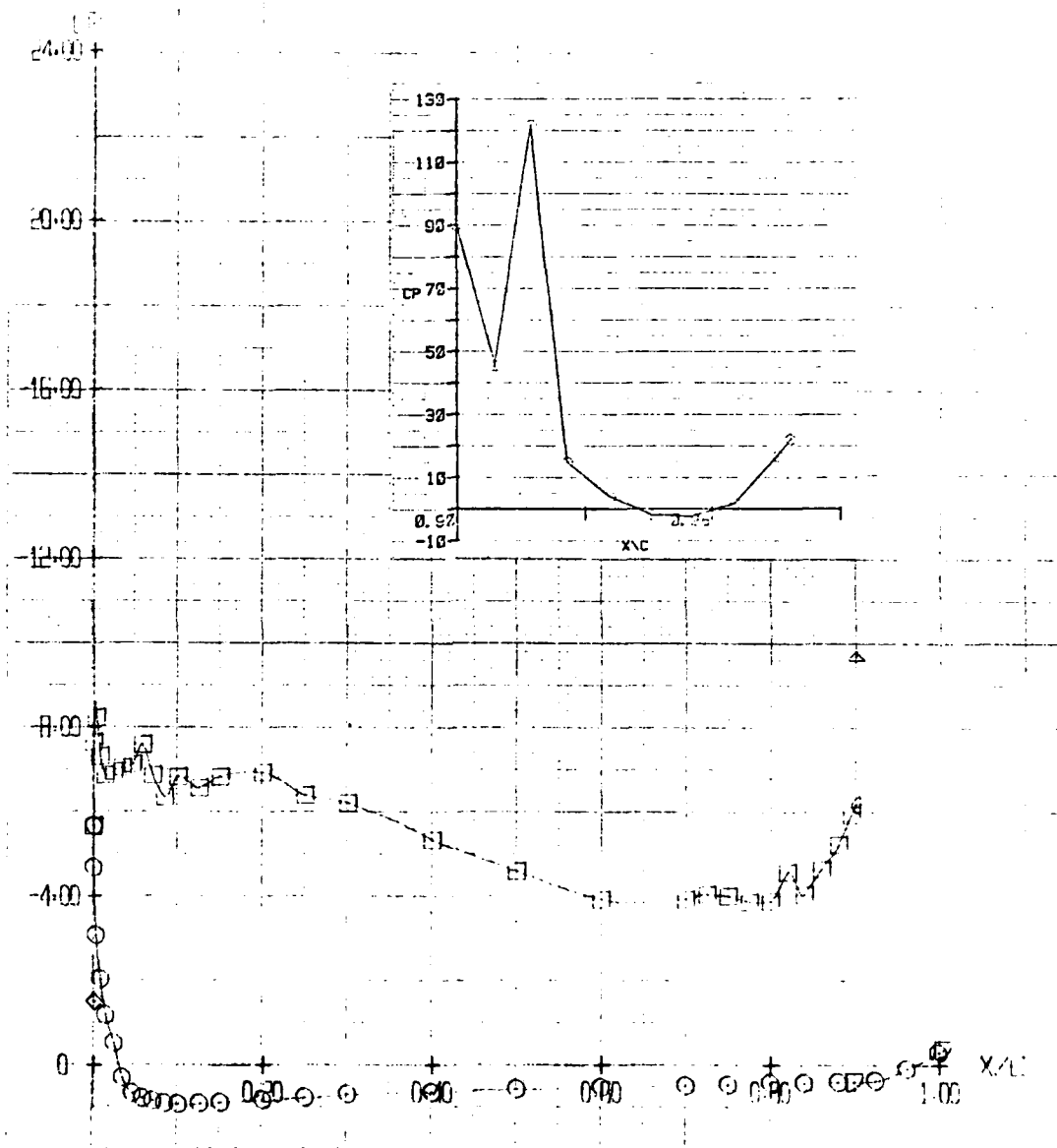
Figure I-11. C_μ = 6.40, Theta = 30°, Alpha = 0° (Test 272, Run 15)
             Q = 4.04 psf

100
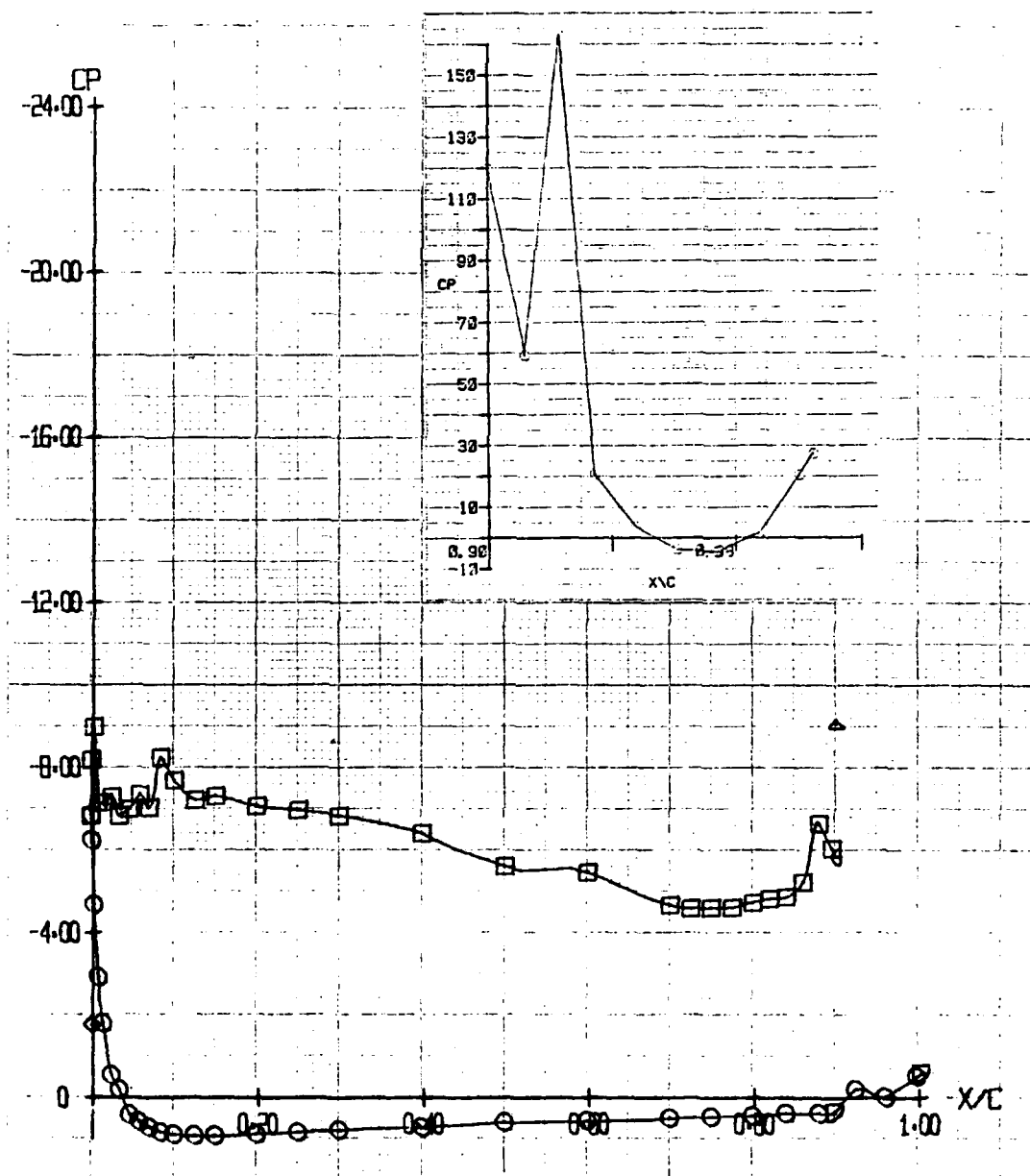
Figure I-12. C_μ = 8.43, Theta = 30°, Alpha = 0° (Test 272, Run 16)
Q = 3.04 psf
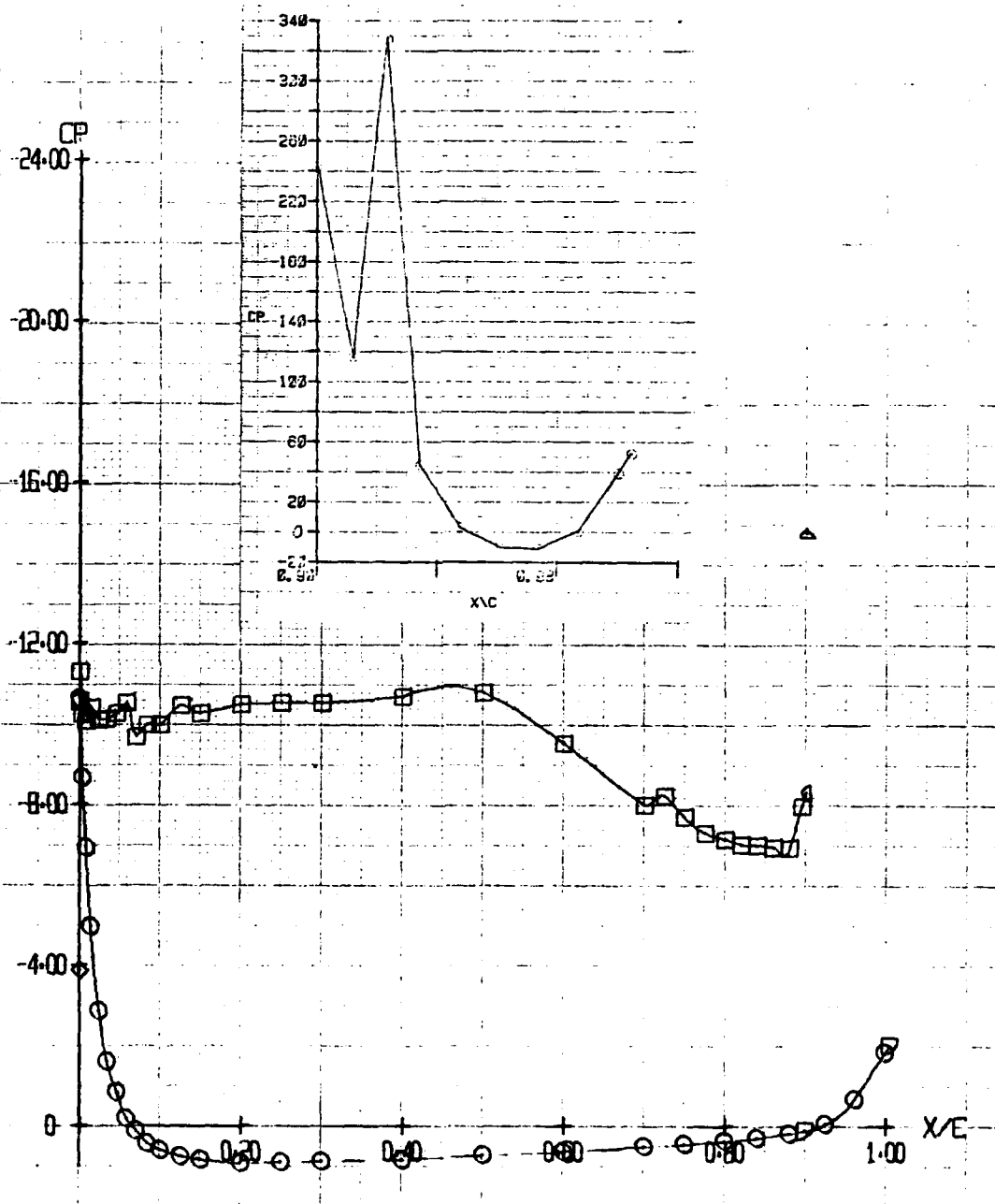
Figure I-13. C_μ = 17.03, Theta = 30°, Alpha = 0° (Test 272, Run 18)
          Q = 1.51 psf
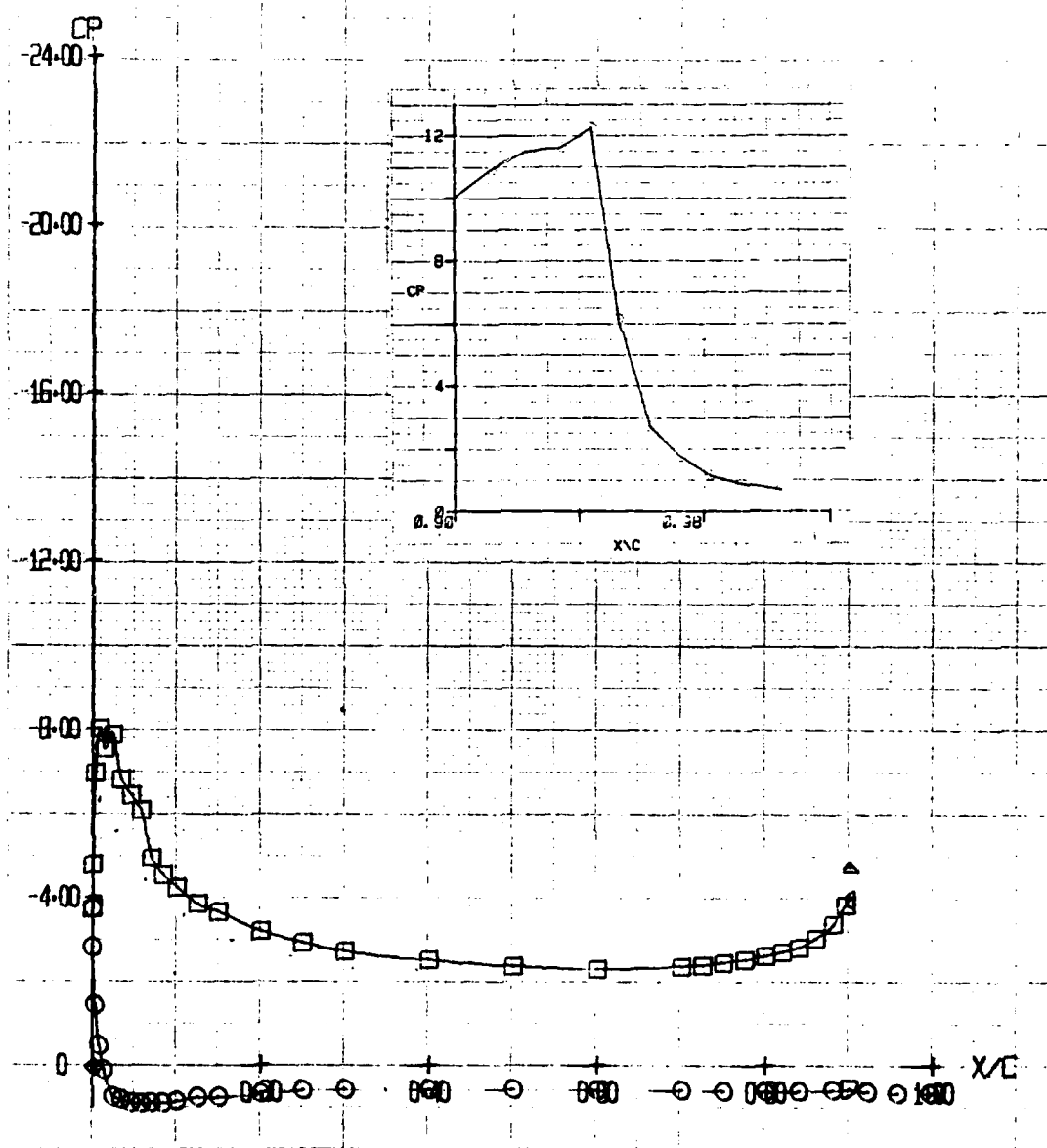
Figure I-14. C_μ = 0.52, Theta = 50°, Alpha = 0° (Test 272, Run 19)
            Q = 7.14 psf

103
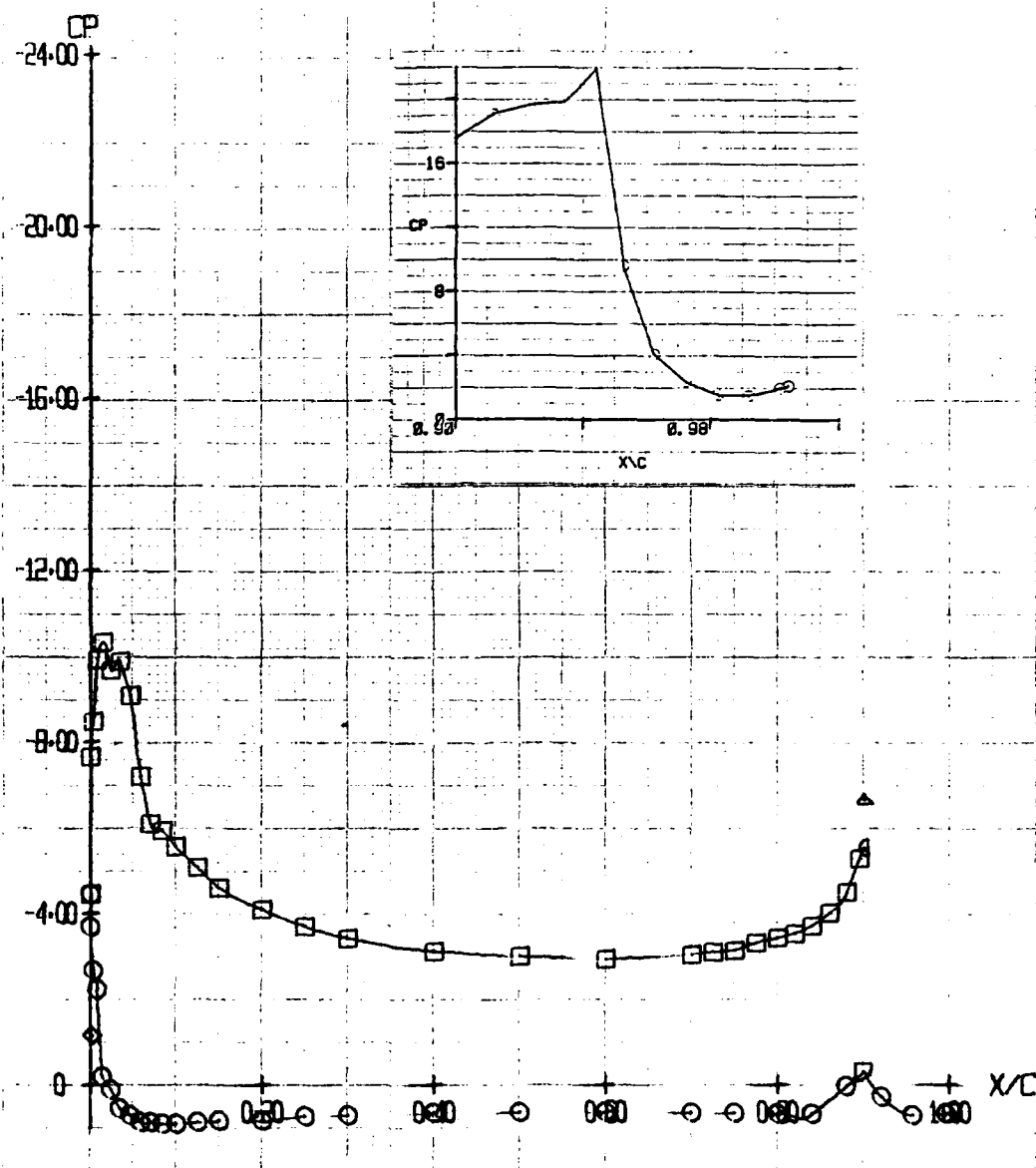
Figure I-15. $C_\mu = 1.01$, Theta = 50°, Alpha = 0° (Test 272, Run 20)
$Q = 7.07$ psf
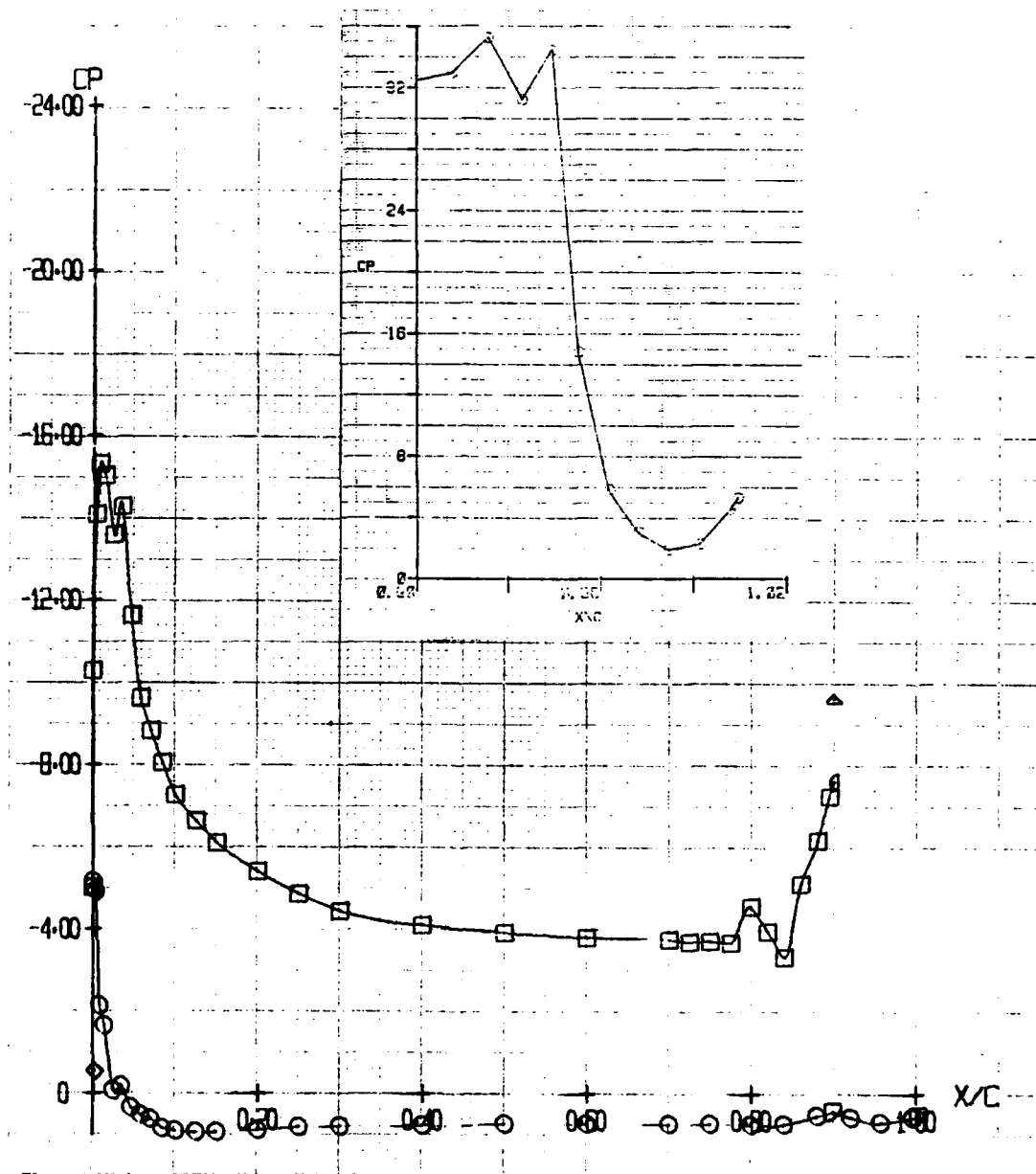
Figure I-16. C_μ = 2.05, Theta = 50°, Alpha = 0° (Test 272, Run 24)
Q = 7.02 psf
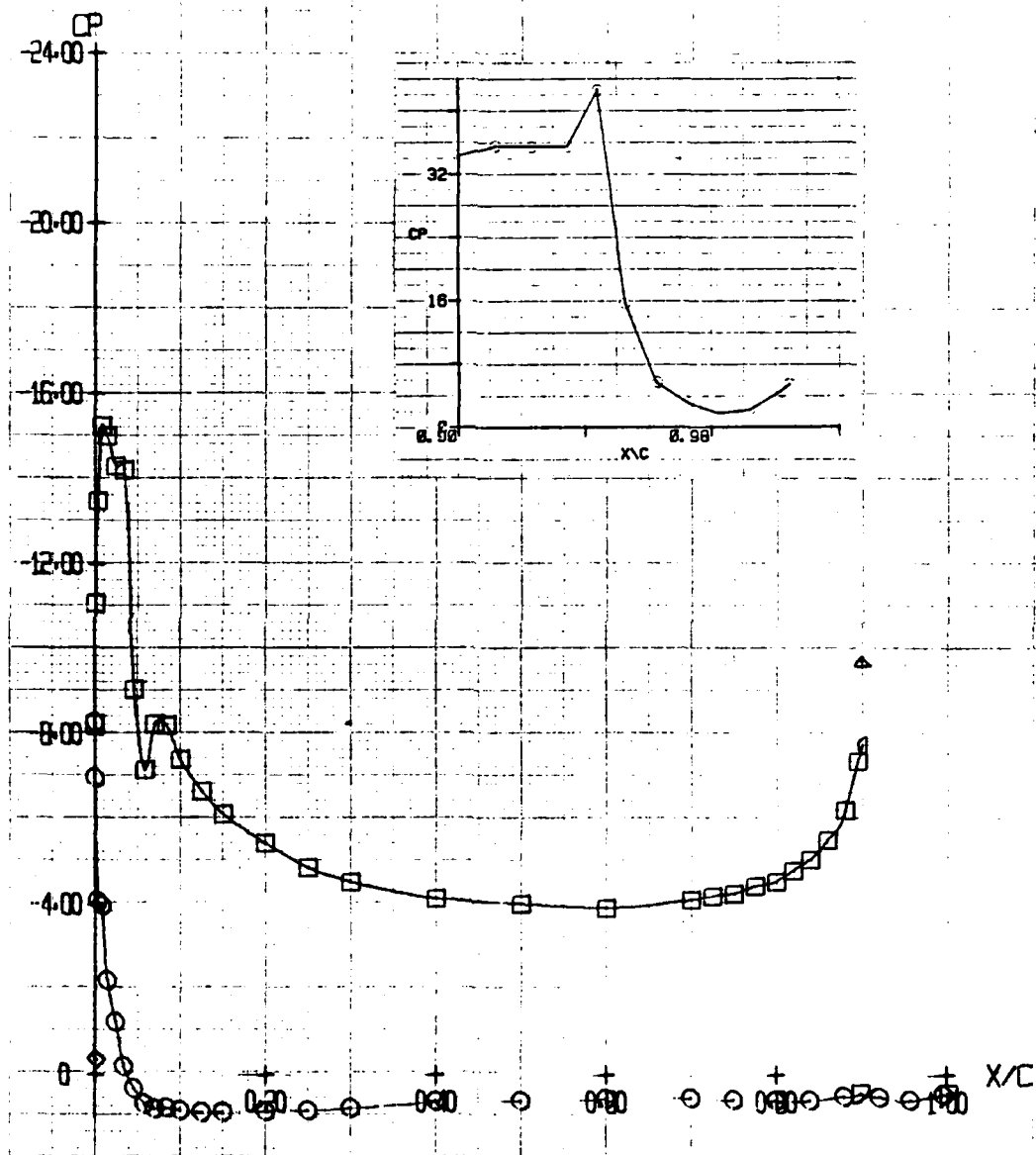
Figure I-17. C_μ = 2.04, Theta = 50°, Alpha = 0° (Test 272, Run 21)
Q = 7.04 psf

106
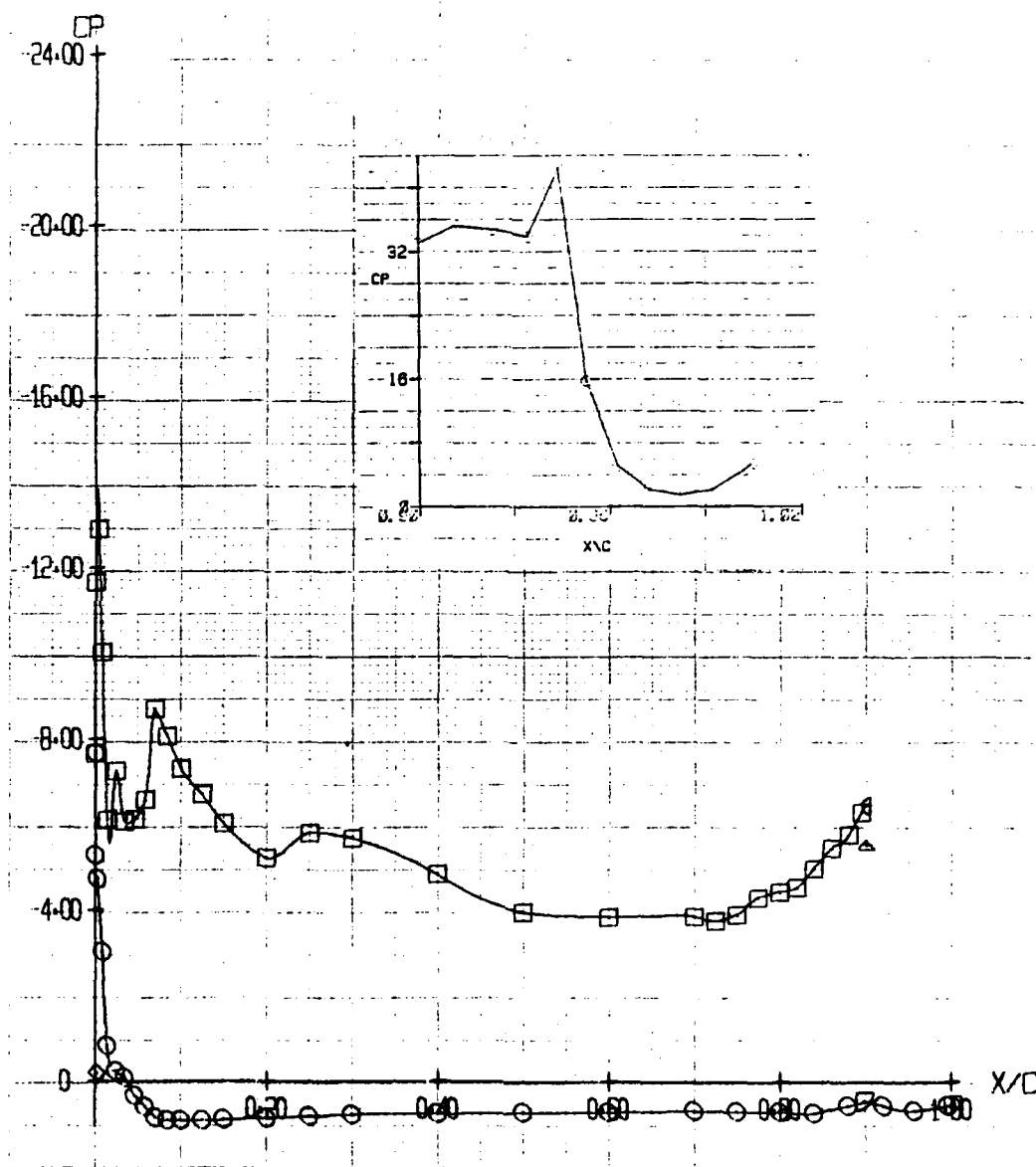
Figure I-18. $C_\mu = 2.04$, Theta = 50°, Alpha = 0° (Test 272, Run 29)
$Q = 7.03$ psf

107
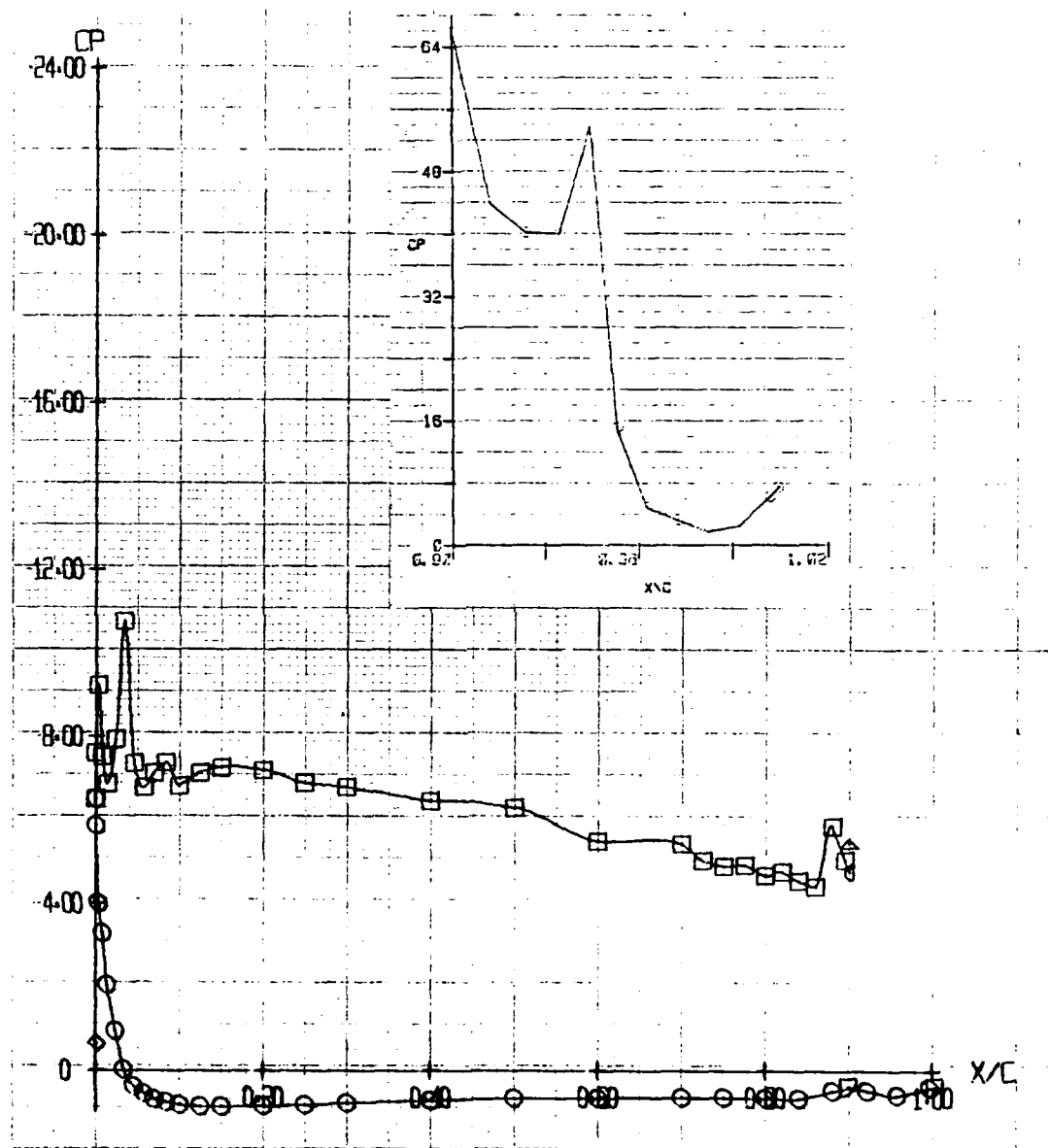
Figure I-19. C_μ = 3.06, Theta = 50°, Alpha = 0° (Test 272, Run 28)
Q = 7.06 psf

108
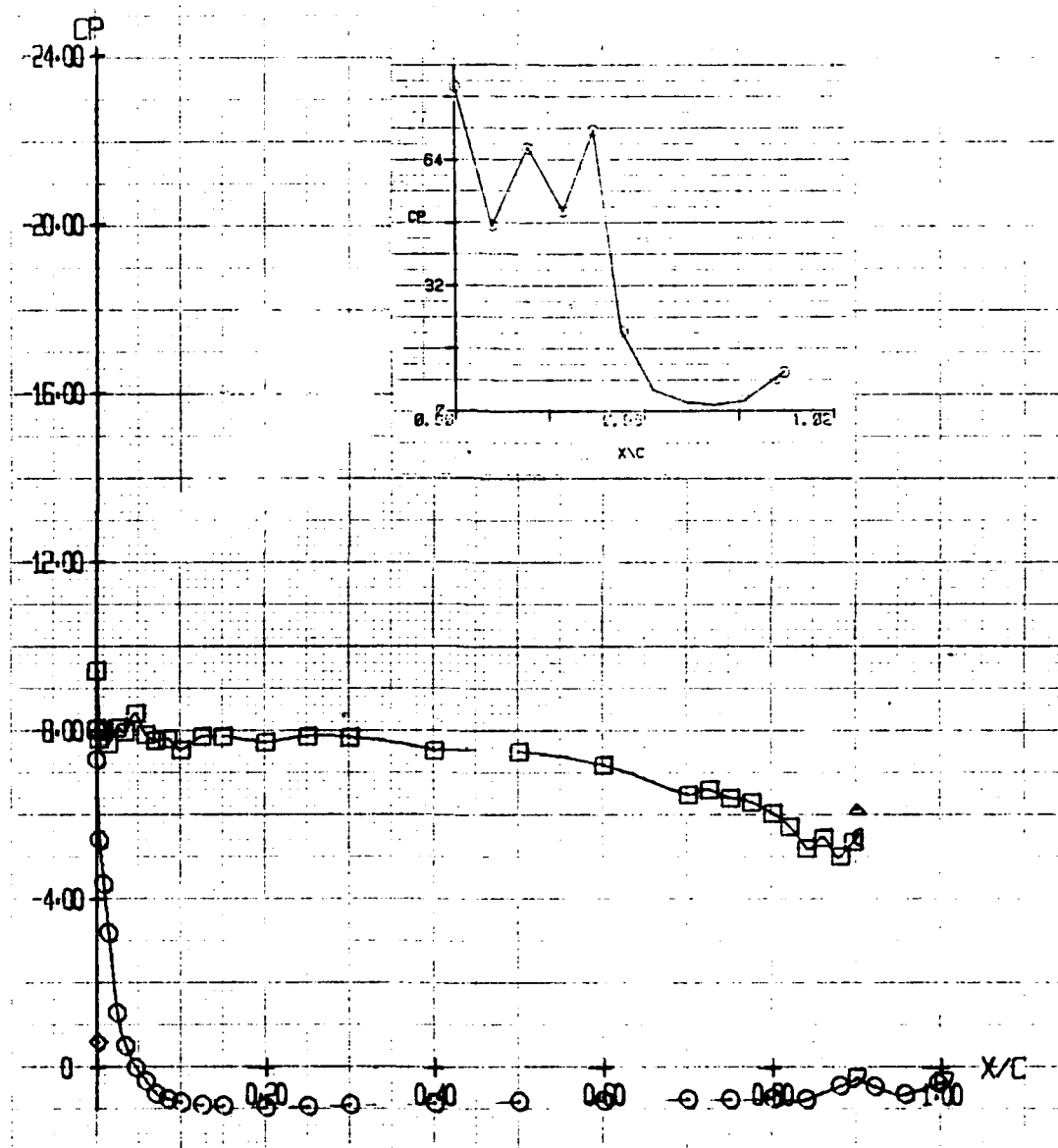
Figure I-20. C_μ = 4.15, Theta = 50°, Alpha = 0° (Test 272, Run 22)
Q = 6.00 psf
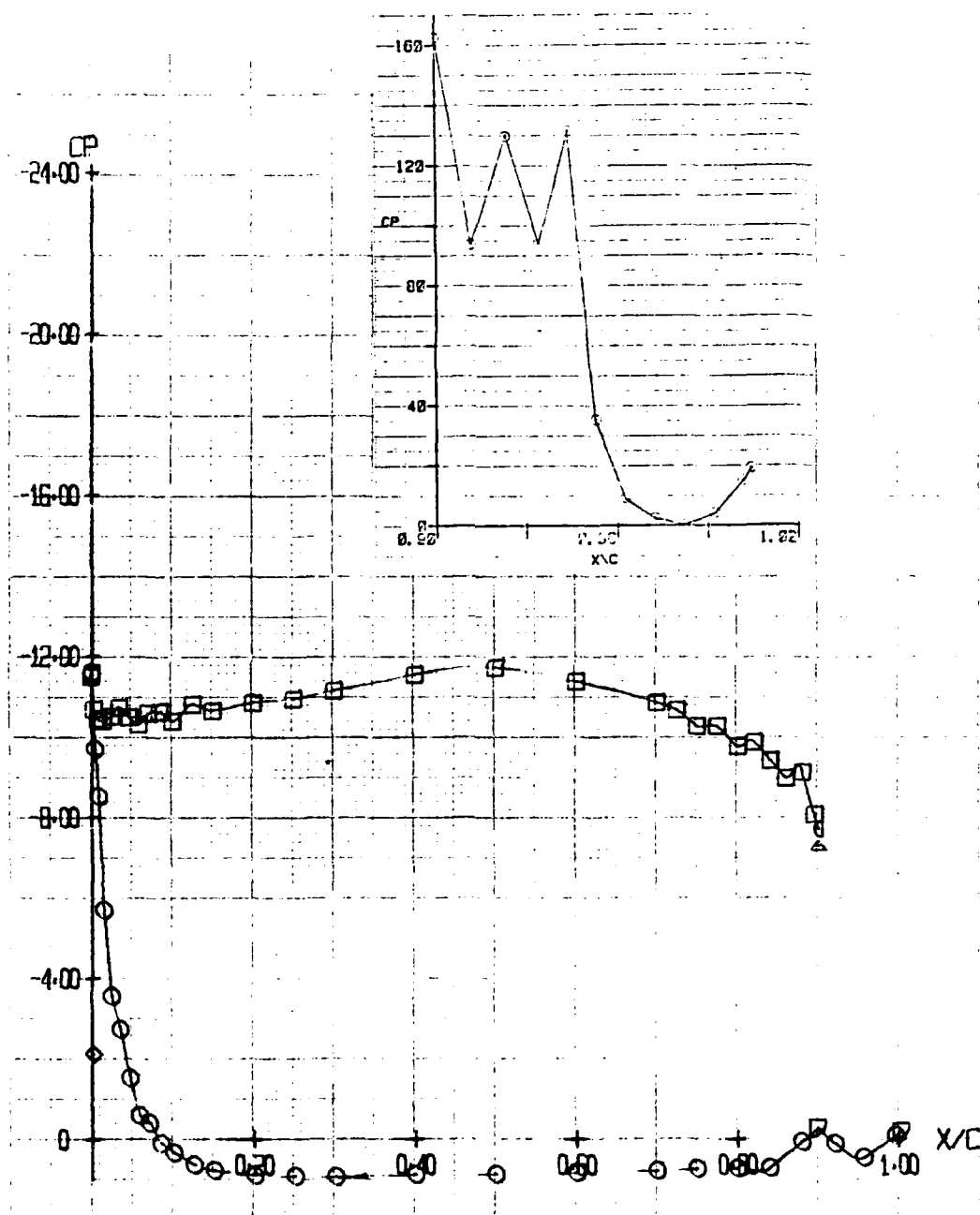
Figure I-21. C_μ = 8.17, Theta = 50°, Alpha = 0° (Test 272, Run 25)
             Q = 3.02 psf

110
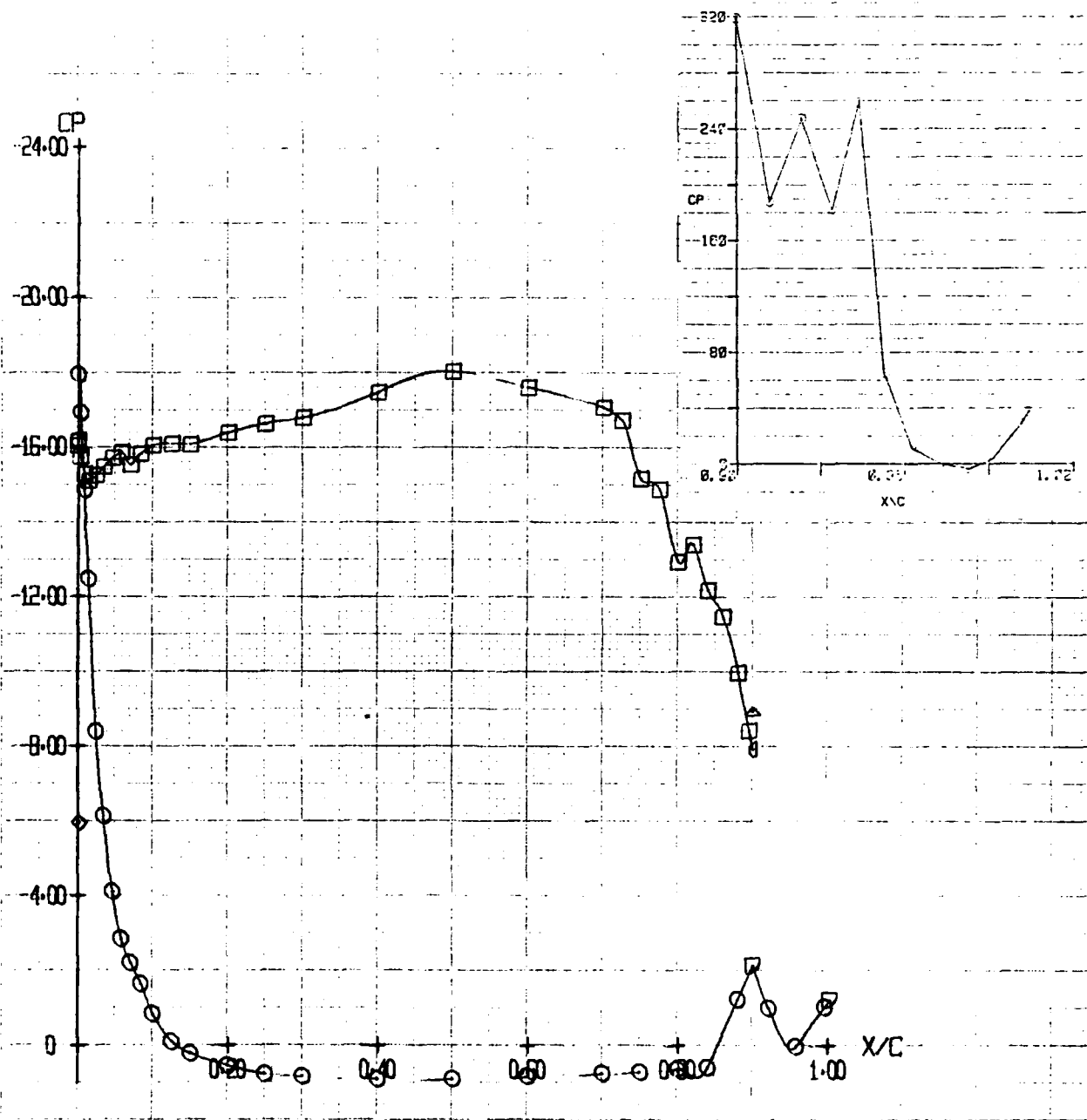
Figure I-22. C_μ = 16.22, Theta = 50°, Alpha = 0° (Test 272, Run 26)
Q = 1.51 psf

111
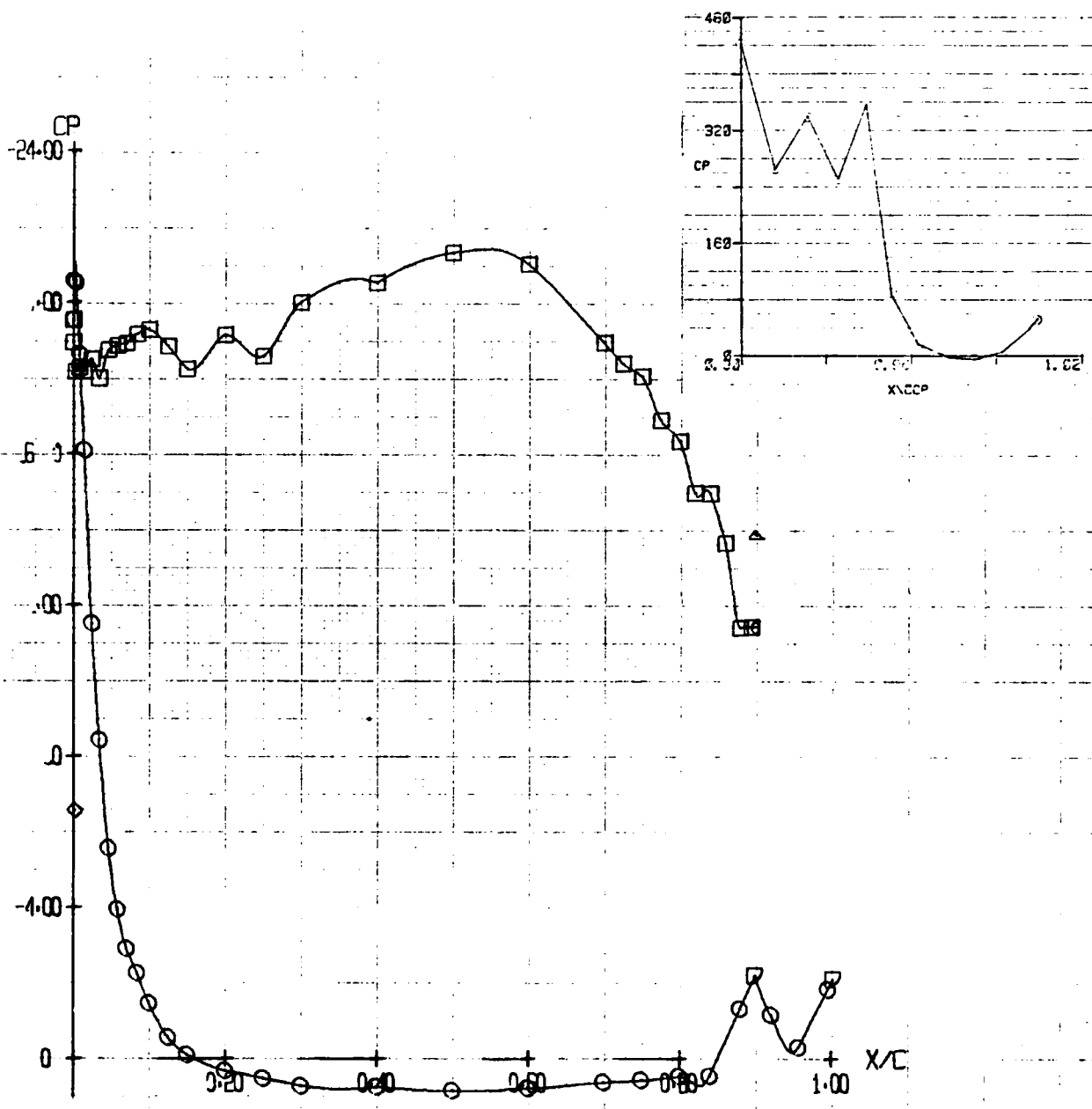
Figure I-23. C_μ = 22.33, Theta = 50°, Alpha = 0° (Test 272, Run 27)
Q = 1.09 psf

112
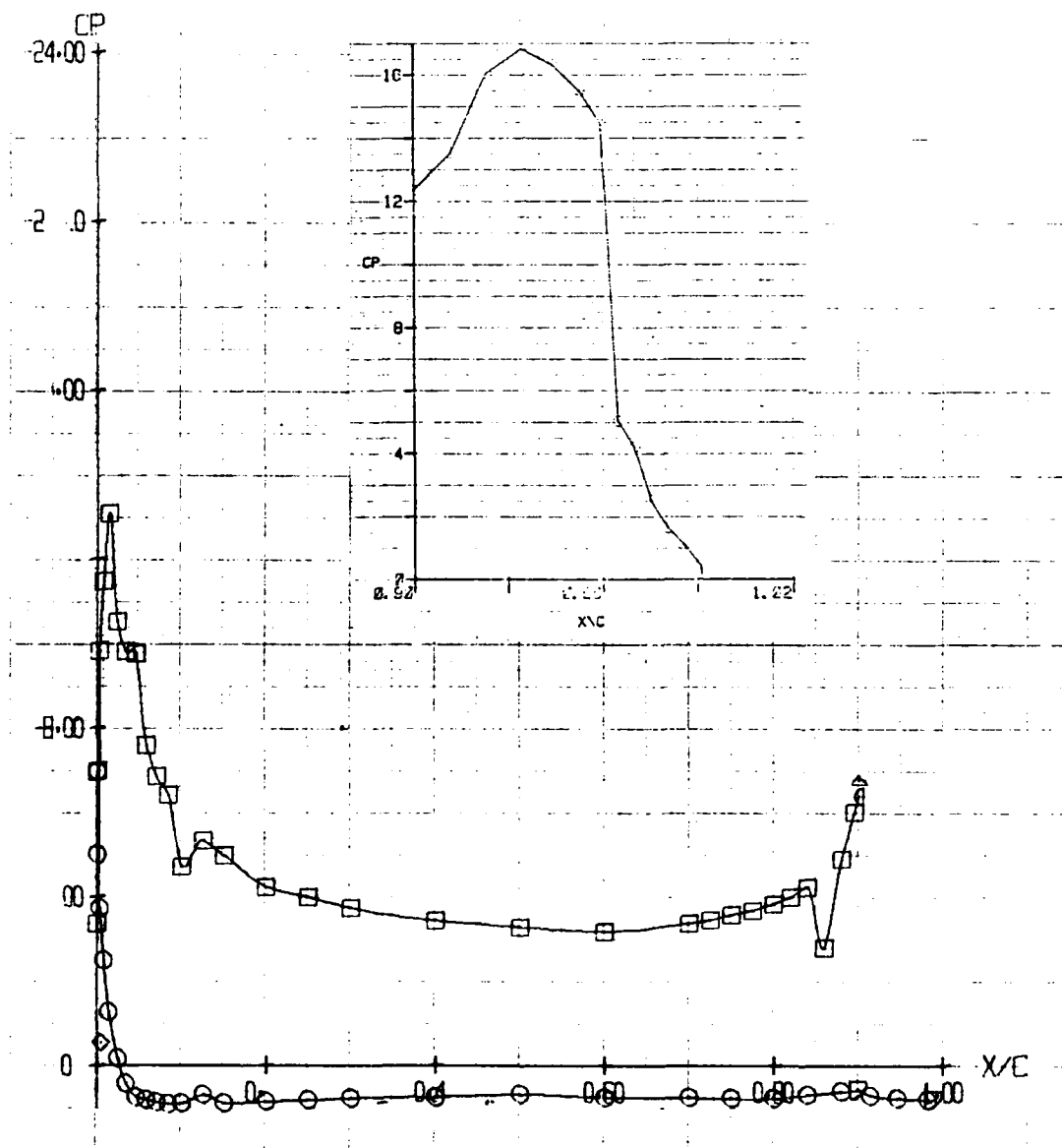
Figure I-24. C_μ = 0.55, Theta = 70°, Alpha = 0° (Test 272, Run 30)
Q = 6.84 psf

113
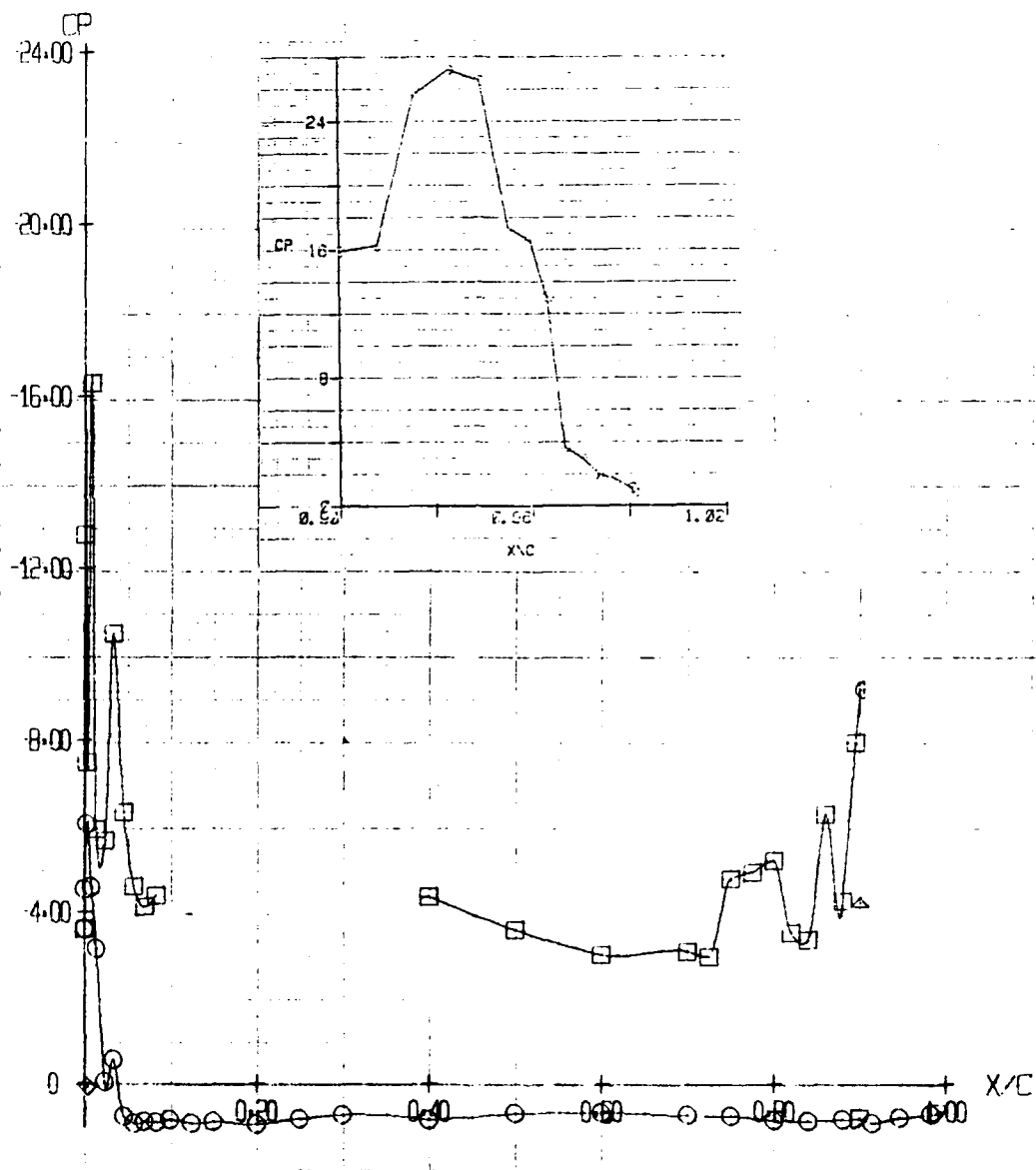
Figure I-25. $C_u = 1.04$, Theta = 70°, Alpha = 0° (Test 272, Run 43) $Q = 6.93$ psf

114
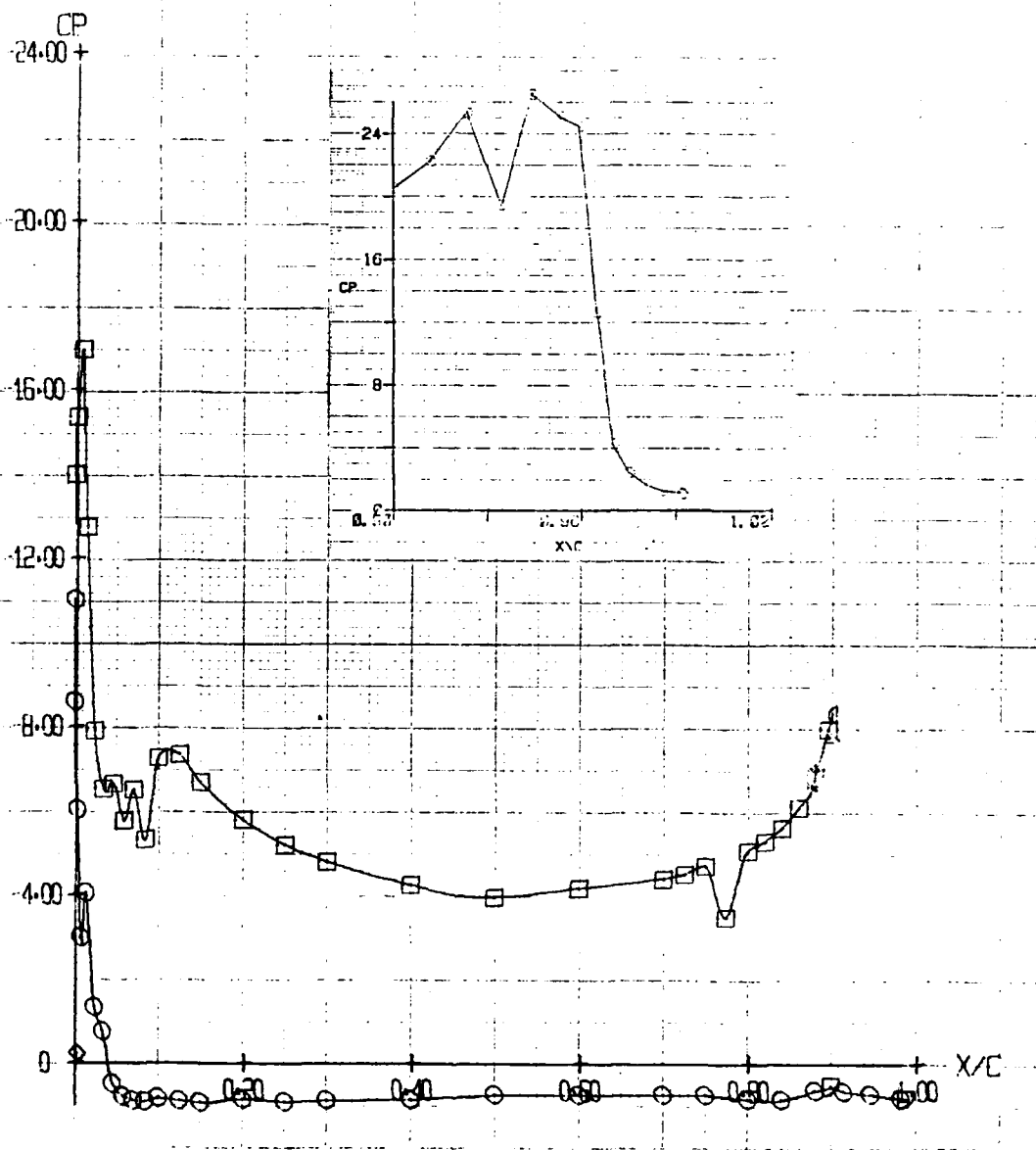
Figure I-26. C_μ = 1.05, Theta = 70°, Alpha = 0° (Test 272, Run 31)
Q = 6.94 psf

115
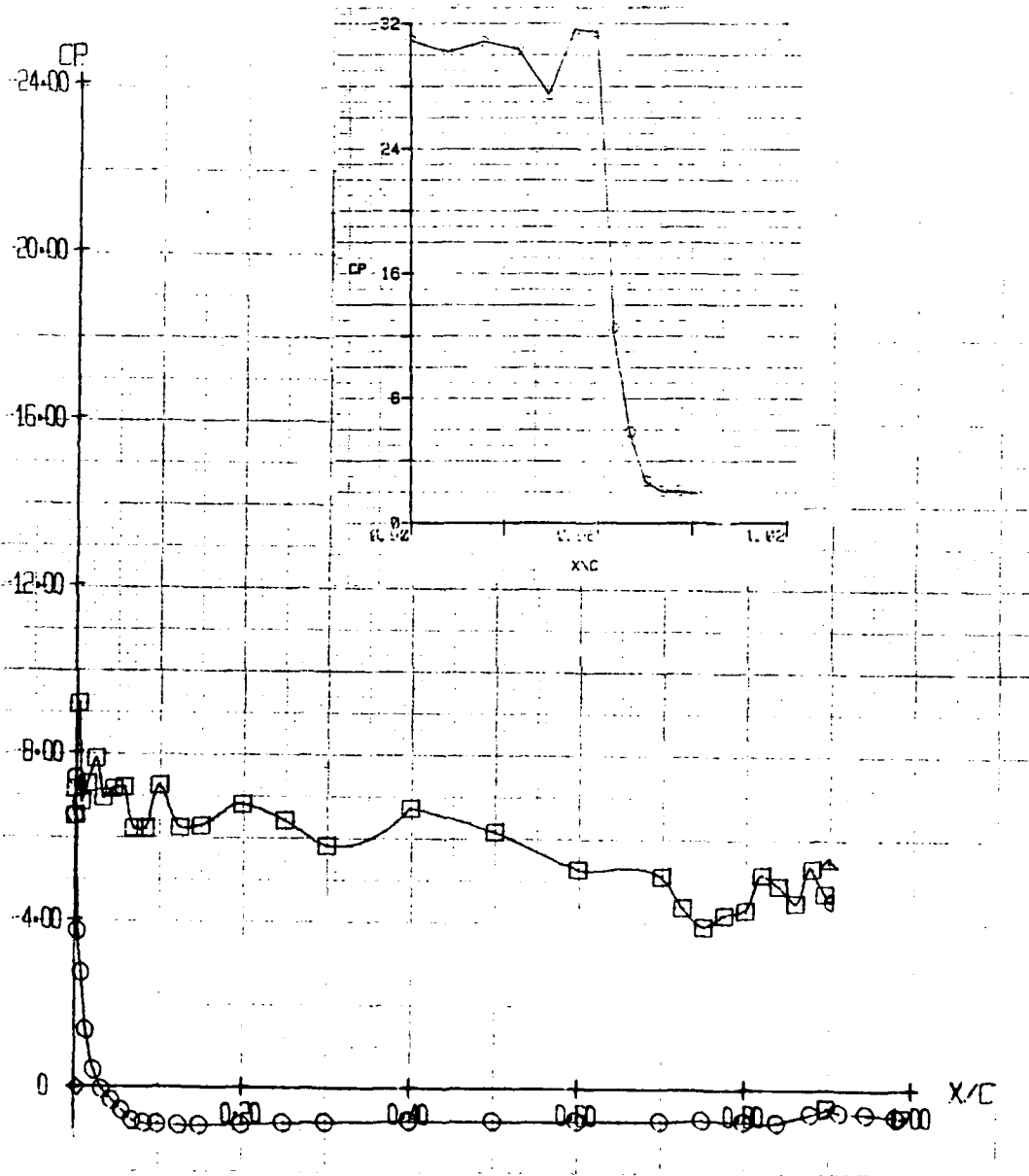
Figure I-27. C_μ = 2.08, Theta = 70°, Alpha = 0° (Test 272, Run 32)
         Q = 7.02 psf
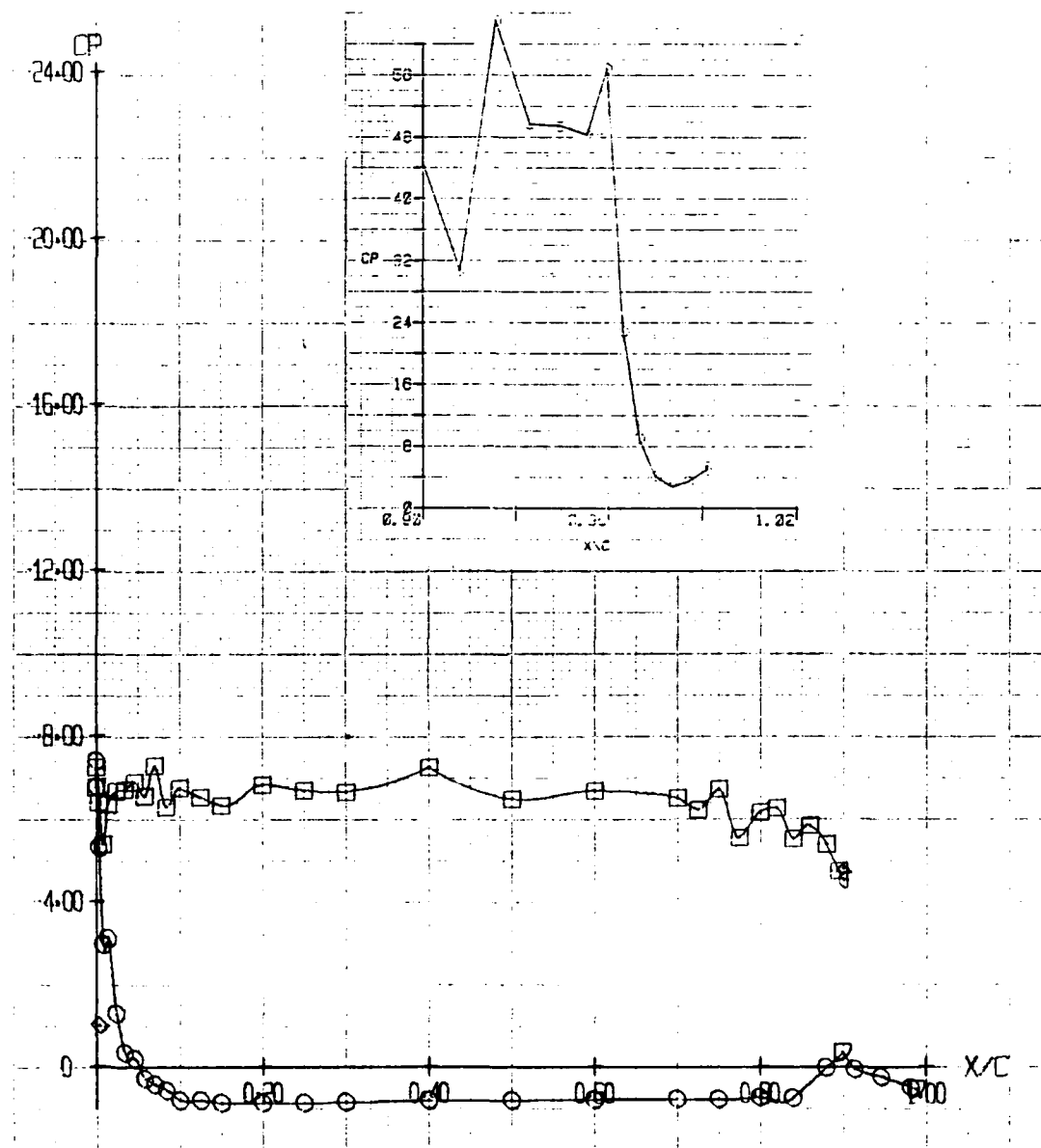
Figure I-28. C_μ = 4.26, Theta = 70°, Alpha = 0° (Test 272, Run 36)
Q = 5.99 psf

117
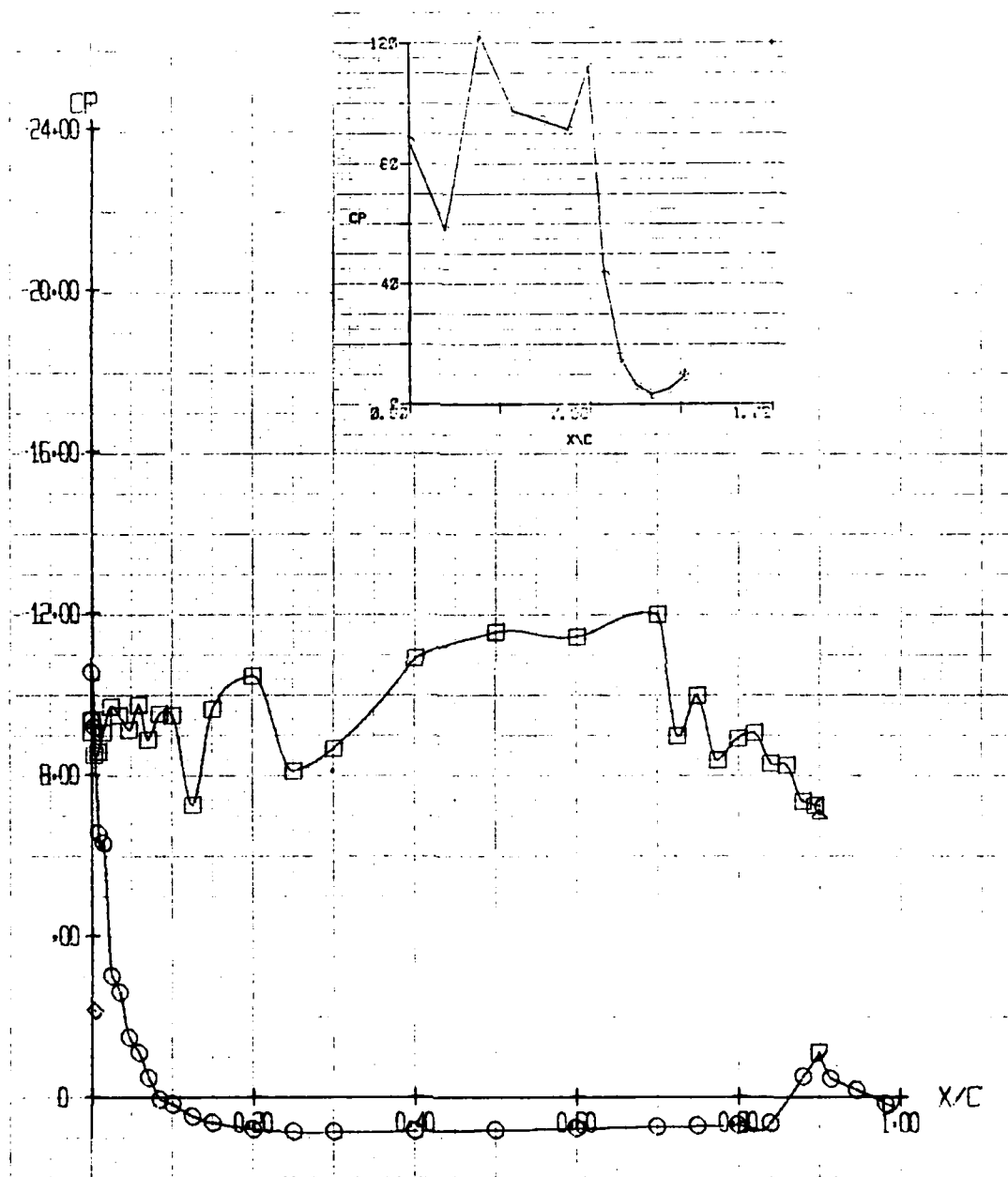
Figure I-29. C_μ = 8.31, Theta = 70°, Alpha = 0° (Test 272, Run 34)
Q = 3.06 psf

118
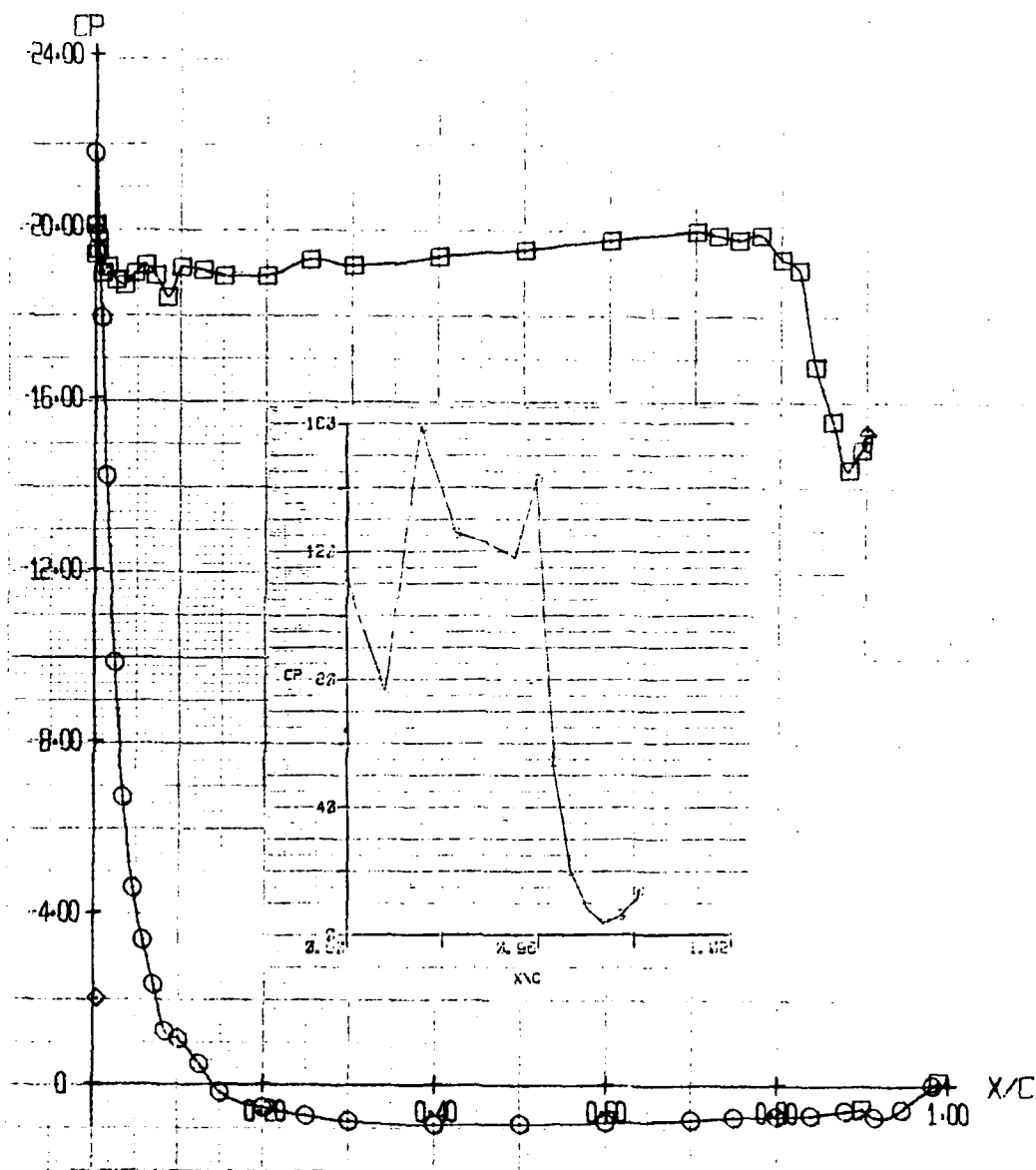
Figure I-30. C_μ = 10.52, Theta = 70°, Alpha = 0° (Test 272, Run 42)
             Q = 2.38 psf

119
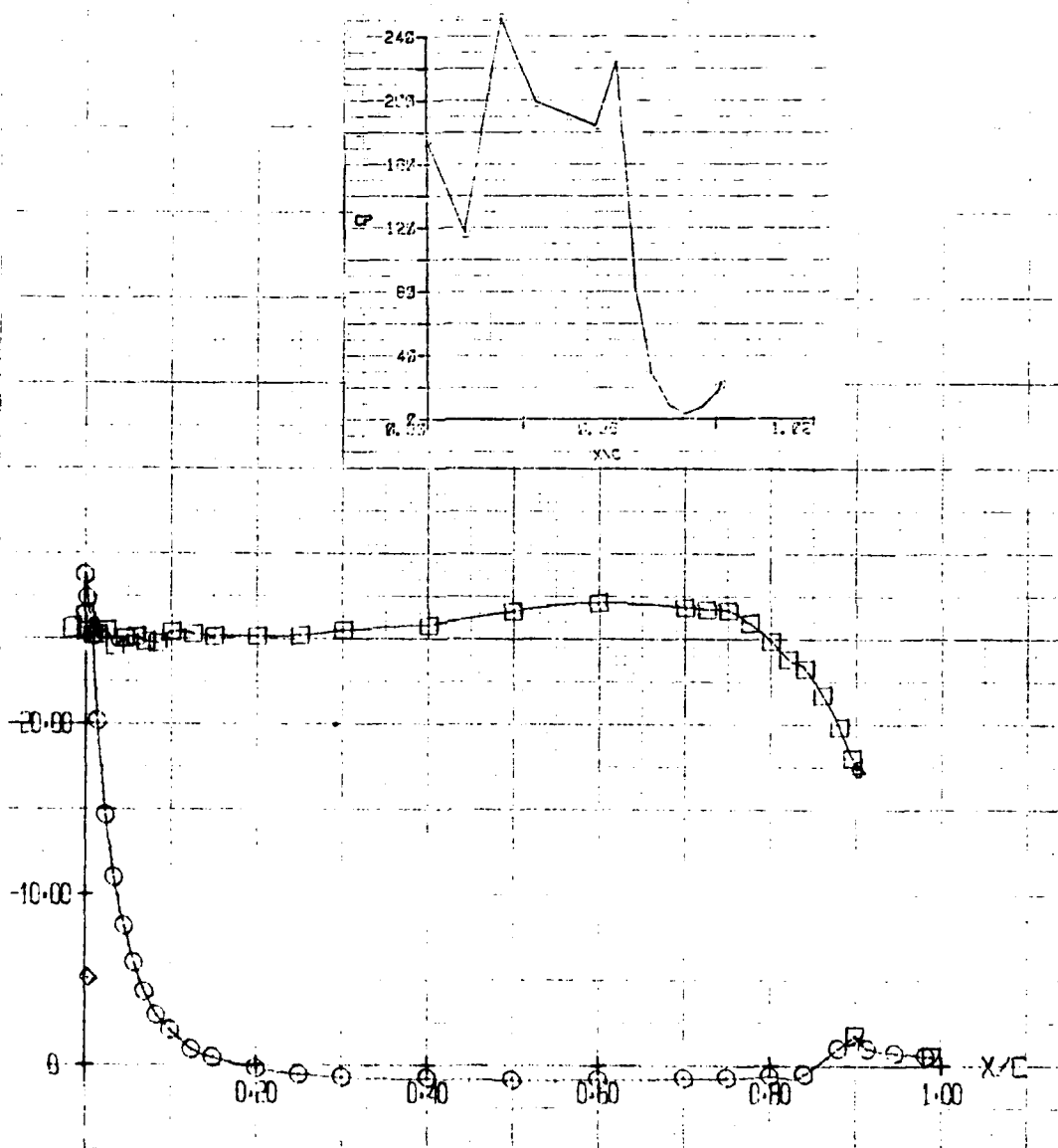
Figure I-31. $C_\mu = 16.60$, Theta = 70°, Alpha = 0° (Test 272, Run 37)
            Q = 1.51 psf

120
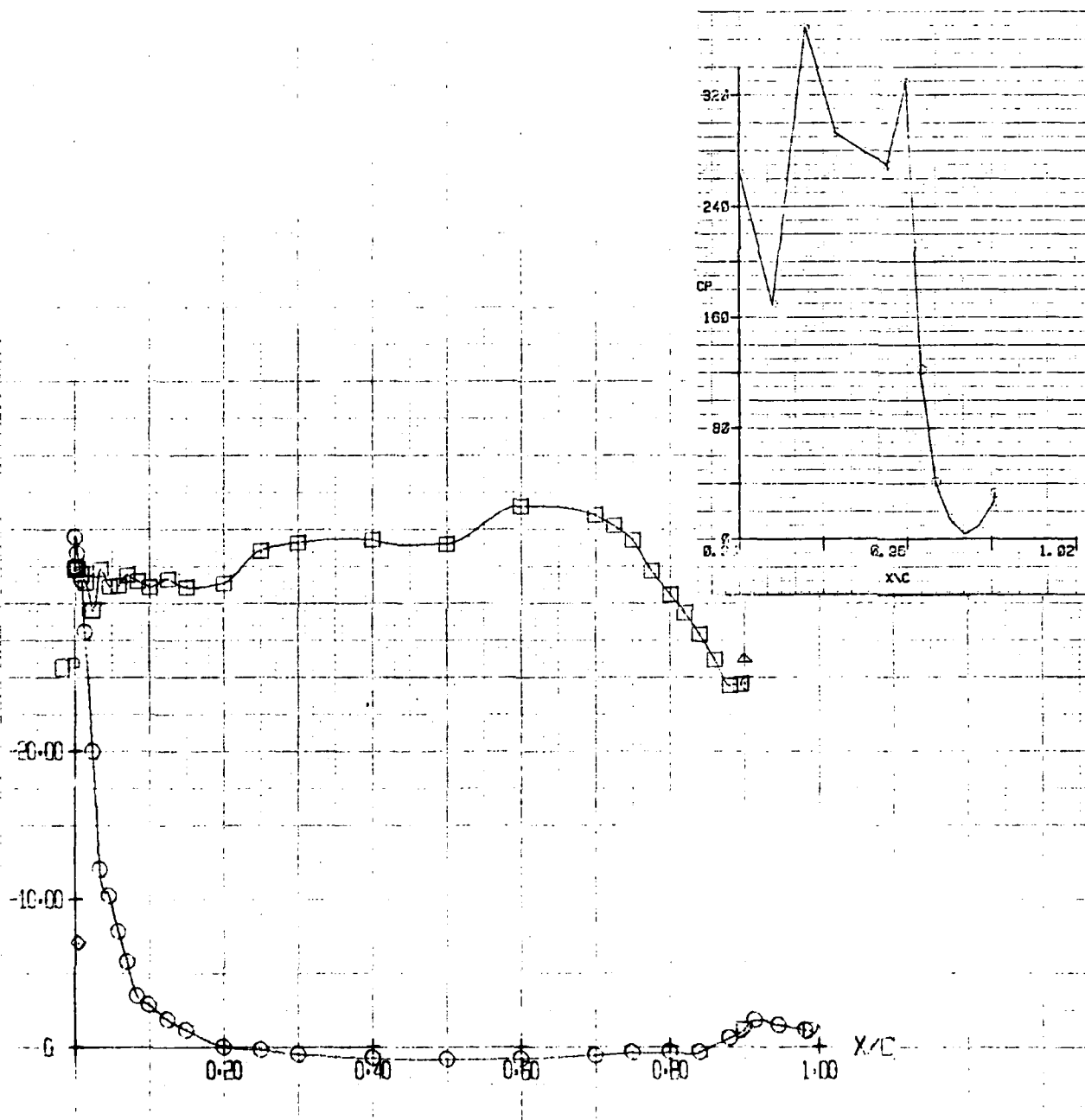
Figure I-32. C_μ = 24.43, Theta = 70°, Alpha = 0° (Test 272, Run 38)
Q = 1.02 psf
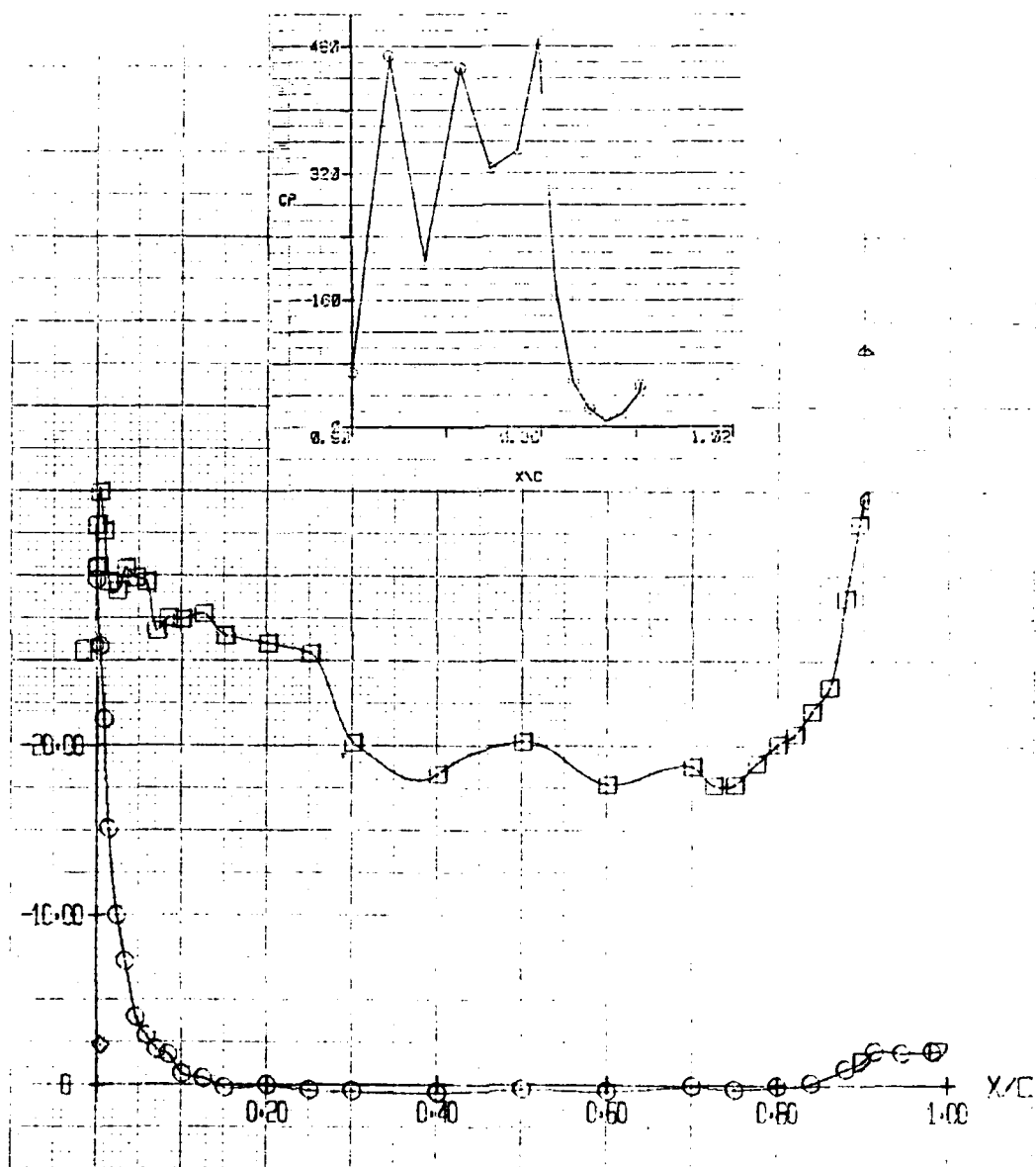
Figure I-33. C_μ = 28.92, Theta = 70°, Alpha = 0° (Test 272, Run 39)
Q = 1.05 psf

122
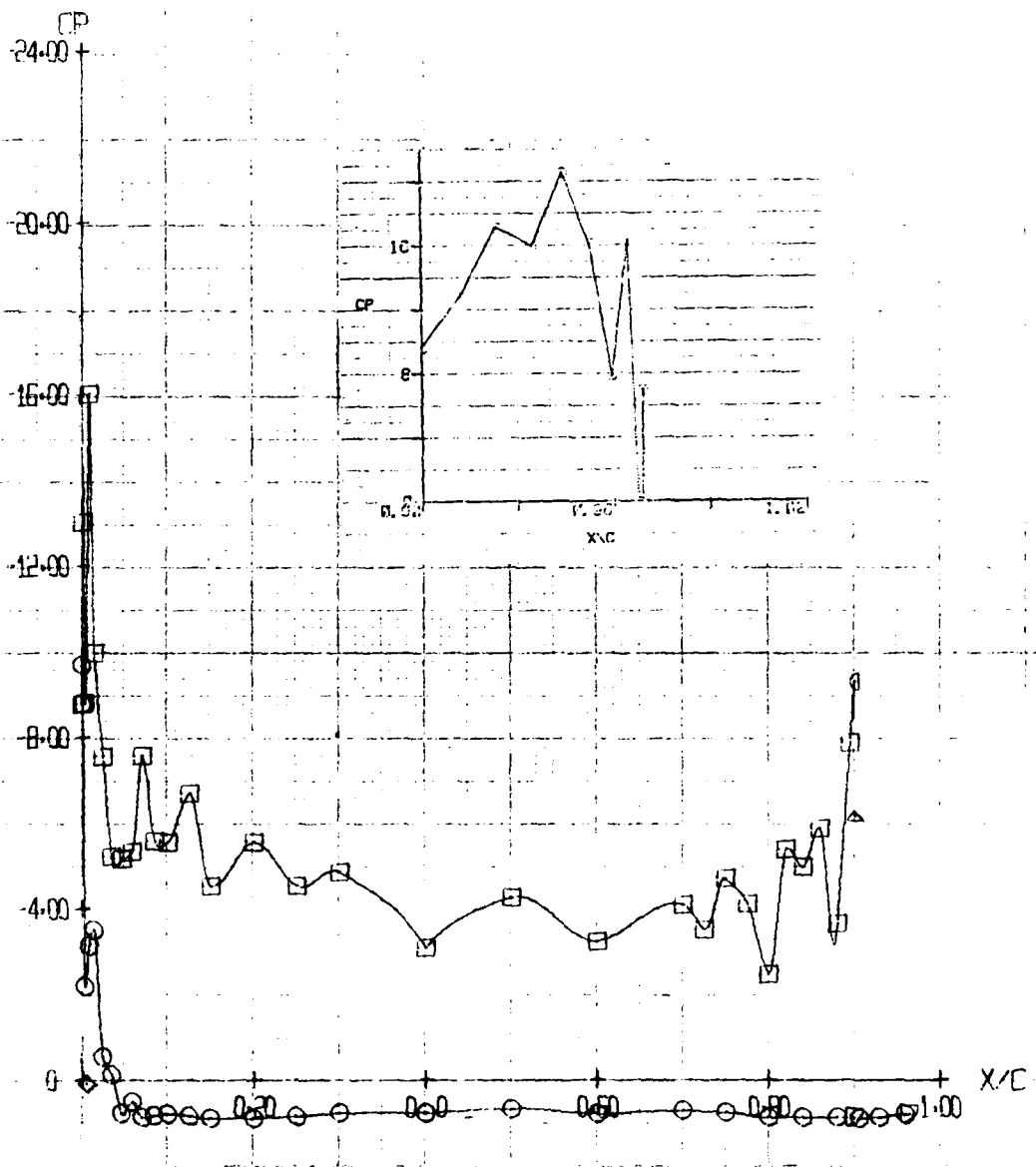
Figure I-34. C_μ = 0.52, Theta = 90°, Alpha = 0° (Test 272, Run 47)
Q = 7.02 psf

123
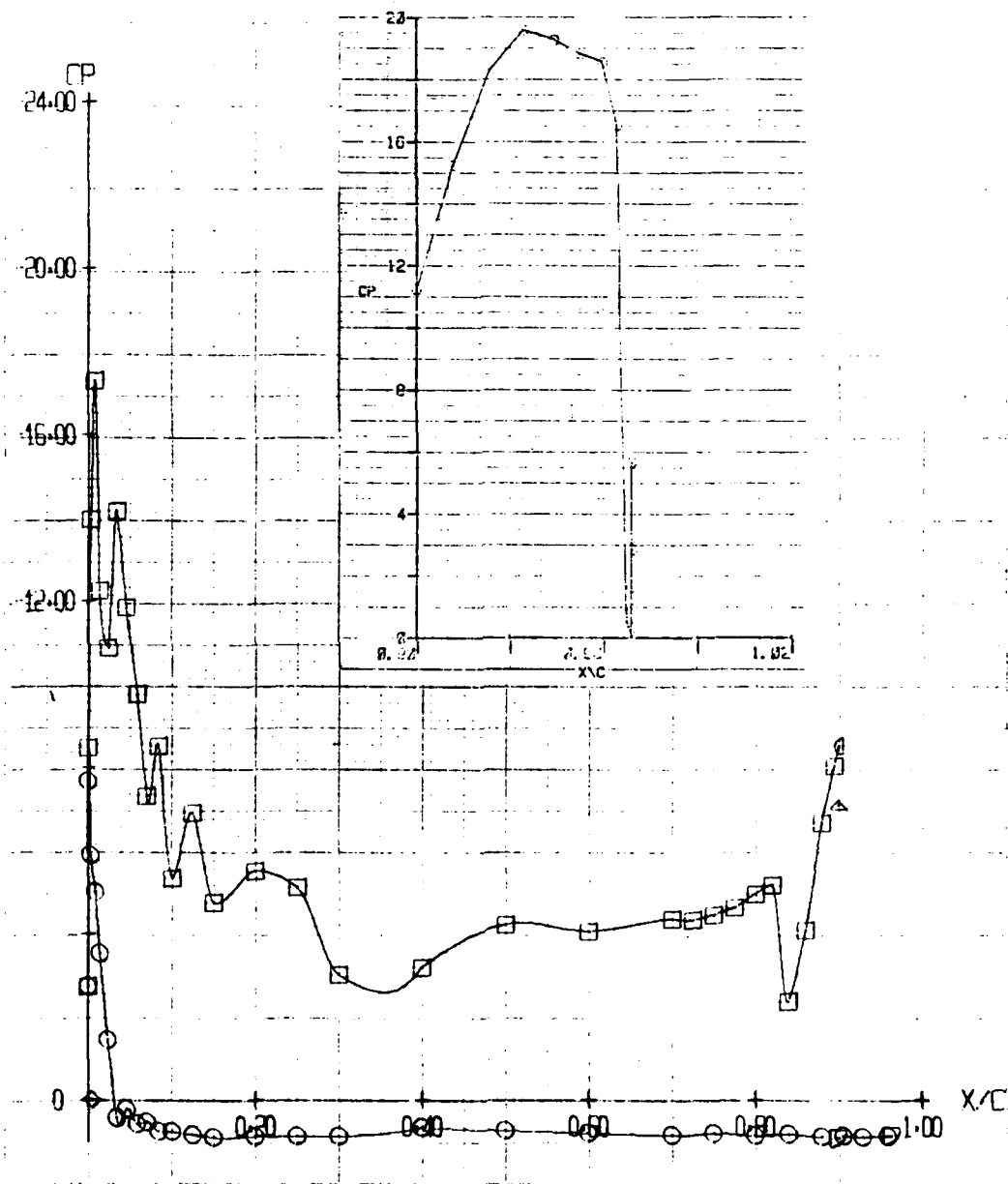
Figure I-35. C_μ = 0.51, Theta = 90°, Alpha = 0° (Test 272, Run 44)
Q = 7.24 psf

124
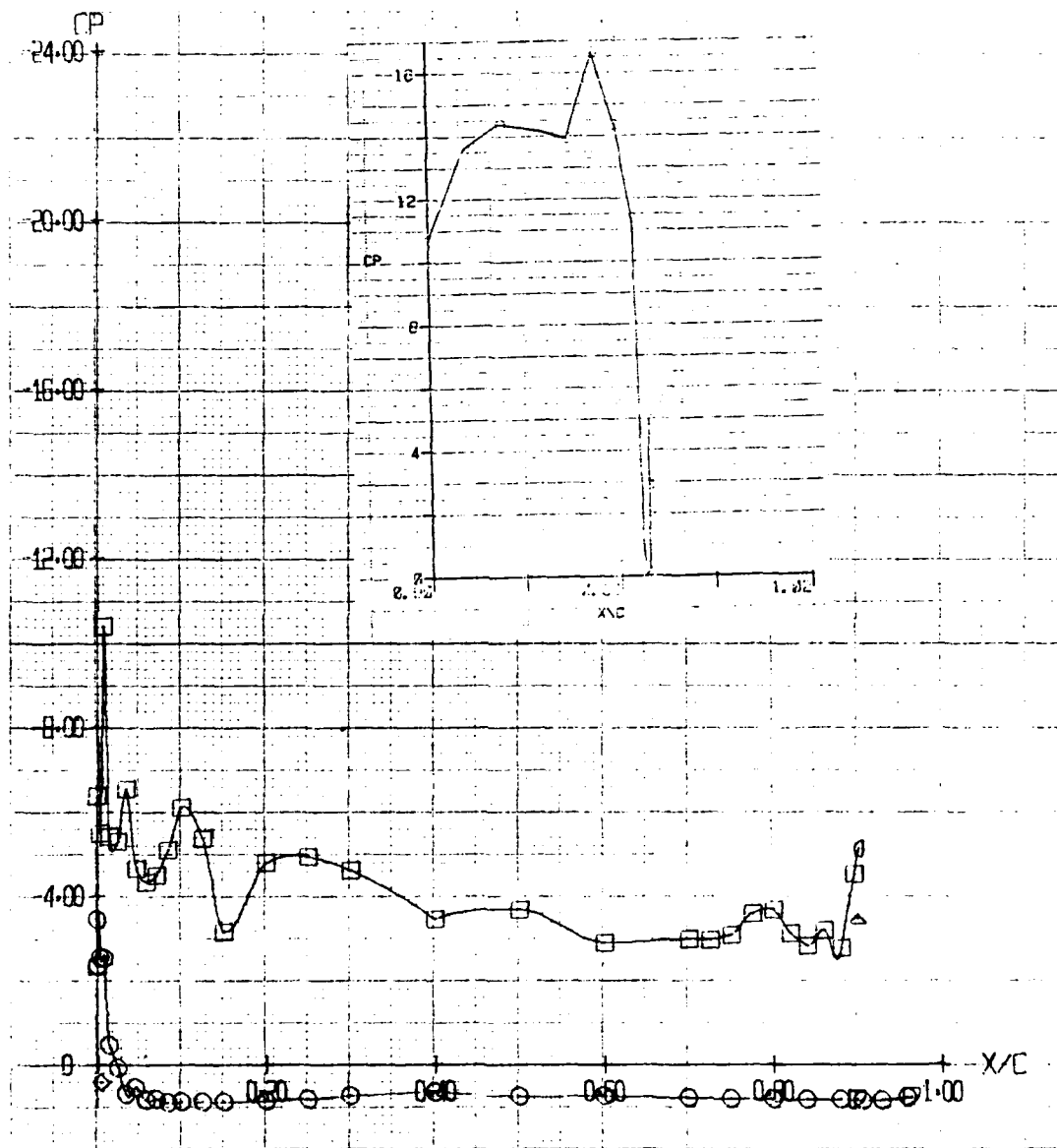
Figure I-36. C_μ = 0.97, Theta = 90°, Alpha = 0° (Test 272, Run 45)
              Q = 6.95 psf
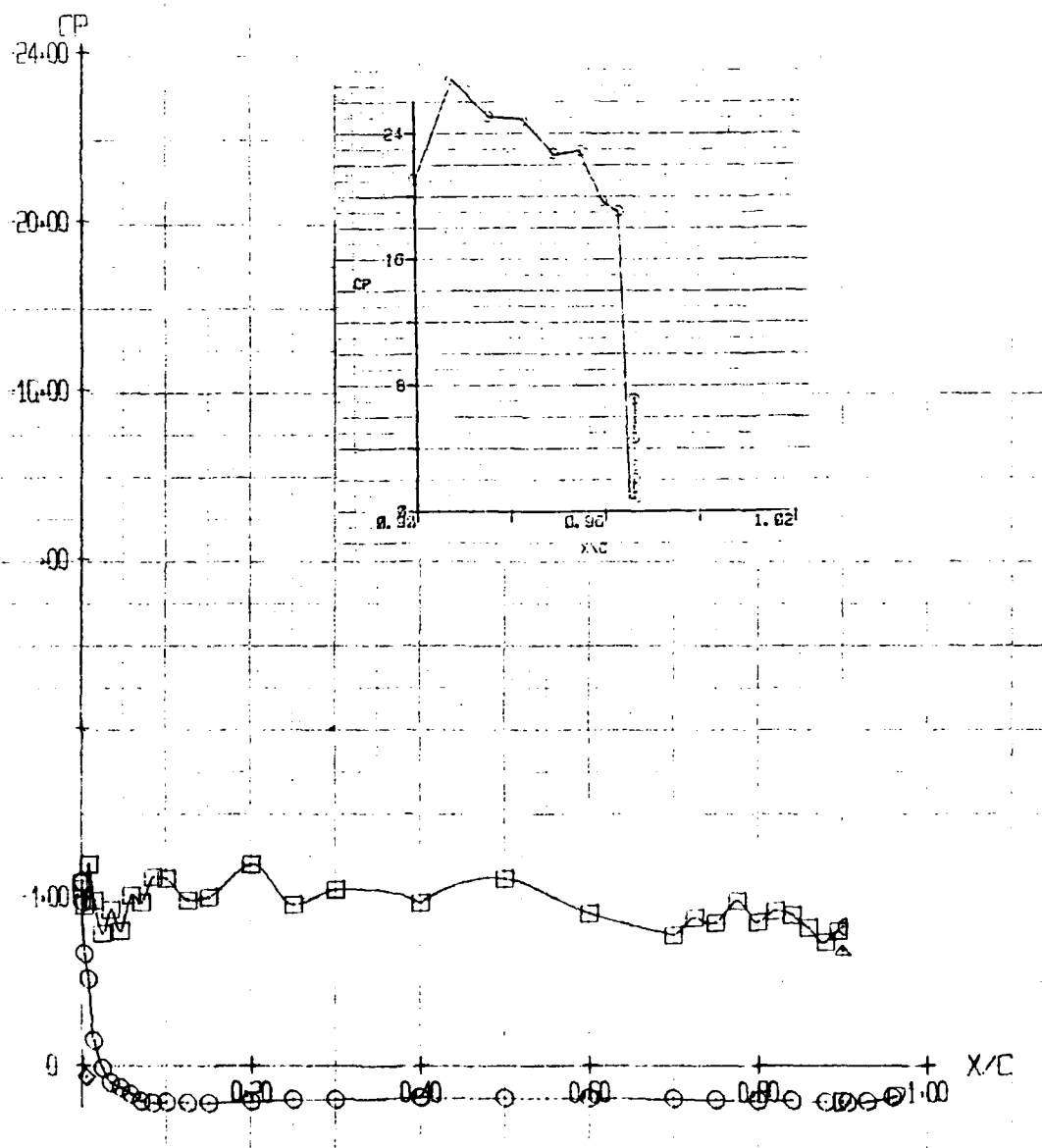
Figure I-37. C_μ = 1.95, Theta = 90°, Alpha = 0° (Test 272, Run 56)
Q = 6.98 psf

126
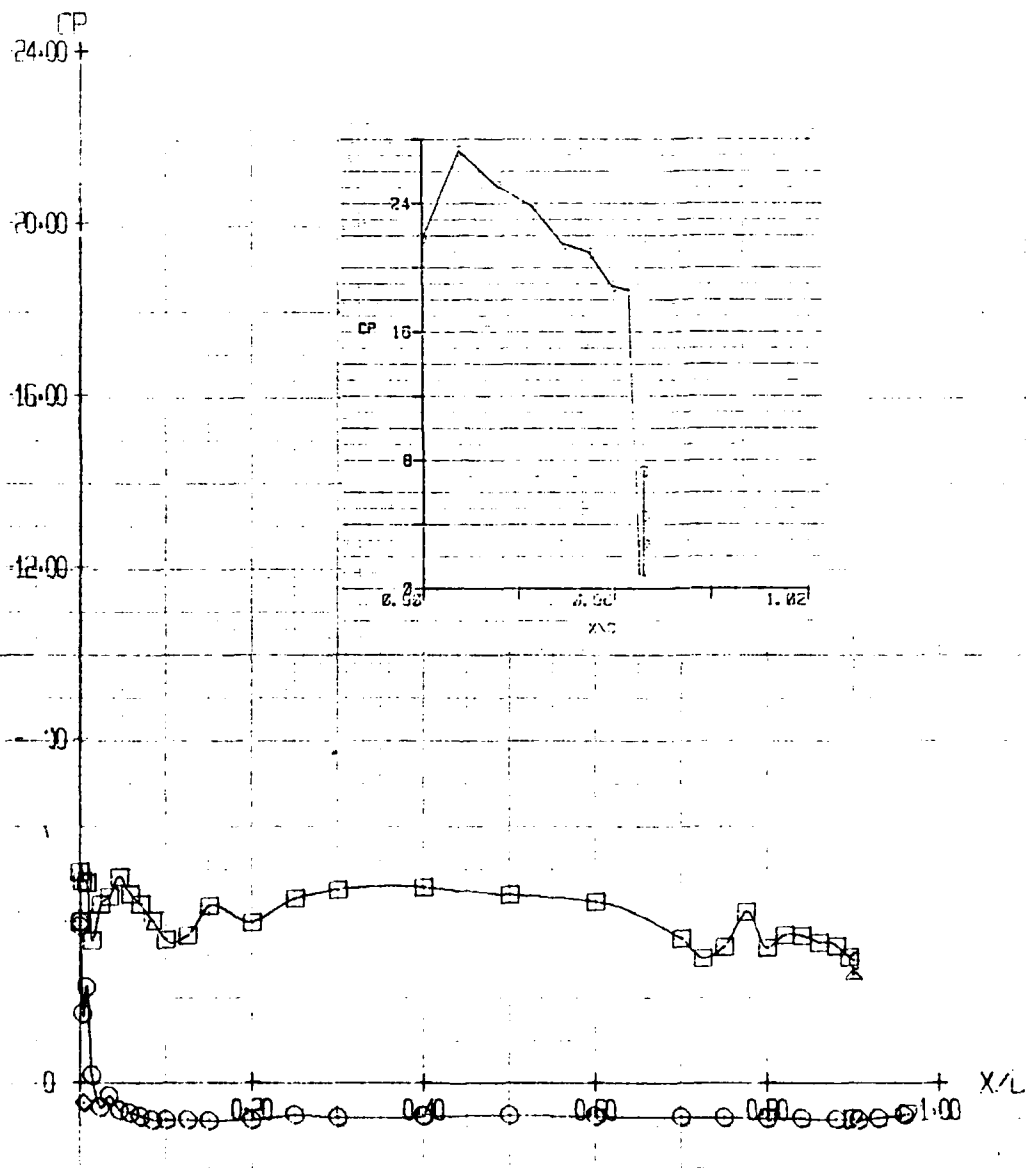
Figure I-38. C_μ = 1.96, Theta = 90°, Alpha = 0° (Test 272, Run 46)
Q = 6.99 psf

127
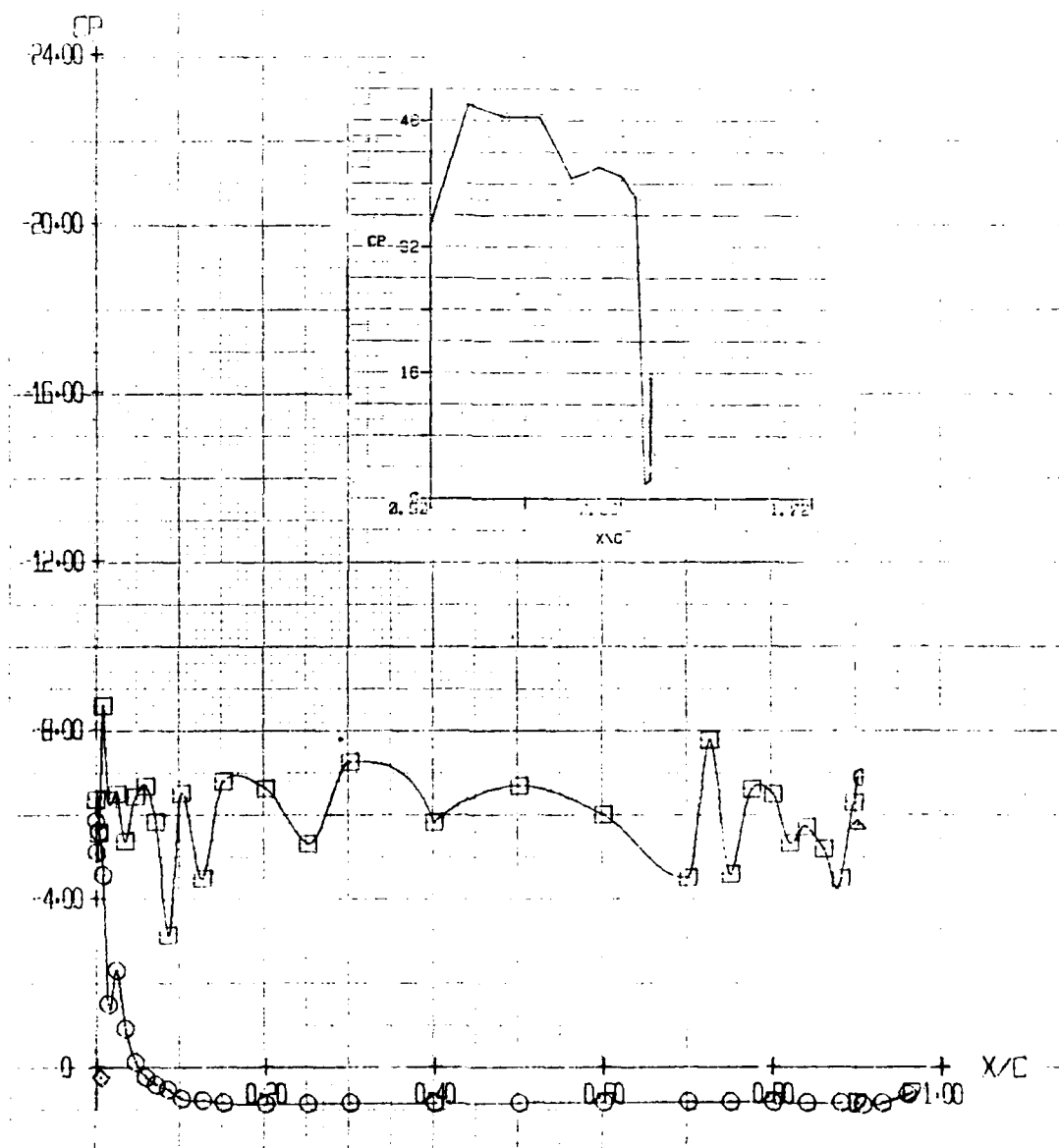
Figure I-39. C_μ = 3.93, Theta = 90°, Alpha = 0° (Test 272, Run 48)
          Q = 5.99 psf

128
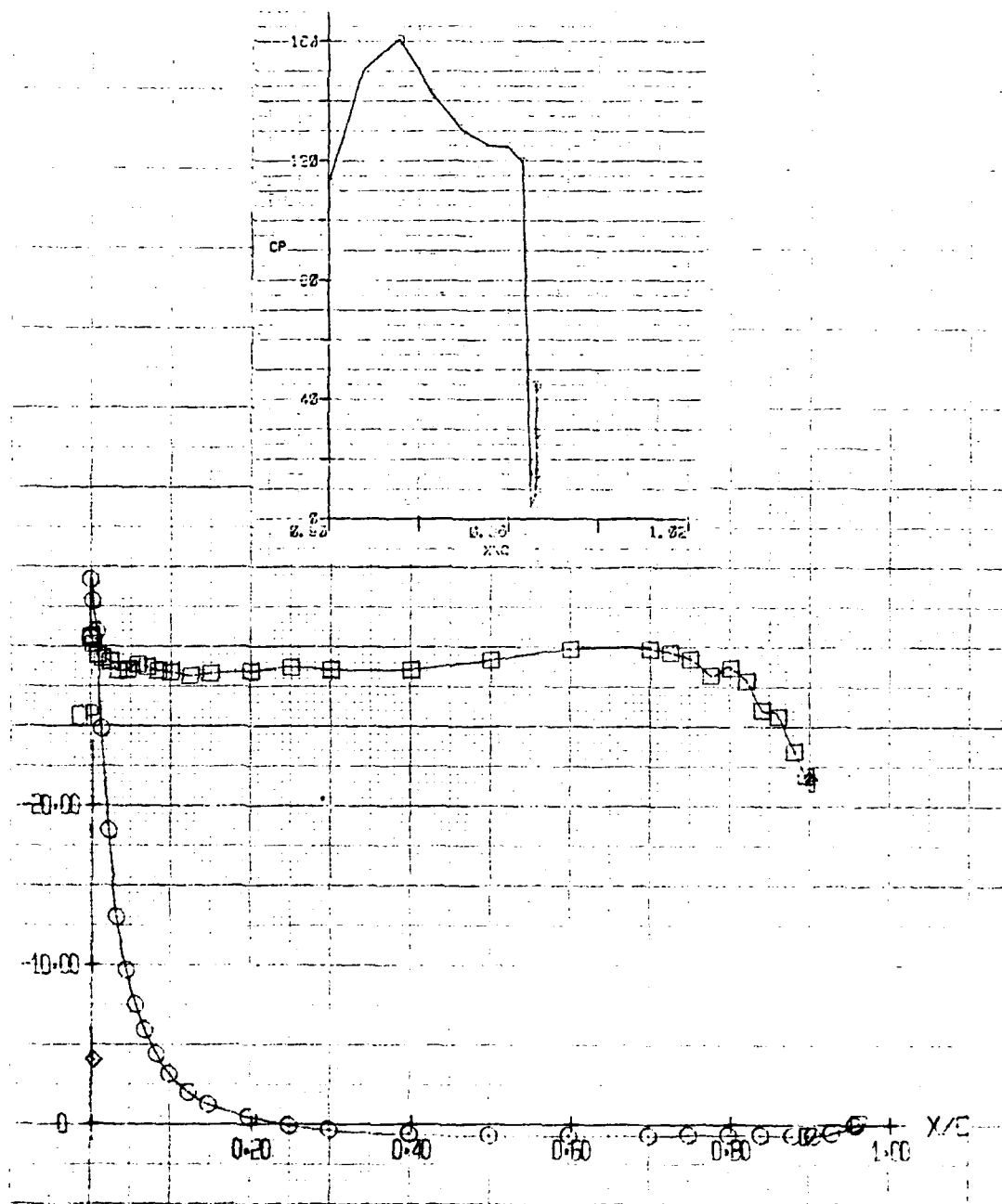
Figure I-40. C_μ = 11.49, Theta = 90°, Alpha = 0° (Test 272, Run 49)
              Q = 2.02 psf

129
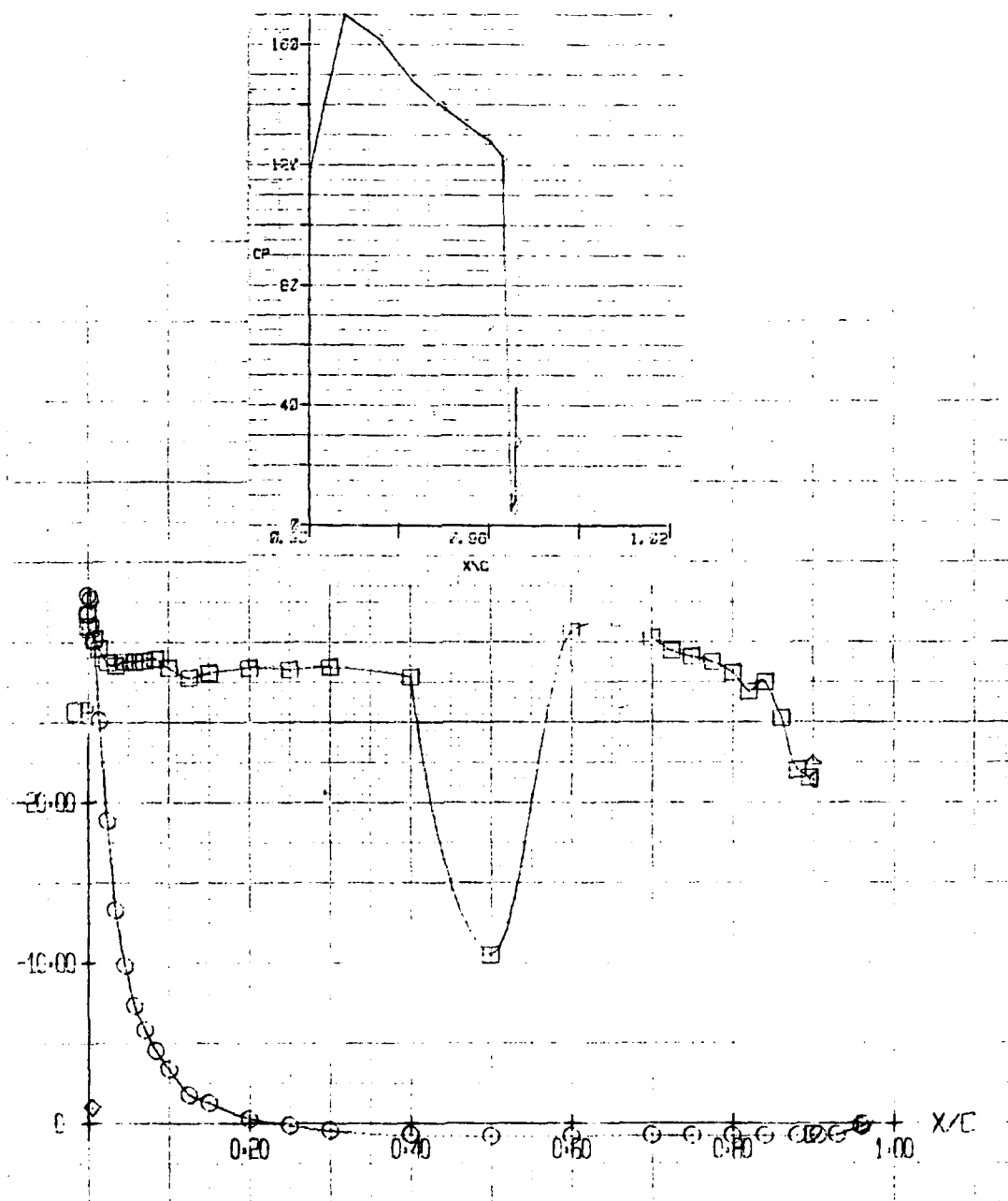
Figure I-41. C_μ = 11.80, Theta = 90°, Alpha = 0° (Test 272, Run 54)
Q = 1.97 psf

130
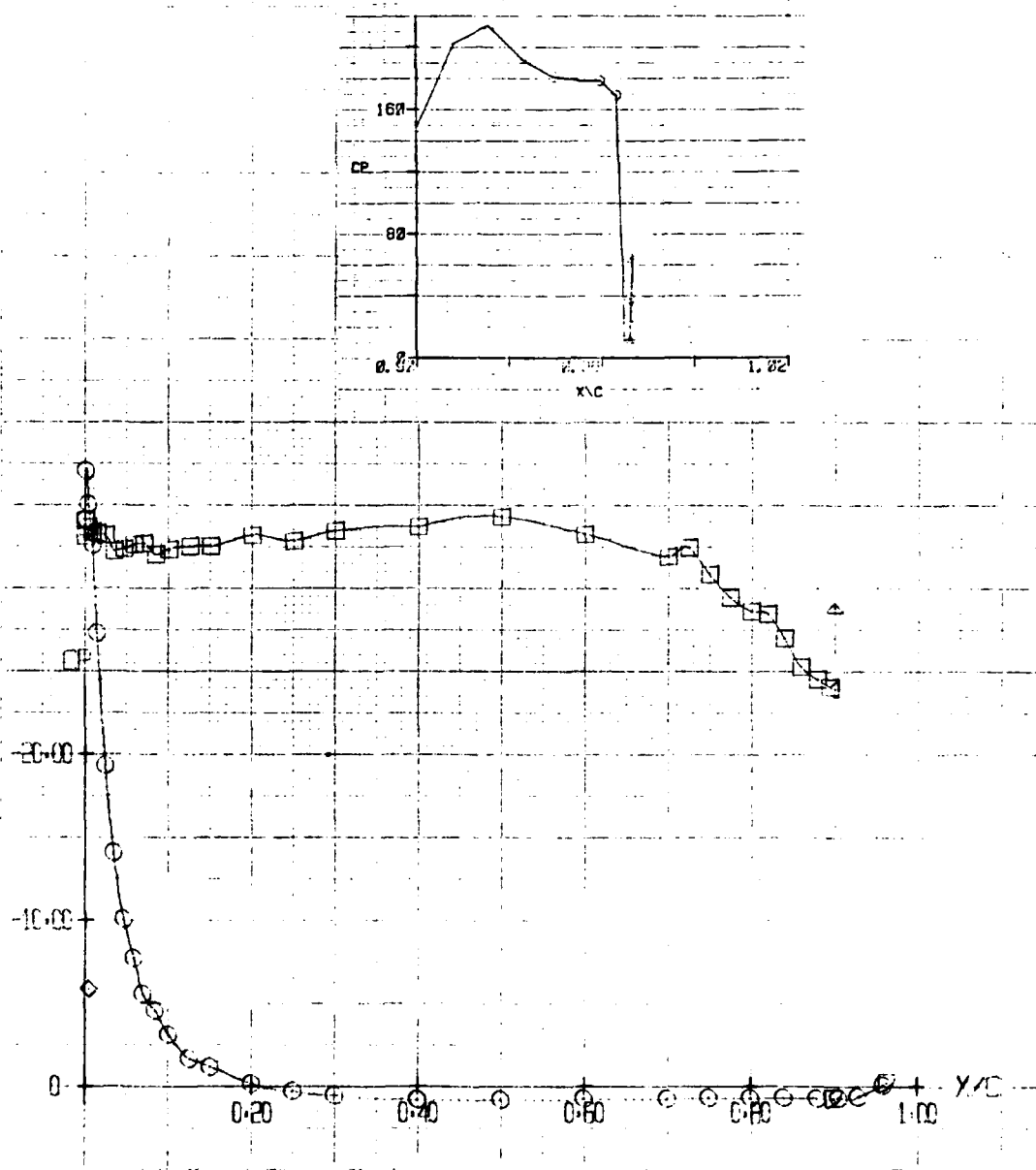
Figure I-42. C_μ = 15.22, Theta = 90°, Alpha = 0° (Test 272, Run 51)
Q = 1.52 psf

131
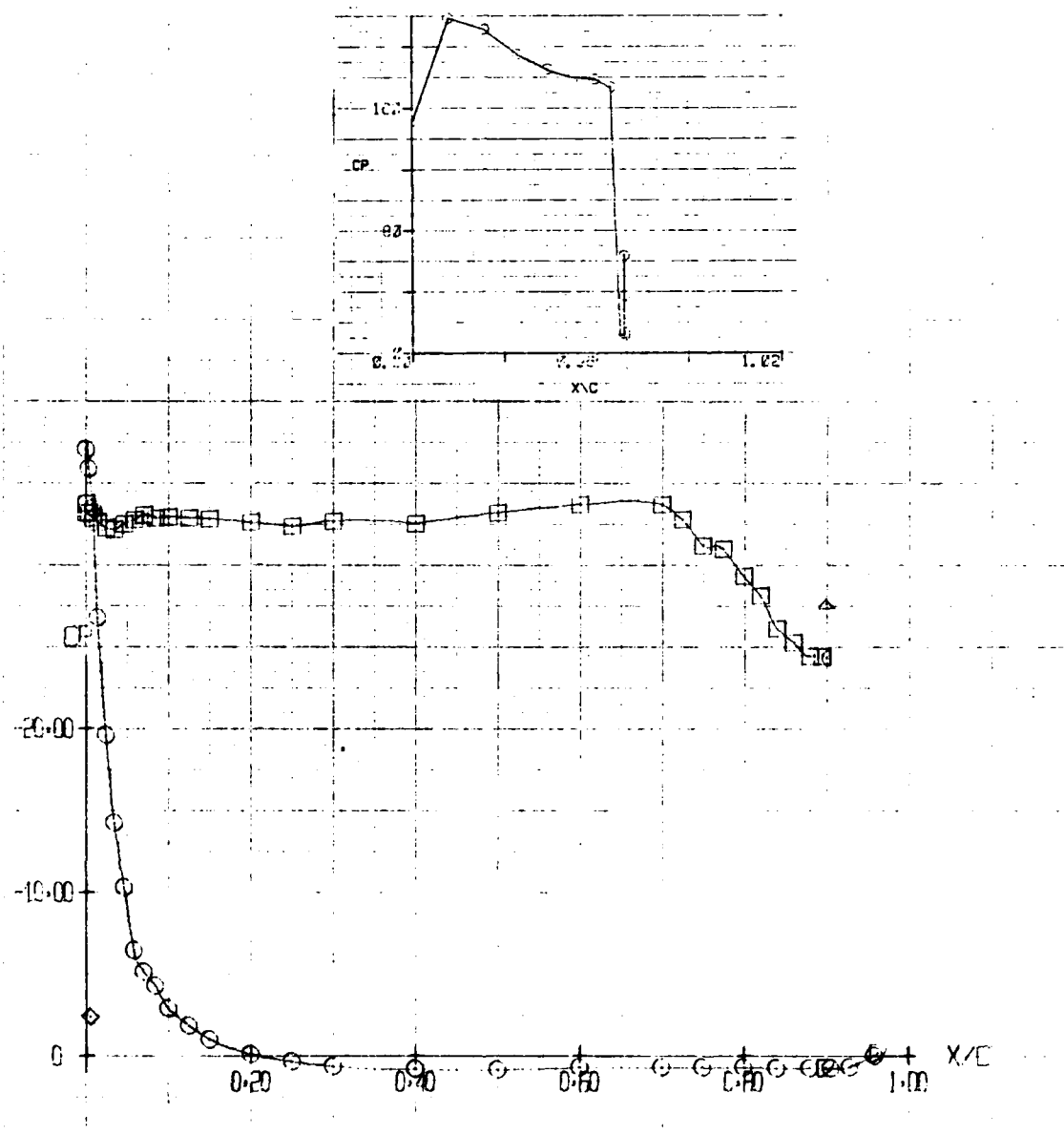
Figure I-43. C_μ = 15.34, Theta = 90°, Alpha = 0° (Test 272, Run 55)
Q = 1.51 psf

132
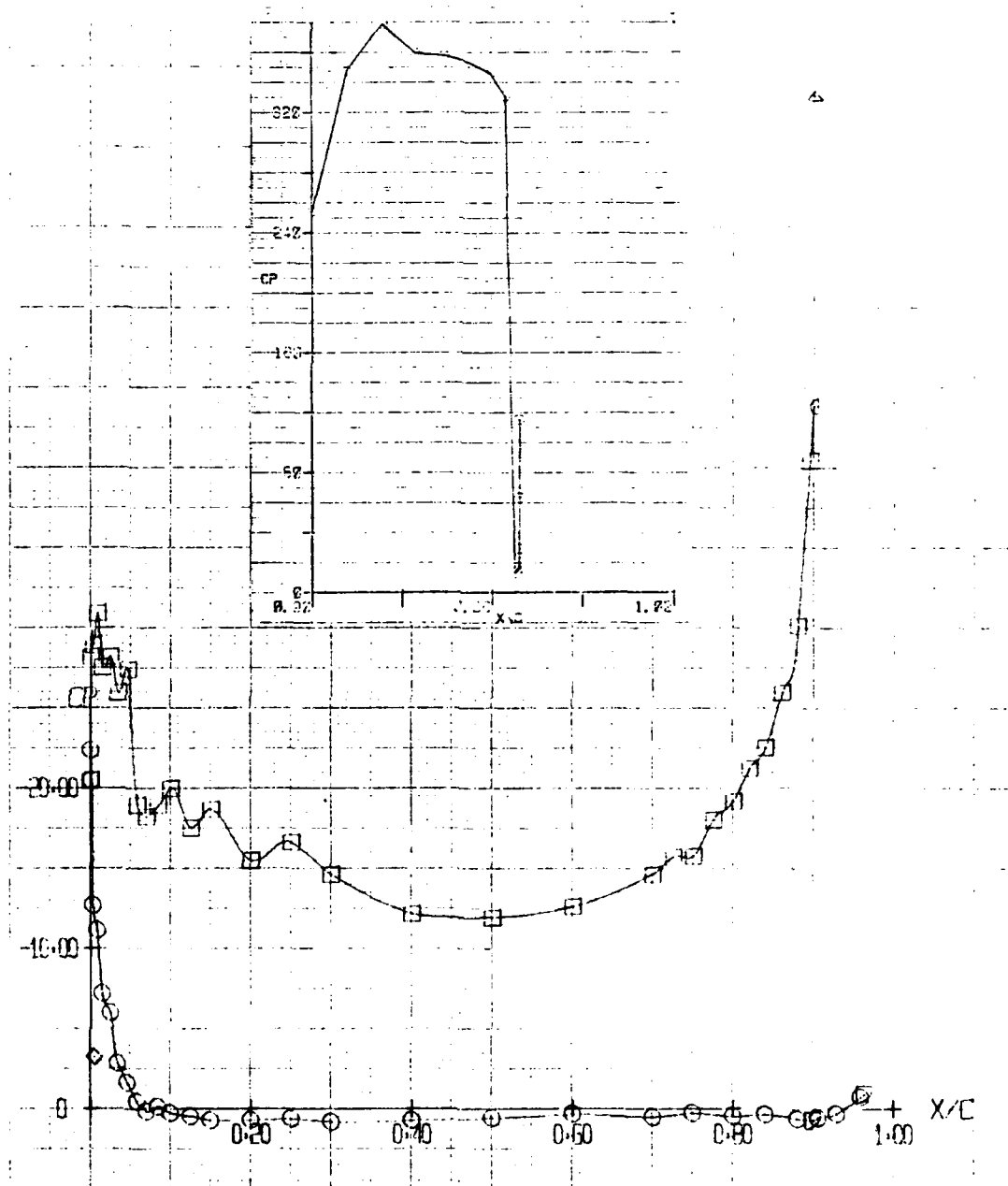
Figure I-44. C_μ = 25.53, Theta = 90°, Alpha = 0° (Test 272, Run 52)
Q = 0.90 psf

133

APPENDIX II

WAKE SURVEY DATA

WAKE SURVEY DATA

TEST _272_ RUN _2_

ANGLE OF ATTACK _-10_ NOMINAL JET ANGLE _—_ C MU _—_

PRESSURE ~ PSIA
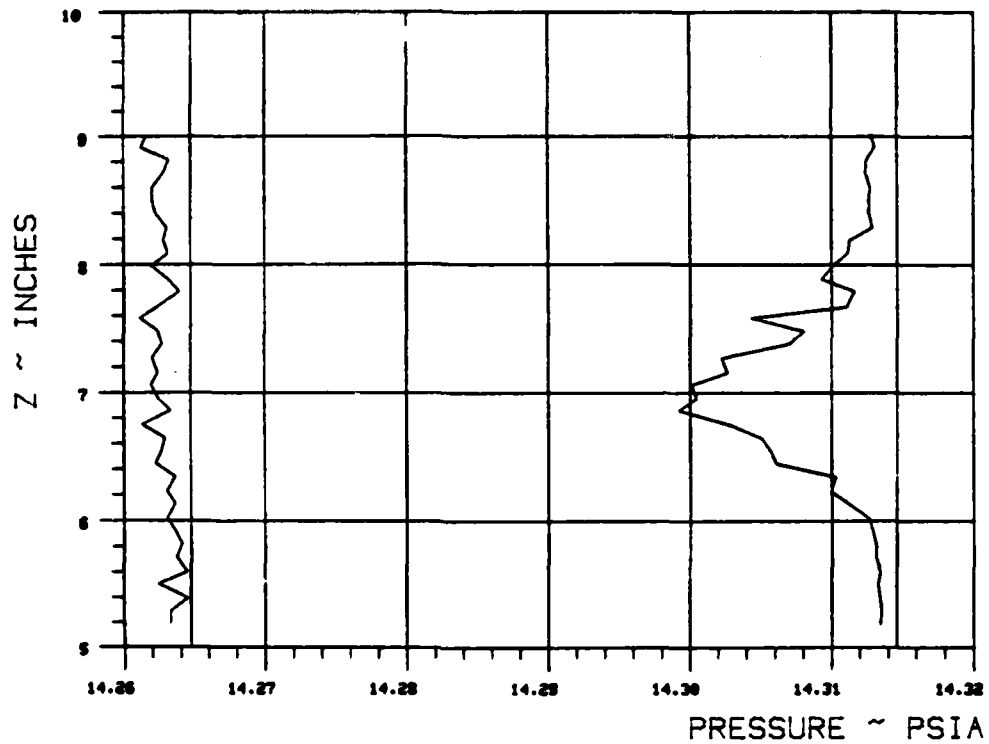
Xss/chord = _—_   Yss/chord = _—_

BETA = _—_

Figure II-1.

ALPHA ~ DEGREES

135
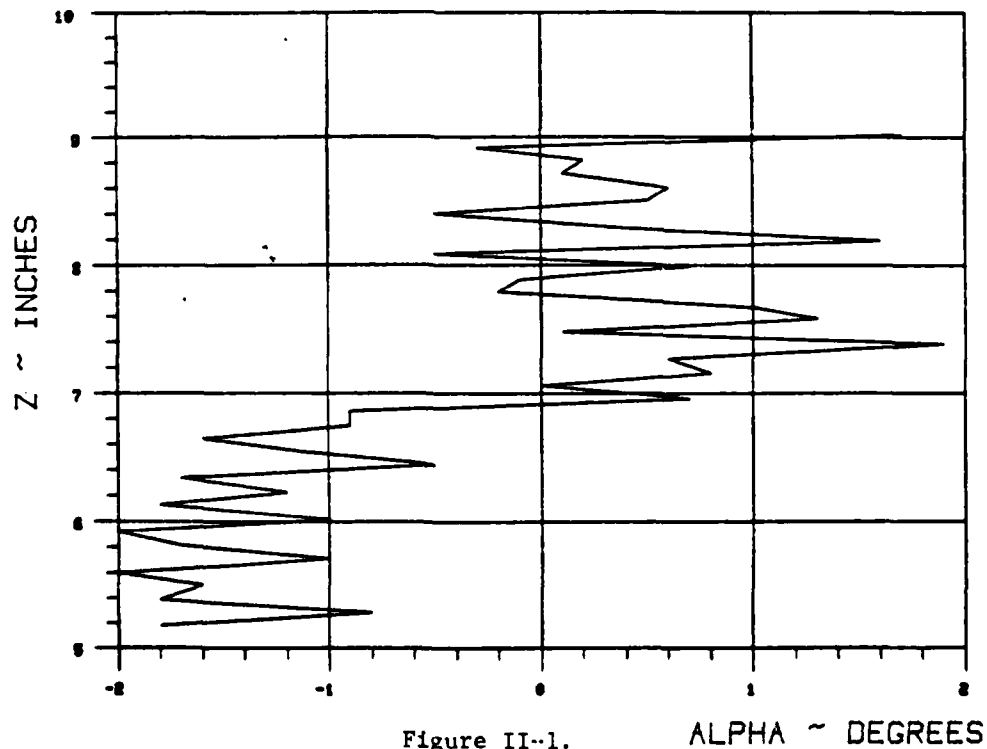
WAKE SURVEY DATA

TEST _272_ RUN _3_

ANGLE OF ATTACK -5 NOMINAL JET ANGLE — C MU —
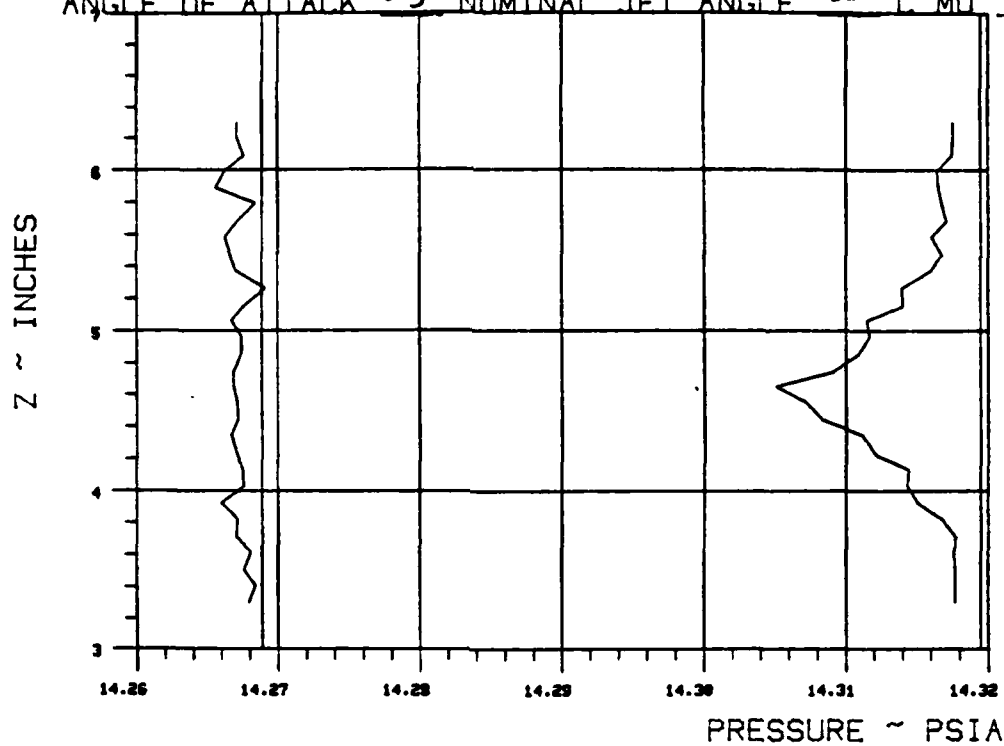
Xss/chord = —   Yss/chord = —
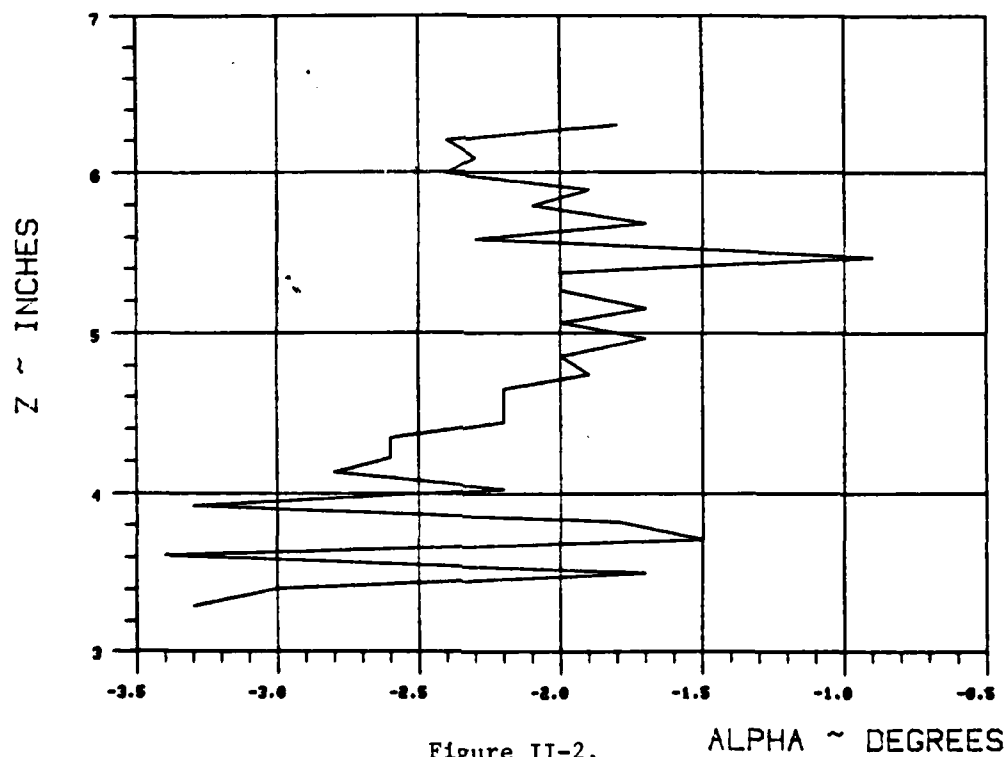
BETA = —

Figure II-2.

WAKE SURVEY DATA

TEST _272_ RUN _12_

ANGLE OF ATTACK _0_ NOMINAL JET ANGLE _30_ C MU __—__

PRESSURE ~ PSIA
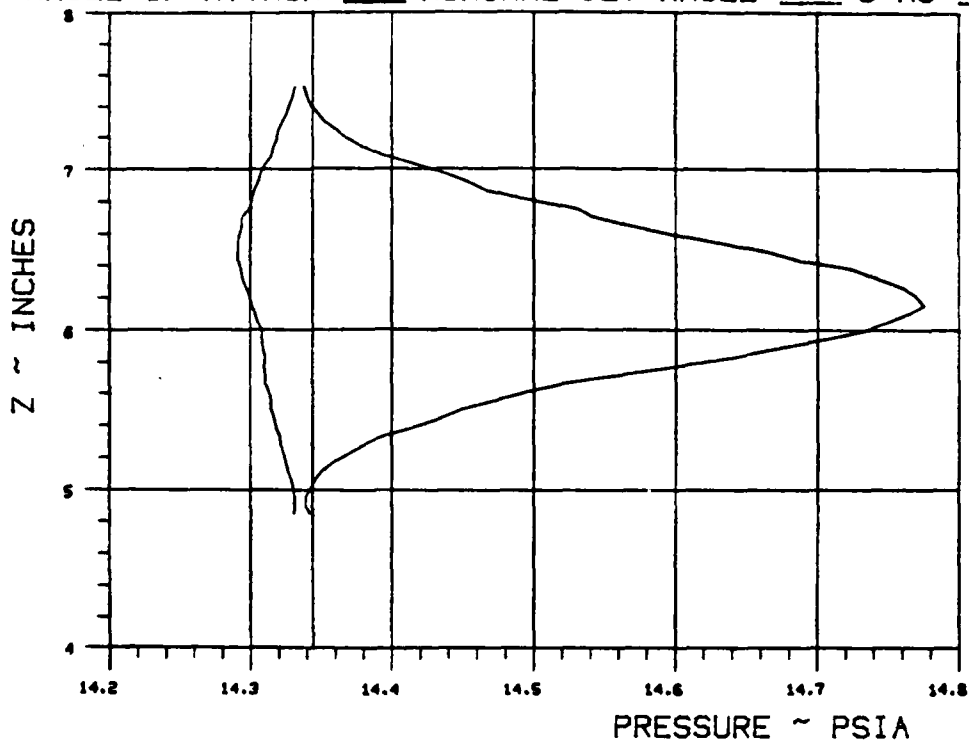
Xss/chord = _.3581_ Yss/chord = _.1014_

BETA = _20.83_

ALPHA ~ DEGREES

Figure II-3.

137
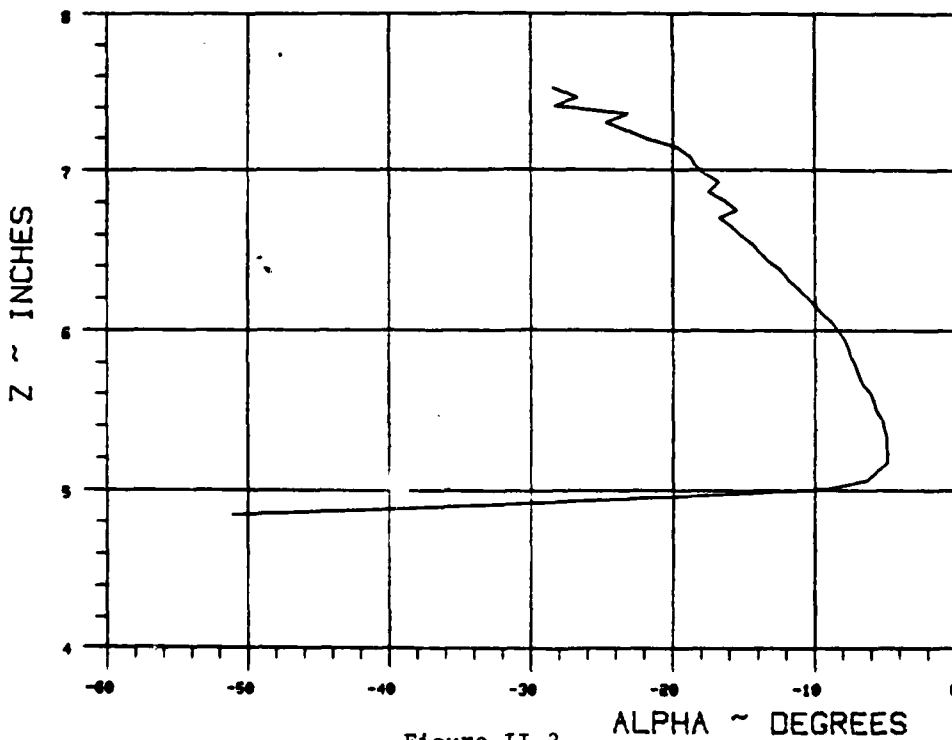
WAKE SURVEY DATA

TEST _272_ RUN _4_

ANGLE OF ATTACK __5__ NOMINAL JET ANGLE __—__ C MU __—__
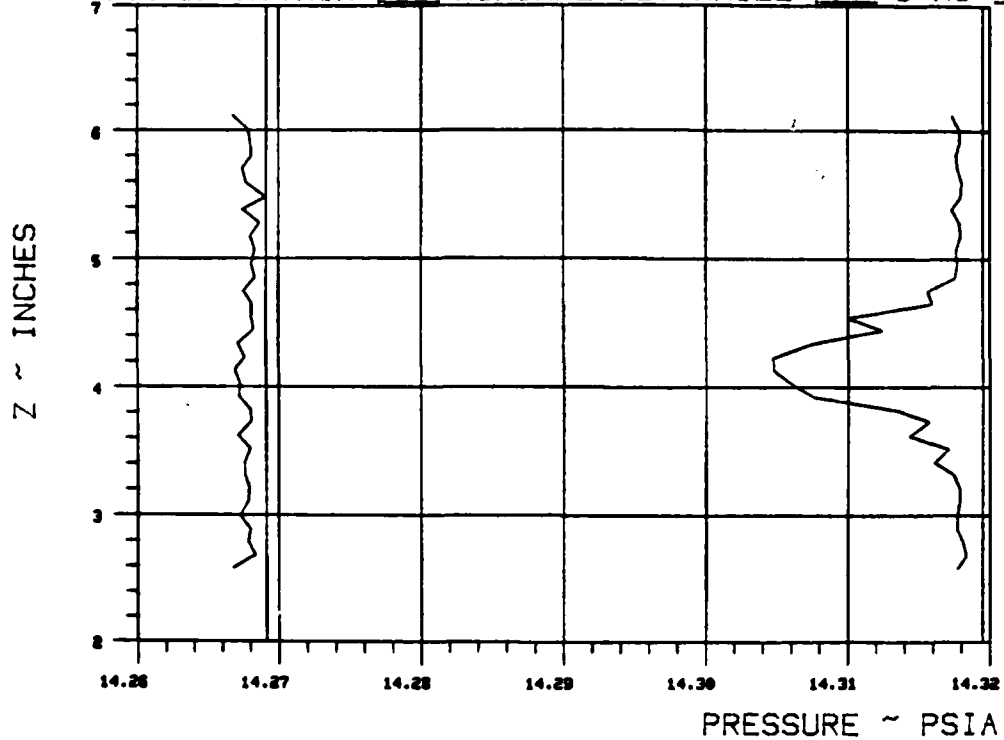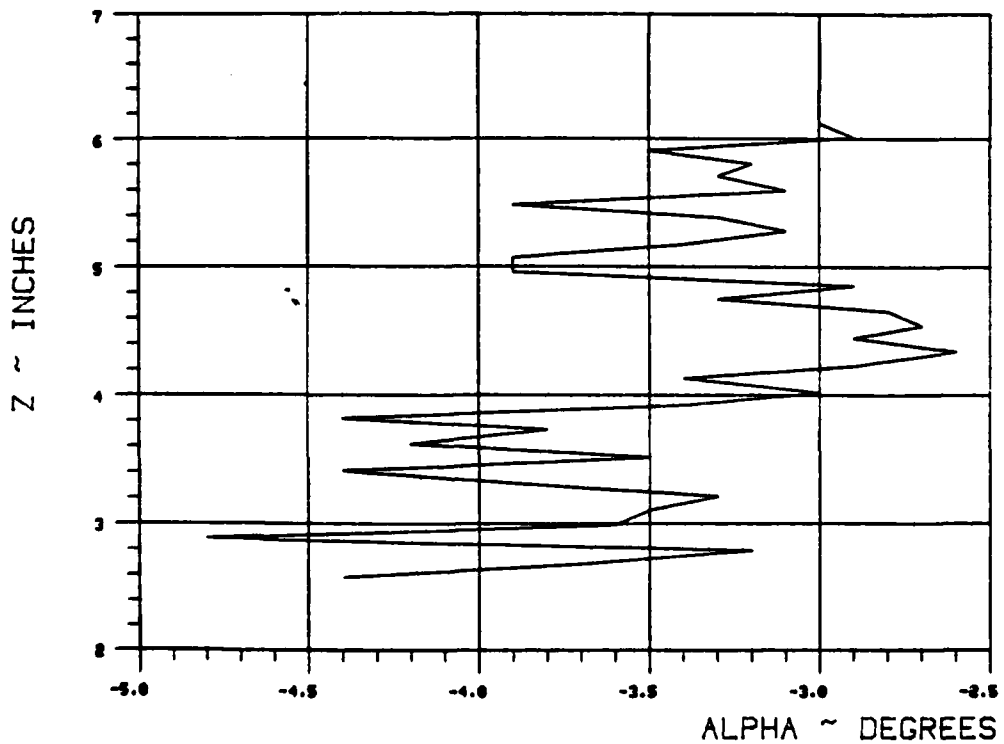
Xss/chord = __—__   Yss/chord = __—__

BETA = __—__

Figure II-4.

138

WAKE SURVEY DATA
TEST _272_ RUN _5_
ANGLE OF ATTACK _10_ NOMINAL JET ANGLE ___ C MU ___

PRESSURE ~ PSIA
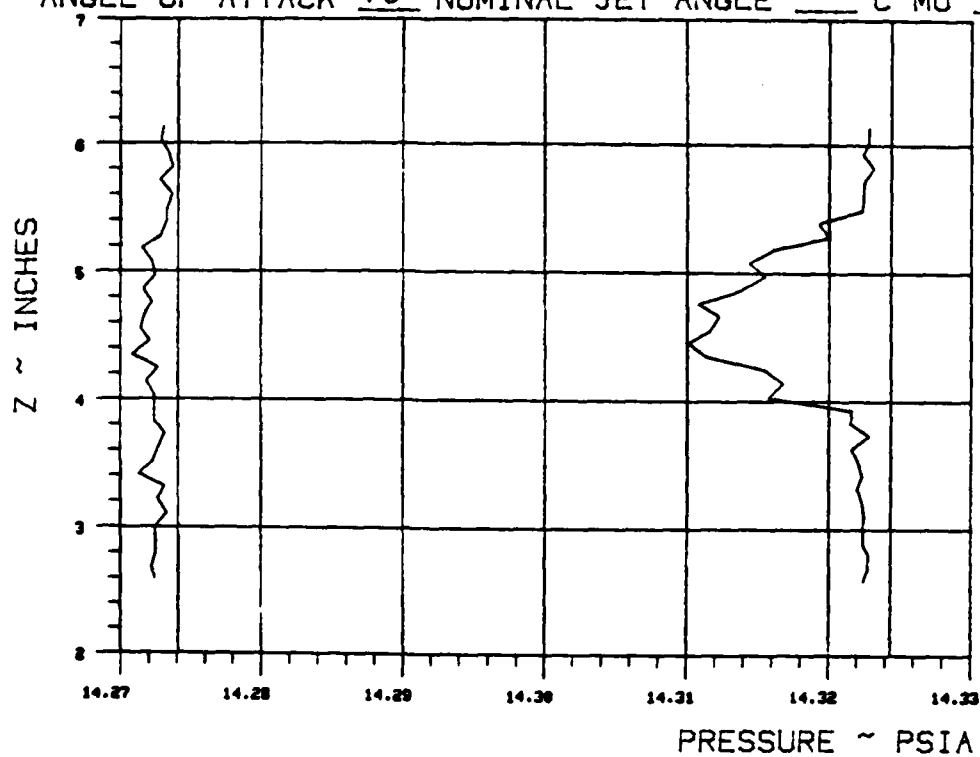
Xss/chord = ___   Yss/chord = ___

BETA = ___

Figure II-5.

ALPHA ~ DEGREES

139
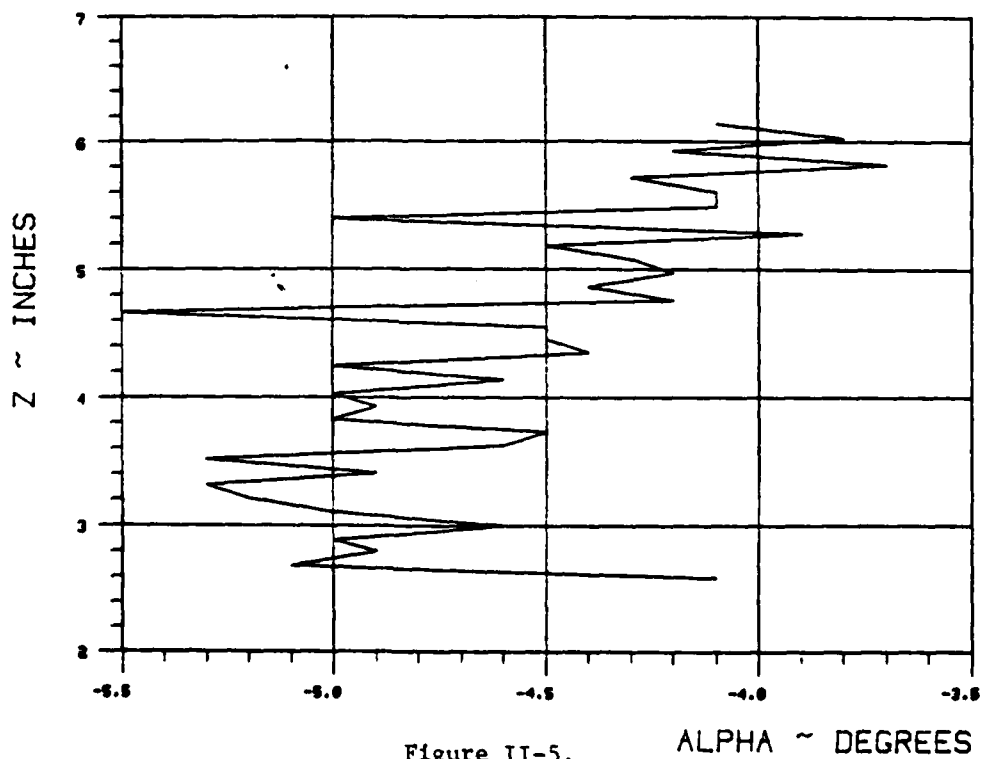
WAKE SURVEY DATA

TEST *272* RUN *8*

ANGLE OF ATTACK *15* NOMINAL JET ANGLE _____ C MU _____
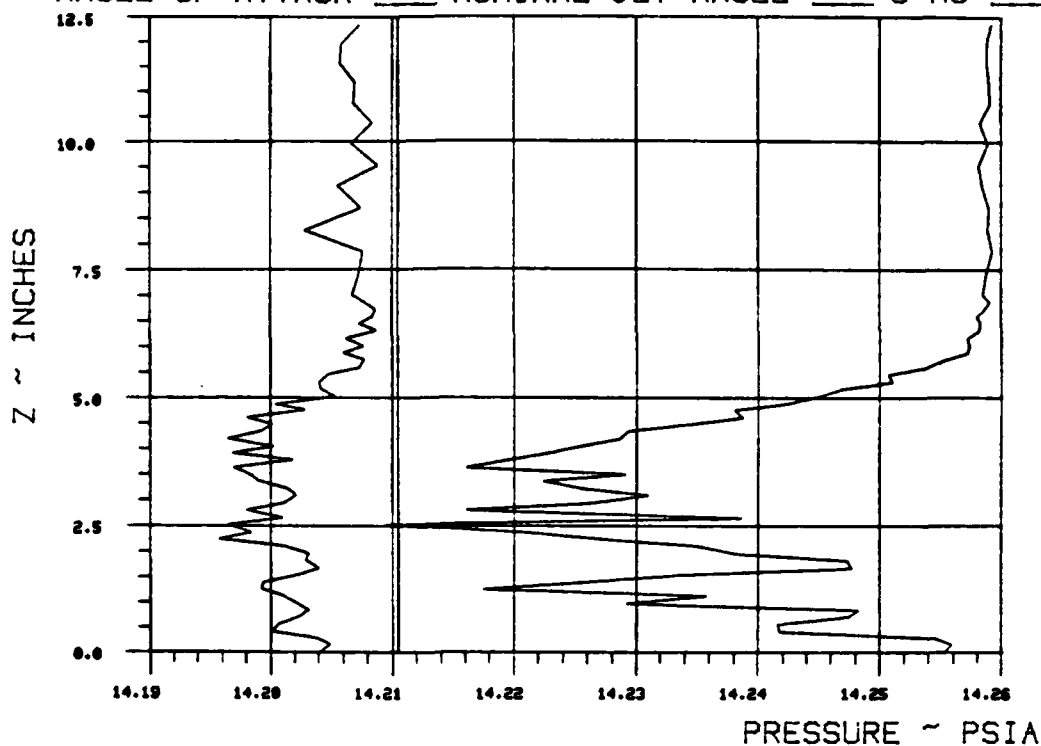
Xss/chord = _____ Yss/chord = _____
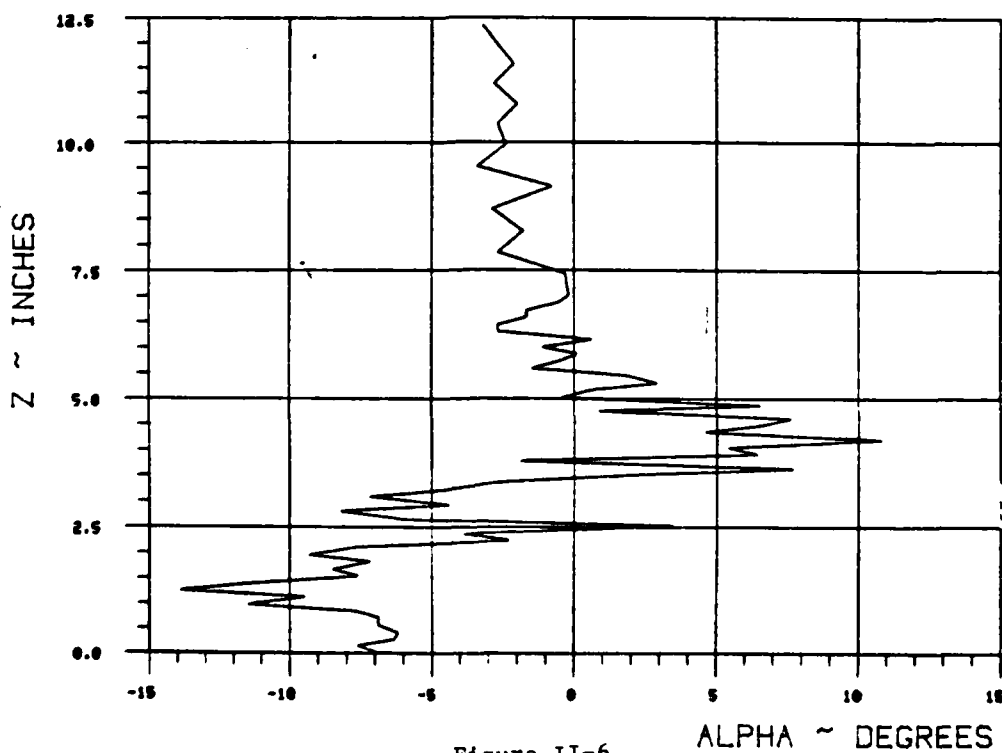
BETA = _____

Figure II-6.

WAKE SURVEY DATA

TEST _272_ RUN _9_

ANGLE OF ATTACK _0_ NOMINAL JET ANGLE _30_ C MU _.5327_

PRESSURE ~ PSIA

Xss/chord = _.3733_ Yss/chord = _.141_

BETA = _20.83_

ALPHA ~ DEGREES

Figure II-7.

141
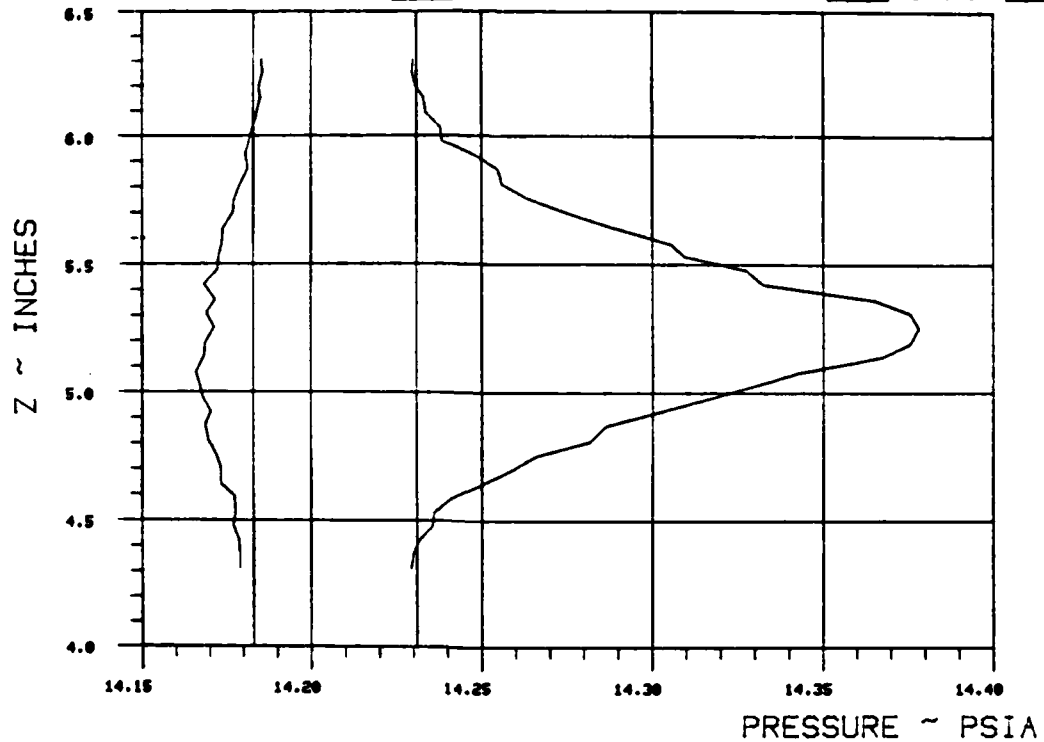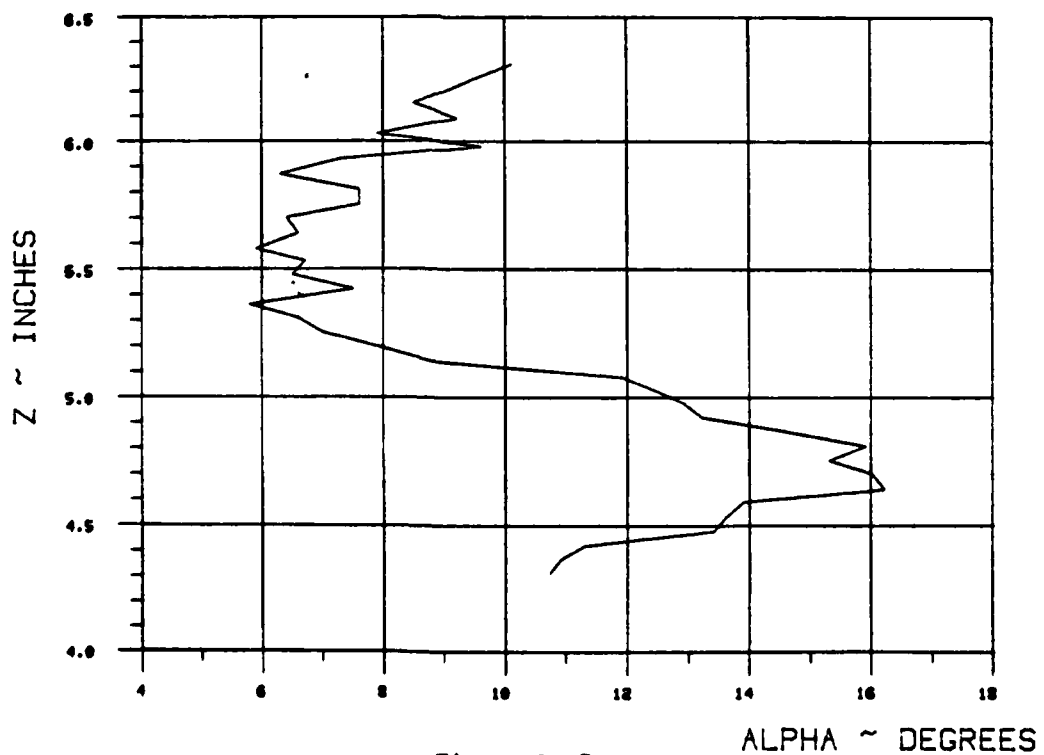
WAKE SURVEY DATA
TEST _272_ RUN _10_
ANGLE OF ATTACK _0_ NOMINAL JET ANGLE _30_ C MU _1.07_

Z ~ INCHES

PRESSURE ~ PSIA
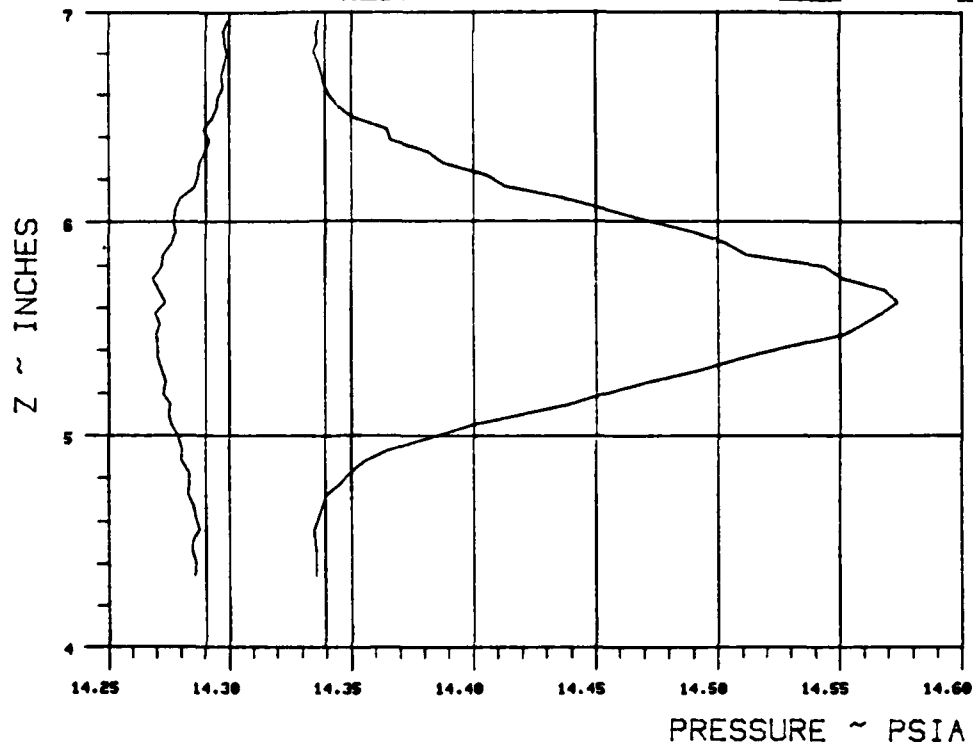
Xss/chord = _.374_   Yss/chord = _.1433_

BETA = _20.83_

Z ~ INCHES

ALPHA ~ DEGREES
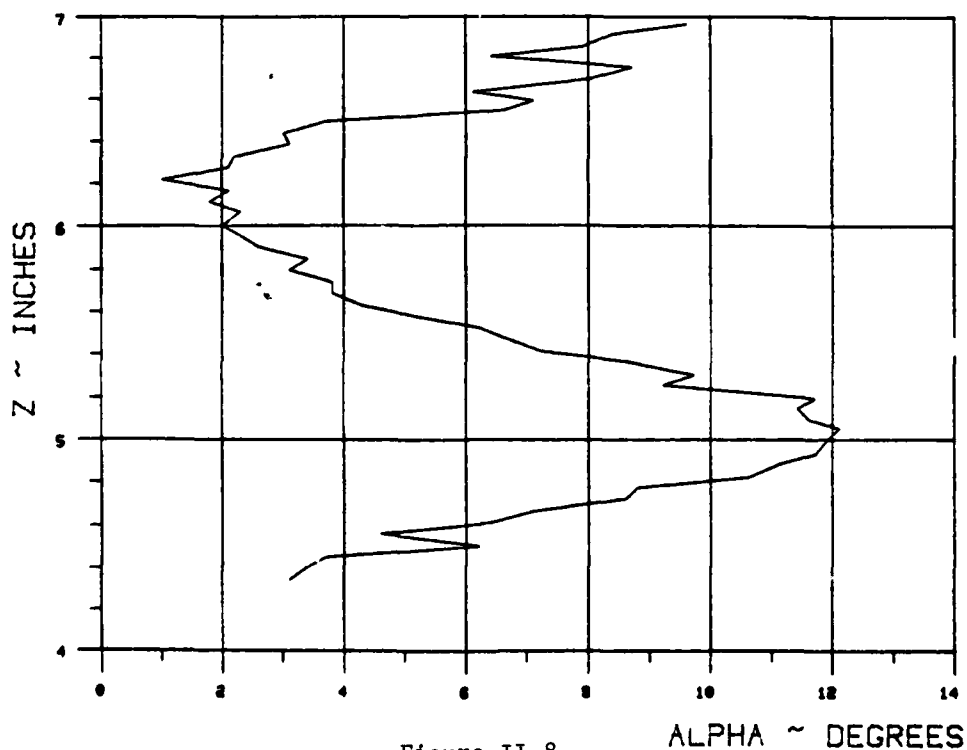
Figure II-8.

WAKE SURVEY DATA
TEST _272_ RUN _11_
ANGLE OF ATTACK _O_ NOMINAL JET ANGLE _30_ C MU _2.1154_

PRESSURE ~ PSIA
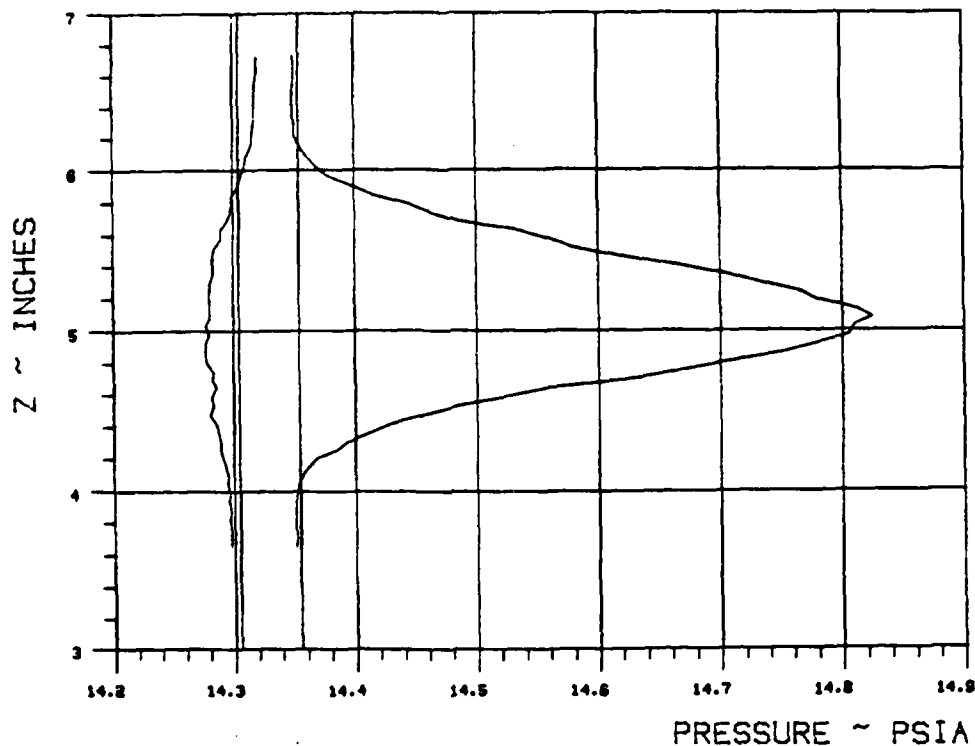
Xss/chord = _.3581_   Yss/chord = _.1015_

BETA = _20.83_

ALPHA ~ DEGREES
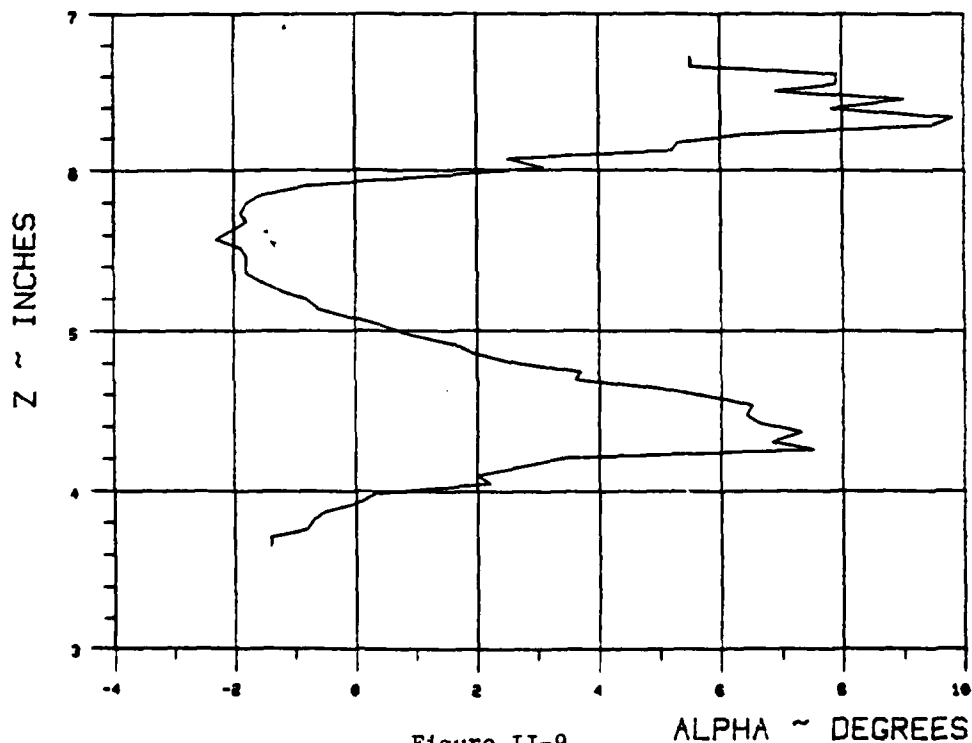
Figure II-9.
143

WAKE SURVEY DATA
TEST _272_ RUN _13_
ANGLE OF ATTACK _0_ NOMINAL JET ANGLE _30_ C MU _4.2601_

PRESSURE ~ PSIA
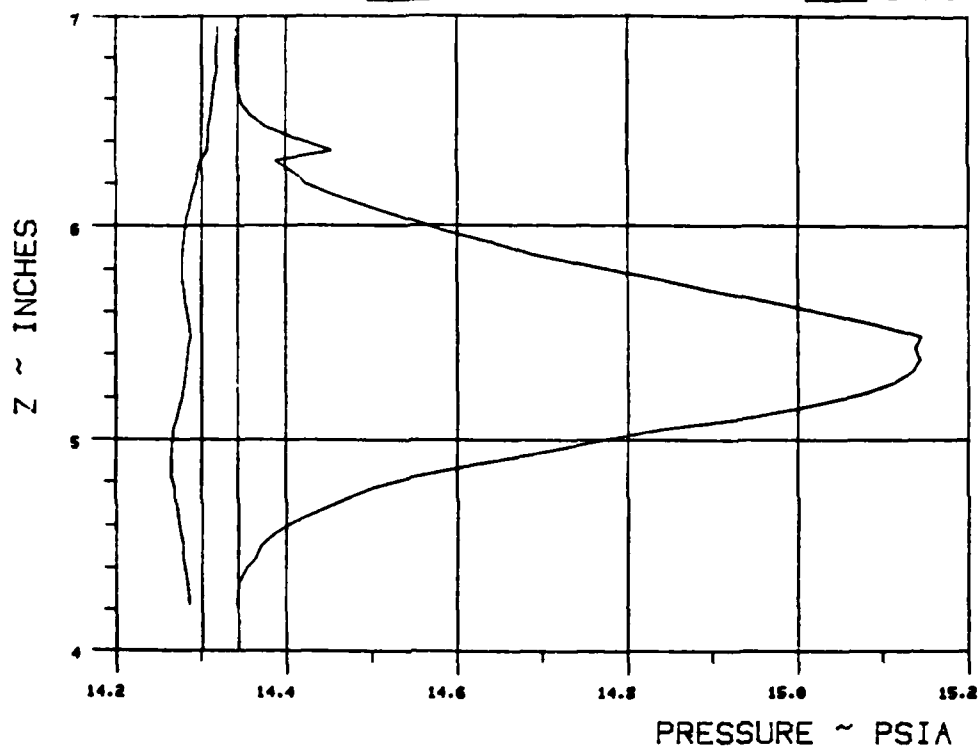
Xse/chord = _.3581_ Yse/chord = _.1016_

BETA = _20.83_

ALPHA ~ DEGREES
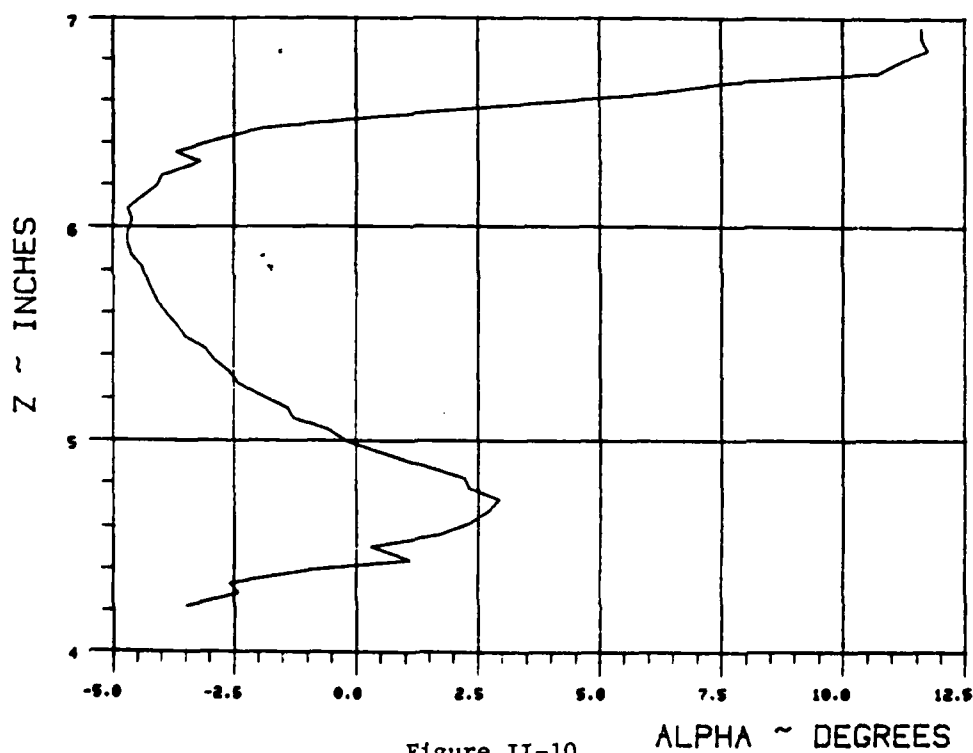
Figure II-10.

WAKE SURVEY DATA

TEST 272 RUN 14

ANGLE OF ATTACK 0 NOMINAL JET ANGLE 30 C MU 4.2694
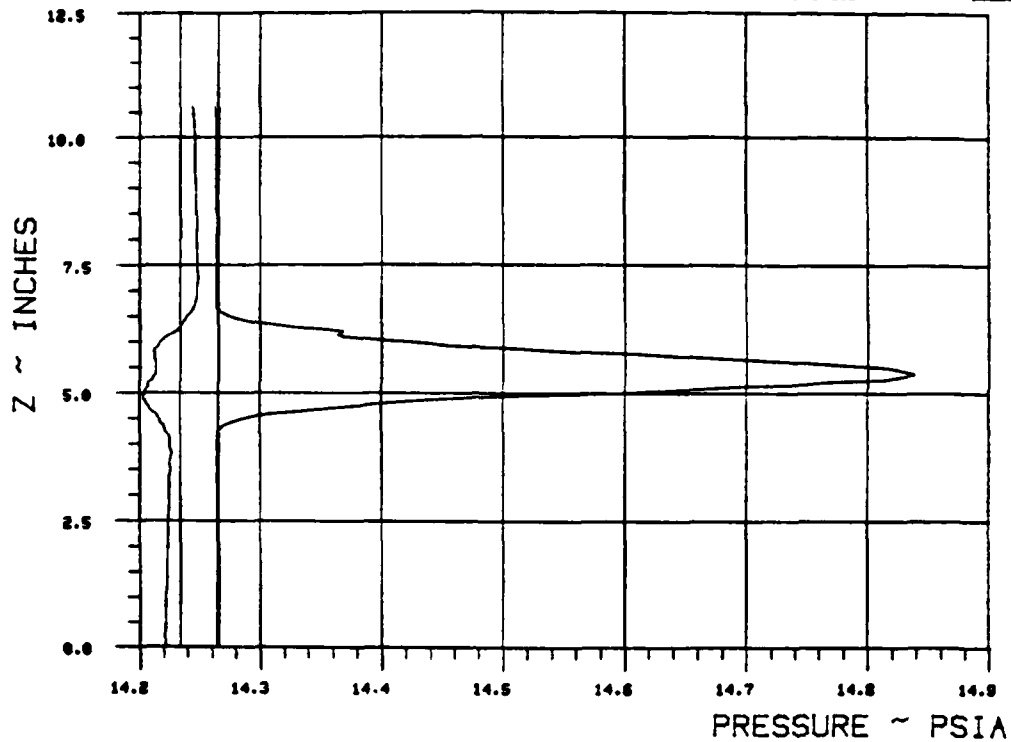
Xse/chord = .3587 Yse/chord = .1032

BETA = 20.83
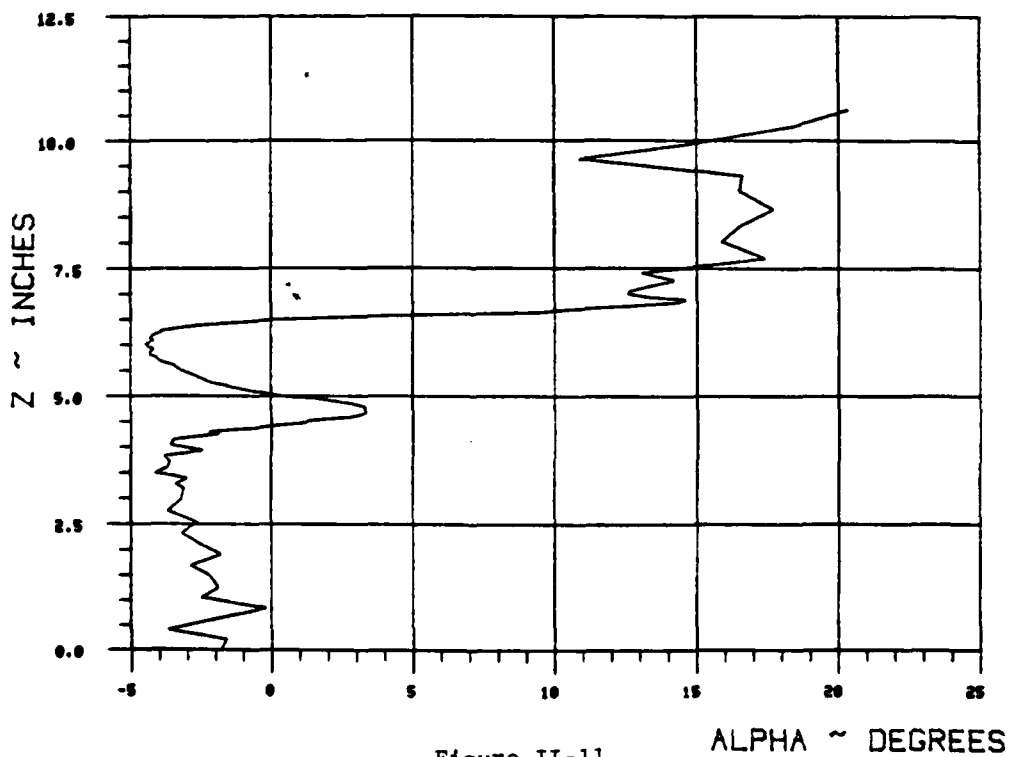
Figure II-11.

WAKE SURVEY DATA

TEST _272_ RUN _15_

ANGLE OF ATTACK _0_ NOMINAL JET ANGLE _30_ C MU _6.4062_

PRESSURE ~ PSIA
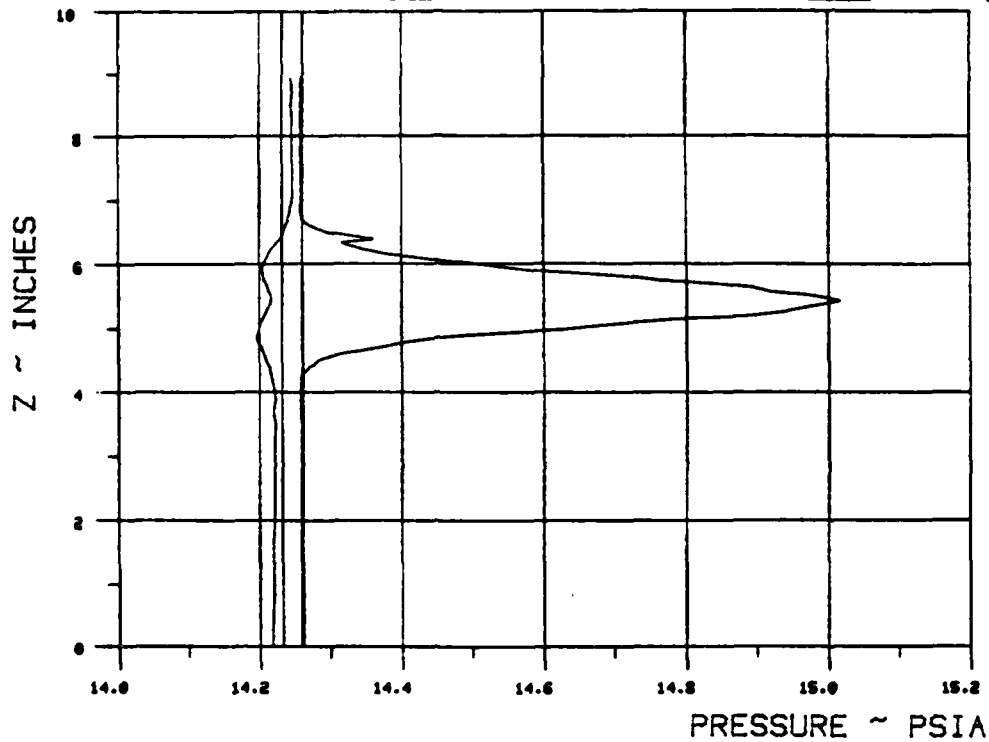
Xss/chord = _.3564_   Yss/chord = _.097_

BETA = _20.83_

ALPHA ~ DEGREES
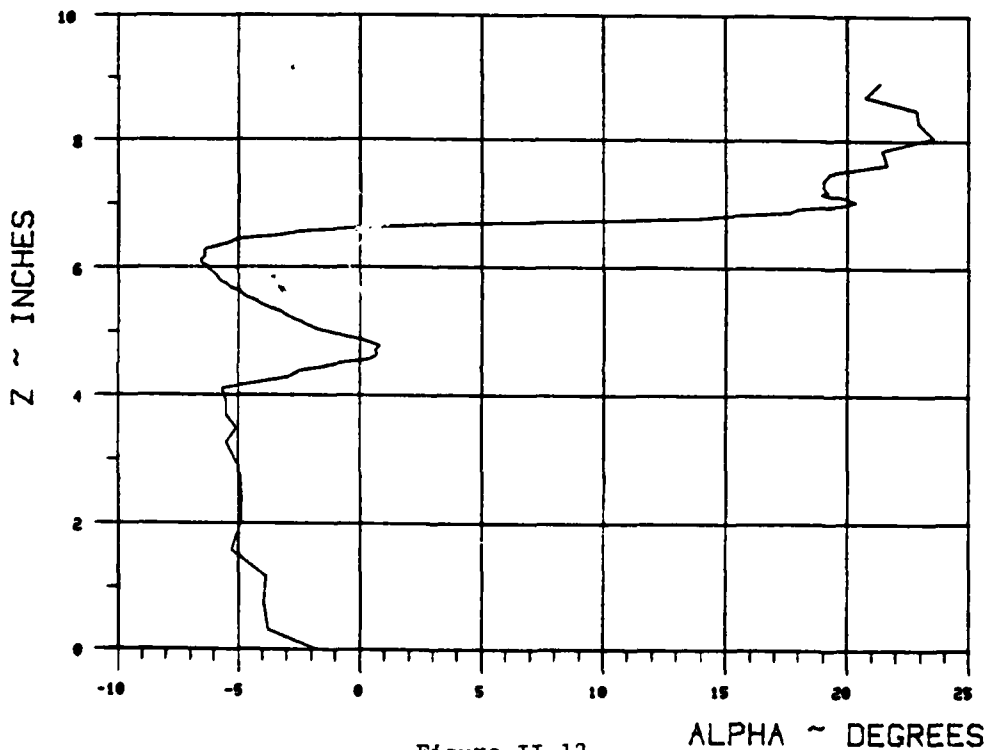
Figure II-12.

WAKE SURVEY DATA

TEST 272 RUN 16

ANGLE OF ATTACK O NOMINAL JET ANGLE 30 C MU 8.4348
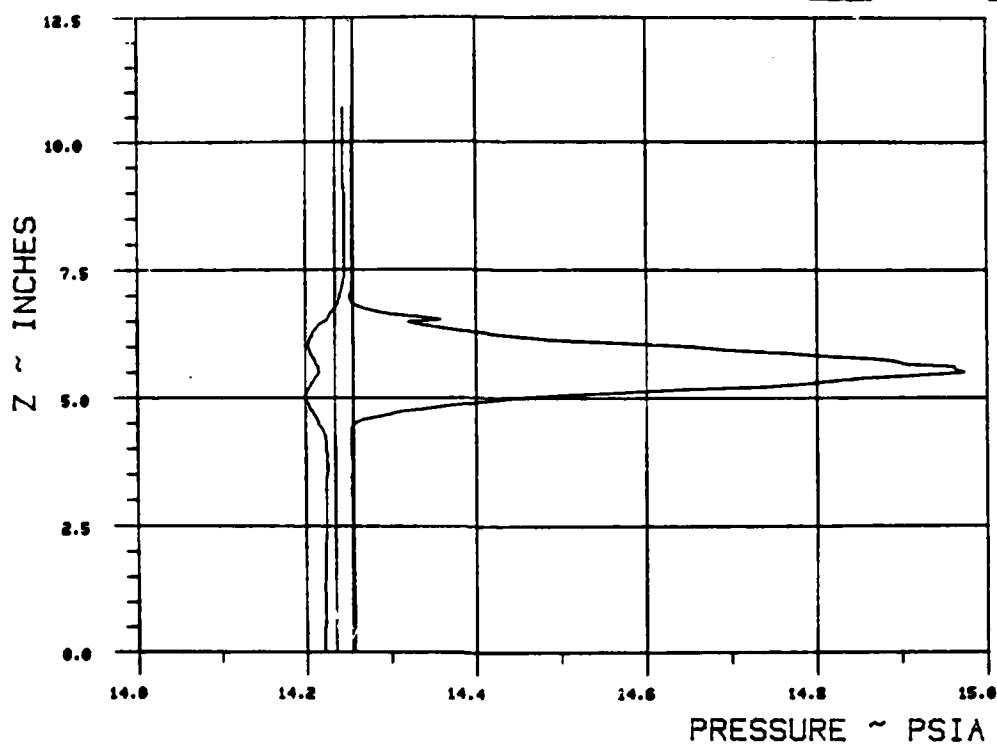
Xee/chord = .3569   Yee/chord = .0985

BETA = 20.83
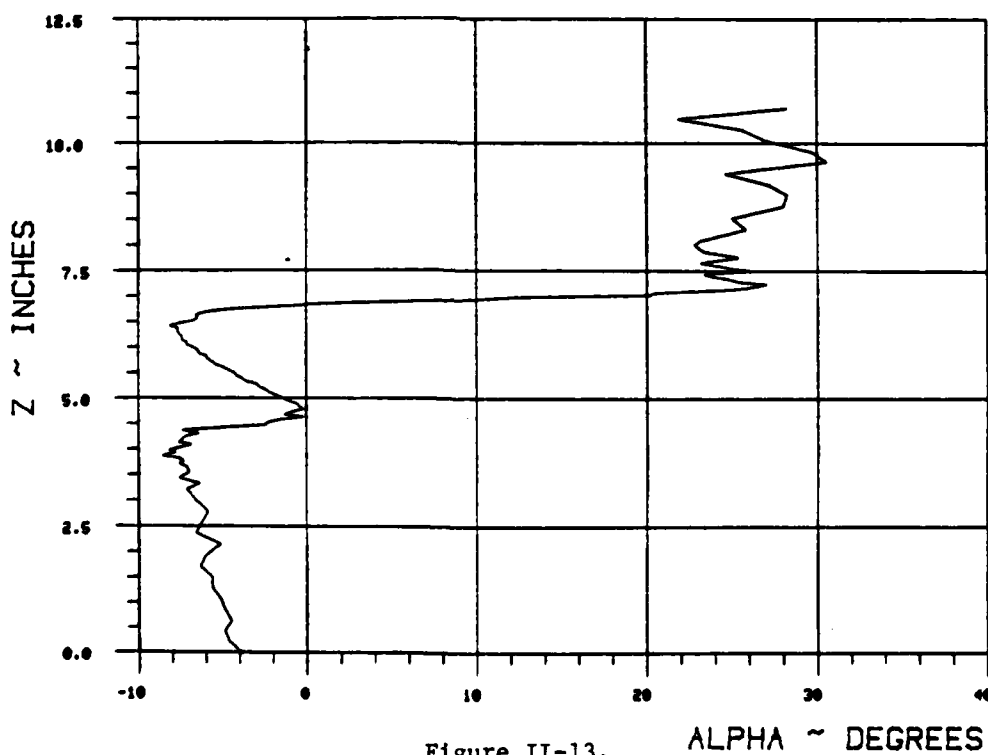
Figure II-13.

WAKE SURVEY DATA

TEST _272_ RUN _17_

ANGLE OF ATTACK _0_ NOMINAL JET ANGLE _30_ C MU _8.6019_
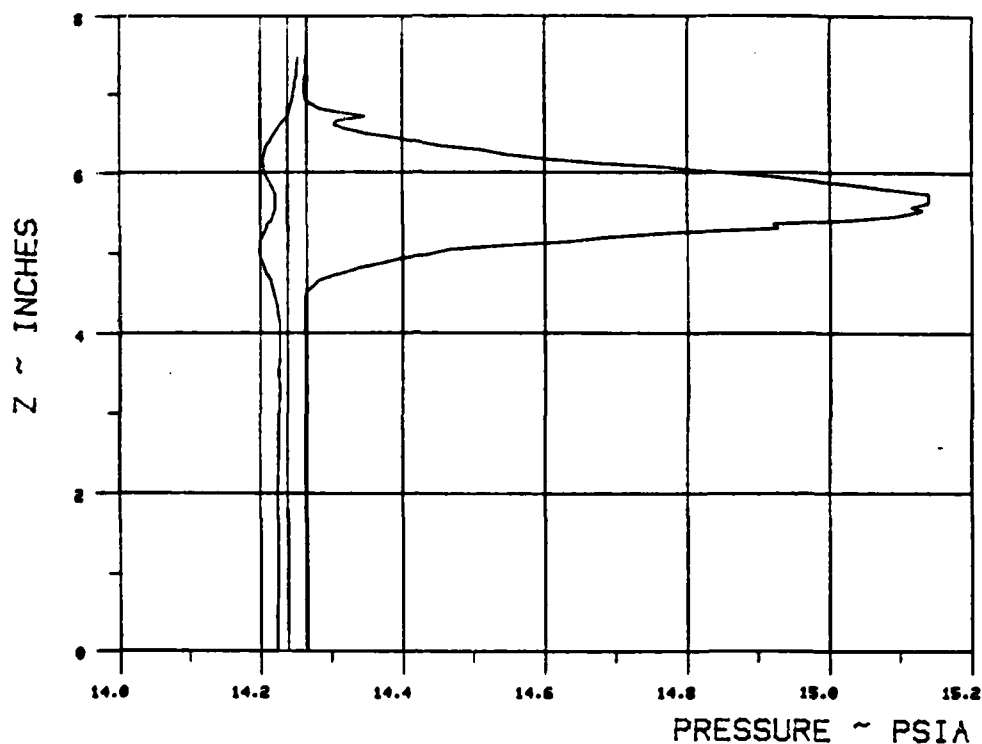
Xss/chord = _.3578_ Yss/chord = _.1008_

BETA = _20.83_
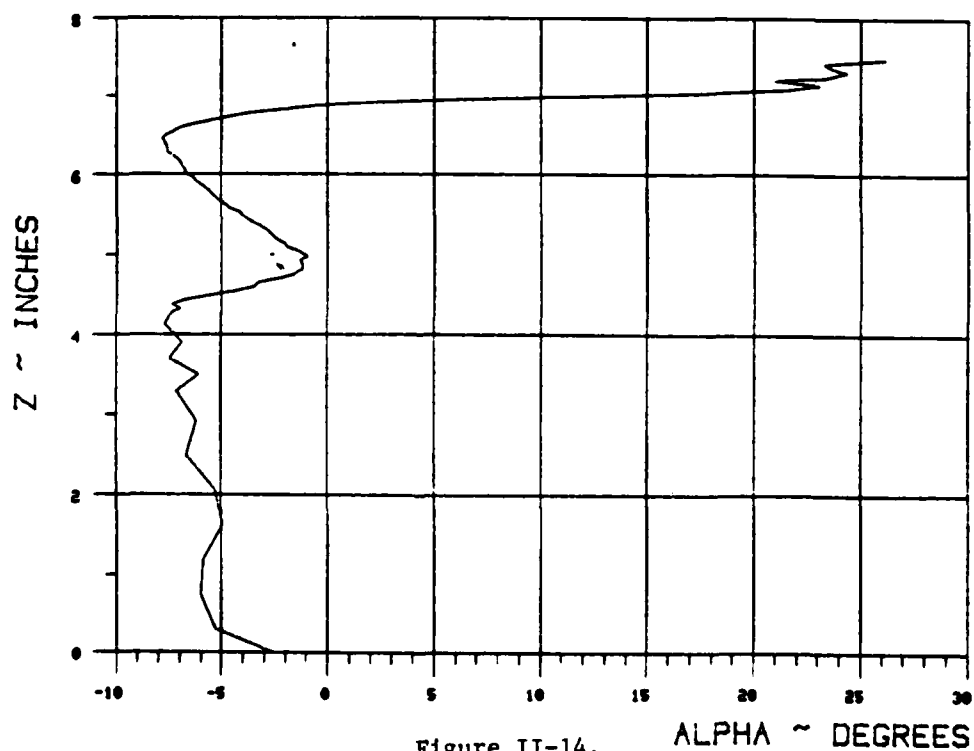
Figure II-14.

WAKE SURVEY DATA
TEST _272_ RUN _1B_
ANGLE OF ATTACK _O_ NOMINAL JET ANGLE _30_ C MU _17.0312_

PRESSURE ~ PSIA

Xss/chord = _.3578_ Yss/chord = _.1008_

BETA = _20.93_

ALPHA ~ DEGREES

Figure II-15.

149
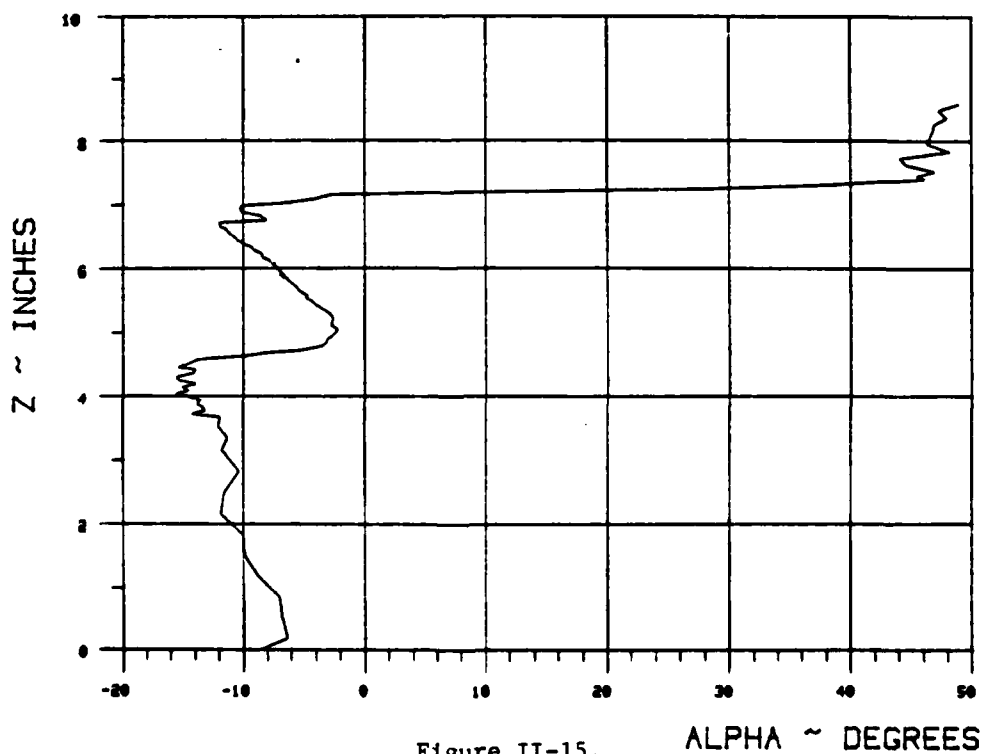
TEST __272__ RUN __19__

ANGLE OF ATTACK __0__ NOMINAL JET ANGLE __50__ C MU __.5257__

PRESSURE ~ PSIA
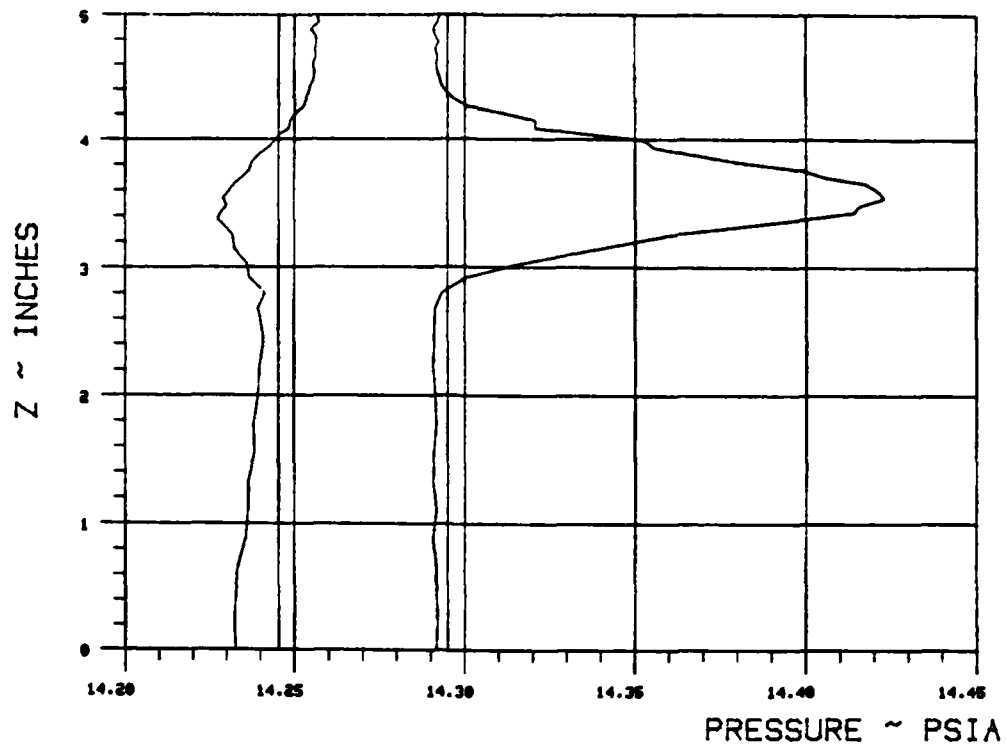
Xee/chord = __.225__ Yee/chord = __.011__

BETA = __30__

ALPHA ~ DEGREES
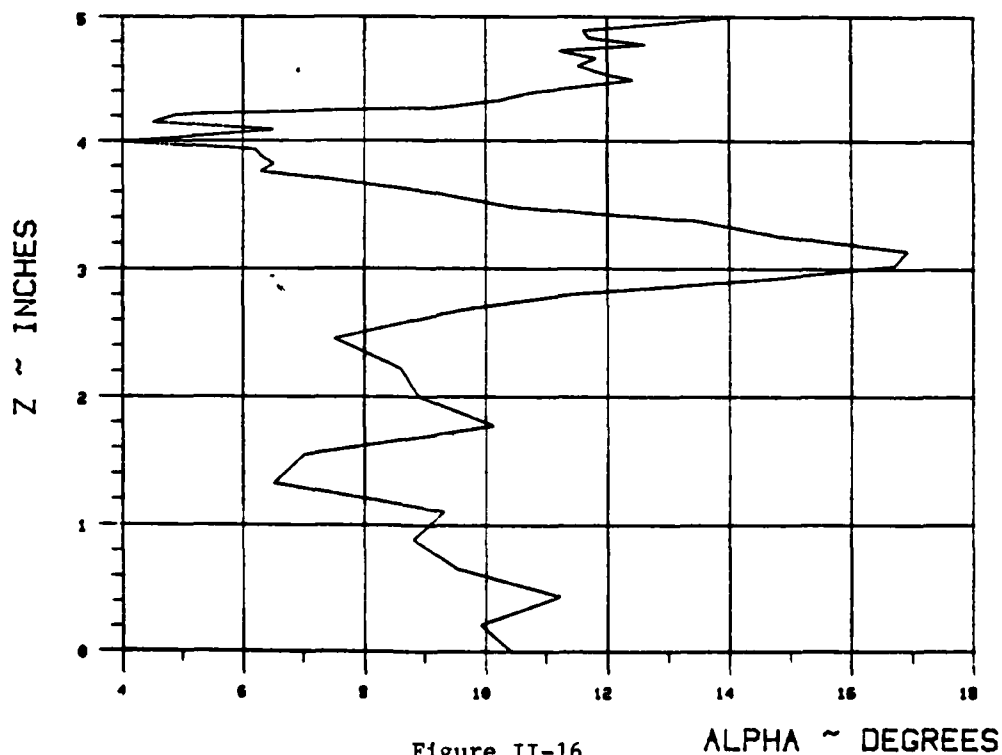
Figure II-16.

WAKE SURVEY DATA

TEST 272 RUN 20

ANGLE OF ATTACK 0 NOMINAL JET ANGLE 50 C MU 1.013
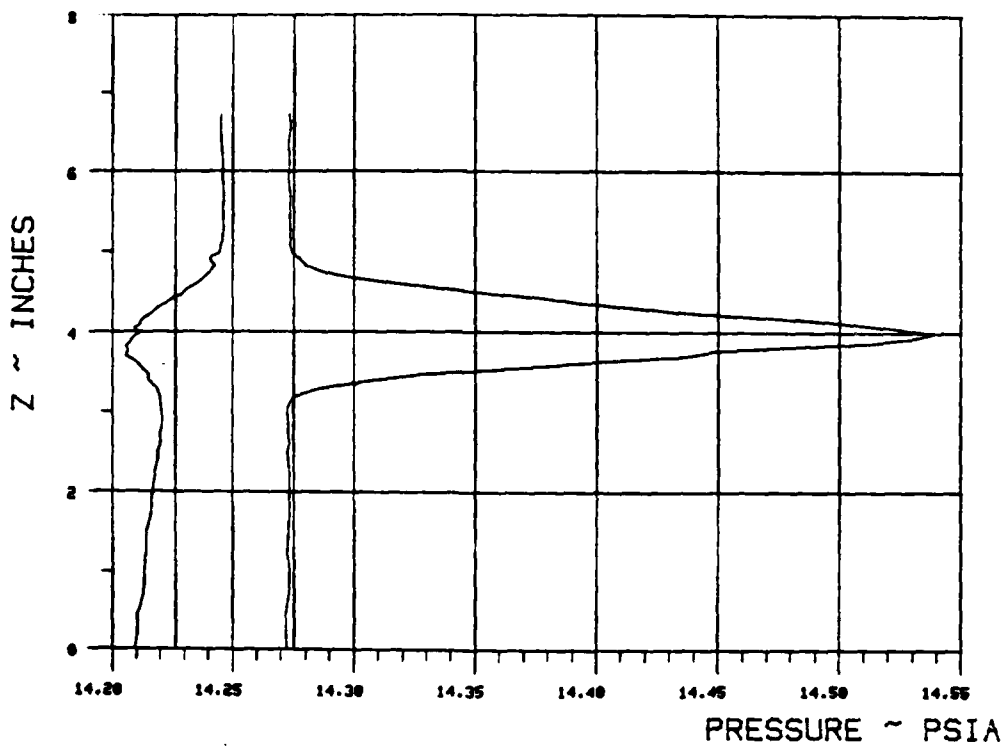
X_{ee}/chord = .2252 Y_{ee}/chord = .0113

BETA = 30
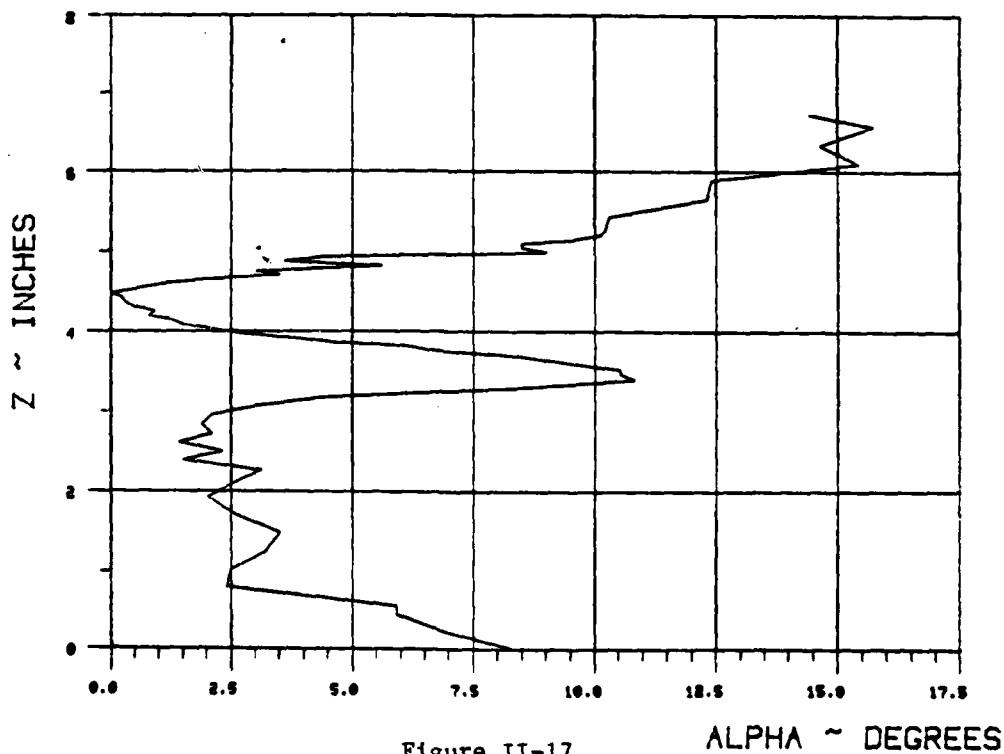
Figure II-17.

WAKE SURVEY DATA
TEST _272_ RUN _21_
ANGLE OF ATTACK _0_ NOMINAL JET ANGLE _50_ C MU _2.045_
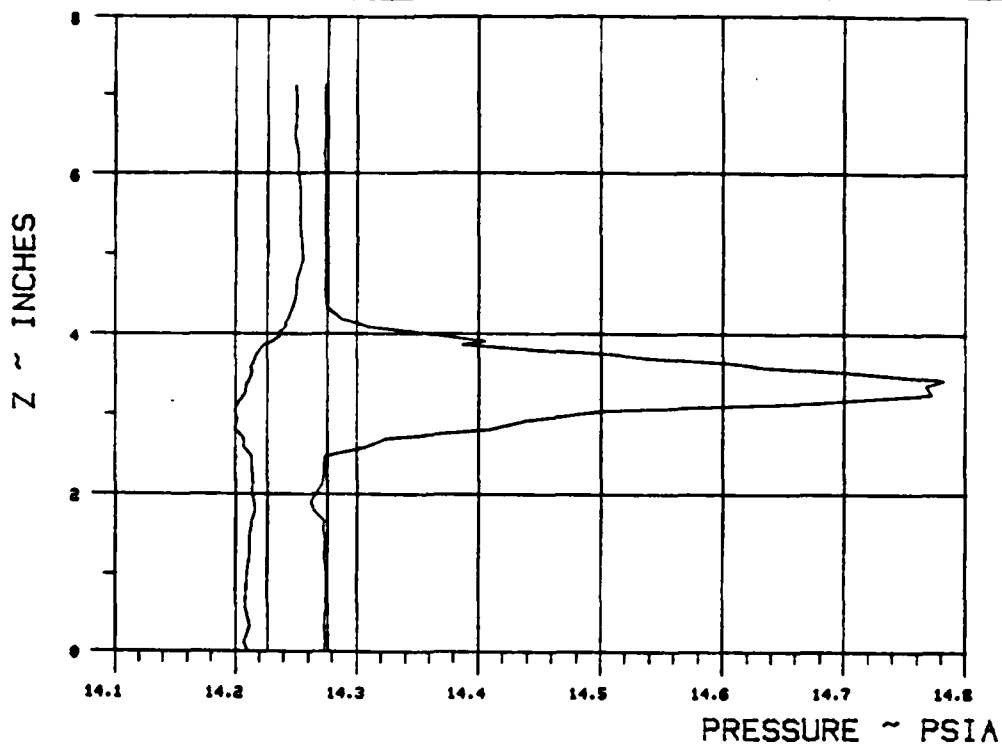
Xss/chord = _.2091_   Yss/chord = _-.0166_

BETA = _30_

Figure II-18.

152
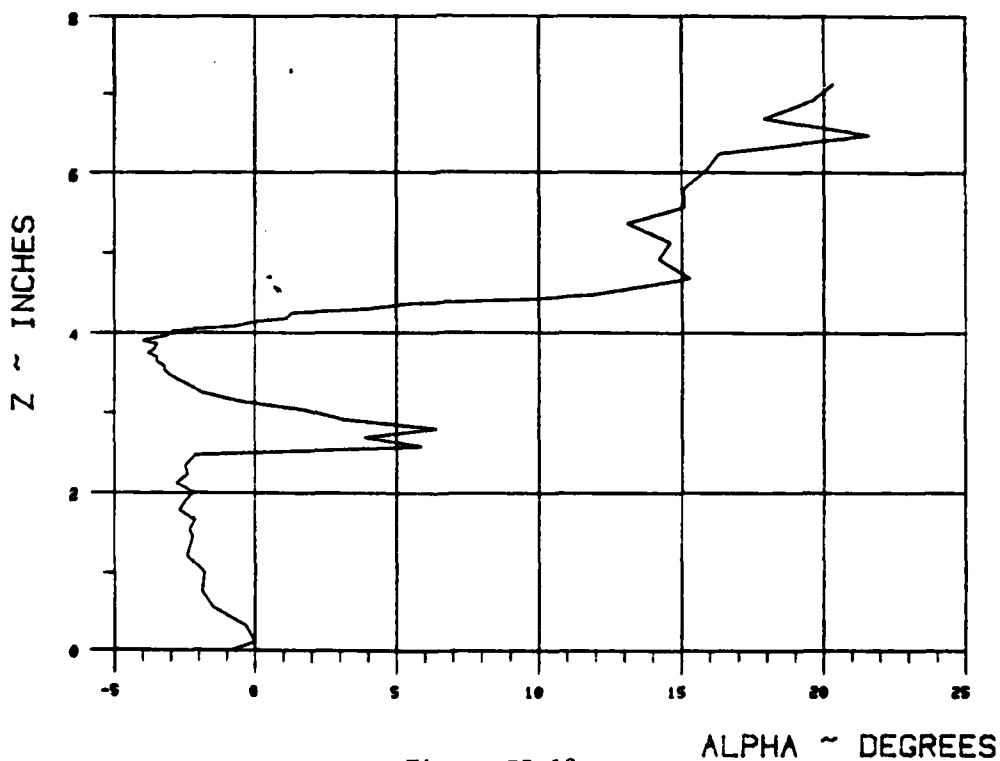
WAKE SURVEY DATA
TEST _272_ RUN _24_
ANGLE OF ATTACK _O_ NOMINAL JET ANGLE _50_ C MU _2.0403_
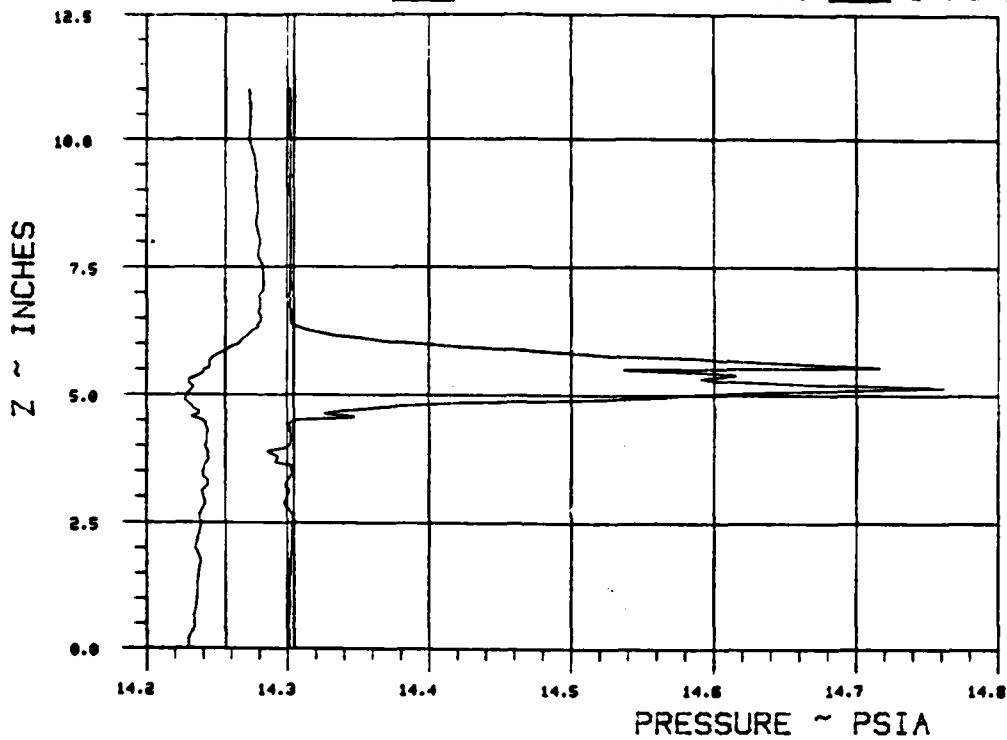
X_{ss}/chord = _.2419_ Y_{ss}/chord = _.0402_

BETA = _30_
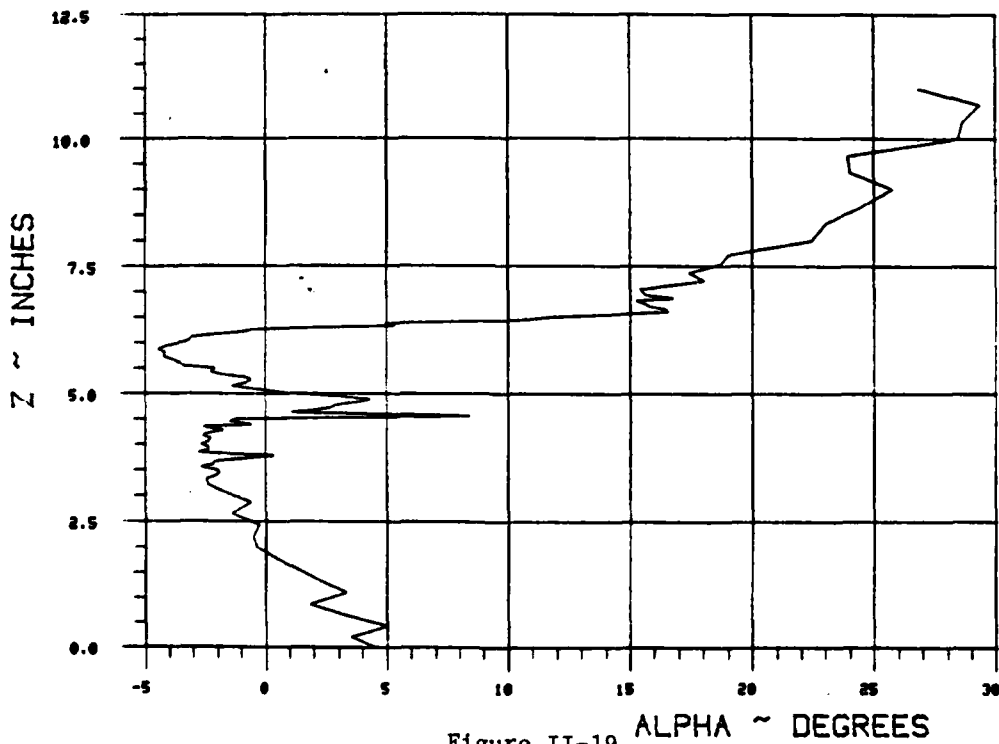
Figure II-19.

WAKE SURVEY DATA

TEST _272_ RUN _24_

ANGLE OF ATTACK _0_ NOMINAL JET ANGLE _50_ C MU _2.0576_

PRESSURE ~ PSIA
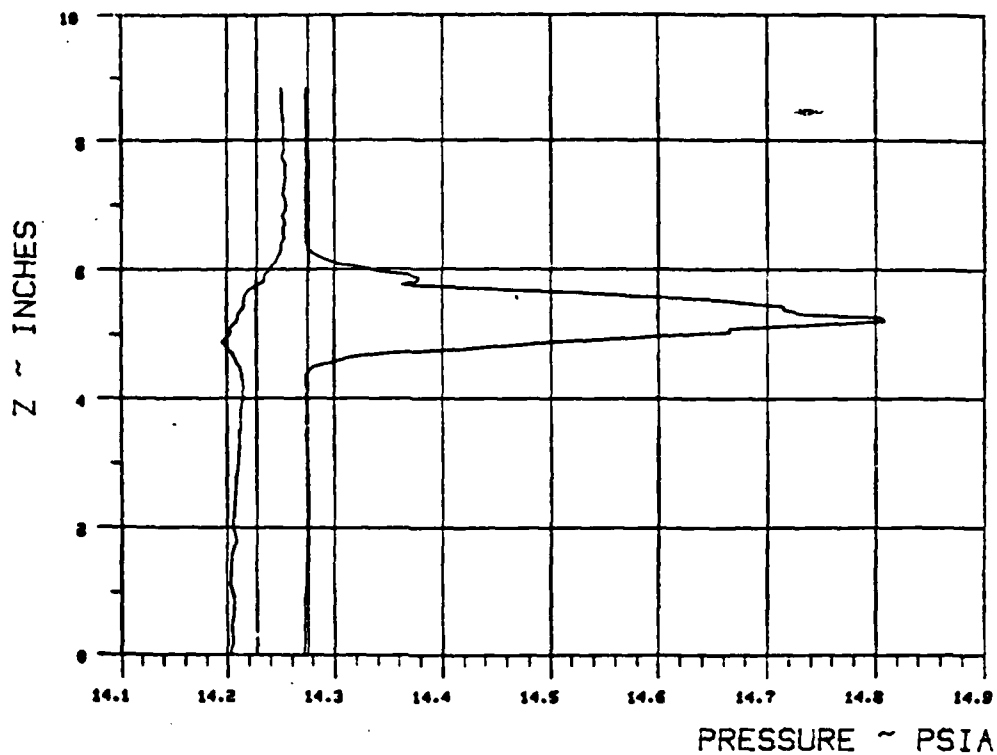
Xss/chord = _.2411_   Yss/chord = _.0389_

BETA = _30_

ALPHA ~ DEGREES

Figure II-20.

154
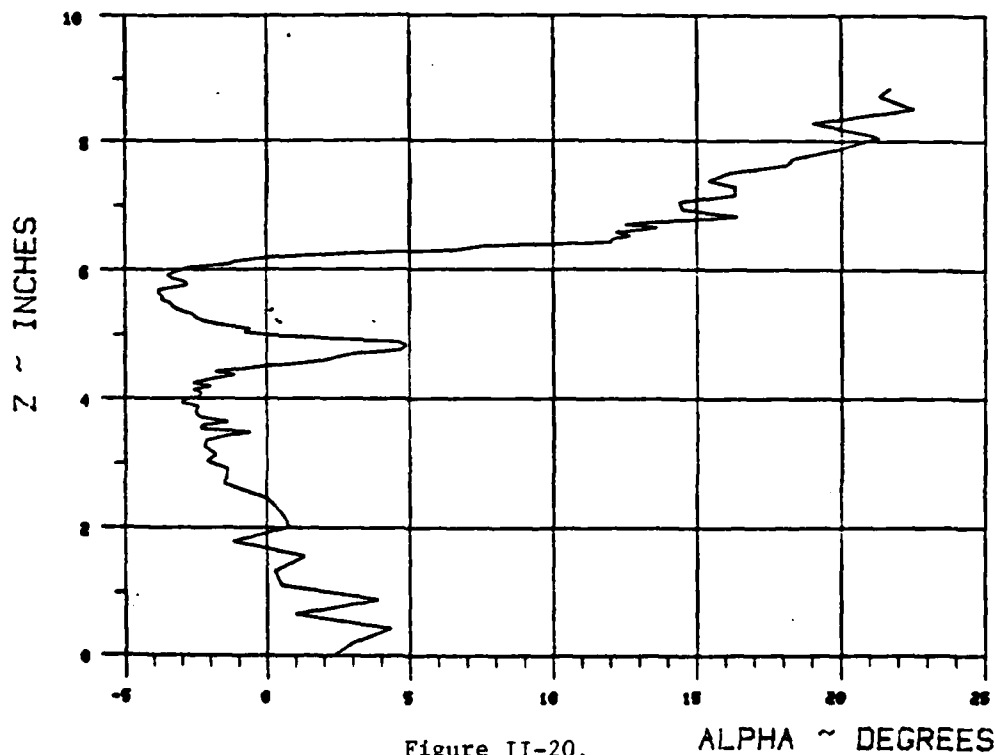
WAKE SURVEY DATA

TEST _272_ RUN _28_

ANGLE OF ATTACK _0_ NOMINAL JET ANGLE _50_ C MU _3.0647_

PRESSURE ~ PSIA
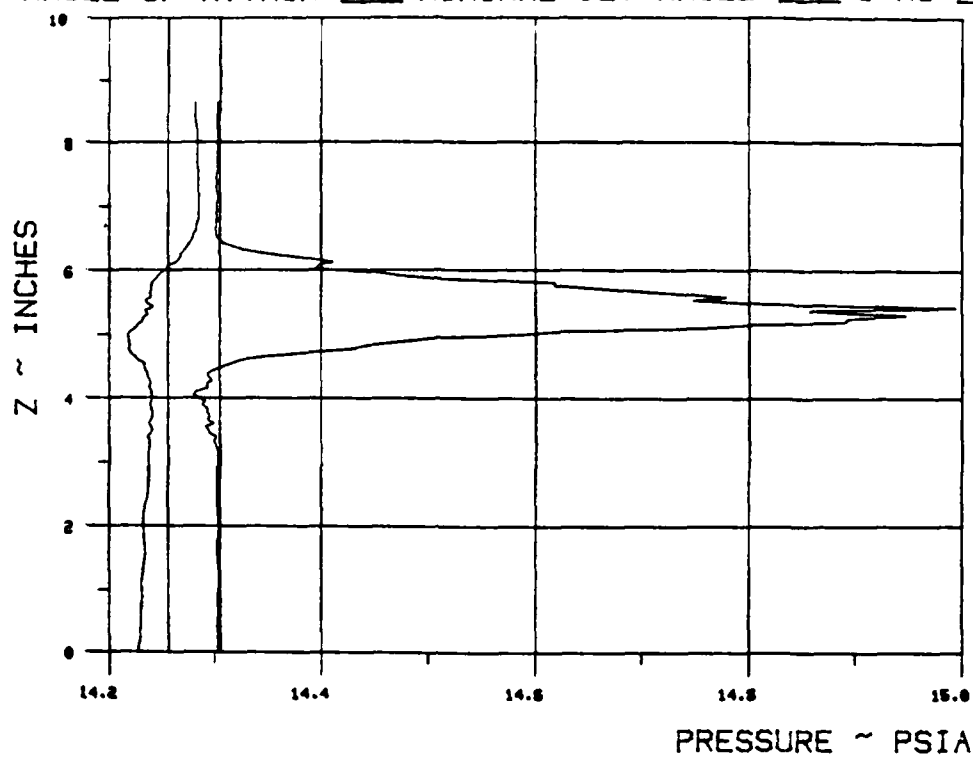
Xss/chord = _.2409_   Yss/chord = _.0386_

BETA = _30_

ALPHA ~ DEGREES

Figure II-21.

155
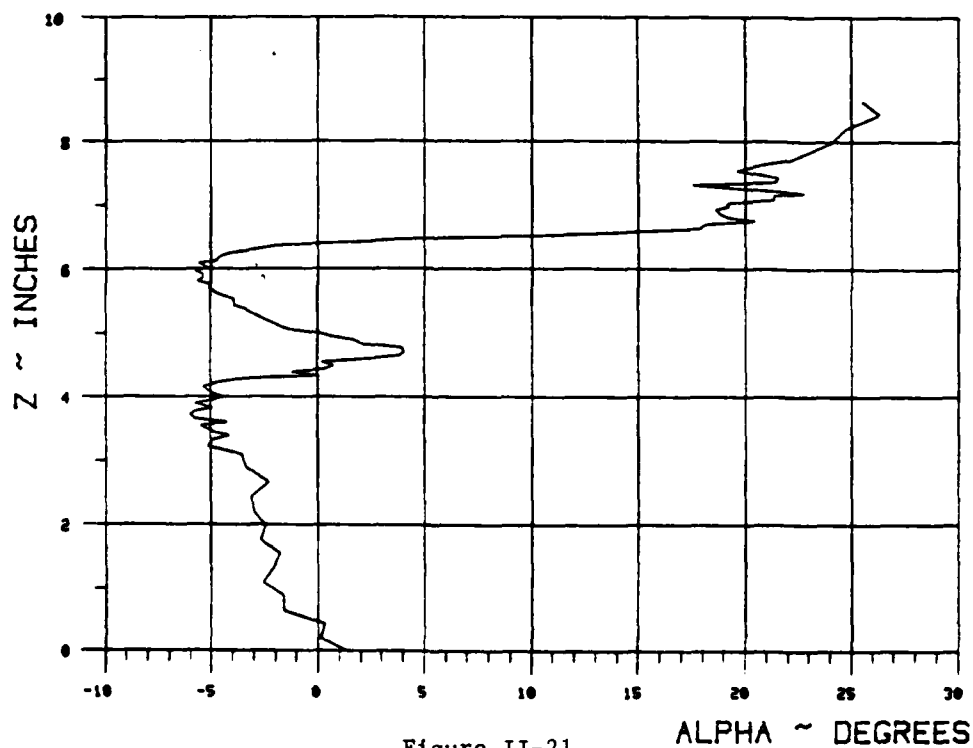
WAKE SURVEY DATA

TEST 272 RUN 22

ANGLE OF ATTACK _0_ NOMINAL JET ANGLE _60_ C MU _4.1525_

PRESSURE ~ PSIA

Xaa/chord = _.2413_ Yaa/chord = _.0392_

BETA = _30_

ALPHA ~ DEGREES

Figure II-22.

156
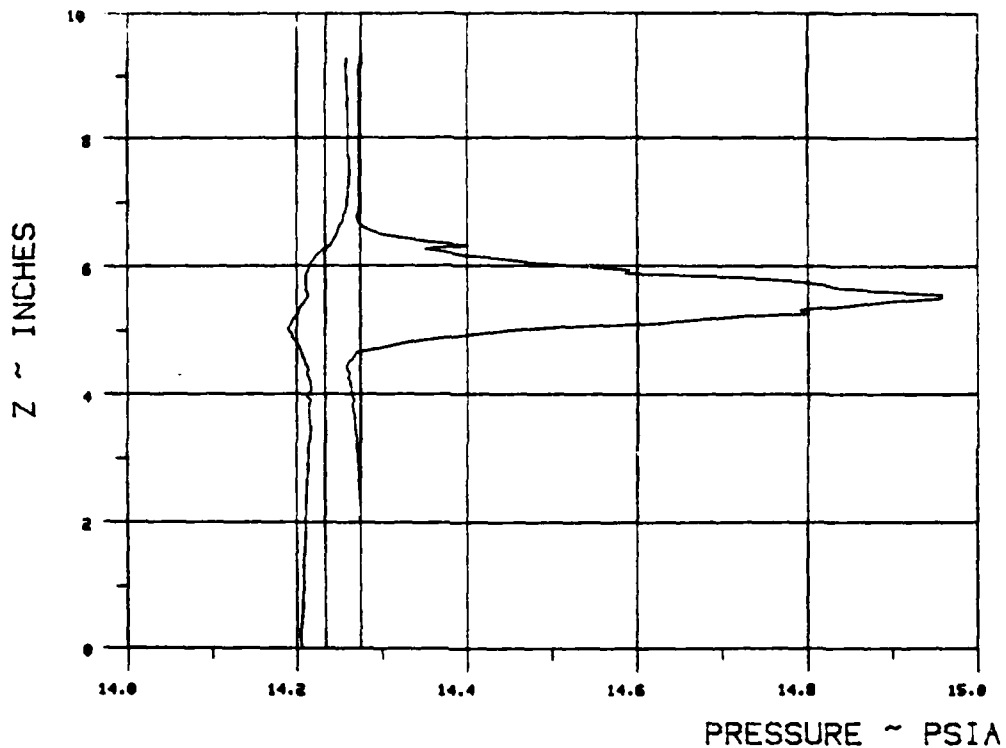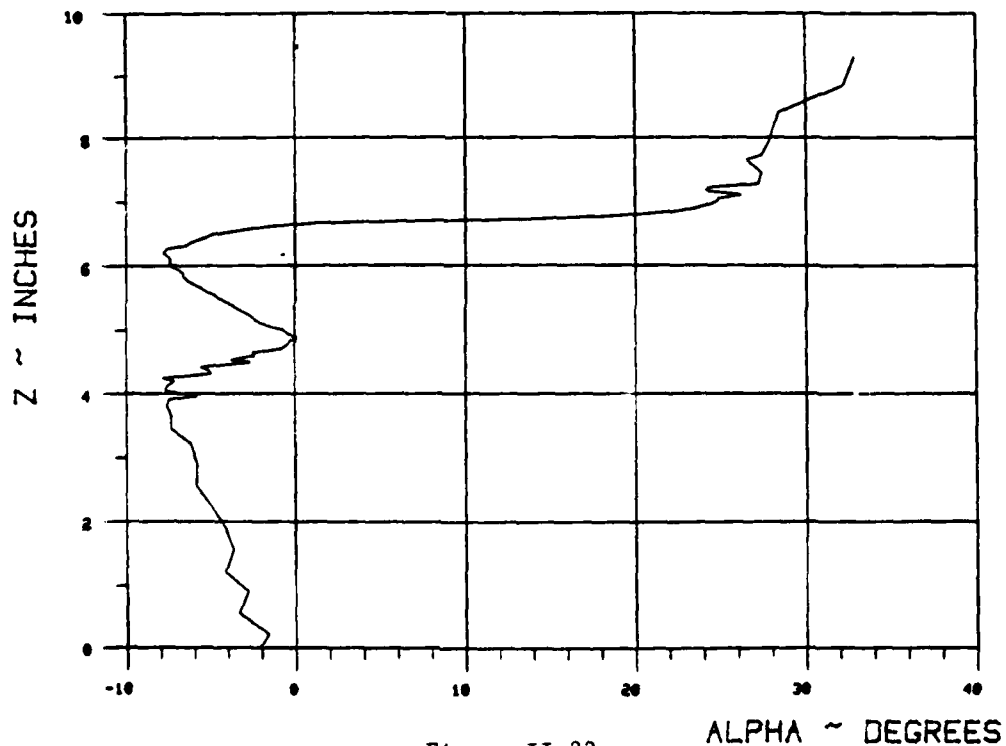
WAKE SURVEY DATA
TEST _272_ RUN _25_
ANGLE OF ATTACK _0_ NOMINAL JET ANGLE _50_ C MU _B.1708_
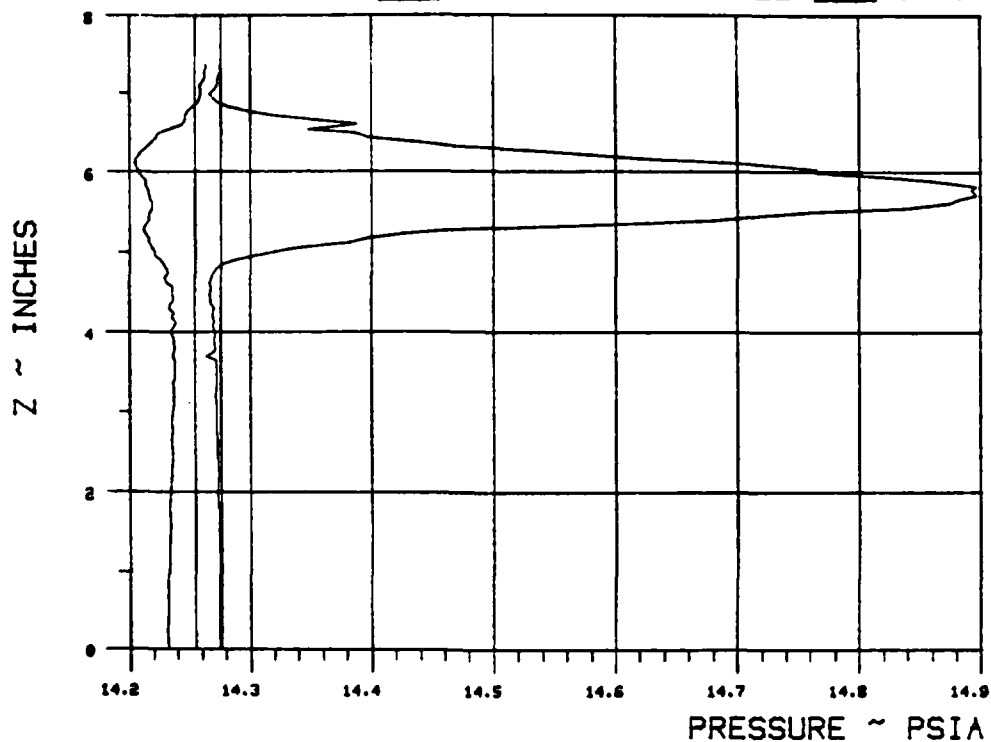
Xaa/chord = _.2406_   Yaa/chord = _.0379_

BETA = _30_

Figure II-23.

157
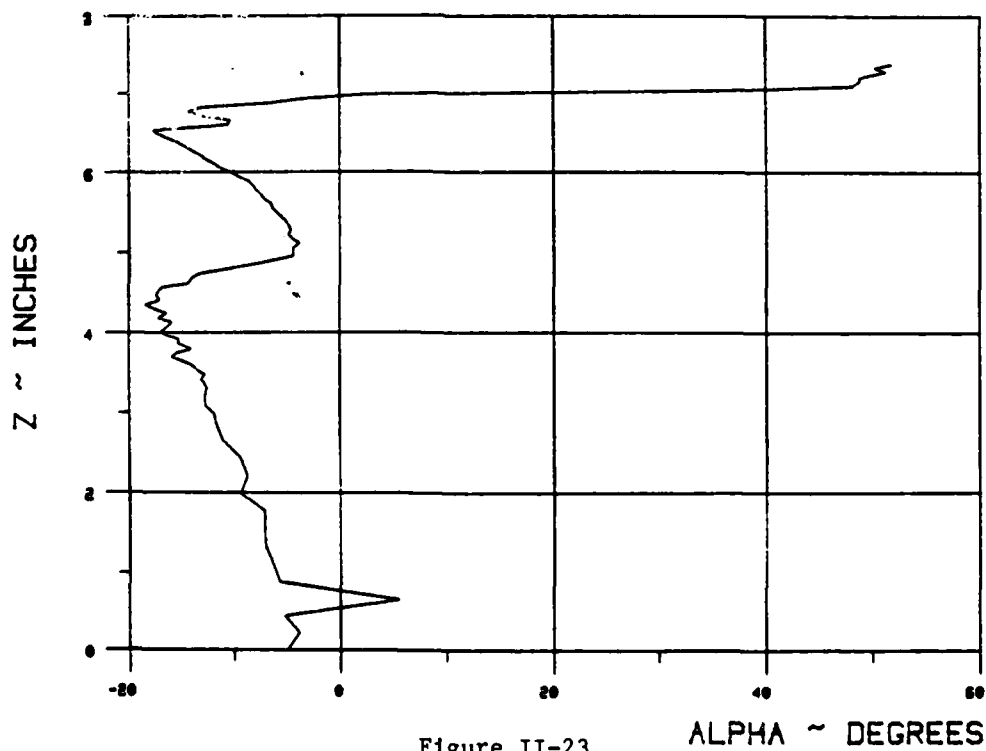
WAKE SURVEY DATA

TEST _272_ RUN _26_

ANGLE OF ATTACK _O_ NOMINAL JET ANGLE _50_ C MU _16.2213_
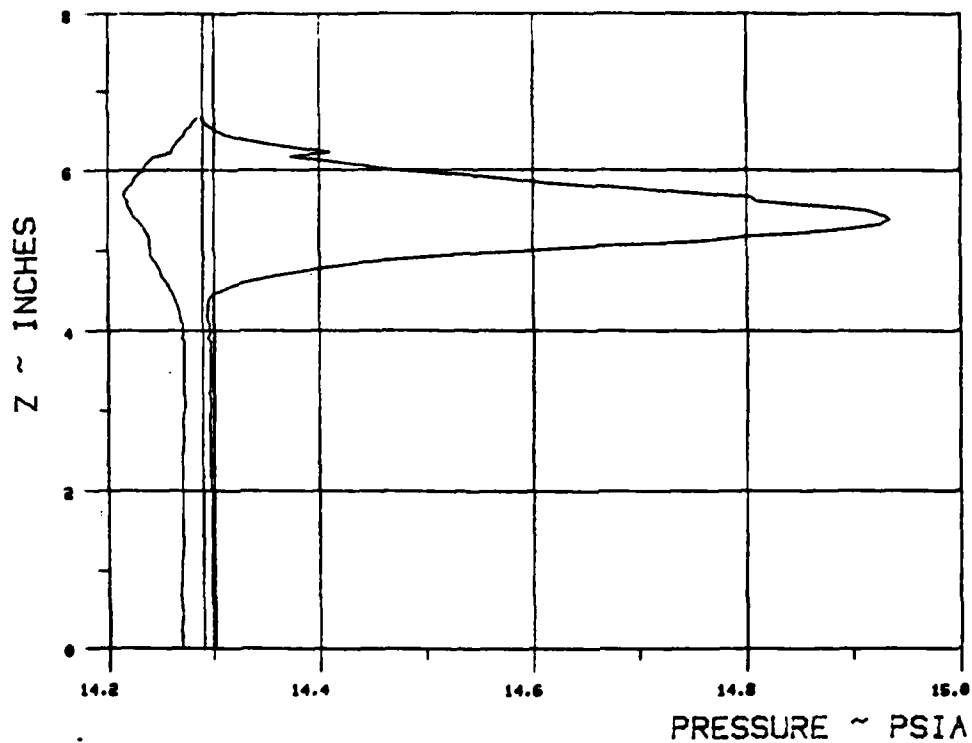
Xee/chord = _.2305_ Yee/chord = _.0205_

BETA = _30_

Figure II-24.

158
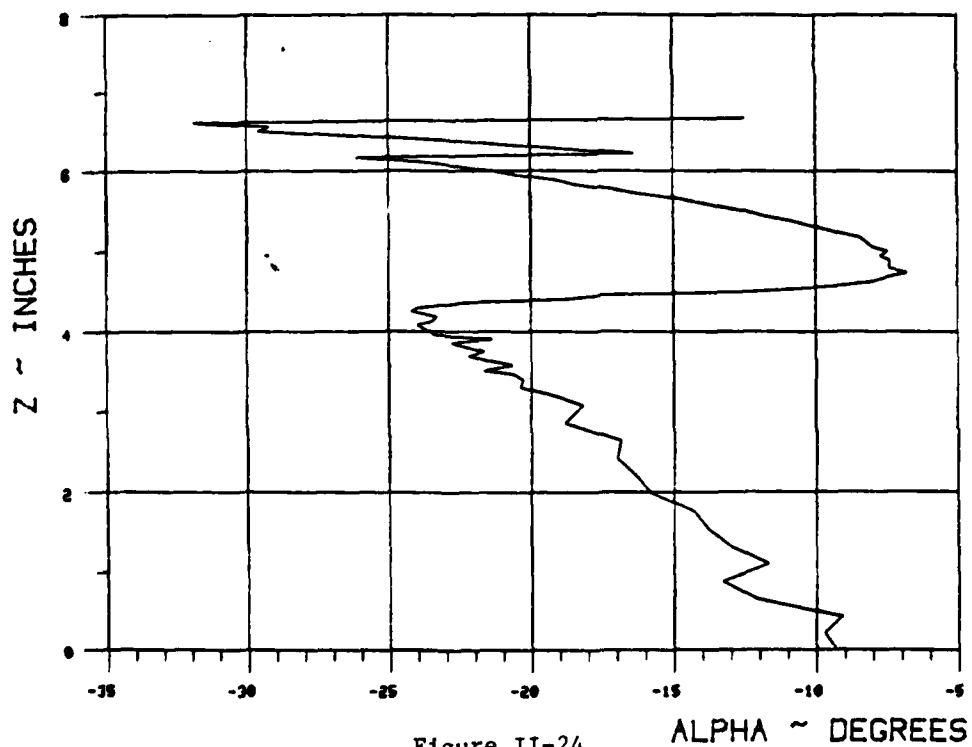
WAKE SURVEY DATA

TEST 272 RUN 27

ANGLE OF ATTACK 0 NOMINAL JET ANGLE 50 C MU 22.33 48

Z ~ INCHES

PRESSURE ~ PSIA

14.2   14.4   14.6   14.8   15.0

Xss/chord = .2309   Yss/chord = .0212

BETA = 30

Z ~ INCHES

-45   -40   -35   -30   -25   -20   -15   -10   -5

ALPHA ~ DEGREES

Figure II-25.

159
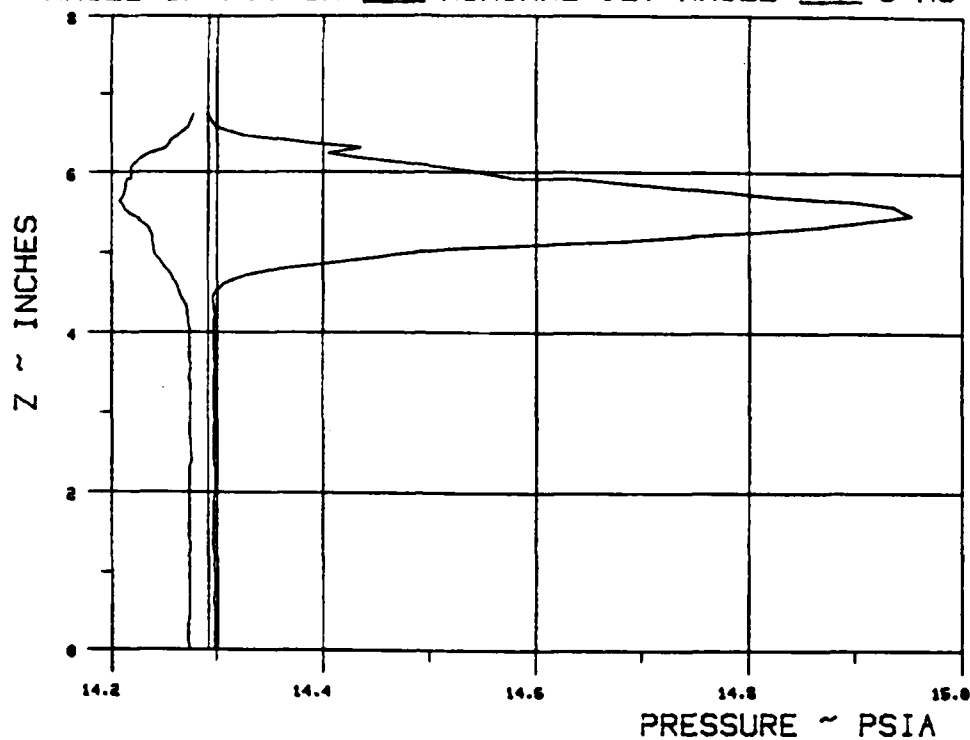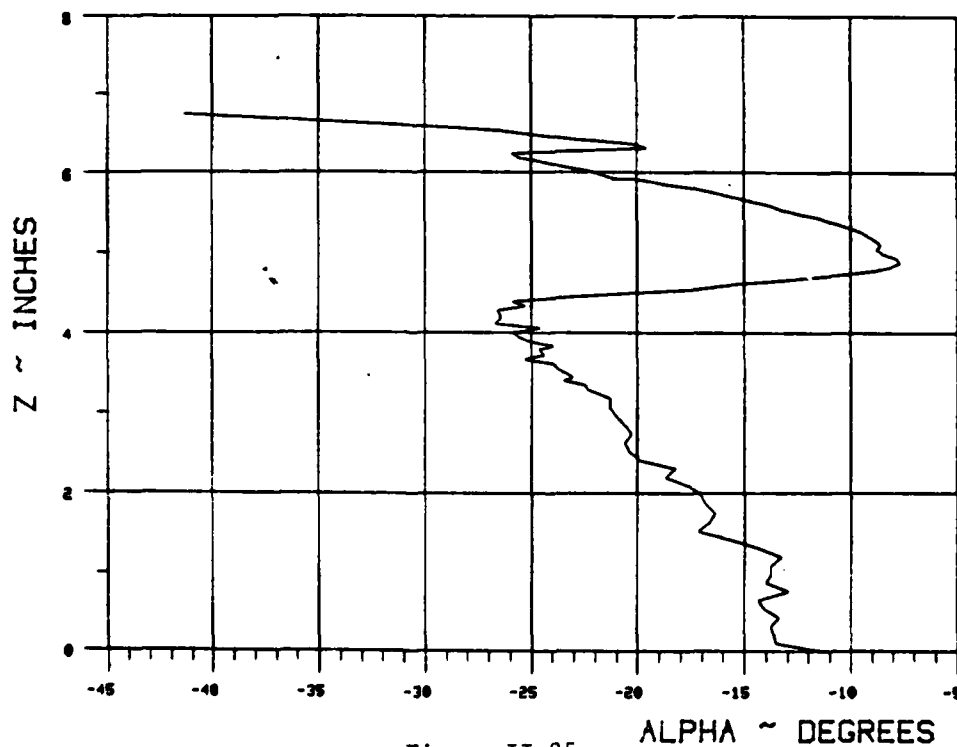
WAKE SURVEY DATA

TEST _272_ RUN _30_

ANGLE OF ATTACK _0_ NOMINAL JET ANGLE _70_ C MU _.5513_

PRESSURE ~ PSIA
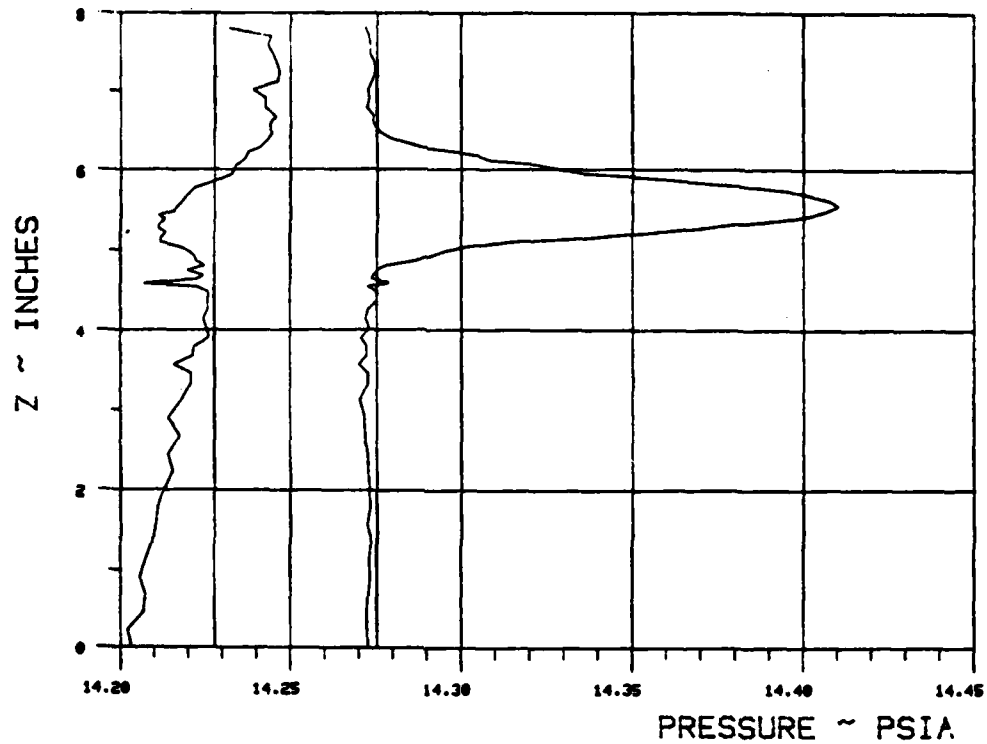
Xss/chord ≈ _.1615_   Yss/chord = _-.0038_

BETA = _45.2_

ALPHA ~ DEGREES
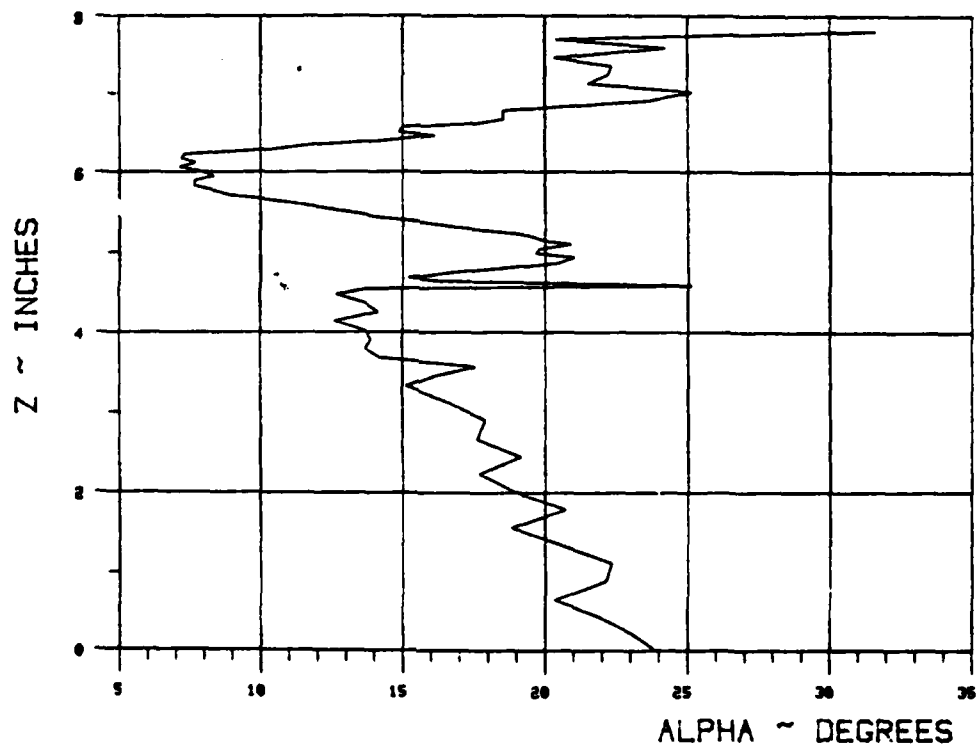
Figure II-26.

WAKE SURVEY DATA

TEST 272 RUN 43

ANGLE OF ATTACK 0 NOMINAL JET ANGLE 70 C MU 1.0486
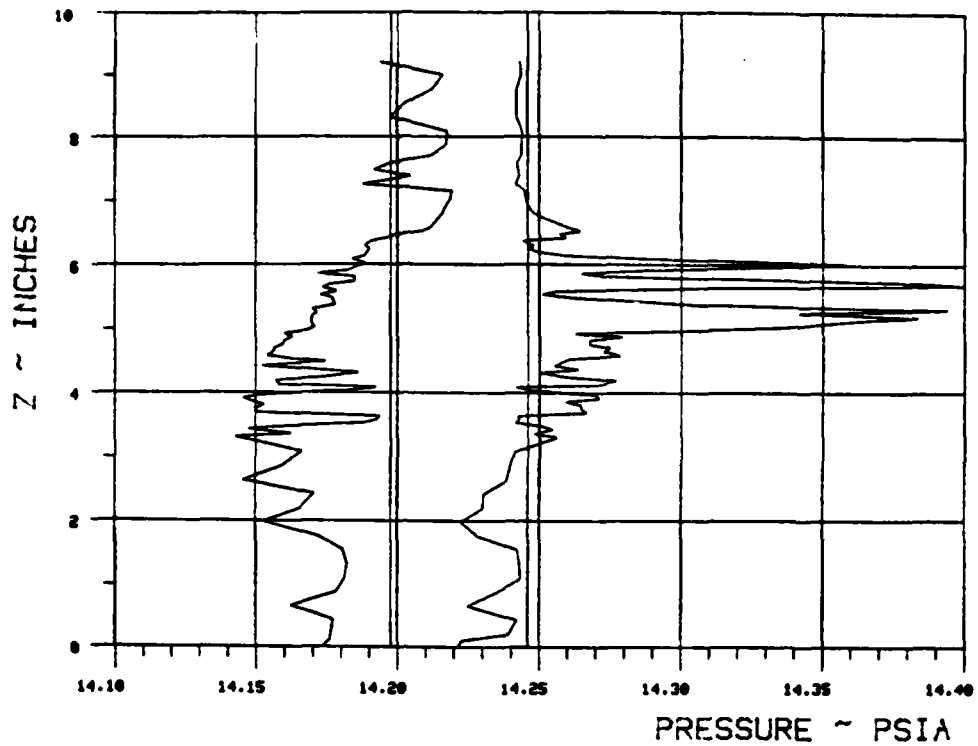
Xss/chord = .1926   Yss/chord = -.0353

BETA = 45.2
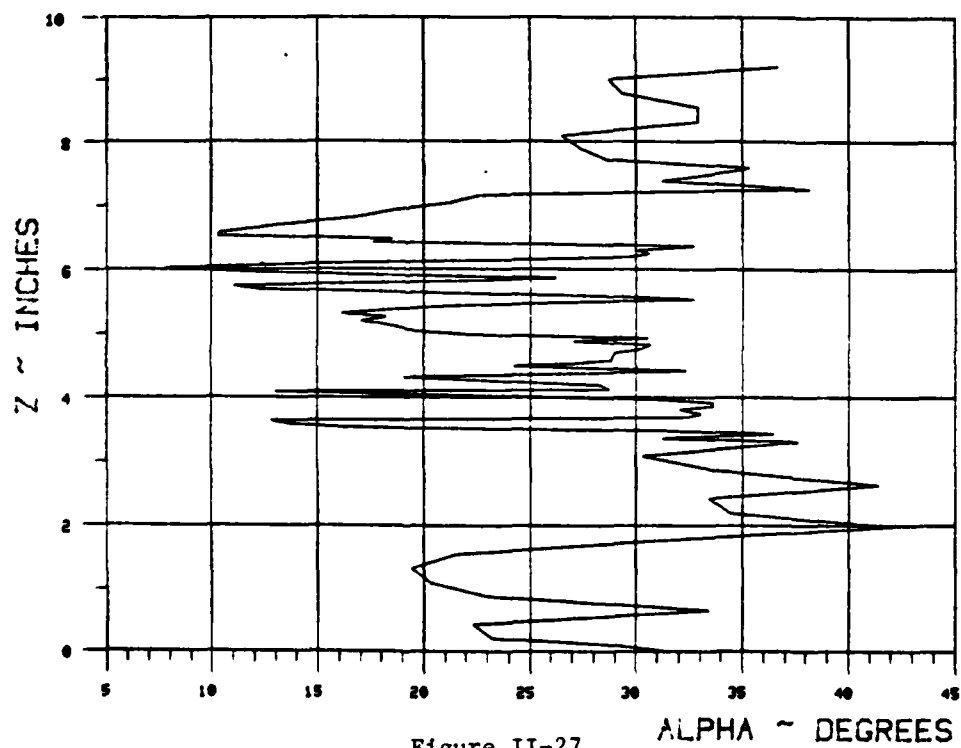
Figure II-27.

WAKE SURVEY DATA
TEST _272_ RUN _41_
ANGLE OF ATTACK _0_ NOMINAL JET ANGLE _70_ C MU _1.051_
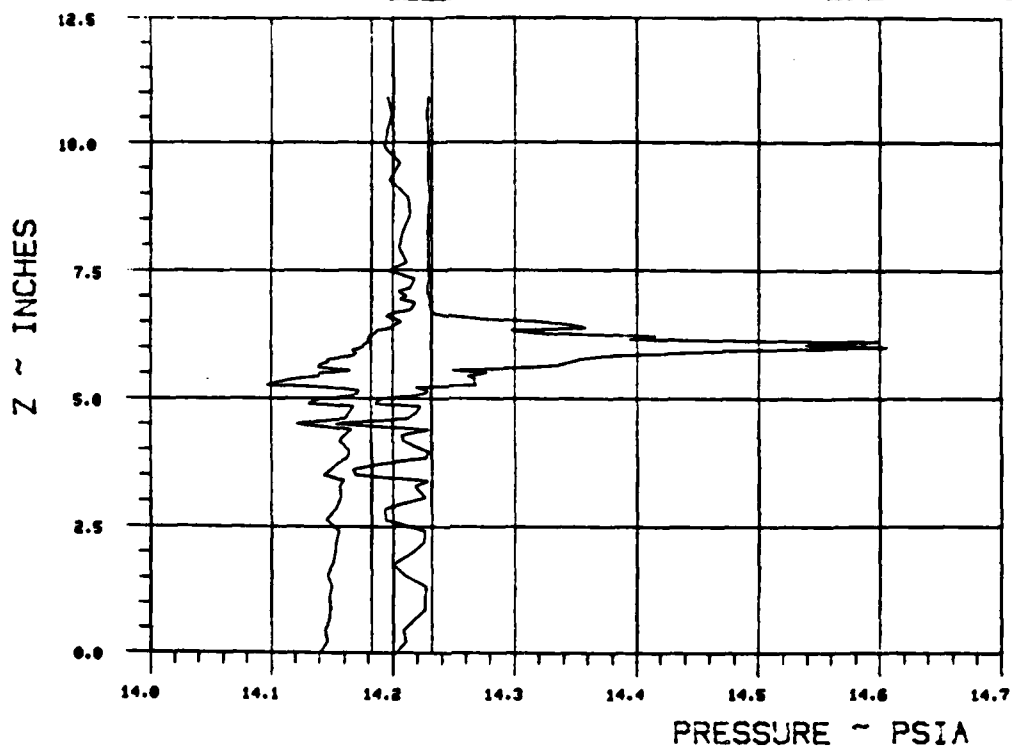
Xss/chord = _.1299_ Yss/chord = _.0273_

BETA = _45.2_
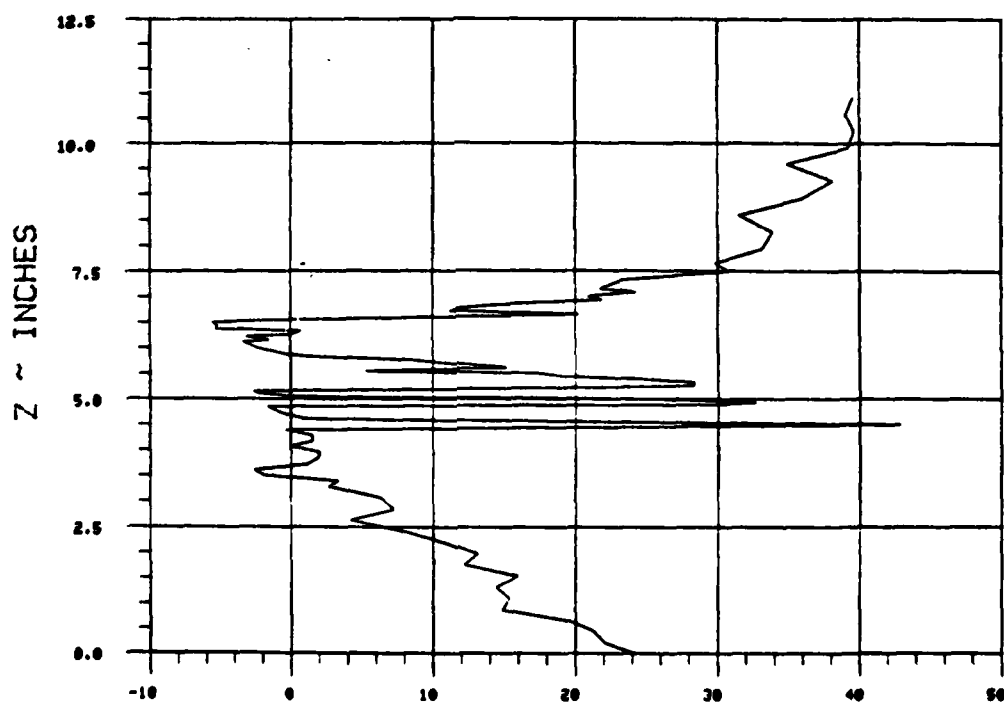
Figure II-28.

WAKE SURVEY DATA

TEST _272_ RUN _31_

ANGLE OF ATTACK _0_ NOMINAL JET ANGLE _70_ C MU _1.0553_
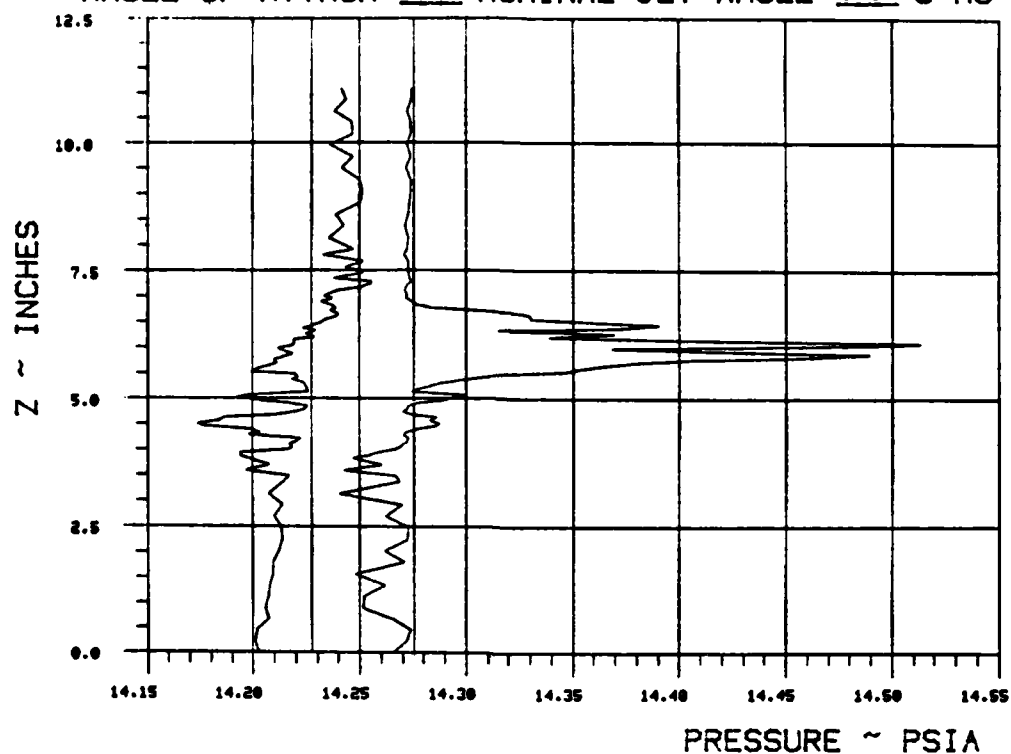
Xss/chord = _.1612_ Yss/chord = _-.004_
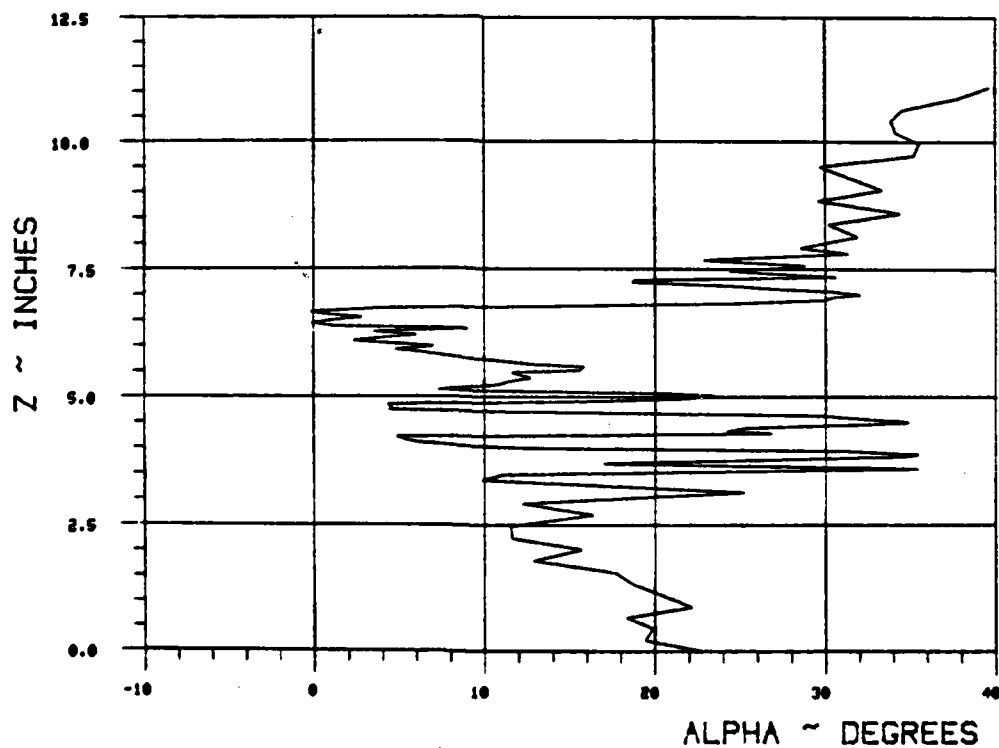
BETA = _45.2_

Figure II-29.

WAKE SURVEY DATA

TEST _272_ RUN _32_

ANGLE OF ATTACK _O_ NOMINAL JET ANGLE _70_ C MU _2.0638_
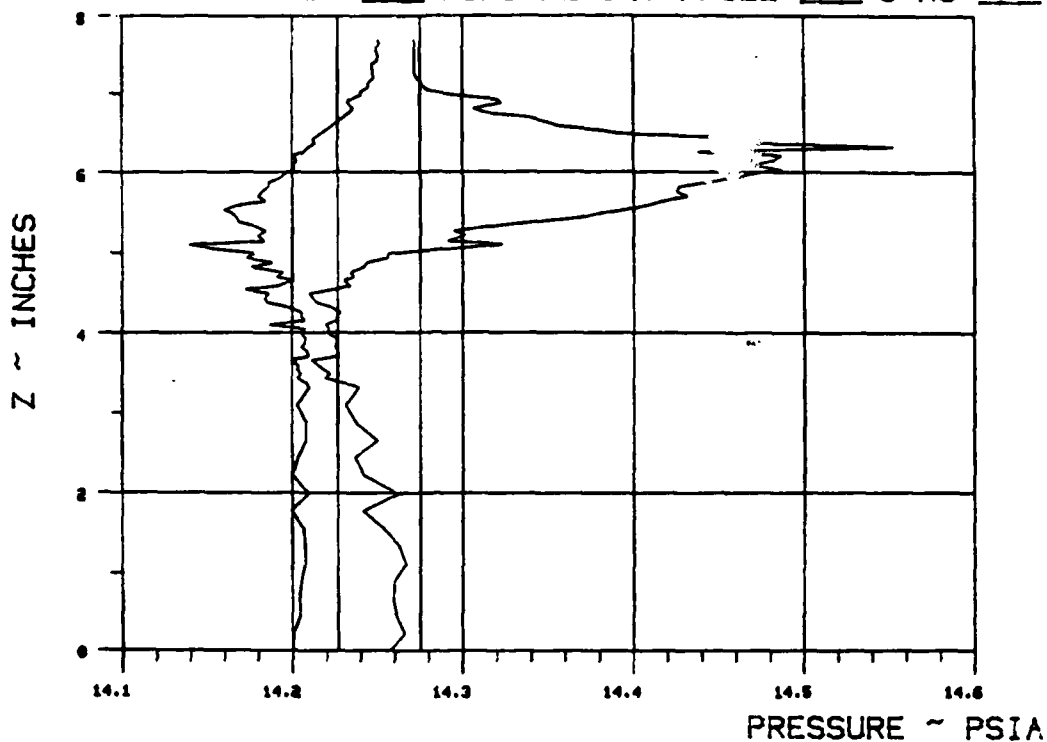
Xss/chord = _.1619_   Yss/chord = _-.0033_

BETA = _45.2_
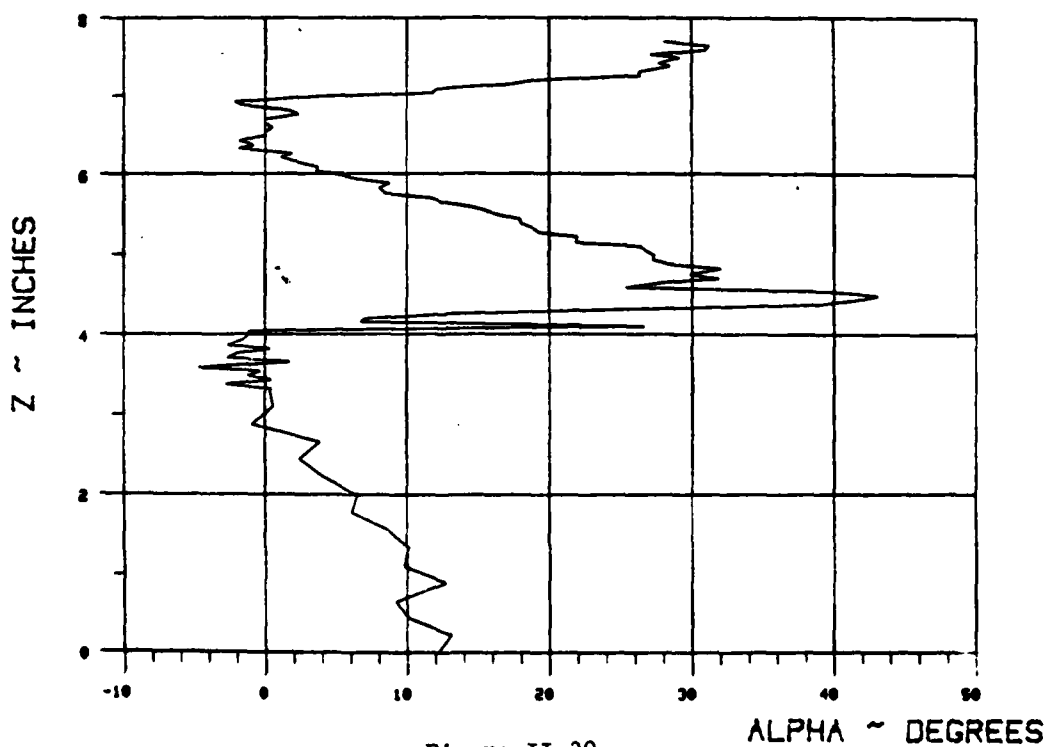
Figure II-30.

WAKE SURVEY DATA

TEST 272 RUN 31

ANGLE OF ATTACK 0 NOMINAL JET ANGLE 70 C MU 1.0553
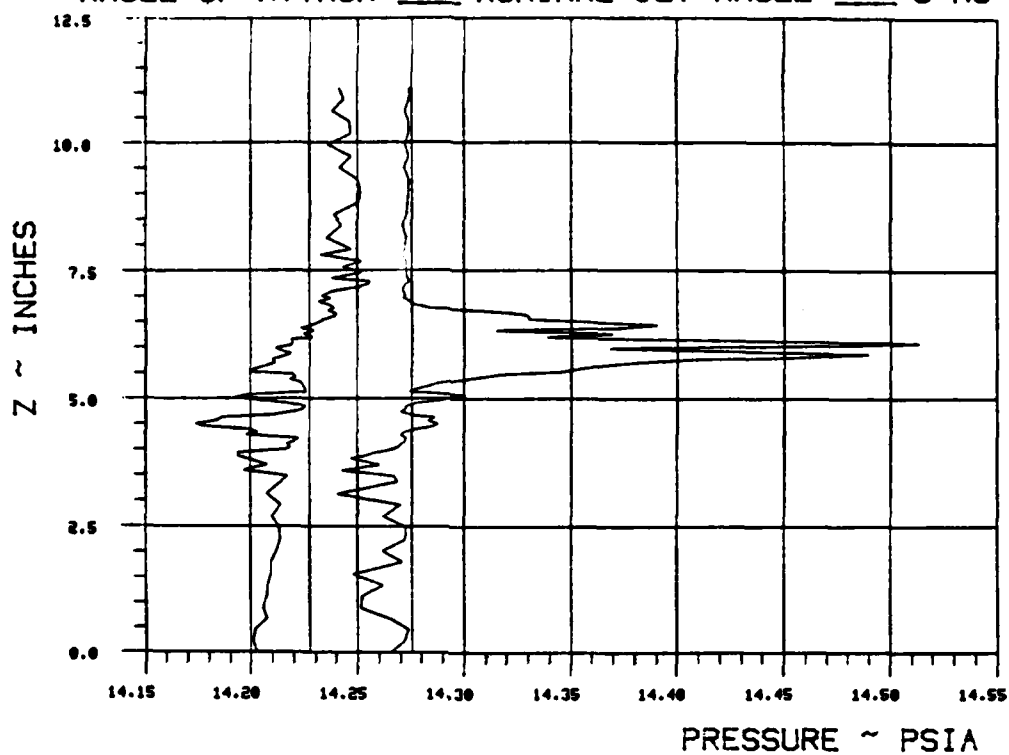
Xss/chord = .1612   Yss/chord = -.004
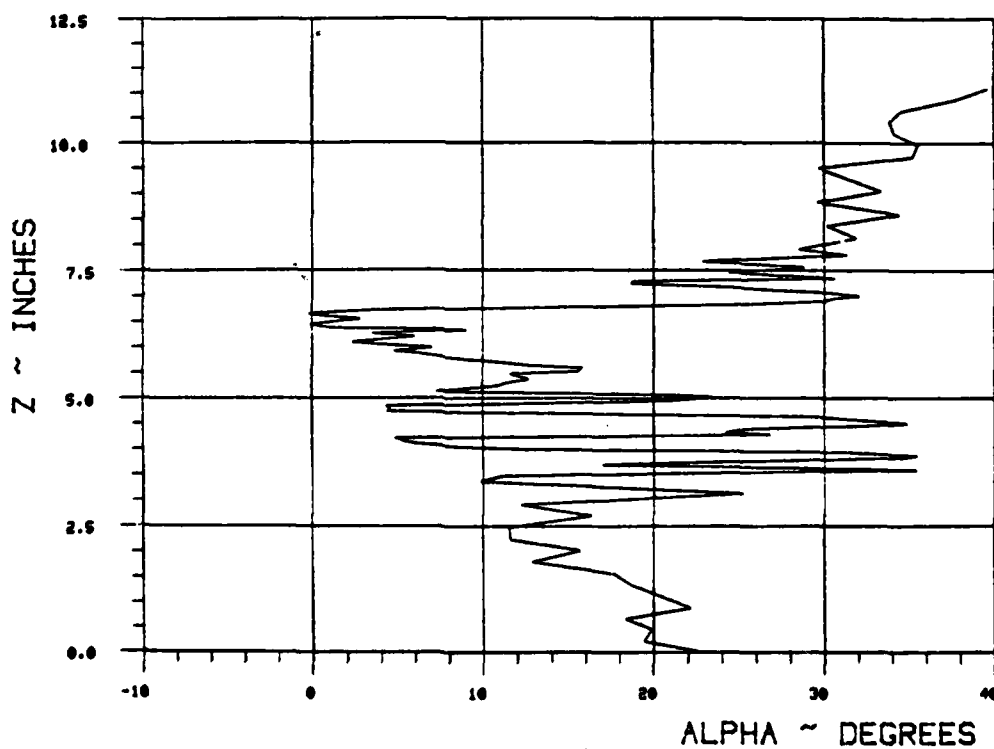
BETA = 45.2

Figure II-29.

WAKE SURVEY DATA

TEST _272_ RUN _36_

ANGLE OF ATTACK _0_ NOMINAL JET ANGLE _70_ C MU _4.2603_
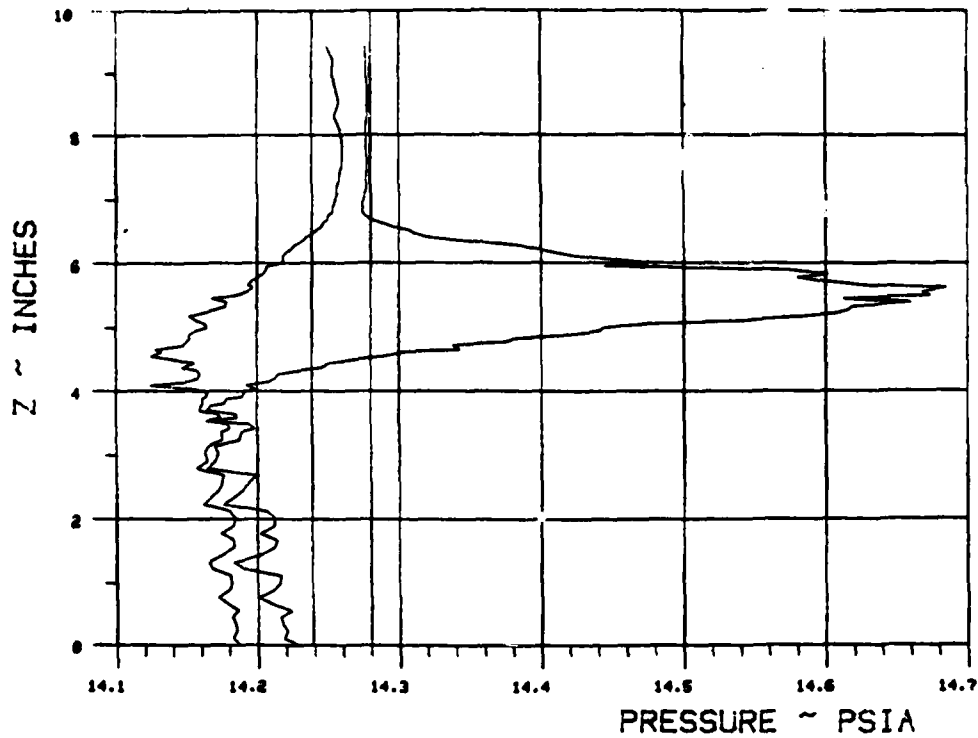
Xss/chord = _.1468_ Yss/chord = _-.0185_

BETA = _45.2_

Figure II-31.

165
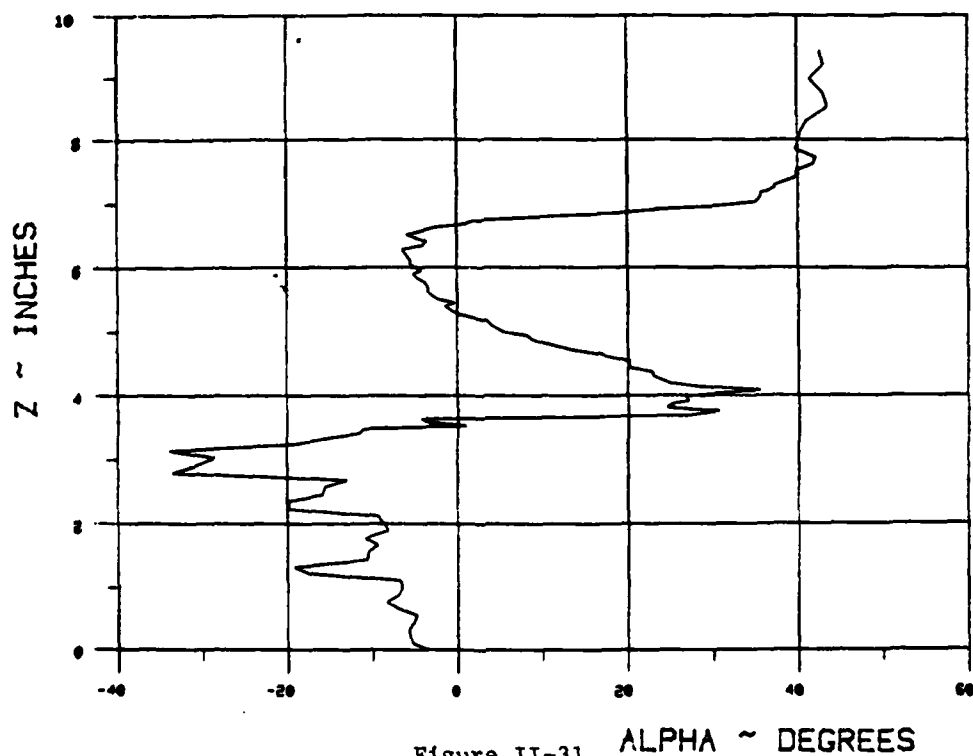
WAKE SURVEY DATA

TEST _272_ RUN _34_

ANGLE OF ATTACK _O_ NOMINAL JET ANGLE _70_ C MU _8.319_
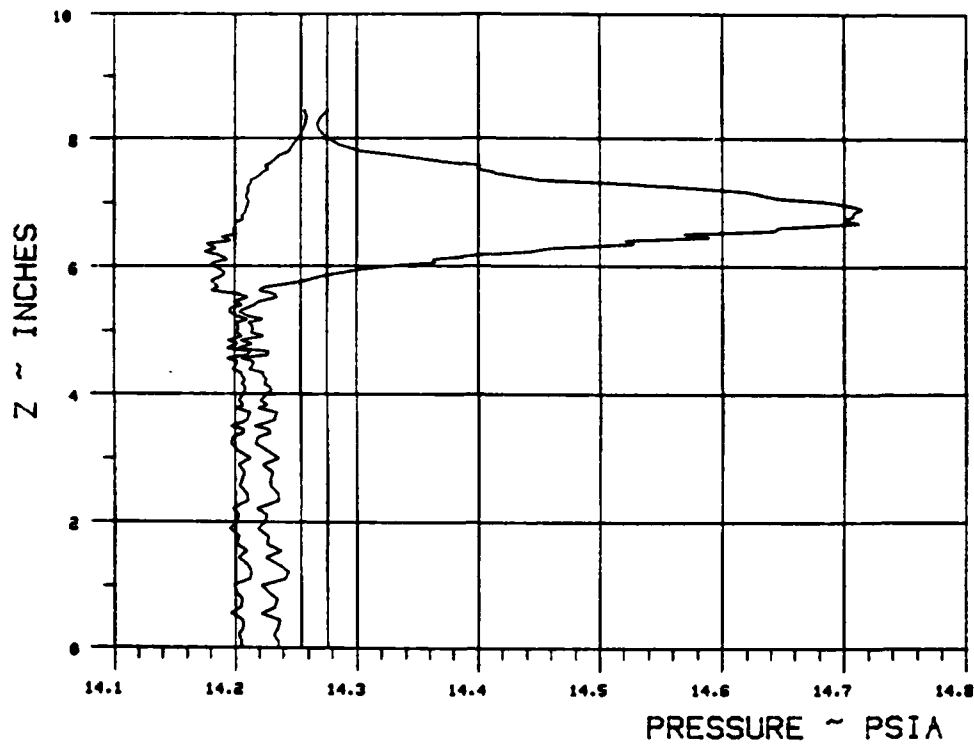
Xss/chord = _.1622_ Yss/chord = _-.0031_

BETA = _45.2_
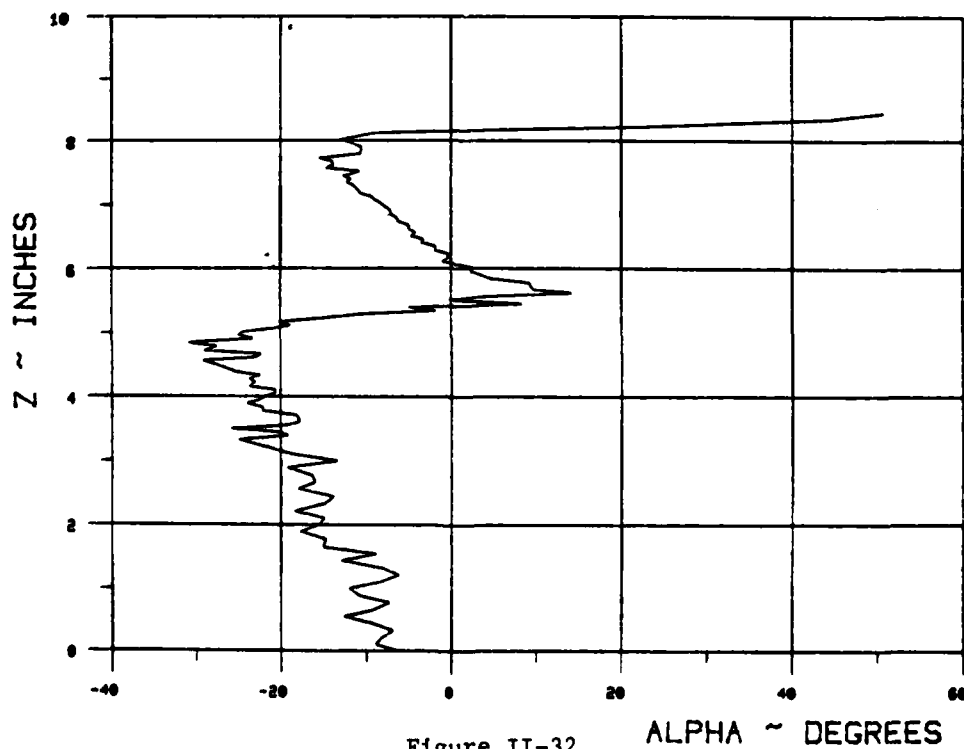
Figure II-32.

WAKE SURVEY DATA
TEST 272 RUN 42
ANGLE OF ATTACK 0 NOMINAL JET ANGLE 70 C MU 10.524

PRESSURE ~ PSIA

Xss/chord = .1472 Yss/chord = -.018

BETA = 45.2

ALPHA ~ DEGREES

Figure II-33.

167
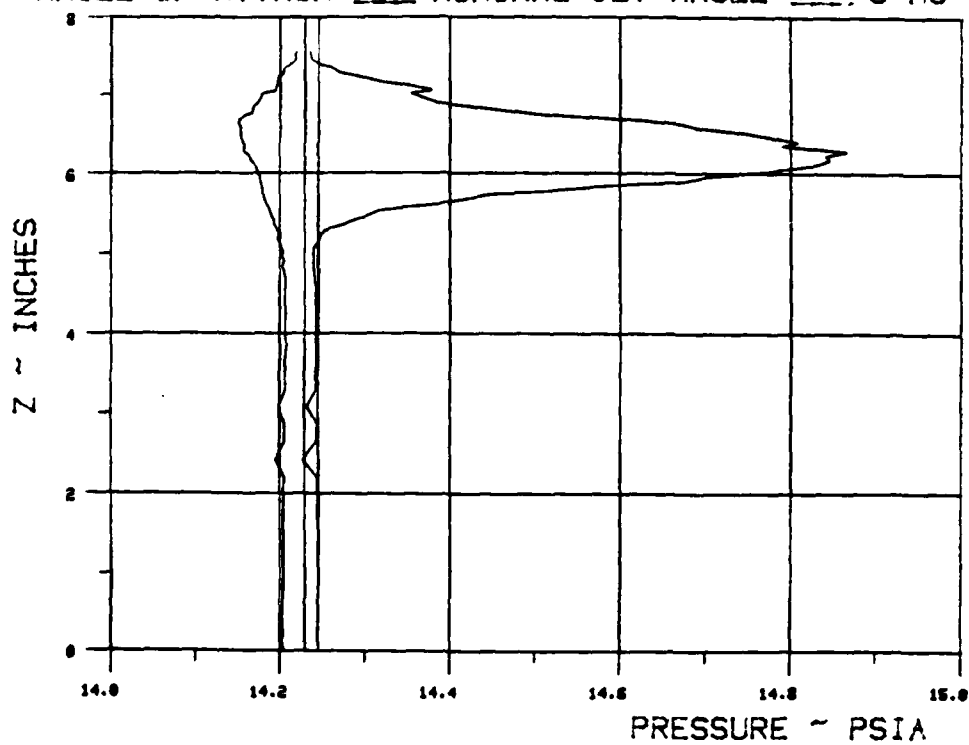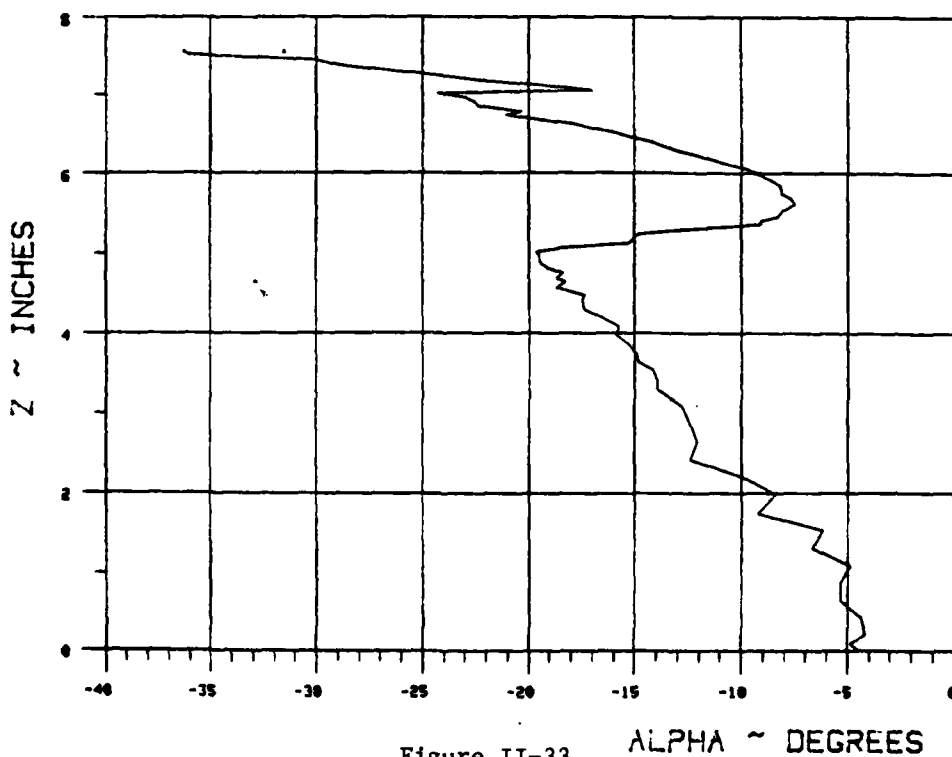
WAKE SURVEY DATA
TEST _272_ RUN _37_
ANGLE OF ATTACK _O_ NOMINAL JET ANGLE _70_ C MU _16.6099_

PRESSURE ~ PSIA
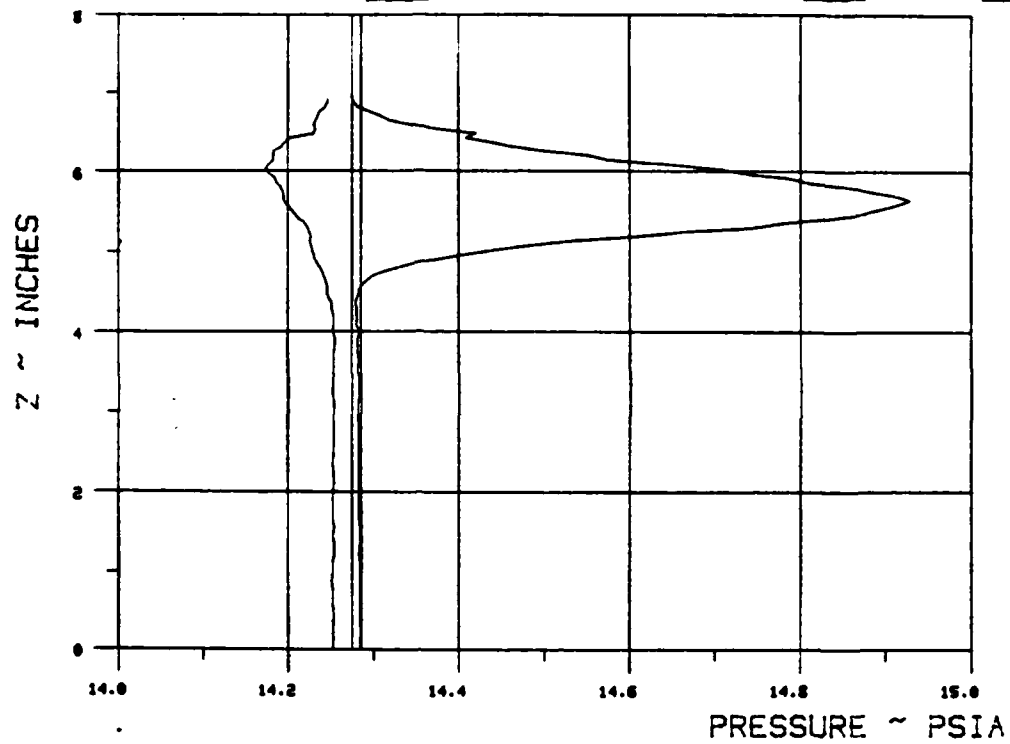
Xss/chord = _.136_   Yss/chord = _-.0291_

BETA = _45.2_

ALPHA ~ DEGREES

Figure II-34.

168

WAKE SURVEY DATA

TEST _272_ RUN _38_

ANGLE OF ATTACK _O_ NOMINAL JET ANGLE _70_ C MU _24.4346_
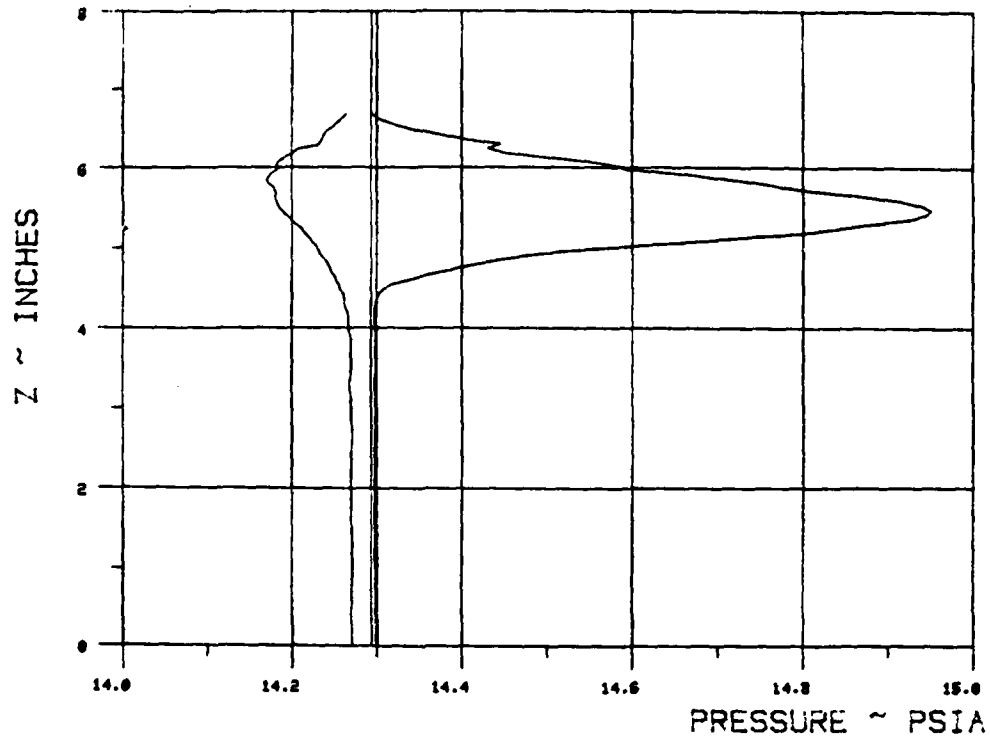
Xss/chord = _.1322_   Yss/chord = _-.0329_

BETA = _45.2_

Figure II-35.

169
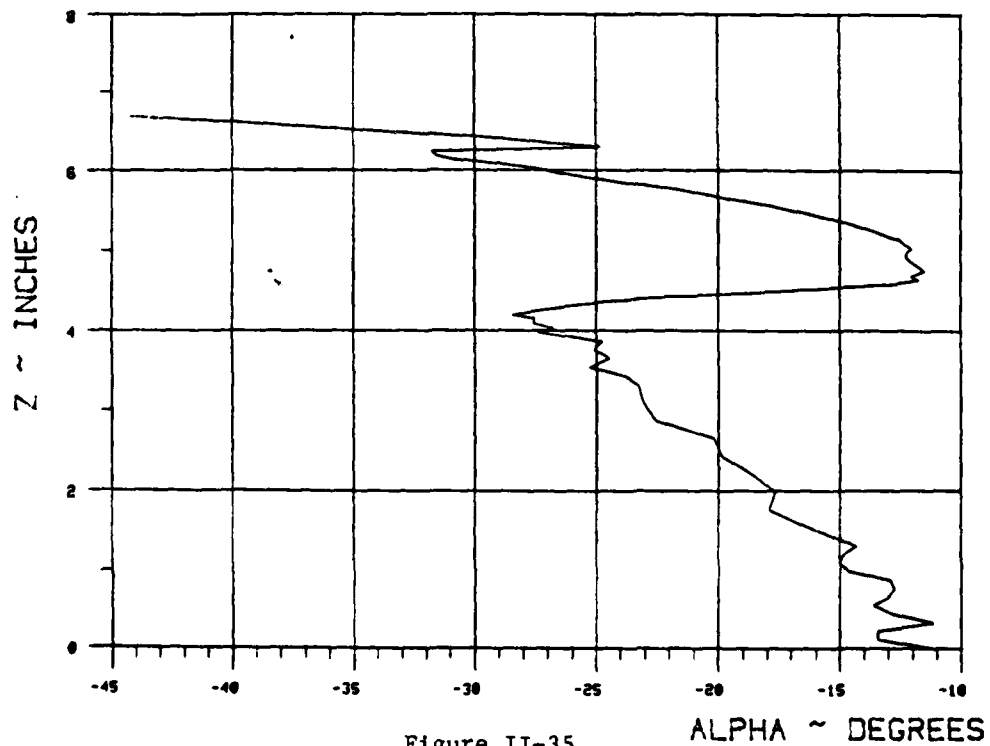
WAKE SURVEY DATA

TEST _272_ RUN _39_

ANGLE OF ATTACK _O_ NOMINAL JET ANGLE _70_ C MU _28.9276_
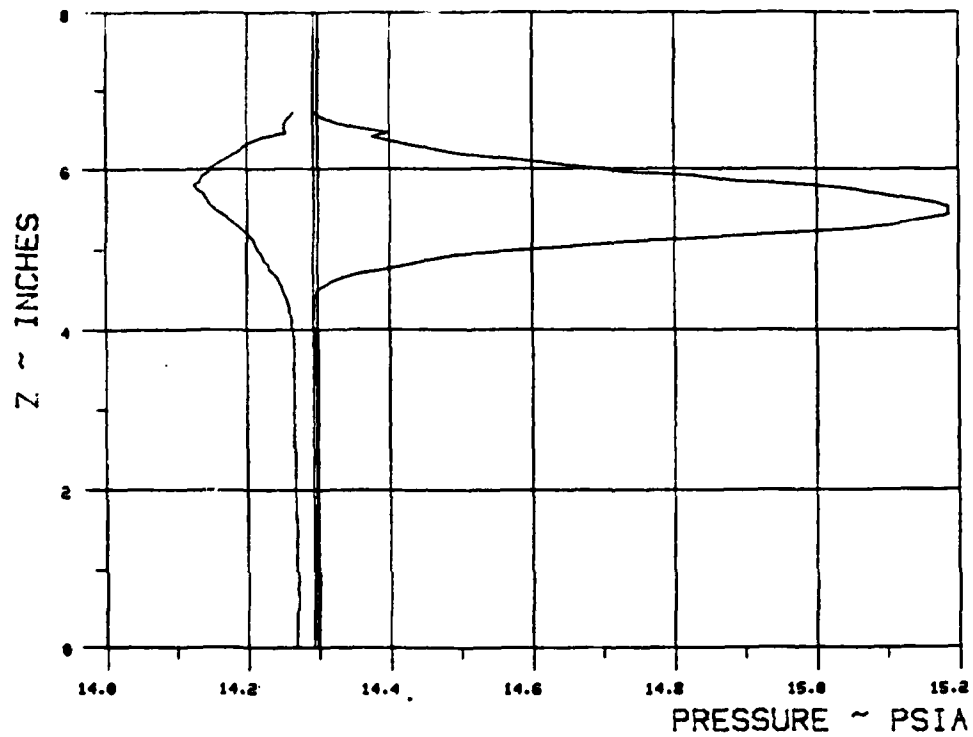
Xss/chord = _.132_ Yss/chord = _-.0331_
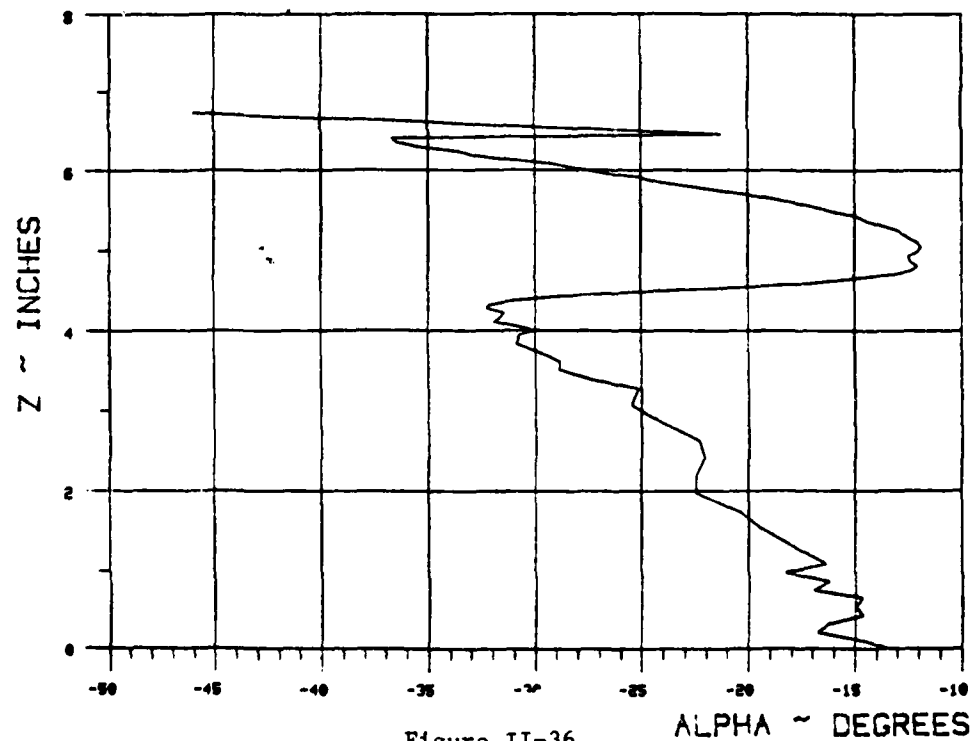
BETA = _45.2_

Figure II-36.

WAKE SURVEY DATA
TEST 272 RUN 44
ANGLE OF ATTACK 0 NOMINAL JET ANGLE 90 C MU .5101

PRESSURE ~ PSIA

Xss/chord = .1922 Yss/chord = .0267

BETA = 45.2

ALPHA ~ DEGREES

Figure II-37.

171
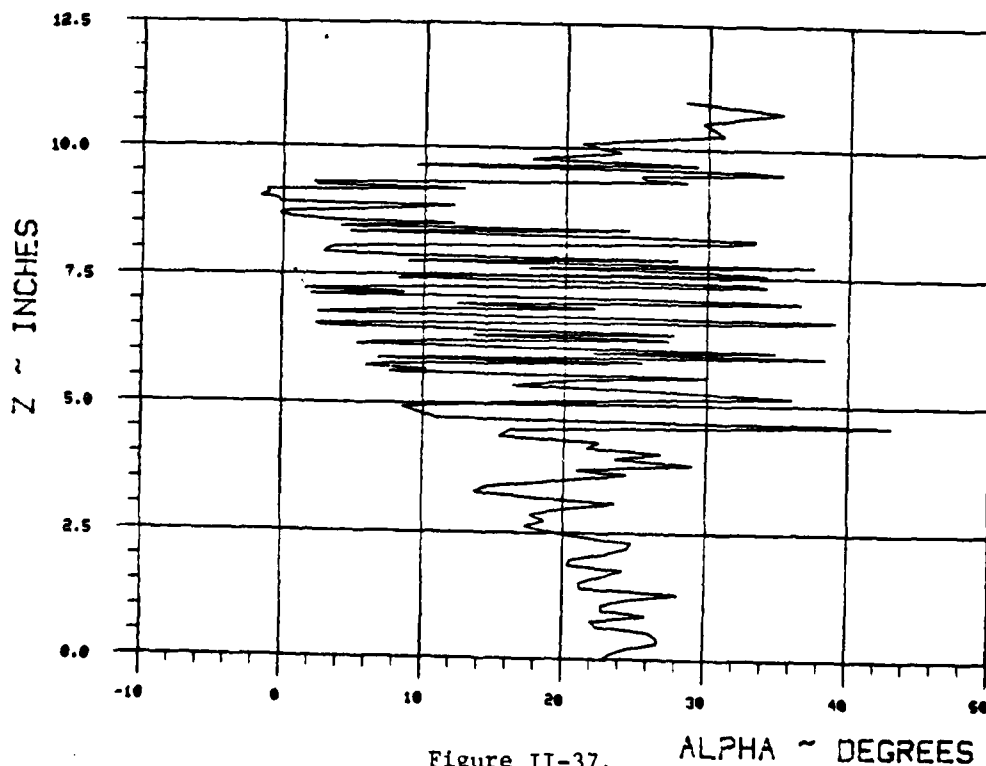
WAKE SURVEY DATA
TEST _272_ RUN _47_
ANGLE OF ATTACK _O_ NOMINAL JET ANGLE _90_ C MU _.5201_

PRESSURE ~ PSIA
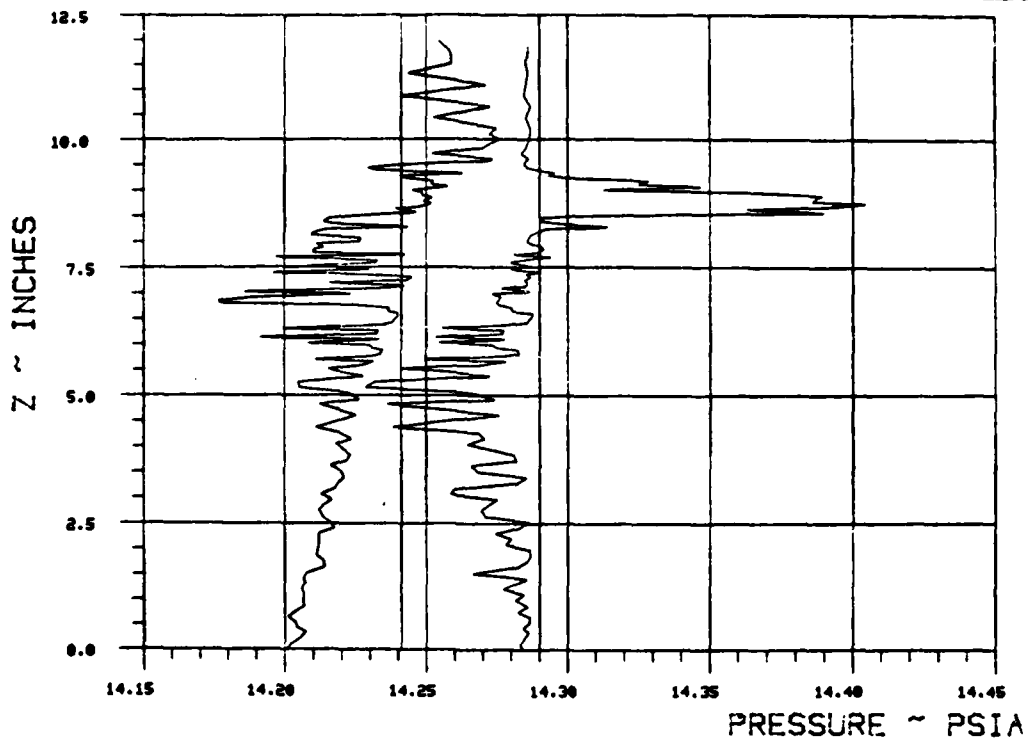
Xss/chord. = _.1759_ Yss/chord = _.0418_

BETA = _45.2_
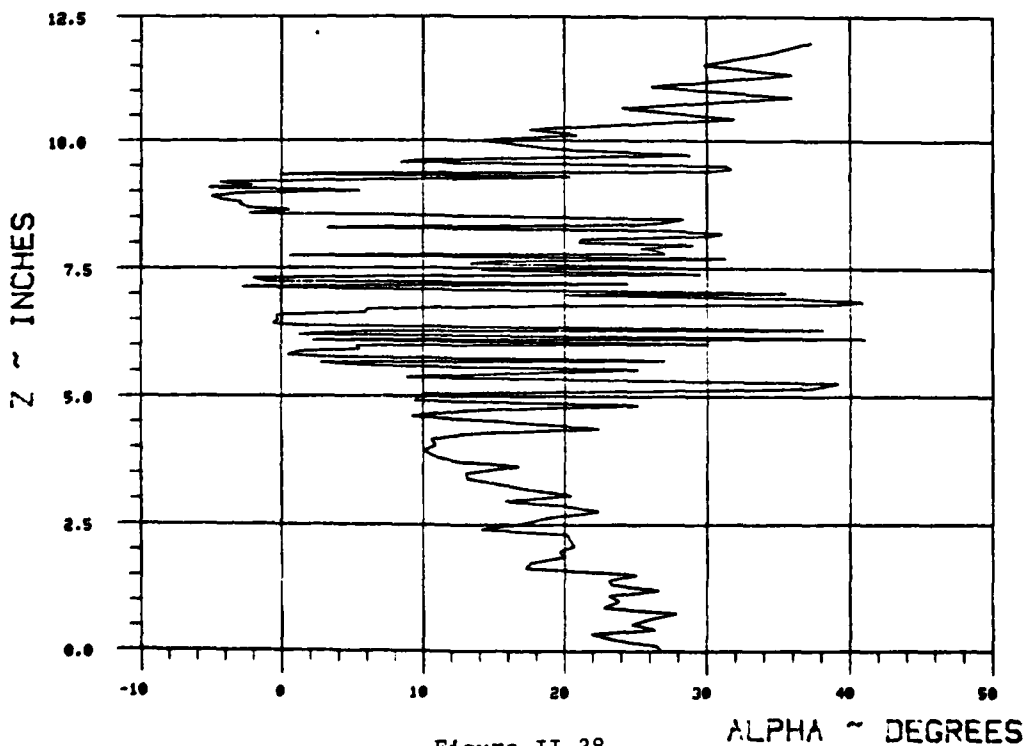
ALPHA ~ DEGREES

Figure II-38.

WAKE SURVEY DATA

TEST _272_ RUN _45_

ANGLE OF ATTACK _O_ NOMINAL JET ANGLE _90_ C MU _.9785_

PRESSURE ~ PSIA
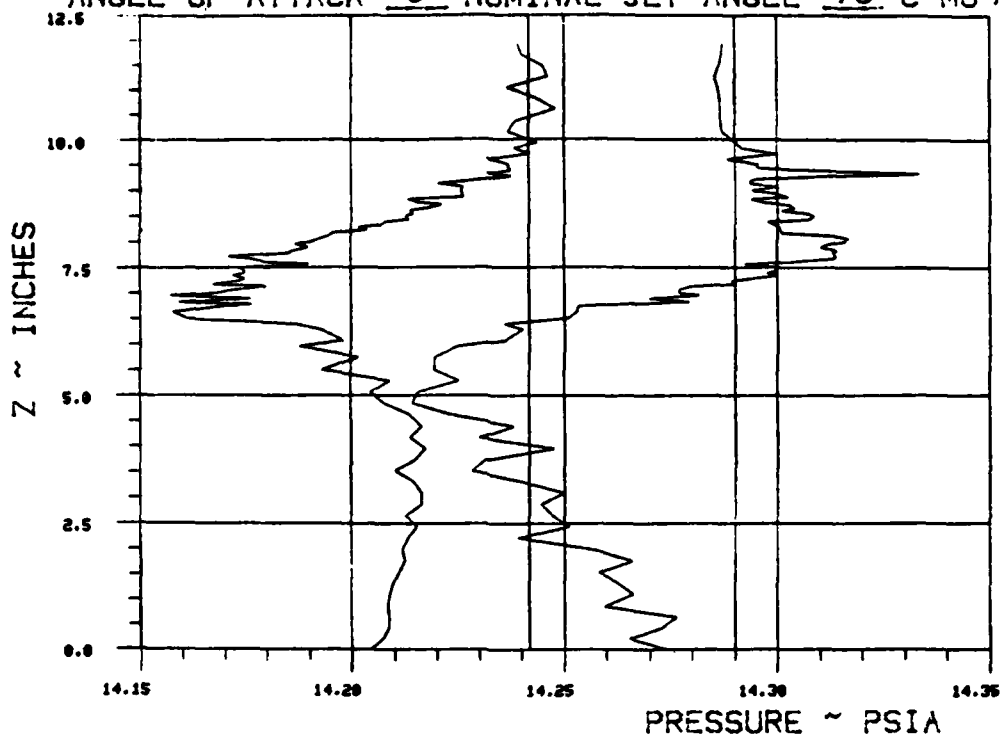
Xss/chord = _.1922_ Yss/chord = _.0267_

BETA = _45.2_
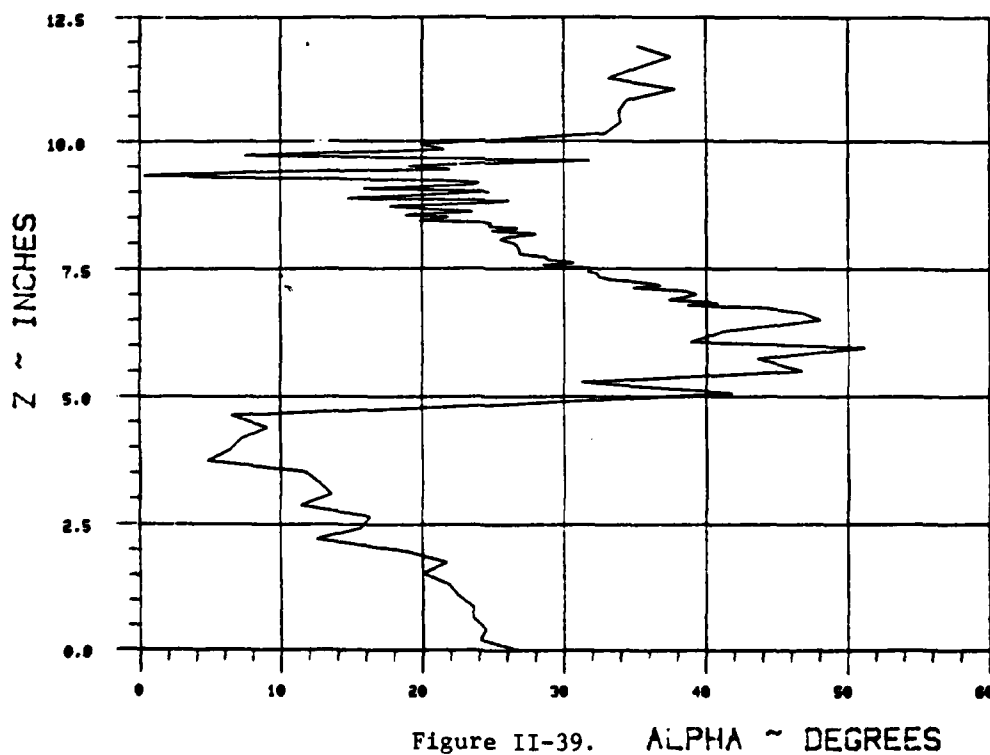
Figure II-39.   ALPHA ~ DEGREES

173

WAKE SURVEY DATA

TEST 272 RUN 56

ANGLE OF ATTACK 0 NOMINAL JET ANGLE 90 C MU 1.9504
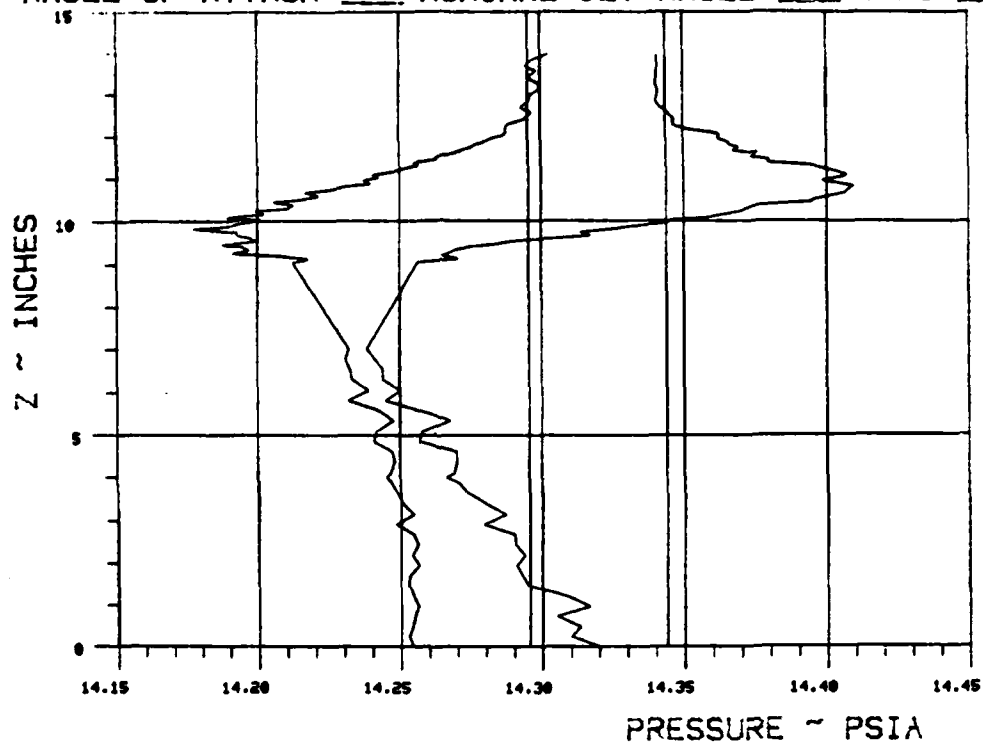
Xss/chord = .1995   Yss/chord = .0444

BETA = 55

Figure II-40.

174
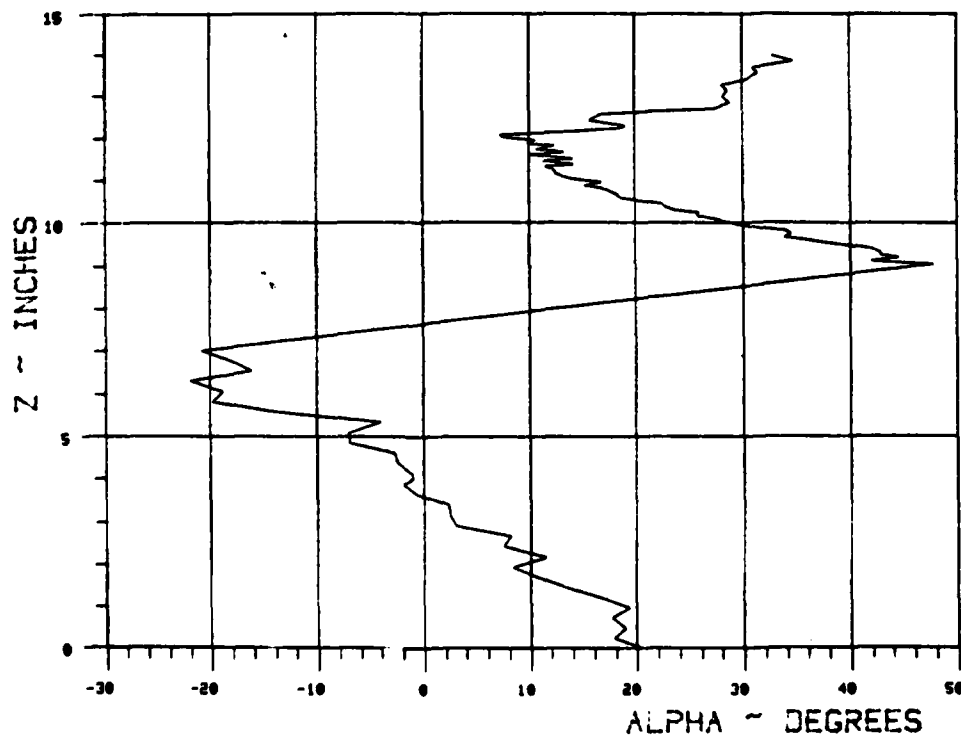
WAKE SURVEY DATA
TEST 272 RUN 48
ANGLE OF ATTACK 0 NOMINAL JET ANGLE 90 C MU 3.9373
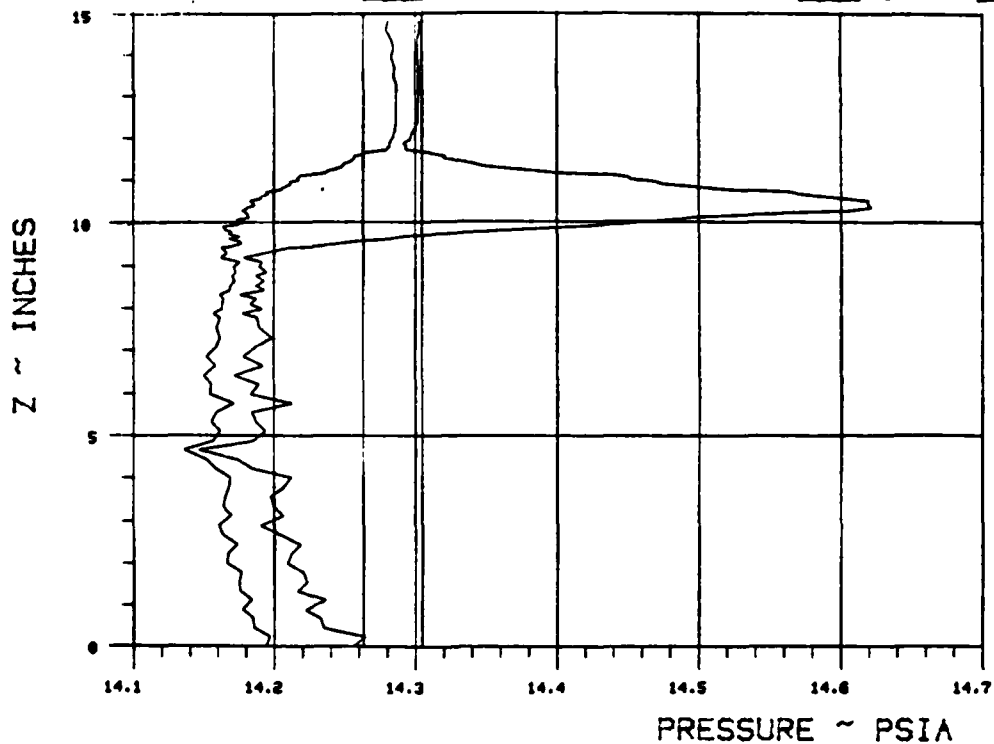
Xss/chord = .191   Yss/chord = .0568

BETA = 45.2
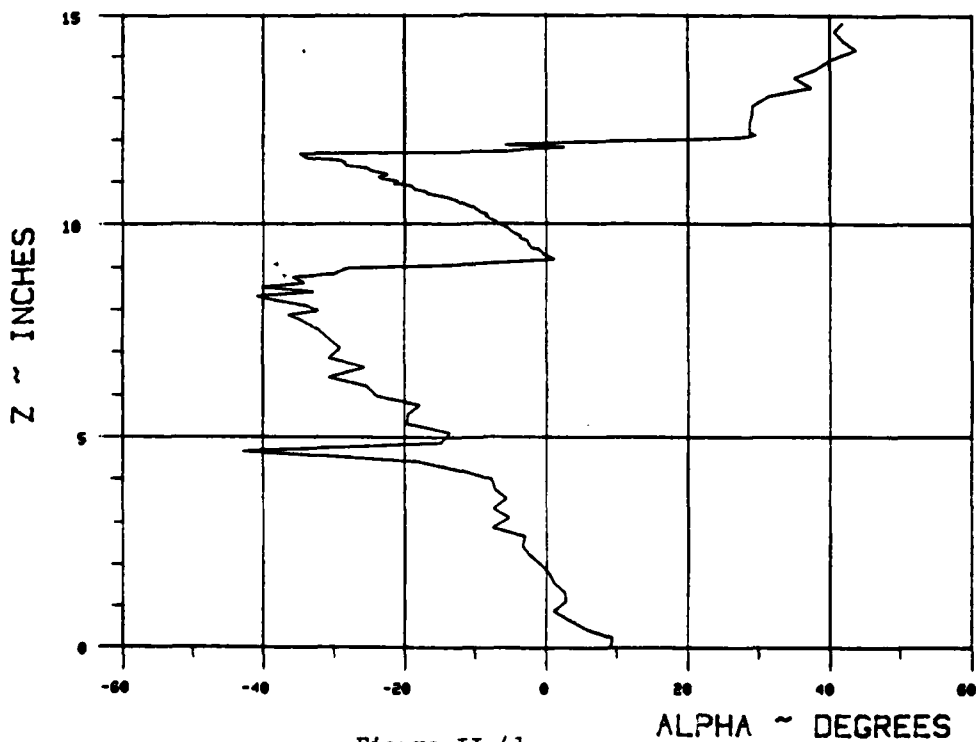
Figure II-41.

WAKE SURVEY DATA

TEST _272_ RUN _49_

ANGLE OF ATTACK _0_ NOMINAL JET ANGLE _90_ C MU _11.4979_
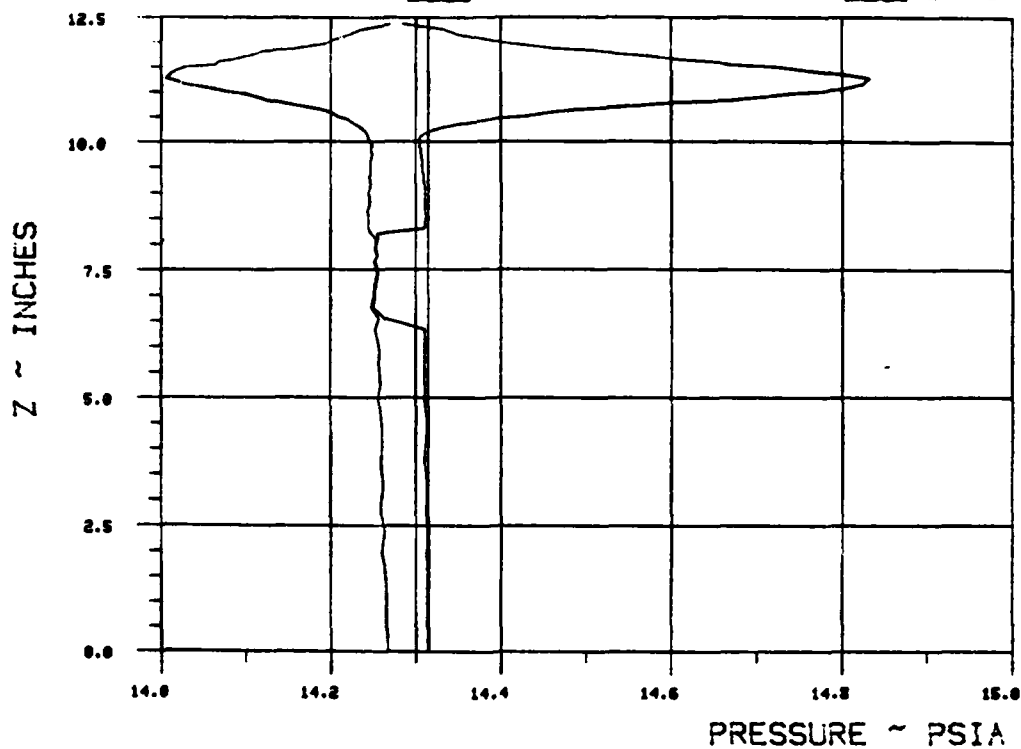
Xss/chord = _.1914_ Yss/chord = _.0573_

BETA = _45.2_
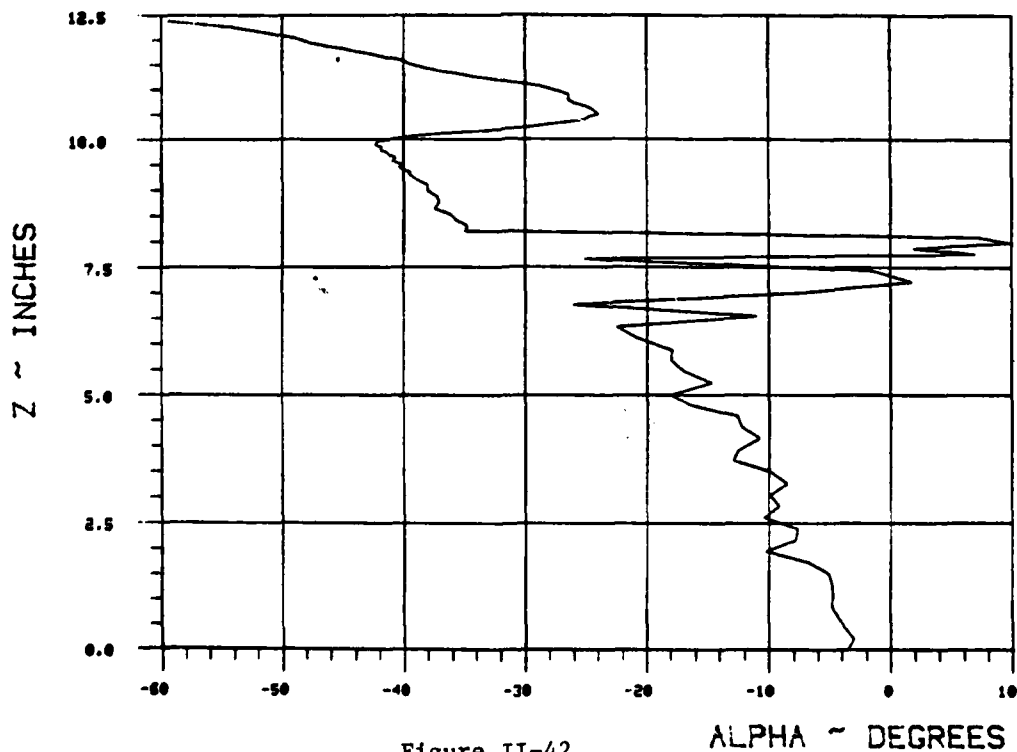
Figure II-42.

WAKE SURVEY DATA

TEST 272 RUN 54

ANGLE OF ATTACK O NOMINAL JET ANGLE 40 C MU 11.803
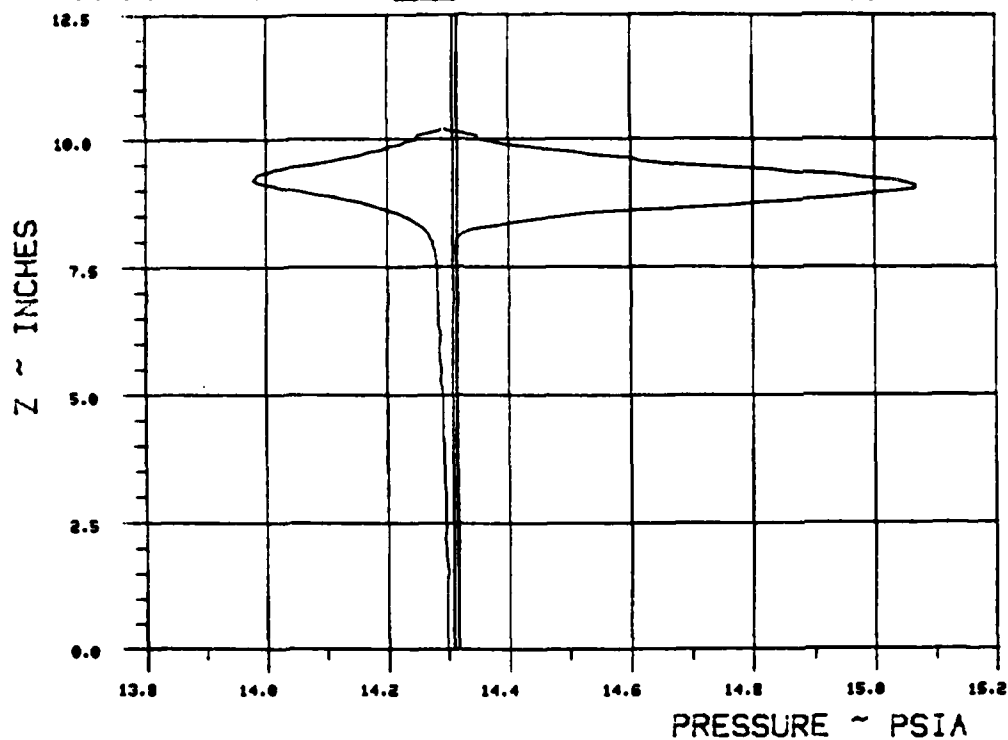
Xse/chord = .1834 Yse/chord = .0335

BETA = 55
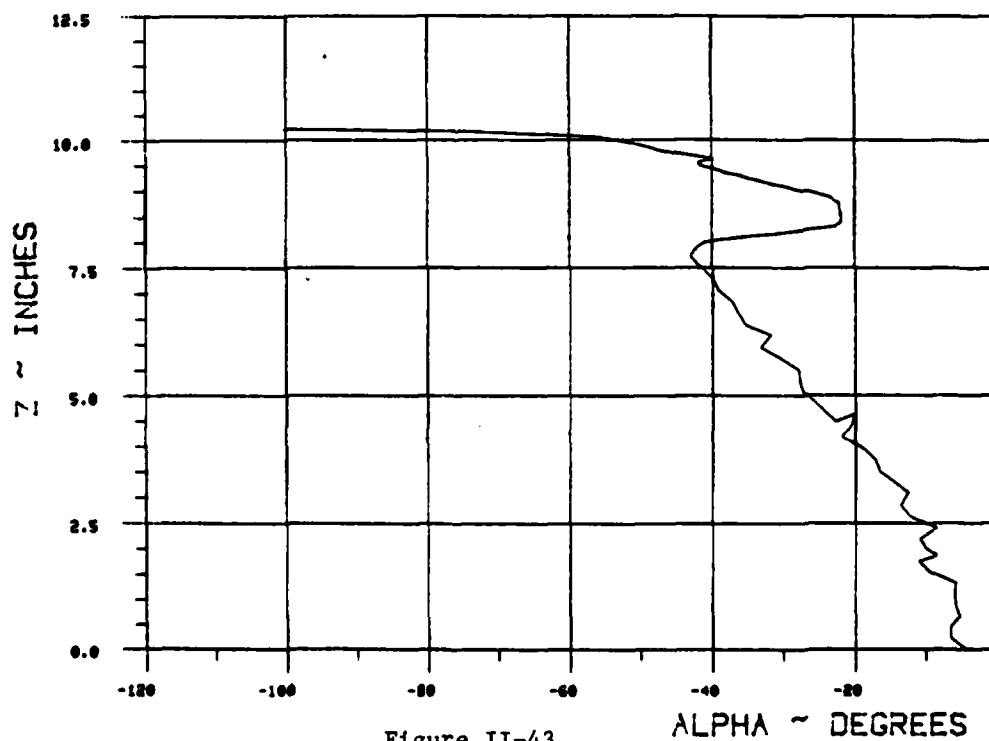
Figure II-43.

WAKE SURVEY DATA
TEST 272 RUN 51
ANGLE OF ATTACK 0 NOMINAL JET ANGLE 90 C MU 15.2237
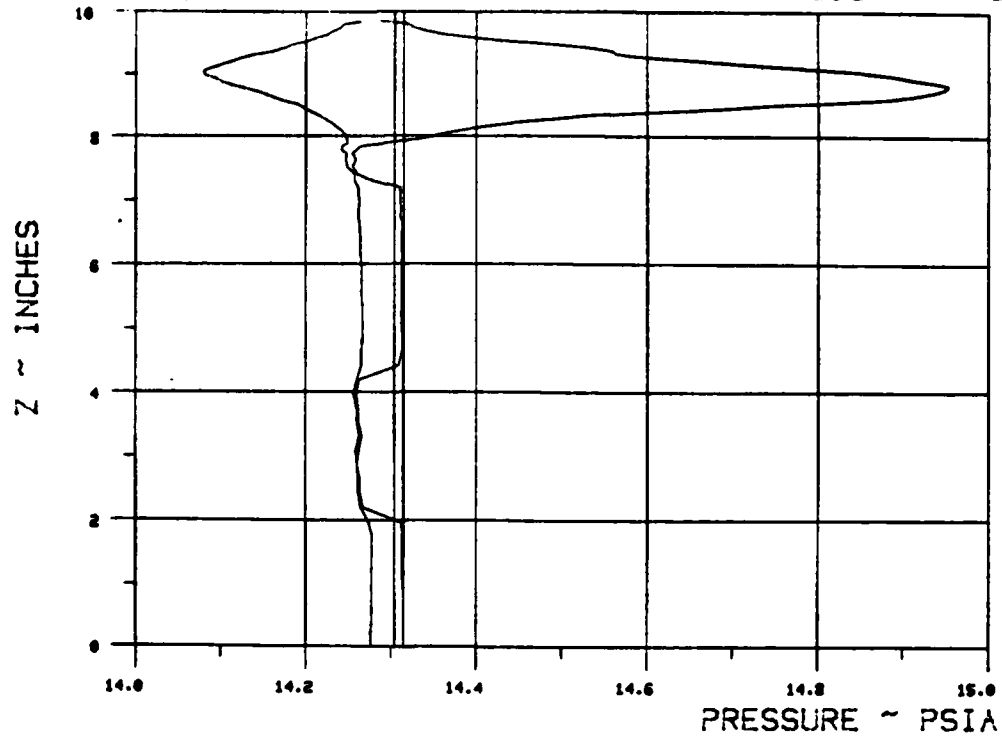
Xss/chord = .1385   Yss/chord = .0017

BETA = 55
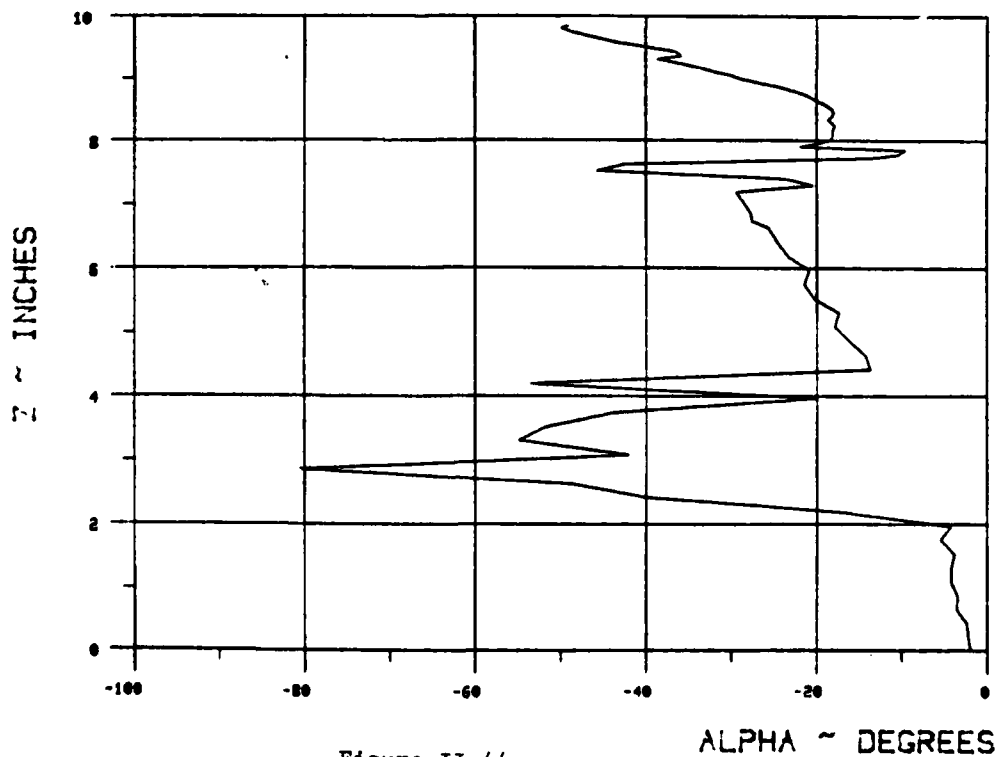
Figure II-44.

WAKE SURVEY DATA
TEST 272 RUN 55
ANGLE OF ATTACK 0 NOMINAL JET ANGLE 90 C MU 15.3477
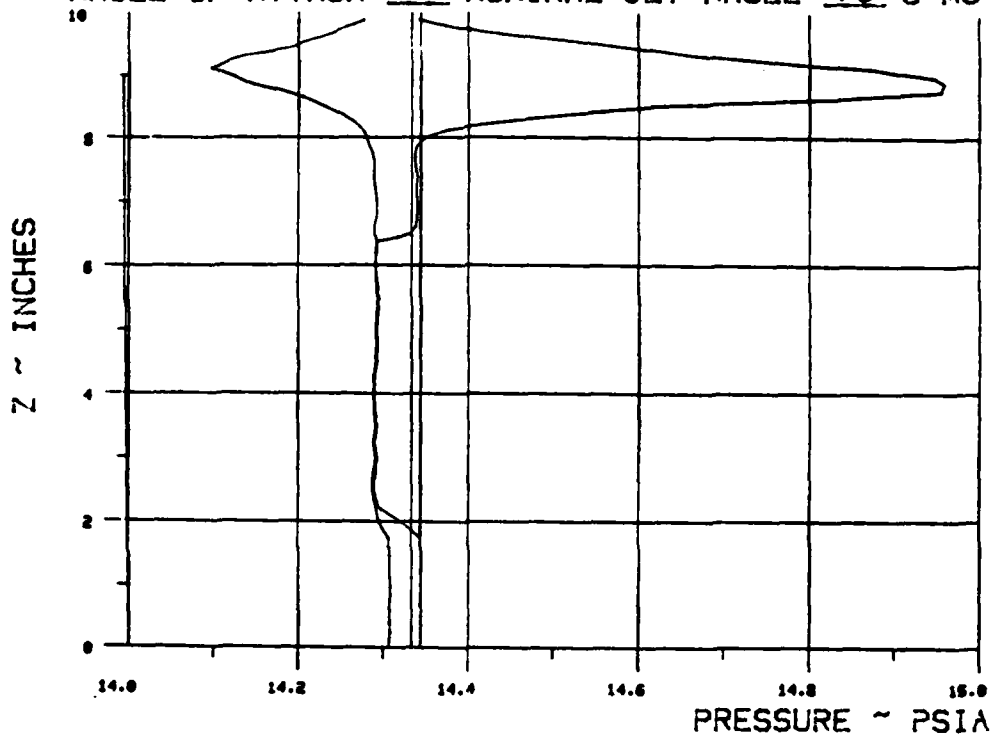
Xss/chord = .138   Yss/chord = .0014

BETA = 55
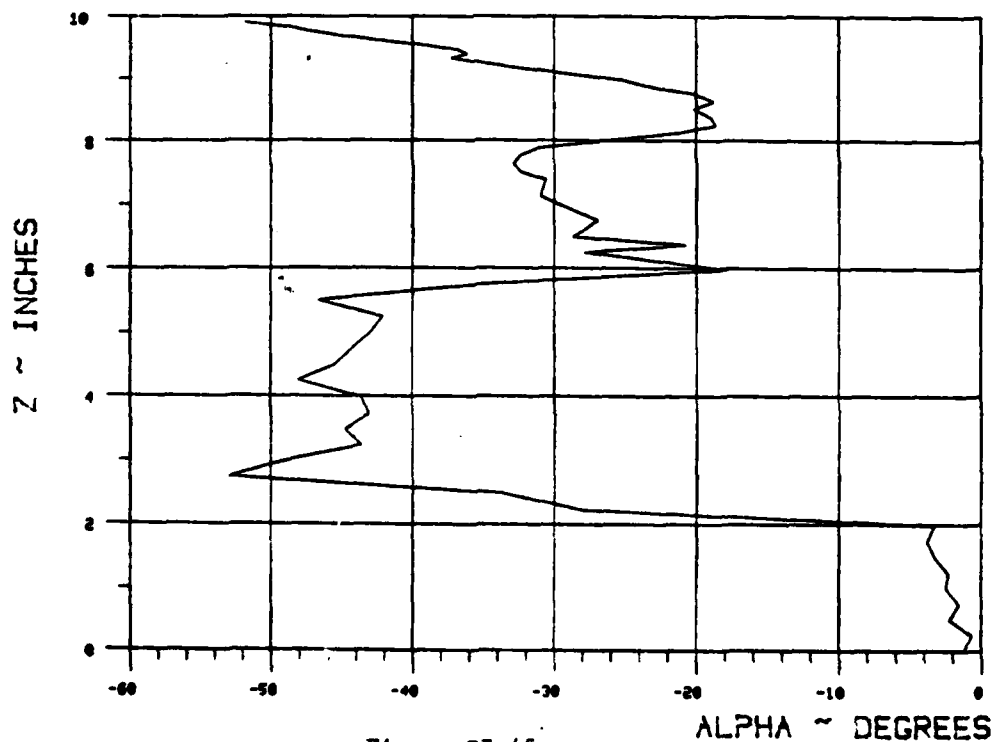
Figure II-45.

WAKE SURVEY DATA

TEST 272 RUN 52

ANGLE OF ATTACK 0 NOMINAL JET ANGLE 90 C MU 25.5336
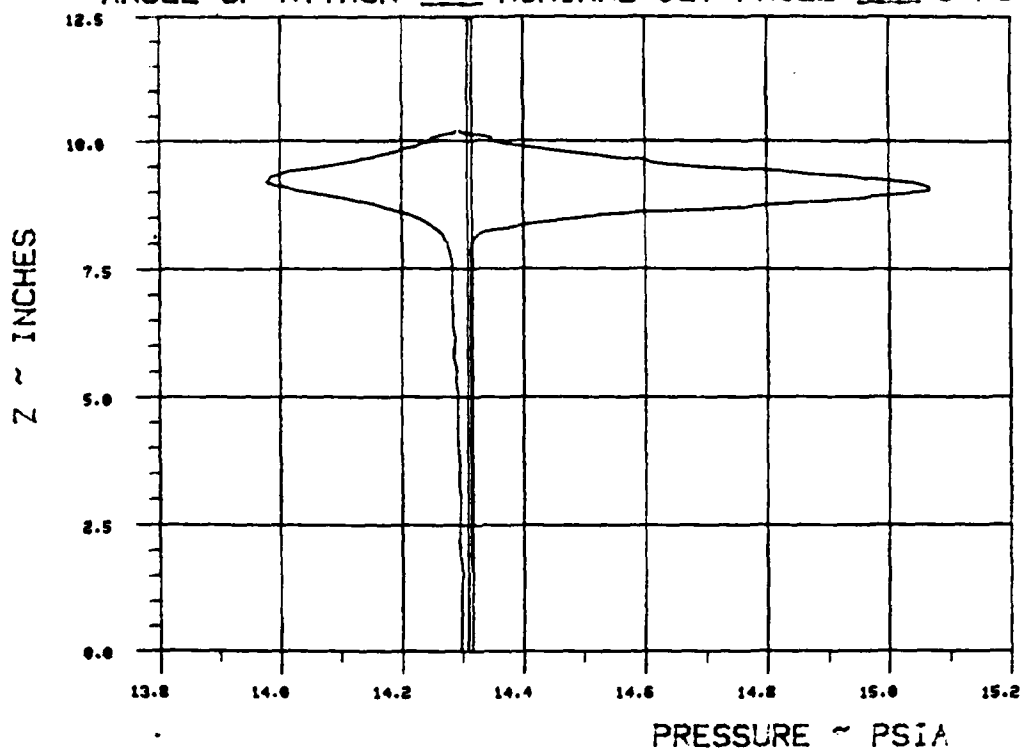
Xss/chord = .1384   Yss/chord = .0016

BETA = 55
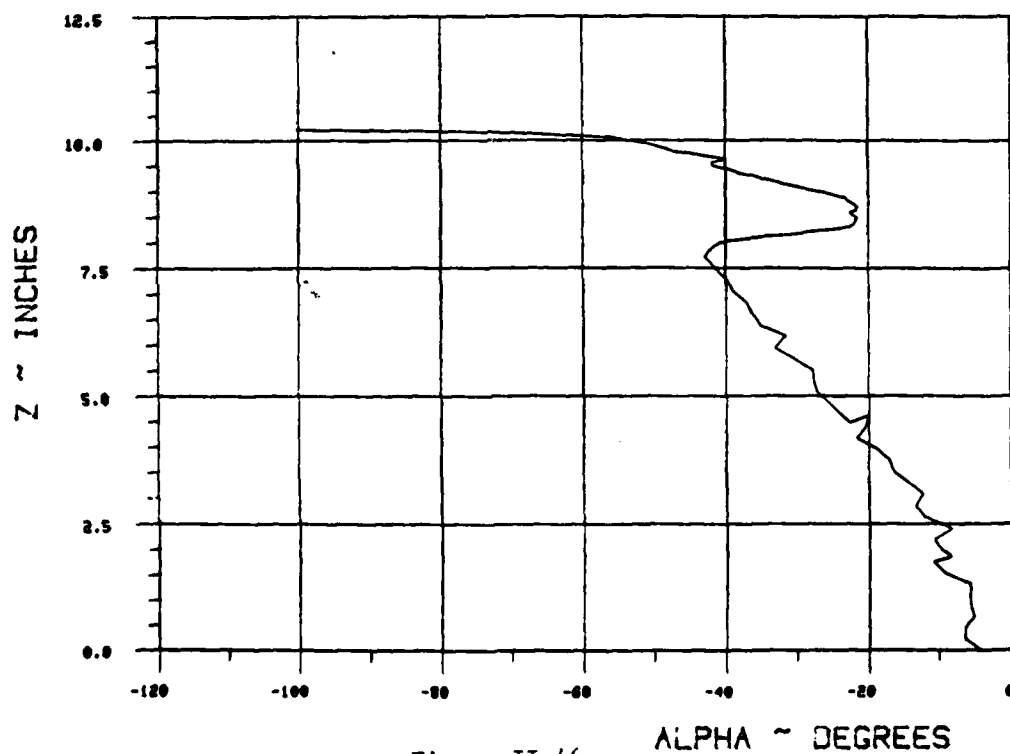
Figure II-46.

APPENDIX III

WAKE SURVEY DATA

WAKE SURVEY DATA

TEST *287* RUN *42*

ANGLE OF ATTACK *0* NOMINAL JET ANGLE *30* C MU *1.0404*
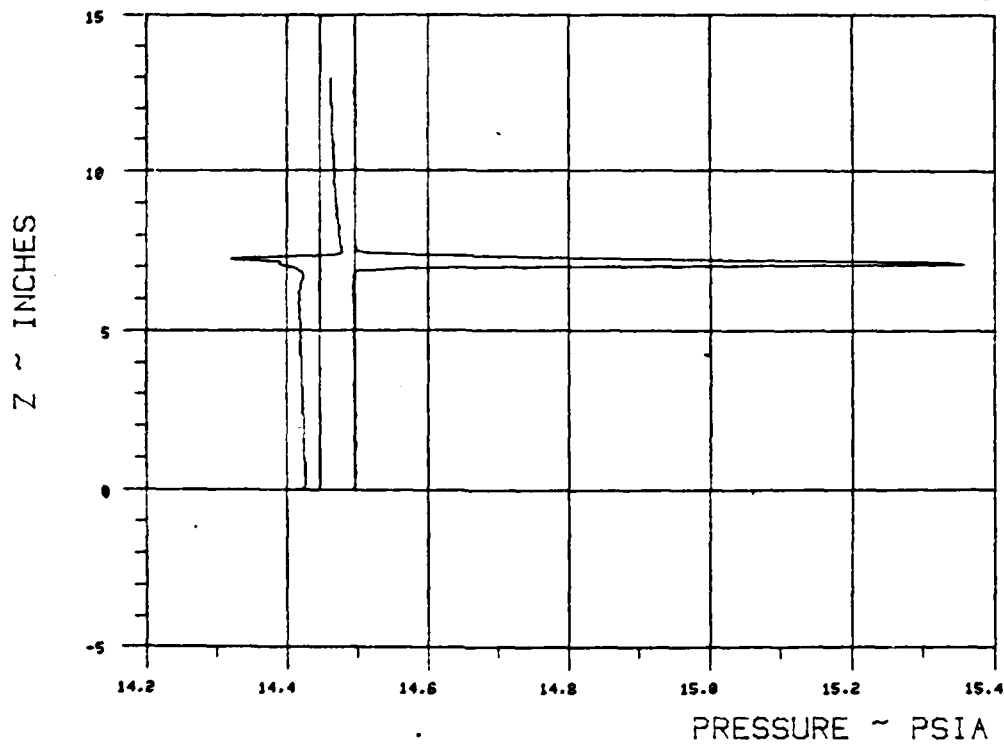
Xss/chord = *.29*   Yss/chord = *.76*
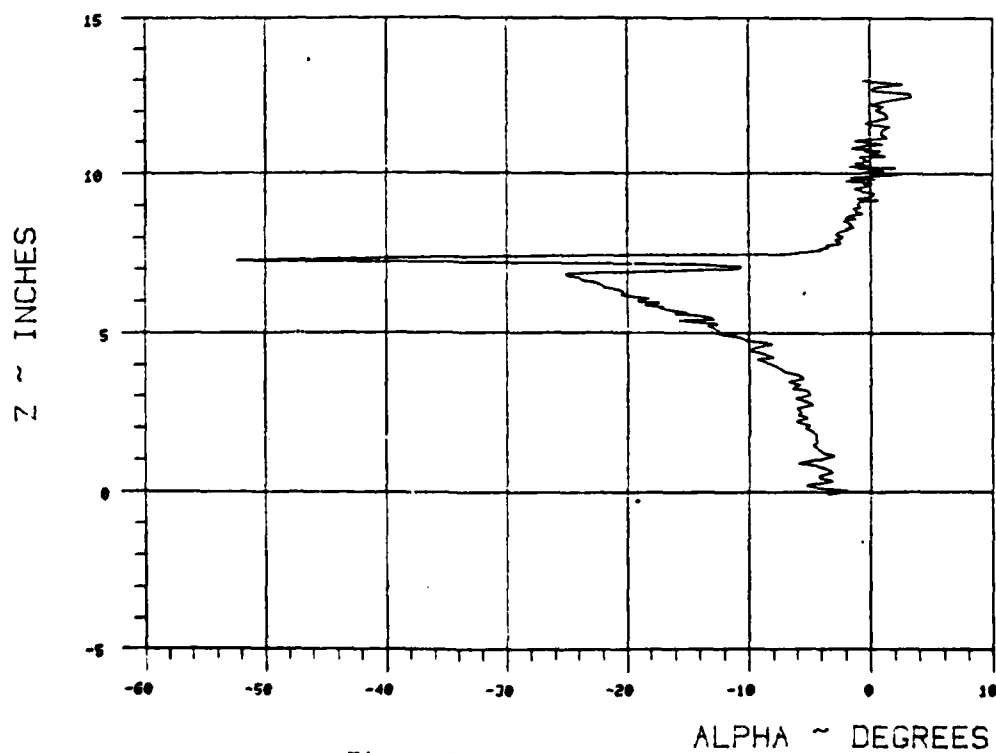
BETA = *10*

Figure III-1.

WAKE SURVEY DATA
TEST _287_ RUN _43_
ANGLE OF ATTACK _0_ NOMINAL JET ANGLE _30_ C MU _1.0286_

PRESSURE ~ PSIA
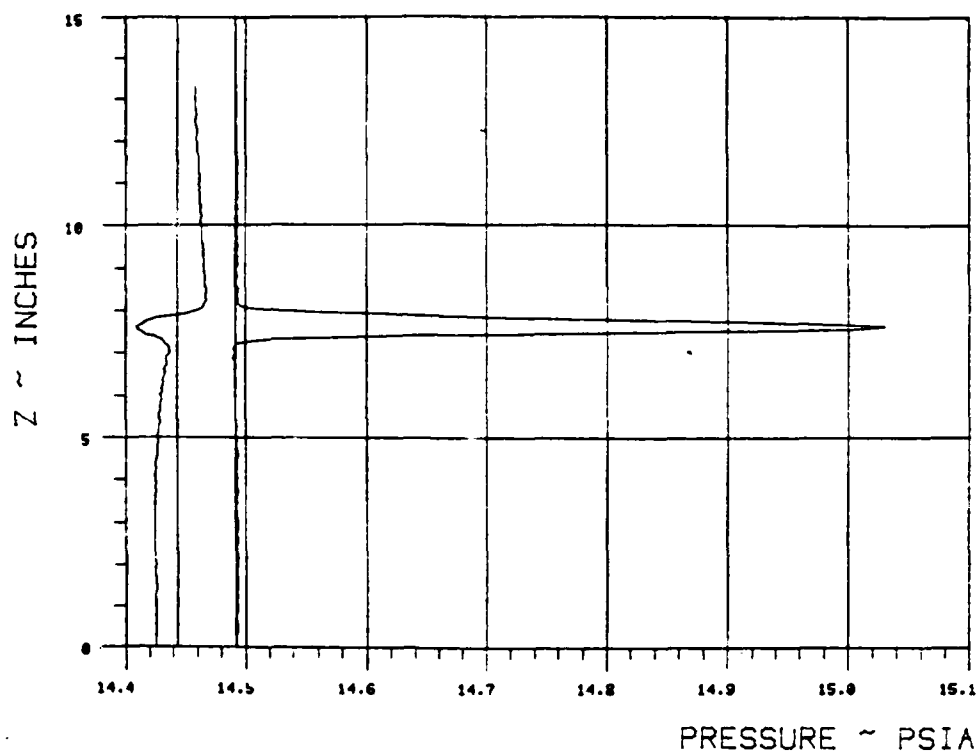
Xss/chord = _.413_   Yss/chord = _.738_

BETA = _10_
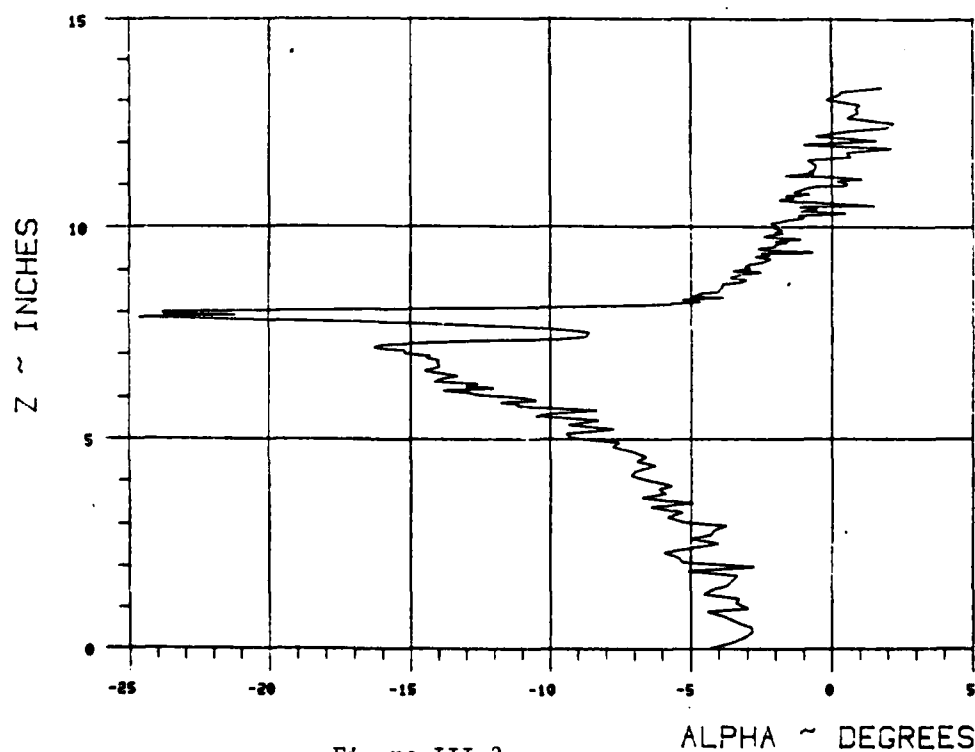
ALPHA ~ DEGREES

Figure III-2.

MICROCOPY RESOLUTION TEST CHART

NATIONAL BUREAU OF STANDARDS 1963-A

WAKE SURVEY DATA

TEST _287_ RUN _44_

ANGLE OF ATTACK _0_ NOMINAL JET ANGLE _30_ C MU _1.0395_

PRESSURE ~ PSIA

Xss/chord = _.536_   Yss/chord = _.717_

BETA = _10_

ALPHA ~ DEGREES

Figure III-3.

184
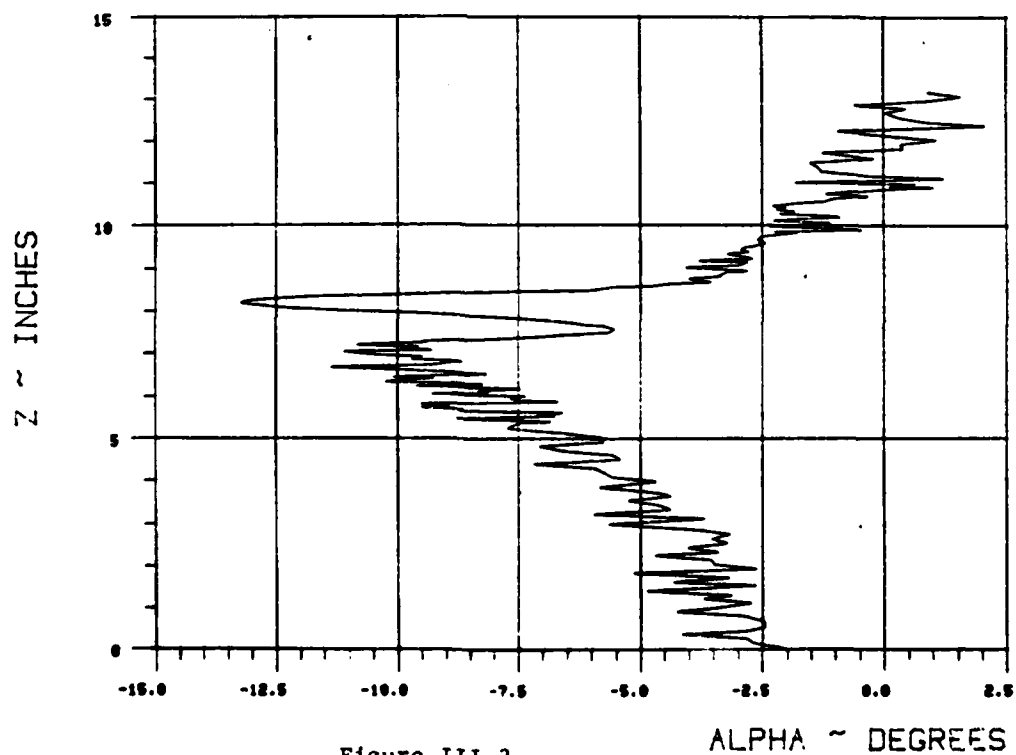
WAKE SURVEY DATA
TEST _287_ RUN _45_
ANGLE OF ATTACK _0_ NOMINAL JET ANGLE _30_ C MU _1.059_
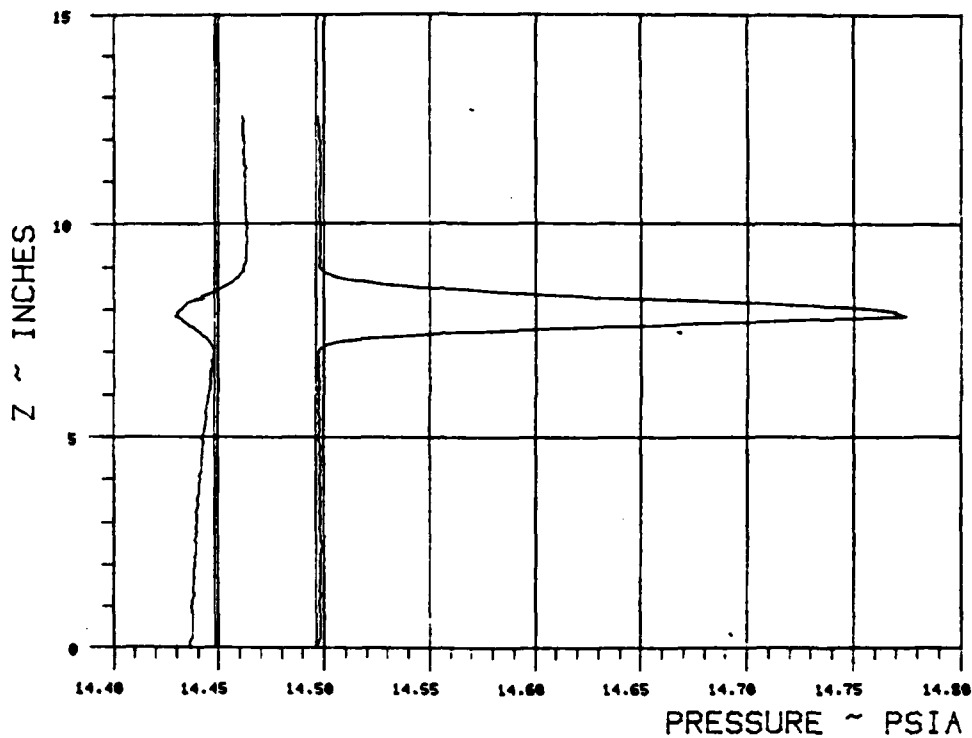
Xss/chord = _.783_ Yss/chord = _.673_
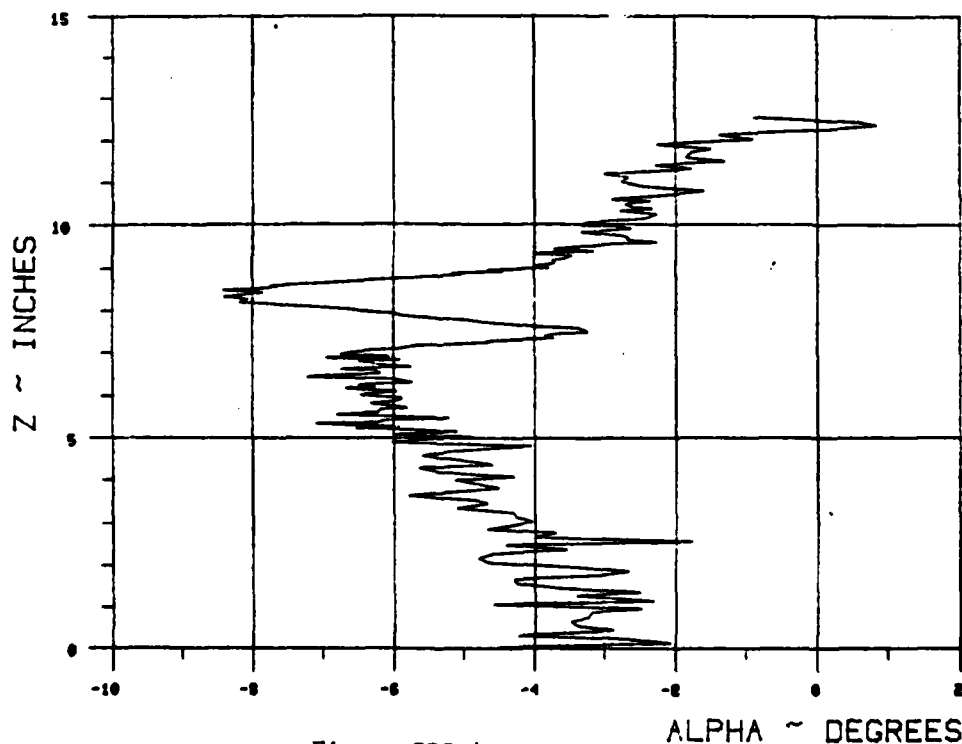
BETA = _10_

Figure III-4.

WAKE SURVEY DATA
TEST _287_ RUN _46_
ANGLE OF ATTACK _0_ NOMINAL JET ANGLE _30_ C MU _1.0268_
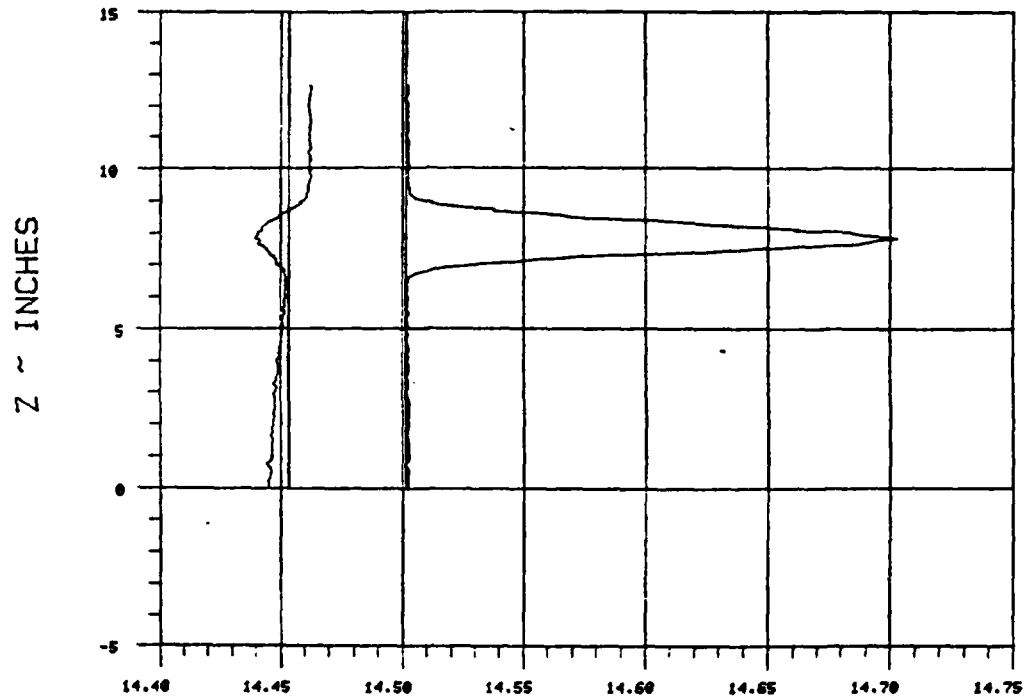
PRESSURE ~ PSIA .

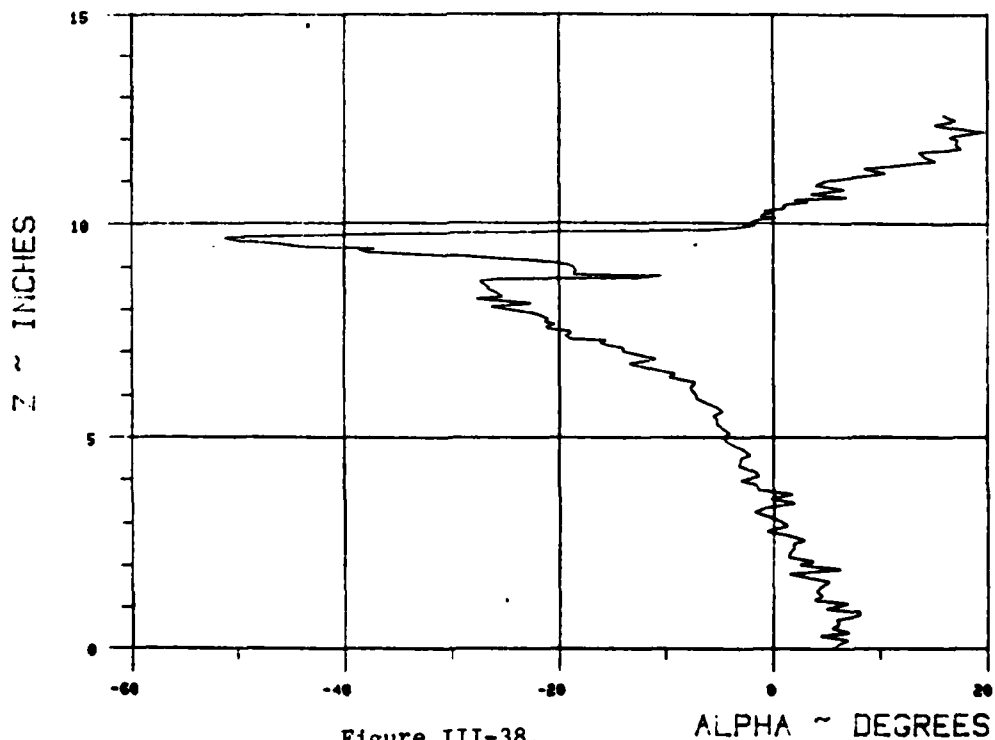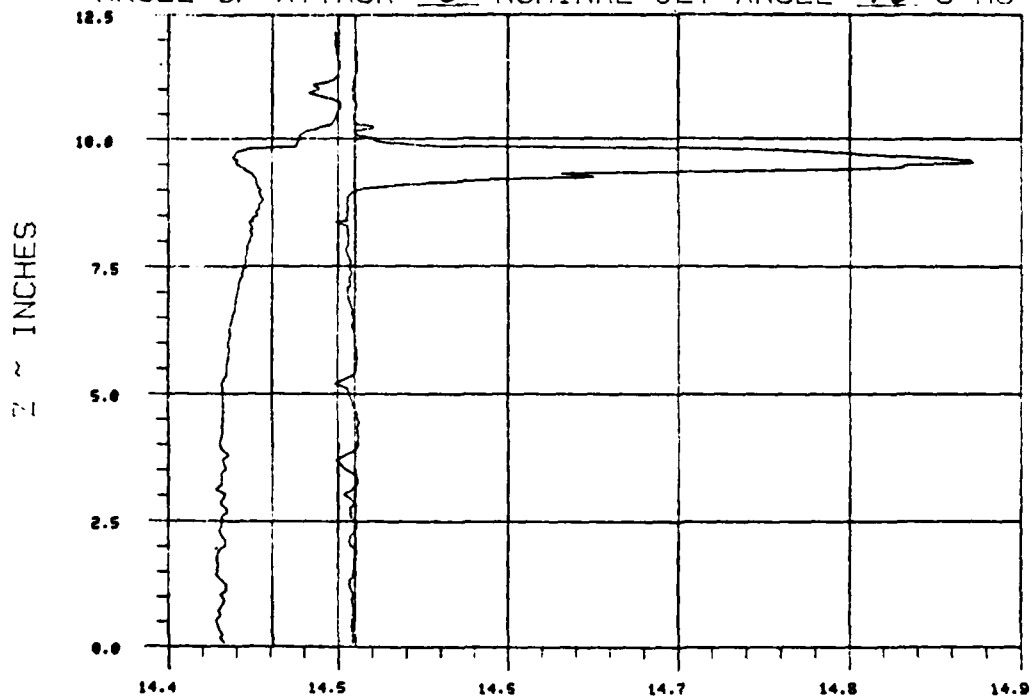Xss/chord = _1.152_   Yss/chord = _.608_
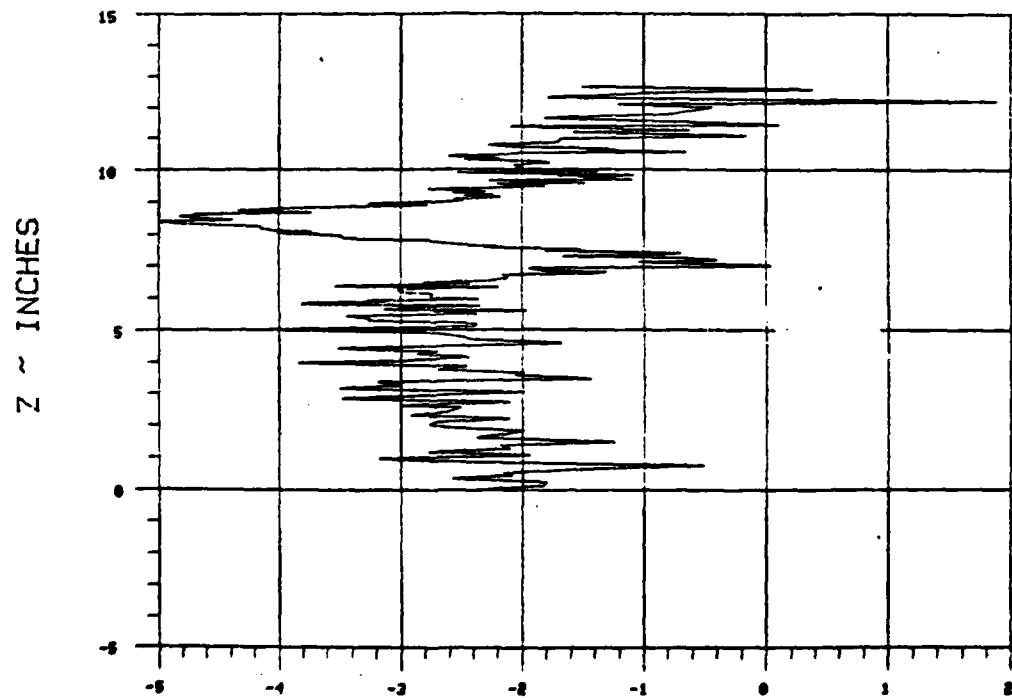
BETA = _10_

ALPHA ~ DEGREES

Figure III-5.

WAKE SURVEY DATA

TEST 287 RUN 47

ANGLE OF ATTACK 0 NOMINAL JET ANGLE 30 C MU 2.098

PRESSURE ~ PSIA

Xss/chord = .29   Yss/chord = .76

BETA = 10

ALPHA ~ DEGREES
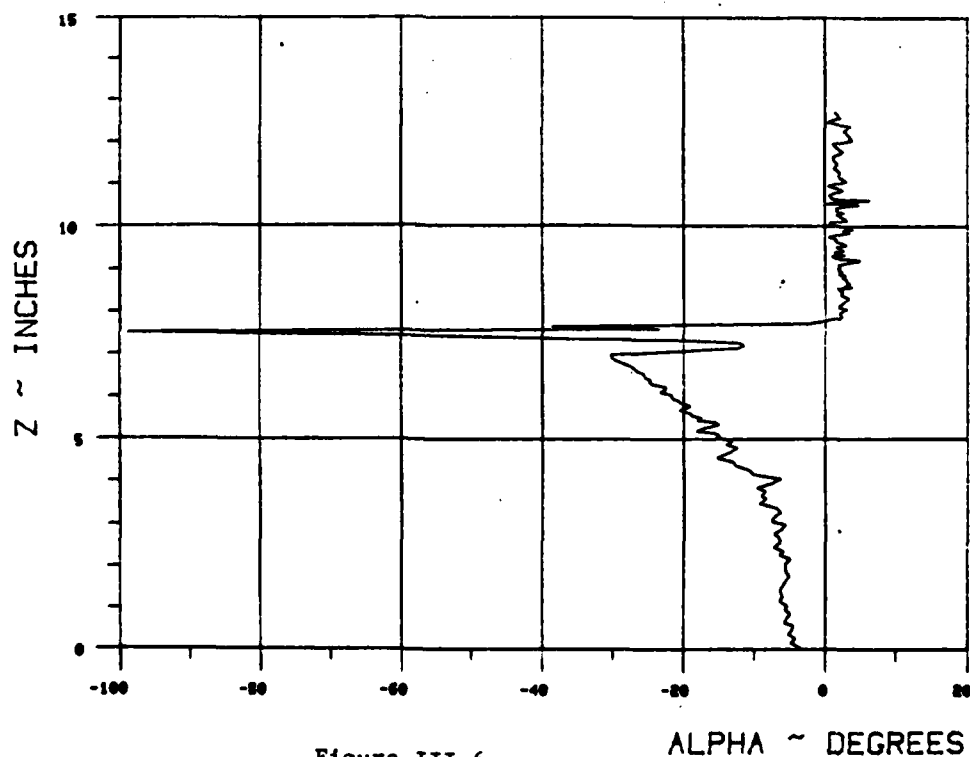
Figure III-6.

WAKE SURVEY DATA

TEST _287_ RUN _48_

ANGLE OF ATTACK _0_ NOMINAL JET ANGLE _30_ C MU _2.0862_
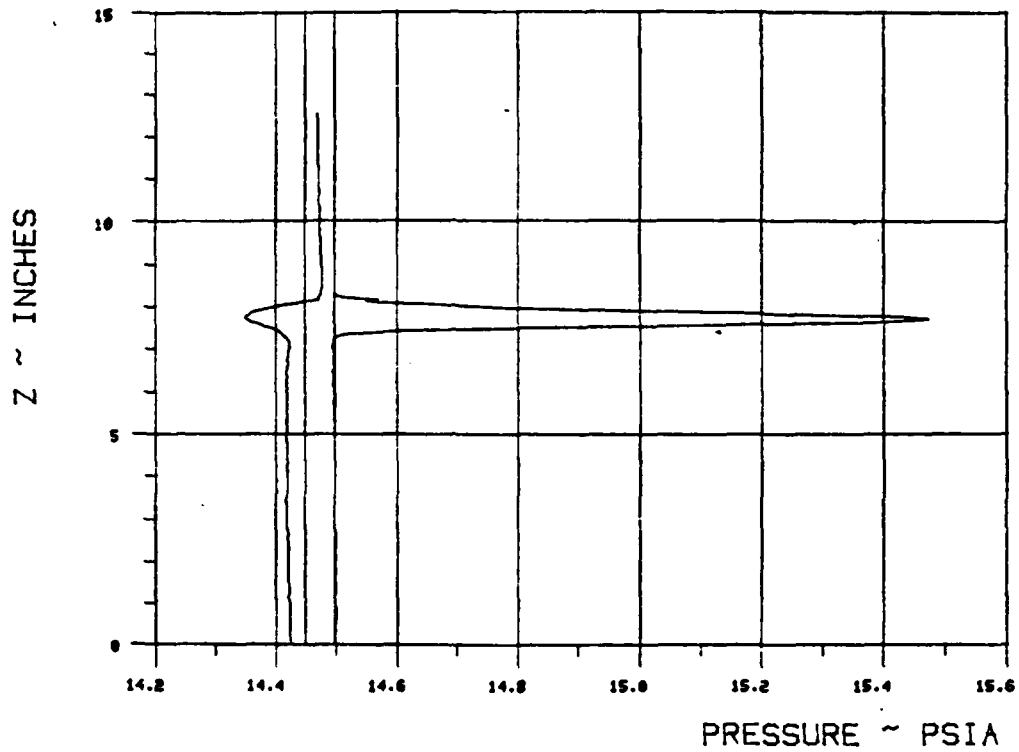
Xse/chord = _.413_   Yse/chord = _.738_

BETA = _10_

Figure III-7.

188
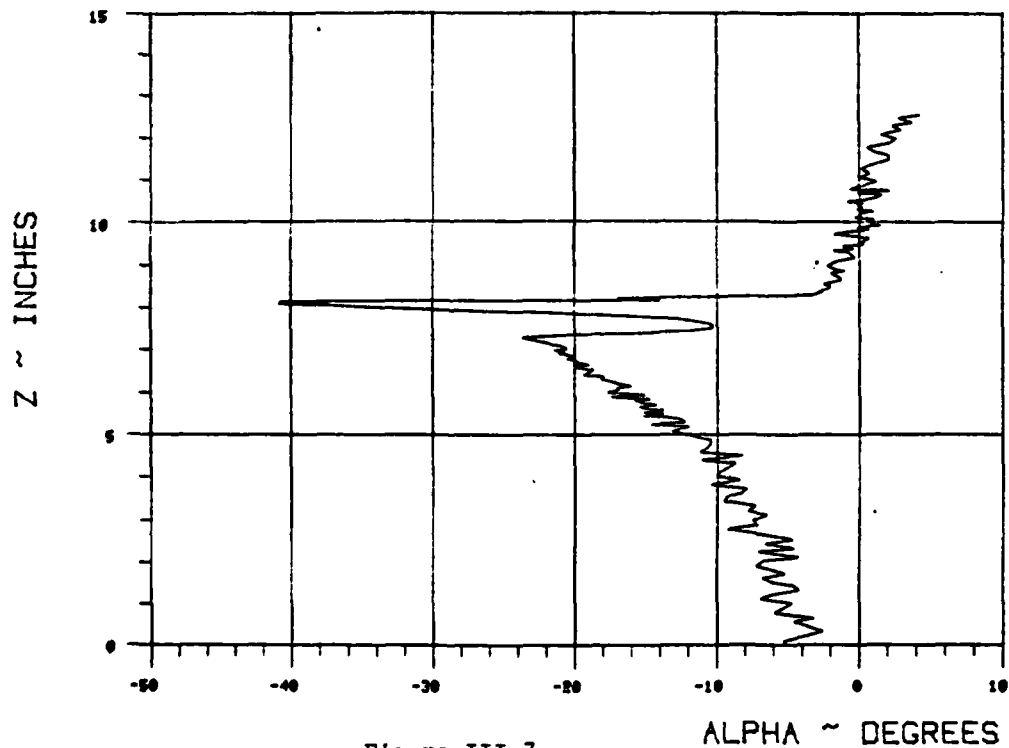
WAKE SURVEY DATA

TEST *287* RUN *49*

ANGLE OF ATTACK *0* NOMINAL JET ANGLE *30* C MU *2.0959*

Xss/chord = *.536*   Yss/chord = *.717*

BETA = *10*

Figure III-8.

189

WAKE SURVEY DATA

TEST _287_ RUN _50_

ANGLE OF ATTACK _0_ NOMINAL JET ANGLE _30_ C MU _2.0595_

PRESSURE ~ PSIA

Xss/chord = _.783_   Yss/chord = _.673_

BETA = _10_

ALPHA ~ DEGREES
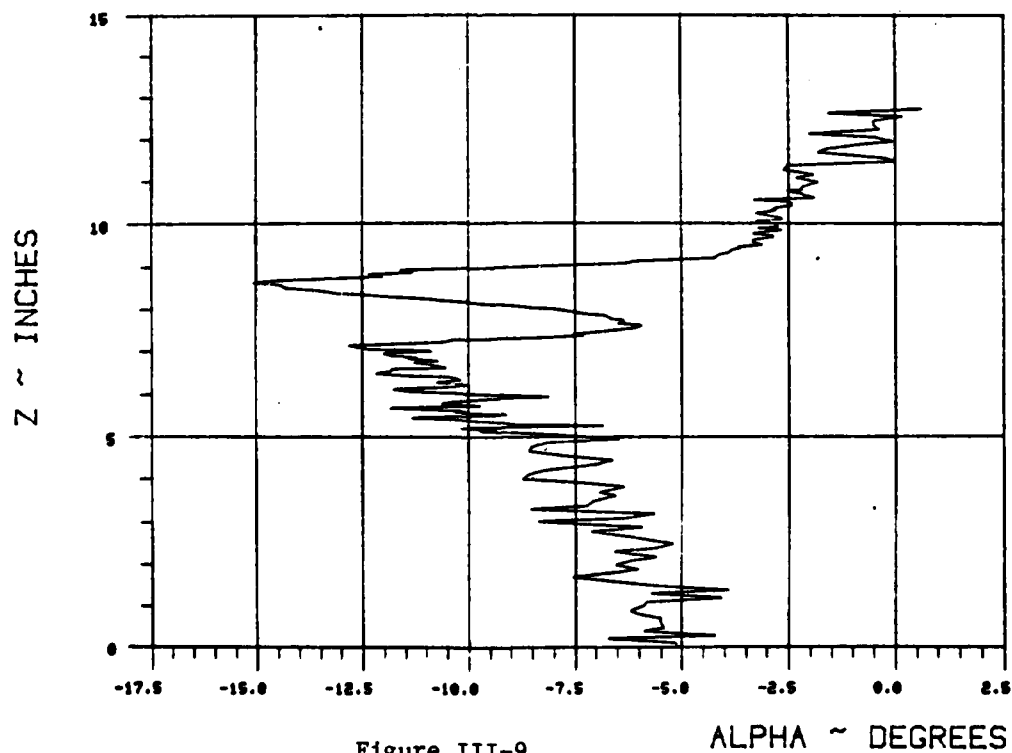
Figure III-9.

WAKE SURVEY DATA
TEST _287_ RUN _51_
ANGLE OF ATTACK _0_ NOMINAL JET ANGLE _30_ C MU _2.0646_

PRESSURE ~ PSIA

Xss/chord = _1.152_   Yss/chord = _.608_

BETA = _10_

ALPHA ~ DEGREES

Figure III-10.

191
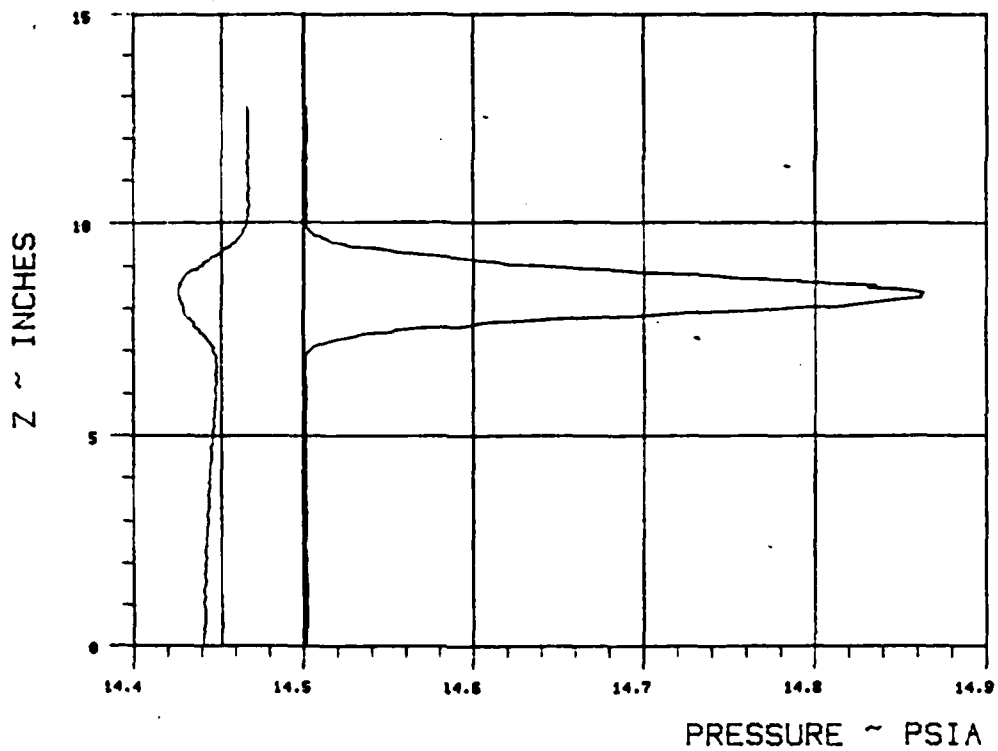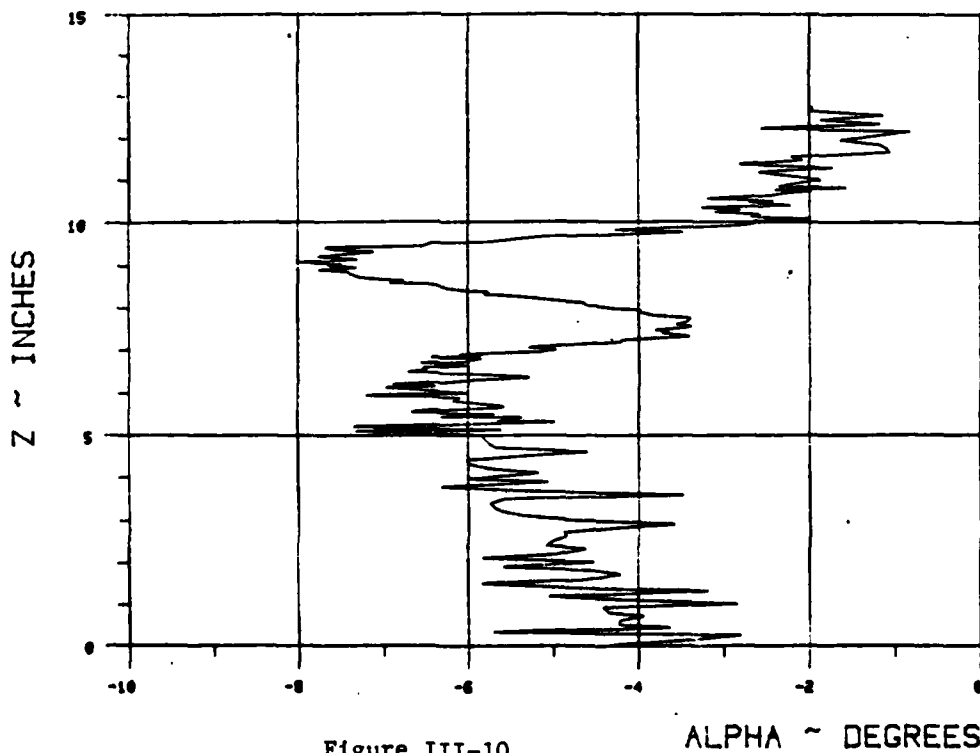
WAKE SURVEY DATA

TEST _287_ RUN _52_

ANGLE OF ATTACK _0_ NOMINAL JET ANGLE _30_ C MU _4.1134_
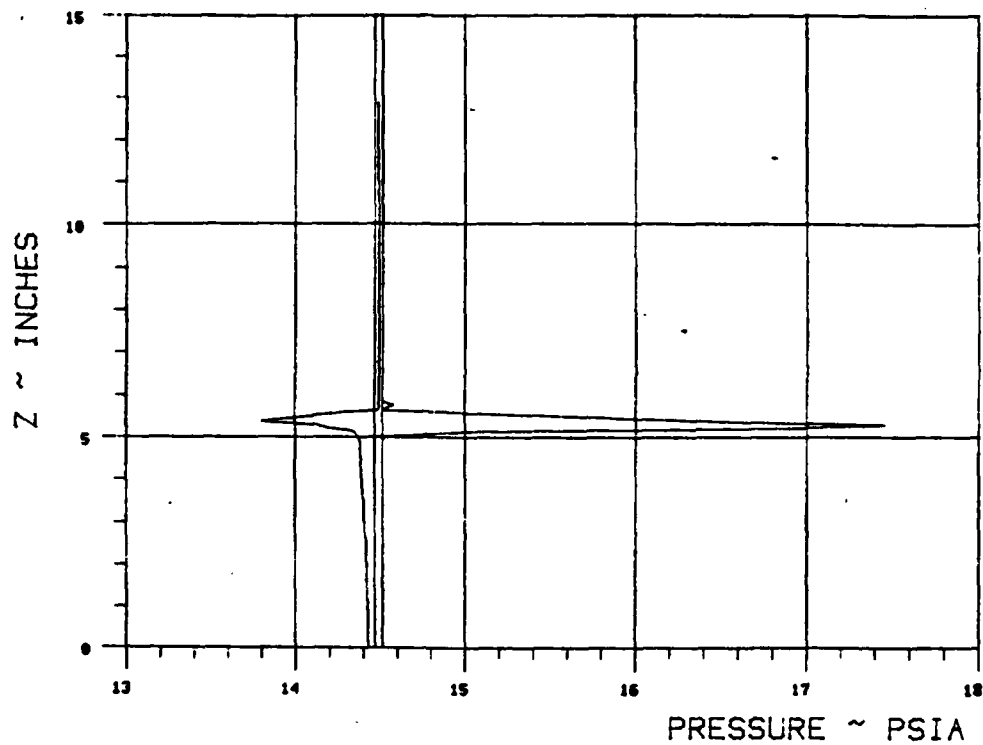
Xss/chord = _.247_ Yss/chord = _.514_

BETA = _10_

Figure III-11.

192
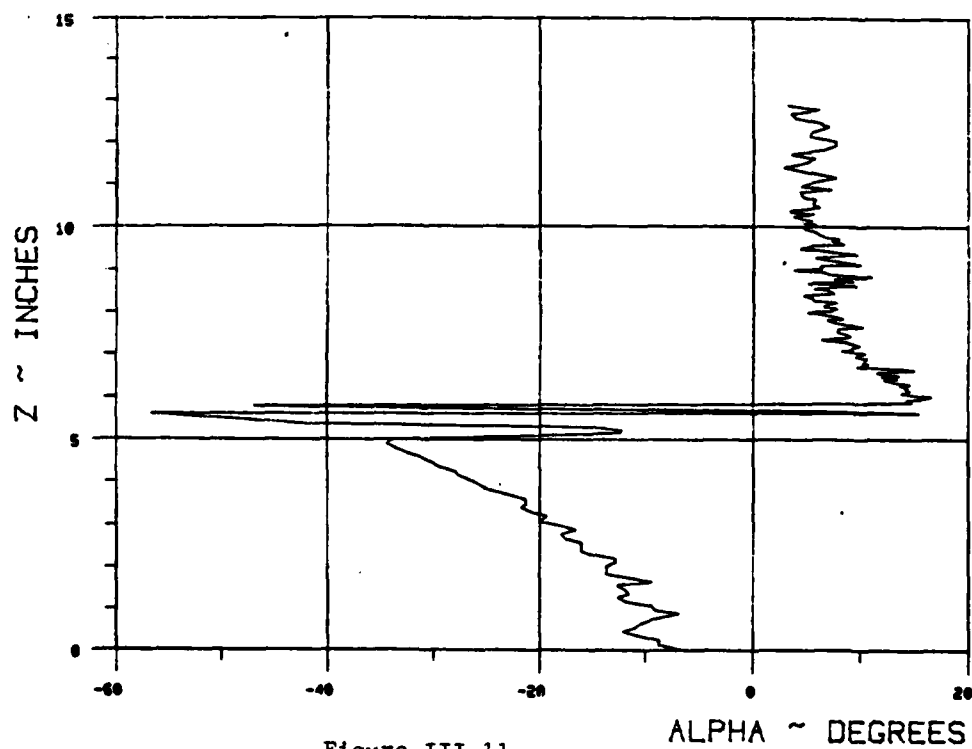
WAKE SURVEY DATA
TEST _287_ RUN _53_
ANGLE OF ATTACK _0_ NOMINAL JET ANGLE _30_ C MU _4.1205_
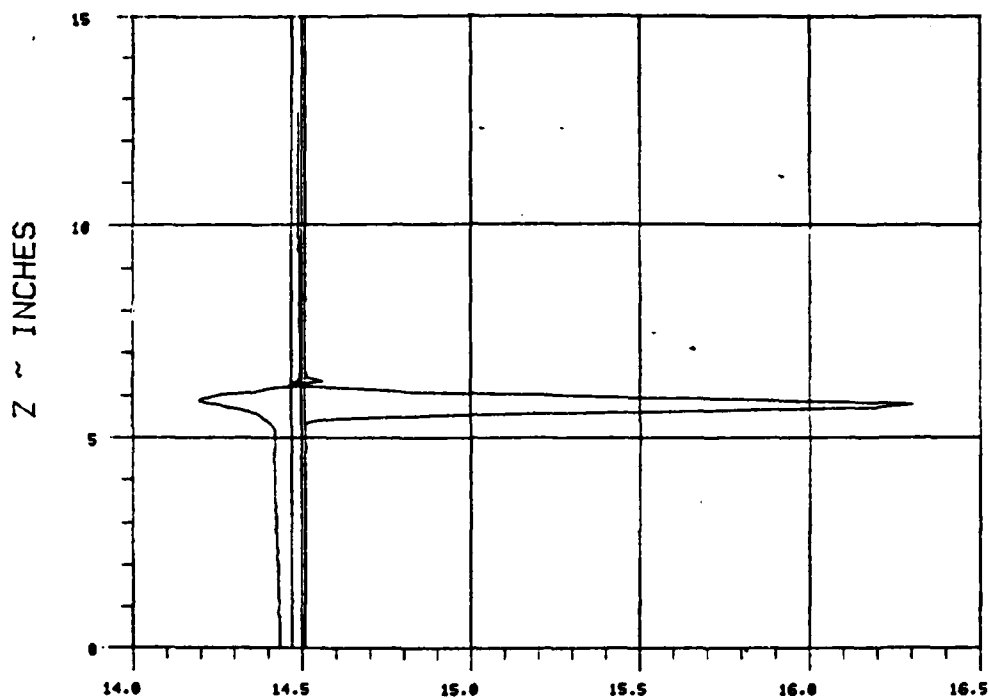
PRESSURE ~ PSIA

Xss/chord = _.37_   Yss/chord = _.492_

BETA = _10_
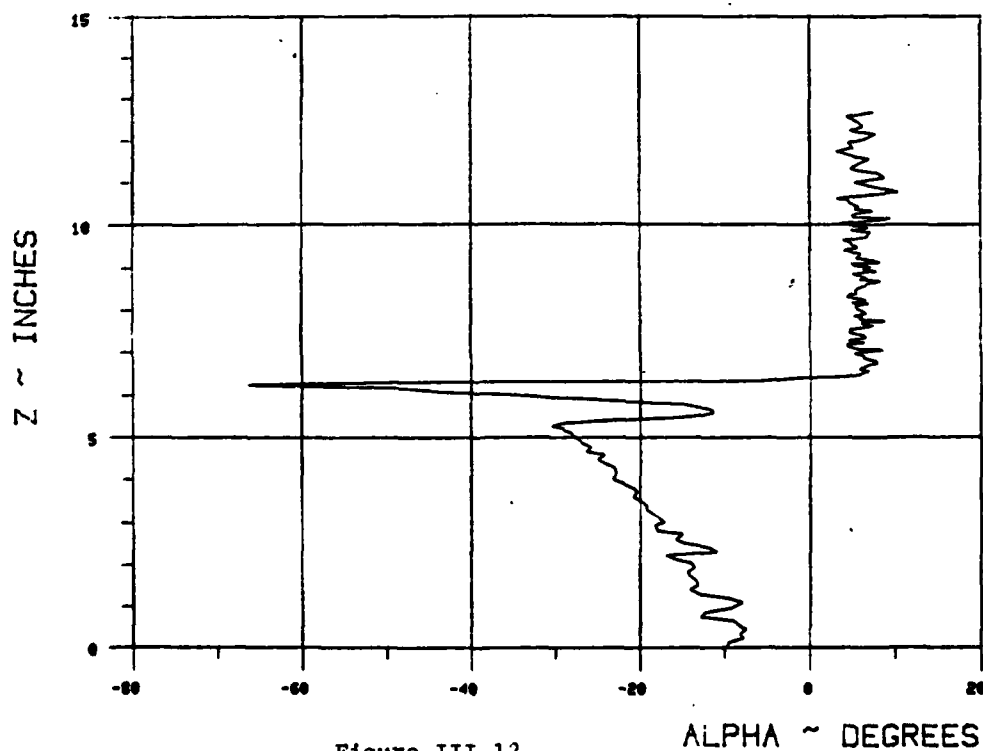
ALPHA ~ DEGREES

Figure III-12.

WAKE SURVEY DATA
TEST _287_ RUN _54_
ANGLE OF ATTACK _0_ NOMINAL JET ANGLE _30_ C MU _4.1363_

PRESSURE ~ PSIA

Xes/chord = _.493_   Yes/chord = _.47_

BETA = _10_

ALPHA ~ DEGREES

Figure III-13.

194
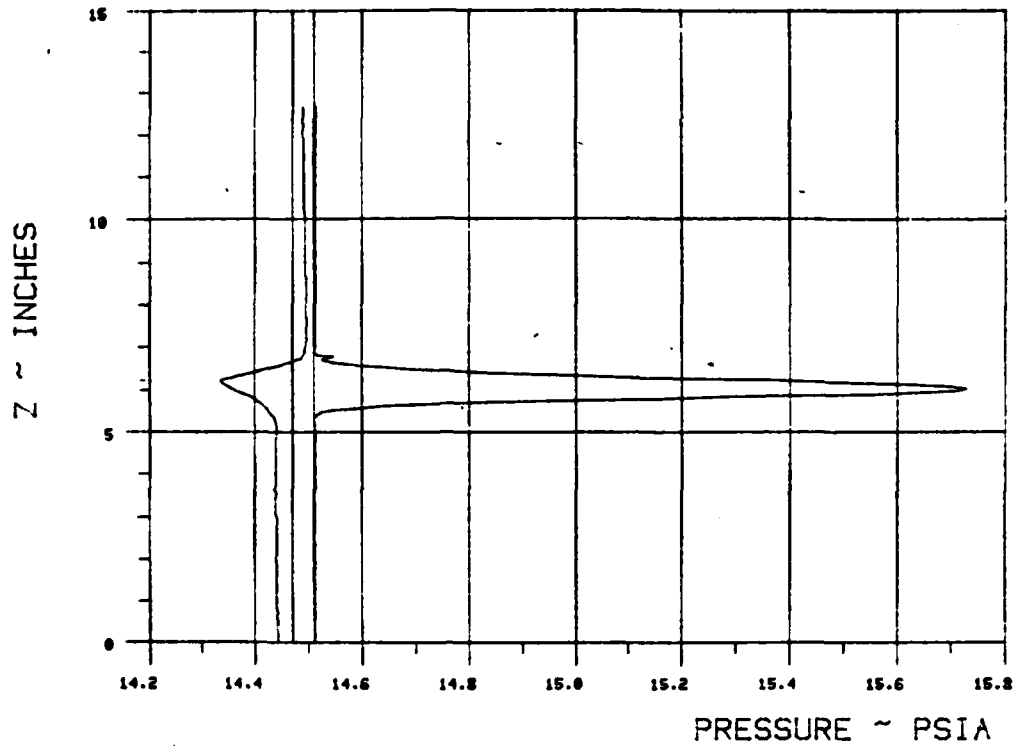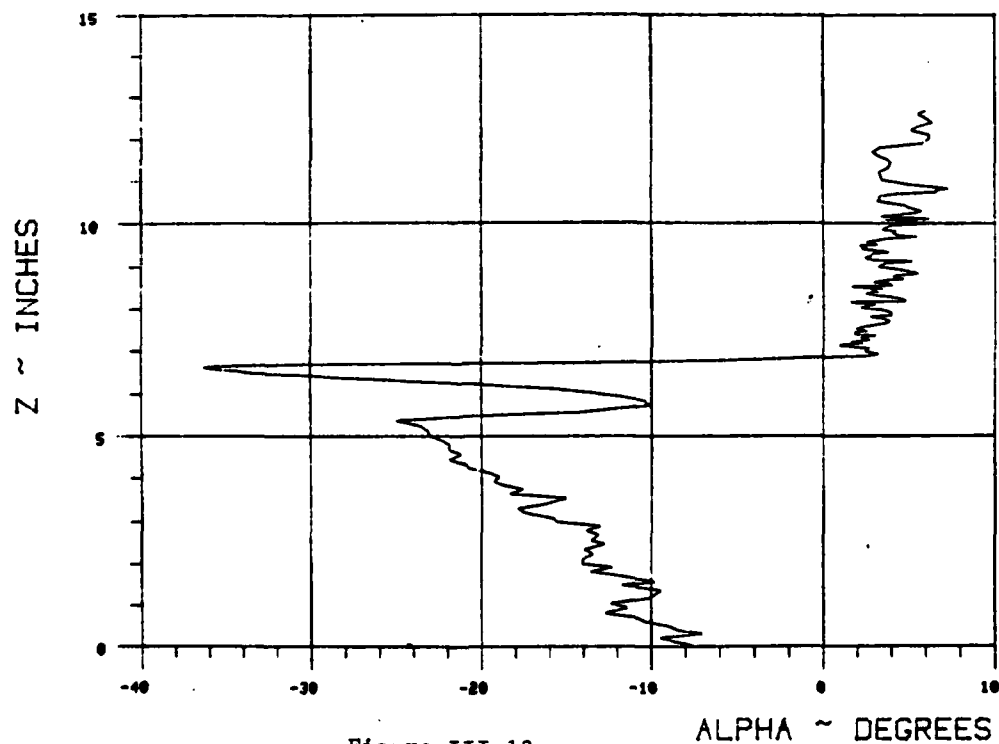
WAKE SURVEY DATA

TEST _287_ RUN _55_

ANGLE OF ATTACK _0_ NOMINAL JET ANGLE _30_ C MU _4.1113_

PRESSURE ~ PSIA

Xss/chord = _.739_ Yss/chord = _.427_

BETA = _10_

ALPHA ~ DEGREES

Figure III-14.

195
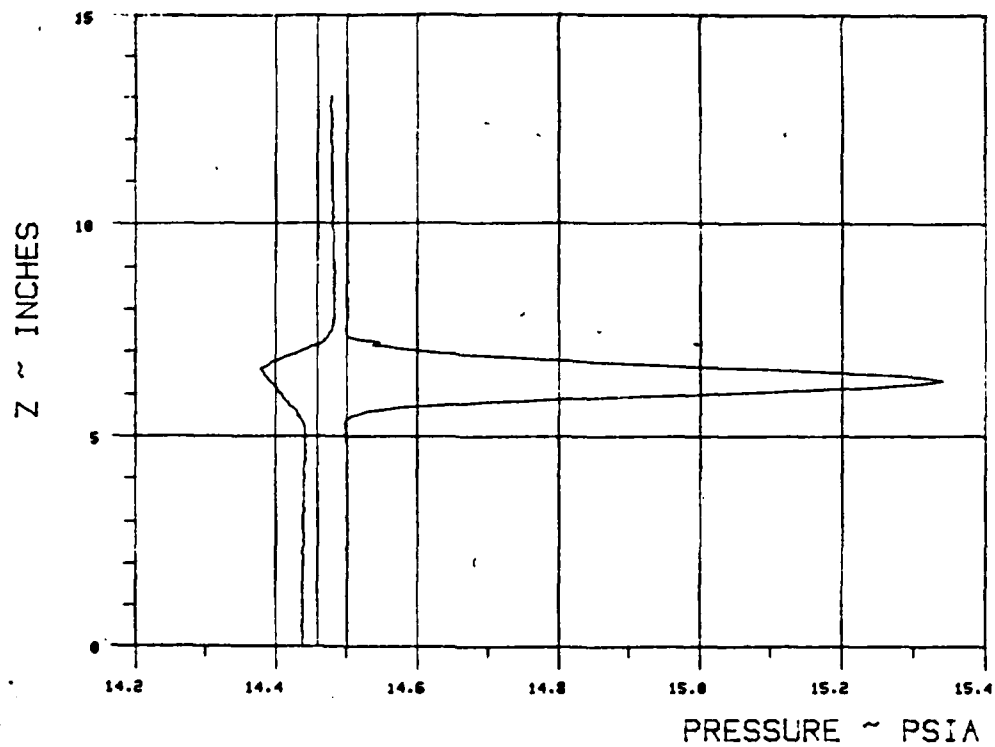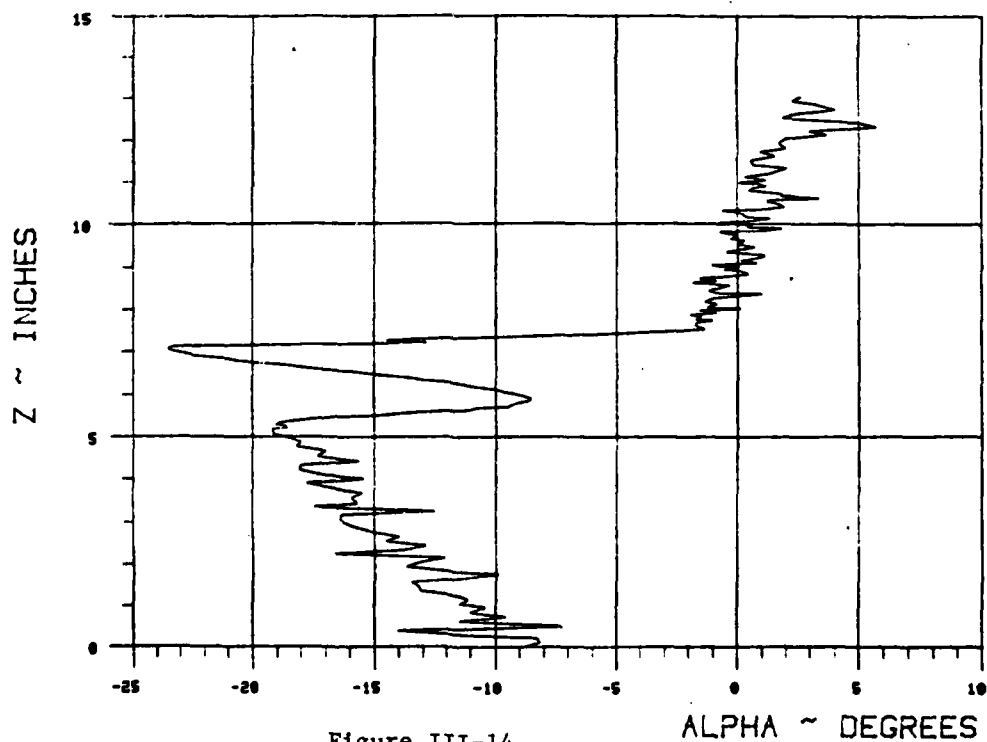
WAKE SURVEY DATA

TEST _287_ RUN _56_

ANGLE OF ATTACK _0_ NOMINAL JET ANGLE _30_ C MU _4.102_
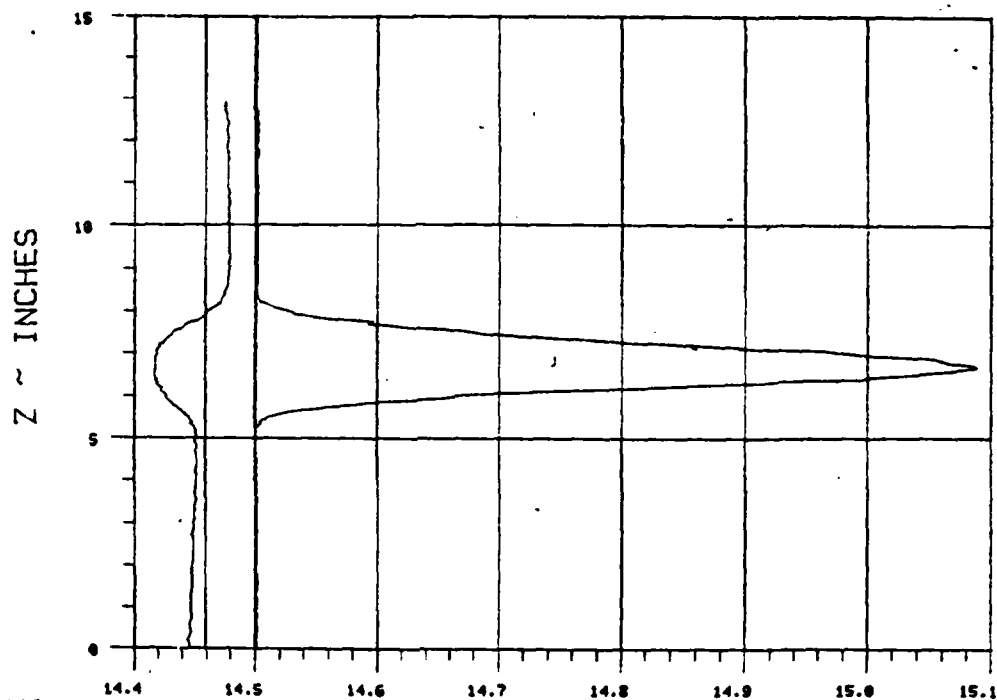
PRESSURE ~ PSIA

Xss/chord = _1.108_   Yss/chord = _.362_

BETA = _10_
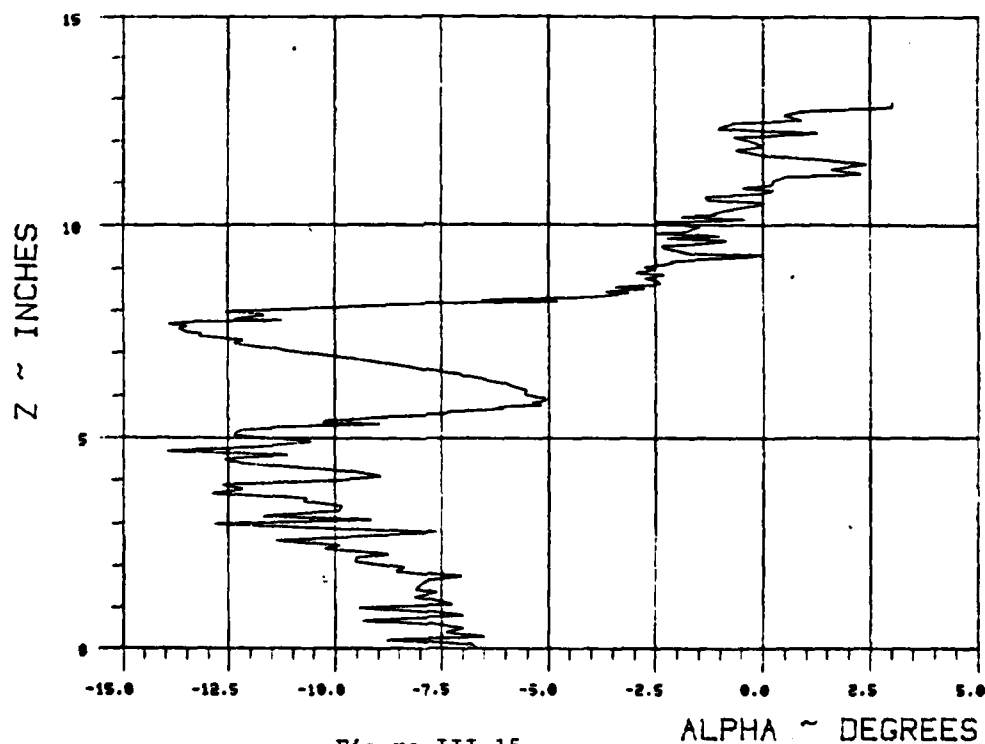
ALPHA ~ DEGREES

Figure III-15.

WAKE SURVEY DATA

TEST _287_ RUN _57_

ANGLE OF ATTACK _0_ NOMINAL JET ANGLE _30_ C MU _8.329_

PRESSURE ~ PSIA
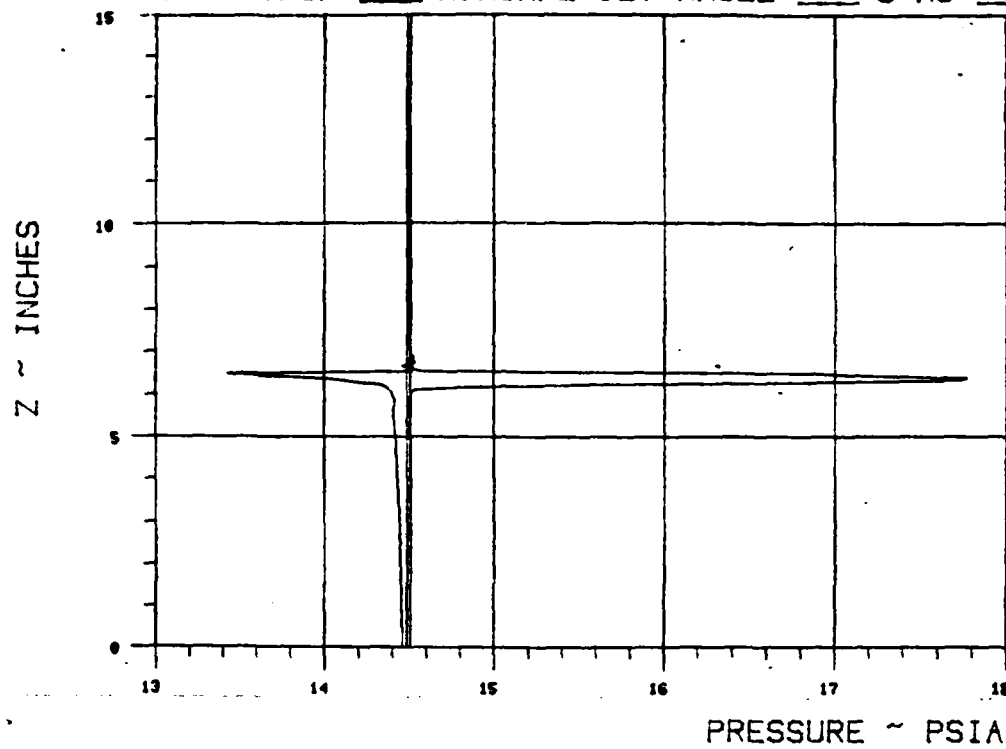
Xss/chord = _.268_ Yss/chord = _.637_

BETA = _10_
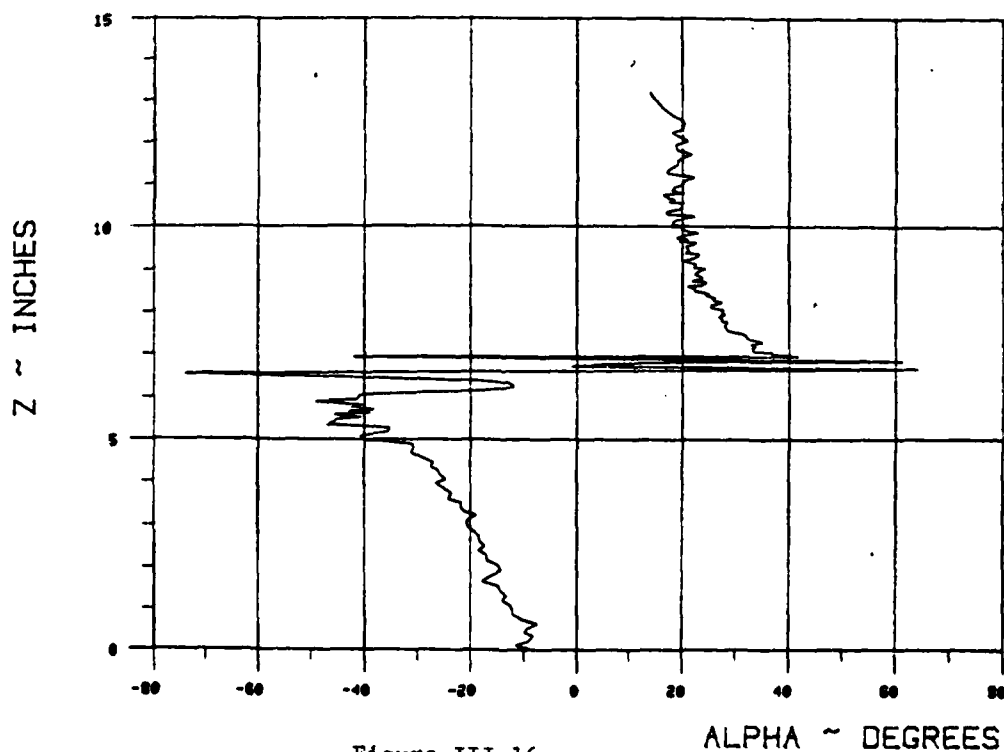
ALPHA ~ DEGREES

Figure III-16.

WAKE SURVEY DATA

TEST _287_ RUN _58_

ANGLE OF ATTACK _O_ NOMINAL JET ANGLE _30_ C MU _8.3877_

PRESSURE ~ PSIA

Xss/chord = _.392_ Yss/chord = _.616_

BETA = _10_

ALPHA ~ DEGREES

Figure III-17.

198
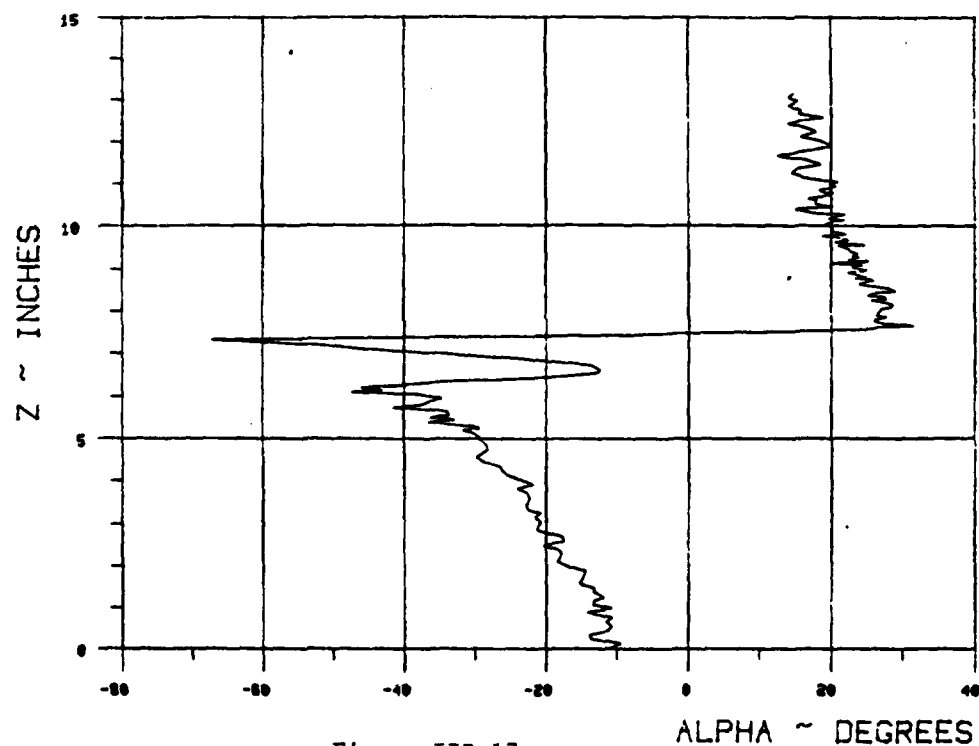
WAKE SURVEY DATA
TEST _287_ RUN _59_ .

ANGLE OF ATTACK _0_ NOMINAL JET ANGLE _30_ C MU _8.6606_
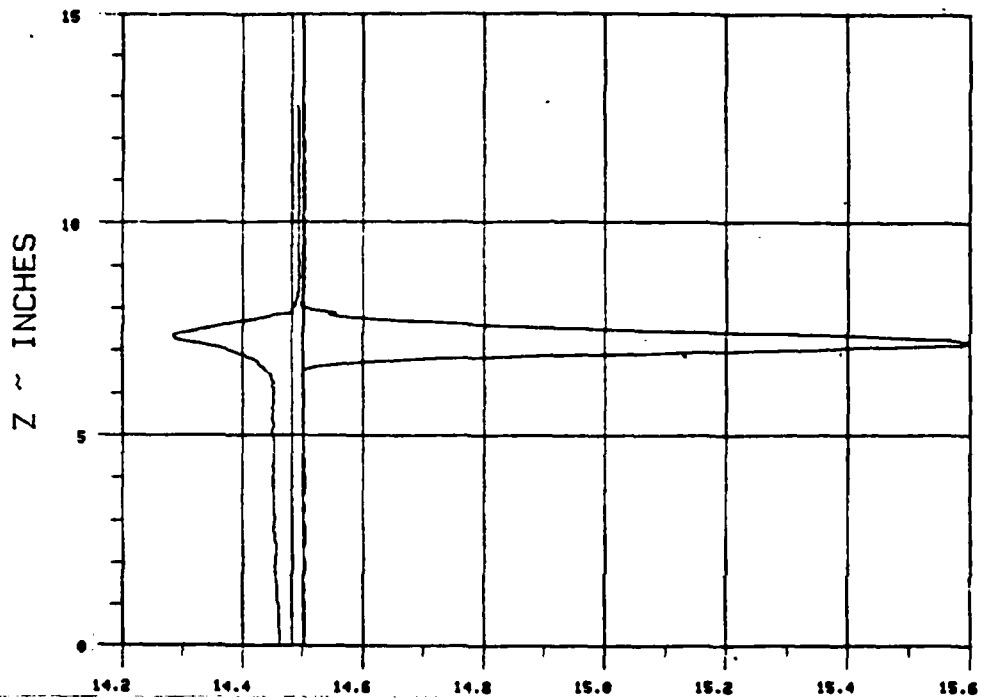
PRESSURE ~ PSIA

Xss/chord = _.515_   Yss/chord = _.594_
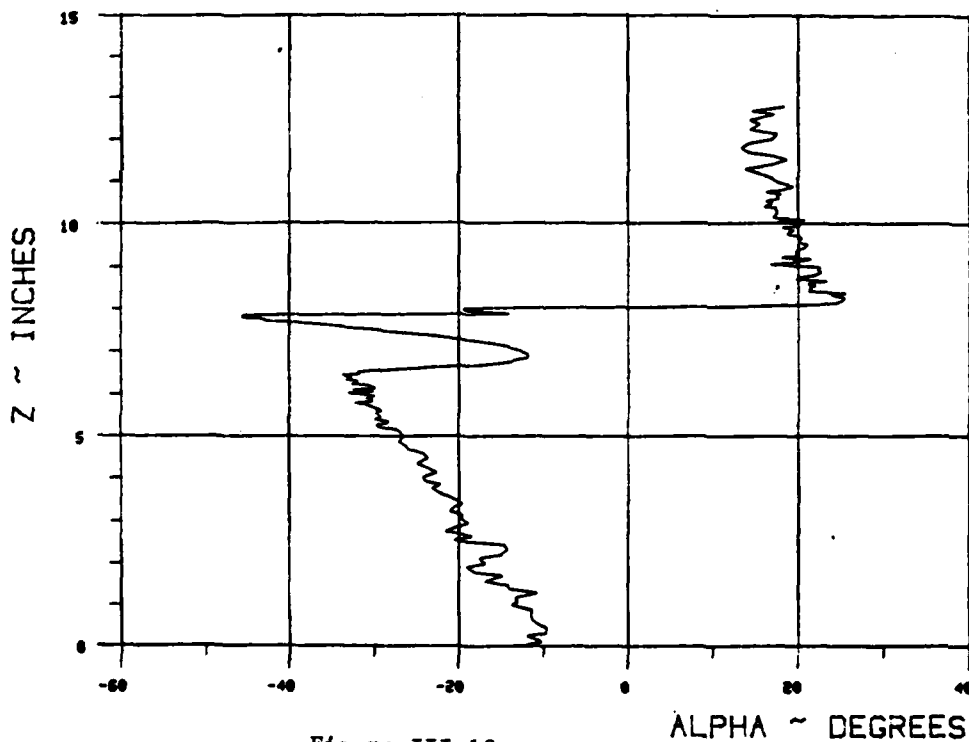
BETA = _10_

ALPHA ~ DEGREES

Figure III-18.

199

WAKE SURVEY DATA

TEST _287_ RUN _60_ ·

ANGLE OF ATTACK _0_ NOMINAL JET ANGLE _30_ C MIJ _8.4272_

PRESSURE ~ PSIA

Xss/chord = _.761_ Yss/chord = _.55_

BETA = _10_

ALPHA ~ DEGREES

Figure III-19.

200

WAKE SURVEY DATA

TEST _287_ RUN _6L_

ANGLE OF ATTACK _0_ NOMINAL JET ANGLE _30_ C MU _0.5653_

PRESSURE ~ PSIA

Xss/chord = _1.13_   Yss/chord = _.485_

BETA = _10_

ALPHA ~ DEGREES
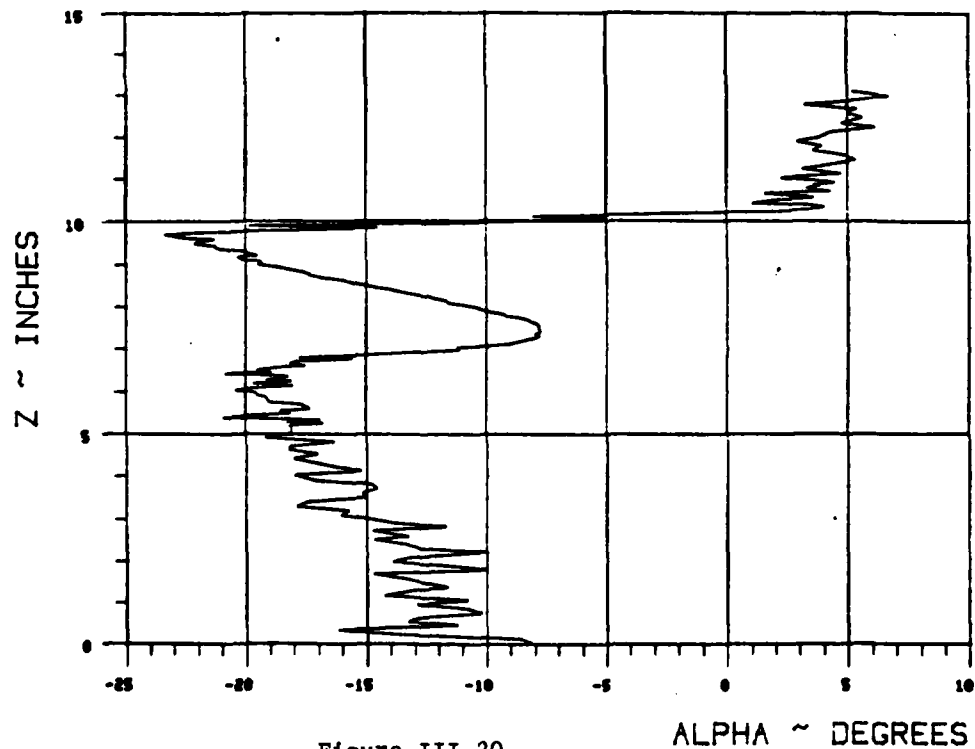
Figure III-20.

WAKE SURVEY DATA

TEST _287_ RUN _62_

ANGLE OF ATTACK _0_ NOMINAL JET ANGLE _30_ C MU _17.2768_
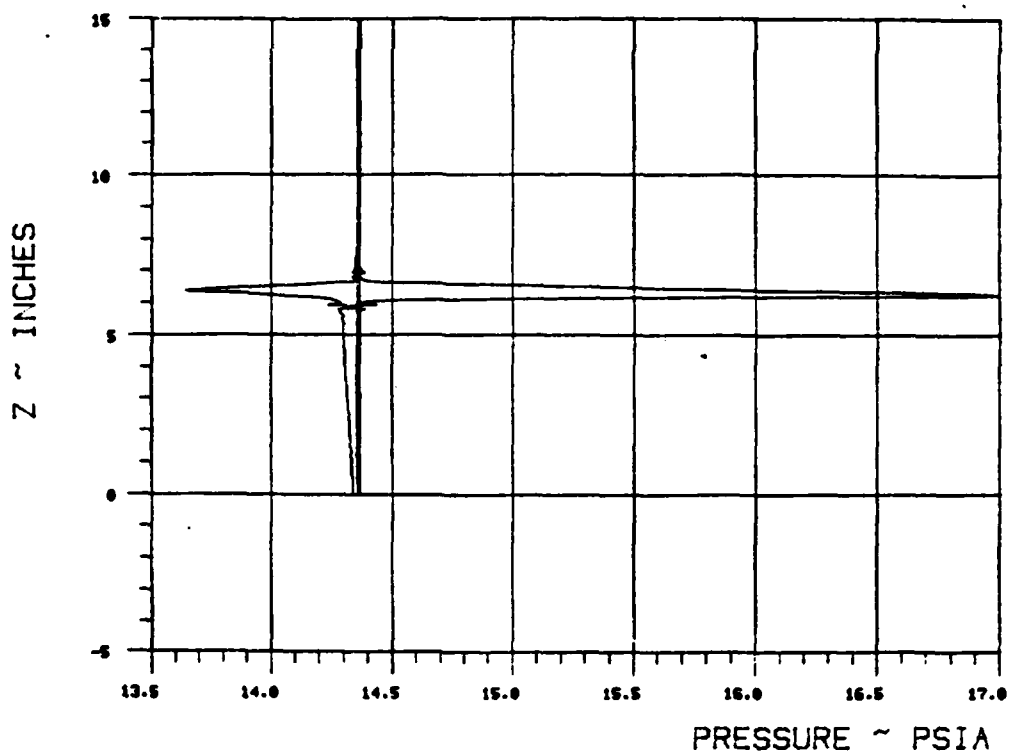
Xss/chord = _.268_   Yss/chord = _.637_
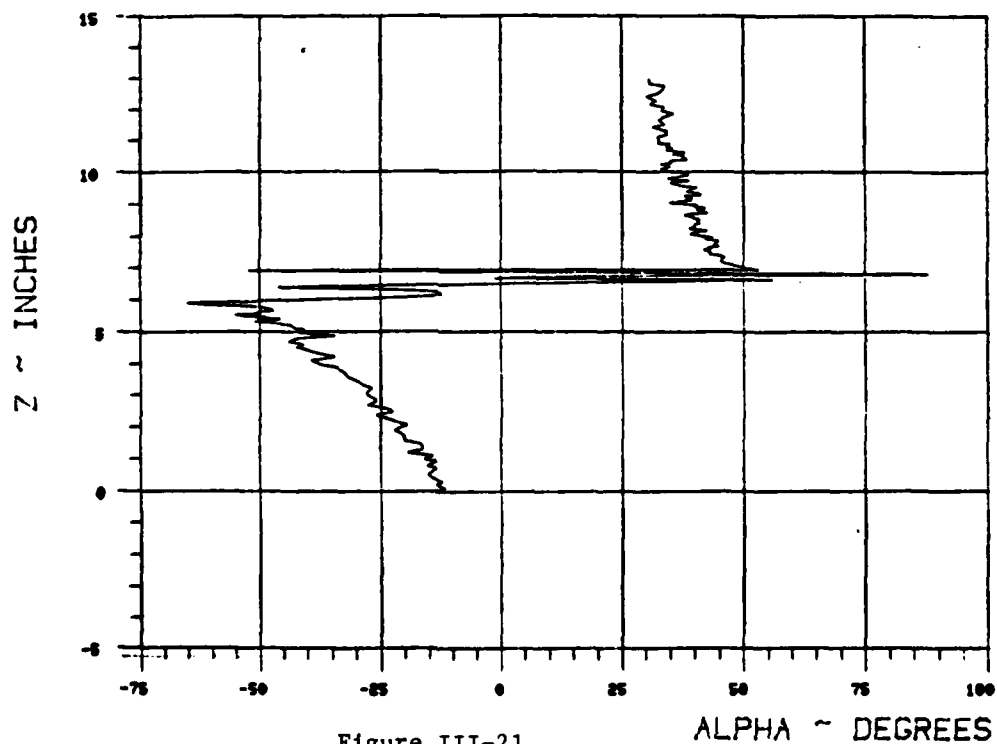
BETA = _10_

Figure III-21.

WAKE SURVEY DATA

TEST _287_ RUN _63_.

ANGLE OF ATTACK _O_ NOMINAL JET ANGLE _30_ C MU _16.8459_

PRESSURE ~ PSIA

Xss/chord = _.392_ Yss/chord = _.616_

BETA = _10_

ALPHA ~ DEGREES

Figure III-22.

203
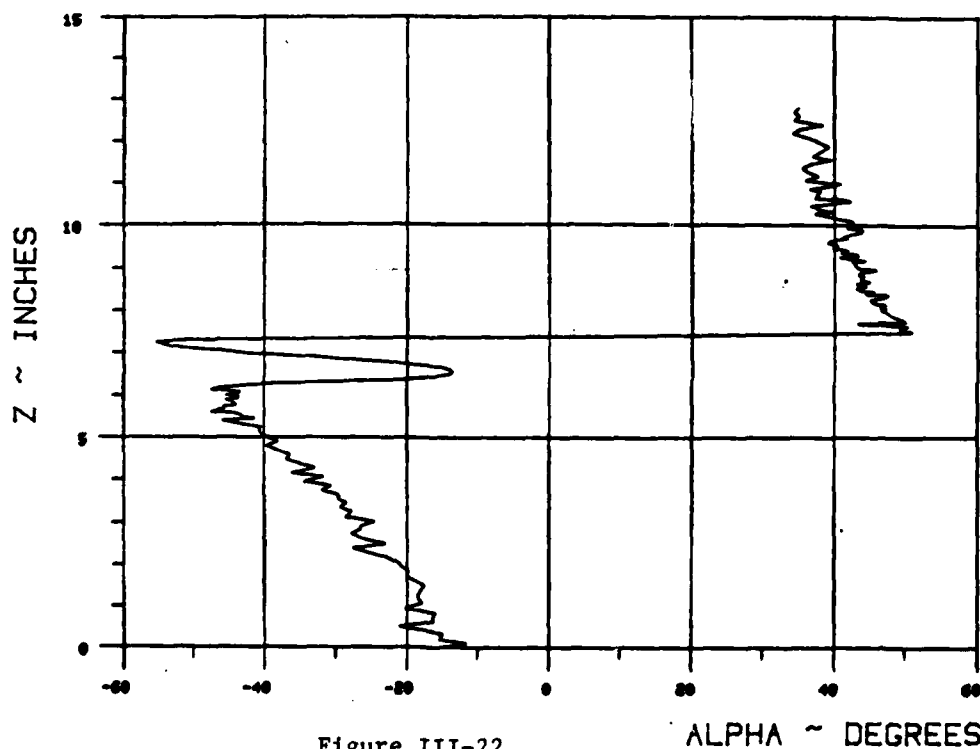
WAKE SURVEY DATA

TEST _287_ RUN _64_

ANGLE OF ATTACK _0_ NOMINAL JET ANGLE _30_ C MU _17.3211_
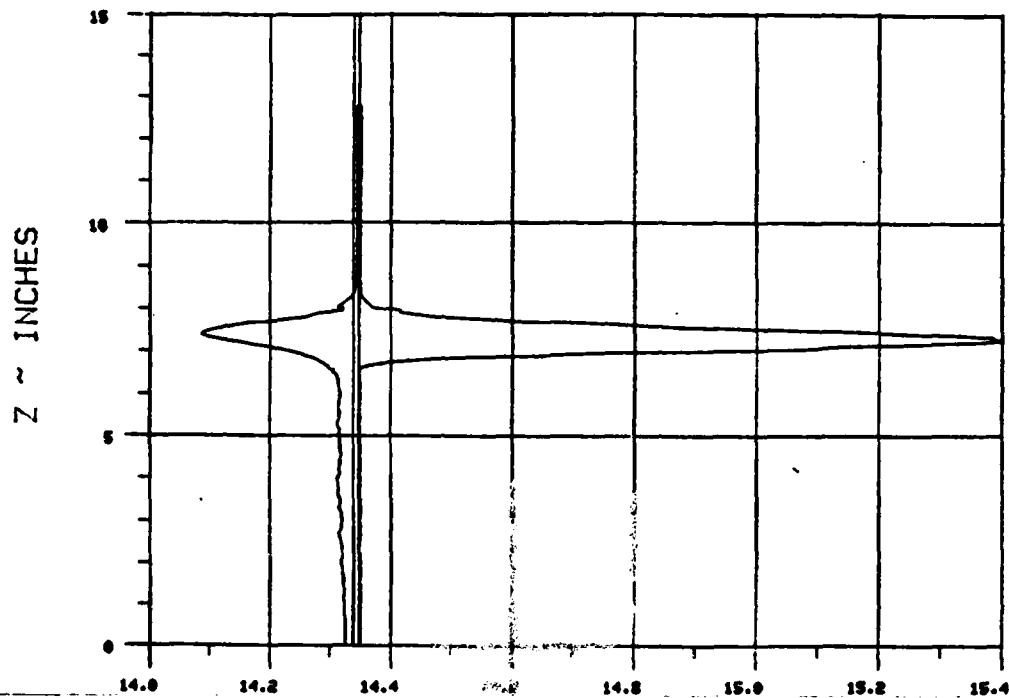
PRESSURE ~ PSIA

Xss/chord = _.515_   Yss/chord = _.594_

BETA = _10_

ALPHA ~ DEGREES

Figure III-23.

204
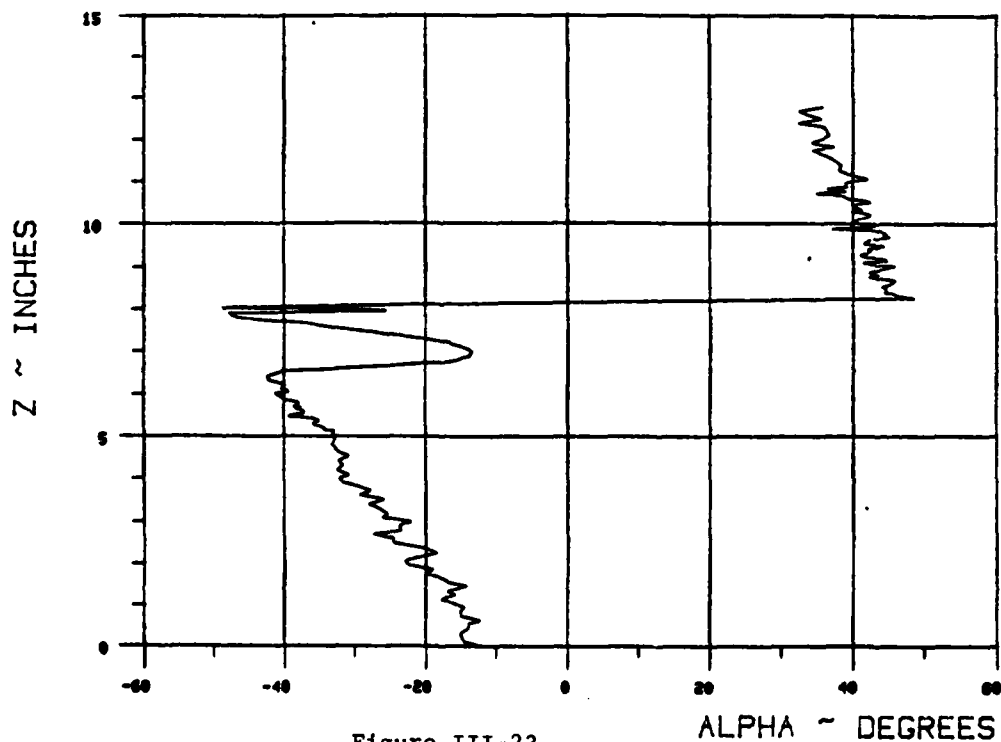
WAKE SURVEY DATA

TEST 287 RUN 65

ANGLE OF ATTACK 0 NOMINAL JET ANGLE 30 C MU 16.9019
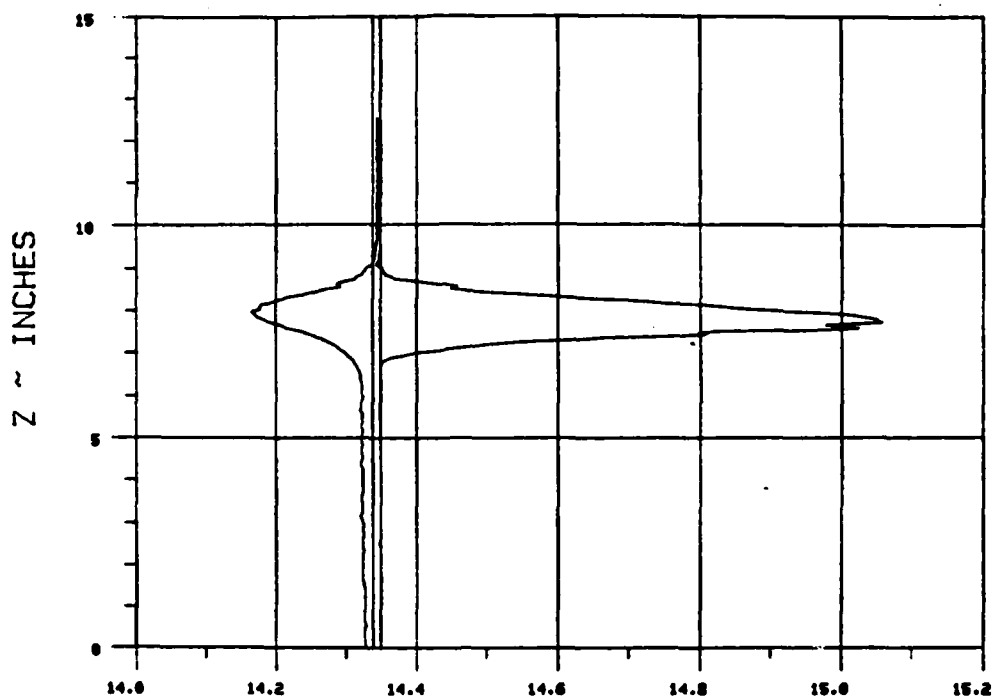
PRESSURE ~ PSIA

Xss/chord = .761   Yss/chord = .55
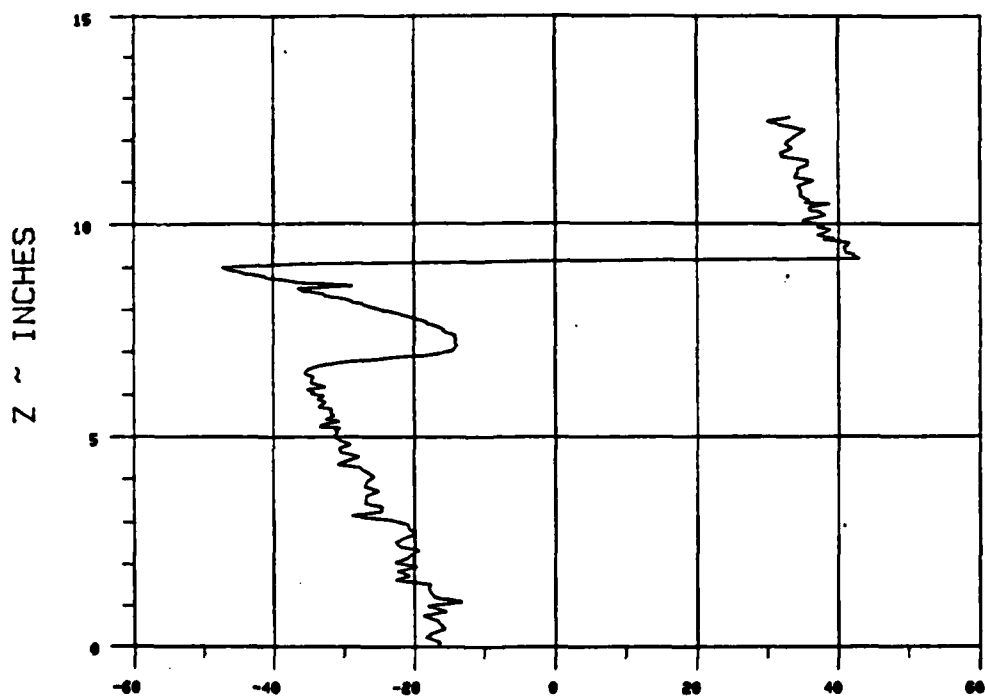
BETA = 10

ALPHA ~ DEGREES

Figure III-24.

WAKE SURVEY DATA
TEST *287* RUN *66*
ANGLE OF ATTACK *O* NOMINAL JET ANGLE *30* C MU *17.6394*
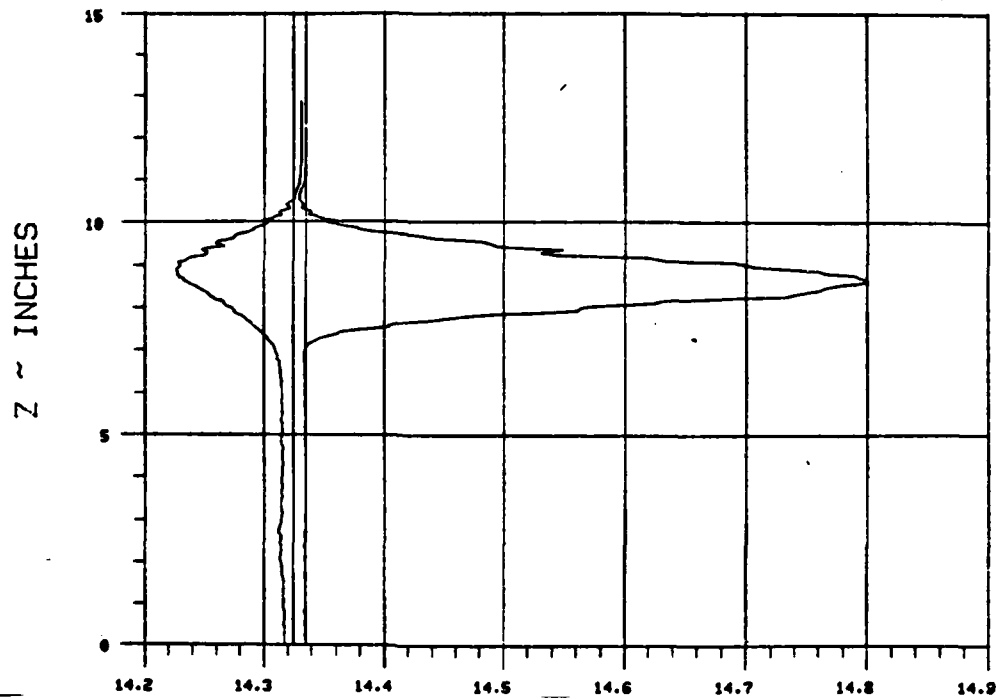
PRESSURE ~ PSIA

Xss/chord = *1.13*   Yss/chord = *.485*
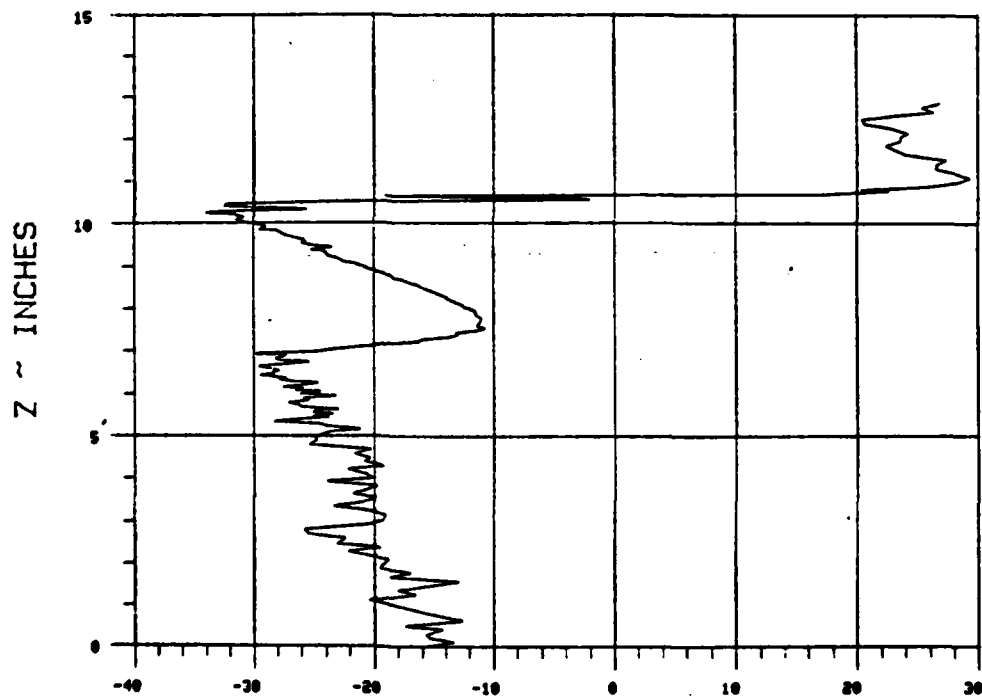
BETA = *10*

ALPHA ~ DEGREES

Figure III-25.

WAKE SURVEY DATA
TEST _287_ RUN _67_
ANGLE OF ATTACK _0_ NOMINAL JET ANGLE _30_ C MU _25.4067_
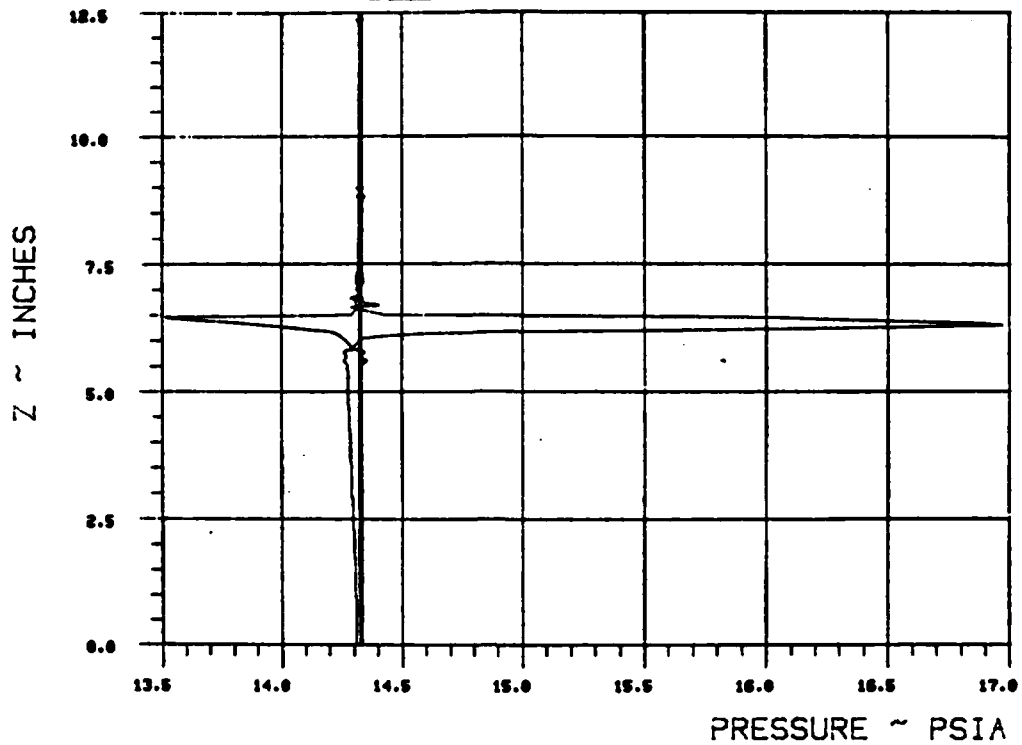
Xss/chord = _.268_   Yss/chord = _.637_
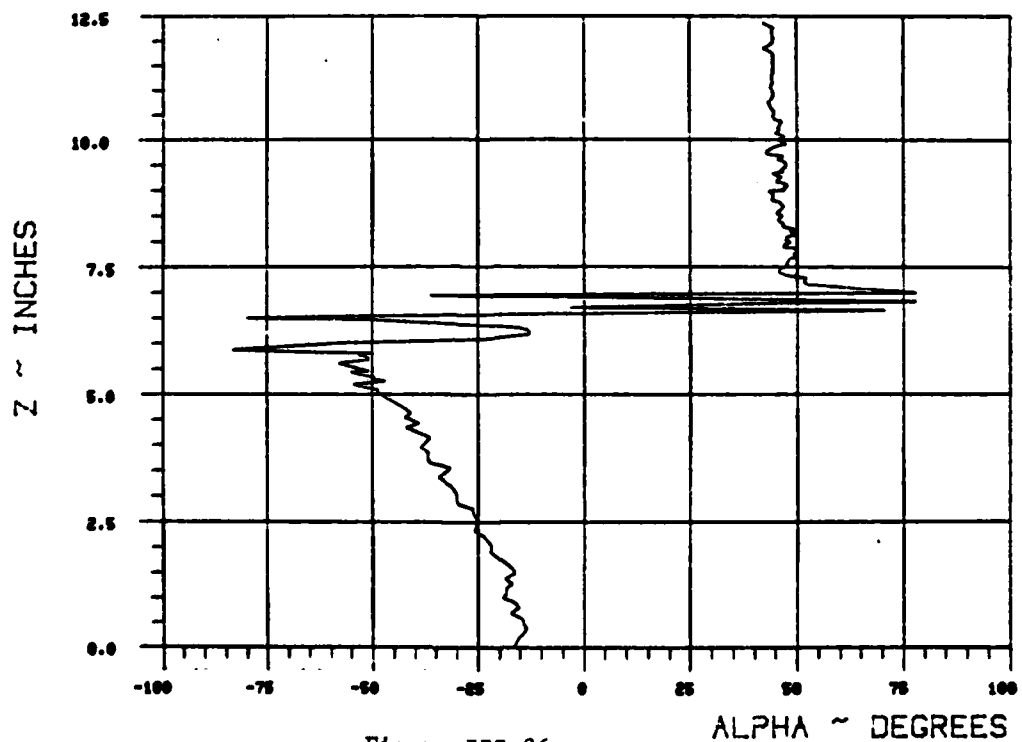
BETA = _10_

Figure III-26.

WAKE SURVEY DATA
TEST _287_ RUN _68_
ANGLE OF ATTACK _O_ NOMINAL JET ANGLE _30_ C MU _26.7713_
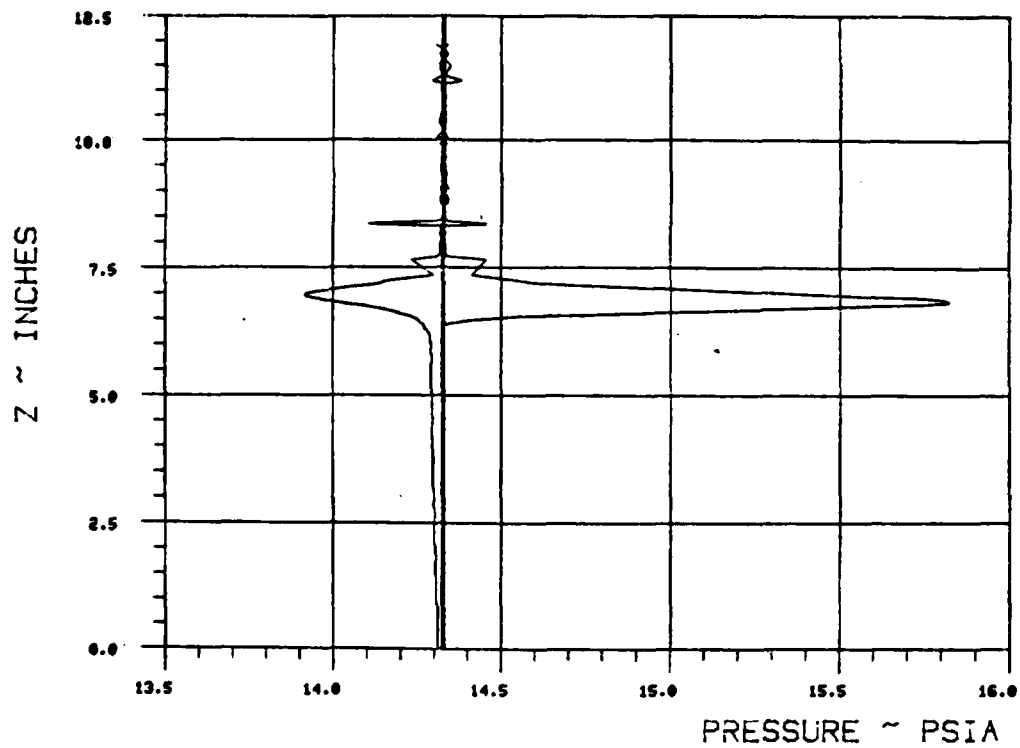
Xss/chord = _.392_ Yss/chord = _.616_
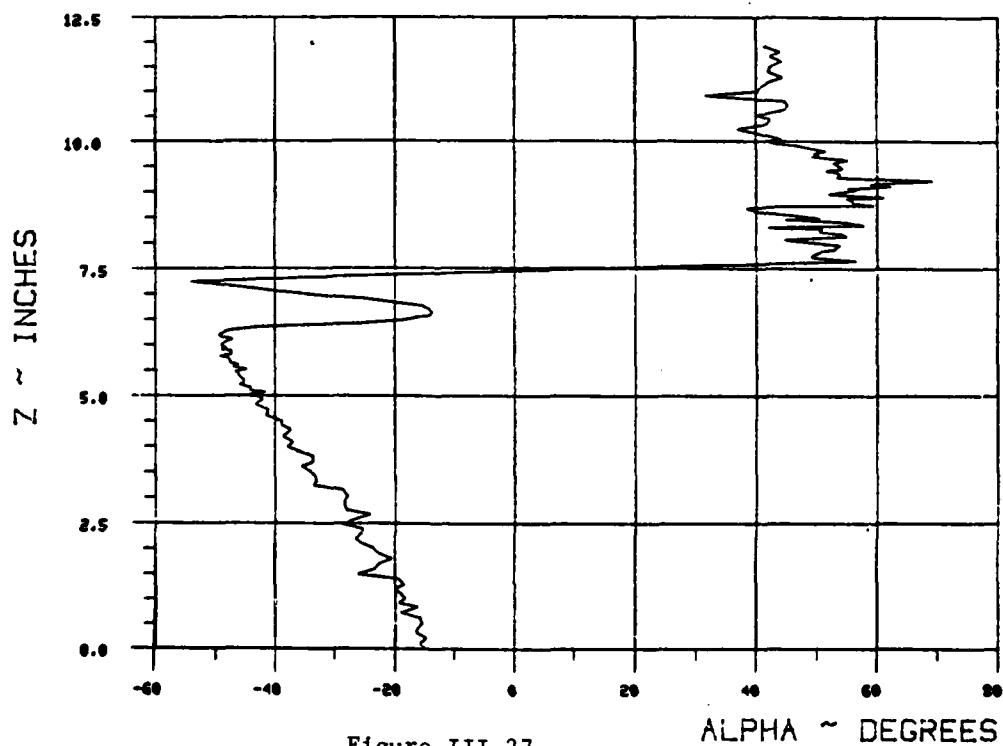
BETA = _10_

Figure III-27.

Figure III-28.

209
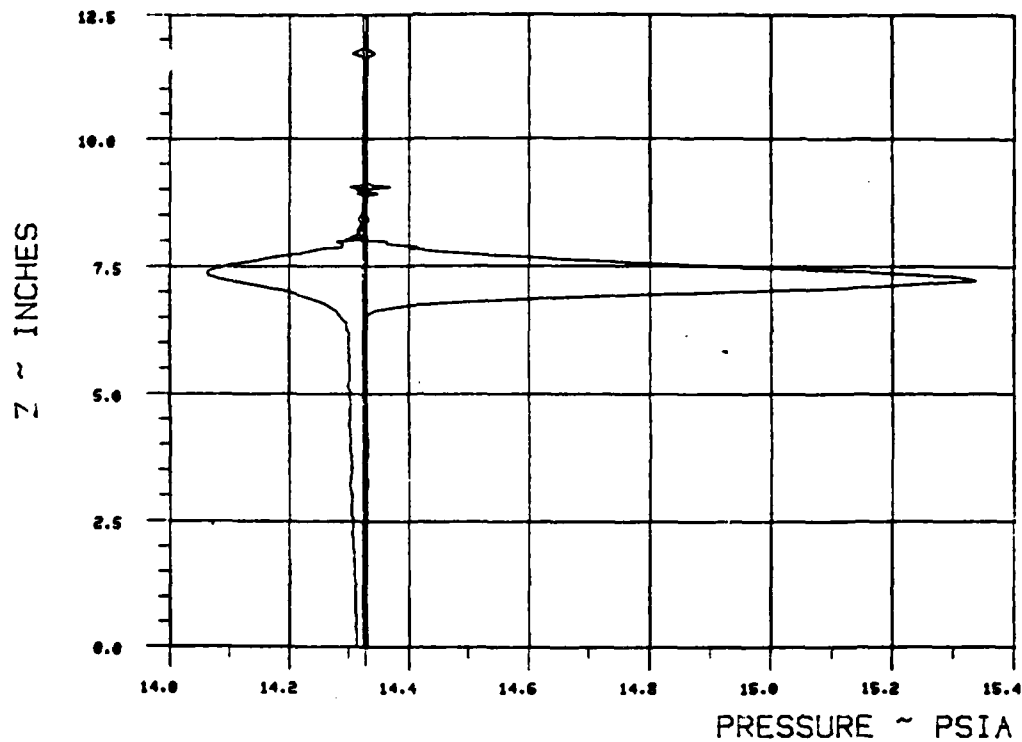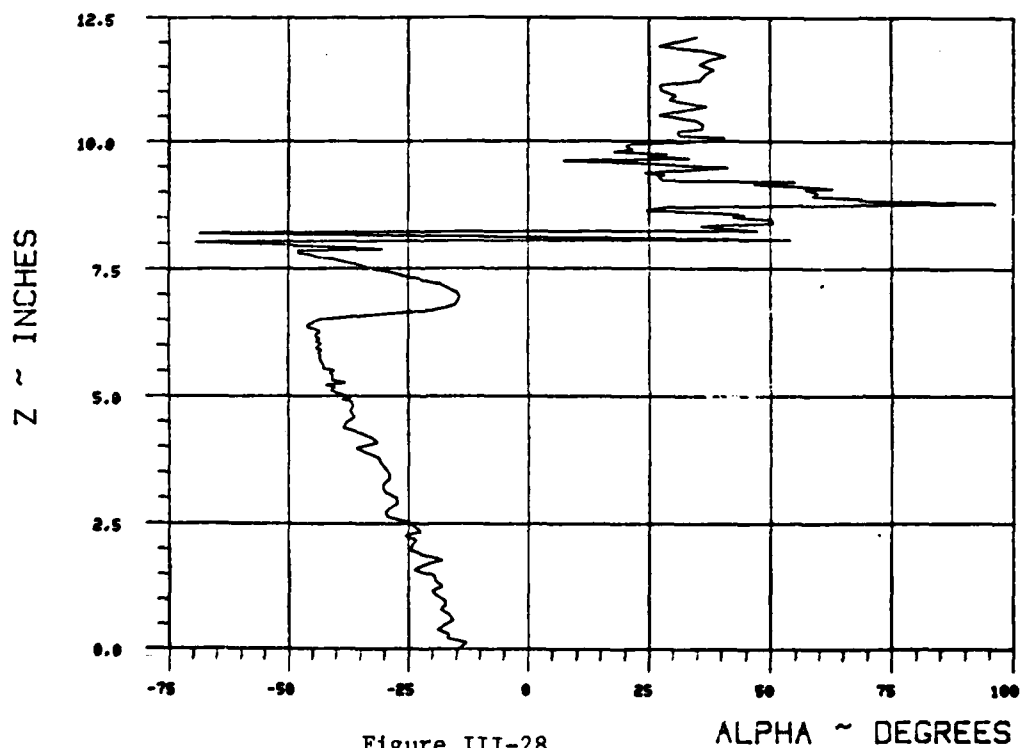
WAKE SURVEY DATA

TEST _287_ RUN _70_

ANGLE OF ATTACK _0_ NOMINAL JET ANGLE _30_ C MU _24.9456_
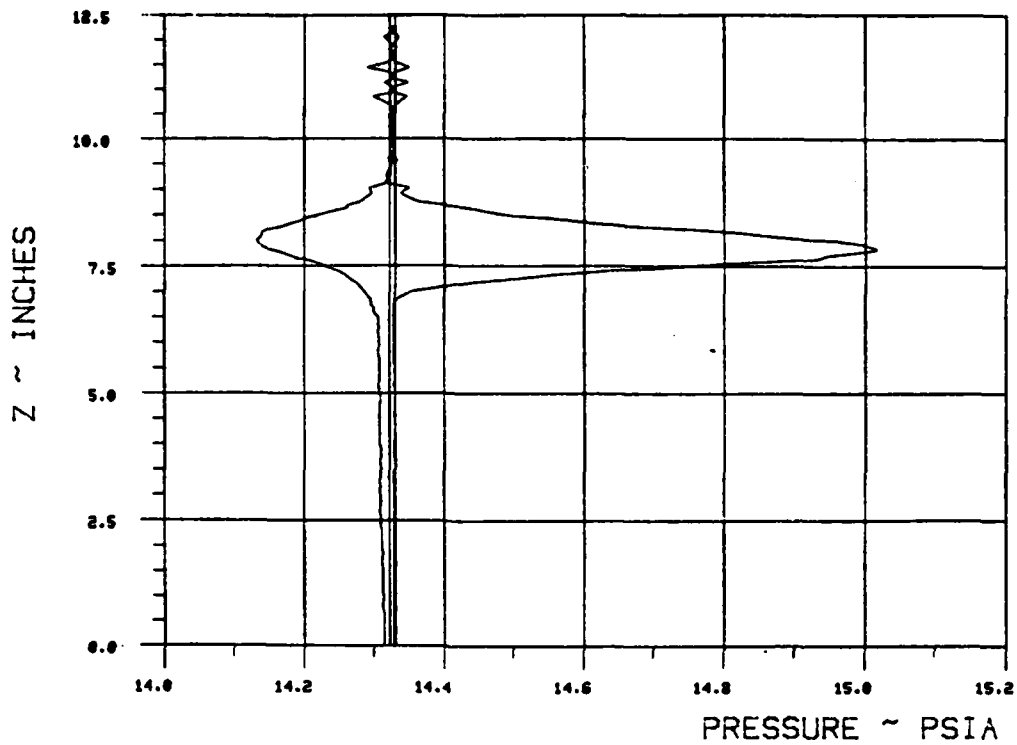
Xss/chord = _.761_   Yss/chord = _.55_
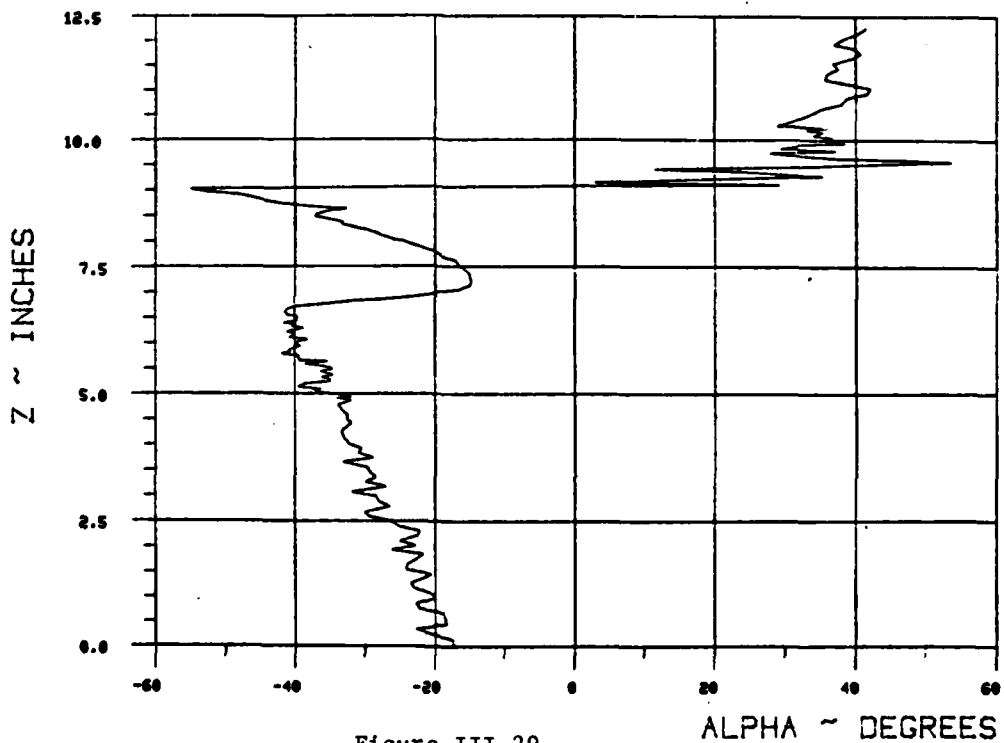
BETA = _10_

Figure III-29.

WAKE SURVEY DATA
TEST 287 RUN 71
ANGLE OF ATTACK 0 NOMINAL JET ANGLE 30 C MU 26.8944
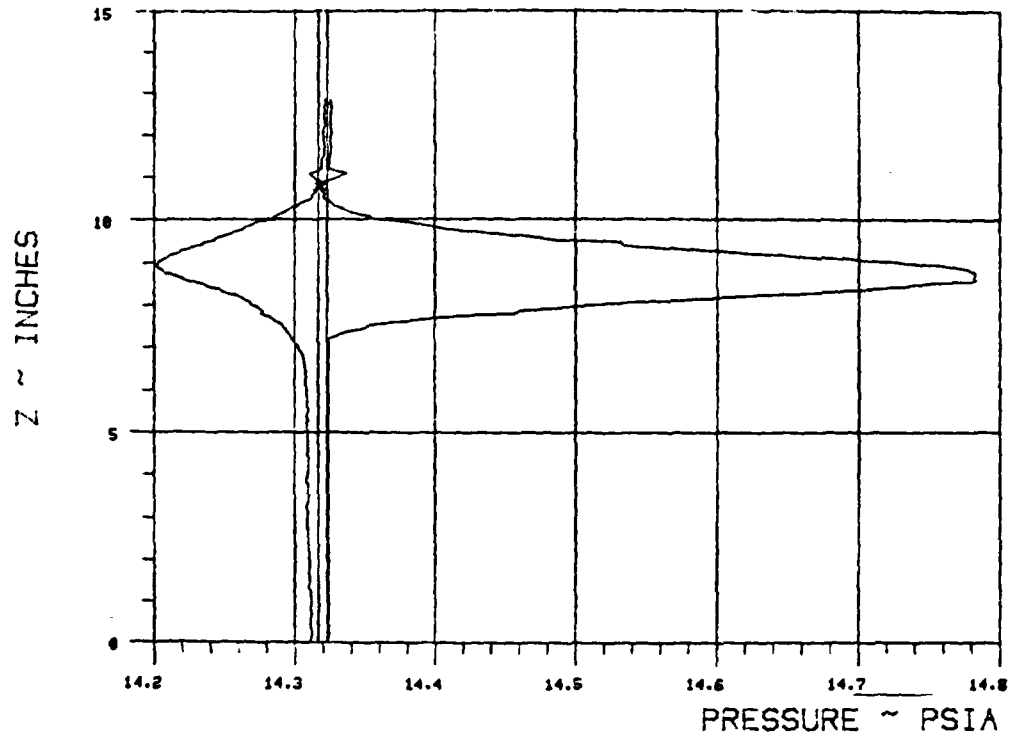
Xss/chord = 1.13   Yss/chord = .485

BETA = 10
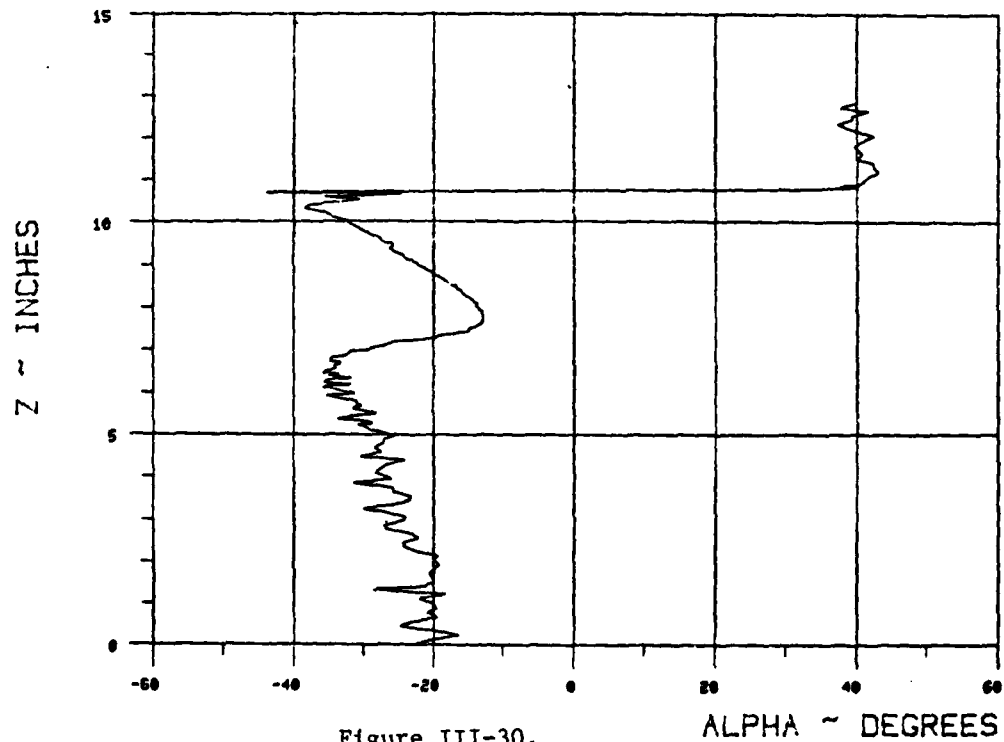
Figure III-30.

WAKE SURVEY DATA

TEST _287_. RUN _36_

ANGLE OF ATTACK _0_ NOMINAL JET ANGLE _50_ C MU _.9947_
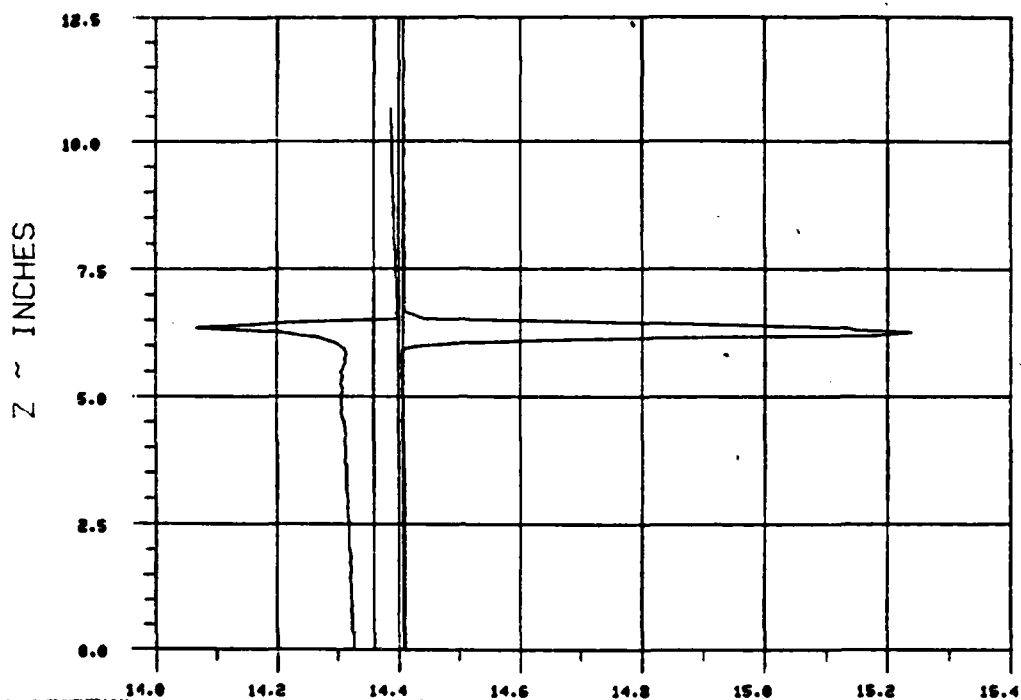
FRESSURE ~ PSIA

Xss/chord = _.368_ Yss/chord = _.565_

BETA = _20_

ALPHA ~ DEGREES

Figure III-31.

212
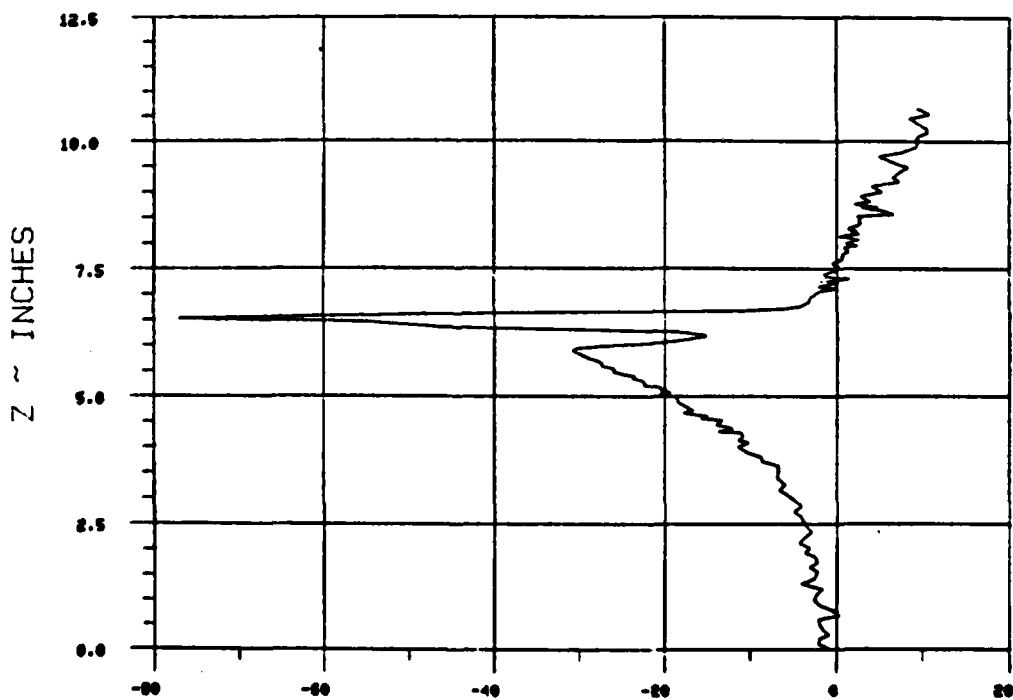
WAKE SURVEY DATA

TEST _287_ RUN _37_

ANGLE OF ATTACK _0_ NOMINAL JET. ANGLE _50_ C MU _1.0013_
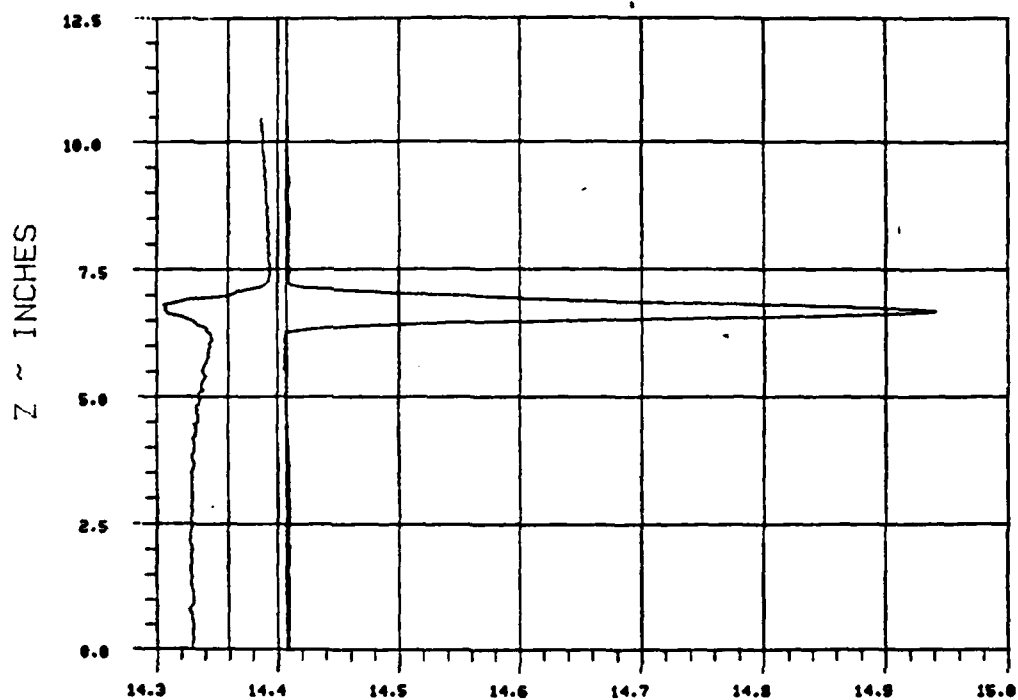
PRESSURE ~ PSIA

Xss/chord = _.485_ Yss/chord = _.522_

BETA = _20_

ALPHA ~ DEGREES

Figure III-32.

213
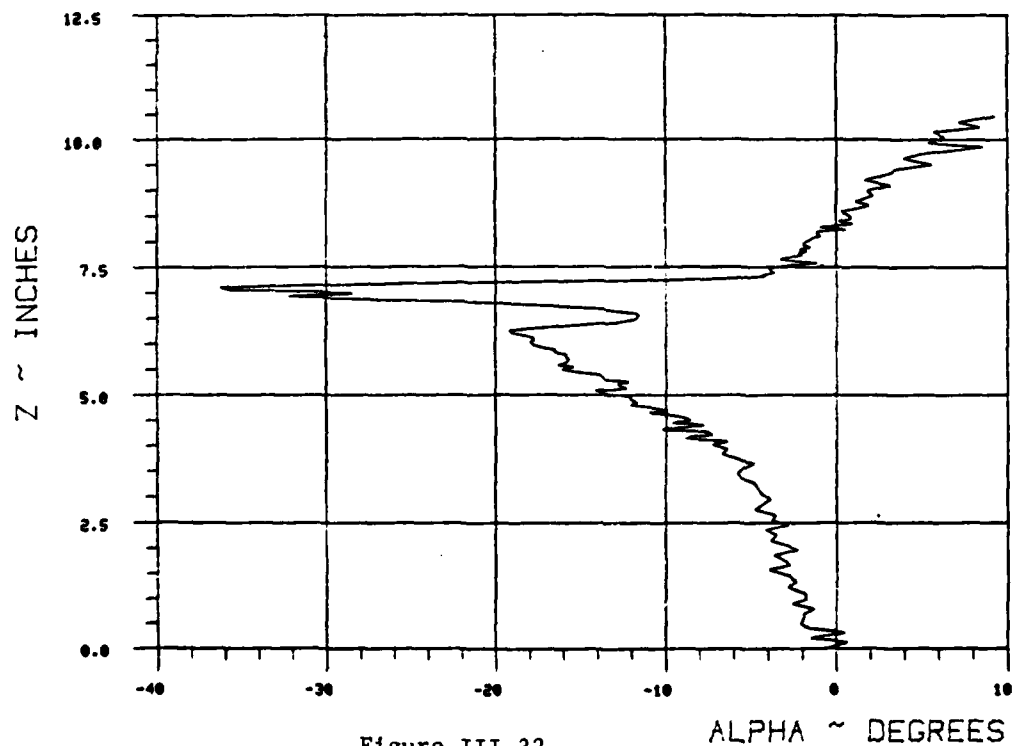
WAKE SURVEY DATA

TEST _287_ RUN _38_

ANGLE OF ATTACK _0_ NOMINAL JET ANGLE _50_ C MU _1.0041_

PRESSURE ~ PSIA
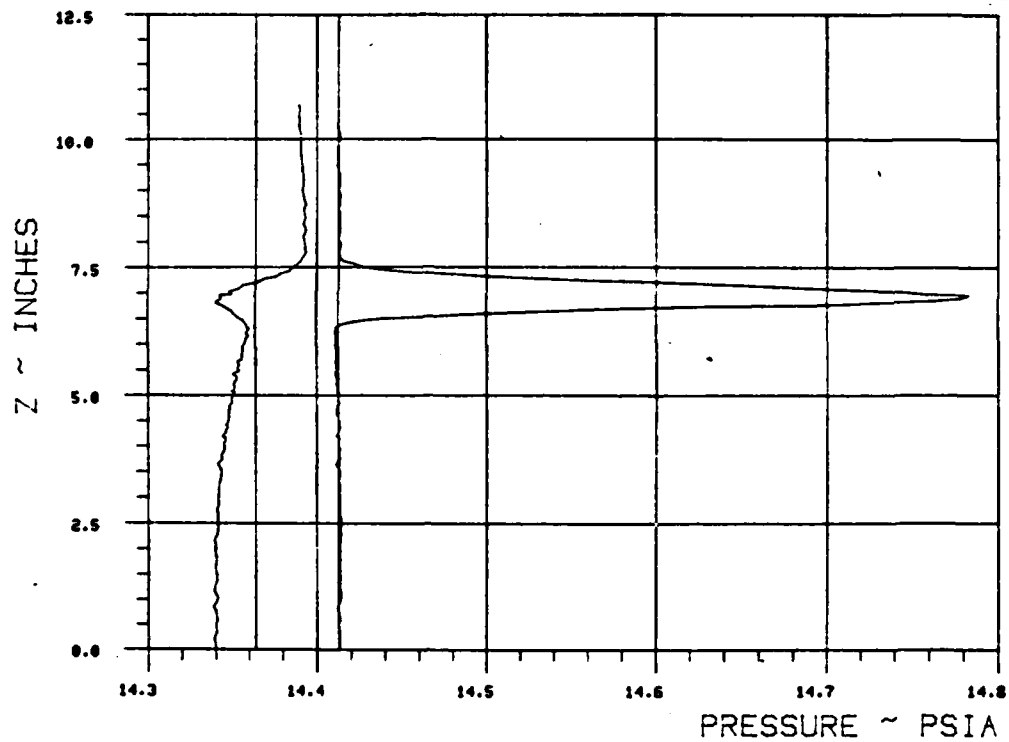
Xss/chord = _.602_ Yss/chord = _.479_

BETA = _20_

ALPHA ~ DEGREES
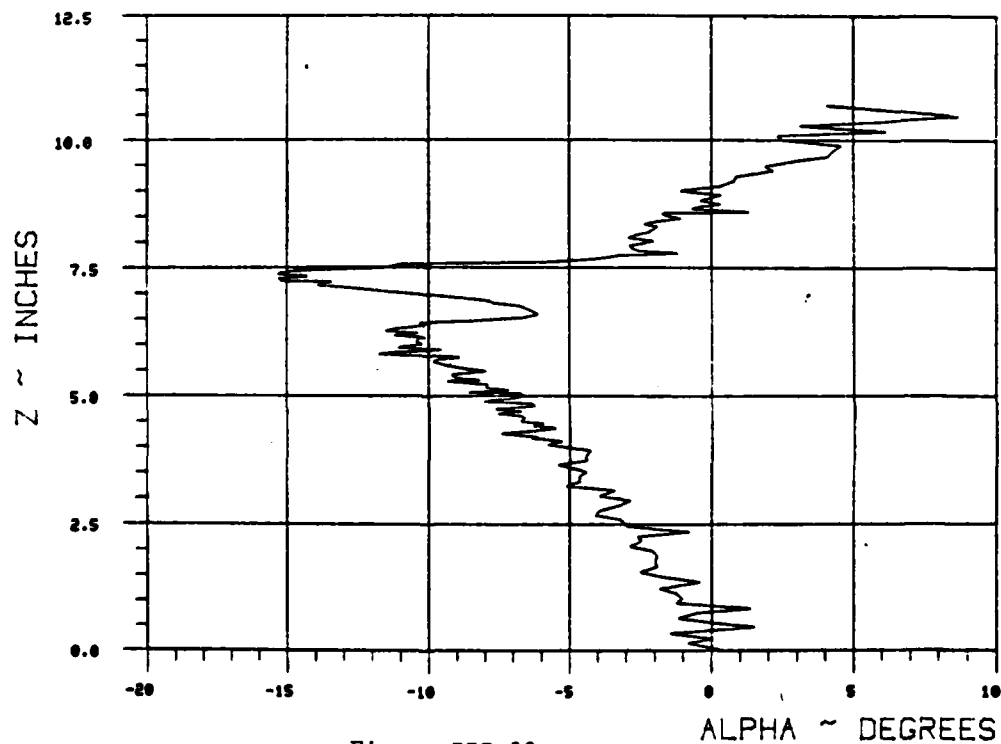
Figure III-33.

WAKE SURVEY DATA
TEST _2B7_ RUN _41_
ANGLE OF ATTACK _0_ NOMINAL JET ANGLE _56_ C MU _1.011_

PRESSURE ~ PSIA
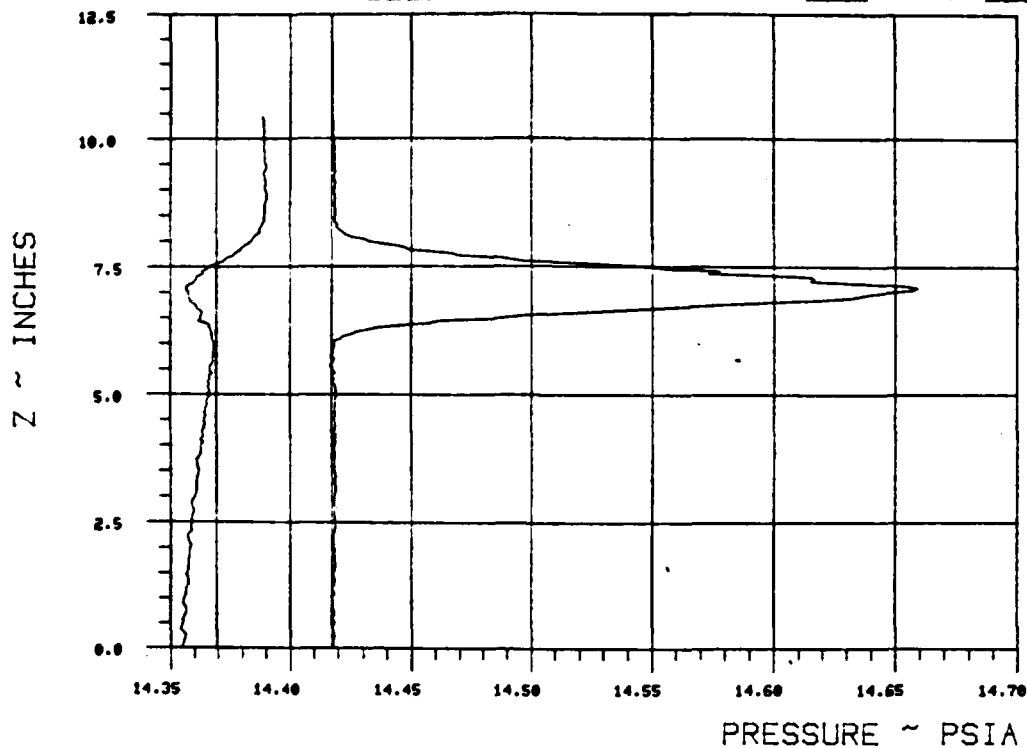
Xss/chord = _.837_   Yss/chord = _.394_

BETA = _20_

ALPHA ~ DEGREES
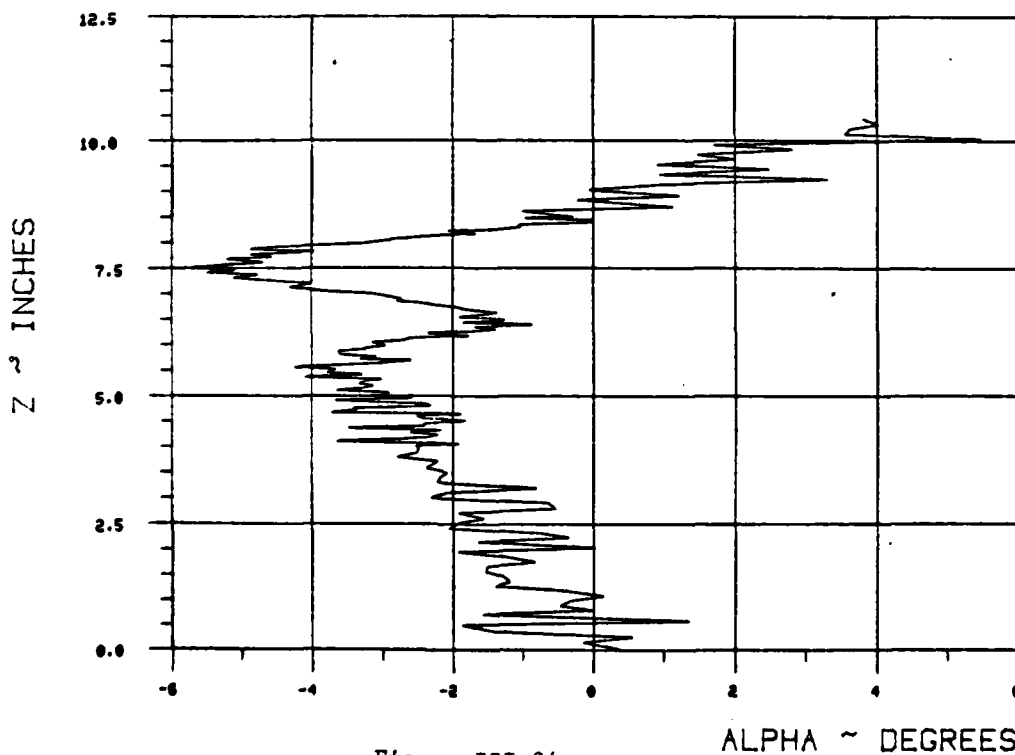
Figure III-34.

WAKE SURVEY DATA

TEST _287_ RUN _39_

ANGLE OF ATTACK _0_ NOMINAL JET ANGLE _50_ C MU _.9893_
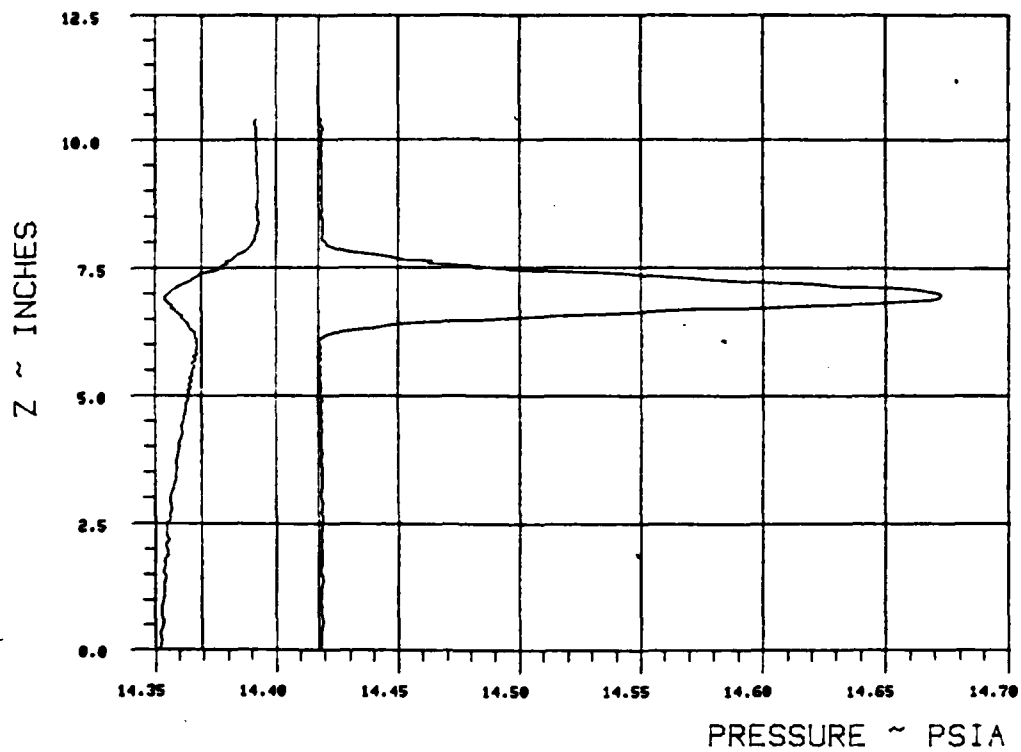
PRESSURE ~ PSIA

Xss/chord = _.837_ Yss/chord = _.397_

BETA = _20_

ALPHA ~ DEGREES

Figure III-35.

216
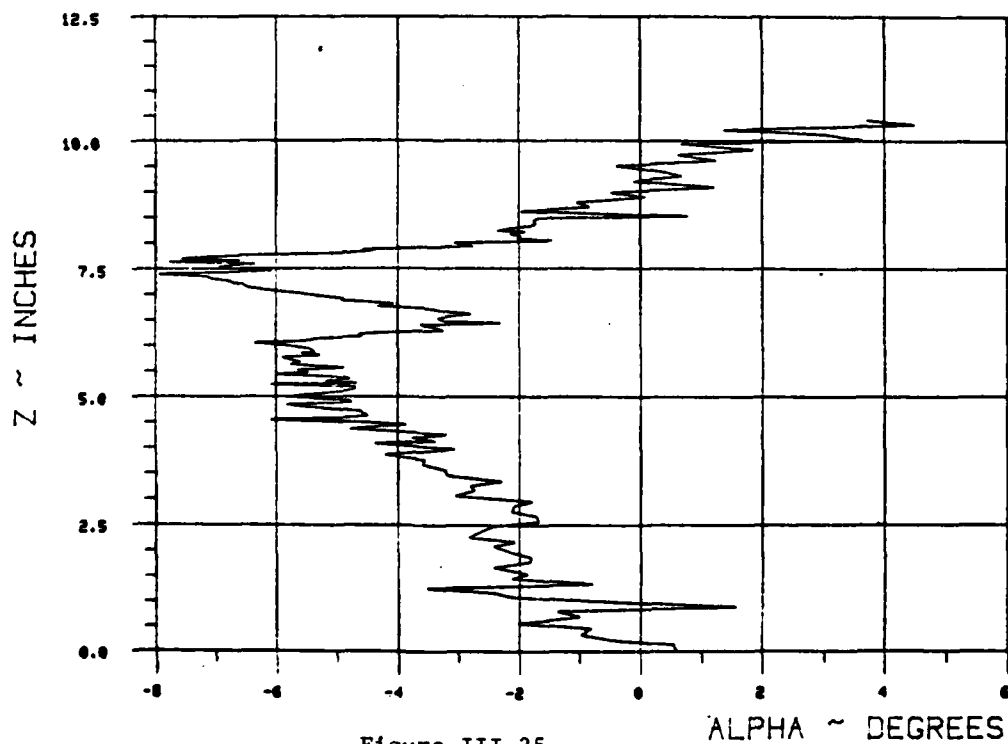
WAKE SURVEY DATA

TEST 287 RUN 40

ANGLE OF ATTACK 0 NOMINAL JET ANGLE 50 C MU .9868
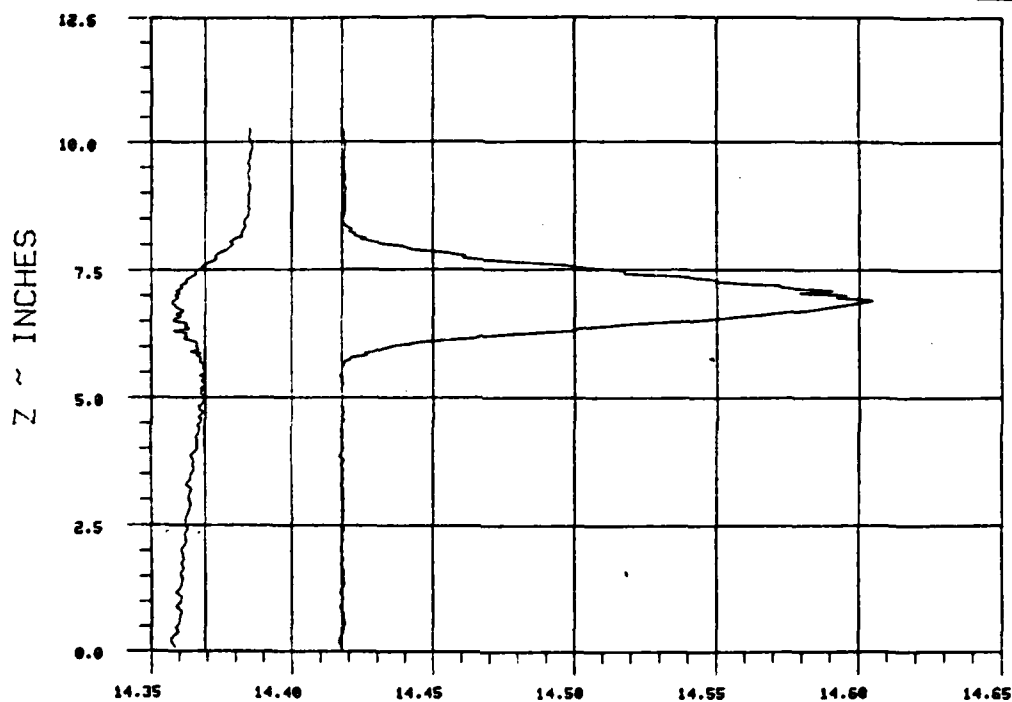
Xss/chord = 1.19   Yss/chord = .265

BETA = 20
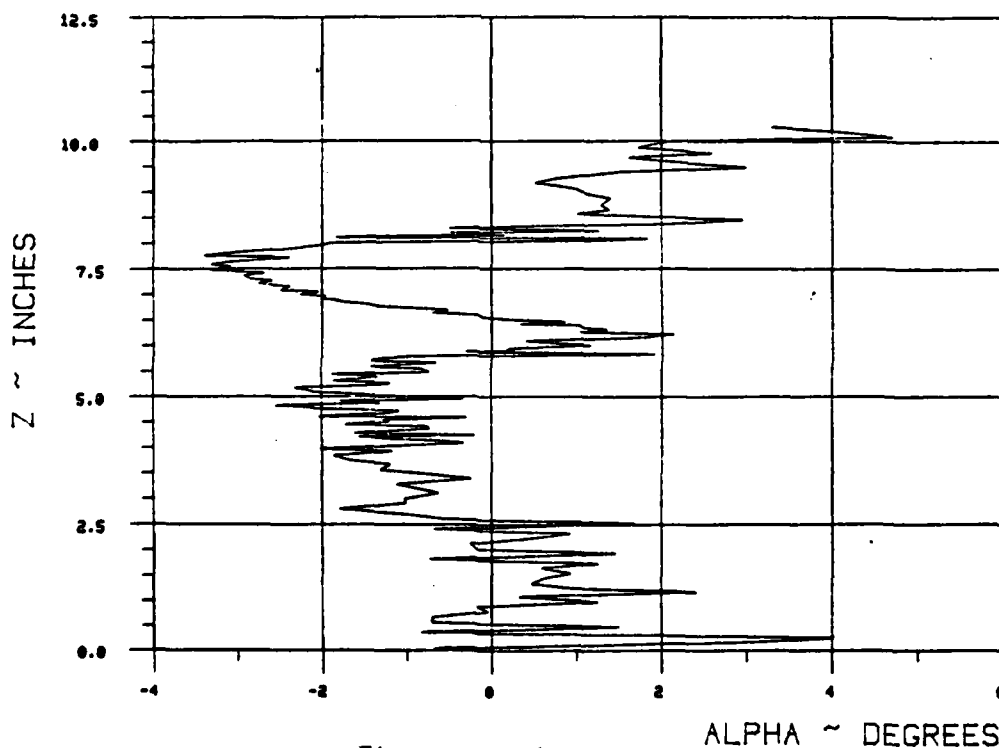
Figure III-36.

WAKE SURVEY DATA
TEST 287 RUN 29
ANGLE OF ATTACK 0 NOMINAL JET ANGLE 70 C MU 1.
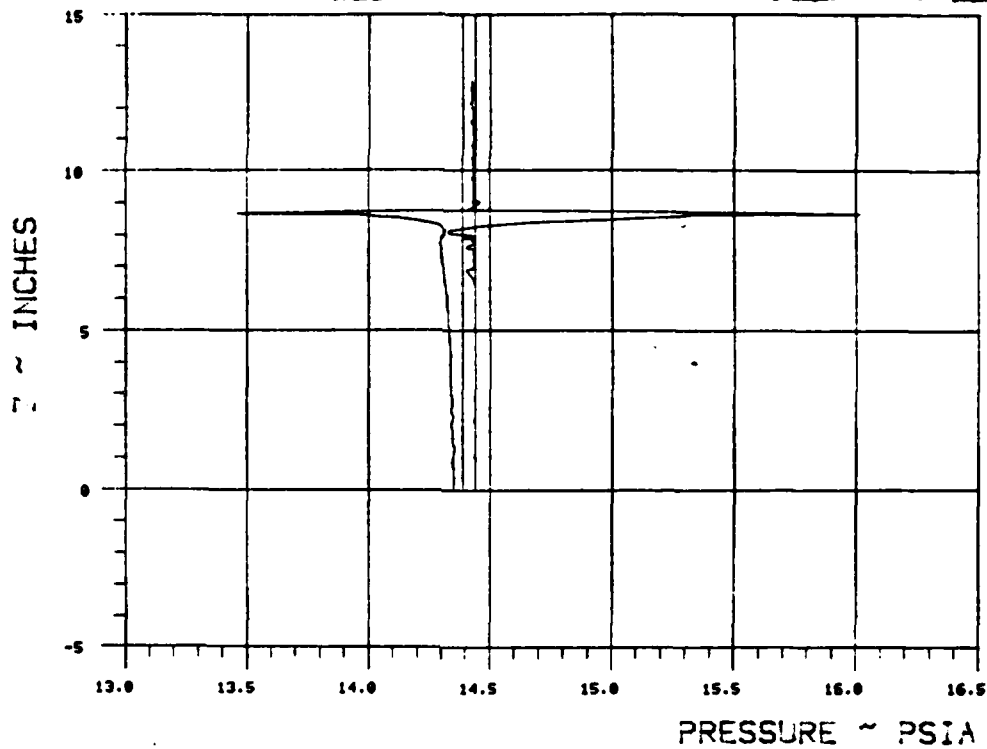
Xss/chord = .582   Yss/chord = .722

BETA = 30
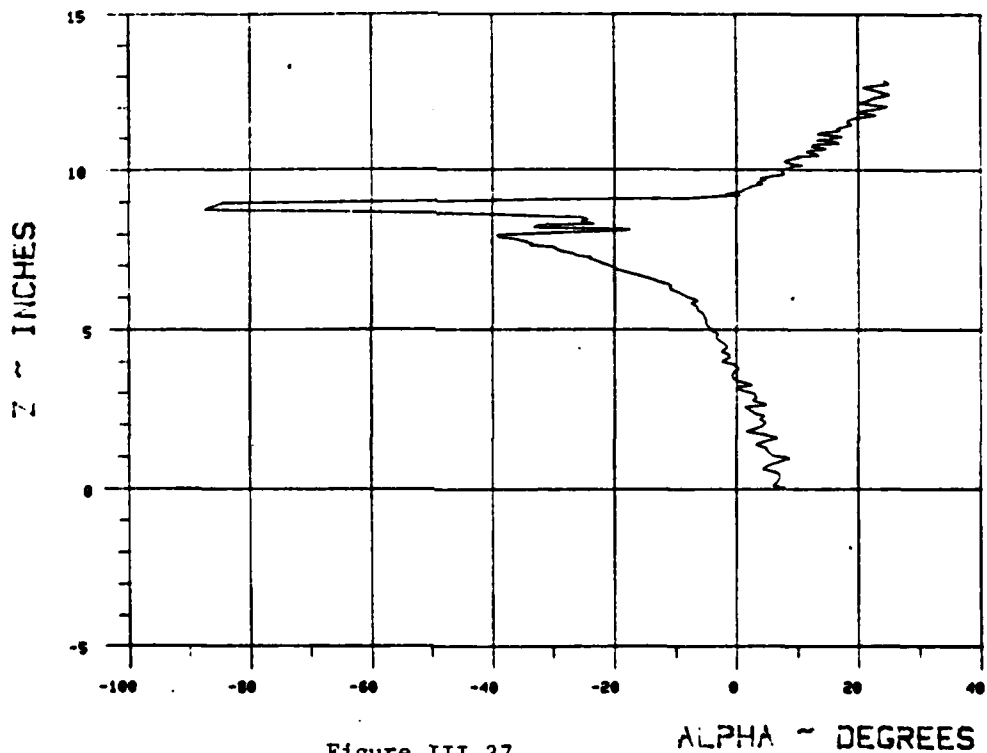
Figure III-37.

WAKE SURVEY DATA
TEST 287 RUN 30
ANGLE OF ATTACK 0 NOMINAL JET ANGLE 76 C MU 1.0512

PRESSURE ~ PSIA

Xss/chord = .69   Yss/chord = .66

BETA = 30

ALPHA ~ DEGREES

Figure III-38.

219
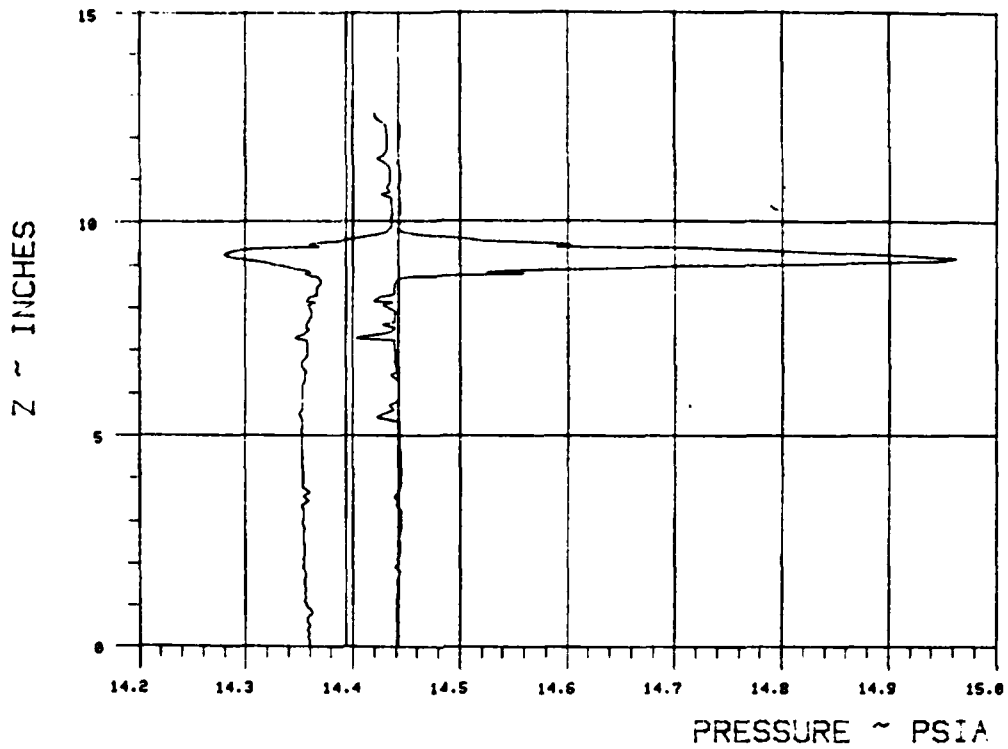
WAKE SURVEY DATA
TEST _287_ RUN _31_
ANGLE OF ATTACK _0_ NOMINAL JET ANGLE _70_ C MU _1.0314_

Xss/chord = _.798_   Yss/chord = _.547_
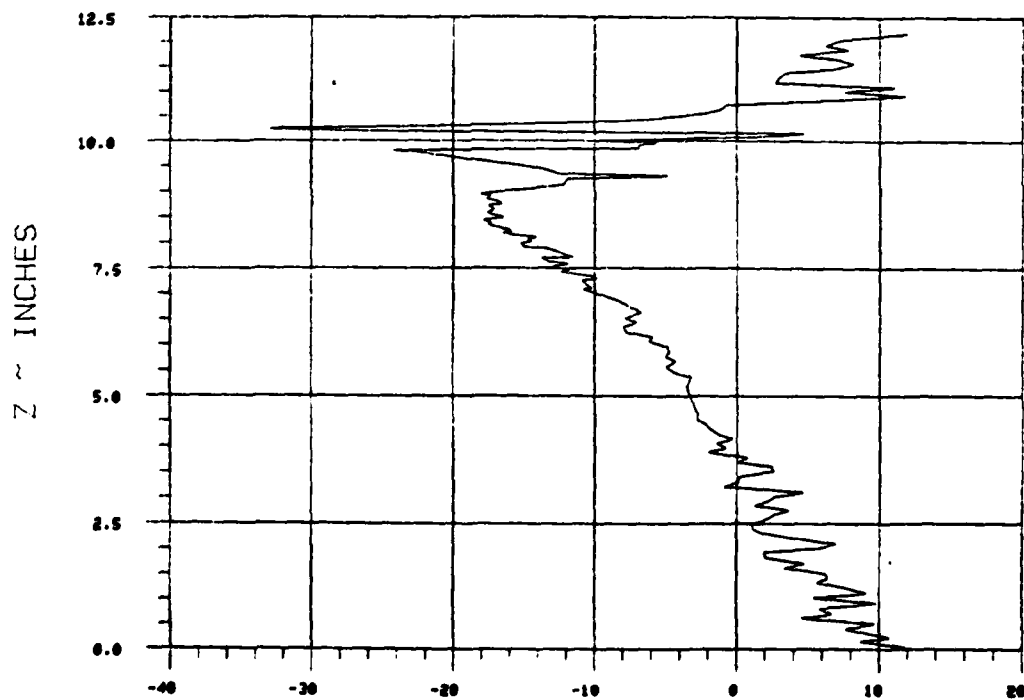
BETA = _30_

Figure III-39.

WAKE SURVEY DATA

TEST _287_ . RUN _32_

ANGLE OF ATTACK _0_ NOMINAL JET ANGLE _70_ C MU _1.0394_
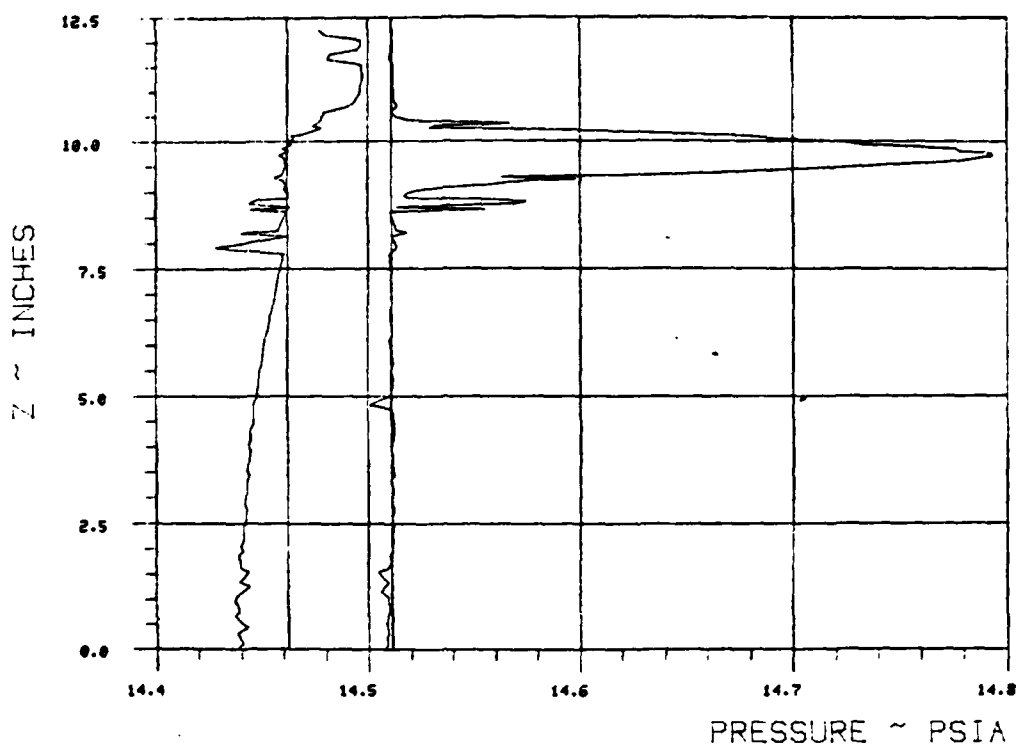
PRESSURE ~ PSIA

Xss/chord = _1.015_   Yss/chord = _.472_

BETA = _30_

ALPHA ~ DEGREES

Figure III-40.

221
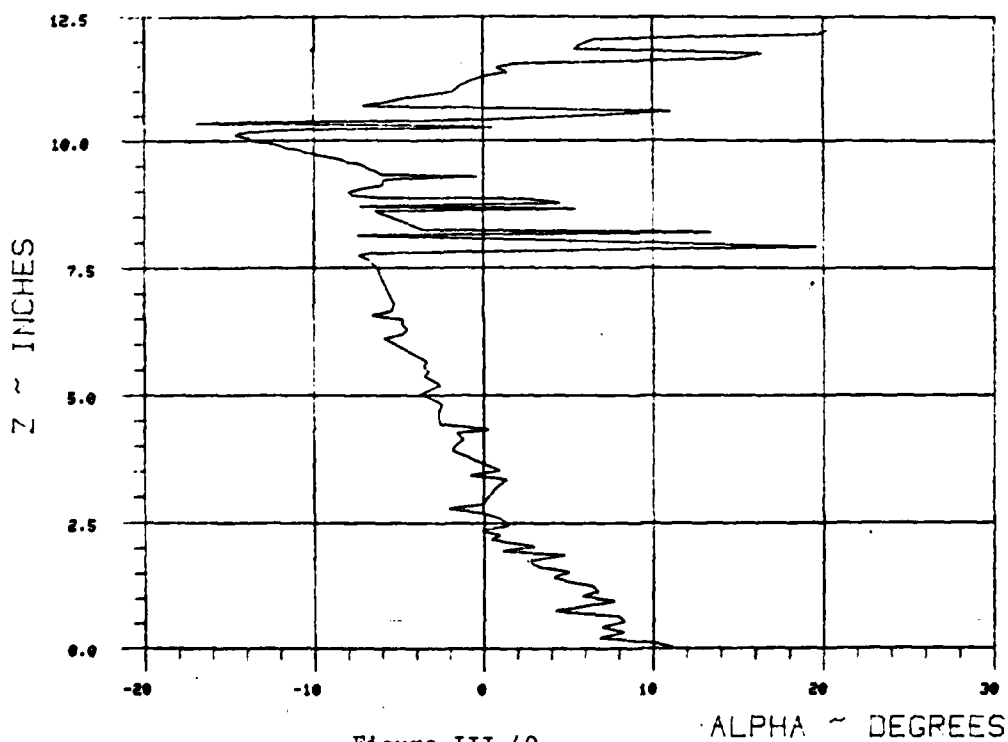
WAKE SURVEY DATA

TEST _287_ RUN _33_

ANGLE OF ATTACK _0_ NOMINAL JET ANGLE _70_ C MU _1.0639_
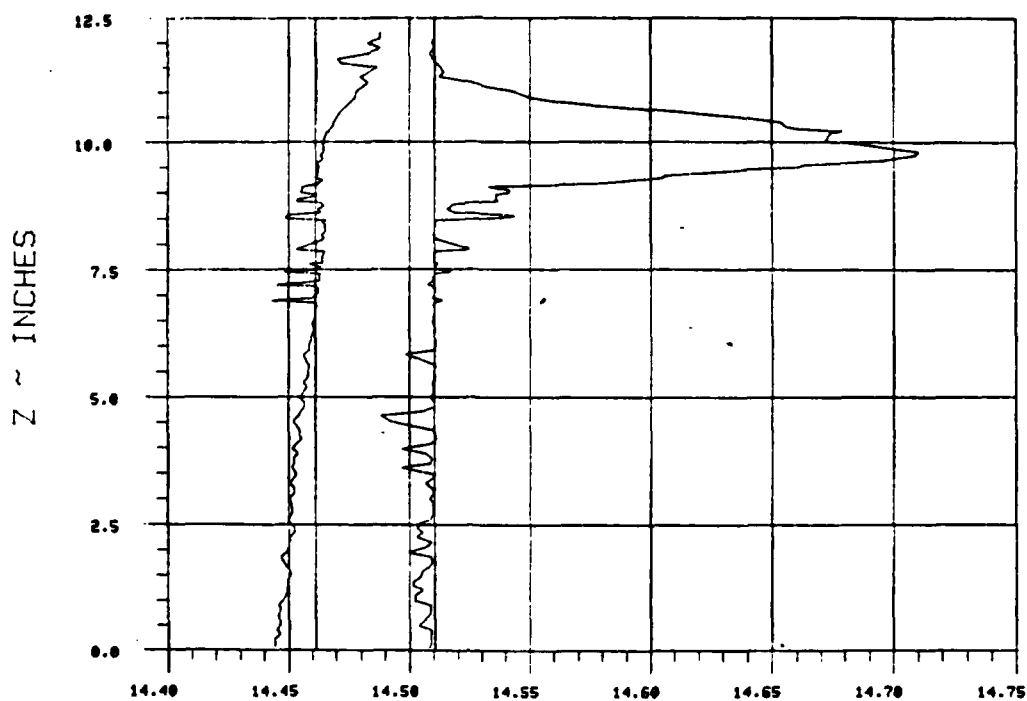
Xss/chord = _1.34_   Yss/chord = _.285_

BETA = _30_
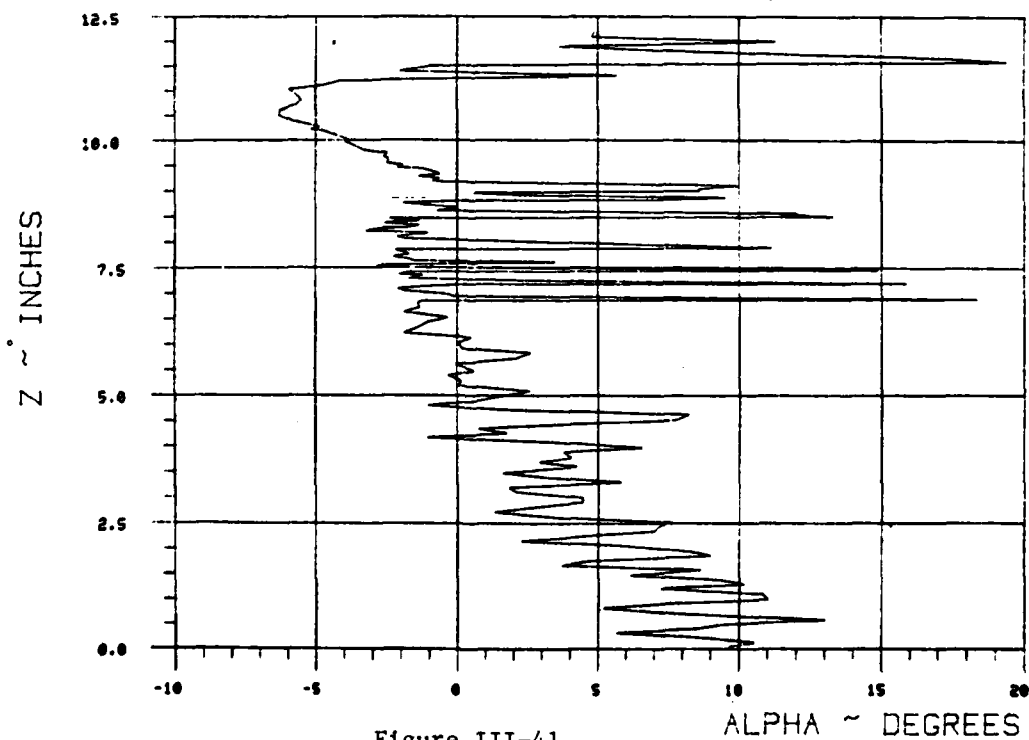
Figure III-41.

WAKE SURVEY DATA

TEST **287** RUN **34**

ANGLE OF ATTACK **0** NOMINAL JET ANGLE **70** C MU **2.1181**
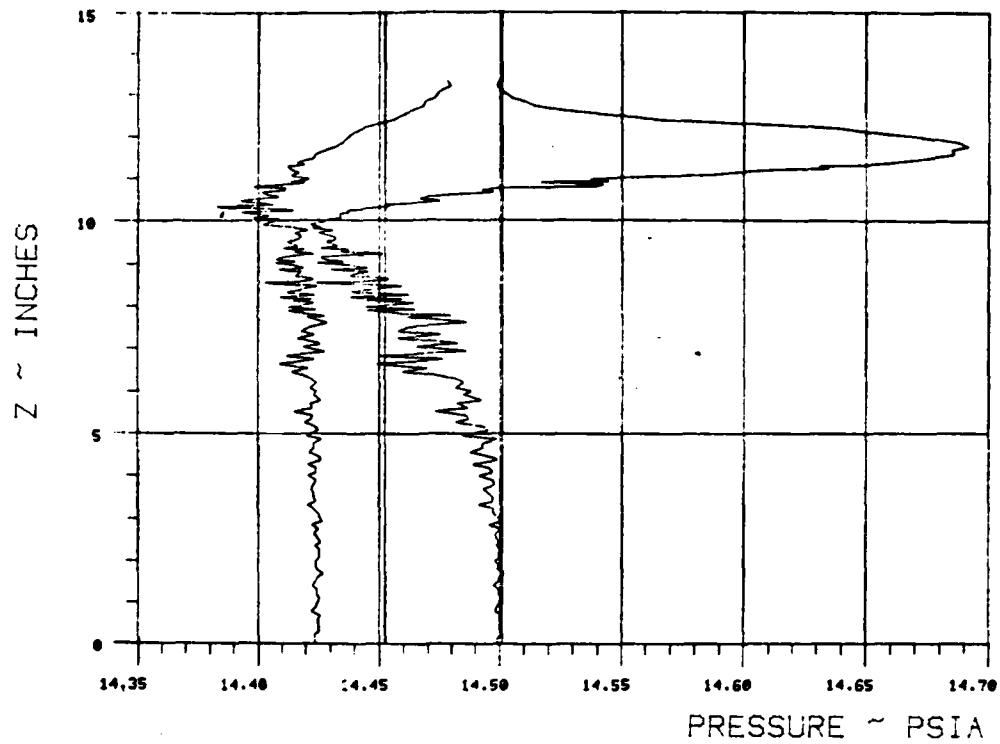
X_{ss}/chord = **1.14** Y_{ss}/chord = **.688**

BETA = **30**

Figure III-42.

223
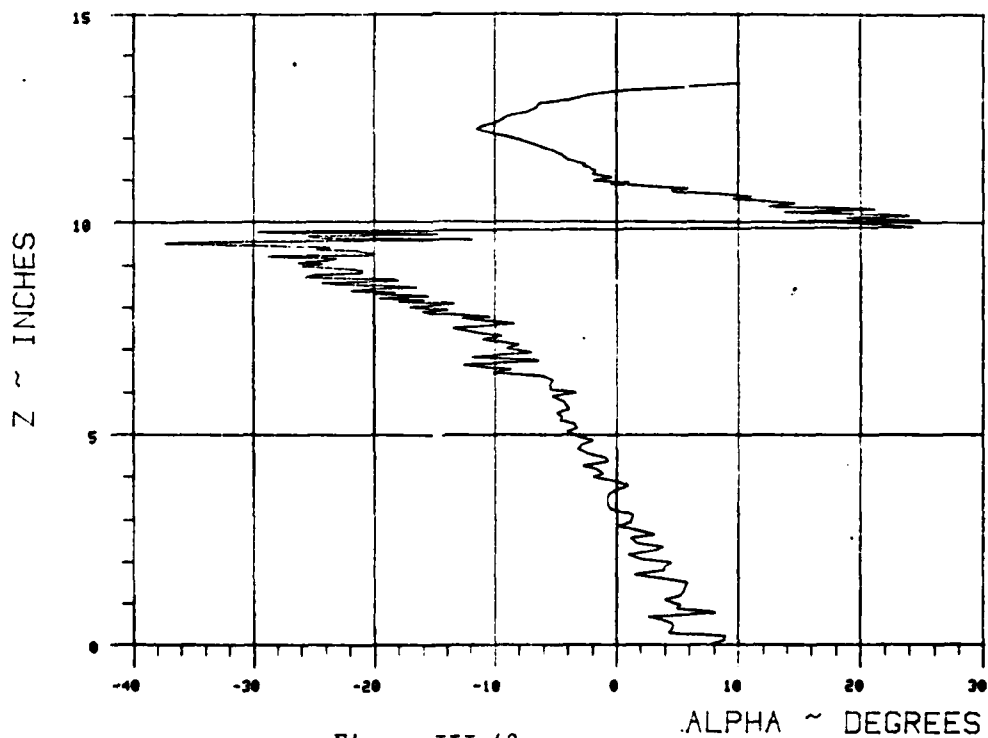
WAKE SURVEY DATA

TEST _287_ RUN _35_

ANGLE OF ATTACK _0_ NOMINAL JET ANGLE _70_ C MU _4.1694_
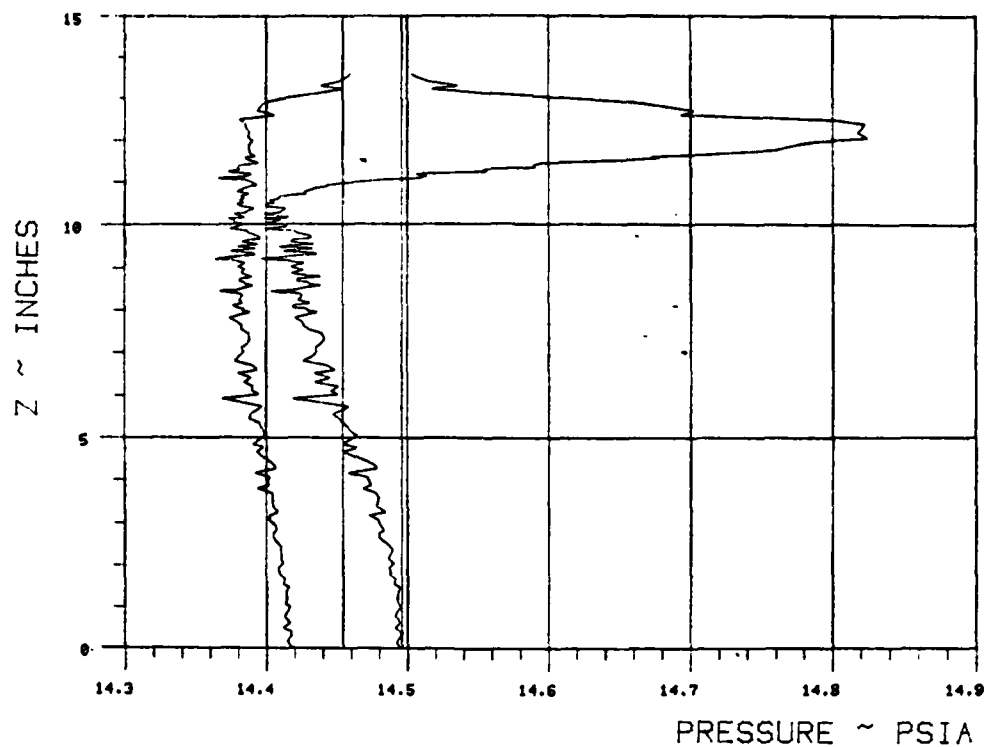
Xss/chord = _1.14_   Yss/chord = _.688_

BETA = _30_

Figure III-43.

224
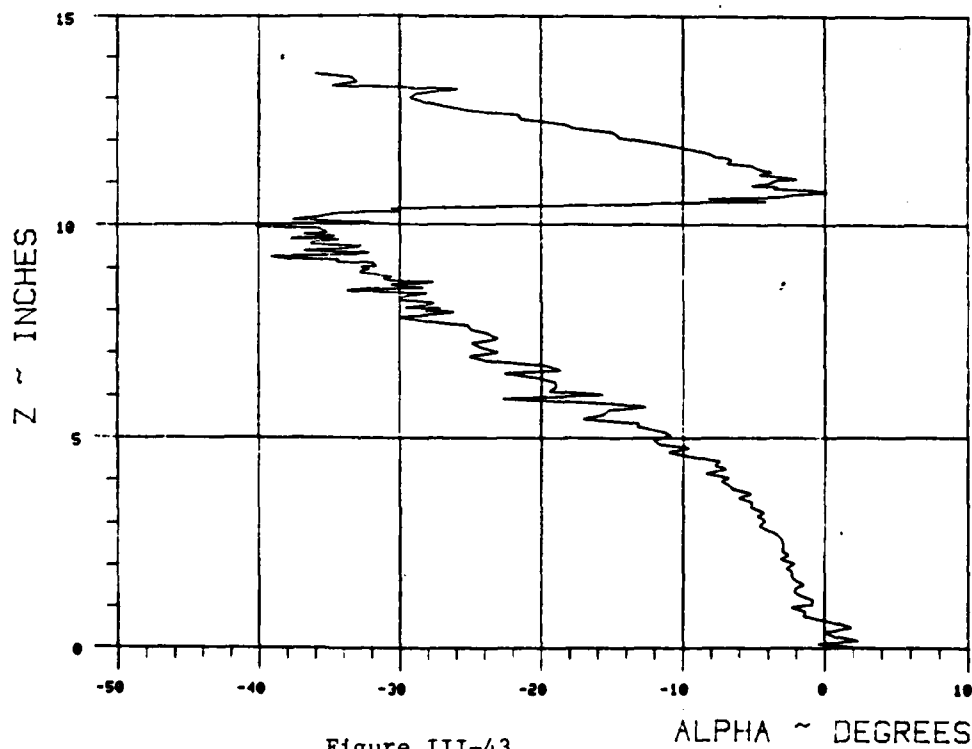
WAKE SURVEY DATA

TEST _287_ RUN _1_

ANGLE OF ATTACK _O_ NOMINAL JET ANGLE _90_ C MU _.9412_
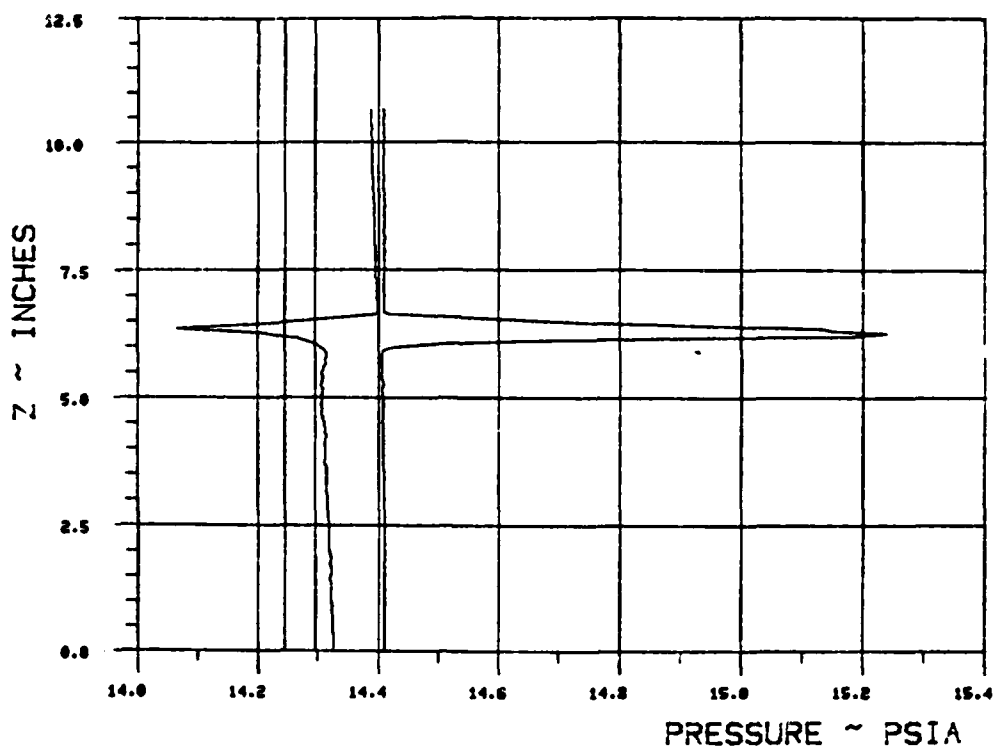
Xss/chord = _.6733_ Yss/chord = _.7222_

BETA = _30_
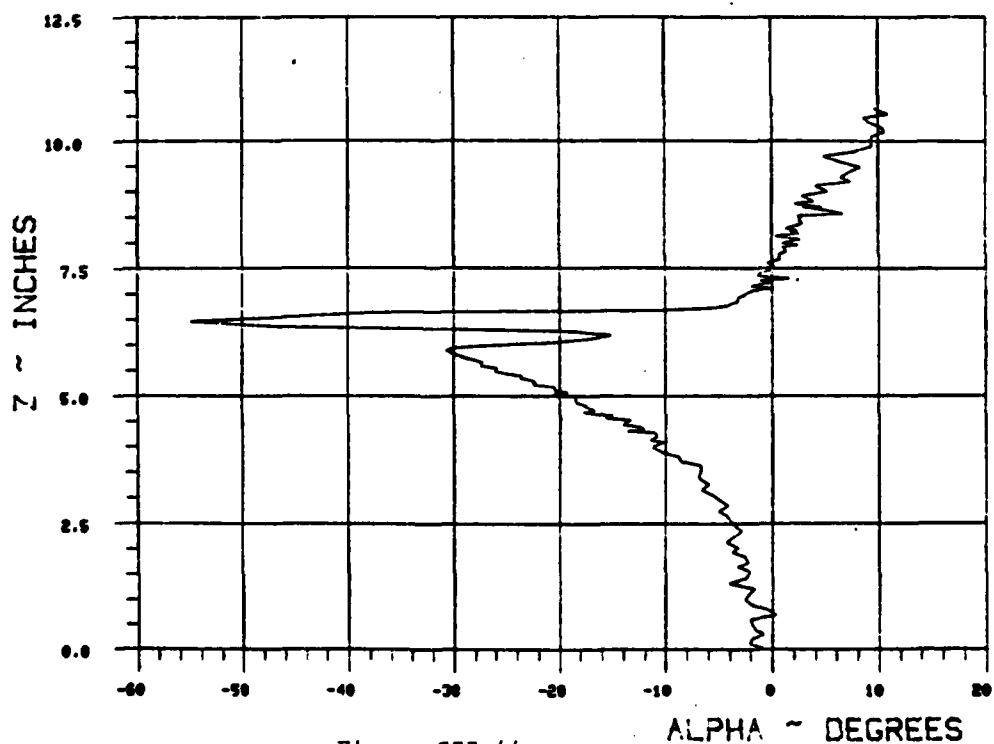
Figure III-44.

WAKE SURVEY DATA

TEST 287 RUN 2

ANGLE OF ATTACK 0 NOMINAL JET ANGLE 90 C MU .9367
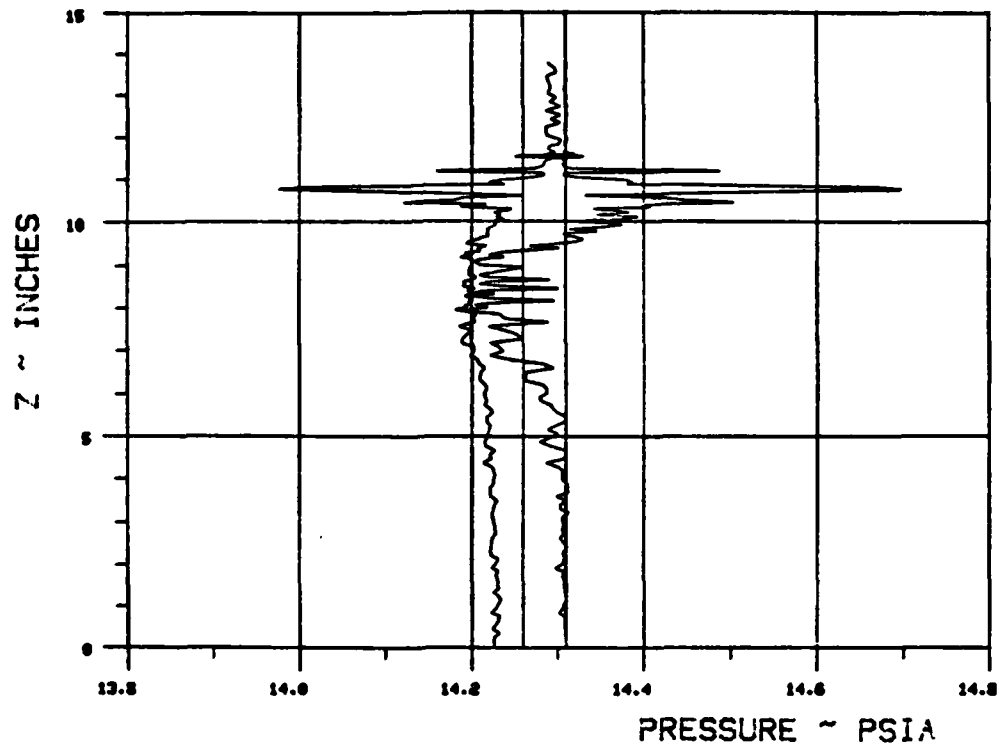
Xss/chord = .7816   Yss/chord = .6597

BETA = 30
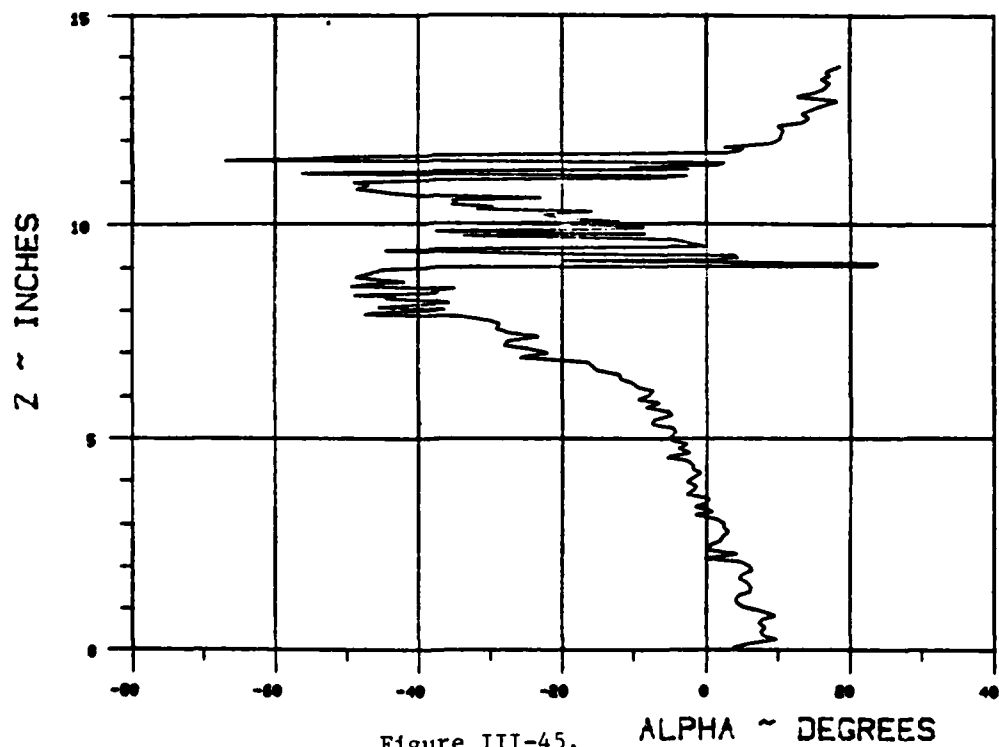
Figure III-45.

WAKE SURVEY DATA

TEST *287* RUN *3*

ANGLE OF ATTACK *6* NOMINAL JET ANGLE *90* C MU *.9319*
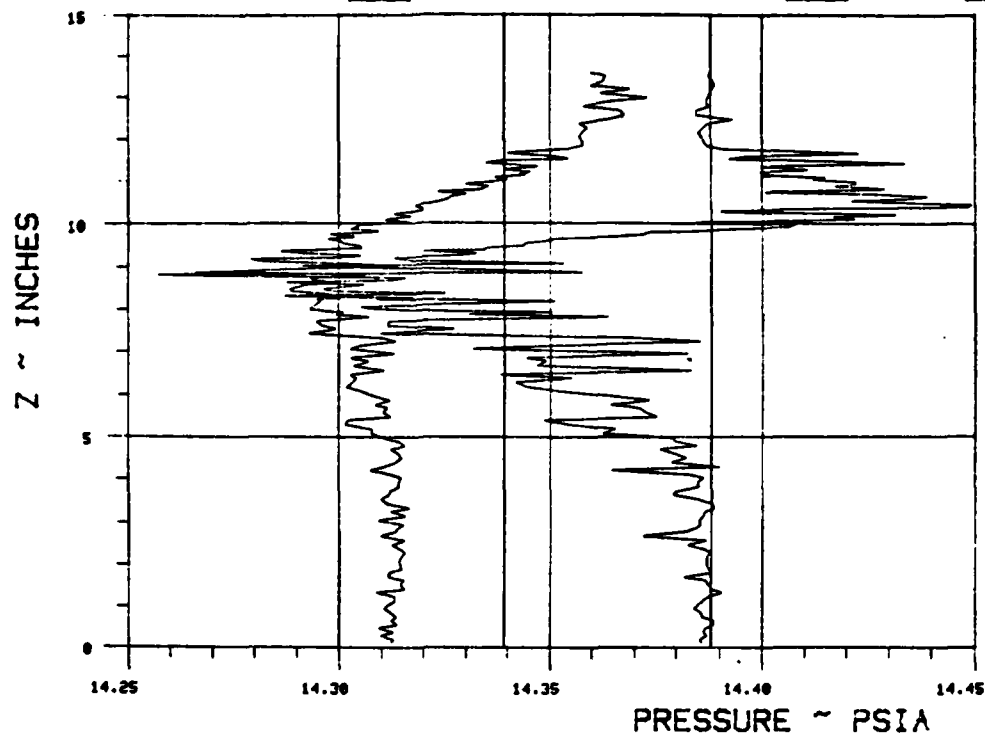
Xee/chord = *.8898* Yee/chord = *.5972*

BETA = *30*
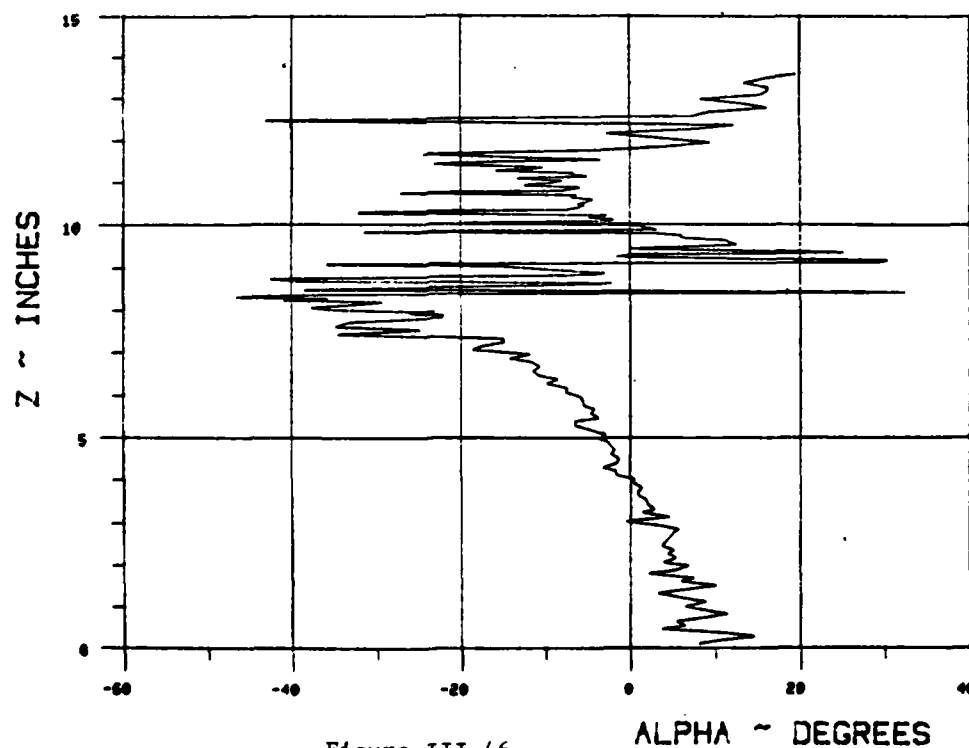
Figure III-46.

WAKE SURVEY DATA

TEST _287_ RUN _4_

ANGLE OF ATTACK _O_ NOMINAL JET ANGLE _90_ C MU _.9774_

PRESSURE ~ PSIA

Xee/chord = _1.1064_ Yee/chord = _.4722_

BETA = _30_

ALPHA ~ DEGREES
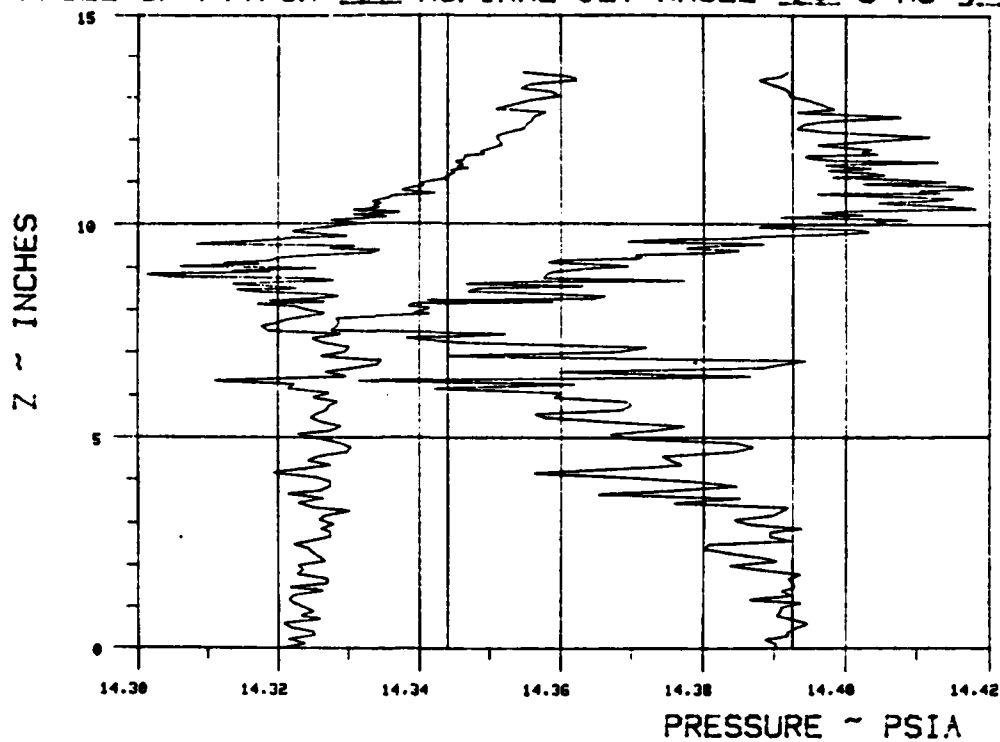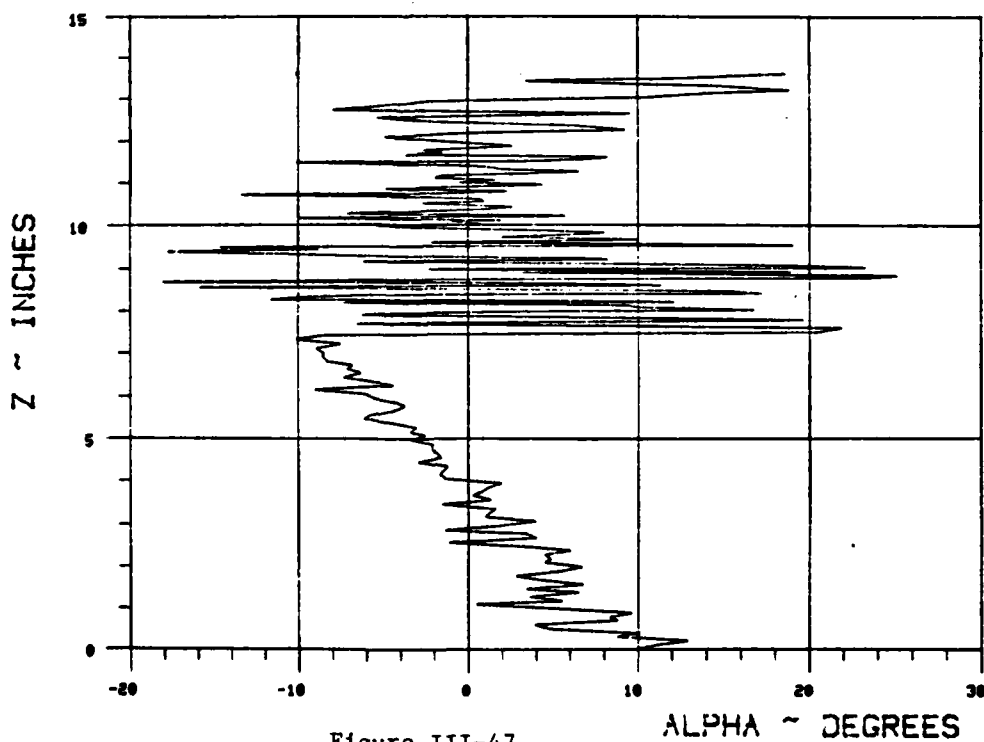
Figure III-47.

WAKE SURVEY DATA
TEST _287_ RUN _5_
ANGLE OF ATTACK _0_ NOMINAL JET ANGLE _90_ C MU _.9256_
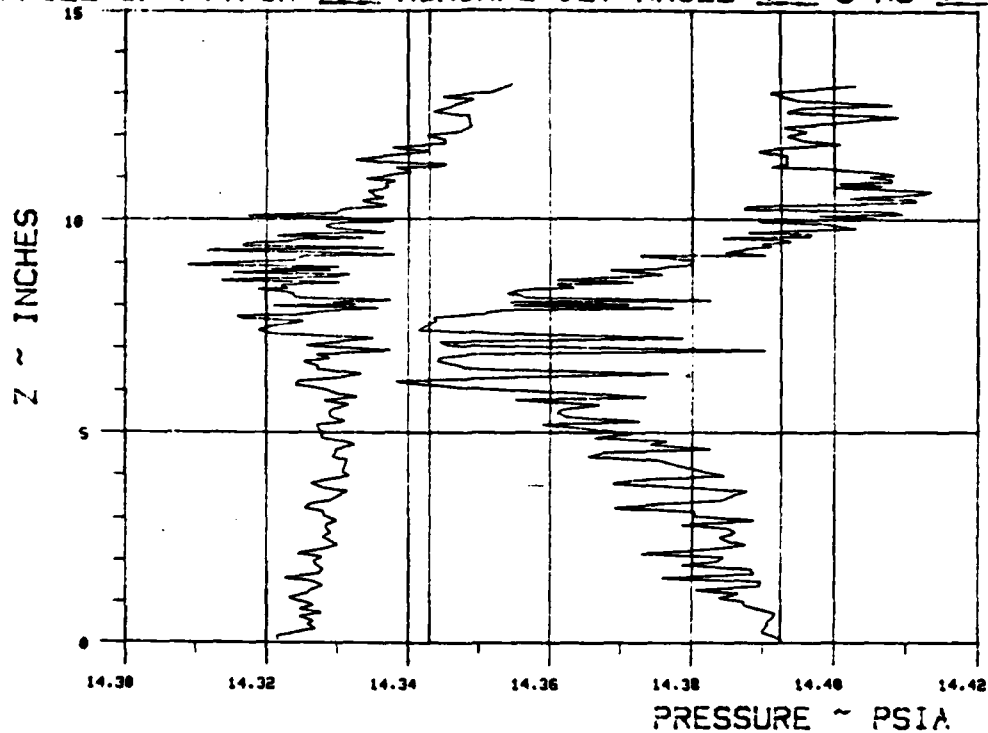
Xee/chord = _1.2146_ Yee/chord = _.4097_

BETA = _30_
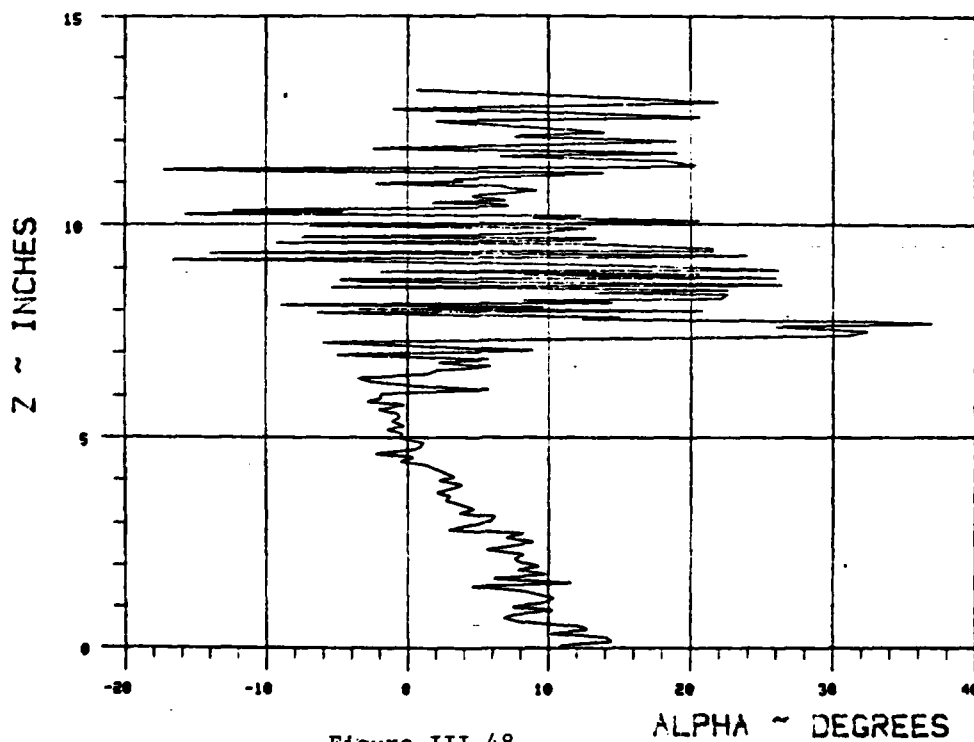
Figure III-48.

WAKE SURVEY DATA
TEST _287_ RUN _6_
ANGLE OF ATTACK _O_ NOMINAL JET ANGLE _90_ C MU _1.8816_

PRESSURE ~ PSIA
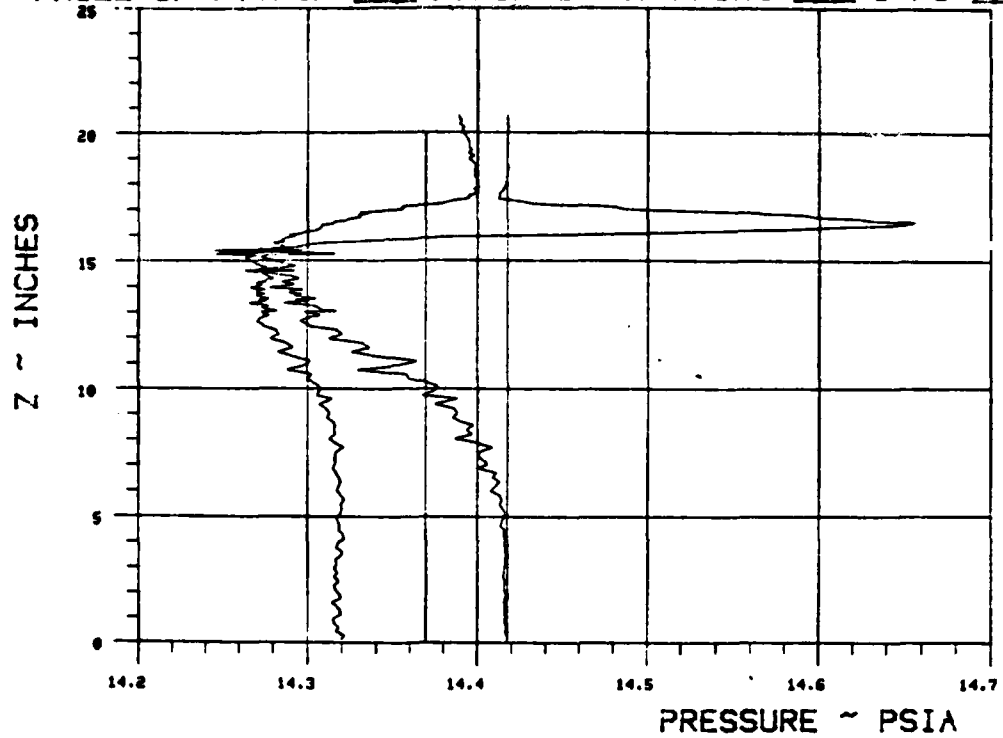
Xₑₑ/chord = _1.4419_ Yₑₑ/chord = _1.1244_

BETA = _45_

ALPHA ~ DEGREES

Figure III-49.

230
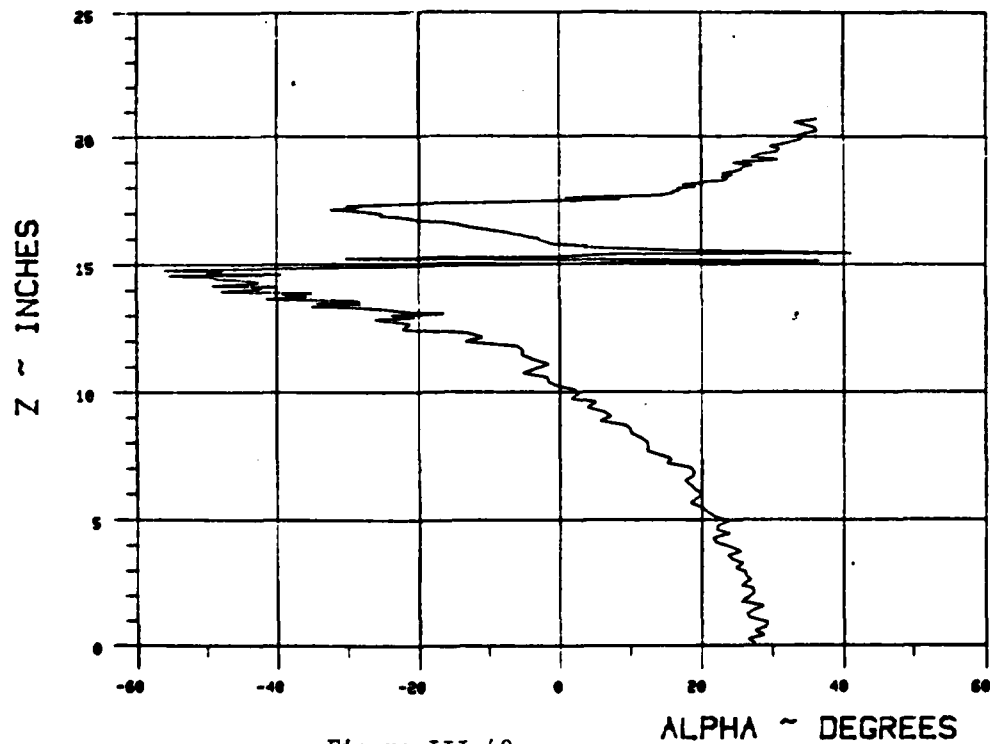
WAKE SURVEY DATA

TEST _287_ RUN _1_

ANGLE OF ATTACK _0_ NOMINAL JET ANGLE _90_ C MU _1.9165_
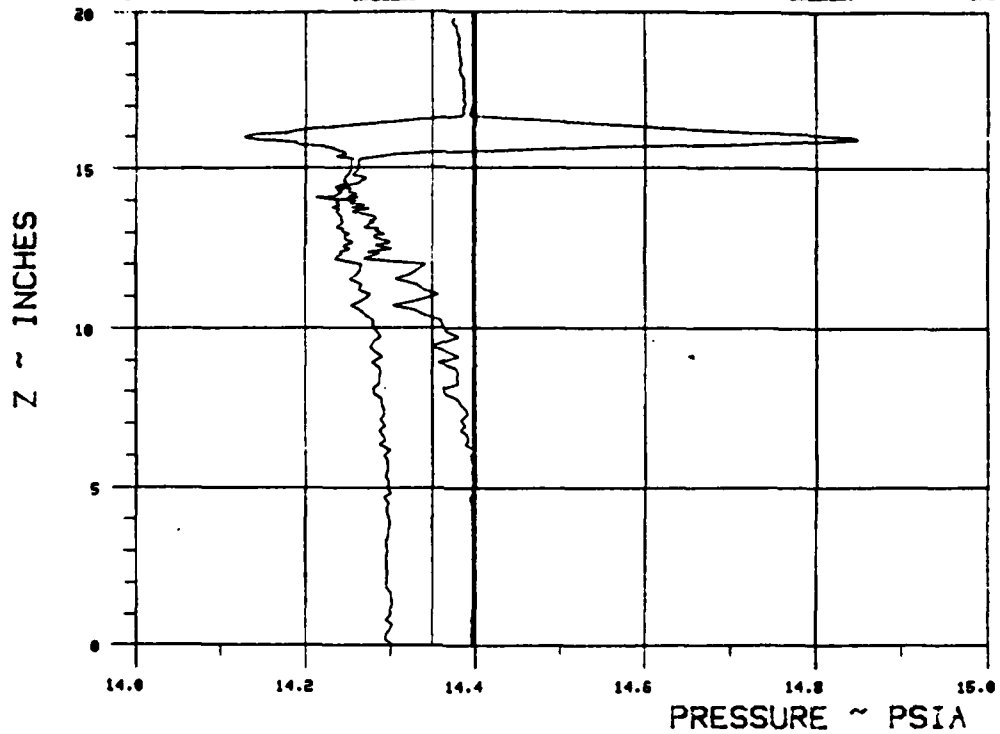
Xss/chord = _1.5303_ Yss/chord = _1.036_

BETA = _45_
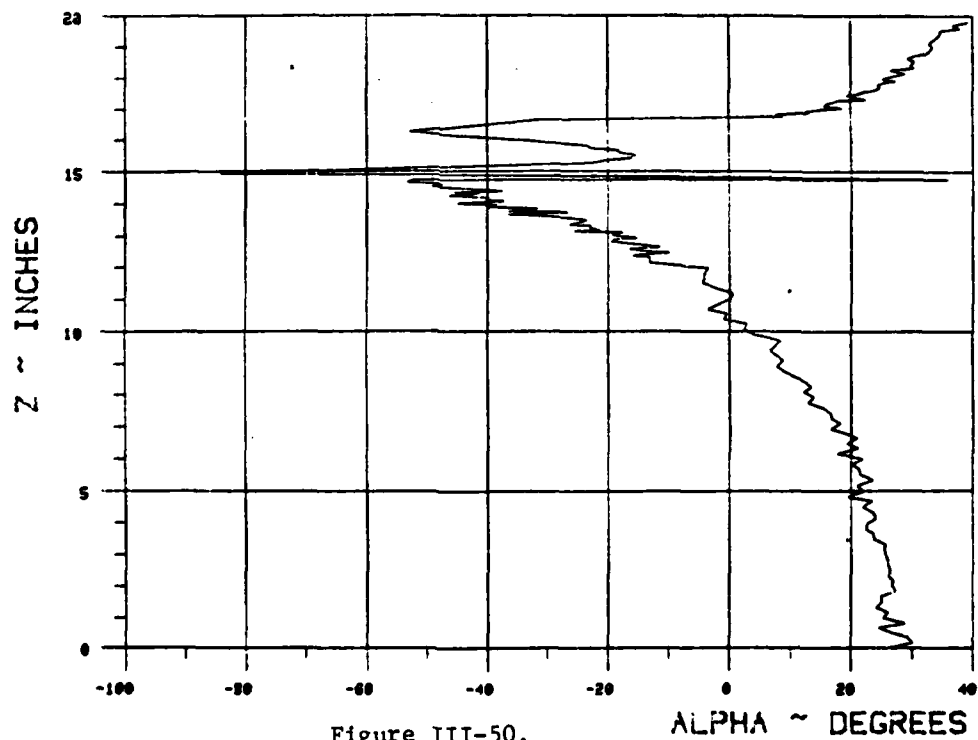
Figure III-50.

WAKE SURVEY DATA

TEST _287_ RUN _8_

ANGLE OF ATTACK _6_ NOMINAL JET ANGLE _90_ C MU _1.8849_

PRESSURE ~ PSIA
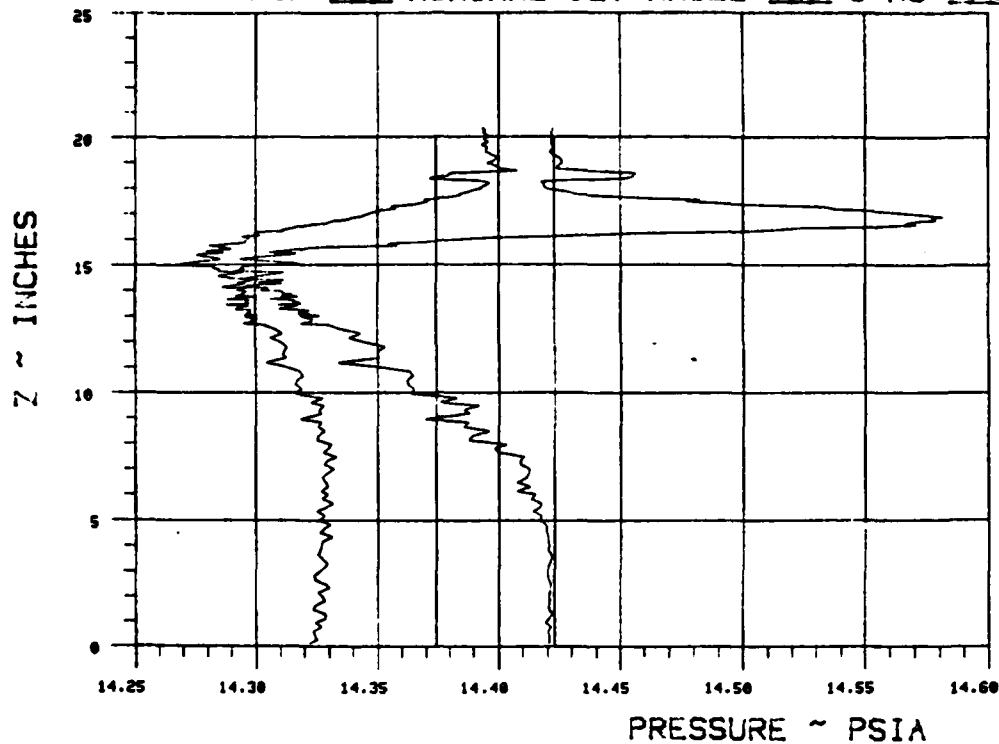
Xss/chord = _1.6187_ Yss/chord = _.9477_

BETA = _45_

ALPHA ~ DEGREES
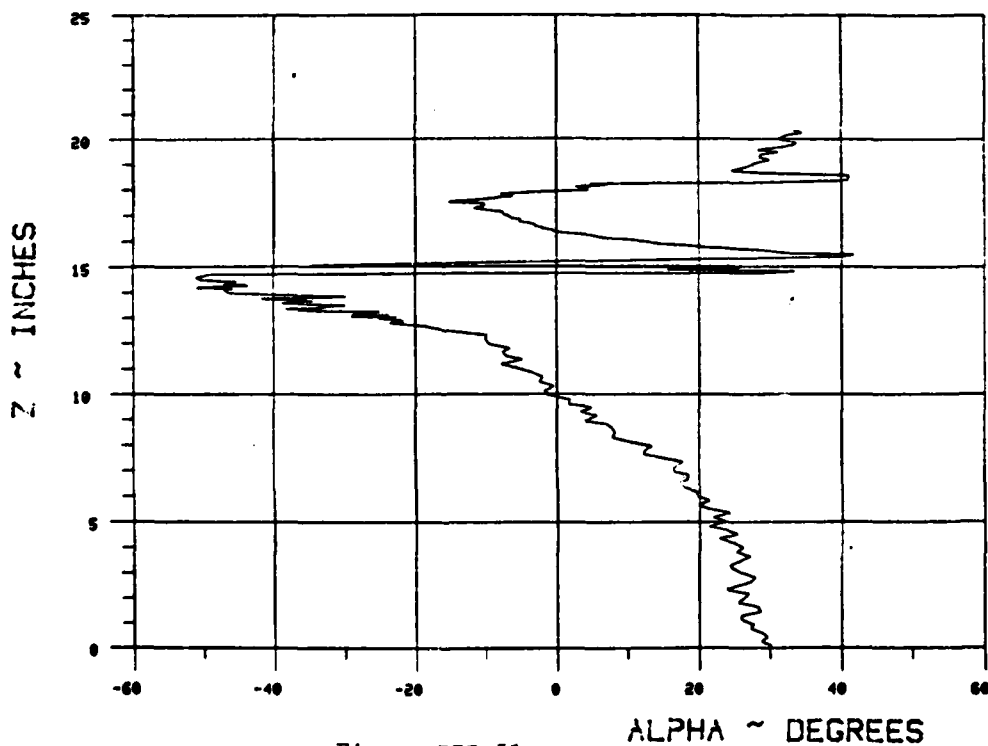
Figure III-51.

WAKE SURVEY DATA
TEST 287 RUN 9
ANGLE OF ATTACK 0 NOMINAL JET ANGLE 90 C MU 1.9428

PRESSURE ~ PSIA
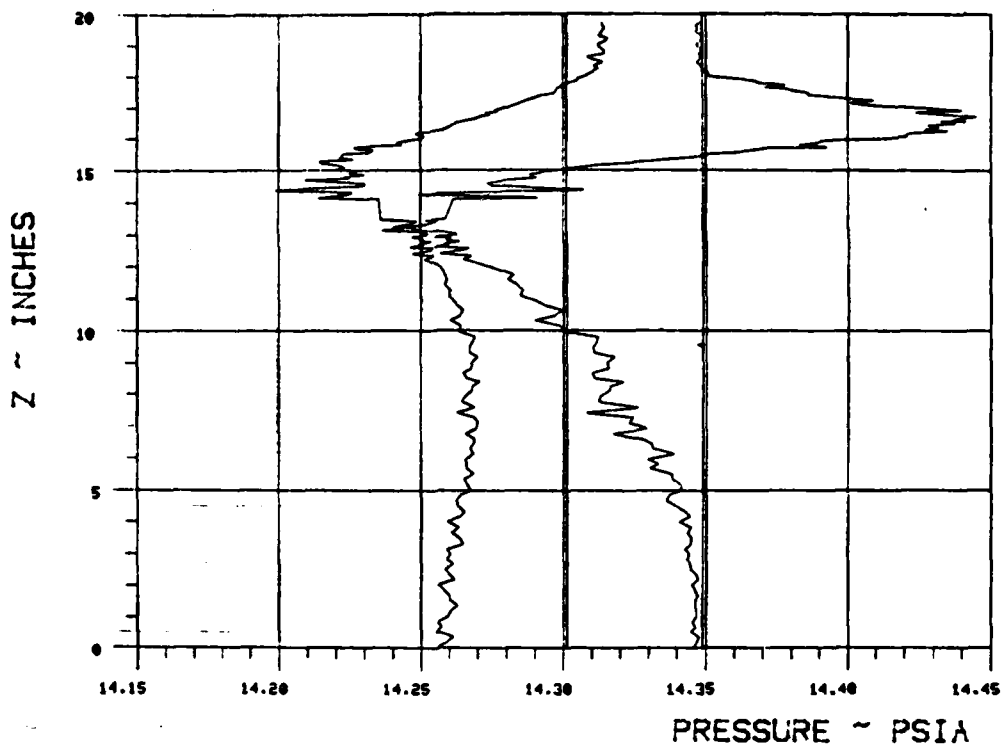
X_{ee}/chord = 1.7955 Y_{ee}/chord = .7109

BETA = 45

ALPHA ~ DEGREES

Figure III-52.

233
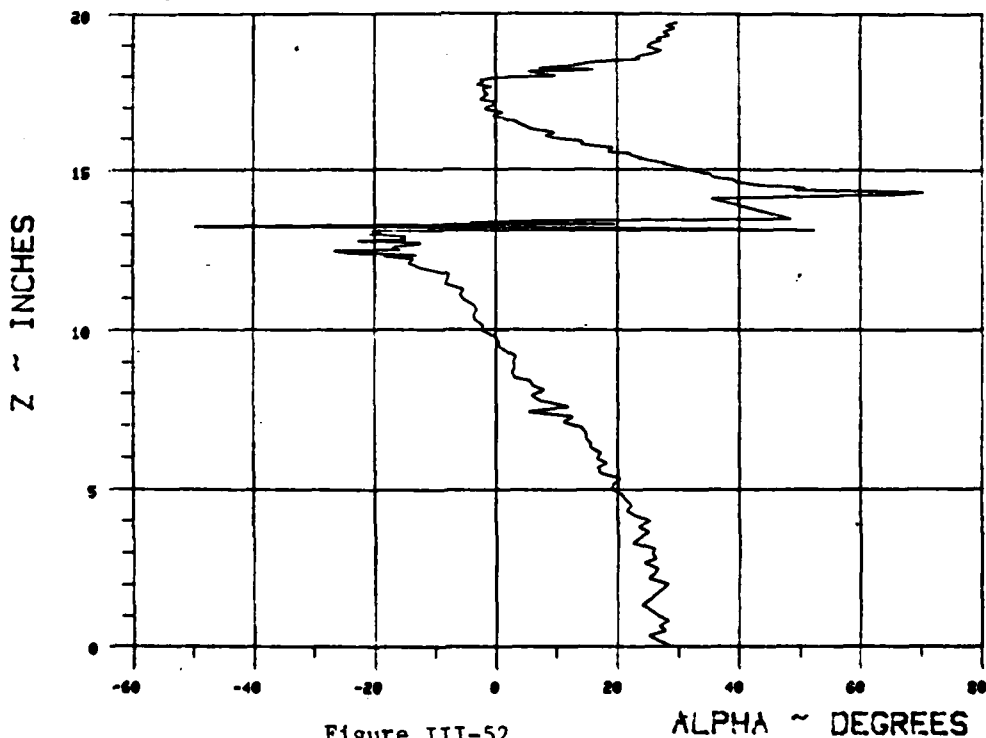
WAKE SURVEY DATA
TEST _287_ RUN _10_

ANGLE OF ATTACK _O_ NOMINAL JET ANGLE _90_ C MU _1.8989_
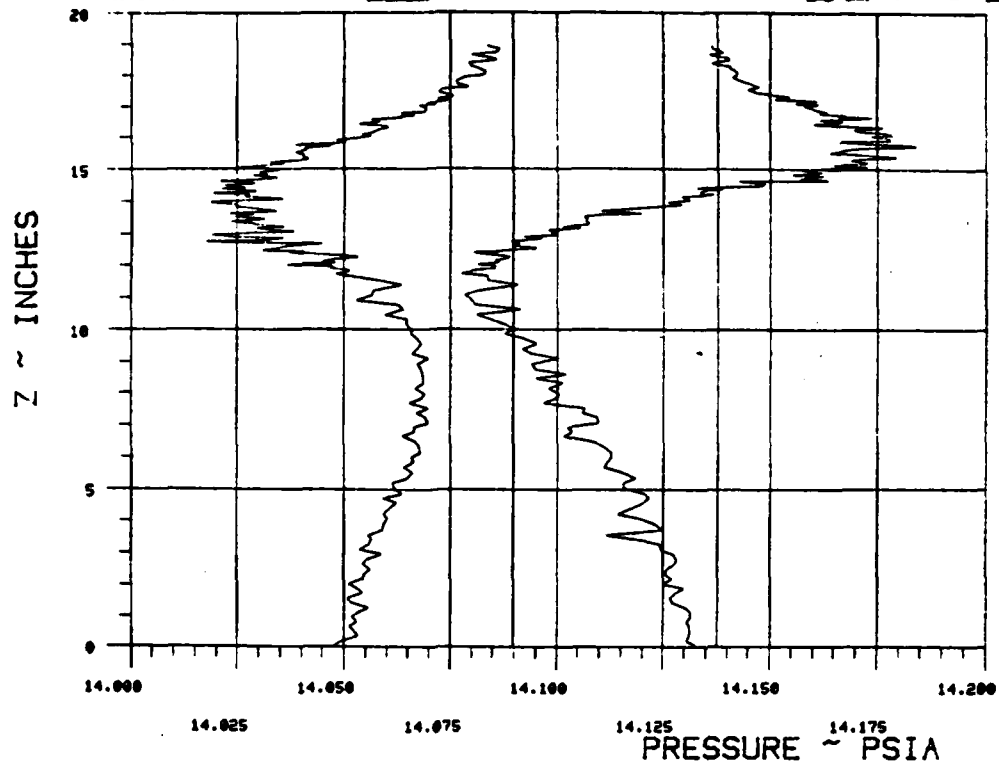
Xee/chord = _2.0607_ Yee/chord = _.5057_

BETA = _45_

Figure III-53.

234
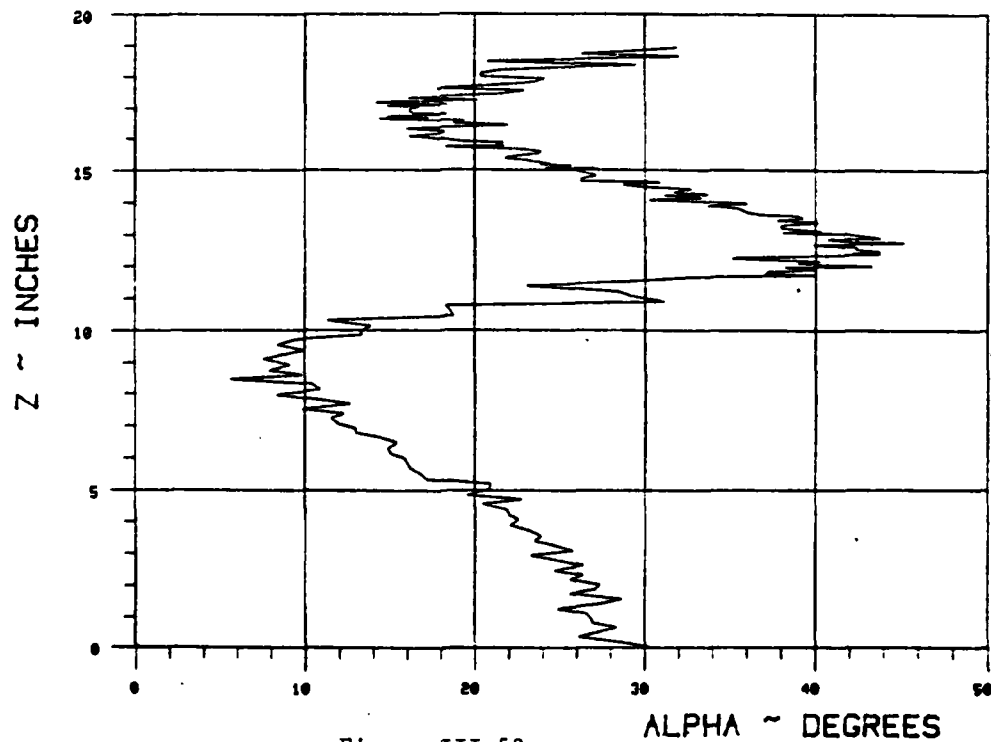
WAKE SURVEY DATA

TEST 287 RUN 11

ANGLE OF ATTACK 0 NOMINAL JET ANGLE 90 C MU 3.7314

PRESSURE ~ PSIA
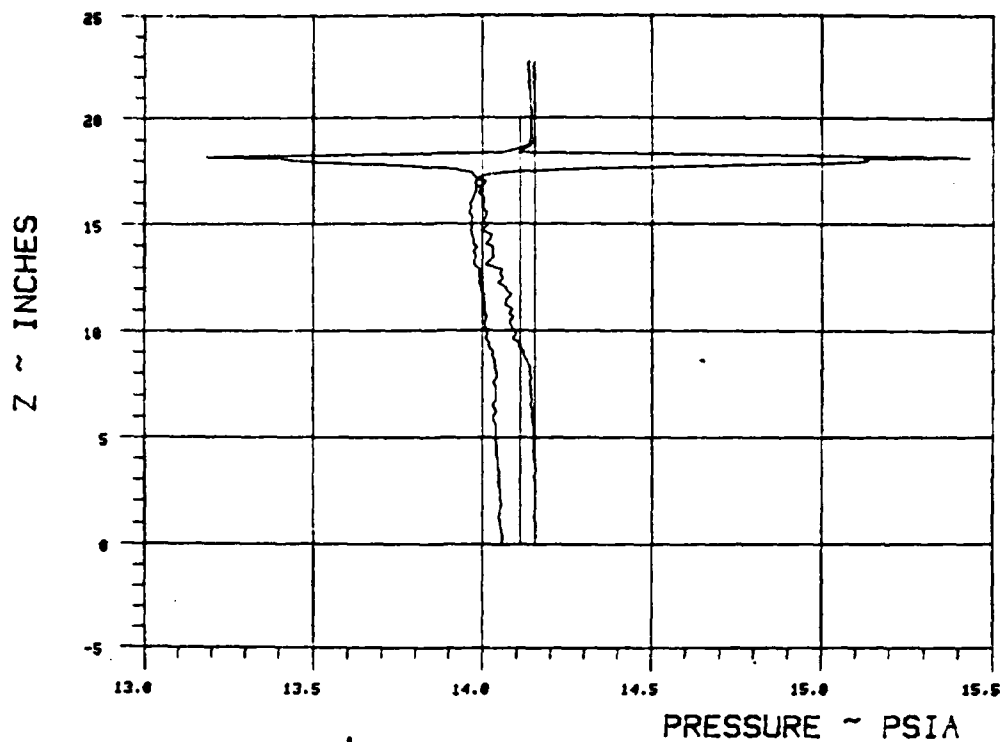
Xss/chord = 1.6189 Yss/chord = 1.3014

BETA = 45

ALPHA ~ DEGREES
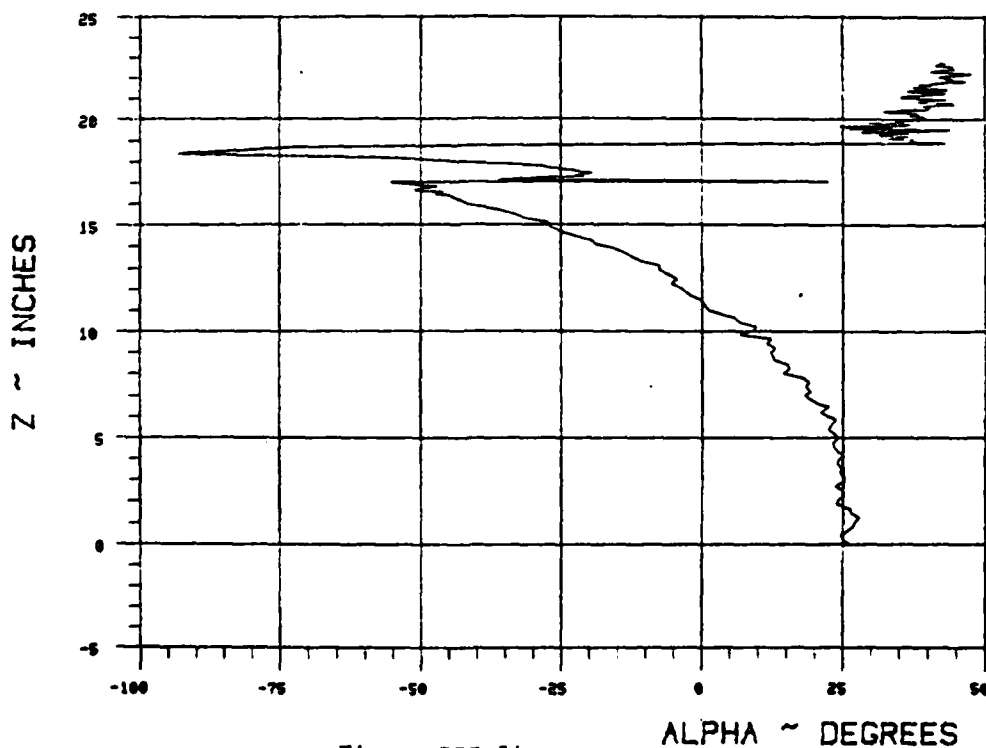
Figure III-54.

WAKE SURVEY DATA
TEST _287_ RUN _12_
ANGLE OF ATTACK _O_ NOMINAL JET ANGLE _90_ C MU _3.7542_

PRESSURE ~ PSIA
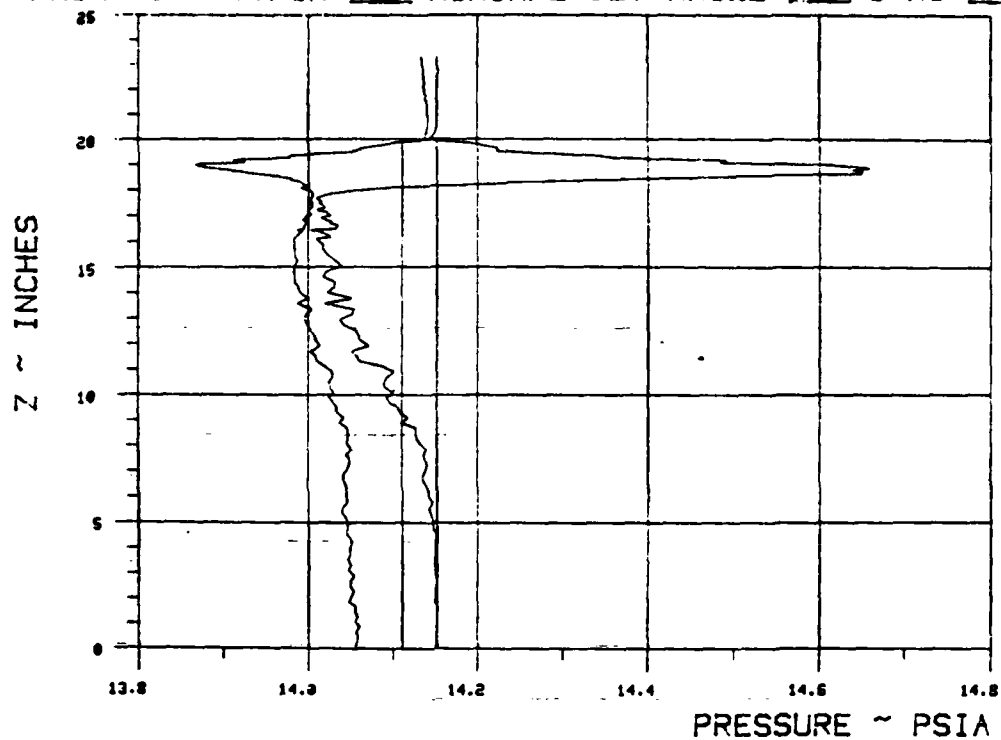
Xss/chord = _1.7073_ Yss/chord = _1.213_

BETA = _45_

ALPHA ~ DEGREES

Figure III-55.

236
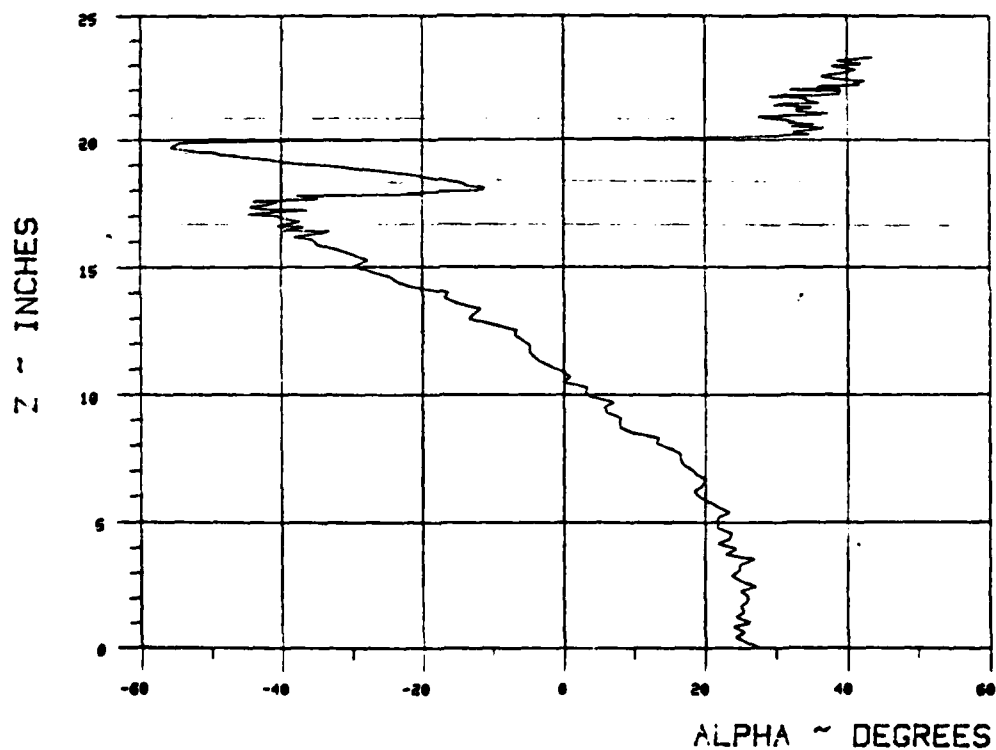
WAKE SURVEY DATA

TEST 287 RUN 13

ANGLE OF ATTACK 0 NOMINAL JET ANGLE 90 C MU 3.741
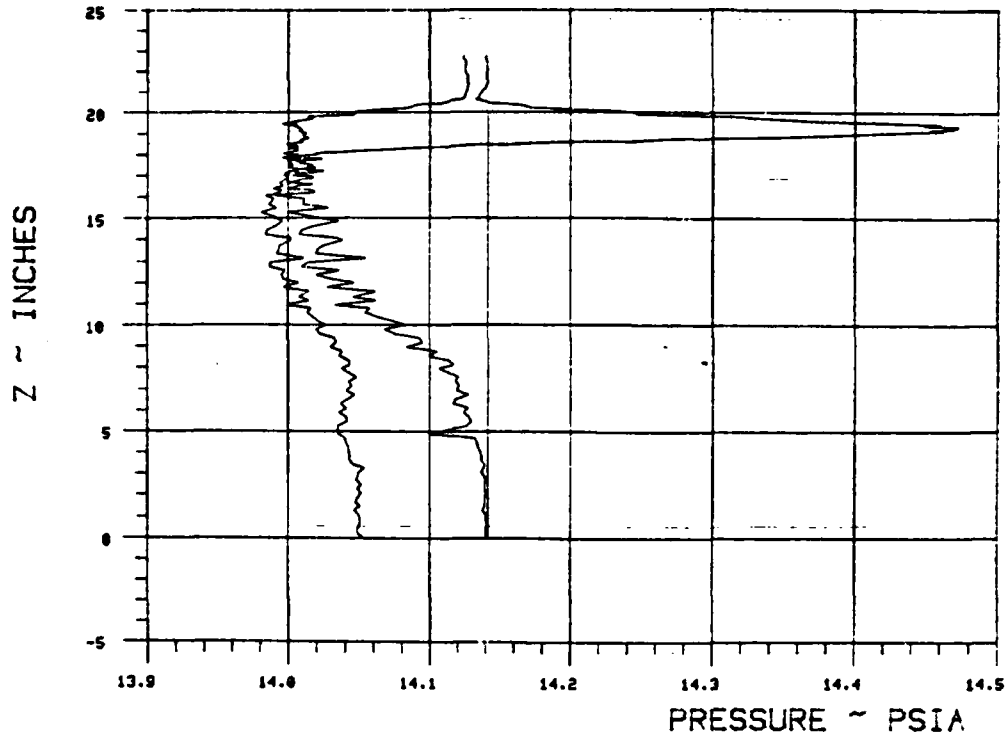
Xes/chord = 1.7956 Yes/chord = 1.1246

BETA = 45
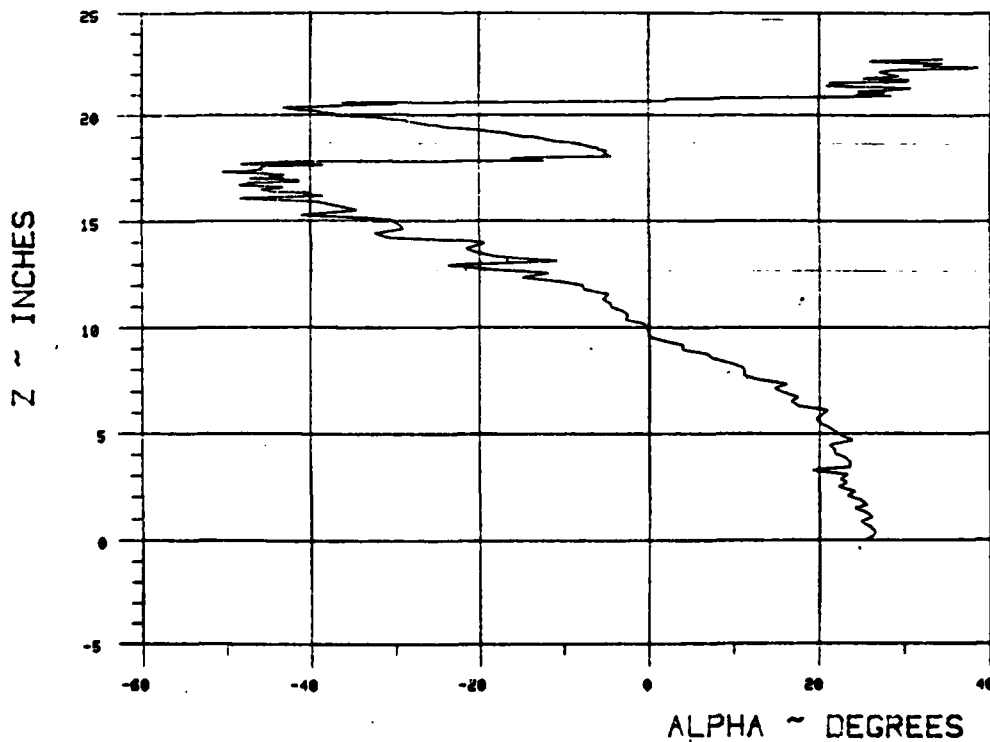
Figure III-56.

WAKE SURVEY DATA
TEST _287_ RUN _14_
ANGLE OF ATTACK _0_ NOMINAL JET ANGLE _90_ C MU _3.7669_
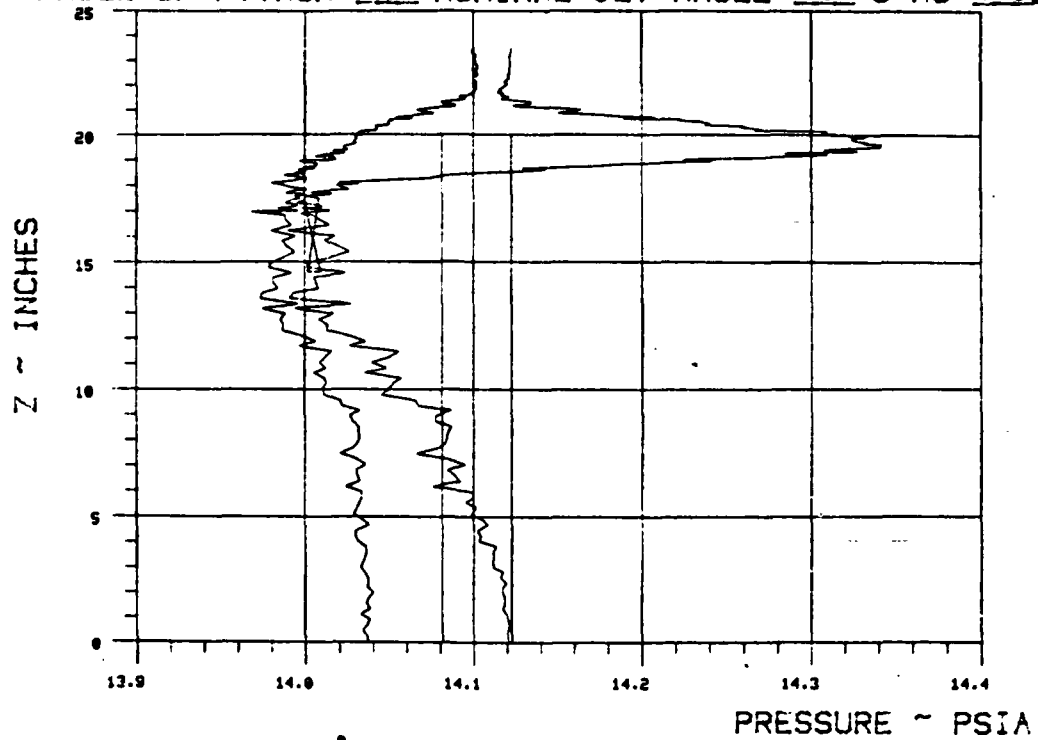
Xss/chord = _1.9724_ Yss/chord = _.9478_

BETA = _45_
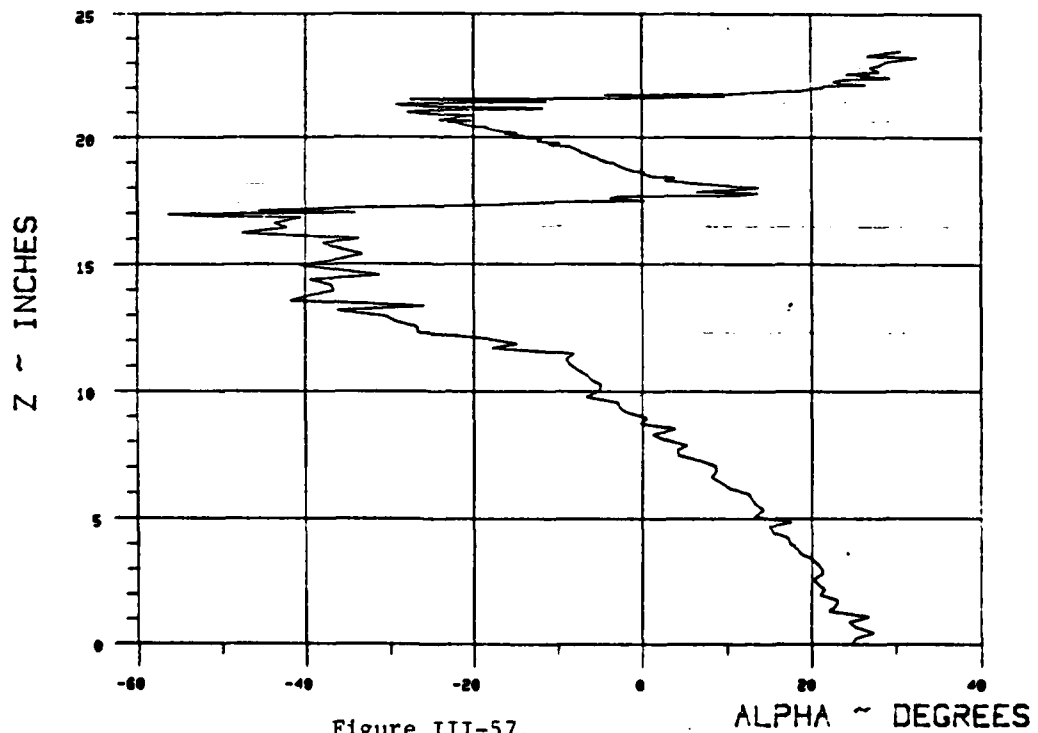
Figure III-57.

WAKE SURVEY DATA
TEST _287_ RUN _15_

ANGLE OF ATTACK _0_ NOMINAL JET ANGLE _90_ C MU _3.6752_
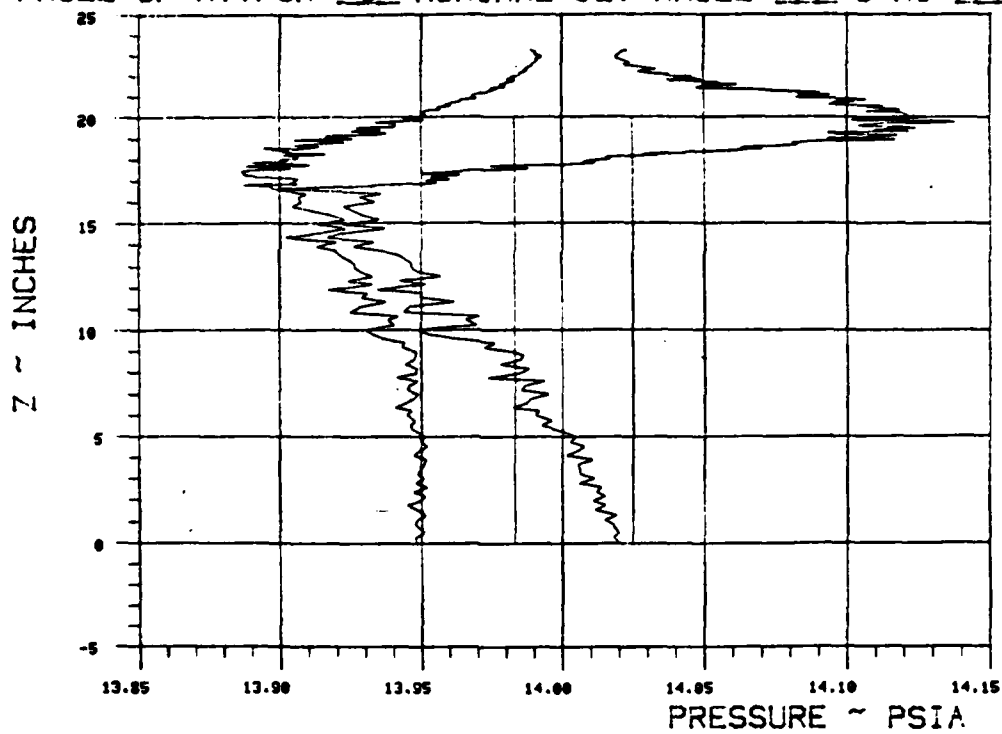
Xee/chord = _2.2376_ Yee/chord = _.6827_

BETA = _45_
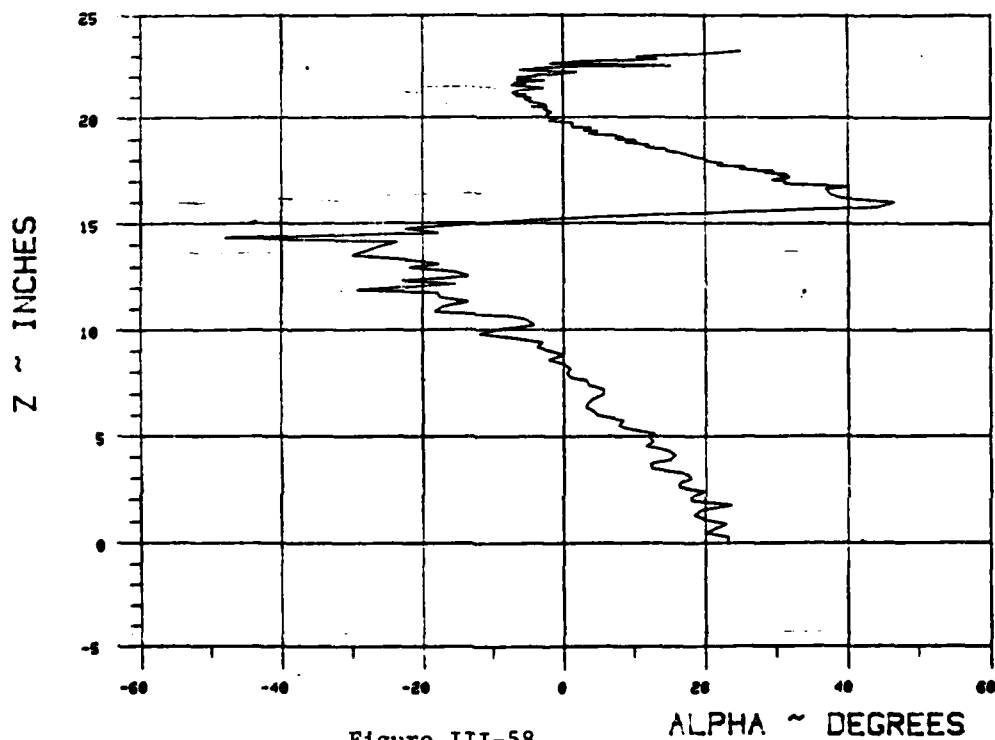
Figure III-58.

WAKE SURVEY DATA

TEST 287 RUN 16

ANGLE OF ATTACK 0 NOMINAL JET ANGLE 90 C MU 7.431
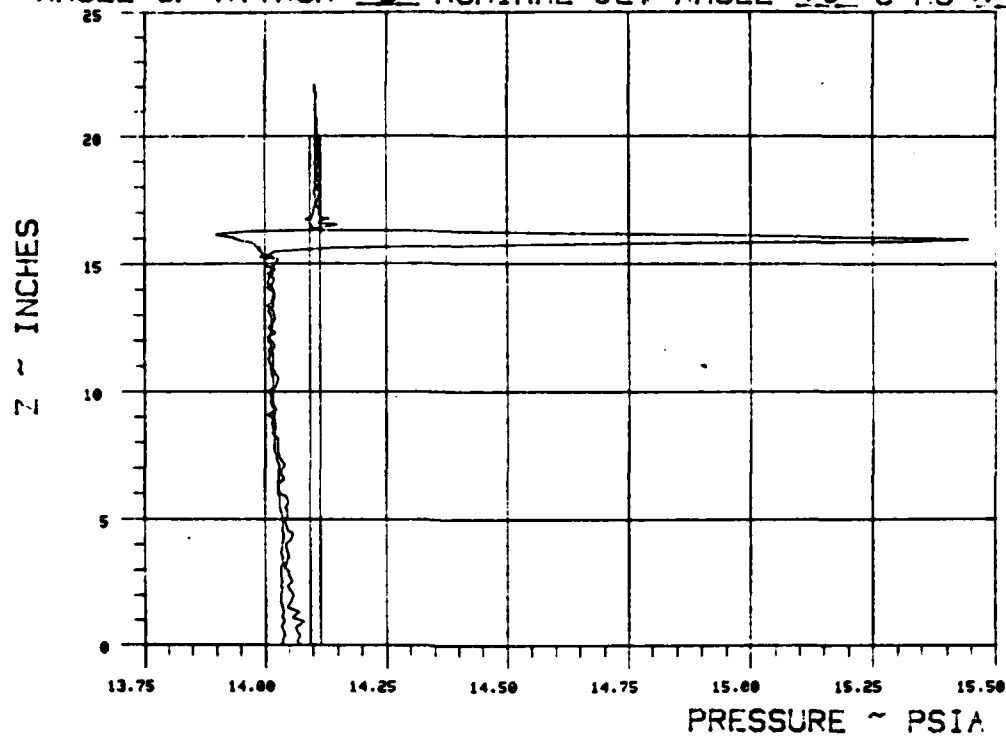
Xss/chord = 1.857 Yss/chord = .382
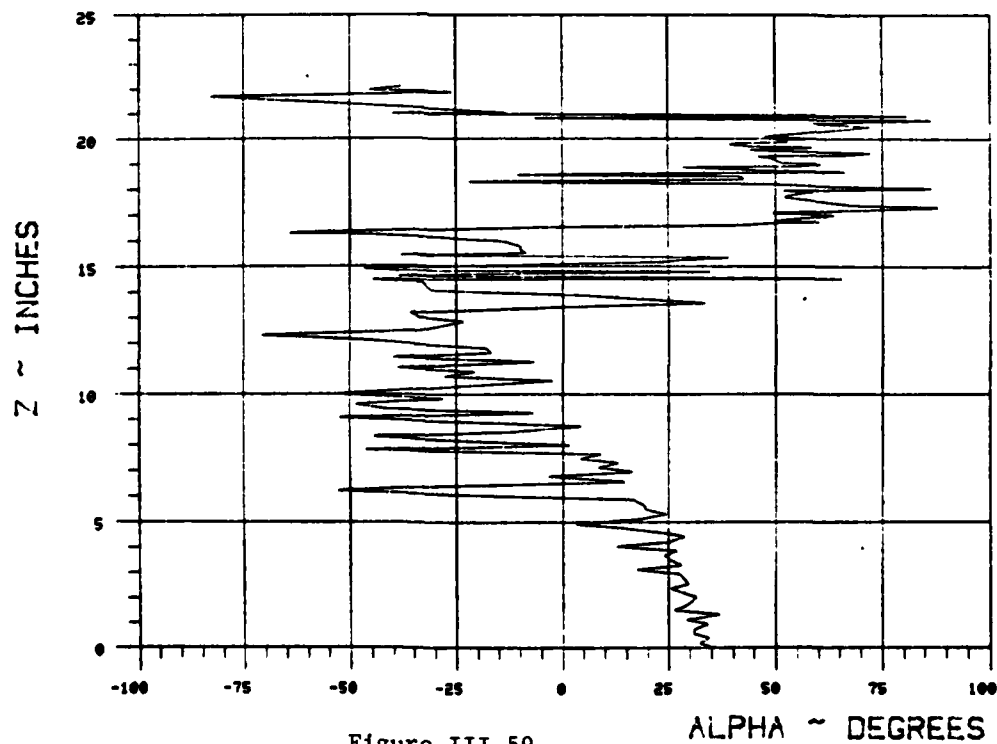
BETA = 70

Figure III-59.

WAKE SURVEY DATA

TEST _2B7_ RUN _17_

ANGLE OF ATTACK _0_ NOMINAL JET ANGLE _90_ C MU _7.4362_

PRESSURE ~ PSIA

Xss/chord = _1.899_   Yss/chord = _.265_

BETA = _70_

ALPHA ~ DEGREES
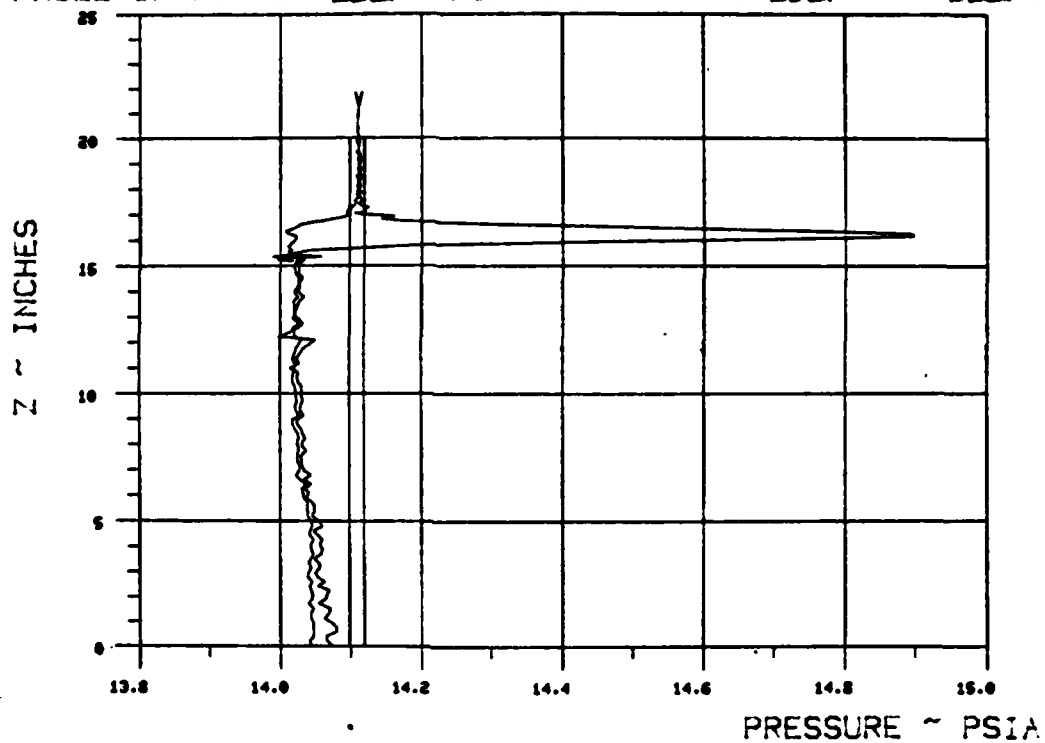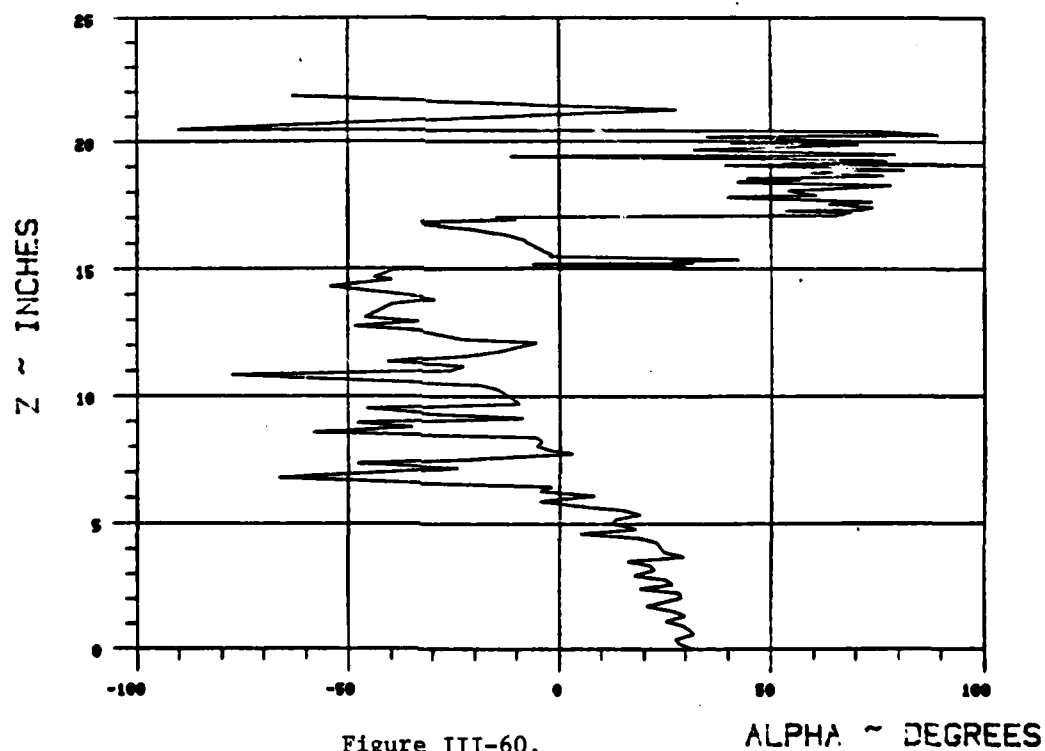
Figure III-60.

WAKE SURVEY DATA
TEST 287 RUN 18
ANGLE OF ATTACK O NOMINAL JET ANGLE 90 C MU 7.3527
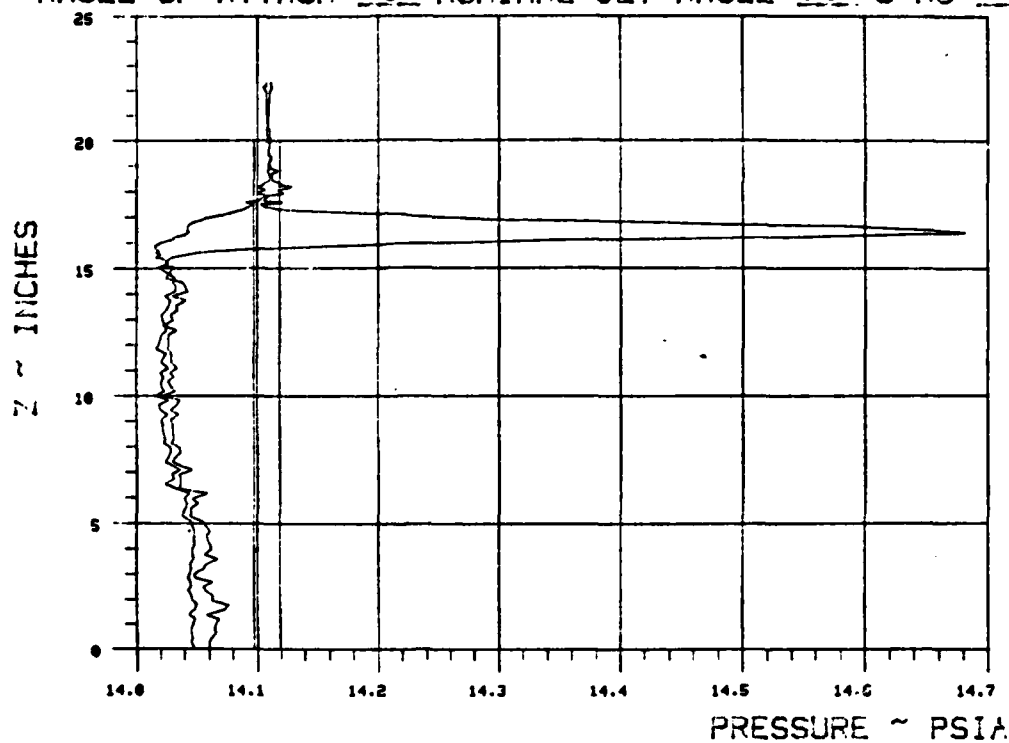
Xss/chord = 1.942 Yss/chord = .147
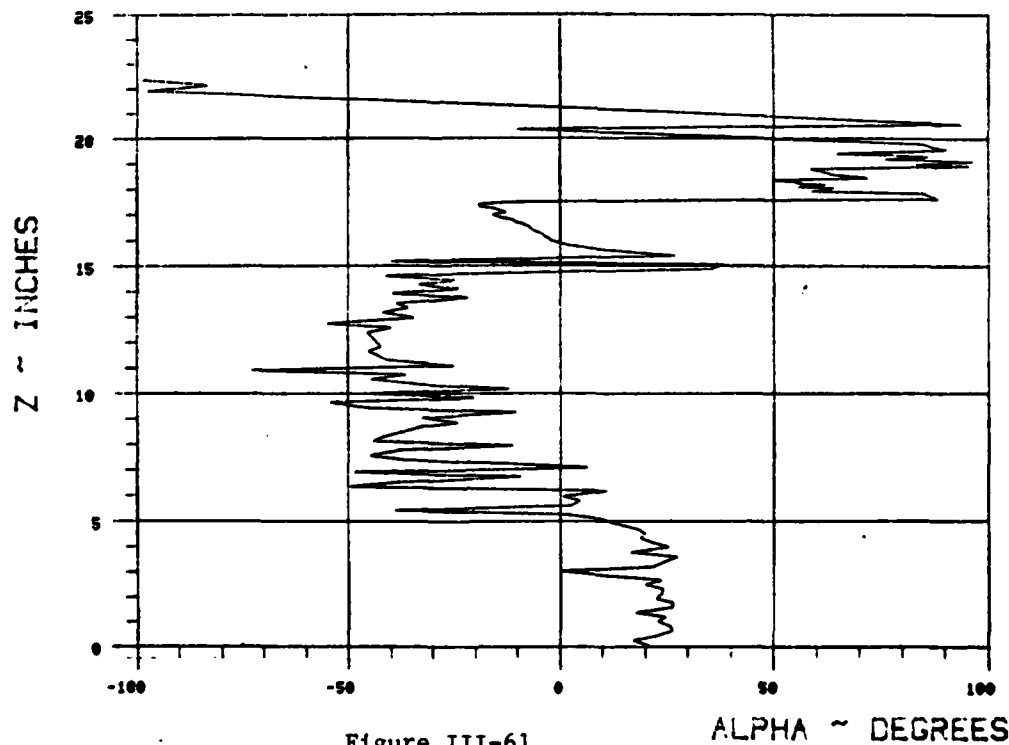
BETA = 70

Figure III-61.

WAKE SURVEY DATA
TEST 287 RUN 19

ANGLE OF ATTACK _0_ NOMINAL JET ANGLE _90_ C MU _7.7259_
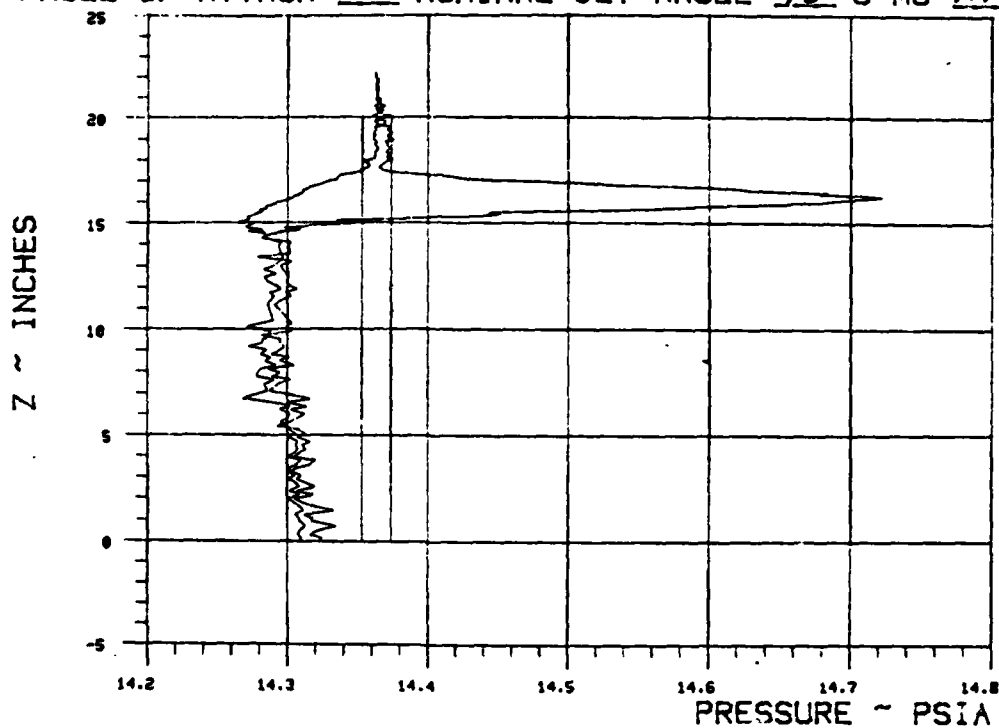
Xss/chord = _2.028_   Yss/chord = _-.088_

BETA = _70_

Figure III-62.

243
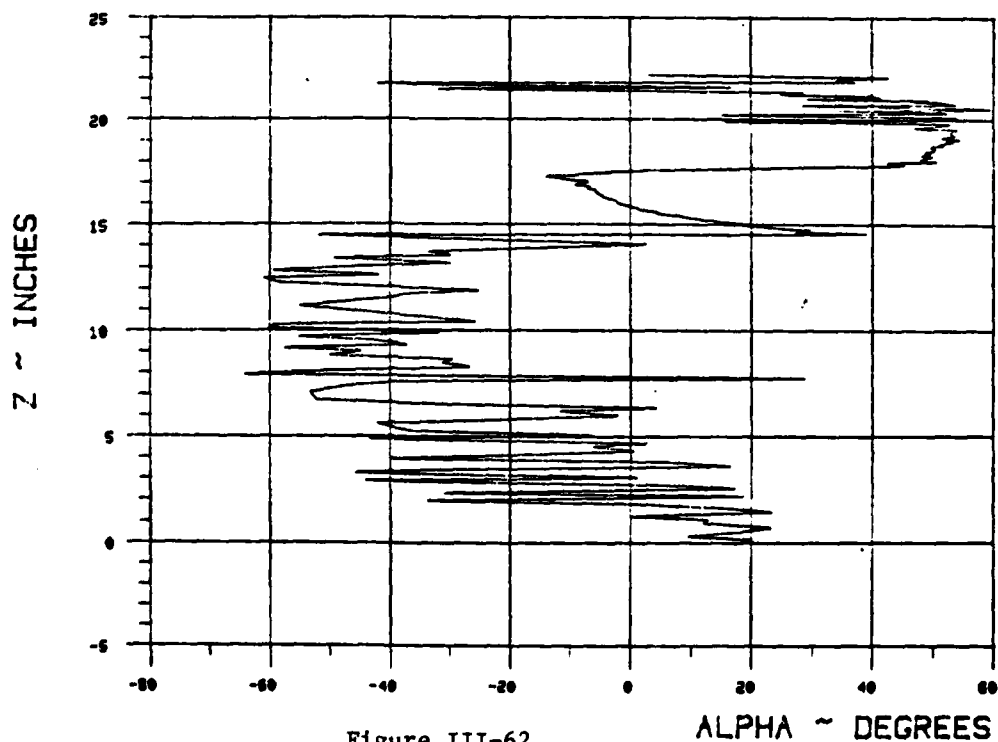
WAKE SURVEY DATA
TEST _287_ RUN _20_
ANGLE OF ATTACK _O_ NOMINAL JET ANGLE _90_ C MU _7.6749_

PRESSURE ~ PSIA

Xss/chord = _2.156_ Yss/chord = _-.44_

BETA = _70_

ALPHA ~ DEGREES

Figure III-63.

244
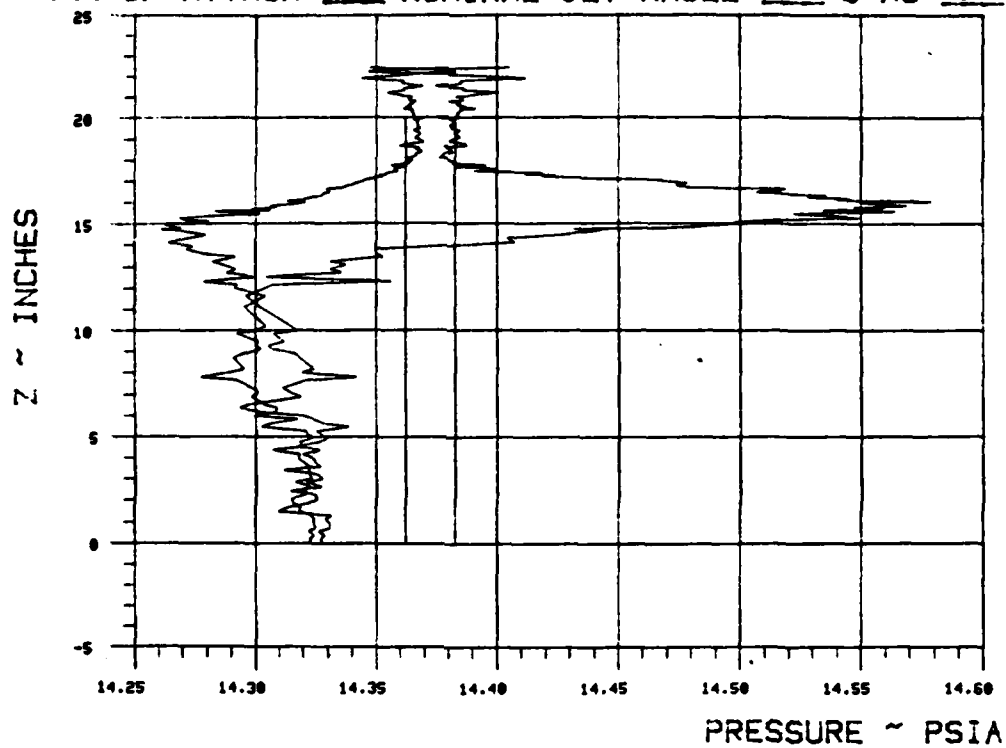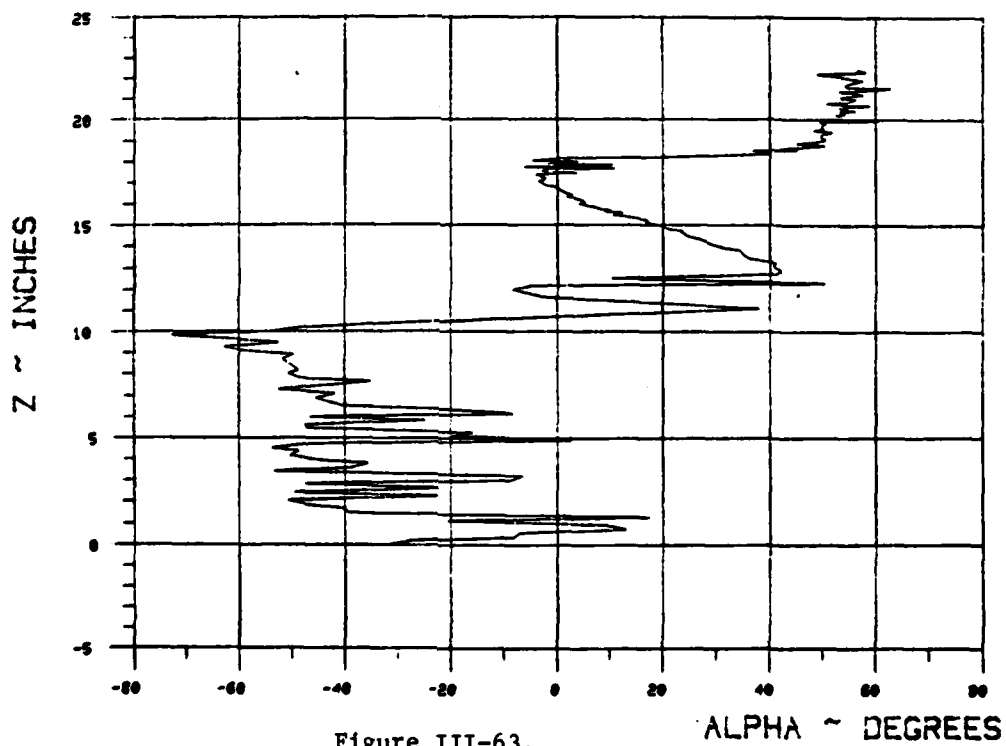
WAKE SURVEY DATA
TEST _287_ RUN _21_
ANGLE OF ATTACK _0_ NOMINAL JET ANGLE _90_ C MU _1.4013_

PRESSURE ~ PSIA
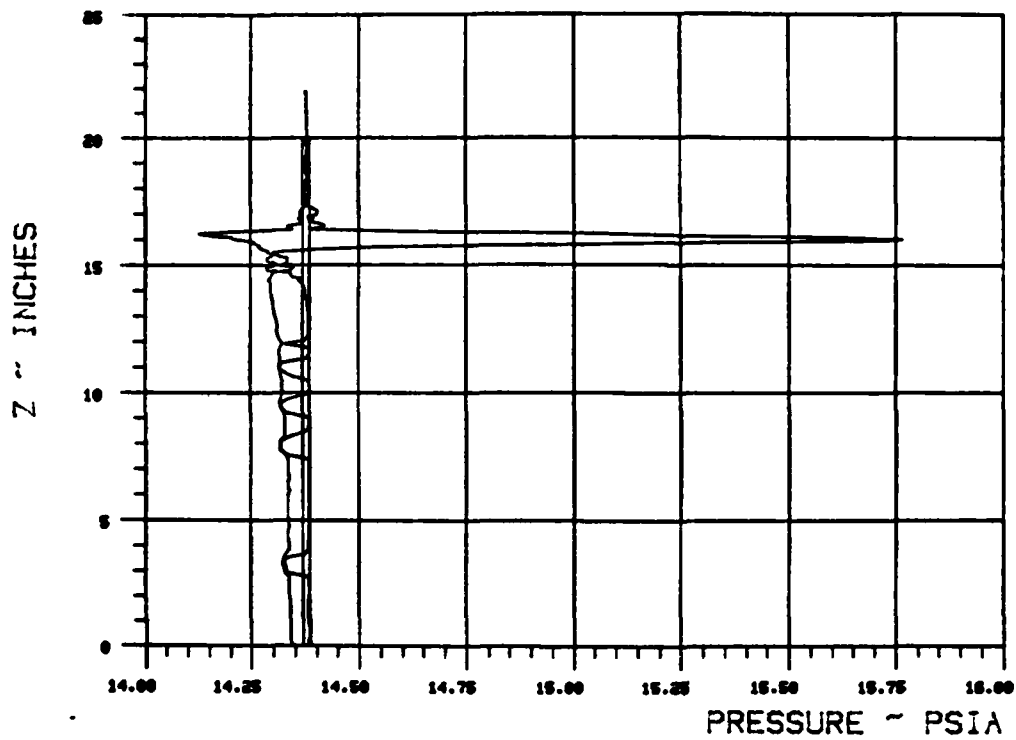
Xee/chord = _1.857_ Yee/chord = _.382_

BETA = _70_

ALPHA ~ DEGREES
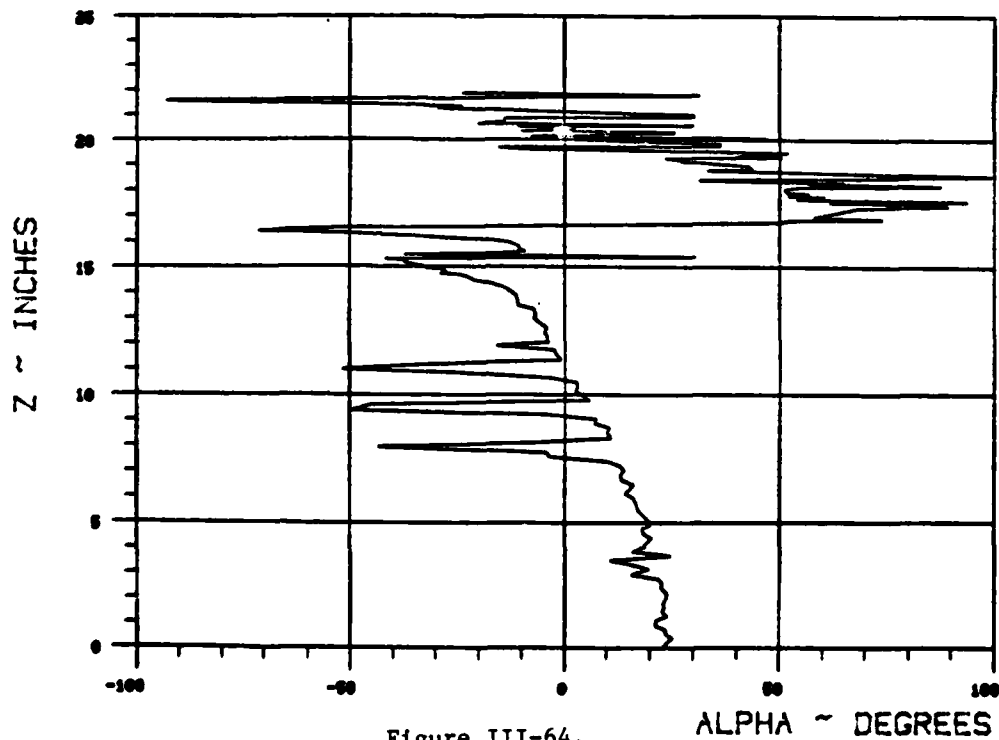
Figure III-64.

WAKE SURVEY DATA

TEST _287_ RUN _22_

ANGLE OF ATTACK _0_ NOMINAL JET ANGLE _90_ C MU _11.4289_

PRESSURE ~ PSIA

Xss/chord = _1.899_   Yss/chord = _.265_

BETA = _70_

ALPHA ~ DEGREES

Figure III-65.

246
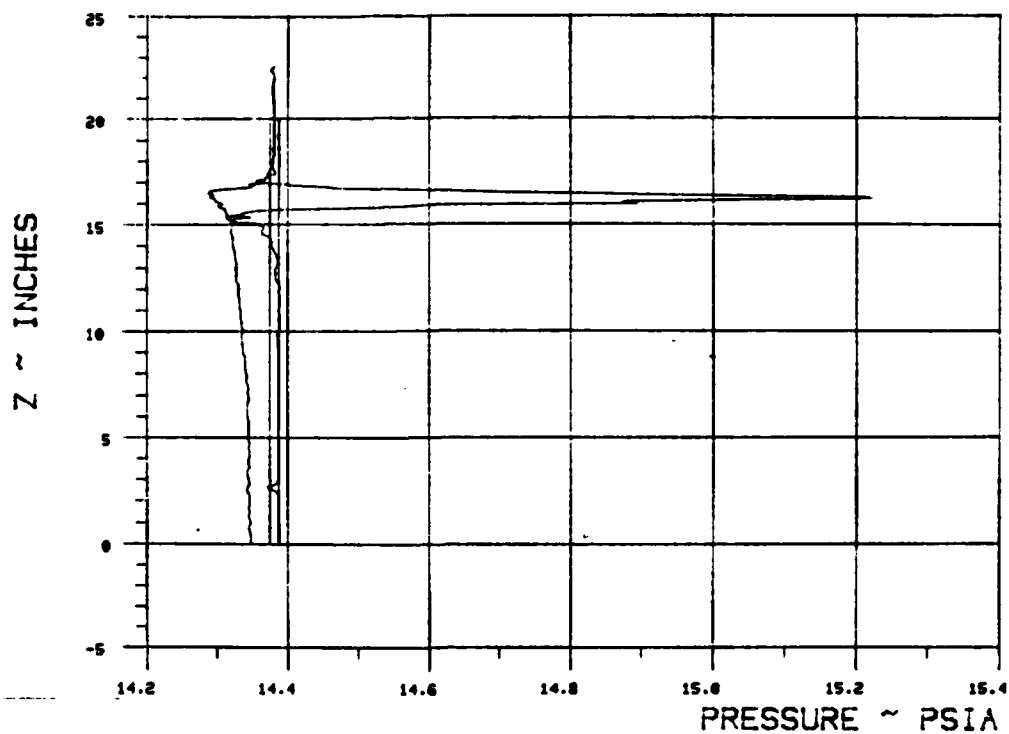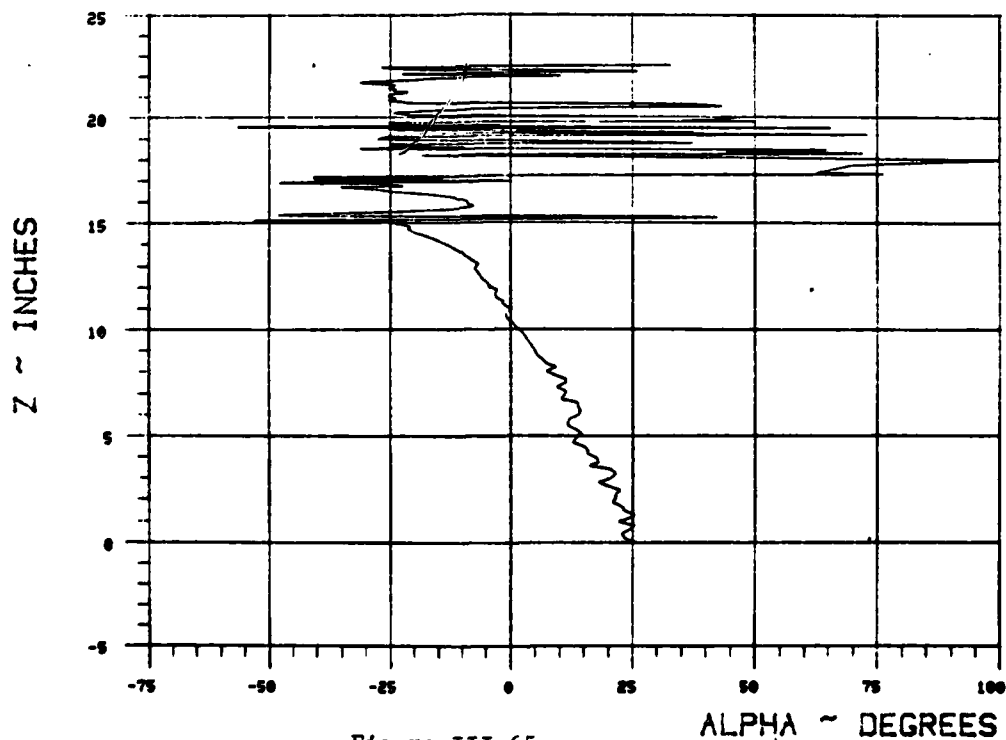
WAKE SURVEY DATA
TEST 287 RUN 23
ANGLE OF ATTACK 6 NOMINAL JET ANGLE 90 C MU 11.2001

PRESSURE ~ PSIA
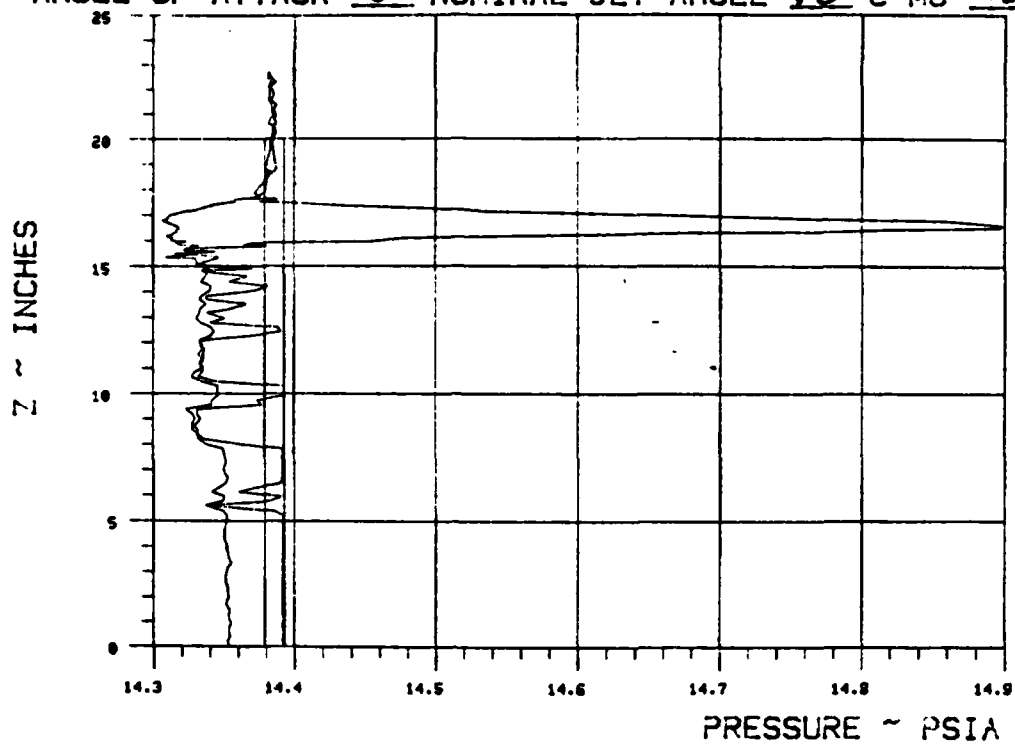
Xss/chord = 1.942 Yss/chord = .147

BETA = 70
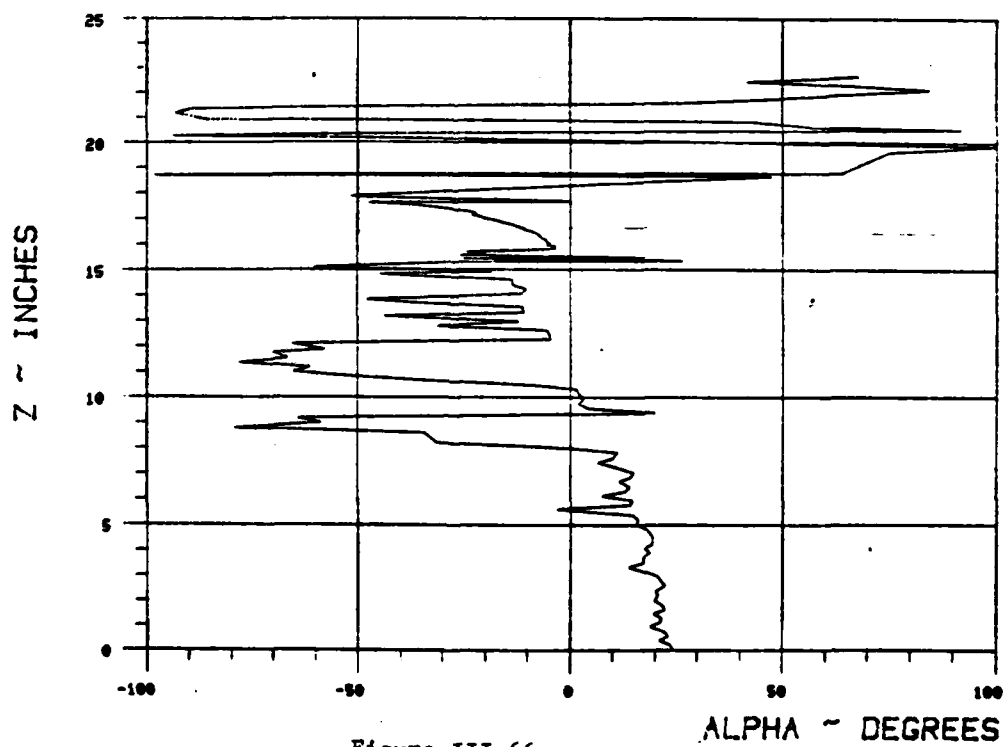
ALPHA ~ DEGREES

Figure III-66.

WAKE SURVEY DATA

TEST _287_ RUN _24_

ANGLE OF ATTACK _0_ NOMINAL JET ANGLE _90_ C MU _11.133_
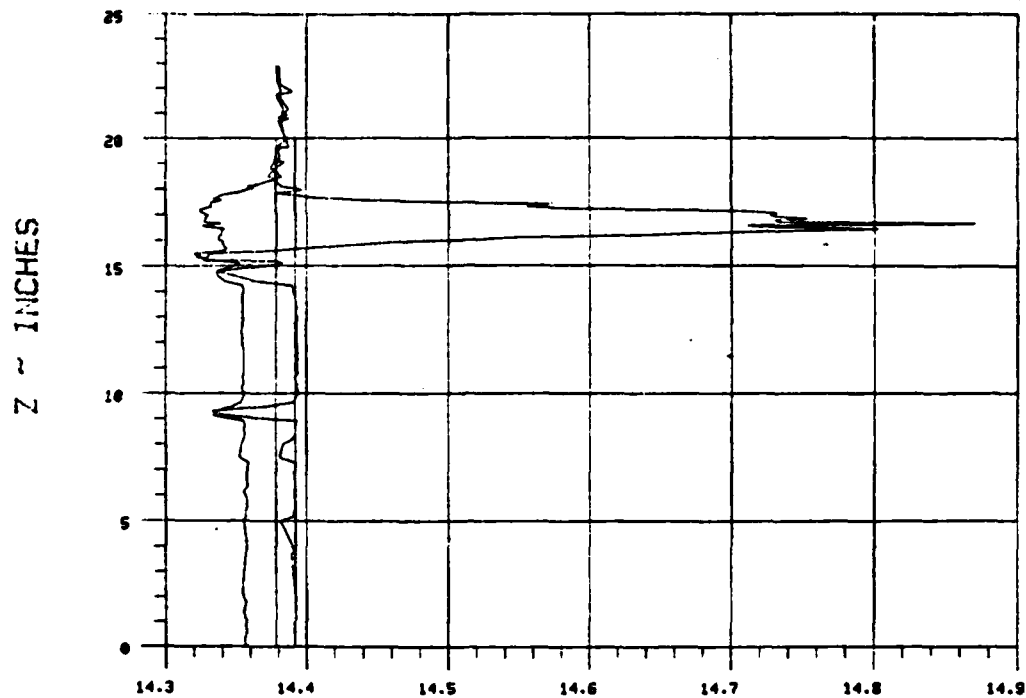
PRESSURE ~ PSIA

Xss/chord = _2.028_ Yss/chord = _-.088_
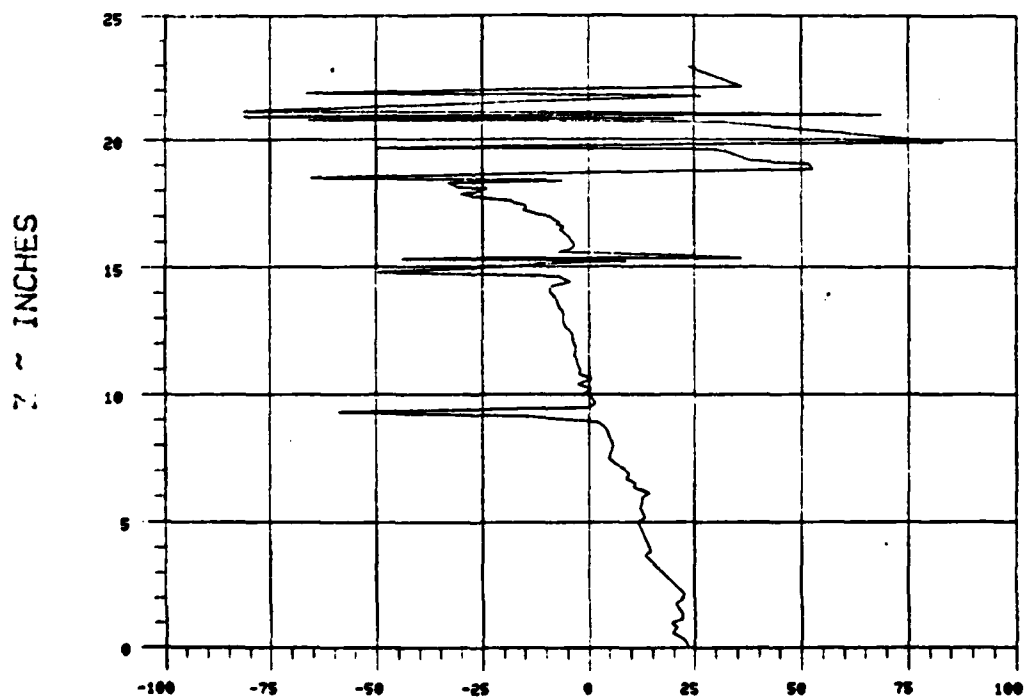
BETA = _70_

Figure III-67.

ALPHA ~ DEGREES

248

WAKE SURVEY DATA

TEST 287 RUN 25

ANGLE OF ATTACK 0 NOMINAL JET ANGLE 90 C MU 11.4093
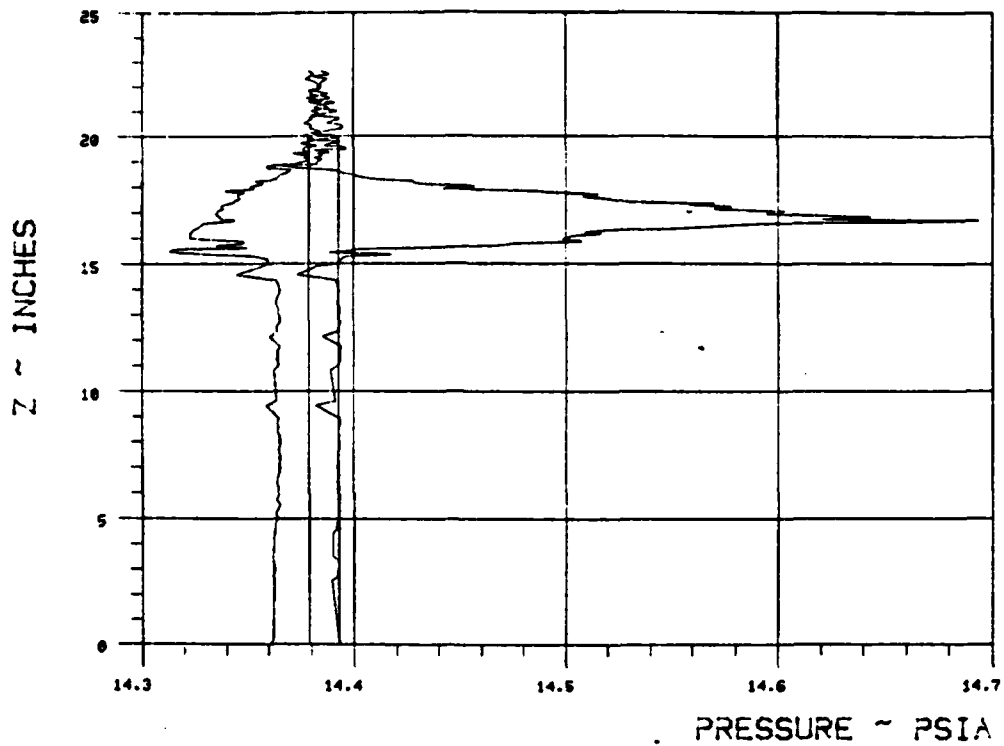
PRESSURE ~ PSIA

Xss/chord = 2.156 Yss/chord = -.44

BETA = 70

ALPHA ~ DEGREES

Figure III-68.

249
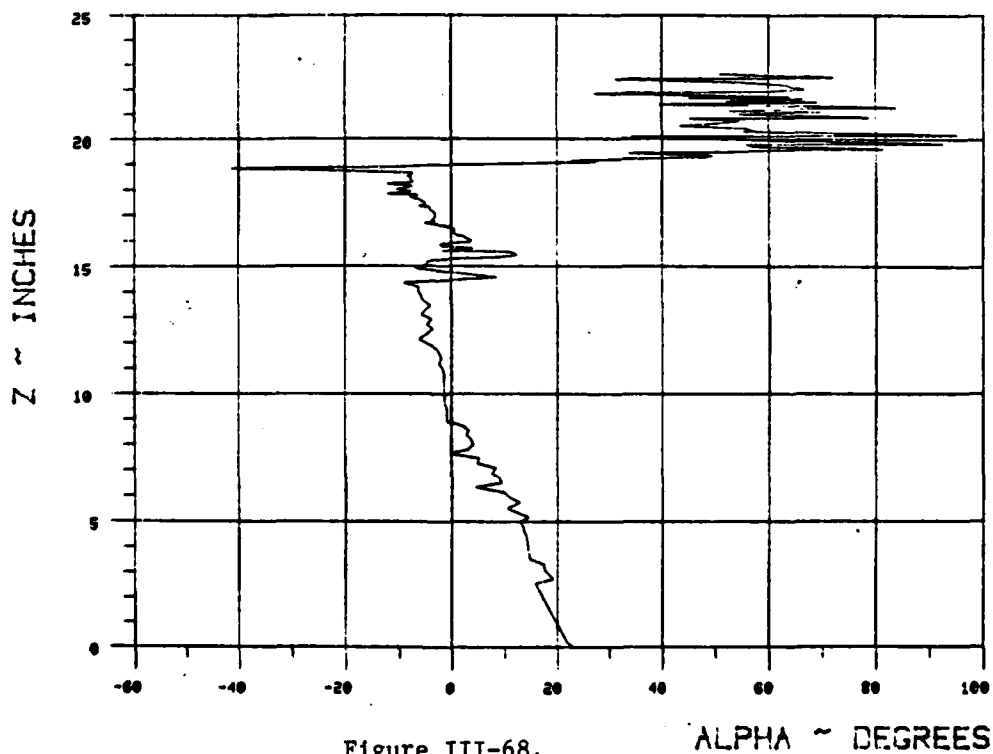
WAKE SURVEY DATA

TEST 287 RUN 26

ANGLE OF ATTACK 0 NOMINAL JET ANGLE 90 C MU 14.3862

PRESSURE ~ PSIA

Xss/chord = 1.857 Yss/chord = .382

BETA = 70
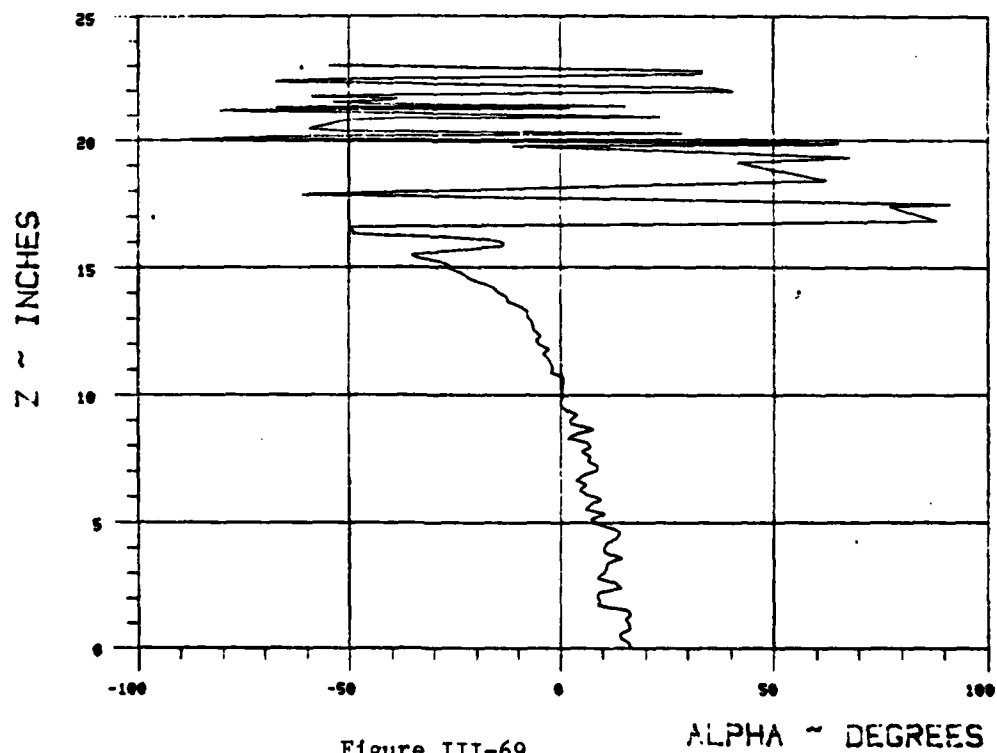
ALPHA ~ DEGREES

Figure III-69.

WAKE SURVEY DATA

TEST _287_ RUN _27_

ANGLE OF ATTACK _0_ NOMINAL JET ANGLE _90_ C MU _14.4717_
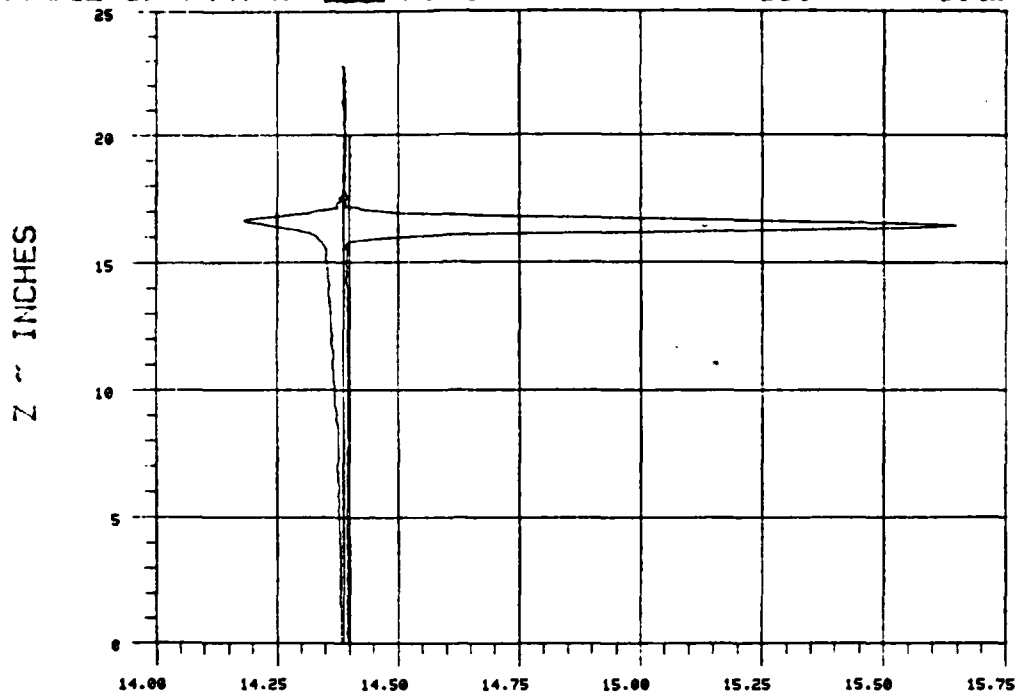
PRESSURE ~ PSIA

Xss/chord = _1.899_   Yss/chord = _.265_
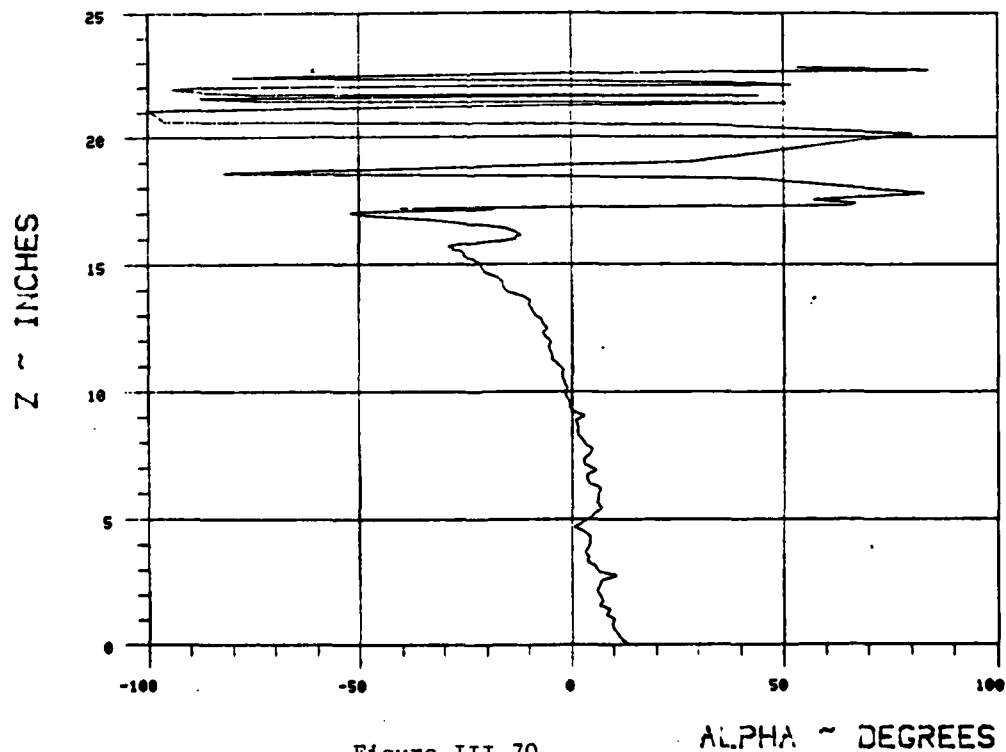
BETA = _70_
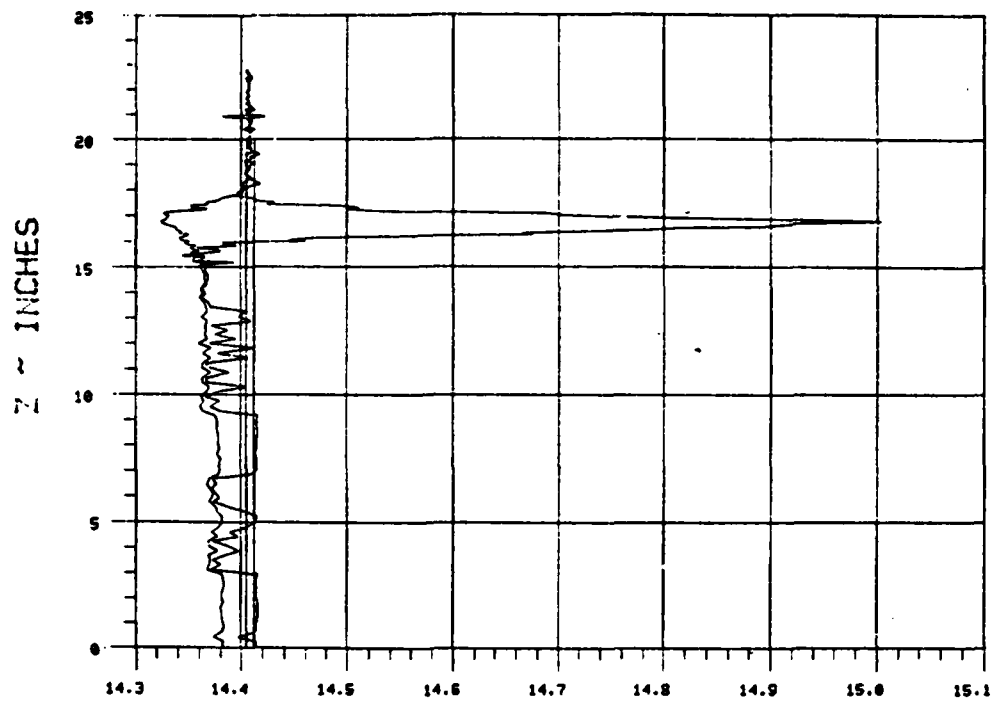

ALPHA ~ DEGREES

Figure III-70.

251

WAKE SURVEY DATA
TEST _287_ RUN _28_

ANGLE OF ATTACK _O_ NOMINAL JET ANGLE _90_ C MU _20.9048_

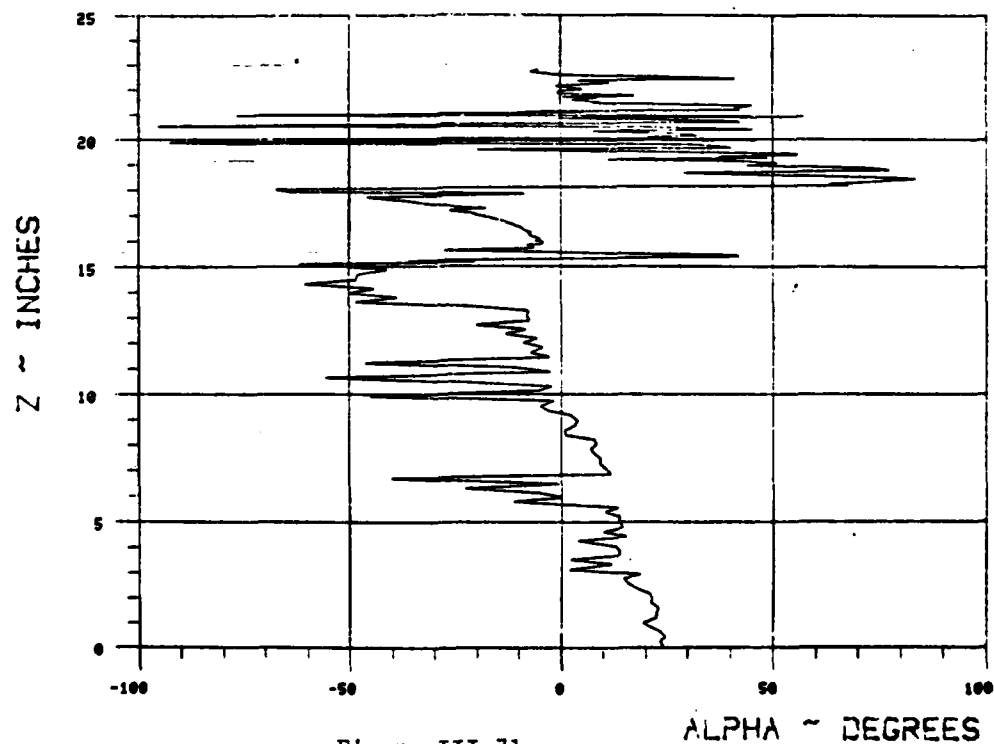PRESSURE ~ PSIA

Xas/chord = _1.942_ Yas/chord = _.147_

BETA = _70_

ALPHA ~ DEGREES

Figure III-71.

252

DATE FILMED
'8